

Electronic Thesis and Dissertation Repository

6-20-2016 12:00 AM


The Corrosion of Carbon Steel under Deep Geologic Nuclear Waste Disposal Conditions

Shannon L.W. Hill
The University of Western Ontario

Supervisor
David W. Shoemith
The University of Western Ontario

Graduate Program in Chemistry
A thesis submitted in partial fulfillment of the requirements for the degree in Doctor of Philosophy
© Shannon L.W. Hill 2016

Follow this and additional works at: <https://ir.lib.uwo.ca/etd>

 Part of the [Analytical Chemistry Commons](#), [Materials Chemistry Commons](#), and the [Physical Chemistry Commons](#)

Recommended Citation

Hill, Shannon L.W., "The Corrosion of Carbon Steel under Deep Geologic Nuclear Waste Disposal Conditions" (2016). *Electronic Thesis and Dissertation Repository*. 3820.
<https://ir.lib.uwo.ca/etd/3820>

This Dissertation/Thesis is brought to you for free and open access by Scholarship@Western. It has been accepted for inclusion in Electronic Thesis and Dissertation Repository by an authorized administrator of Scholarship@Western. For more information, please contact wlsadmin@uwo.ca.

Abstract

The proposed disposal scenario for high-level nuclear waste (spent fuel) in Canada is emplacement within a sealed, deep geological repository (DGR) located in either granitic rock or sedimentary clay. Disposal is based on a multi-barrier approach, with the primary barrier being a sealed container which could be either dual-walled with a copper shell over an inner carbon steel vessel for granitic rock or a single thick-walled steel container for sedimentary clay. This study focuses on the corrosion behaviour of A516 Gr70 carbon steel as well as the corrosion products formed in a variety of groundwater compositions and concentrations expected within a sedimentary clay DGR environment. In particular, the effects of groundwater anions such as Cl^- , $\text{HCO}_3^-/\text{CO}_3^{2-}$, and SO_4^{2-} on the corrosion behaviour and corrosion product compositions and morphologies were studied. Several electrochemical and surface characterization techniques were employed to investigate the corrosion behaviour of the steel as well as the identities and morphologies of the subsequent corrosion products.

It was shown that in the presence of trace levels of O_2 , Cl^- is able to induce passivation of the steel surface by the catalytic conversion of Fe^{2+} to Fe^{3+} with passivation induced in this manner then leading to the initiation of breakdown sites. The addition of $\text{HCO}_3^-/\text{CO}_3^{2-}$ to highly concentrated Cl^- solutions led to a competition between the catalytic formation of Fe^{III} oxides and the stabilization of soluble Fe^{2+} by complexation with $\text{HCO}_3^-/\text{CO}_3^{2-}$. In addition, an increase in the total carbonate concentration increased the breakdown potential by preventing the stabilization of pits by buffering the development of acidity required for propagation. In contrast, SO_4^{2-} was shown not to interfere with the Cl^- -catalyzed oxidation to Fe^{III} oxides in the presence of trace O_2 but to have a significant effect on the breakdown potential, possibly due to its ability to be more strongly adsorbed to the Fe^{III} surface.

Electrochemical experiments performed under totally anaerobic conditions showed that an increase in $[\text{Cl}^-]$ promoted corrosion leading to an increased roughening of the steel surface. This was attributed to an acceleration of the cathodic reaction on exposed Fe_3C bands from the pearlite structure. The addition of groundwater ions led to a suppression of the anodic kinetics due to the accumulation of CaCO_3 crystals. Addition of $\text{HCO}_3^-/\text{CO}_3^{2-}$ to buffer the pH to 8.85 led to a significant decrease in the corrosion rate. This was attributed to the growth of a Fe_3O_4 barrier layer with additional protection provided by an outer layer of $\text{Fe}_2(\text{OH})_2\text{CO}_3$.

Complementary long-term corrosion studies showed that an initial period of humid air exposure led to the formation of a γ -Fe₂O₃ layer which was subsequently reduced to Fe₃O₄ by galvanic coupling to steel dissolution over approximately the first 100 days of exposure. Corrosion occurred preferentially at pearlite grains due to the lower cathodic overpotential on the Fe₃C lamellae. Addition of groundwater ions suppressed steel corrosion due to the rapid deposition of CaSO₄ and CaCO₃ crystals. High levels of Mg²⁺ were shown to promote the formation of aragonite, a polymorph of CaCO₃ known to cause a reduction in steel corrosion rates. Finally, the addition of HCO₃⁻/CO₃²⁻ led to the rapid formation of Fe₂(OH)₂CO₃, attributed to the initial γ -Fe₂O₃ layer whose reduction led to high [Fe²⁺] and the promotion of Fe₂(OH)₂CO₃ deposition. However, thermodynamic transformation of Fe₂(OH)₂CO₃ to FeCO₃ appeared to induce some localized corrosion/pitting processes.

The influence of H₂O₂ on steel corrosion under deaerated and totally anaerobic conditions was studied to determine whether radiolytic oxidants produced by the radiation fields in the fuel waste form would influence corrosion of the inside of a failed waste container. The interaction of the H₂O₂ with the steel was confirmed by the presence of Fe^{III}-containing corrosion products. The results showed that continuous steel corrosion can be expected in an anaerobic environment but that passivation occurred in the deaerated experiment. However, passivation was attributed to the higher levels of dissolved O₂ present and not the addition of H₂O₂ used as a surrogate for radiolytic oxidants. As such, active steel corrosion should be maintained inside a failed container and the soluble corrosion products (Fe²⁺ and H₂) will be available to suppress fuel corrosion and radionuclide release.

Keywords:

Carbon Steel, corrosion, corrosion product, corrosion rate, chloride, carbonate, sulphate, Raman spectroscopy, SEM, electrochemistry

Co-Authorship Statement

For the following chapters I was the primary investigator and writer with the following additional aid:

Chapter 3: Computational modelling was performed by N. Liu with the aid of Z. Qin. D.W. Shoemith assisted with editing.

Chapter 4: D.W. Shoemith assisted with editing.

Chapter 5: Z. Qin assisted with the data analysis of EIS experiments. D.W. Shoemith assisted with editing.

Chapter 6: D. Zagidulin aided in the experimental design and D.W. Shoemith assisted with editing.

Acknowledgements

First and foremost I must thank my supervisor, Dr. David Shoesmith, without whom this thesis would not have been possible. I cannot put into words how grateful I am to have had the opportunity to work with such an amazing supervisor. Thank you for your endless guidance through this process, for providing such a wonderful environment in which to work and learn, and for being the one that had all the patience when I was lacking. I firmly believe that there is no better supervisor, mentor, or role model and I will continue to use the lessons I have learned from you in all aspects of my life yet to come.

I would like to thank the members of the Shoesmith lab, both past and present, for making the lab such an enjoyable place to work and spend the last five years. I will forever value the time I have spent with such amazing people and the lessons I have learned from everyone who has passed through the lab during my time here. Specifically, I would like to thank Dr. Dmitrij Zagidulin for his expertise in experimental set-ups and his help in designing my experiments over the years, Dr. Zack Qin for his guidance in the area of EIS analysis, and to Dr. Jamie Noel for his invaluable lessons in electrochemistry and corrosion science which aided in my further understanding of the topics.

I am sincerely grateful to the amazing people at Surface Science Western who were always available for consultation on matters of surface analysis. Particularly I would like to extend my heartfelt appreciation to Mary Jane Walzak for her guidance and expertise in the area of Raman spectroscopy and FTIR. In addition I would like to thank Dr. Brad Kobe for his assistance in training me with the SEM instrumentation. Finally, I would like to thank Dr. Todd Simpson of the UWO Nanofab for his support with SEM and FIB analyses.

To my wonderful friends, I am grateful for all of our time together which allowed me to just be me. To Sarah, Melanie, and Zara, thanks for managing to help me retain my sanity. To Becky, my thesis writing buddy, here is to the finish line and whatever may come next.

To my parents and my Papa, I cannot thank you enough for your support and guidance throughout my life, never pushing me but allowing me to carve out my own path in this world. Without you I would not be here. Whatever success I may see in life I know it is due to the lessons and values which you have instilled upon me throughout my life. To my sister, Rachael,

thank you for being my little sister and always keeping me on my toes. I wouldn't trade you for the world.

Finally, to Anthony, for believing in me and seeing me through this journey, no matter how hard things got. Here's to the future and whatever it might have in store for us.

This thesis is dedicated to my parents,

Pauline and Jeff Hill

For their unwavering love and support

And to my grandparents,

John and Alice Wright

and

Thelma Hill

“If there ever comes a day when we can’t be together,
keep me in your heart, I’ll stay there forever.”

- Winnie the Pooh

Table of Contents

Abstract	ii
Co-Authorship Statement	iv
Acknowledgements	v
Table of Contents	viii
List of Tables	xiv
List of Figures	xv
List of Symbols and Acronyms	xxxi
Chapter 1: Introduction	1
1.1. Project Background	1
1.2. Aqueous Corrosion	2
1.2.1. Thermodynamics of Corrosion	2
1.2.2. Kinetics of Corrosion	8
1.3. Materials Background	13
1.3.1. Carbon Steel	13
1.3.2. Iron Oxides	17
1.3.2.1. Magnetite (Fe_3O_4)	17
1.3.2.2. Maghemite ($\gamma\text{-Fe}_2\text{O}_3$)	17
1.3.2.3. Akaganeite ($\beta\text{-FeOOH}$)	18
1.3.2.4. Lepidocrocite ($\gamma\text{-FeOOH}$)	19
1.3.2.5. Green Rusts	19
1.3.2.6. Ferrihydrite ($\text{Fe}_5\text{O}_7(\text{OH})\cdot 4\text{H}_2\text{O}$)	19
1.3.2.7. Chukanovite ($\text{Fe}_2(\text{OH})_2\text{CO}_3$)	20
1.4. Corrosion of Carbon Steel in Aqueous Systems	20
1.4.1. Corrosion under Disposal Conditions	20
1.4.1.1. Evolution of the Waste Vault	20
1.4.1.2. Steel Corrosion under Nuclear Waste Disposal Conditions	23
1.4.2. The Role of Dissolved O_2	25
1.4.3. The Role of Groundwater Anions	26
1.4.3.1. The Effects of Chloride	26
1.4.3.2. The Effects of Bicarbonate/Carbonate	27

1.4.3.3.	The Effects of Sulphate	29
1.5.	Thesis Objectives.....	29
1.6.	Thesis Summary	30
1.7.	References	31
Chapter 2:	Experimental Techniques and Details	37
2.1.	Experimental Design	37
2.1.1.	Electrochemical Cell and Equipment	37
2.1.2.	A516 Gr70 Carbon Steel Working Electrode.....	37
2.1.3.	Solution Preparation	38
2.1.4.	Anaerobic Exposure Experiments	38
2.2.	Electrochemical Techniques	39
2.2.1.	Corrosion Potential (E_{CORR})	39
2.2.2.	Linear Polarization Resistance (LPR) Measurements.....	41
2.2.2.1.	Basic Principles of LPR.....	41
2.2.2.2.	LPR Experimental Details	43
2.2.3.	Cyclic Voltammetry	43
2.2.3.1.	Basic Principles of Cyclic Voltammetry	43
2.2.3.2.	Cyclic Voltammetry Experimental Details.....	45
2.2.4.	Electrochemical Impedance Spectroscopy (EIS)	45
2.2.4.1.	Basic Principles of EIS.....	45
2.2.4.2.	EIS Experimental Details	46
2.3.	Surface Analytical Techniques	48
2.3.1.	Scanning Electron Microscopy (SEM)	48
2.3.1.1.	Basic Principles of SEM	48
2.3.1.2.	SEM Experimental Details.....	50
2.3.2.	Energy Dispersive X-Ray (EDX) Spectroscopy	51
2.3.2.1.	Basic Principles of EDX	51
2.3.2.2.	EDX Experimental Details.....	52
2.3.3.	Focused Ion Beam (FIB) Milling.....	52
2.3.3.1.	Basic Principles of FIB.....	52
2.3.3.2.	FIB Experimental Details	54
2.3.4.	Vibrational Spectroscopies	54

2.3.4.1.	Basic Principles of Raman Spectroscopy	54
2.3.4.2.	Basic Principles of Fourier Transform Infrared (FTIR) Spectroscopy	57
2.3.4.3.	Raman vs. IR Spectroscopy	59
2.3.4.4.	Raman Experimental Details	59
2.3.4.5.	FTIR Experimental Details	60
2.4.	References	60
Chapter 3: Interactions between Carbon Steel and UO₂ Corrosion Fronts inside a Failed Nuclear Waste Container		61
3.1.	Introduction	61
3.2.	Experimental Details	62
3.2.1.	Materials and Electrode Preparations	62
3.2.2.	Electrochemical Cell and Equipment	63
3.2.3.	Experimental Solutions	63
3.2.4.	Experimental Procedure	63
3.2.5.	Surface Analysis	64
3.2.6.	Computational Modelling	64
3.3.	Results and Discussion	64
3.3.1.	Electrochemical Analysis	64
3.3.2.	Surface Analysis of Steel in the Deaerated Solution	68
3.3.3.	Surface Analysis of Steel in the Anaerobic Solution	71
3.3.4.	Computational Modelling	73
3.4.	Conclusions	75
3.5.	References	76
Chapter 4: The Effects of Groundwater Anions on the Corrosion of A516 Gr70 Carbon Steel ..		79
4.1.	Introduction	79
4.2.	Experimental Details	80
4.2.1.	Materials and Electrode Preparations	80
4.2.2.	Electrochemical Cell and Equipment	80
4.2.3.	Experimental Procedure	81
4.2.4.	Experimental Solutions	81
4.2.5.	Surface Analysis	81
4.3.	Results	82

4.3.1.	Effects of Chloride.....	82
4.3.1.1.	E_{CORR} and R_p Measurements	82
4.3.1.2.	Raman Spectroscopy.....	85
4.3.1.3.	Scanning Electron Microscopy on Surfaces and Cross-Sections Prepared by Focused Ion Beam Milling.....	89
4.3.1.4.	Cyclic Voltammetry	94
4.3.2.	Effects of Carbonate	95
4.3.2.1.	E_{CORR} and R_p Measurements	95
4.3.2.2.	Raman and Infrared Spectroscopies	99
4.3.2.3.	Scanning Electron Microscopy	104
4.3.2.4.	Cyclic Voltammetry	106
4.3.3.	Effects of Sulphate	108
4.3.3.1.	E_{CORR} and R_p Measurements	108
4.3.3.2.	Raman Spectroscopy.....	108
4.3.3.3.	Scanning Electron Microscopy	114
4.3.3.4.	Cyclic Voltammetry	115
4.4.	Discussion.....	117
4.4.1.	Effects of Chloride.....	117
4.4.2.	Effects of Carbonate	120
4.4.3.	Effects of Sulphate	123
4.5.	Summary and Conclusions.....	124
4.6.	References	125
Chapter 5: The Electrochemical Behaviour of A516 Gr70 Carbon Steel Exposed to Anoxic Simulated Groundwater Environments.....		131
5.1.	Introduction	131
5.2.	Experimental Details	132
5.2.1.	Materials and Electrode Preparations	132
5.2.2.	Electrochemical Cell and Equipment	132
5.2.3.	Experimental Procedure	133
5.2.4.	Experimental Solutions	133
5.2.5.	Surface Analysis	134
5.3.	Results.....	134

5.3.1.	E_{CORR} and R_p Measurements	134
5.3.2.	Electrochemical Impedance Spectroscopy	138
5.3.3.	Surface Analyses	144
5.4.	Discussion.....	153
5.5.	Summary and Conclusions.....	157
5.6.	References	158
Chapter 6: Long Term Analysis of the Corrosion Product Identities and Morphologies Formed on A516 Gr70 Carbon Steel Exposed to Anoxic Simulated Groundwater Environments		
6.1.	Introduction	161
6.2.	Experimental Details	161
6.2.1.	Materials and Electrode Preparations	161
6.2.2.	Experimental Setup.....	161
6.2.3.	Experimental Solutions	163
6.2.4.	Surface Analysis	164
6.3.	Results.....	165
6.3.1.	Solution (i): Low Chloride Concentration.....	165
6.3.1.1.	Raman Spectroscopy.....	165
6.3.1.2.	Scanning Electron Microscopy	171
6.3.1.3.	Focused Ion Beam Milling.....	179
6.3.2.	Solution (ii): High Chloride Concentration	183
6.3.2.1.	Raman Spectroscopy.....	183
6.3.2.2.	Scanning Electron Microscopy	188
6.3.2.3.	Focused Ion Beam Milling	195
6.3.3.	Solution (iii): Buffered, High Chloride Concentration	199
6.3.3.1.	Raman and Infrared Spectroscopies	199
6.3.3.2.	Scanning Electron Microscopy	204
6.3.3.3.	Focused Ion Beam Milling.....	211
6.3.4.	Solution (iv): Simulated Groundwater Solution	215
6.3.4.1.	Raman Spectroscopy.....	215
6.3.4.2.	Scanning Electron Microscopy	219
6.3.4.3.	Focused Ion Beam Milling.....	226
6.4.	Discussion.....	228

6.5.	Summary and Conclusions	233
6.6.	References	234
Chapter 7: Conclusions and Future Research		239
Appendix A: Supporting Raman Spectra and SEM Images for the Long-Term Evolution of Carbon Steel Corrosion under Anoxic Simulated Groundwater Environments		245
A.1.	Reference Raman spectra	245
A.2.	Solution (i): Low Chloride Concentration.....	247
A.2.1.	Raman Spectroscopy.....	247
A.2.2.	Scanning Electron Microscopy	255
A.3.	Solution (ii): High Chloride Concentration	262
A.3.1.	Raman Spectroscopy.....	262
A.3.2.	Scanning Electron Microscopy	271
A.4.	Solution (iii): Buffered, High Chloride Concentration	279
A.4.1.	Raman Spectroscopy.....	279
A.4.2.	Scanning Electron Microscopy	286
A.5.	Solution (iv): Simulated Groundwater Solution	293
A.5.1.	Raman Spectroscopy.....	293
A.5.2.	Scanning Electron Microscopy	298

List of Tables

Table 4-1: Summary of corrosion products identified by Raman spectroscopy in the range of chloride environments investigated	89
Table 4-2: Summary of corrosion products identified by Raman spectroscopy for $\text{HCO}_3^-/\text{CO}_3^{2-}$ containing exposure environments.	103
Table 4-3: Summary of corrosion products identified by Raman spectroscopy for SO_4^{2-} containing exposure environments.	112
Table 5-1: Chemical composition of solutions (i-iii) containing Cl^- and $\text{HCO}_3^-/\text{CO}_3^{2-}$	133
Table 5-2: Chemical composition of solution (iv) representing the expected composition of sedimentary clay groundwater in the Canadian Shield.	134
Table 6-1: Removal times for steel coupons exposed to a series of four exposure environments.	163
Table 6-2: Chemical compositions of exposure solutions (i) to (iii).	164
Table 6-3: Chemical composition of solution (iv) made up to simulate sedimentary clay groundwater in the Canadian Shield.	164

List of Figures

Figure 1-1: Proposed design for a Canadian deep geologic repository (DGR) using (a) a dual-walled copper coated container for crystalline host rock; (b) a single-walled carbon steel container for sedimentary host clay [7].....	2
Figure 1-2: Pourbaix diagram for the Fe-H ₂ O system with various Fe ²⁺ activities at 25°C. Solid lines represent the stability ranges for the solid species while the dotted lines show the stability ranges for aqueous species (not considered here) [9].	5
Figure 1-3: Simplified Pourbaix diagram for the Fe-H ₂ O system showing the regions of immunity, corrosion, and passivation (by Fe ₃ O ₄ and Fe ₂ O ₃) at 25°C. Dashed lines (a) and (b) represent the stability regions of H ₂ O [9].	8
Figure 1-4: Potential-current (Butler-Volmer) relationship for the Fe dissolution/deposition reaction. Solid lines indicate the measureable current while the dashed lines show the partial currents for the forward and reverse reactions [10].	10
Figure 1-5: Current-potential relationships for the Fe dissolution and proton reduction reactions (solid black lines). As shown, the anodic reaction has a large i_0 while the cathodic reaction has a small i_0 . The dashed red line shows the current that would be measured for the coupled reaction. As shown, the anodic reaction has a large i_0 compared to the cathodic reaction and hence determines the position of E_{CORR} [10].....	11
Figure 1-6: Current-potential relationships for the anodic dissolution of Fe and the cathodic reduction of protons plotted as an Evan's diagram [10].	12
Figure 1-7: Cooling curve showing the allotropic conversions for pure Fe at atmospheric pressure [14].	14
Figure 1-8: Triple point showing the possible interconversions of Fe allotropes α (BCC), γ (FCC), and ϵ (HCP) [12].	14
Figure 1-9: The iron-carbon phase diagram showing the distinction between steels and cast irons as a function of carbon content [15].	15
Figure 1-10: Illustration of the microstructures of a hypoeutectoid steel (containing less than 0.76 wt% C) as it is cooled from the austenite phase region to below the eutectoid temperature [15].	16
Figure 1-11: Optical images of the A516 Gr70 carbon steel used within this thesis showing grains of α -Fe (white) and pearlite (brown).	16
Figure 1-12: Illustrative representation of the akaganeite tunnel structure. Triangular prisms represent the edge-sharing octahedra while the spheres are the Cl ⁻ ions which stabilize the tunnels [17].	18
Figure 1-13: Evolution of the environmental conditions expected within a DGR as a function of the stage of saturation. Overlaid colours represent the transition over time of the temperature from hot to cool [6].	22
Figure 1-14: Corrosion rates as a function of time illustrating the evolution in the stages of corrosion for a reference time for full saturation of 10,000 years [34].	24
Figure 1-15: Effect of saturation time on the corrosion rate of the steel container [34].	24

Figure 1-16: General reaction scheme for iron corrosion product films formed in oxidizing and reducing conditions [36].	26
Figure 1-17: Pourbaix diagram of iron in carbonate containing aqueous media at 25°C for equilibria involving $\text{Fe}_2(\text{OH})_2\text{CO}_3$ (dotted lines) and FeCO_3 (solid lines) [67].	28
Figure 2-1: (a) Magnified image of carbon steel coupons emplaced in the sample slots of a Teflon holder; (b) image of the Teflon sample holder placed in a modified 2 L beaker.	39
Figure 2-2: Current-potential (Butler-Volmer) relationships for the Fe dissolution/deposition and water reduction/ H_2 oxidation reactions illustrating their coupling at the E_{CORR} .	40
Figure 2-3: Current-potential relationship for a corrosion process demonstrating the linearization for small overpotentials from E_{CORR} used in polarization resistance measurements.	42
Figure 2-4: Potential-time profile used to generate a CV in which the potential is increased from t_0 to the switching potential at t_1 and then back to the initial potential at t_2 .	44
Figure 2-5: Schematic of a typical CV recorded for a reversible electrochemical reaction involving soluble species.	44
Figure 2-6: Illustrative representation of the sinusoidal potential excitation used in EIS and the corresponding sinusoidal current response. The phase shift is given by θ .	46
Figure 2-7: Graphical representation of a typical Nyquist plot.	46
Figure 2-8: Graphical representation of Bode plots of $\log Z $ and θ against the log of the frequency.	47
Figure 2-9: Equivalent circuit representative of a passive metal covered with an oxide film.	47
Figure 2-10: General schematic for an SEM instrumental arrangement [6].	49
Figure 2-11: Excitation volume caused by an incident electron beam showing the regions of signal generation, and the effects of increasing the incident energy (E_0) and atomic number (Z).	50
Figure 2-12: Schematic showing the creation of an electron hole due to an incident electron beam and the subsequent X-Ray photon released due to an outer shell electron filling the inner shell hole.	52
Figure 2-13: General schematic of a dual-beam FIB and SEM arrangement [10].	53
Figure 2-14: Schematic of a Renishaw Raman microscope system [12, 13].	56
Figure 2-15: Energy level diagram showing the electron transitions for Rayleigh scattering and Stokes and Anti-Stokes Raman shifts. E_1 and E_2 represent the first and second discrete energy levels. The ground state is given by $v=0$ and $v=1$, and 2 represent the first and second vibrational excited states within the molecule.	56
Figure 2-16: Comparison of a reference spectrum for magnetite (Fe_3O_4) to an experimentally collected Fe_3O_4 spectrum.	57
Figure 2-17: Example of an experimental FTIR spectrum obtained for a chukanovite ($\text{Fe}_2(\text{OH})_2\text{CO}_3$) corrosion product.	58
Figure 3-1: Interactions of the steel and UO_2 corrosion products and radiolytically produced oxidants within a failed spent nuclear fuel container.	62
Figure 3-2: Corrosion potential (E_{CORR}) under deaerated conditions. Points indicate the R_p values, with the red points showing R_p values recorded after an addition of H_2O_2 .	65

Figure 3-3: Corrosion potential (E_{CORR}) under anaerobic conditions ($[O_2] \sim 0.1$ ppb). Points indicate R_p values, with the red points showing R_p values recorded after the addition of H_2O_2 .	66
Figure 3-4: Metastable transients in E_{CORR} recorded under (a) deaerated and (b) anaerobic corrosion conditions.	66
Figure 3-5: SEM micrographs showing the morphology of the corrosion film and deposits on the steel surface after corrosion under deaerated conditions.	69
Figure 3-6: Raman spectra (a-c) recorded at various locations on the steel after corrosion under deaerated conditions (Figure 3-2).	70
Figure 3-7: SEM micrographs showing the morphology of the corrosion film and deposits on the steel surface after corrosion under anaerobic conditions.	71
Figure 3-8: Raman spectra (a-d) recorded at various locations on the steel after corrosion under anaerobic conditions (Figure 3-3).	73
Figure 3-9: (a) $[H_2O_2]$ profile from the UO_2 surface (0.0 mm) to the surface of the carbon steel (1.0 mm) after 500 s: (b) plot of $[H_2O_2]$ at the carbon steel surface as a function of the period of α -radiolysis at the fuel surface (surface separation, 1 mm). The different coloured points are for a series of simulations using different time intervals in the calculation with slight variations being produced due to the fact the calculated values are for a boundary parameter (a discontinuity in the calculation).	74
Figure 3-10: The influence of the steel corrosion rate on the $[H_2O_2]$ at the steel surface as a function of the period of α -radiolysis at the fuel surface (surface separation, 1 mm).	75
Figure 4-1: Corrosion potentials (E_{CORR}) measured in solutions containing various $[Cl^-]$. Dashed lines represent the thermodynamic boundaries for the oxidation of Fe to Fe_3O_4 and $Fe(OH)_2$ to α - Fe_2O_3 . The latter equilibrium is subsequently designated $Fe^{II} ox/Fe^{III} ox$.	83
Figure 4-2: Polarization resistance (R_p) measurements for solutions containing various $[Cl^-]$ as given in Figure 4-1.	84
Figure 4-3: Corrosion potential (E_{CORR}) and polarization resistance (R_p) measurements recorded in the $[Cl^-]=5.00$ M (#1) solution.	85
Figure 4-4: Ex-situ Raman spectra (1-7) recorded at various locations on the steel surface after exposure to (a) $[Cl^-]=0.01$ M and (b) $[Cl^-]=1.00$ M.	86
Figure 4-5: Ex-situ Raman spectra (1-11) recorded at various locations on the steel surface after exposure to $[Cl^-]=5.00$ M environments.	88
Figure 4-6: SEM micrographs showing the morphology of the corrosion product after exposure to the solution containing $[Cl^-]=0.01$ M.	90
Figure 4-7: SEM micrographs showing the morphology of the corrosion product after exposure to the solution containing $[Cl^-]=1.00$ M.	90
Figure 4-8: FIB cross-sections for the general corrosion film on the steel exposed to $[Cl^-]=1.00$ M.	91
Figure 4-9: FIB cross-sections for corrosion deposits formed on the steel surface exposed to $[Cl^-]=1.00$ M.	91
Figure 4-10: SEM micrographs showing the morphology of the corrosion product after exposure to the $[Cl^-]=5.00$ M (#1) solution.	92

Figure 4-11: FIB cross-sections through corrosion deposit accumulations on the steel exposed to $[\text{Cl}^-]=5.00 \text{ M}$ (#1).	93
Figure 4-12: SEM micrographs showing the corrosion product morphology after exposure to $[\text{Cl}^-]=5.00 \text{ M}$ (#2).	93
Figure 4-13: SEM micrographs showing the corrosion product morphology after exposure to $[\text{Cl}^-]=5.00 \text{ M}$ (#3).	93
Figure 4-14: Cyclic voltammograms recorded to increasing anodic limits on steel coupons exposed to (a) $[\text{Cl}^-]=0.01 \text{ M}$; (b) $[\text{Cl}^-]=0.01 \text{ M}$ & $[\text{ClO}_4^-]=0.10 \text{ M}$; (c) $[\text{Cl}^-]=1.00 \text{ M}$; and (d) $[\text{Cl}^-]=5.00 \text{ M}$. Dashed vertical lines represent the range of E_{CORR} measured during the corrosion experiments.	94
Figure 4-15: Corrosion potentials (E_{CORR}) for solutions in $[\text{Cl}^-]=5.00 \text{ M}$ containing $\text{HCO}_3^-/\text{CO}_3^{2-}$ at concentrations of 0.001 M and 0.01 M. Dashed horizontal lines represent the thermodynamic boundaries for the oxidation of Fe to Fe_3O_4 and $\text{Fe}(\text{OH})_2$ to $\alpha\text{-Fe}_2\text{O}_3$	96
Figure 4-16: Polarization resistance (R_p) measurements for solutions containing $[\text{Cl}^-]=5.00 \text{ M}$ and $\text{HCO}_3^-/\text{CO}_3^{2-}$ at concentrations of 0.001 M and 0.01 M as given in Figure 4-15.	97
Figure 4-17: Corrosion potential (E_{CORR}) (solid line) and polarization resistance (R_p) (points) values recorded in $[\text{Cl}^-]=5.00 \text{ M}$ and $[\text{HCO}_3^-/\text{CO}_3^{2-}]=0.10 \text{ M}$ (#1). The dashed vertical lines indicate points at which the Ar sparging system needed to be replaced due to precipitate build-up.	98
Figure 4-18: Corrosion potential (E_{CORR}) (solid line) and polarization resistance (R_p) (points) values recorded in $[\text{Cl}^-]=5.00 \text{ M}$ and $[\text{HCO}_3^-/\text{CO}_3^{2-}]=0.10 \text{ M}$ (#2). The dashed vertical lines indicate points at which the Ar sparging system needed to be replaced due to precipitate build-up.	99
Figure 4-19: Ex-situ Raman spectra (1-12) recorded at various locations on the steel surface after exposure to 5.0 M Cl^- solutions containing (a) $[\text{HCO}_3^-/\text{CO}_3^{2-}]=0.001 \text{ M}$; and (b-c) $[\text{HCO}_3^-/\text{CO}_3^{2-}]=0.01 \text{ M}$	100
Figure 4-20: Ex-situ Raman spectra (1-7) recorded at various locations on the steel surface after exposure to 5.0 M Cl^- solutions containing $[\text{HCO}_3^-/\text{CO}_3^{2-}]=0.10 \text{ M}$	102
Figure 4-21: Ex-situ FTIR spectra recorded at two locations on the steel surface after exposure to a 5.0 M Cl^- solution with $[\text{HCO}_3^-/\text{CO}_3^{2-}]=0.10 \text{ M}$ (#1).	103
Figure 4-22: SEM micrographs showing the corrosion product morphology after exposure to a 5.0 M Cl^- solution containing $[\text{HCO}_3^-/\text{CO}_3^{2-}]=0.001 \text{ M}$	104
Figure 4-23: SEM micrographs showing the corrosion product morphology after exposure to a 5.0 M Cl^- solution containing $[\text{HCO}_3^-/\text{CO}_3^{2-}]=0.01 \text{ M}$ (#1).	105
Figure 4-24: SEM micrographs showing the corrosion product morphology after exposure to a 5.0 M Cl^- solution containing $[\text{HCO}_3^-/\text{CO}_3^{2-}]=0.10 \text{ M}$ (#1).	105
Figure 4-25: (a) Cyclic voltammograms starting at a potential of -1.1 V recorded on steel in a $[\text{Cl}^-]=5.00 \text{ M}$ solution containing either 0.01 M or 0.20 M $\text{HCO}_3^-/\text{CO}_3^{2-}$; (b) anodic currents at -0.7 V as a function of $[\text{HCO}_3^-/\text{CO}_3^{2-}]$; (c) anodic polarization scans starting at a potential of -1.1 V recorded up to the onset of film breakdown in a $[\text{Cl}^-]=5.00 \text{ M}$ solution containing increasing $[\text{HCO}_3^-/\text{CO}_3^{2-}]$; (d) breakdown potentials as a function of $[\text{HCO}_3^-/\text{CO}_3^{2-}]$	107
Figure 4-26: Corrosion potentials (E_{CORR}) for solutions containing 5.00 M Cl^- and various concentrations of SO_4^{2-} . The dashed horizontal line represents the thermodynamic boundary for the transformation of $\text{Fe}(\text{OH})_2$ to $\alpha\text{-Fe}_2\text{O}_3$	109

Figure 4-27: Polarization resistance (R_p) measurements for solutions containing 5.00 M Cl^- and various concentrations of SO_4^{2-} as given in Figure 4-26.	110
Figure 4-28: Ex-situ Raman spectra (1-7) recorded at various locations on the steel surface after exposure to 5.0 M Cl^- solutions with (a) $[\text{SO}_4^{2-}] = 0.001 \text{ M}$; (b) $[\text{SO}_4^{2-}] = 0.01 \text{ M}$	111
Figure 4-29: Raman optical image recorded on the steel surface exposed to a 5.0 M Cl^- solution containing $[\text{SO}_4^{2-}] = 0.10 \text{ M}$ (#1). Crosshairs indicate location of Raman spectra collection.	112
Figure 4-30: Ex-situ Raman spectra (1-4) recorded at various locations on the steel surface after exposure to 5.0 M Cl^- solutions containing $[\text{SO}_4^{2-}] = 0.10 \text{ M}$	113
Figure 4-31: Raman optical image recorded on the steel surface exposed to a 5.0 M Cl^- solution containing $[\text{SO}_4^{2-}] = 0.50 \text{ M}$ (#1). Crosshairs indicate location of Raman spectra collection.	113
Figure 4-32: Ex-situ Raman spectra (1-9) recorded at various locations on the steel surface after exposure to 5.0 M Cl^- solutions containing $[\text{SO}_4^{2-}] = 0.50 \text{ M}$	114
Figure 4-33: SEM micrographs showing the corrosion product morphology after exposure to a 5.0 M Cl^- solution containing $[\text{SO}_4^{2-}] = 0.01 \text{ M}$	115
Figure 4-34: (a) cyclic voltammograms recorded for steel exposed to a $[\text{Cl}^-] = 5.00 \text{ M}$ solution containing 0.01 M or 0.20 M SO_4^{2-} ; (b) anodic dissolution currents measured at -0.7 V as a function of anion concentration; (c) anodic polarization scans recorded up to the onset of film breakdown in a $[\text{Cl}^-] = 5.00 \text{ M}$ solution containing increasing $[\text{SO}_4^{2-}]$; (d) breakdown potentials as a function of $[\text{SO}_4^{2-}]$ and $[\text{HCO}_3^-/\text{CO}_3^{2-}]$	116
Figure 4-35: Pourbaix diagram of iron in carbonate containing aqueous media at 25°C for equilibria involving $\text{Fe}_2(\text{OH})_2\text{CO}_3$ (dotted lines) and FeCO_3 (solid lines) [89].	123
Figure 5-1: Corrosion potential (E_{CORR}) measurements recorded on steel exposed to solutions (i) to (iv) (Table 5-1 and Table 5-2).	135
Figure 5-2: Polarization resistance (R_p) measurements recorded on steel exposed to solutions (i) to (iv) (Table 5-1 and Table 5-2).	136
Figure 5-3: Corrosion potential (E_{CORR}) (solid line) and polarization resistance (R_p) (points) measurements for steel exposed to solution (iii) (Table 5-1) over a period of 5-35 days showing simultaneous fluctuations in the values of both E_{CORR} and R_p	138
Figure 5-4: EIS data for steel exposed to solution (i) (Table 5-1) showing (a) and (b) Bode plots; (c) Nyquist plots; (d) the first three Nyquist plots on a larger scale; (e) the low frequency plot for the spectra taken after 3 days (black); (f) a comparison of R_p (from LPR) and $(R_p)_{\text{EIS}}$ (from fitted EIS plots) and the capacitance (C) (from the fitted EIS plots). Inset legends show the exposure time, in days, at the time of the EIS measurement.	140
Figure 5-5: One time-constant equivalent circuit used to fit impedance spectra for solutions (i) to (iv) consisting of a constant phase element representative of the film capacitance (CPE), a polarization resistance $(R_p)_{\text{EIS}}$, and the solution resistance (R_s).	141
Figure 5-6: EIS data for steel exposed to solution (ii) (Table 5-1) showing (a) and (b) Bode plots; (c) Nyquist plots; (d) a comparison of R_p (from LPR) and $(R_p)_{\text{EIS}}$ (from fitted EIS plots) and the capacitance (C) (from the fitted EIS plots). Inset legends show the exposure time, in days, at the time of the EIS measurement.	141
Figure 5-7: EIS data for steel exposed to solution (iii) (Table 5-1) showing (a) and (b) Bode plots; (c) Nyquist plots; (d) a comparison of R_p (from LPR) and $(R_p)_{\text{EIS}}$ (from fitted EIS plots) and the	

capacitance (C) (from the fitted EIS plots). Inset legends show the exposure time, in days, at the time of the EIS measurement.	142
Figure 5-8: EIS data for steel exposed to solution (iv) (Table 5-2) showing (a) and (b) Bode plots; (c) Nyquist plots; (d) a comparison of R_p (from LPR) and $(R_p)_{EIS}$ (from fitted EIS plots) and the capacitance (C) (from the fitted EIS plots). Inset legends show the exposure time, in days, at the time of the EIS measurement.	143
Figure 5-9: SEM micrographs of the corrosion product formed after 60 days of exposure to solution (i) (Table 5-1) for (a-c) the general steel surface; (d-f) patches of crystalline $Fe_2(OH)_2CO_3$; and (g-i) additional locations showing distribution (g) and the morphology ((h) and (i)) of the crystalline patches.	145
Figure 5-10: Ex-situ Raman spectra recorded on the steel coupon after 60 days of exposure to solution (i) (Table 5-1).....	146
Figure 5-11: Ex-situ FTIR spectra recorded on three locations of the steel after 60 days of exposure to solution (i) (Table 5-1).....	146
Figure 5-12: Ex-situ Raman spectra (1-3) recorded at various locations on the steel coupon after 47 days of exposure to solution (ii) (Table 5-1).	147
Figure 5-13: SEM micrographs recorded on three locations on the surface after 47 days of exposure to solution (ii) (Table 5-1).....	148
Figure 5-14: SEM micrographs recorded on the steel surface after 57 days of exposure to solution (iii) (Table 5-1) showing: (a-c) a large patch of $Fe_2(OH)_2CO_3$; (d-f) the uneven distribution of $Fe_2(OH)_2CO_3$ on the steel surface; (g-h) a location covered by small multi-faceted cubic crystals.	149
Figure 5-15: Ex-situ Raman spectra recorded on the steel coupon after 57 days of exposure to solution (iii) (Table 5-1).....	150
Figure 5-16: Ex-situ FTIR spectra recorded on the steel coupon after 57 days exposure to solution (iii) (Table 5-1).....	150
Figure 5-17: SEM micrographs recorded on the steel surface after 60 days of exposure to solution (iv) (Table 5-2) showing: (a-f) two regions on the sample surface with different coverages by deposits but exhibiting the same underlying morphology; (g) a region covered by a more dense crystal layer with the morphology of the disc-shaped and spherical star-shaped crystals shown in (h) and (i).	151
Figure 5-18: Raman spectra (1-5) recorded at various locations on the steel coupon after 60 days of exposure to solution (iv) (Table 5-2). Dotted spectrum represents the reference spectrum of Fe_3O_4	152
Figure 6-1: Schematic showing the top and bottom views of the Teflon sample holder used to support 16 steel coupons in each of 4 exposure solutions.	162
Figure 6-2: Steel coupons emplaced on a Teflon holder which was subsequently placed in a modified 2 L beaker. The coupons shown had not been polished and are shown to demonstrate the experimental set-up.	163
Figure 6-3: Sample Raman spectrum highlighting the three regions in which characteristic features aiding in the identification of corrosion products can be found.....	166

Figure 6-4: (a) Raman spectra (1-6) recorded at various locations on a steel specimen after 4 days of exposure to solution (i); (b) deconvolution of the spectrum closest to the sample average.....	168
Figure 6-5: (a) Raman spectra (1-7) recorded at various locations on a steel specimen after 14 days of exposure to solution (i); (b) deconvolution of the spectrum closest to the sample average.....	168
Figure 6-6: (a) Raman spectra (1-5) recorded at various locations on a steel specimen after 110 days exposure to solution (i); (b) deconvolution of the spectrum closest to the sample average.	169
Figure 6-7: (a) Raman spectra (1-8) recorded at various locations on a steel specimen after 252 days exposure to solution (i); (b) deconvolution of the spectrum closest to the sample average.	169
Figure 6-8: (a) Raman spectra (1-8) recorded at various locations on a steel specimen after 365 days exposure to solution (i); (b) deconvolution of the spectrum closest to the sample average.	170
Figure 6-9: (a) Raman spectra (1-7) recorded at various locations on a steel specimen after 604 days exposure to solution (i); (b) deconvolution of the spectrum closest to the sample average.	170
Figure 6-10: Evolution of the area ratio for the Fe_3O_4 (672 cm^{-1}) and $\gamma\text{-Fe}_2\text{O}_3$ (705 cm^{-1}) Raman peaks after exposure to solution (i), calculated from the deconvoluted spectra.	171
Figure 6-11: SEM micrographs recorded on three locations of a specimen surface (a-c), (d-f), and (g-h) after 4 days of exposure to solution (i) showing the distributions of crystalline $\gamma\text{-Fe}_2\text{O}_3$ and the general surface morphology.....	173
Figure 6-12: SEM micrographs recorded on a specimen surface after 14 days of exposure to solution (i) showing: (a-f) the general surface morphology; (g-i) a region exhibiting a higher degree of corrosion damage.....	174
Figure 6-13: SEM micrographs recorded on a specimen surface after 110 days of exposure to solution (i) showing: (a-f) the general surface morphology; (g-i) a layered morphology consistent with the remnants of Fe_3C from ferrite dissolution of pearlite grains.	175
Figure 6-14: SEM micrographs recorded on a specimen surface after 252 days of exposure to solution (i) showing: (a-e) the general surface morphology; (f) the preferential corrosion of ferrite in pearlite grains; (g-i) a region of localized damage.....	176
Figure 6-15: SEM micrographs recorded on a specimen surface after 365 days of exposure to solution (i) showing: (a-f) the general surface morphology; (g-i) a region exhibiting a more significant corrosion deposit.....	177
Figure 6-16: SEM micrographs recorded on a specimen surface after 604 days of exposure to solution (i) showing: (a-c) the increased roughening of the specimen surface; (d-f) the increase in corrosion product coverage.....	178
Figure 6-17: FIB cross-section micrographs recorded on a specimen surface after 252 days of exposure to solution (i) showing: (a-b) and (d-e) the thin nature of the corrosion film; (c) and (f) the residual bands of Fe_3C left behind after preferential dissolution of the $\alpha\text{-Fe}$ in the pearlite	

grains; (g-i) a region exhibiting void spaces created by corrosion under the surface oxide layer.	180
Figure 6-18: FIB cross-section micrographs recorded on a specimen surface after 540 days of exposure to solution (i) showing: (a-b) a region of shallow localized corrosion; (c) the formation of a localized pit; (d-f) a region which has undergone significant localized damage. Backscatter images in (b), (c), and (f) highlight the interface between the base metal (bright) and the oxide film (dark).....	181
Figure 6-19: FIB cross-section micrographs recorded on a specimen surface after 604 days of exposure to solution (i) showing: (a-f) the thin nature of the corrosion film; (c) lamellae of Fe ₃ C left after the preferential dissolution of α-Fe from the pearlite grains; (g-i) a region exhibiting void spaces created by corrosion under the surface oxide layer.	182
Figure 6-20: (a) Raman spectra (1-7) recorded at various locations on a steel specimen after 4 days exposure to solution (ii); (b) deconvolution of the spectrum closest to the sample average.	184
Figure 6-21: (a) Raman spectra (1-6) recorded at various locations on a steel specimen after 110 days exposure to solution (ii); (b) deconvolution of the spectrum closest to the sample average.	184
Figure 6-22: (a) Raman spectra (1-8) recorded at various locations on a steel specimen after 252 days exposure to solution (ii); (b) deconvolution of the spectrum closest to the sample average.	185
Figure 6-23: (a) Raman spectra (1-9) recorded at various locations on a steel specimen after 548 days exposure to solution (ii); (b) deconvolution of the spectrum closest to the sample average.	185
Figure 6-24: (a) Raman spectra (1-7) recorded at various locations on a steel specimen after 716 days exposure to solution (ii); (b) deconvolution of the spectrum closest to the sample average.	186
Figure 6-25: Raman spectra (1-7) recorded at various locations on a steel specimen after 910 days exposure to solution (ii).....	186
Figure 6-26: Evolution of the area ratio for the Fe ₃ O ₄ (672 cm ⁻¹) and γ-Fe ₂ O ₃ (705 cm ⁻¹) Raman peaks after exposure to solution (ii), calculated from the deconvoluted spectra.	187
Figure 6-27: SEM micrographs recorded on a specimen surface after 4 days of exposure to solution (ii) showing a lightly corroded surface with (c) early stages of visible pearlite corrosion; (d-f) a region of crystalline corrosion product; (g-i) a more heavily corroded location.	189
Figure 6-28: SEM micrographs recorded on a specimen surface after 110 days of exposure to solution (ii) showing: (a-f) regions of the general surface with a compact underlying film with interspersed platelet structures; (g-h) regions with overlying corrosion product deposits; (i) localized corrosion products on the order of 15-30 μm.	190
Figure 6-29: SEM micrographs recorded on a specimen surface after 252 days of exposure to solution (ii) showing: (a-f) the general surface and underlying corrosion layer; (g-i) corrosion product deposits, possible γ-Fe ₂ O ₃	191

Figure 6-30: SEM micrographs recorded on a specimen surface after 548 days of exposure to solution (ii) showing: (a-f) the general surface with increasing levels of corrosion product deposits; (g-i) the morphology of the overlying corrosion product deposits..... 192

Figure 6-31: SEM micrographs recorded on a specimen surface after 716 days of exposure to solution (ii) showing: (a-f) regions with a visible underlying corrosion layer; (g-i) a region exhibiting extensive overlying corrosion product deposits..... 193

Figure 6-32: SEM micrographs recorded on a specimen surface after 910 days of exposure to solution (ii) showing: (a-c) the general underlying corrosion film; (d-i) the increasing extent of surface coverage by corrosion product deposits..... 194

Figure 6-33: FIB cross-section micrographs recorded on a specimen surface after 252 days of exposure to solution (ii) showing: (a-c) that penetration beneath the compact film is minor; (d-f) a cut through an overlying deposit which has experienced more extensive penetration; (g-i) a cut through a large corrosion deposit at a location which has experienced more extensive corrosion. The backscatter image in (b) highlights the interface between the base metal (bright) and the oxide film (dark). EDX maps (f and i) further highlight the interface by mapping of elemental oxygen (pink) and iron (blue)..... 196

Figure 6-34: FIB cross-section micrographs recorded on a specimen surface after 548 days of exposure to solution (ii) showing: (a-f) a thickening of the film to $\sim 3 \mu\text{m}$ with more penetrating damage beneath thicker regions; (e) bright bands within the oxide structure, which the EDX map (f) for iron (blue) and carbon (green), shows are residual Fe_3C bands of the pearlite grains; (g-i) a cut through a large deposit which appears porous and non-protective. The EDX maps (c,i) highlight the interface between the base metal and the oxide film by mapping of elemental oxygen (pink) and iron (blue)..... 197

Figure 6-35: FIB cross-section micrographs recorded on a specimen surface after 910 days of exposure to solution (ii) showing: (a-c) a $\sim 3\text{-}5 \mu\text{m}$ thick corrosion layer which appears generally uniform and protective; (d-i) regions showing deeper penetration which has spread laterally rather than developing as deep pits. The backscatter images ((b-c), (e-f), (i)) highlight the interface between the base metal (bright) and the oxide film (dark)..... 198

Figure 6-36: Raman spectra (1-5) recorded at various locations on a steel specimen after 4 days of exposure to solution (iii)..... 201

Figure 6-37: (a) Raman spectra (1-5) and (b) FTIR spectra recorded at various locations on a steel specimen after 14 days of exposure to solution (iii). 201

Figure 6-38: (a) Raman spectra (1-6) and (b) FTIR spectra recorded at various locations on a steel specimen after 109 days of exposure to solution (iii). 202

Figure 6-39: (a) Raman spectra (1-3) and (b) FTIR spectra recorded at various locations on a steel specimen after 252 days of exposure to solution (iii). 202

Figure 6-40: (a) Raman spectra (1-6) and (b) FTIR spectra recorded at various locations on a steel specimen after 365 days of exposure to solution (iii). 203

Figure 6-41: (a) Raman spectra (1-5) and (b) FTIR spectra recorded at various locations on a steel specimen after 639 days of exposure to solution (iii). 203

Figure 6-42: SEM micrographs recorded on a steel specimen after 4 days of exposure to solution (iii) showing: (a-c) needle-like acicular crystals expected of $\text{Fe}_2(\text{OH})_2\text{CO}_3$; (d-i) large localized corrosion products 60-100 μm in diameter..... 205

Figure 6-43: SEM micrographs recorded on a steel specimen after 14 days of exposure to solution (iii) showing that the morphology of the corrosion product has remained unchanged but that small hexagonal crystals (c, e-f) appear across the surface and evidence for small locally corroded sites (g-i). 206

Figure 6-44: SEM micrographs recorded on a steel specimen after 109 days of exposure to solution (iii) showing the emergence of a different morphology of cubic structure best observed in (c) which suggests the formation of FeCO_3 207

Figure 6-45: SEM micrographs recorded on a steel specimen after 252 days of exposure to solution (iii) showing a general $\text{Fe}_2(\text{OH})_2\text{CO}_3$ film with an increase in the density of the cubic structure, supporting FeCO_3 formation as well as hexagonal crystals in (e) and (g) which may indicate the presence of GR..... 208

Figure 6-46: SEM micrographs recorded on a steel specimen after 365 days of exposure to solution (iii) showing: (a-c) the dominance of $\text{Fe}_2(\text{OH})_2\text{CO}_3$ with small amorphous deposits (c) visible on top of the $\text{Fe}_2(\text{OH})_2\text{CO}_3$ deposit; (d-i) two regions of localized corrosion deposits..... 209

Figure 6-47: SEM micrographs recorded on a steel specimen after 639 days of exposure to solution (iii) showing: (a-c) a $\text{Fe}_2(\text{OH})_2\text{CO}_3$ film with more numerous small deposits; (d-f) a region with a localized corrosion deposit; (g-i) the size distribution of additional localized corrosion deposits..... 210

Figure 6-48: FIB cross-section micrographs recorded on a steel specimen after 252 days of exposure to solution (iii) showing: (a-b) the general $\text{Fe}_2(\text{OH})_2\text{CO}_3$ film in which the crystals are attached directly to the substrate which is confirmed by the backscatter image (b); (c-d) a cut through a region of isolated deposit showing that they are located over regions of active localized corrosion; (e-f) a cut through a region of active corrosion suggesting $\text{Fe}_2(\text{OH})_2\text{CO}_3$ has reformed at the metal/oxide interface under the original deposit..... 212

Figure 6-49: FIB cross-section micrographs recorded on a steel specimen after 546 days of exposure to solution (iii) showing: (a-c) a cut through a localized deposit indicating a more active location with shallow penetration shown in the backscatter image (c); (d-f) a cut through a region with significant penetration indicating an active pitting process had occurred; (g-h) a cut through the general $\text{Fe}_2(\text{OH})_2\text{CO}_3$ film showing that its thickness has remained unchanged..... 213

Figure 6-50: FIB cross-section micrographs recorded on a steel specimen after 639 days of exposure to solution (iii) showing: (a-c) a cut through a large deposit showing the film at this location to be porous and suggesting this site remained active; (d-f) a cut through the general $\text{Fe}_2(\text{OH})_2\text{CO}_3$ covered surface which shows little penetration into the metal. The backscatter images in (b), and (d) highlight the interface between the base metal (bright) and oxide film (dark)..... 214

Figure 6-51: Raman spectra (1-4) recorded at various locations on a steel specimen after 5 days of exposure to solution (iv). 217

Figure 6-52: Raman spectra (1-6) recorded at various locations on a steel specimen after 42 days of exposure to solution (iv). 217

Figure 6-53: Raman spectra (1-6) recorded at various locations on a steel specimen after 110 days of exposure to solution (iv).....	218
Figure 6-54: Raman spectra (1-5) recorded at various locations on a steel specimen after 728 days of exposure to solution (iv).....	218
Figure 6-55: Raman spectra (1-4) recorded at various locations on a steel specimen after 910 days of exposure to solution (iv).....	219
Figure 6-56: SEM micrographs recorded on a steel specimen after 5 days of exposure to solution (iv) showing: (a-c) the extend of CaSO ₄ and CaCO ₃ crystal coverage; (d-f) the fine crystal morphology with the long rectangular crystals the expected structure of CaSO ₄ and the star-shaped crystals the expected structure of CaCO ₃ (aragonite); (g-i) a region of the exposed steel exhibiting a roughening of the surface.	221
Figure 6-57: SEM micrographs recorded on a steel specimen after 42 days of exposure to solution (iv) showing that the underlying steel surface is almost completely obscured by the CaSO ₄ and CaCO ₃ crystals.....	222
Figure 6-58: SEM micrographs recorded on a steel specimen after 56 days of exposure to solution (iv) showing that the crystal coverage continues while regions of visible surface (b-c) appear roughened.	223
Figure 6-59: SEM micrographs recorded on a steel specimen after 728 days of exposure to solution (iv) showing: (a-f) the visible surface which exhibits a coherent oxide layer; (g-i) a region with a significant corrosion product deposit.	224
Figure 6-60: SEM micrographs recorded on a steel specimen after 910 days of exposure to solution (iv) showing an apparently thick protective layer of Fe ₃ O ₄ with scattered corrosion deposits.....	225
Figure 6-61: FIB cross-section micrographs recorded on a steel specimen after 728 days of exposure to solution (iv) showing: (a-c) a cut through a localized deposit showing some undercutting of the substrate; (d-f) a cut through a general corroded region showing no significant penetration into the steel. The backscatter image in (f) highlights the interface between the base metal (bright) and oxide film (dark).....	227
Figure 6-62: FIB cross-section micrographs recorded on a steel specimen after 910 days of exposure to solution (iv) showing regions exhibiting considerable void space between the product and substrate. Backscatter images (b, d) highlight the separation of the oxide film (dark) and the base metal (bright).	227
Figure 6-63: Pourbaix diagram of iron in carbonated aqueous media at 25°C for equilibria involving Fe ₂ (OH) ₂ CO ₃ (dotted lines) and FeCO ₃ (solid lines) [26].	231
Figure A-1: Reference Raman spectrum for Fe ₃ O ₄ (magnetite).....	245
Figure A-2: Reference Raman spectrum for γ-Fe ₂ O ₃ (maghemite).	246
Figure A-3: Reference Raman spectrum for α-FeOOH (goethite).....	246
Figure A-4: Reference Raman spectrum for γ-FeOOH (lepidocrocite).	247
Figure A-5: (a) Raman spectra recorded at various locations on a steel specimen after 2 days of exposure to solution (i); (b) deconvolution of the spectrum closest to the sample average.	247
Figure A-6: (a) Raman spectra recorded at various locations on a steel specimen after 4 days of exposure to solution (i); (b) deconvolution of the spectrum closest to the sample average.	248

Figure A-7: (a) Raman spectra recorded at various locations on a steel specimen after 7 days of exposure to solution (i); (b) deconvolution of the spectrum closest to the sample average. 248

Figure A-8: (a) Raman spectra recorded at various locations on a steel specimen after 14 days of exposure to solution (i); (b) deconvolution of the spectrum closest to the sample average. 249

Figure A-9: (a) Raman spectra recorded at various locations on a steel specimen after 28 days of exposure to solution (i); (b) deconvolution of the spectrum closest to the sample average. 249

Figure A-10: (a) Raman spectra recorded at various locations on a steel specimen after 42 days of exposure to solution (i); (b) deconvolution of the spectrum closest to the sample average. 250

Figure A-11: (a) Raman spectra recorded at various locations on a steel specimen after 56 days of exposure to solution (i); (b) deconvolution of the spectrum closest to the sample average. 250

Figure A-12: (a) Raman spectra recorded at various locations on a steel specimen after 110 days of exposure to solution (i); (b) deconvolution of the spectrum closest to the sample average. 251

Figure A-13: (a) Raman spectra recorded at various locations on a steel specimen after 182 days of exposure to solution (i); (b) deconvolution of the spectrum closest to the sample average. 251

Figure A-14: (a) Raman spectra recorded at various locations on a steel specimen after 252 days of exposure to solution (i); (b) deconvolution of the spectrum closest to the sample average. 252

Figure A-15: (a) Raman spectra recorded at various locations on a steel specimen after 365 days of exposure to solution (i); (b) deconvolution of the spectrum closest to the sample average. 252

Figure A-16: (a) Raman spectra recorded at various locations on a steel specimen after 540 days of exposure to solution (i); (b) deconvolution of the spectrum closest to the sample average. 253

Figure A-17: (a) Raman spectra recorded at various locations on a steel specimen after 604 days of exposure to solution (i); (b) deconvolution of the spectrum closest to the sample average. 253

Figure A-18: Evolution of the area ratio between the Fe_3O_4 (672 cm^{-1}) and $\gamma\text{-Fe}_2\text{O}_3$ (705 cm^{-1}) Raman peaks after exposure to solution (i), calculated from the deconvoluted Raman spectra. 254

Figure A-19: SEM micrographs recorded on a specimen surface after 2 days of exposure to solution (i) showing: (a-c) the distribution of crystalline corrosion product; (d-f) the general surface morphology; (g-i) a region exhibiting a more significant degree of corrosion. 255

Figure A-20: SEM micrographs recorded on a specimen surface after 7 days of exposure to solution (i) showing: (a-c) the general surface morphology; (d-f) a region of crystalline corrosion product; (g-i) a region exhibiting a larger corrosion deposit and the surrounding surface morphology..... 256

Figure A-21: SEM micrographs recorded on a specimen surface after 28 days of exposure to solution (i) showing: (a-c) the general surface morphology; (d-f) a region of minor corrosion product accumulation; (g-i) a region of heavier corrosion product accumulation. 257

Figure A-22: SEM micrographs recorded on a specimen surface after 42 days of exposure to solution (i) showing: (a-c) the general surface morphology; (d-e) a location with deposited corrosion product; (f) a region exhibiting the characteristic lamella of Fe_3C left after the preferential dissolution of $\alpha\text{-Fe}$ from pearlite grains; (g-h) a region of localized damage; (i) a possible pitted location..... 258

Figure A-23: SEM micrographs recorded on a specimen surface after 56 days of exposure to solution (i) showing: (a-f) the general surface morphology; (g-h) a region with a larger corrosion

deposit; (i) a region exhibiting the characteristic lamella of Fe ₃ C left after the preferential dissolution of α-Fe from pearlite grains.	259
Figure A-24: SEM micrographs recorded on a specimen surface after 182 days of exposure to solution (i) showing: (a-f) the general surface morphology; (g-i) a region of localized corrosion damage.	260
Figure A-25: SEM micrographs recorded on a specimen surface after 540 days of exposure to solution (i) showing: (a-c) the general surface morphology; (d-f) a region exhibiting additional corrosion deposits; (g-i) a region of localized corrosion damage.....	261
Figure A-26: (a) Raman spectra recorded at various locations on a steel specimen after 2 days of exposure to solution (ii); (b) deconvolution of the spectrum closest to the sample average.....	262
Figure A-27: (a) Raman spectra recorded at various locations on a steel specimen after 4 days of exposure to solution (ii); (b) deconvolution of the spectrum closest to the sample average.....	262
Figure A-28: (a) Raman spectra recorded at various locations on a steel specimen after 7 days of exposure to solution (ii); (b) deconvolution of the spectrum closest to the sample average.....	263
Figure A-29: (a) Raman spectra recorded at various locations on a steel specimen after 14 days of exposure to solution (ii); (b) deconvolution of the spectrum closest to the sample average.	263
Figure A-30: (a) Raman spectra recorded at various locations on a steel specimen after 28 days of exposure to solution (ii); (b) deconvolution of the spectrum closest to the sample average.	264
Figure A-31: (a) Raman spectra recorded at various locations on a steel specimen after 42 days of exposure to solution (ii); (b) deconvolution of the spectrum closest to the sample average.	264
Figure A-32: (a) Raman spectra recorded at various locations on a steel specimen after 56 days of exposure to solution (ii); (b) deconvolution of the spectrum closest to the sample average.	265
Figure A-33: (a) Raman spectra recorded at various locations on a steel specimen after 110 days of exposure to solution (ii); (b) deconvolution of the spectrum closest to the sample average.	265
Figure A-34: (a) Raman spectra recorded at various locations on a steel specimen after 182 days of exposure to solution (ii); (b) deconvolution of the spectrum closest to the sample average.	266
Figure A-35: (a) Raman spectra recorded at various locations on a steel specimen after 252 days of exposure to solution (ii); (b) deconvolution of the spectrum closest to the sample average.	266
Figure A-36: (a) Raman spectra recorded at various locations on a steel specimen after 365 days of exposure to solution (ii); (b) deconvolution of the spectrum closest to the sample average.	267
Figure A-37: (a) Raman spectra recorded at various locations on a steel specimen after 548 days of exposure to solution (ii); (b) deconvolution of the spectrum closest to the sample average.	267
Figure A-38: (a) Raman spectra recorded at various locations on a steel specimen after 716 days of exposure to solution (ii); (b) deconvolution of the spectrum closest to the sample average.	268
Figure A-39: Raman spectra recorded at various locations on a steel specimen after 910 days of exposure to solution (ii).....	268
Figure A-40: Evolution of the area ratio between the Fe ₃ O ₄ (672 cm ⁻¹) and γ-Fe ₂ O ₃ (705 cm ⁻¹) Raman peaks after exposure to solution (ii), calculated from the deconvoluted spectra.	269
Figure A-41: Comparison of the evolution in the area ratio for the Fe ₃ O ₄ (672 cm ⁻¹) and γ-Fe ₂ O ₃ (705 cm ⁻¹) Raman peaks between solutions (i) and (ii), calculated from the deconvoluted Raman spectra.	270

Figure A-42: SEM micrographs recorded on a specimen surface after 2 days of exposure to solution (ii) showing: (a-c) the general surface morphology; (d-f) a region of localized crystalline corrosion product; (g-i) the distribution and morphology of heavily corroded locations..... 271

Figure A-43: SEM micrographs recorded on a specimen surface after 7 days of exposure to solution (ii) showing: (a-c) the general surface morphology; (d-f) a region with crystalline corrosion product; (g-h) a region exhibiting more extensive corrosion damage; (i) a location with a large localized corrosion product deposit..... 272

Figure A-44: SEM micrographs recorded on a specimen surface after 14 days of exposure to solution (ii) showing: (a-c) crystalline corrosion product; (d-f) a region of secondary corrosion product morphology; (g-i) the general surface morphology. 273

Figure A-45: SEM micrographs recorded on a specimen surface after 28 days of exposure to solution (ii) showing: (a-c) a region of general corrosion product deposit; (d-f) a more significantly corroded region with crystalline morphology; (g-i) a region of localized corrosion damage. 274

Figure A-46: SEM micrographs recorded on a specimen surface after 42 days of exposure to solution (ii) showing: (a-c) the general surface morphology; (d-f) a region of more significant corrosion product deposit; (g-i) a region of localized corrosion damage..... 275

Figure A-47: SEM micrographs recorded on a specimen surface after 56 days of exposure to solution (ii) showing: (a-f) the general surface morphology; (g-i) a region of localized corrosion damage. 276

Figure A-48: SEM micrographs recorded on a specimen surface after 182 days of exposure to solution (ii) showing: (a-c) the general surface morphology; (d-f) a region of more significant corrosion damage; (g-h) a region exhibiting more significant corrosion product deposits; (i) the underlying general surface morphology beneath the corrosion product deposits..... 277

Figure A-49: SEM micrographs recorded on a specimen surface after 365 days of exposure to solution (ii) showing: (a-c) the general surface morphology; (d-f) a more significant crystalline corrosion product deposit; (g-i) a region of the general surface highlighting the smooth underlying corrosion product layer. 278

Figure A-50: Raman spectra recorded at various locations on a steel specimen after 2 days of exposure to solution (iii). 279

Figure A-51: Raman spectra recorded at various locations on a steel specimen after 4 days of exposure to solution (iii). 280

Figure A-52: Raman spectra recorded at various locations on a steel specimen after 7 days of exposure to solution (iii). 280

Figure A-53: (a) Raman and (b) FTIR spectra recorded at various locations on a steel specimen after 14 days of exposure to solution (iii). 281

Figure A-54: (a) Raman and (b) FTIR spectra recorded at various locations on a steel specimen after 30 days of exposure to solution (iii). 281

Figure A-55: (a) Raman and (b) FTIR spectra recorded at various locations on a steel specimen after 38 days of exposure to solution (iii). 282

Figure A-56: (a) Raman and (b) FTIR spectra recorded at various locations on a steel specimen after 56 days of exposure to solution (iii). 282

Figure A-57: (a) Raman and (b) FTIR spectra recorded at various locations on a steel specimen after 109 days of exposure to solution (iii).....	283
Figure A-58: (a) Raman and (b) FTIR spectra recorded at various locations on a steel specimen after 182 days of exposure to solution (iii).....	283
Figure A-59: (a) Raman and (b) FTIR spectra recorded at various locations on a steel specimen after 252 days of exposure to solution (iii).....	284
Figure A-60: (a) Raman and (b) FTIR spectra recorded at various locations on a steel specimen after 365 days of exposure to solution (iii).....	284
Figure A-61: (a) Raman and (b) FTIR spectra recorded at various locations on a steel specimen after 546 days of exposure to solution (iii).....	285
Figure A-62: (a) Raman and (b) FTIR spectra recorded at various locations on a steel specimen after 639 days of exposure to solution (iii).....	285
Figure A-63: SEM micrographs recorded on a specimen surface after 2 days of exposure to solution (iii) showing: (a-c) the general surface with no apparent corrosion product; (d-f) a region of crystalline corrosion product; (g-i) a region of localized corrosion product deposit....	286
Figure A-64: SEM micrographs recorded on a specimen surface after 7 days of exposure to solution (iii) showing: (a-f) the general surface morphology, consistent with $Fe_2(OH)_2CO_3$; (g-i) a region of localized corrosion product deposit.....	287
Figure A-65: SEM micrographs recorded on a specimen surface after 30 days of exposure to solution (iii) showing: (a-f) the general surface morphology, consistent with $Fe_2(OH)_2CO_3$; (g-i) a region of localized corrosion product deposit.....	288
Figure A-66: SEM micrographs recorded on a specimen surface after 38 days of exposure to solution (iii) showing: (a-i) the general surface morphology, consistent with $Fe_2(OH)_2CO_3$	289
Figure A-67: SEM micrographs recorded on a specimen surface after 56 days of exposure to solution (iii) showing: (a-f) the general surface morphology, consistent with $Fe_2(OH)_2CO_3$	290
Figure A-68: SEM micrographs recorded on a specimen surface after 182 days of exposure to solution (iii) showing: (a-i) the general surface morphology, consistent with $Fe_2(OH)_2CO_3$	291
Figure A-69: SEM micrographs recorded on a specimen surface after 546 days of exposure to solution (iii) showing: (a-f) the general surface morphology, consistent with $Fe_2(OH)_2CO_3$; (g-i) the size distribution of localized corrosion product deposits.....	292
Figure A-70: Raman spectra recorded at various locations on a steel specimen after 3 days of exposure to solution (iv).	293
Figure A-71: Raman spectra recorded at various locations on a steel specimen after 5 days of exposure to solution (iv).	294
Figure A-72: Raman spectra recorded at various locations on a steel specimen after 7 days of exposure to solution (iv).	294
Figure A-73: Raman spectra recorded at various locations on a steel specimen after 28 days of exposure to solution (iv).	295
Figure A-74: Raman spectra recorded at various locations on a steel specimen after 42 days of exposure to solution (iv).	295
Figure A-75: Raman spectra recorded at various locations on a steel specimen after 56 days of exposure to solution (iv).	296

Figure A-76: Raman spectra recorded at various locations on a steel specimen after 110 days of exposure to solution (iv).	296
Figure A-77: Raman spectra recorded at various locations on a steel specimen after 728 days of exposure to solution (iv).	297
Figure A-78: Raman spectra recorded at various locations on a steel specimen after 910 days of exposure to solution (iv).	297
Figure A-79: SEM micrographs recorded on a specimen surface after 2 days of exposure to solution (iv) showing: (a-c) the morphology of crystal deposits; (d-f) the general surface morphology beneath the crystals; (g-i) three locations showing the distribution of crystal coverage.....	298
Figure A-80: SEM micrographs recorded on a specimen surface after 7 days of exposure to solution (iv) showing: (a-b) a region where the underlying surface remains visible; (c) the preferential dissolution of α -Fe from the pearlite grains; (d-f) a region of significant crystal coverage; (g-i) a secondary location of crystal coverage and the morphology of the formed crystals.	299
Figure A-81: SEM micrographs recorded on a specimen surface after 14 days of exposure to solution (iv) showing: (a-f) regions in which the underlying surface morphology remains visible; (g-i) a region of significant crystal coverage.	300
Figure A-82: SEM micrographs recorded on a specimen surface after 28 days of exposure to solution (iv) showing: (a-c) a region of significant crystal coverage; (d-i) two regions where the underlying surface morphology is visible.	301

List of Symbols and Acronyms

Symbols

α_i	Activity of species i
α	Transfer coefficient
β	Tafel coefficient
C	Capacitance
E_0	Incident energy
E	Electrochemical potential
E°	Standard potential
E^e	Equilibrium potential
E_{CORR}	Corrosion potential
E_b	Breakdown potential
$E_{x,y,z}$	Field strength of Raman radiation
F	Faraday's constant
ΔG_{rxn}	Gibbs free energy change
I	Absolute current
i	Current density
i_0	Exchange current density
i_{CORR}	Corrosion current density
m	Mass
M	Molar mass
n	Moles of electrons
η	Overpotential
θ	Phase angle
P	Dipole moment
ρ	Resistivity
R	Universal gas constant
R_p	Polarization resistance
R_s	Solution resistance
R_{film}	Film resistance

T	Temperature
t	Time
μ	Chemical potential
μ°	Standard chemical potential
ν	Stoichiometric coefficient
ω	Angular frequency
Z	Atomic number
Z	Absolute impedance
Z'	Real impedance
Z''	Imaginary impedance

Acronyms

BCC	Body-centered cubic
BSE	Backscattered electrons
B-V	Butler-Volmer
CANDU	Canadian deuterium uranium
CCD	Charge-coupled detector
CCP	Cubic close-packed
CV	Cyclic voltammogram
DGR	Deep geologic repository
EDX	Energy dispersive x-ray spectroscopy
EIS	Electrochemical impedance spectroscopy
FCC	Face-centered cubic
FIB	Focused ion beam
FTIR	Fourier transform infrared spectroscopy
GR	Green rust
HCP	Hexagonal close-packed
IR	Infrared spectroscopy
LDH	Layered double hydroxide
LMIS	Liquid metal ion source
LPR	Linear polarization resistance

PMT	Photo multiplier tube
SCE	Saturated calomel electrode
SE	Secondary electron
SEM	Scanning electron microscopy
SHE	Standard hydrogen electrode
STXM	Scanning transmission x-ray microscopy
UHP	Ultra-high purity
WDX	Wavelength dispersive x-ray spectroscopy
XPS	X-ray photoelectron spectroscopy
XRD	X-ray diffraction spectroscopy

Chapter 1

Introduction

1.1. PROJECT BACKGROUND

Currently, nuclear power accounts for over 50% of Ontario's electricity needs and 15% of Canada's overall electricity supply [1, 2]. Nuclear power is an attractive means of generating electricity as it is one of the safest and cleanest forms of energy generation. However, for nuclear energy to remain a viable and sustainable option, the issue of waste disposal must be addressed. The main waste product produced from nuclear energy in Canada is the used CANDU (CANadian Deuterium Uranium) fuel bundles, consisting of high-density ceramic pellets of uranium dioxide (UO_2), which are discharged from the reactor core. Canada presently has 19 operational reactors which are producing ~88,000 used fuel bundles per year [3]. Currently, there are a total of 2.6 million used fuel bundles being stored at the reactor sites with a projected scenario of 4.4 million bundles by the end of all nuclear reactor lifetimes [3].

The current design for the long-term management of used nuclear fuel in Canada is based on a multi-barrier approach and deep geological disposal. The barrier system consists of the used fuel bundles, a durable metal container, a clay buffer/sealing system, a deep, stable, geologic environment and the geologic formation. The current proposal is to place the repository at a nominal depth between 500 and 1000 m in either the crystalline rock of the Canadian Shield or the Ordovician sedimentary rock formations in Ontario's Michigan Basin [4, 5]. A key barrier is the container in which the fuel bundles will be sealed. For a crystalline repository environment the proposed container will consist of an inner carbon steel vessel to provide the structural support for an outer corrosion resistant copper coating. For sedimentary clay environments, a single-walled container made only from carbon steel has been considered due to the significant cost reduction over the coated container design and the fact a shorter-lived steel container can be considered due to the enhanced sealing properties provided by the sedimentary clay. Figure 1-1 illustrates the concept for the deep geological repository (DGR) for both crystalline rock and sedimentary clay host environments.

While Canada has chosen to proceed with the copper coated container design, many countries (for example, France, Switzerland, and Belgium) are still considering the single-walled carbon steel container [6]. It is therefore judicious to assess the corrosion damage which the steel

container may experience in the saline groundwaters anticipated. Furthermore, while not expected to fail, it remains beneficial to study the corrosion behaviour of the steel vessel should the copper coating of the dual-walled design be compromised.

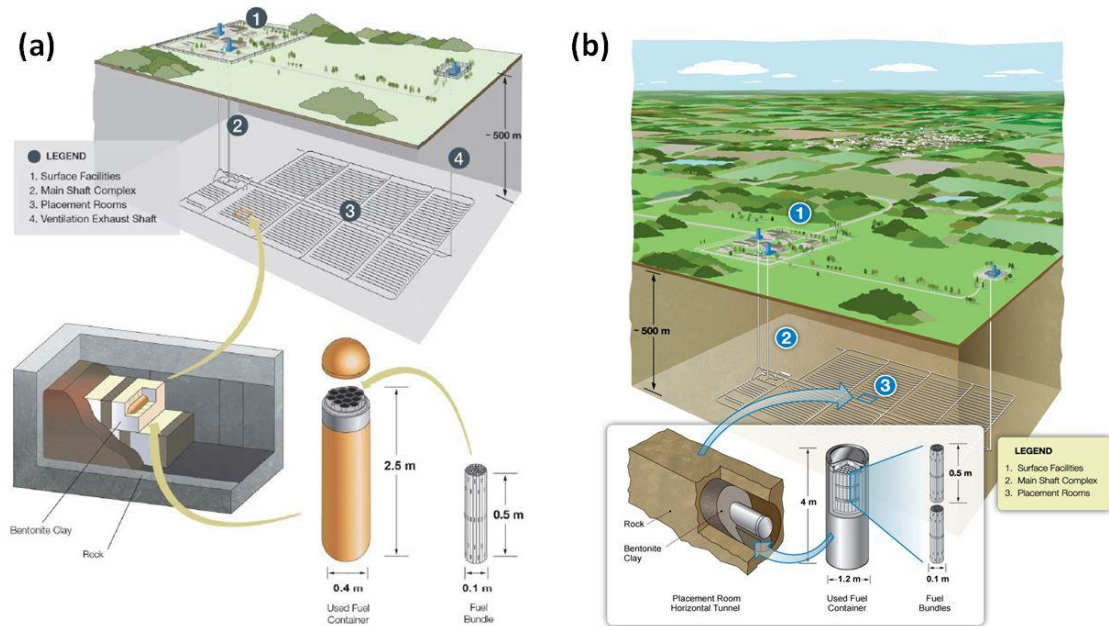


Figure 1-1: Proposed design for a Canadian deep geologic repository (DGR) using (a) a dual-walled copper coated container for crystalline host rock; (b) a single-walled carbon steel container for sedimentary host clay [7].

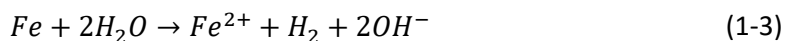
1.2. AQUEOUS CORROSION

1.2.1. Thermodynamics of Corrosion

Corrosion is the degradation of a substance (usually a metal) caused by an interfacial reaction with the environment to which it is exposed [8]. Corrosion processes can be viewed as a short circuited galvanic cell in which an anodic reaction is coupled to a cathodic reaction. For example, the oxidation of Fe in anaerobic aqueous media involves the oxidation of Fe and the reduction of water,



The overall corrosion reaction is the sum of these two half reactions:



For the overall reaction in equation 1-3 to occur spontaneously, the free energy (ΔG_{rxn}) of the reaction given by

$$\Delta G_{rxn} = \sum v_P \mu_P - \sum v_R \mu_R \quad (1-4)$$

must be negative. In equation 1-4 v_P and v_R are the stoichiometric coefficients of the products and reactants and μ_P and μ_R are the chemical potentials of the products and reactants. The chemical potential of any species i can then be written as a function of its activity which accounts for deviations from ideality

$$\mu_i = \mu_i^\circ + RT \ln \alpha_i \quad (1-5)$$

where μ_i° represents the chemical potential of species i in its standard state, R is the gas constant ($8.314 \text{ J mol}^{-1} \text{ K}^{-1}$), T is the temperature in Kelvin, and α_i is the activity of species i . Substitution of equation 1-5 into equation 1-4 for the simple reaction given in equation 1-6 would yield equation 1-7,



$$\Delta G = \Delta G^\circ + RT \ln \left(\frac{\alpha_C^c \alpha_D^d}{\alpha_A^a \alpha_B^b} \right) \quad (1-7)$$

Additionally, the free energy (ΔG) and standard free energy (ΔG°) of an electrochemical system can be described by

$$\Delta G = -nFE \quad (1-8)$$

$$\Delta G^\circ = -nFE^\circ \quad (1-9)$$

where n is the number of electrons transferred in the reaction, F is Faraday's constant (96485 C mol^{-1}), E is the equilibrium potential, and E° is the standard equilibrium potential. Substituting equations 1-8 and 1-9 into equation 1-7 yields the Nernst Equation

$$E^e = E^\circ - \frac{RT}{nF} \ln \left(\frac{\alpha_C^c \alpha_D^d}{\alpha_A^a \alpha_B^b} \right) \quad (1-10)$$

which can be used to calculate the equilibrium potential for a reversible reaction under conditions other than the standard state. However, in dilute solutions the activity of each species can be adequately approximated by their concentration and equation 1-10 can be rewritten as

$$E^e = E^\circ - \frac{RT}{nF} \ln \left(\frac{[C]^c [D]^d}{[A]^a [B]^b} \right) \quad (1-11)$$

For corrosion reactions, the driving force will be the difference in the equilibrium potentials, derived from the Nernst Equation, between the anodic half reaction,



$$E_{M^{n+}/M}^e = E_{M^{n+}/M}^\circ - \frac{RT}{nF} \ln \left(\frac{1}{[M^{n+}]} \right) \quad (1-13)$$

and the cathodic half reaction.



$$E_{Red/Ox}^e = E_{Red/Ox}^\circ - \frac{RT}{nF} \ln \left(\frac{[Red]}{[Ox]} \right) \quad (1-15)$$

The thermodynamic possibilities for a material exposed to an aqueous medium can be calculated from the Nernst equation and a table of standard potentials and represented in the form of a Pourbaix (E-pH) diagram, which summarizes these possibilities as a function of potential and pH [9]. Figure 1-2 shows the Pourbaix diagram for the Fe-H₂O system for different activities of Fe²⁺ at 25°C. Since most corrosion reactions take place in aqueous media, the stability limits for the oxidation and reduction of H₂O define the range of applicable conditions. The Nernst equation for the reduction of water is given by,



$$E^e = E^\circ - \frac{(8.314)(295.15)}{(2)(96485)} \ln[OH^-]^2 \quad (1-17)$$

$$E^e = E^\circ - \frac{0.059}{2} \log[OH^-]^2 \quad (1-18)$$

where the partial pressure of H_2 is assumed to be 1. Rearranging the equation in terms of pH yields

$$E^e = -0.059 \text{ pH} \quad (1-19)$$

Similarly for the oxidation of water with an O_2 partial pressure of 1,



and,

$$E^e = 1.23 \text{ V} - 0.059 \text{ pH} \quad (1-21)$$

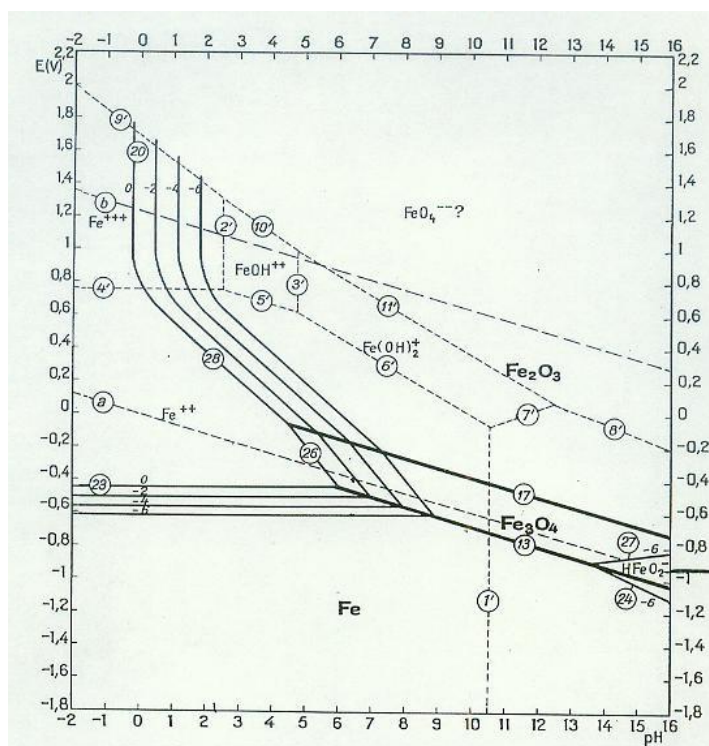


Figure 1-2: Pourbaix diagram for the Fe- H_2O system with various Fe^{2+} activities at 25°C. Solid lines represent the stability ranges for the solid species while the dotted lines show the stability ranges for aqueous species (not considered here) [9].

Plotting these two equations in Figure 1-2 yields the diagonal dashed lines (a) and (b) between which H₂O is thermodynamically stable and aqueous corrosion may be supported.

For Fe dissolution,



$$E^{\circ} = -0.447 V \quad (1-23)$$

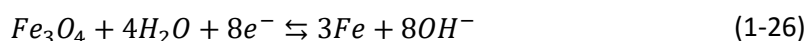
the Nernst equation is

$$E_{Fe^{2+}/Fe}^e = E_{Fe^{2+}/Fe}^{\circ} - \frac{RT}{2F} \log \frac{1}{[Fe^{2+}]} \quad (1-24)$$

$$E_{Fe^{2+}/Fe}^e = -0.447 V + 0.0295 \log [Fe^{2+}] \quad (1-25)$$

Since the dissolution reaction (equation 1-22) involves no protons, the equilibrium potential is independent of pH and appears as a series of horizontal lines (line (23) in Figure 1-2) dependent only on the concentration of the Fe²⁺. At potentials below this line Fe is stable while at potentials above this line it will oxidize to aqueous Fe²⁺. While the stability region of the Fe metal is seen to become larger as [Fe²⁺] increases, it can be noted from Figure 1-2 that there is no region on the E-pH diagram in which Fe metal is stable in the presence of water. As such, Fe is considered to be a base metal.

In addition, Fe can react to form Fe₃O₄ via the reaction

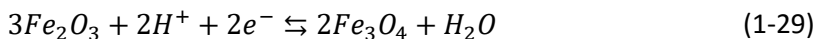


for which the Nernst Equation can be expressed as

$$E_{Fe/Fe_3O_4}^e = E_{Fe_3O_4/Fe}^{\circ} - \frac{RT}{8F} \log [OH^{-}]^8 \quad (1-27)$$

$$E_{Fe/Fe_3O_4}^e = -0.085 V - 0.059 pH \quad (1-28)$$

It is clear from equation 1-28 that the equilibrium potential for the formation of Fe₃O₄ is dependent on both the potential and the pH. As such, this reaction will be represented by a diagonal line with a slope of -0.059, line (13) in Figure 1-2. Above this line Fe₃O₄ is the stable species, while below Fe metal is stable. Fe₃O₄ can then be oxidized to form Fe₂O₃ by the reaction



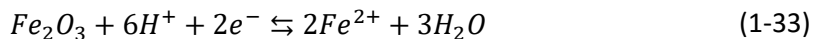
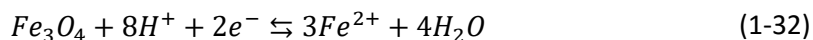
for which the Nernst equation can be expressed as

$$E_{Fe_3O_4/Fe_2O_3}^e = E_{Fe_3O_4/Fe_2O_3}^\circ - \frac{RT}{2F} \log \frac{1}{[H^+]^2} \quad (1-30)$$

$$E_{Fe_3O_4/Fe_2O_3}^e = 0.221 V - 0.059 pH \quad (1-31)$$

The oxidation of Fe_3O_4 to Fe_2O_3 is seen as the diagonal line (17) in Figure 1-2 below which Fe_3O_4 is the stable species and above which Fe_2O_3 is the stable species.

Furthermore, the Fe^{2+} species produced via equation 1-22 can also oxidize to either Fe_3O_4 or Fe_2O_3 via the following reactions



leading to lines (26) and (28) in Figure 1-2 calculated by the following Nernst Equations

$$E_{Fe^{2+}/Fe_3O_4}^e = 0.980 V - 0.2364 pH - 0.0886 \log[Fe^{2+}] \quad (1-34)$$

$$E_{Fe^{2+}/Fe_2O_3}^e = 0.728 V - 0.1773 pH - 0.059 \log[Fe^{2+}] \quad (1-35)$$

Figure 1-3 shows a simplified Pourbaix diagram highlighting the regions in which the Fe is immune to corrosion, in a passive state due to Fe_3O_4 or Fe_2O_3 film formation, and in active corrosion conditions. From Figure 1-3 it is clear that passivation of Fe is only possible for alkaline, oxidizing conditions. While Pourbaix diagrams are useful in determining which species may be thermodynamically stable under specific conditions, they do not give any information on the properties of the oxide species produced, in particular its ability to passivate the Fe. In addition, Pourbaix diagrams are unable to provide any information on the kinetics of the system.

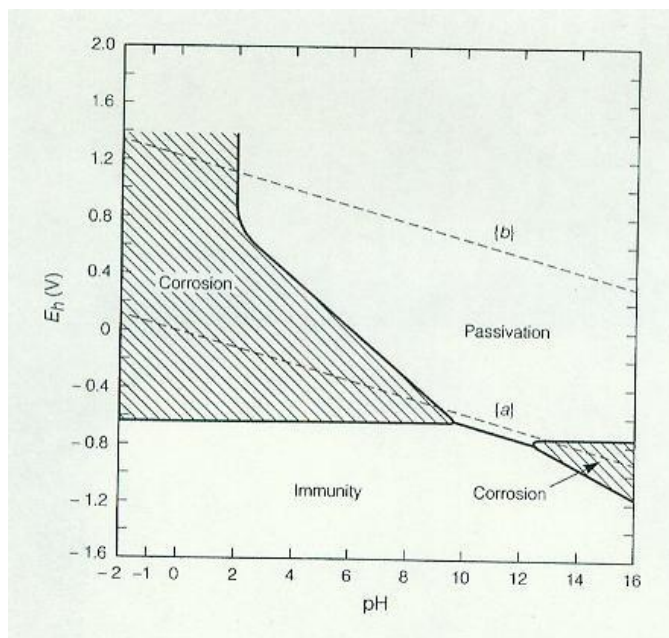


Figure 1-3: Simplified Pourbaix diagram for the Fe-H₂O system showing the regions of immunity, corrosion, and passivation (by Fe₃O₄ and Fe₂O₃) at 25°C. Dashed lines (a) and (b) represent the stability regions of H₂O [9].

1.2.2. Kinetics of Corrosion

While thermodynamics is useful in predicting which reactions may occur in a corrosion process, the corrosion kinetics express the rates at which corrosion can occur. In a corrosion cell, the positive anodic current due to the dissolution of the metal is equal and opposite in sign to the negative current from the reduction of the oxidant. The resulting corrosion current (I_{CORR}), is carried by the electrons through the metal and by ions in the solution.

$$I_{CORR} = I_a = |I_c| \quad (1-36)$$

A simple way to measure the corrosion current is through mass loss measurements using Faraday's law,

$$I_{CORR} = \frac{mnF}{Mt} \quad (1-37)$$

$$Rate = \frac{I_{CORR}M}{nF} \quad (1-38)$$

where m is the mass (g) of corroded metal, M is the molar mass of the material (g mol^{-1}), and t

is the duration of exposure in seconds. While this is a relatively straightforward way to determine the corrosion rate, i_{CORR} is often unknown since it cannot be readily measured.

The equal rates of the cathodic and anodic reactions for a metal dissolution reaction at equilibrium can be expressed as an exchange current density (i_0),

$$i_0 = i_a = |i_c| \quad (1-39)$$

where i_a is the anodic current density for the forward reaction and i_c is the cathodic current density for the reverse reaction. The current-potential relationship can be described by the Butler-Volmer (B-V) equation

$$i_{net} = i_0 \left[e^{\left(\frac{\alpha n F}{RT} \eta\right)} - e^{\left(-\frac{(1-\alpha) n F}{RT} \eta\right)} \right] \quad (1-40)$$

where α is the transfer coefficient of the reversible reaction and η is the overpotential defined with reference to the equilibrium potential ($\eta = E \pm E^e$). Figure 1-4 illustrates the B-V relationship for the reversible Fe dissolution/precipitation reaction. When the reaction is polarized to a large anodic overpotential, the current can be simplified to

$$i_a = i_0 \left[e^{\left(\frac{\alpha n F}{RT} \eta\right)} \right] \quad (1-41)$$

Similarly, for large cathodic overpotentials the current can be expressed by

$$i_c = i_0 \left[-e^{\left(-\frac{(1-\alpha) n F}{RT} \eta\right)} \right] \quad (1-42)$$

Writing equations 1-41 and 1-42 logarithmically yields the following linear relationships

$$\log i_a = \log i_0 + \frac{\alpha n F \eta}{2.303 RT} \quad (1-43)$$

$$\log i_c = \log i_0 - \frac{(1 - \alpha) n F \eta}{2.303 RT} \quad (1-44)$$

Plotting the η versus $\log i_a$ gives an intercept of i_0 and a slope of

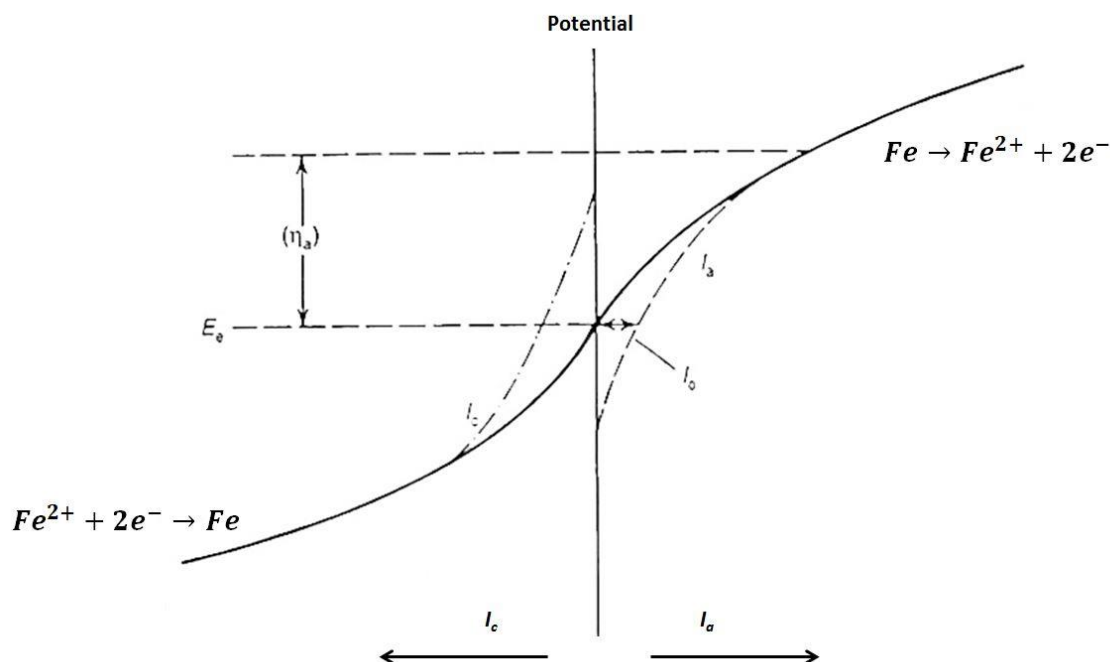


Figure 1-4: Potential-current (Butler-Volmer) relationship for the Fe dissolution/deposition reaction. Solid lines indicate the measurable current while the dashed lines show the partial currents for the forward and reverse reactions [10].

$$\frac{2.303RT}{\alpha nF} \quad (1-45)$$

which is known as the anodic Tafel slope, commonly denoted by the coefficient β . A similar process can be performed for $\log i_c$ to obtain the cathodic Tafel slope.

However, a corrosion reaction involves the coupling of two separate reactions at the unique potential at which the anodic and cathodic currents are equal and opposite in sign (equation 1-36), Figure 1-5. If the equilibrium potentials of the half reactions are sufficiently separated, the point at which E_{CORR} occurs will involve only the anodic current for Fe dissolution and the cathodic current for proton reduction. As such, i_{CORR} will exhibit a BV-like relationship as given by the Wagner-Traud equation,

$$i_{net} = i_{CORR} \left[e^{\left(\frac{2.3(E-E_{CORR})}{\beta_a} \right)} - e^{\left(\frac{2.3(E-E_{CORR})}{\beta_c} \right)} \right] \quad (1-46)$$

where β_a and β_c are the anodic and cathodic Tafel coefficients. Plotting equation 1-46 logarithmically yields an Evans' diagram which can be used to predict the behaviour of the anodic and cathodic half reactions based on changes in E_{CORR} and i_{CORR} , Figure 1-6. The position of E_{CORR} will be determined by the half reaction with the larger i_0 while the kinetics of the reaction with the smaller i_0 will control the value of i_{CORR} .

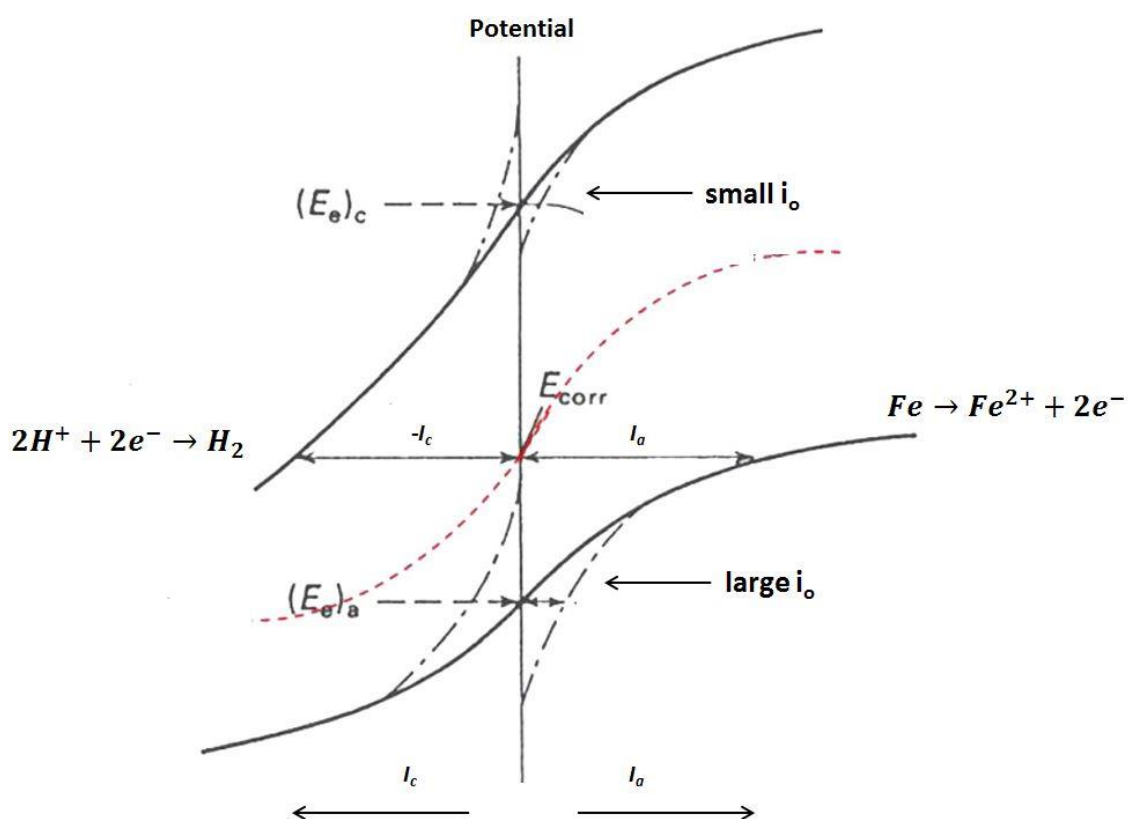


Figure 1-5: Current-potential relationships for the Fe dissolution and proton reduction reactions (solid black lines). As shown, the anodic reaction has a large i_0 while the cathodic reaction has a small i_0 . The dashed red line shows the current that would be measured for the coupled reaction. As shown, the anodic reaction has a large i_0 compared to the cathodic reaction and hence determines the position of E_{CORR} [10].

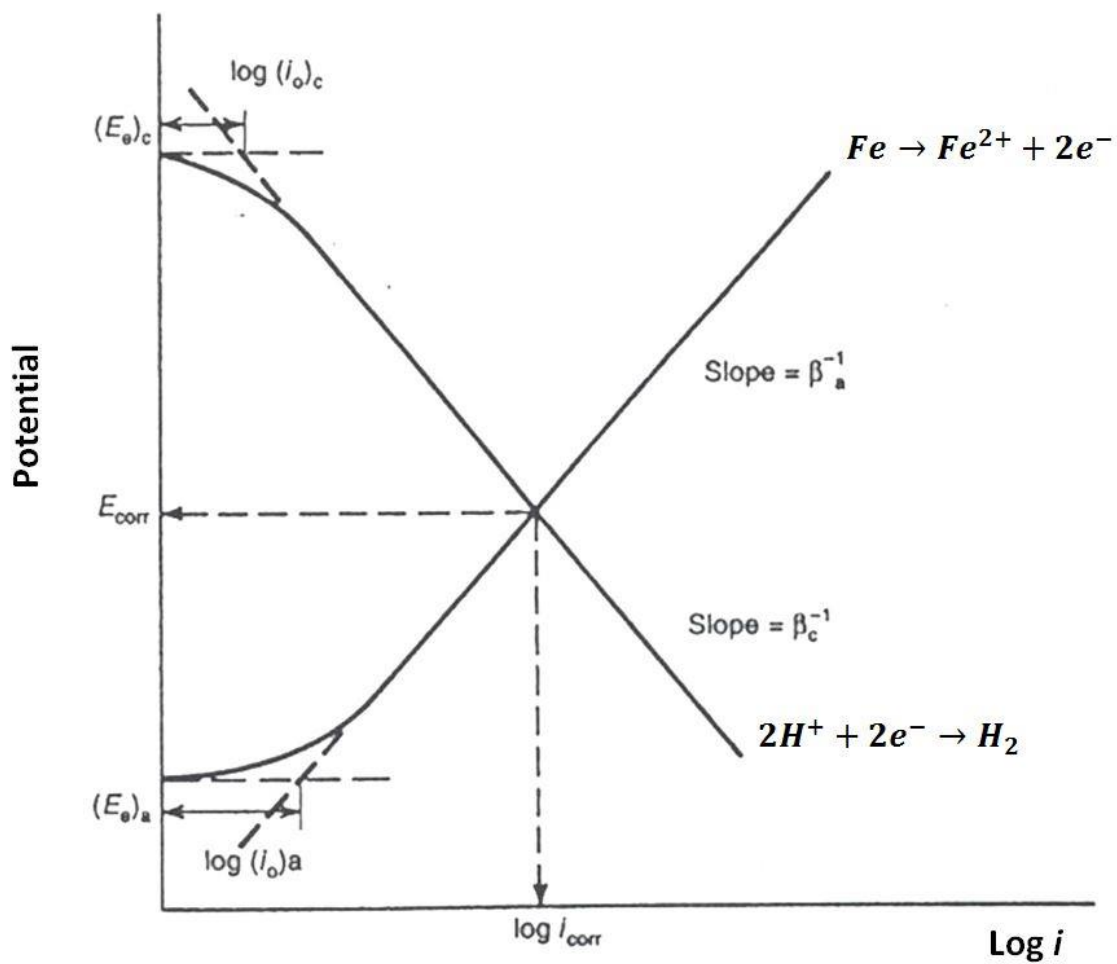


Figure 1-6: Current-potential relationships for the anodic dissolution of Fe and the cathodic reduction of protons plotted as an Evan's diagram [10].

1.3. MATERIALS BACKGROUND

1.3.1. Carbon Steel

Iron is an allotropic metal which, depending on temperature, can exist in at least three different structures [11, 12]. Figure 1-7 shows that as liquid Fe metal is cooled it first forms a solid body-centered cubic (BCC) δ -phase, known as delta ferrite, followed by a face-centered cubic (FCC) γ -phase, known as austenite, before finally reverting back to a BCC structure, designated the α -phase. The α -phase, also known as ferrite, can exist in both a non-magnetic and a magnetic form above and below 768 °C, respectively. While the magnetic properties change at this temperature, the Fe structure remains unchanged based on X-ray studies [11]. At increased pressures, a third allotrope (ϵ -Fe) of hexagonal close-packed (HCP) structure is possible, Figure 1-8 [12]. The alloying elements within the steel, most importantly the C content, will determine the point at which these structural changes occur. Fe alloys are classified as either steels (<2.14 wt% C) or cast irons (>2.14 wt% C) [11]. The equilibrium phase diagram for the Fe-C system showing these distinctions is given in Figure 1-9. Carbon steel, or mild steel, is a Fe-C alloy with low levels of impurities such as Mn, S and Si, where C atoms are located interstitially within the octahedral holes of the BCC structure of the α -Fe [12]. Carbon steels can be classified into three major categories: low, medium, and high-carbon steel based on an increasing C content. Low-carbon steels are generally classified by a C content of less than 0.25% and are the most widely produced [13].

Figure 1-10 shows the equilibrium diagram for steels with a C content lower than 2%. The vertical dashed lined indicates a low-carbon steel containing roughly 0.25% C. Initially, at point c, only the austenitic phase is present. Upon cooling to point d, the steel begins to undergo an allotropic change to BCC α -Fe, indicated in red. Because C is more soluble in the interstitial spaces of the FCC structure, the change to BCC results in a decrease in C solubility, leading to the removal of C atoms from solid solution in regions undergoing transition to α -Fe and their re-dissolution in the residual austenite. When the temperature reaches the point designated by the horizontal red line, the remaining FCC austenite, with a C content which has been increased to 0.8%, undergoes a eutectoid reaction to form α -Fe and the precipitation of cementite (Fe_3C , 6.67 wt% C) in regions surrounding the α -Fe. This process leads to the formation of alternating bands of α -Fe and Fe_3C , collectively known as pearlite. As indicated by point f in Figure 1-10,

there is a mixture of two different types of α -Fe. The ferrite initially formed before the eutectoid temperature is known as proeutectoid α -Fe while the ferrite within the pearlite structure is

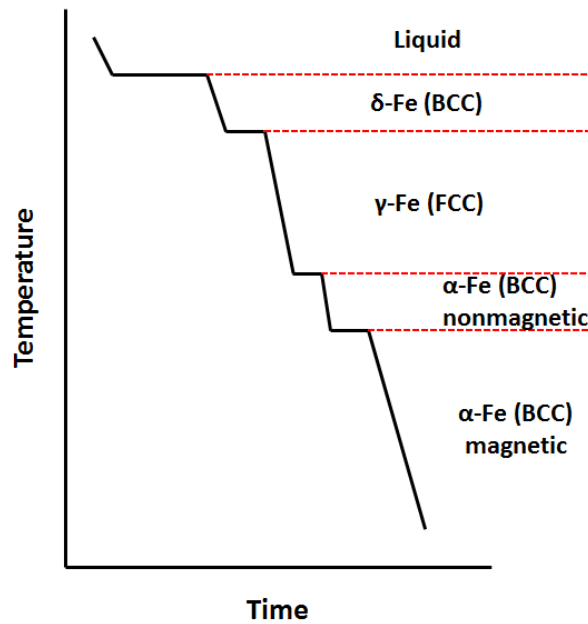


Figure 1-7: Cooling curve showing the allotropic conversions for pure Fe at atmospheric pressure [14].

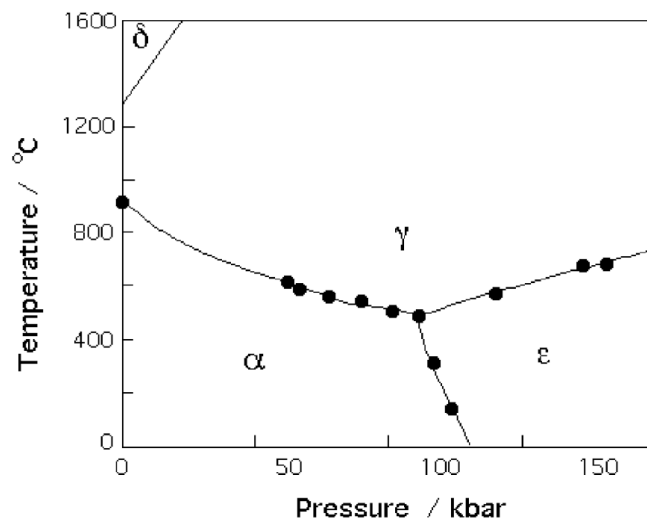


Figure 1-8: Triple point showing the possible interconversions of Fe allotropes α (BCC), γ (FCC), and ϵ (HCP) [12].

known as eutectoid α -Fe due to its formation about the eutectoid temperature [15]. The amount of Fe_3C , and therefore pearlite, is dependent on the amount of C present within the alloy. Increasing the C content will increase the pearlite percentage until it is the only phase present (0.8 wt% C) [12]. Figure 1-11 shows optical images of the α -Fe and pearlite structure for the A516 Gr70 (0.23 wt% C) steel used in the studies presented in this thesis. The interstitial C atoms and the Fe_3C within the pearlite are what help to inhibit the glide of dislocations within the lattice structure, thus increasing the strength of the material over that of pure iron [11, 12].

While the low carbon levels (< 0.25 wt%) of low-carbon steels mean that they are softer and weaker than their high-carbon counterparts, they are an ideal structural material as they maintain their toughness and ductility as well as ease of machinability and weldability [12, 13]. More than a billion tonnes of steel are consumed annually with low-carbon steels being used in castings, structural shapes, automobile components and sheets which are used in the fabrication of pipelines, storage tanks, pressure vessels, bridges, and buildings [12, 13].

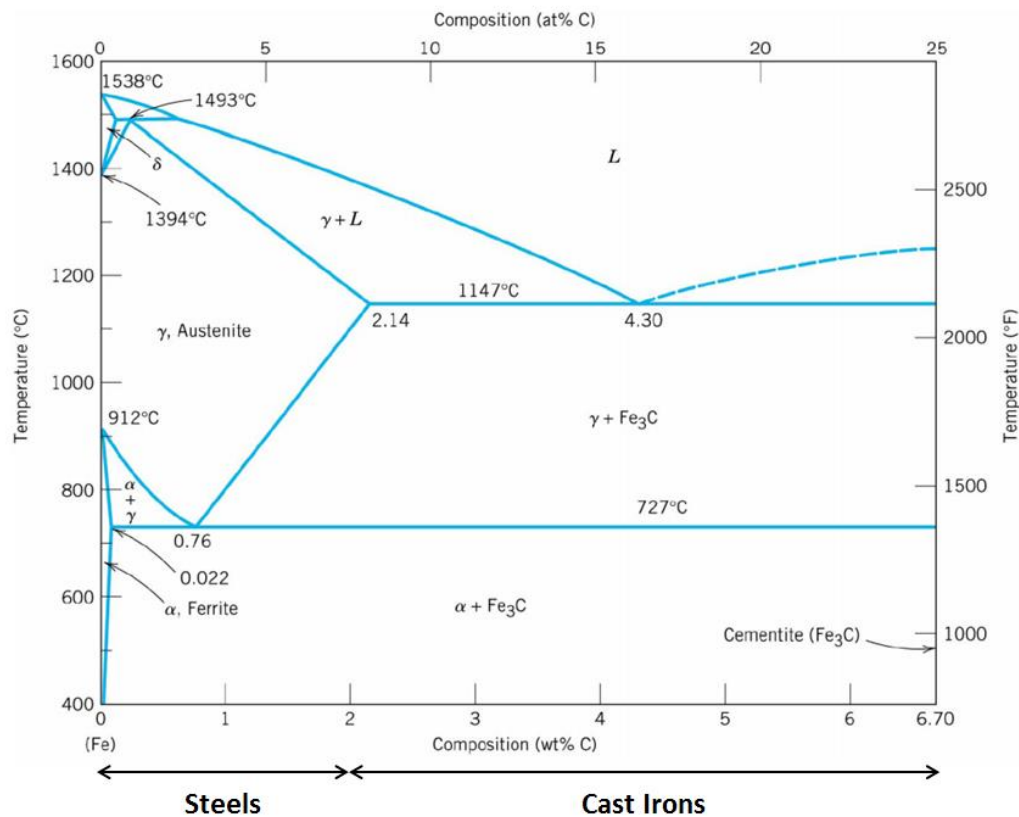


Figure 1-9: The iron-carbon phase diagram showing the distinction between steels and cast irons as a function of carbon content [15].

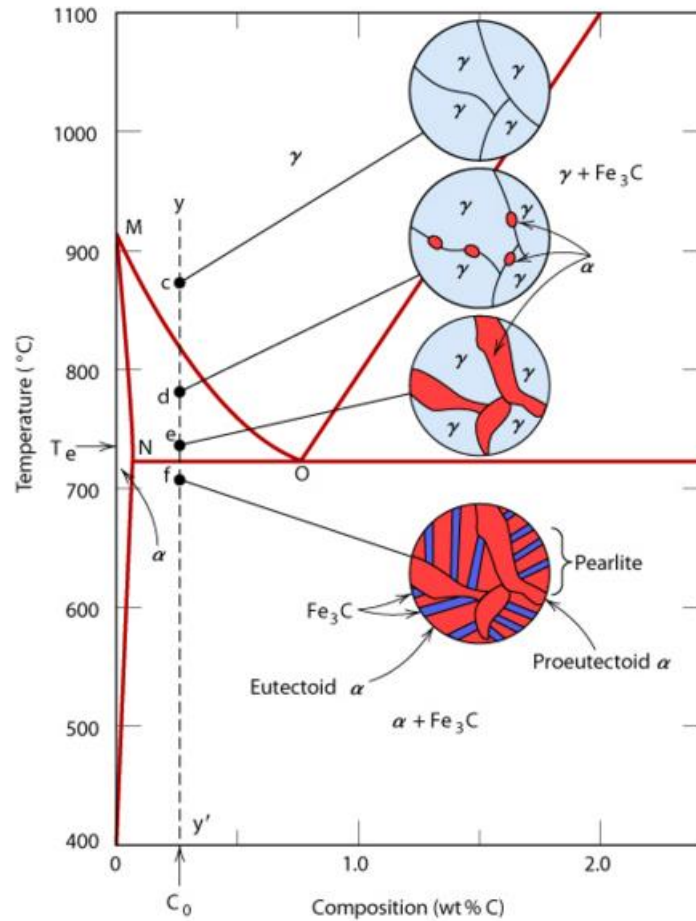


Figure 1-10: Illustration of the microstructures of a hypo-eutectoid steel (containing less than 0.76 wt% C) as it is cooled from the austenite phase region to below the eutectoid temperature [15].

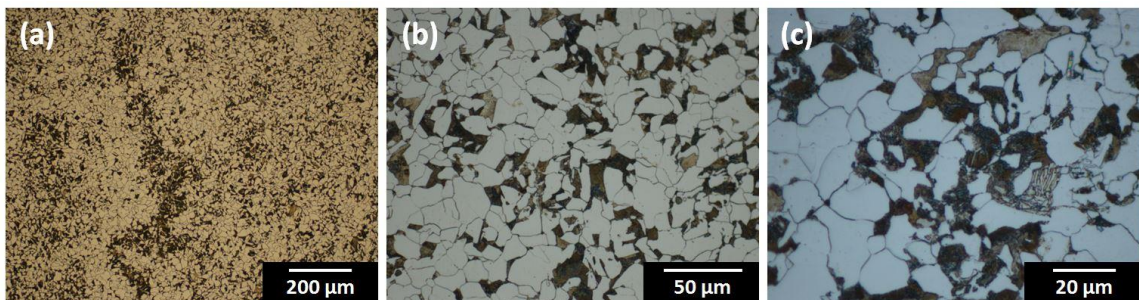


Figure 1-11: Optical images of the A516 Gr70 carbon steel used within this thesis showing grains of α -Fe (white) and pearlite (brown).

1.3.2. Iron Oxides

Fe based alloys have become so prevalent in construction materials due to the large abundance of Fe, the relative ease of alloying and fabrication techniques available, and the extreme versatility of their mechanical and physical properties [13]. However, the main downfall of Fe based alloys is their low corrosion resistance. Upon contact with aqueous media, Fe will corrode to produce a variety of oxides and hydroxides. The phase formed will depend on a multitude of factors including the pH, temperature, oxidant availability, and the ion content of the exposure environment. The following sections describe the properties of the oxide and hydroxide phases found to form in the studies presented in this thesis.

1.3.2.1. Magnetite (Fe_3O_4)

Magnetite is a black phase with an inverse spinel structure of mixed oxidation state and formula $Fe^{II}Fe^{III}_2O_4$, simplified to Fe_3O_4 [16, 17]. The inverse spinel consists of a cubic close-packed array of oxygen ions where the cations are located within the tetrahedral and octahedral interstices. The unit cell is FCC with 32 O^{2-} ions leaving 16 octahedral and eight tetrahedral locations for the Fe cations. In Fe_3O_4 the Fe^{III} ions occupy the tetrahedral locations along with half of the octahedral locations. The remaining eight octahedral locations are occupied by the Fe^{II} ions [18]. The resulting oxide is comprised of alternating layers of octahedra (Fe^{II}) and mixed octahedra/tetrahedra (Fe^{III}). The anti-parallel and unequal magnitude of the spins in these layers causes the ferrimagnetic properties of Fe_3O_4 [17]. In fact, Fe_3O_4 is the world's oldest known magnetic material.

1.3.2.2. Maghemite ($\gamma-Fe_2O_3$)

Maghemite ($\gamma-Fe_2O_3$) is a defect spinel structure which differs from Fe_3O_4 , and contains only the Fe^{III} oxidation state. The increased charge is compensated for by the random introduction of cation vacancies into the octahedral sites. As such, $\gamma-Fe_2O_3$ is often referred to as an Fe^{II} deficient form of Fe_3O_4 [17, 18]. The overall formula, Fe_2O_3 , is derived from a unit cell which contains 32 O^{2-} ions (as in Fe_3O_4), 21.3 Fe^{III} ions and 2.3 vacancies [17]. The γ -designation is used to distinguish the maghemite phase from that of hematite ($\alpha-Fe_2O_3$). Like Fe_3O_4 , $\gamma-Fe_2O_3$ is ferrimagnetic at room temperatures due to the location of Fe^{III} in both tetrahedral and octahedral sites. $\gamma-Fe_2O_3$ has been shown to form via transformation from other iron oxide states. In such cases the crystal structure of the produced $\gamma-Fe_2O_3$ is generally the same as that

of the oxide from which it formed. For example, oxidation of Fe_3O_4 results in cubic or irregularly shaped particles while dehydroxylation of lepidocrocite ($\gamma\text{-FeOOH}$) will lead to the growth of thin and narrow crystals [17]. $\gamma\text{-Fe}_2\text{O}_3$ appears brown or brownish-red in colouring.

1.3.2.3. Akaganeite ($\beta\text{-FeOOH}$)

Akaganeite ($\beta\text{-FeOOH}$) is a polymorph of the iron oxyhydroxide grouping. It possesses a tetragonal unit cell structure with the O^{2-} and OH^- anions in a BCC array causing $\beta\text{-FeOOH}$ to be less dense than either α - or $\gamma\text{-FeOOH}$ [17, 19]. The Fe^{III} cations occupy octahedral locations. The structure of $\beta\text{-FeOOH}$ is composed of double chains of edge-shared octahedra which share corners with adjacent chains. This gives rise to a 3D structure, Figure 1-12, which contains tunnels confined by rows of octahedra [17, 19]. Occupation of these tunnels by chloride ions aids in their stabilization. Removal of the chloride ions has been shown to induce transformation to goethite ($\alpha\text{-FeOOH}$) or $\alpha\text{-Fe}_2\text{O}_3$ [17]. As such, akaganeite is only formed in chloride containing environments. $\beta\text{-FeOOH}$ is paramagnetic at room temperature but becomes antiferromagnetic below 290 K (however this temperature has been known to change based on synthesis conditions) [17]. $\beta\text{-FeOOH}$ is yellow-brown in appearance.

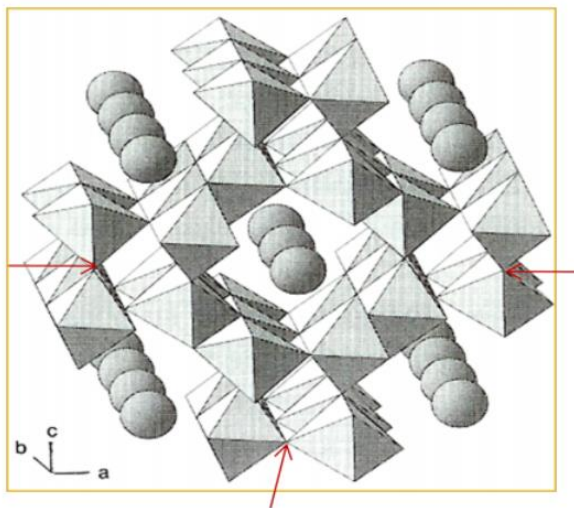


Figure 1-12: Illustrative representation of the akaganeite tunnel structure. Triangular prisms represent the edge-sharing octahedra while the spheres are the Cl^- ions which stabilize the tunnels [17].

1.3.2.4. *Lepidocrocite (γ -FeOOH)*

A second iron oxyhydroxide polymorph, lepidocrocite (γ -FeOOH), has an orthorhombic unit cell where the O^{2-} and OH^- anions are located in cubic close-packed (CCP) arrays and the Fe^{III} ions are found within the octahedral interstitial spaces. While both β -FeOOH and γ -FeOOH are formed from double chain octahedra of $Fe(O,OH)_6$, γ -FeOOH forms corrugated sheets of octahedra separated by empty octahedral locations rather than a tunnel structure like β -FeOOH [17]. On the macroscale, γ -FeOOH generally forms tabular crystal morphologies. However, slow crystal growth or high temperatures have been shown to lead to the formation of long and narrow crystal structures while rapid precipitation has led to thin, crumpled sheets [17]. γ -FeOOH is paramagnetic at room temperature and due to the layered structure antiferromagnetic below 77 K, which is much lower than any other iron oxide or hydroxide [17]. γ -FeOOH is yellow to orange in appearance.

1.3.2.5. *Green Rusts*

Green rusts (GRs) are Fe^{II} - Fe^{III} layered double-hydroxide compounds isostructural with pyroaurite ($Mg_6Fe_2(OH)_{16}CO_3$) and are made up of HCP sheets of $Fe^{II}(OH)_6$ octahedra exhibiting an $Fe(OH)_2$ structure. The substitution of Fe^{III} into the layers gives the structure a positive charge which is then balanced by anions located between the octahedral sheets [17, 20-22]. The most common anions found within GR are chloride (GR1) and sulphate (GR2), although halogens, carbonate, perchlorate and nitrate have also been seen [17]. In the absence of other anions it has been suggested that OH^- anions are found between the layer structures [23]. Due to the $Fe(OH)_2$ structure incorporated into the layers, GRs exist in the form of hexagonal platelets, are blue-green in colour, and a common corrosion product associated with high concentrations of Fe^{2+} [17].

1.3.2.6. *Ferrihydrite ($Fe_5O_7(OH) \cdot 4H_2O$)*

Synthetic and natural ferrihydrite are poorly ordered with two forms being reported, 2-line and 6-line, due to their XRD pattern which give 2 or 6-8 reflections as the structural order increases [17]. Due to the poor ordering of ferrihydrite and the inability to separate the OH and adsorbed H_2O within the structure, an exact formula is not yet agreed upon. Several groups report a structure of $Fe_5O_7(OH) \cdot 4H_2O$ for the bulk formula [24-26]. Music et al. [25] report a hexagonal crystal system for the ferrihydrite structure. Ferrihydrite is characterized by small crystal sizes

and low structural order. However, the higher ordered 6-line ferrihydrite has been shown to appear with a hexagonal structure [17]. The 2-line ferrihydrite easily transforms into either α -FeOOH or α -Fe₂O₃ in water at room temperatures [27]. Ferrihydrite ranges from pale to bright yellow, orange or brown-yellow in colour [16]. However, it is generally less yellow in hue than β -FeOOH, γ -FeOOH, and γ -Fe₂O₃ [17].

1.3.2.7. *Chukanovite (Fe₂(OH)₂CO₃)*

Chukanovite (Fe₂(OH)₂CO₃) is an iron hydroxycarbonate from the rosasite-malachite mineral group. It is composed of edge-sharing Fe octahedra forming ribbons interlinked via corner-shared locations to form corrugated octahedral layers. The carbonate groups are inserted within the structure which allows interlayer linking. Two octahedral Fe locations exist within the structure, one in which the Fe cation is coordinated to four oxygen atoms and two hydroxyl groups, and a second where the Fe is coordinated to four hydroxyl groups and two oxygen atoms. The former location is a larger octahedron with a higher level of distortion than the latter [28]. Chukanovite has been shown to grow as plate-like crystals during corrosion processes [29-31]. Saheb et al. [32] have shown that Fe₂(OH)₂CO₃ forms in carbonate rich anaerobic environments while work by Remazeilles et al. [33] showed its formation is dependent on the ratio of Fe²⁺ to both OH⁻ and CO₃²⁻ concentrations.

1.4. CORROSION OF CARBON STEEL IN AQUEOUS SYSTEMS

1.4.1. Corrosion under Disposal Conditions

1.4.1.1. *Evolution of the Waste Vault*

The corrosion behaviour of a steel container will be dependent on the environmental conditions to which it is exposed including: water saturation of the repository, temperature gradients, redox conditions, pore-water chemistry, microbial activity, mass transport, residual stress and external loads, and gas transport mechanism. Generally, the repository environment will evolve such that corrosion of the container will become less severe over time, with possible short term localized corrosion processes eventually giving way to uniform corrosion [6]. Initially, when the container temperature is high, the repository will contain insufficient moisture to support container corrosion. However, as the temperature at the container surface begins to decrease and the relative humidity increases, the deliquescence of salt deposits will allow corrosion to

begin. While the supply of H₂O will initially be rate-limiting, the DGR will eventually become fully saturated and corrosion will progress in a continuous aqueous phase. It has been estimated that saturation of the DGR in a sedimentary clay environment could take 100's to 1000's of years due to the low permeability of the host rock [4, 6]. The low hydraulic conductivity of the sedimentary host rock may even push saturation times to tens of thousands of years [34].

Initially, the DGR redox conditions will be oxidizing due to O₂ trapped during the sealing process. Over time this O₂ will be consumed by the corrosion of the container, microbial activity, and the oxidation of Fe^{II} and other oxidizable minerals. It is generally accepted that this aerobic phase will last 10's of years to a maximum of 100-200 years [4, 6, 35]. Because the processes of water saturation and O₂ consumption are occurring at the same time, the extent of steel corrosion will be dictated by the transition between these phases. Should the O₂ be consumed at a rate faster than the establishment of saturated conditions, the corrosion of the steel should proceed in a uniform manner with relatively low corrosion rates. However, if saturation were to occur quickly, a period of saturated, aerobic conditions would be established. Under these conditions three exposure phases, based on the evolution of the repository temperature, saturation, and redox conditions, can be defined:

1. An aerobic, unsaturated vapour phase
2. An aerobic, saturated aqueous phase or an anaerobic, unsaturated vapour phase
3. An anaerobic, saturated aqueous phase

Figure 1-13 highlights the evolution of the DGR environment as a function of the saturation [6]. Additionally, the chemistry of the pore-water will evolve over time. Initially, the chemistry will be determined by the nature of the water used to saturate the bentonite back-fill material and the content of the mineral impurities of the clay. King [6] describes the evolution in pore-water chemistry as follows;

1. Dissolution of soluble mineral impurities in the water used for wetting of the sealing materials.
2. Ion exchange with the bentonite, resulting in the uptake of Ca²⁺ and the release of Na⁺ ions.
3. Precipitation of the least soluble minerals as water is driven away from the container by the thermal gradient.

4. Buffering of the pore-water pH by calcite in the range 7-8.
5. Dissolution of minerals as the sealing materials re-wet, starting with the most soluble species.
6. Full saturation of the sealing materials.

Over time, the pore-water will equilibrate with the surrounding groundwater which is expected to be highly saline at the proposed depth of a repository in the reference Michigan Basin host environment.

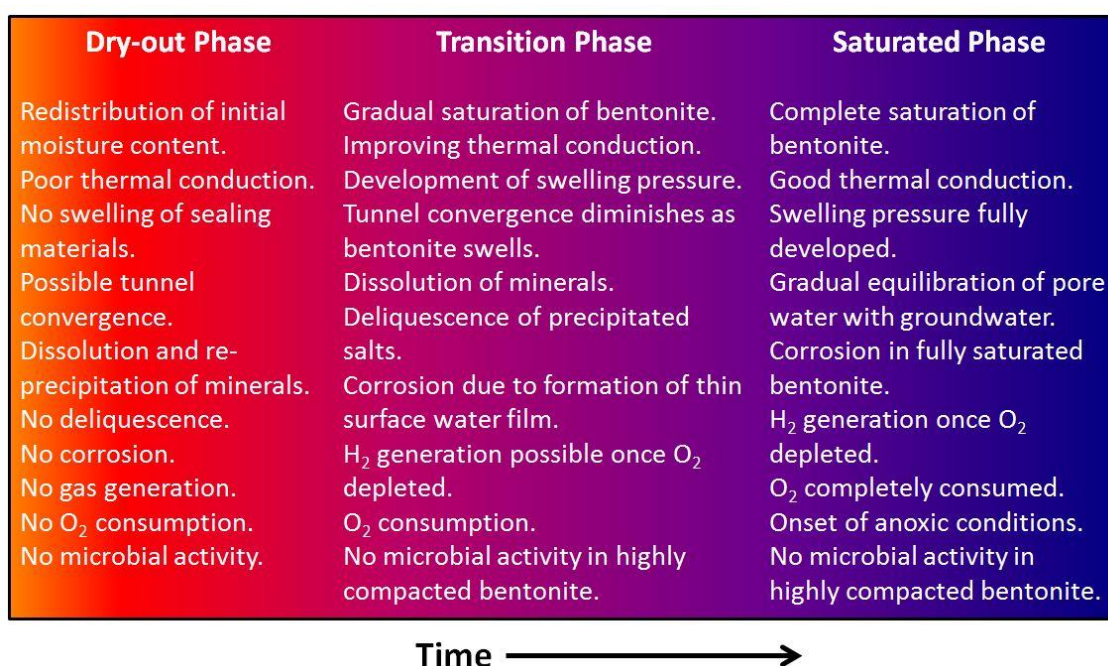


Figure 1-13: Evolution of the environmental conditions expected within a DGR as a function of the stage of saturation. Overlaid colours represent the transition over time of the temperature from hot to cool [6].

1.4.1.2. *Steel Corrosion under Nuclear Waste Disposal Conditions*

In the initial aerobic, unsaturated conditions there will be insufficient moisture to support corrosion. Under the anaerobic conditions in phase 3 (section 1.4.1.1), the steel container will corrode indefinitely in contact with the groundwater, Figure 1-2. King and Kolar [34] have developed a model for the anaerobic corrosion of carbon steel used fuel containers in sedimentary host rock in order to predict long-term container lifetimes. Since the corrosion behaviour will depend on the establishment of saturated conditions in the repository, a reference time for full saturation of 10,000 years was assumed in the initial model calculations. Figure 1-14 shows the evolution of the corrosion rate divided into four distinct stages. Stage (I) corresponds to the initial anaerobic, unsaturated phase in which no significant corrosion is expected to occur. In stage (II) the initial corrosion rate will be high due to dissolution of the base metal. However, the rate will decrease as protective surface films (assumed to be Fe_3O_4) form on the surface. This inhibiting effect dominates until Stage (III) when a minimum porosity of the Fe_3O_4 film is achieved and the corrosion rate begins to increase due to the continued saturation of the area surrounding the container. Beyond 10,000 years when full saturation has been achieved the corrosion rate decreases slowly as the container begins to cool. After 100,000 years, a steady state corrosion rate of ~ 0.1 $\mu\text{m}/\text{year}$ is established. Sensitivity analyses for the time until full saturation were also conducted and are presented in Figure 1-15. For the shortest time to full saturation of 1,000 years the corrosion rate was seen to be highest due to the increased temperature of the fuel container when wetting first occurs. Conversely, for a saturation time of 100,000 years the corrosion rate is shown to decrease due to the lower temperatures of the fuel container upon wetting. From these results it was predicted that fuel container failure would occur after 8,200 years, 19,500 years, and 190,000 years for saturation times of 1,000 years, 10,000 years, and 100,000 years, respectively, for a corrosion allowance of 2 cm.

The rates predicted by the model by King and Kolar [34] are similar to those measured on archaeological artefacts which are often used as long-term analogues for the corrosion behaviour of carbon steel in repository conditions.

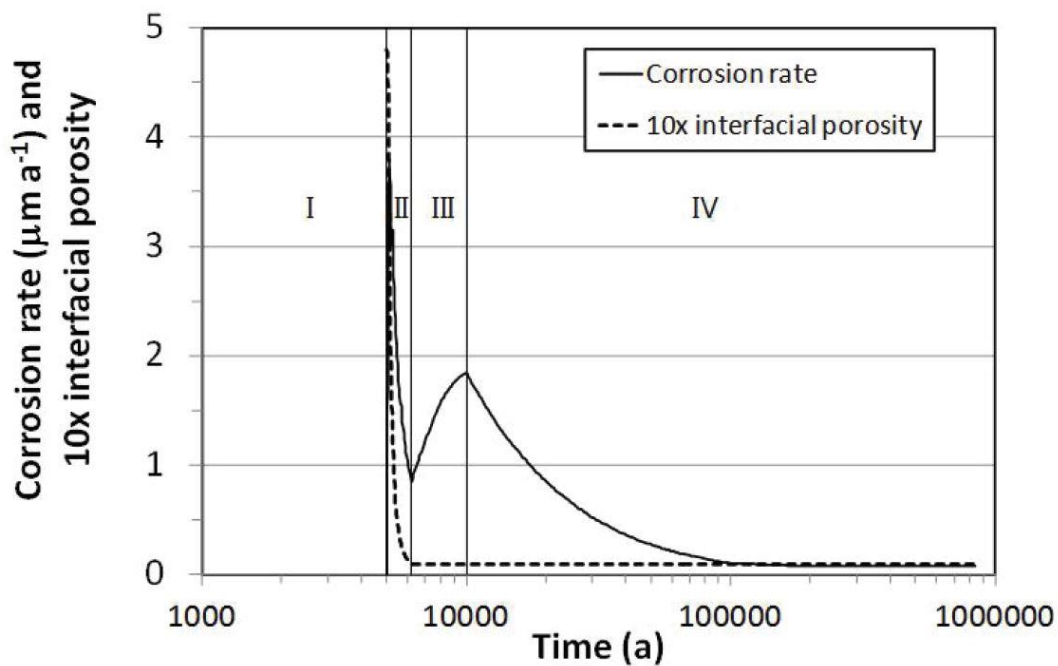


Figure 1-14: Corrosion rates as a function of time illustrating the evolution in the stages of corrosion for a reference time for full saturation of 10,000 years [34].

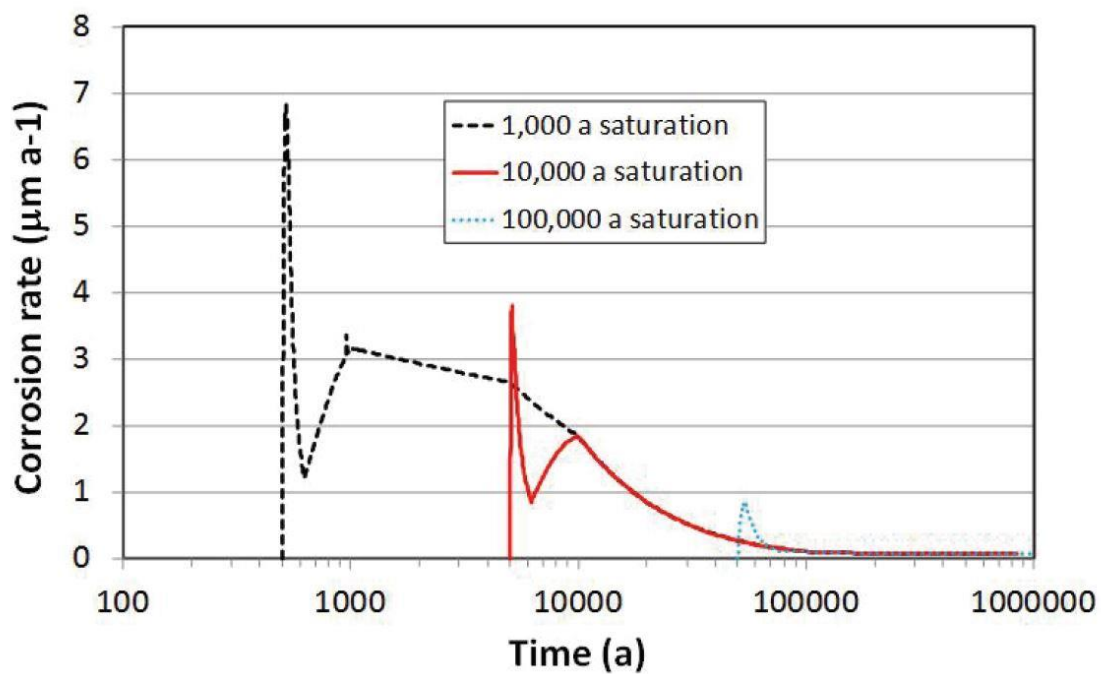
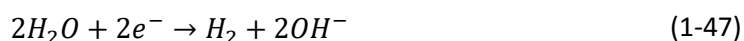


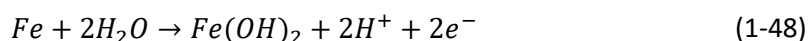
Figure 1-15: Effect of saturation time on the corrosion rate of the steel container [34].

1.4.2. The Role of Dissolved O₂

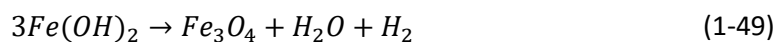
The anaerobic corrosion of carbon steel is thought to occur slowly due to the rate-limiting nature of the H₂O reduction reaction on the steel surface



The primary corrosion product of anaerobic steel corrosion is widely accepted to be Fe(OH)₂ according to the reaction 1-48.



However, Fe(OH)₂ is not considered to be either thermodynamically or kinetically stable [36], and as such will convert to other iron oxides/hydroxides depending on the redox conditions of the exposure environment. Figure 1-16 shows a general reaction scheme illustrating the differences in the corrosion products formed in anaerobic and slightly oxidizing conditions [36]. Under anaerobic conditions Fe(OH)₂ generally converts to Fe₃O₄ via the Schikorr reaction:



Increases in temperature and pH (Figure 1-2) also favour the formation of Fe₃O₄. However, in the presence O₂, Fe^{III} oxides/oxyhydroxides become the favoured corrosion product species. Increased levels of O₂ are seen to favour the formation of α-, β-, and γ-FeOOH while trace levels of O₂ are seen to cause the formation of mixed Fe^{II}/Fe^{III} green rusts (GRs). Under highly oxidizing conditions these species may oxidize further to α- or γ-Fe₂O₃. Mabuchi et al. [37] characterized the corrosion products formed over a range of [O₂] over a 4-day period. They showed that with increasing [O₂], the fraction of Fe^{III} phases increased with γ-Fe₂O₃ and subsequently α-Fe₂O₃ forming over a Fe₃O₄ base layer. Figure 1-16 also indicates that the Fe^{III} containing FeOOH phases can be reduced to Fe₃O₄ under reducing conditions in the presence of excess Fe²⁺. Ishikawa et al. [38] showed that the ease of reduction of the FeOOH species to Fe₃O₄ was in the order β-FeOOH > γ-FeOOH >>> α-FeOOH. As such, it would appear that any FeOOH corrosion products that may be formed on the steel container due to the presence of trace levels of O₂ will be reduced to Fe₃O₄ as conditions become progressively more anoxic with time [36].

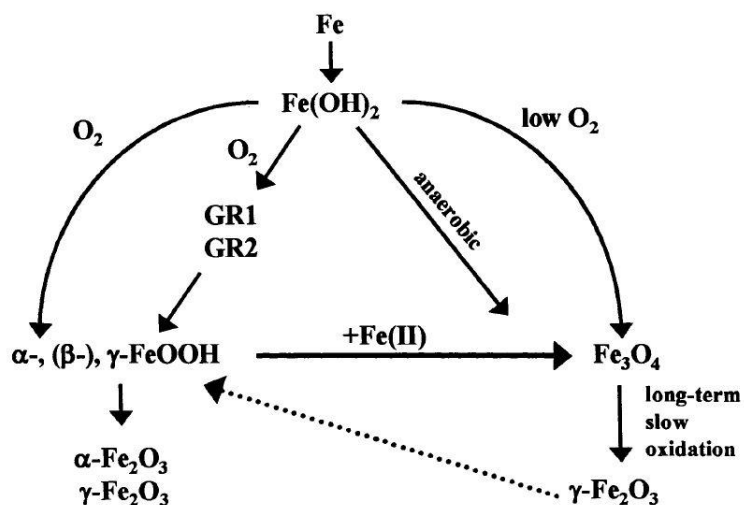


Figure 1-16: General reaction scheme for iron corrosion product films formed in oxidizing and reducing conditions [36].

1.4.3. The Role of Groundwater Anions

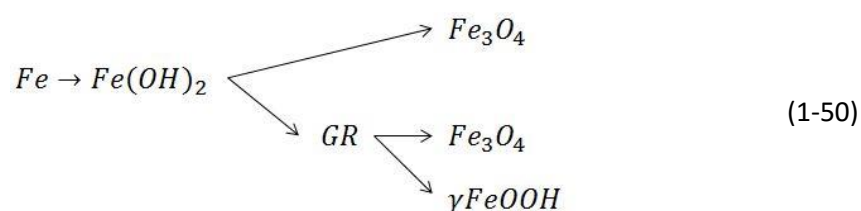
The groundwaters of the sedimentary clay DGR are expected to be highly saline and to contain anions such as $\text{HCO}_3^-/\text{CO}_3^{2-}$ and SO_4^{2-} . Some anion species, such as $\text{HCO}_3^-/\text{CO}_3^{2-}$, are known to increase the stability of Fe^{II} species while others, such as Cl^- , are thought to stabilize Fe^{III} species [36]. Consequently, the products formed on the steel container surface are expected to have a complex dependence on the dissolved $[\text{O}_2]$, pH, and anion content of the solution.

1.4.3.1. The Effects of Chloride

Several authors have previously shown that Cl^- has the ability to accelerate the conversion of Fe^{2+} to Fe^{3+} in the presence of trace O_2 [39-49]. Kurimura et al. [43] proposed that this oxidation was catalyzed by chelation and could be facilitated by a ligand bridging mechanism involving Cl^- as observed for the oxidation of Cr^{2+} to Cr^{3+} [50]. Figure 1-16 shows that in the presence of trace O_2 , GRs can form as intermediate corrosion products. However, in addition to further oxidation to produce FeOOH species, GR is also metastable with respect to Fe_3O_4 at pH values greater than 5 (as expected for DGR groundwaters) making Fe_3O_4 a likely conversion product of GRs via dehydration and oxidation [51]. In the presence of high $[\text{Cl}^-]$, an excess of Cl^- may be incorporated into the GR structure leading to further oxidation of Fe^{II} to Fe^{III} in order for the

structure to remain neutral. This increase in the Cl^- to Fe ratio is seen to cause the formation of $\gamma\text{-FeOOH}$ [46, 51-55].

Refait and Genin [46] studied the effect of Cl^- to OH^- ratios on the distribution of iron corrosion products. They observed that an increase in the $[\text{Cl}^-]$ of the exposure environment favoured the formation of $\gamma\text{-FeOOH}$ at the expense of Fe_3O_4 . Taylor [56] suggested that this effect was due to the preferential adsorption of Cl^- over OH^- at the Fe surface which would hinder the formation of Fe_3O_4 . Therefore, it would appear that a competition exists between the formation of Fe_3O_4 at low $[\text{Cl}^-]$ and the formation of $\gamma\text{-FeOOH}$ at high $[\text{Cl}^-]$, equation 1-50.



Furthermore, at extremely high $[\text{Cl}^-]$ the increased Cl^- intercalation into a GR structure has been shown to cause preferential oxidation to $\beta\text{-FeOOH}$ rather than $\gamma\text{-FeOOH}$ [52]. This is not surprising as $\beta\text{-FeOOH}$ is known to only form in Cl^- containing environments. The Cl^- anion is incorporated into the FeOOH structure which aids in stabilization of the octahedral tunnels, Figure 1-12.

1.4.3.2. *The Effects of Bicarbonate/Carbonate*

The presence of $\text{HCO}_3^-/\text{CO}_3^{2-}$ has been shown to accelerate both the anodic and cathodic reactions involved in corrosion. Acceleration of the cathodic reaction is due to the increased availability of H^+ from the dissociation of HCO_3^- while the acceleration of the anodic reaction is due to stabilization of Fe^{2+} species through complexation to form species such as FeHCO_3^+ , $\text{Fe}(\text{HCO}_3)_2$, and $\text{Fe}(\text{CO}_3)_2^{2-}$ [57-64]. Additionally, an increase in the $\text{HCO}_3^-/\text{CO}_3^{2-}$ content of the exposure environment is shown to favour CO_3^{2-} containing corrosion products [59]. Depending on the conditions, siderite (FeCO_3) is known to form competitively with chukanovite ($\text{Fe}_2(\text{OH})_2\text{CO}_3$) [32, 65-67]. FeCO_3 is known to be the major corrosion product formed on steel pipelines exposed to groundwater saturated soils [68]. $\text{Fe}_2(\text{OH})_2\text{CO}_3$ has been found as a corrosion product of steel in oxygen-poor clay environments such as those expected within the

DGR [31, 32, 59, 65, 69-75]. Previous authors have shown that high $[\text{Fe}^{2+}]$, moderate $[\text{HCO}_3^- / \text{CO}_3^{2-}]$, and slightly alkaline pH will promote the formation of $\text{Fe}_2(\text{OH})_2\text{CO}_3$ over FeCO_3 [31, 33, 59, 67, 71, 73, 76]. Observation of the Pourbaix diagram for Fe in $\text{HCO}_3^- / \text{CO}_3^{2-}$ containing environments shows that $\text{Fe}_2(\text{OH})_2\text{CO}_3$ is favoured in slightly alkaline conditions but that it is metastable with respect to FeCO_3 , Figure 1-17. Consequently, it is possible that over extended periods of time $\text{Fe}_2(\text{OH})_2\text{CO}_3$ may thermodynamically convert to FeCO_3 . This is consistent with the observation of inner $\text{Fe}_2(\text{OH})_2\text{CO}_3$ layers and outer FeCO_3 layers found on archaeological artefacts exposed to anoxic carbonated groundwaters [32, 33, 59, 65, 67, 77].

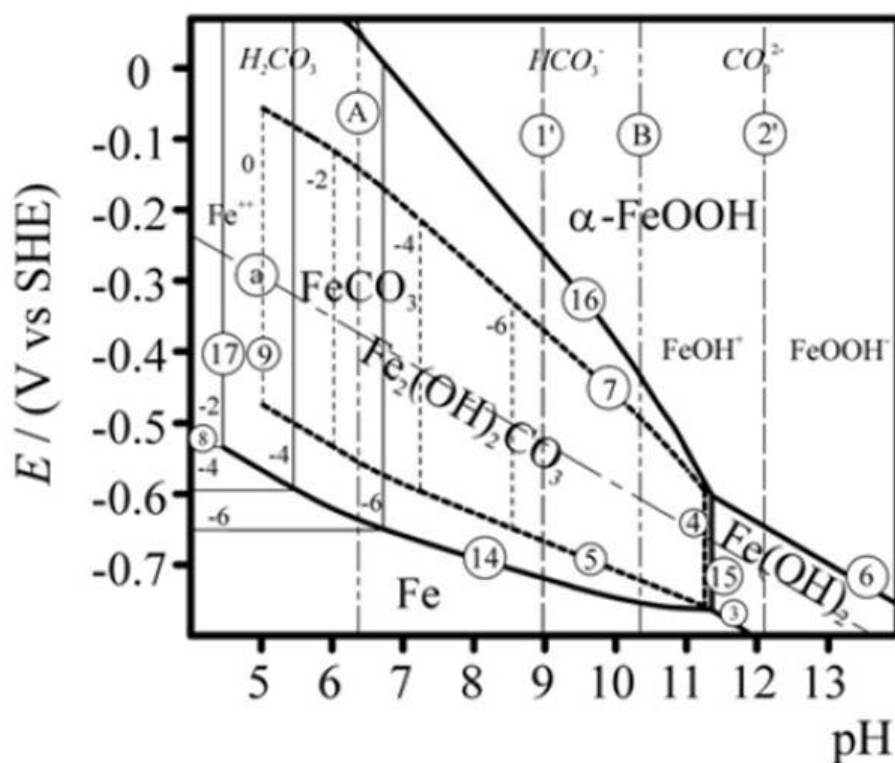


Figure 1-17: Pourbaix diagram of iron in carbonate containing aqueous media at 25°C for equilibria involving $\text{Fe}_2(\text{OH})_2\text{CO}_3$ (dotted lines) and FeCO_3 (solid lines) [67].

1.4.3.3. *The Effects of Sulphate*

Previous studies of the effects of SO_4^{2-} on the corrosion of carbon steel suggest that SO_4^{2-} is an aggressive anion towards steel corrosion in anoxic and alkaline environments [59, 78-85]. Zhu et al. [85] suggest that this is due to the loss of protective oxides due to an accelerated dissolution caused by replacement of adsorbed OH^- ions by SO_4^{2-} leading to a situation in which a small anode is coupled to a large cathode. Others have attributed its aggressiveness to an increase in solution conductivity [86] or to the formation of complexes with iron such as those observed in the case of $\text{HCO}_3^-/\text{CO}_3^{2-}$ [79]. Furthermore, several studies have shown that carbon steel is susceptible to localized pitting events in the presence of SO_4^{2-} [81, 84, 85]. However, these studies were performed in solutions containing HCO_3^- with only little Cl^- which may have changed the behaviour of the steel in comparison to if it had been exposed to SO_4^{2-} only.

1.5. THESIS OBJECTIVES

The overall goal of this thesis was to investigate the corrosion behaviour of A516 Gr70 carbon steel in a variety of solutions containing the species anticipated in the groundwater of a sedimentary clay DGR. In particular, the effects of groundwater anions such as Cl^- , $\text{HCO}_3^-/\text{CO}_3^{2-}$, and SO_4^{2-} on the corrosion behaviour and corrosion product compositions and morphologies were studied. In addition, the effects of trace levels of O_2 were studied in order to investigate how corrosion might progress if saturated conditions are achieved before all the available O_2 has been consumed. The overall thesis objectives are:

- To determine whether corrosion on the inside of a failed container is influenced by water radiolysis products produced by the radioactive decay processes occurring in the fuel waste form.
- To study the effects of $\text{HCO}_3^-/\text{CO}_3^{2-}$ and SO_4^{2-} in highly concentrated Cl^- solutions on the corrosion behaviour of A516 Gr70 carbon steel under anoxic and near anoxic conditions.
- To identify the corrosion products formed on the steel surface after exposure to solutions with different compositions.
- To develop a long term understanding of the evolution of the corrosion behaviour of A516 Gr70 carbon steel in highly concentrated Cl^- solutions under conditions expected in sedimentary clay groundwaters.

1.6. THESIS SUMMARY

This thesis describes the application of electrochemical and surface analysis techniques to determine the corrosion behaviour of carbon steel as applied to nuclear waste storage containers.

Electrochemical methods used included the measurement of corrosion potentials (E_{CORR}) over periods ranging from 14 to 60 days, linear polarization resistance (LPR) measurements to provide insight into the steel corrosion rates, and electrochemical impedance spectroscopy (EIS) to characterize the corroding interface. Surface analytical techniques were used to characterize the composition and morphology of the corrosion product films. Raman spectroscopy and infrared spectroscopy (FTIR) were used to identify the corrosion product deposits formed during exposure to the various environments. Scanning electron microscopy (SEM) was used to determine the morphology of the surface films while focused ion beam (FIB) milling was used to cross-section the corrosion films and determine the influence of corrosion on the steel surface. Energy dispersive X-ray (EDX) spectroscopy was used to determine the elemental composition of the corrosion products.

Chapter 2 briefly outlines the electrochemical and surface analytical techniques used as well as the experimental designs.

In Chapter 3 the influence of H_2O_2 on the corrosion of carbon steel was investigated under deaerated conditions, when traces of dissolved O_2 could be present, and under anaerobic conditions, when the $[\text{O}_2]$ would be expected to be at the ppb level. The goal of this chapter was to determine whether or not H_2 and Fe^{2+} produced from steel corrosion will be continuously produced inside a failed container and available to scavenge radiolytically produced H_2O_2 thereby suppressing fuel corrosion.

In Chapter 4 the effects of Cl^- along with $\text{HCO}_3^-/\text{CO}_3^{2-}$ and SO_4^{2-} in highly concentrated Cl^- solutions were investigated under deaerated conditions when trace levels of O_2 are present. A series of E_{CORR} and R_p measurements were performed in solutions containing increasing concentrations of Cl^- as well as solutions containing 5.0 M Cl^- with increasing concentrations of $\text{HCO}_3^-/\text{CO}_3^{2-}$ or SO_4^{2-} . This chapter describes the possible consequences should the saturation of the DGR environment occur before all of the initial O_2 is consumed.

In Chapters 5 and 6 the effects of $[\text{Cl}^-]$ and $\text{HCO}_3^-/\text{CO}_3^{2-}$ on the corrosion behaviour of carbon steel, specifically the corrosion product identity and morphology, under totally anaerobic conditions was investigated. Four exposure solutions were developed: (i) a low $[\text{Cl}^-]$; (ii) a high $[\text{Cl}^-]$; (iii) a high $[\text{Cl}^-]$ buffered by $\text{HCO}_3^-/\text{CO}_3^{2-}$; (iv) a simulated sedimentary clay groundwater. Chapter 5 focused on the electrochemical behaviour of carbon steel exposed to each of the four exposure solutions by E_{CORR} and R_p measurements over extended 60 day periods. This chapter describes the effect of groundwater composition on the anodic and cathodic reaction kinetics.

Chapter 6 focused on the evolution in corrosion product identities and morphologies over long-term periods of exposure (up to 30 months). A series of 16 steel coupons were exposed to each of the four exposure solutions and removed at periodic intervals to track the evolution in the corrosion products. A combination of surface analysis techniques were used to identify the corrosion products and observe their morphologies.

Chapter 7 summarizes the results and conclusions of the current project as applied to the use of carbon steel containers for the long-term disposal of spent Canadian nuclear fuel in sedimentary clay environments.

1.7. REFERENCES

- [1] OPG, "Nuclear power" (2016) <http://www.opg.com/generating-power/nuclear/Pages/nuclear.aspx> (Accessed March 3, 2016)
- [2] CNSC, "Nuclear power plants" (2016) <https://www.cnsccsn.gc.ca/eng/reactors/power-plants/index.cfm> (Accessed March 10, 2016)
- [3] M. Garamszeghy "Nuclear fuel waste projections in Canada - 2015 update" Nuclear Waste Management Organization Report No. NWMO-TR-2015-19 (2015)
- [4] J. McMurry, B. M. Ikeda, S. Stroes-Gascoyne and D. A. Dixon "Evolution of a Canadian geologic repository: Defective container scenario" Atomic Energy of Canada Ltd. Report No. 06819-REP-01200-10127-R00 (2004)
- [5] R. S. Read "The role of rock engineering in developing a deep geological repository in sedimentary rock" Nuclear Waste Management Organization Report No. NWMO TR-2008-16 (2008)
- [6] F. King "Overview of a carbon steel container corrosion model for a deep geological repository in sedimentary rock" Nuclear Waste Management Organization Report No. NWMO TR-2007-01 (2007)
- [7] J. Read "Deep geological repository design report: Sedimentary rock environment copper used fuel container" Nuclear Waste Management Organization Report No. APM-REP-00440-0002 (2011)
- [8] NACE "Corrosion basics: An introduction" National Association of Corrosion Engineers, Houston, TX, (1984)

- [9] M. Pourbaix "Atlas of electrochemical equilibria in aqueous solutions" Pergamon Press Ltd. , Bristol, **(1966)**
- [10] D. Shoesmith "Kinetics of aqueous corrosion" ASM Handbook Corrosion: Fundamentals, testing, and protection, 13A (42-51) ASM International **(2003)**
- [11] S. H. Avner "Introduction to physical metallurgy" McGraw-Hill Inc. , New York, **(1964)**
- [12] H. K. D. H. Bhadeshia and R. Honeycombe "Steels: Microstructure and properties" Elsevier Ltd., Oxford, UK, **(2006)**
- [13] W. D. Callister and D. G. Rethwisch "Types and applications of materials in fundamentals of materials science: An integrated approach" John Wiley & Sons, Hoboken, NJ, **(2008)**
- [14] J. L. Dossett and H. E. Boyer "Practical heat treating" ASM International, Ohio, USA, **(2006)**
- [15] W. D. Callister "Materials science and engineering: An introduction" John Wiley & Sons, New York, **(2007)**
- [16] J. W. Anthony, R. A. Bideaux, K. W. Blahd and M. C. Nichols "Handbook of mineralogy: Halides, hydroxides, oxides" Mineral Data Publishing, Tucson, AZ, Vol. 3. **(1997)**
- [17] R. M. Cornell and U. Schwertmann "The iron oxides: Structure, properties, reactions, occurrences, and uses" Wiley-VCH GmbH & Co. KGaA, Weinheim, Germany, **(2003)**
- [18] A. J. Davenport, L. J. Oblonsky, M. P. Ryan and M. F. Toney "The structure of the passive film that forms on iron in aqueous environments" *Journal of the Electrochemical Society* 147 (6) **(2000)** 2162-2173
- [19] R. Parameshwari, G. Priyadarshini and G. Chandrasekaran "Optimization, structural, spectroscopic and magnetic studies on stable akaganeite nanoparticles via co-precipitation method" *American Journal of Materials Science* 1 (1) **(2011)** 18-25
- [20] G. W. Brindley, D. L. Bish and A. L. Mackay "Green rust: A Pyroaurite type structure" *Nature* 263 (5575) **(1976)** 353
- [21] R. M. Taylor and R. M. Mckenzie "The influence of aluminum on iron-oxides. VI. The formation of Fe(II)-Al(III) hydroxy-chlorides, -sulfates, and -carbonates as new members of the pyroaurite group and their significance in soils" *Clays and Clay Minerals* 28 (3) **(1980)** 179-187
- [22] P. Refait and J. M. R. Genin "Mechanisms of oxidation of Ni(II)-Fe(II) hydroxides in chloride-containing aqueous media: Role of the pyroaurite-type Ni-Fe hydroxychlorides" *Clay Minerals* 32 (4) **(1997)** 597-613
- [23] F. Trolard, J. M. R. Genin, M. Abdelmoula, G. Bourrie, B. Humbert and A. Herbillon "Identification of a green rust mineral in a reductomorphic soil by Mossbauer and Raman spectroscopies" *Geochimica et Cosmochimica Acta* 63 (5) **(1997)** 1107-1111
- [24] J. L. Jambor and J. E. Dutrizac "Occurrence and constitution of natural and synthetic ferrihydrite, a widespread iron oxyhydroxide" *Chemical Reviews* 98 (7) **(1998)** 2549-2585
- [25] S. Music, M. Gotic and S. Popovic "X-Ray-diffraction and Fourier transform-infrared analysis of the rust formed by corrosion of steel in aqueous solutions" *Journal of Materials Science* 28 (21) **(1993)** 5744-5752
- [26] K. M. Towe and W. F. Bradley "Mineralogical constitution of colloidal 'hydrous ferric oxides'" *Journal of Colloid and Interface Science* 24 **(1967)** 384-392
- [27] U. Schwertmann and R. M. Cornell "Iron oxides in the laboratory: Preparation and characterization" Wiley-VCH Verlag GmbH, Weinheim, Germany, **(2000)**
- [28] I. V. Pekov, N. Perchiazzi, S. Merlini, V. N. Kalachev, M. Merlini and A. E. Zadov "Chukanovite, $\text{Fe}_2(\text{CO}_3)(\text{OH})_2$, a new mineral from the weathered iron meteorite Dronino" *European Journal of Mineralogy* 19 **(2007)** 891-898

- [29] A. S. Ruhl, C. Kotre, U. Gernert and M. Jekel "Identification, quantification and localization of secondary minerals in mixed FeO fixed bed reactors" *Chemical Engineering Journal* 172 (2011) 811-816
- [30] Y. Yang, G. R. Joshi and R. Akid "Electrochemical investigation of the corrosion of different microstructural phases of X65 pipeline steel under saturated carbon dioxide conditions" *Materials* 8 (2015) 2635-2649
- [31] V. Pandarinathan, K. Lepkova and W. van Bronswijk "Chukanovite ($\text{Fe}_2(\text{OH})_2\text{CO}_3$) identified as a corrosion product at sand-deposited carbon steel in CO_2 -saturated brine" *Corrosion Science* 85 (2014) 26-32
- [32] M. Saheb, D. Neff, P. Dillmann, H. Matthiesen and E. Foy "Long term corrosion behavior of low-carbon steel in anoxic environment: Characterisation of archaeological artefacts" *Journal of Nuclear Materials* 379 (1-3) (2008) 118-123
- [33] C. Remazeilles and P. Refait "Fe(II) hydroxycarbonate $\text{Fe}_2(\text{OH})_2\text{CO}_3$ (Chukanovite) as iron corrosion product: Synthesis and study by Fourier transform infrared spectroscopy" *Polyhedron* 28 (4) (2009) 749-756
- [34] F. King and M. Kolar "Simulation of the anaerobic corrosion of carbon steel used fuel containers using the steel corrosion model version 1.0 (SCM V1.0)" Nuclear Waste Management Organization Report No. NWMO TR-2012-07 (2012)
- [35] D. W. Shoesmith "Assessing the corrosion performance of high-level nuclear waste containers" *Corrosion* 62 (8) (2006) 703-722
- [36] F. King and S. Stroes-Gascoyne "An assessment of the long-term corrosion behaviour of C-steel and the impact on the redox conditions inside a nuclear fuel waste disposal container" Ontario Power Generation Report No. 06819-REP-01200-10028-R00 (2000)
- [37] K. Mabuchi, Y. Horii, H. Takahashi and M. Nagayama "Effect of temperature and dissolved-oxygen on the corrosion behavior of carbon-steel in high-temperature water" *Corrosion* 47 (7) (1991) 500-508
- [38] T. Ishikawa, Y. Kondo, A. Yasukawa and K. Kandori "Formation of magnetite in the presence of ferric oxyhydroxides" *Corrosion Science* 40 (7) (1998) 1239-1251
- [39] J. King and N. Davidson "Kinetics of the ferrous iron-oxygen reaction in acidic phosphate-pyrophosphate solutions" *Journal of the American Chemical Society* 80 (7) (1958) 1542-1545
- [40] H. Tamura, K. Goto and M. Nagayama "Effect of anions on oxygenation of ferrous ion in neutral solutions" *Journal of Inorganic & Nuclear Chemistry* 38 (1) (1976) 113-117
- [41] A. M. Posner "The kinetics of autoxidation of ferrous ions in concentrated HCl solutions" *Transactions of the Faraday Society* 49 (4) (1953) 382-388
- [42] W. Stumm and G. F. Lee "Oxygenation of ferrous iron" *Industrial and Engineering Chemistry* 53 (2) (1961) 143-146
- [43] Y. Kurimura, R. Ochiai and N. Matsuura "Oxygen oxidation of ferrous ions induced by chelation" *Bulletin of the Chemical Society of Japan* 41 (10) (1968) 2234-2239
- [44] R. P. Colborn and M. J. Nicol "Investigation into the kinetics and mechanism of oxidation of iron (II) by oxygen in aqueous chloride solutions" *Journal of the Southern African Institute of Mining and Metallurgy* 73 (9) (1973) 281-289
- [45] K. Porsch and A. Kappler "Fe^{II} oxidation by molecular O_2 during HCl extraction" *Environmental Chemistry* 8 (2) (2011) 190-197
- [46] P. Refait and J. M. R. Genin "The oxidation of ferrous hydroxide in chloride-containing aqueous media and Pourbaix diagrams of green rust one" *Corrosion Science* 34 (5) (1993) 797-819

- [47] F. M. Al-Kharafi, B. G. Ateya and R. M. Abdallah "Electrochemical behaviour of low carbon steel in concentrated carbonate chloride brines" *Journal of Applied Electrochemistry* 32 (12) **(2002)** 1363-1370
- [48] S. S. El-Egamy and W. A. Badaway "Passivity and passivity breakdown of 304 stainless steel in alkaline sodium sulphate solutions" *Journal of Applied Electrochemistry* 34 (11) **(2004)** 1153-1158
- [49] N. J. Laycock and R. C. Newman "Localised dissolution kinetics, salt films and pitting potentials" *Corrosion Science* 39 (10-11) **(1997)** 1771-1790
- [50] J. J. Ulrich and F. C. Anson "Ligand bridging by halide in electrochemical oxidation of chromium(II) at mercury electrodes" *Inorganic Chemistry* 8 (2) **(1969)** 195-200
- [51] R. M. Taylor "Influence of chloride on the formation of iron-oxides from Fe(II) chloride. II. Effect of [Cl] on the formation of lepidocrocite and its crystallinity" *Clays and Clay Minerals* 32 (3) **(1984)** 175-180
- [52] P. Refait and J. M. R. Genin "The mechanisms of oxidation of ferrous hydroxychloride beta-Fe₂(OH)₃Cl in aqueous solution: The formation of akaganeite vs goethite" *Corrosion Science* 39 (3) **(1997)** 539-553
- [53] U. Schwertmann and H. Fechter "The formation of green rust and its transformation to lepidocrocite" *Clay Minerals* 29 (1) **(1994)** 87-92
- [54] D. Rezel, P. Bauer and J. M. R. Genin "Superparamagnetic behavior and hyperfine interactions in ferrous hydroxide II and green rust I" *Hyperfine Interactions* 42 (1) **(1988)** 1075-1078
- [55] A. A. Olowe and J. M. R. Genin "The mechanism of oxidation of ferrous hydroxide in sulfated aqueous media: Importance of the initial ratio of the reactants" *Corrosion Science* 32 (9) **(1991)** 965-984
- [56] R. M. Taylor "Influence of chloride on the formation of iron-oxides from Fe(II) Chloride. I. Effect of [Cl]/[Fe] on the formation of magnetite" *Clays and Clay Minerals* 32 (3) **(1984)** 167-174
- [57] C. T. Lee, M. S. Odziemkowski and D. W. Shoesmith "An in situ Raman-electrochemical investigation of carbon steel corrosion in Na₂CO₃/NaHCO₃, Na₂SO₄, and NaCl solutions" *Journal of the Electrochemical Society* 153 (2) **(2006)** B33-B41
- [58] C. T. Lee, Z. Qin, M. Odziemkowski and D. W. Shoesmith "The influence of groundwater anions on the impedance behaviour of carbon steel corroding under anoxic conditions" *Electrochimica Acta* 51 (8-9) **(2006)** 1558-1568
- [59] P. Refait, J. A. Bourdoiseau, M. Jeannin, D. D. Nguyen, A. Romaine and R. Sabot "Electrochemical formation of carbonated corrosion products on carbon steel in deaerated solutions" *Electrochimica Acta* 79 **(2012)** 210-217
- [60] E. B. Castro, C. R. Valentini, C. A. Moina, J. R. Vilche and A. J. Arvia "The influence of ionic composition on the electrodisolution and passivation of iron electrodes in potassium carbonate-bicarbonate solutions in the 8.4-10.5 pH range at 25C" *Corrosion Science* 26 (10) **(1986)** 781-793
- [61] E. B. Castro, J. R. Vilche and A. J. Arvia "Iron dissolution and passivation in K₂CO₃-KHCO₃ solutions. Rotating-ring-disk electrode and XPS studies" *Corrosion Science* 32 (1) **(1991)** 37-50
- [62] B. W. A. Sherar, P. G. Keech, Z. Qin, F. King and D. W. Shoesmith "Nominally anaerobic corrosion of carbon steel in near-neutral pH saline environments" *Corrosion* 66 (4) **(2010)** 045001-1-045001-11
- [63] K. Videm and A. M. Koren "Corrosion, passivity, and pitting of carbon steel in aqueous-solutions of HCO₃⁻, CO₂, and Cl⁻" *Corrosion* 49 (9) **(1993)** 746-754

- [64] L. Legrand, S. Savoye, A. Chausse and R. Messina "Study of oxidation products formed on iron in solutions containing bicarbonate/carbonate" *Electrochimica Acta* 46 (1) **(2000)** 111-117
- [65] M. Saheb, D. Neff, L. Bellot-Gurlet and P. Dillmann "Raman study of a deuterated iron hydroxycarbonate to assess long-term corrosion mechanisms in anoxic soils" *Journal of Raman Spectroscopy* 42 (5) **(2011)** 1100-1108
- [66] M. Saheb, D. Neff, P. Dillmann, H. Matthiesen, E. Foy and L. Bellot-Gurlet "Multisecular corrosion behaviour of low carbon steel in anoxic soils: Characterisation of corrosion system on archaeological artefacts" *Materials and Corrosion* 60 (2) **(2009)** 99-105
- [67] I. Azoulay, C. Remazeilles and P. Refait "Determination of standard Gibbs free energy of formation of chukanovite and Pourbaix diagrams of iron in carbonated media" *Corrosion Science* 58 **(2012)** 229-236
- [68] B. W. A. Sherar "The effect of the environment on the corrosion products and corrosion rates on gas transmission pipelines" PhD Thesis, Department of Chemistry, The University of Western Ontario, **(2011)** 045001-1-045001-11
- [69] J. H. Dong, T. Nishimura and T. Kodama "Corrosion behavior of carbon steel in bicarbonate (HCO_3) solutions" *Scientific Basis for Nuclear Waste Management XXV*, 713, Boston, MA, Materials Research Society, **(2002)** 105-112
- [70] S. Music, I. Nowik, M. Ristic, Z. Orehovec and S. Popovic "The effect of bicarbonate/carbonate ions on the formation of iron rust" *Croatica Chemica Acta* 77 (1-2) **(2004)** 141-151
- [71] M. L. Schlegel, C. Bataillon, C. Blanc, D. Pret and E. Foy "Anodic activation of iron corrosion in clay media under water-saturated conditions at 90 degrees C: Characterization of the corrosion interface" *Environmental Science & Technology* 44 (4) **(2010)** 1503-1508
- [72] A. Romaine, R. Sabot, M. Jeannin, S. Necib and P. Refait "Electrochemical synthesis and characterization of corrosion products on carbon steel under argillite layers in carbonated media at 80 degrees C" *Electrochimica Acta* 114 **(2013)** 152-158
- [73] M. L. Schlegel, C. Bataillon, F. Brucker, C. Blanc, D. Pret, E. Foy and M. Chorro "Corrosion of metal iron in contact with anoxic clay at 90 degrees C: Characterization of the corrosion products after two years of interaction" *Applied Geochemistry* 51 **(2014)** 1-14
- [74] M. Ko, B. Ingham, N. Laycock and D. E. Williams "In situ synchrotron X-ray diffraction study of the effect of chromium additions to the steel and solution on CO_2 corrosion of pipeline steels" *Corrosion Science* 80 **(2014)** 237-246
- [75] M. Ko, B. Ingham, N. Laycock and D. E. Williams "In situ synchrotron X-ray diffraction study of the effect of microstructure and boundary layer conditions on CO_2 corrosion of pipeline steels" *Corrosion Science* 90 **(2015)** 192-201
- [76] S. Savoye, L. Legrand, G. Sagon, S. Lecomte, A. Chausse, R. Messina and P. Toulhoat "Experimental investigations on iron corrosion products formed in bicarbonate/carbonate containing solutions at 90 degrees C" *Corrosion Science* 43 (11) **(2001)** 2049-2064
- [77] Y. Leon, M. Saheb, E. Drouet, D. Neff, E. Foy, E. Leroy, J. J. Dynes and P. Dillmann "Interfacial layer on archaeological mild steel corroded in carbonated anoxic environments studied with coupled micro and nano probes" *Corrosion Science* 88 **(2014)** 23-35
- [78] K. Azumi and M. Seo "Corrosion behavior of titanium-clad carbon steel in weakly alkaline solutions" *Corrosion Science* 45 (2) **(2003)** 413-426

- [79] Y. Benamor, L. Bousselmi, H. Takenouti and E. Triki "Influence of sulphate ions on corrosion mechanism of carbon steel in calcareous media" *Corrosion Engineering Science and Technology* 40 (2) **(2005)** 129-136
- [80] E. M. Rus, I. Baldea and C. Calin "OLT-35 low carbon steel corrosion in presence of sulfate ions" *Studia Universitatis Babeş-Bolyai Chemia* 52 (3) **(2007)** 137-146
- [81] G. Vatankhah, M. Drogowska, H. Menard and L. Brossard "Electrodissolution of iron in sodium sulfate and sodium bicarbonate solutions at pH 8" *Journal of Applied Electrochemistry* 28 (2) **(1998)** 173-183
- [82] M. S. Rahman, S. Divi, D. Chandra and J. Daemen "Effect of different salts on the corrosion properties of friction type A607 steel rock bolt in simulated concentrated water" *Tunnelling and Underground Space Technology* 23 (6) **(2008)** 665-673
- [83] P. Smith, S. Roy, D. Swailes, S. Maxwell, D. Page and J. Lawson "A model for the corrosion of steel subjected to synthetic produced water containing sulfate, chloride and hydrogen sulfide" *Chemical Engineering Science* 66 (23) **(2011)** 5775-5790
- [84] K. Premllal, J. H. Potgieter and S. Sanja "Laser surface treatment to inhibit observed corrosion of reinforcing steel in sulphate: Alkaline media" *Anti-Corrosion Methods and Materials* 58 (5) **(2011)** 267-284
- [85] Z. Zhu, X. Jiao, X. Tang and H. Lu "Effects of SO_4^{2-} concentration on corrosion behaviour of carbon steels" *Anti-Corrosion Methods and Materials* 62 (5) **(2015)** 322-326
- [86] G. Singh "A survey of underground mine waters from Indian coal mines" *International Journal of Mine Waters* 5 (1) **(2006)** 21-32

Chapter 2

Experimental Techniques and Details

2.1. EXPERIMENTAL DESIGN

2.1.1. Electrochemical Cell and Equipment

All electrochemical experiments were conducted in a standard three-electrode, three-compartment glass cell. The cell was comprised of a main central chamber separated by glass frits from two side arms. The reference electrode was a commercial saturated calomel reference electrode (SCE, Fisher Scientific) placed in one side arm of the cell and connected to the main chamber by a Luggin capillary, the tip of which was placed just below the surface of the working electrode. All potentials throughout this thesis are reported on the SCE scale (+0.241 V vs. SHE). The counter electrode was a Pt sheet, spot welded to a Pt wire and housed in the second side arm of the cell. The cell was fitted with a glass gas dispersion tube with a fritted end used to deaerate the solution by sparging with Ar gas.

In bench-top experiments, the cell was housed within a grounded Faraday cage to minimize interference from external noise. For anaerobic experiments, the cell was placed in an anaerobic chamber to avoid the influx of atmospheric O₂. Experiments performed on the bench-top were run with a Solartron 1480 multistat running CorrWare™ software to control applied potentials and to record current responses. For experiments performed within the anaerobic chamber, a Solartron Analytical Modulab running Modulab XM ECS software was used.

2.1.2. A516 Gr70 Carbon Steel Working Electrode

All electrodes were fabricated from A516 Gr70 carbon steel (0.23 C; 1.11 Mn; 0.07 P; 0.03 S; 0.26 Si; 0.01 Cu; 0.01 Ni; 0.02 Cr; 0.004 Mo; 0.036 Al; 0.019 V; 0.003 O [wt.%], balance Fe). The steel coupons were first prepared by ultrasonication in ethanol and type 1 water to remove adhered contaminants from the steel surface. Once cleaned, coupons were mounted in a high-performance epoxy resin (Hysol EE 4190) with a single exposed flat face (0.7854 cm²). The connection between the electrode and the stainless steel rod used to connect the electrode to external measuring circuits was covered, first with laboratory film (Parafilm), and then with several layers of Teflon tape to prevent exposure of the connection to the electrolyte. Prior to each experiment, the electrode was wet polished with 180, 600, 800, 1000, and 1200 grit SiC

paper and rinsed with type 1 water before being placed directly into solution or into the anaerobic chamber.

2.1.3. Solution Preparation

All solutions were prepared using Type 1 water with a resistance of 18.2 MΩ.cm, purified using a Thermo Scientific Barnstead Nanopure Model 7143 filtration system to remove organic and inorganic impurities. Specific details of the composition of the electrolyte solutions used are provided in the individual experimental sections found in subsequent chapters. A Thermo Scientific Orion Star A211 pH meter was used to measure the pH before and after electrochemical measurements, with either a Thermo Scientific Orion 8104BNUWP or 9156DJWP pH electrode for the anaerobic chamber and benchtop measurements, respectively. For experiments performed on the bench-top, all solutions were deaerated at a high flow rate with ultra-high purity (UHP) Ar (Praxair) for at least 60 minutes prior to experimentation. Ar sparging was continued at a decreased flow rate throughout the duration of each experiment. For anaerobic experiments, the Type 1 water was sparged with UHP Ar at a high flow rate for at least 90 minutes prior to being sealed and transferred into the anaerobic chamber. The flask was sealed with the entire volume filled with the Ar sparged water to avoid any trapped air. Preparation of the solution was completed within the anaerobic chamber and no additional Ar sparging was necessary.

2.1.4. Anaerobic Exposure Experiments

A series of four exposure environments were examined to determine the effects of simulated groundwater, various chloride concentrations, and pH buffering on the corrosion behaviour of A516 Gr70 carbon steel. For each exposure environment, a total of 16 carbon steel coupons were prepared with dimensions of 1 cm x 1 cm x 0.5 cm. Each face of the steel coupon was polished with 180, 600, 800, 1000, and 1200 grit SiC paper and rinsed with type 1 water before being left exposed to air for one week to mimic the natural oxides which would form on the steel waste container surface before emplacement in a repository. Samples were then placed within sample slots on a specially designed Teflon sample holder housed within a 2 L beaker, Figure 2-1. All solutions were prepared as outlined for anaerobic experiments in section 2.1.3. The pH of the simulated groundwater and chloride solutions was set to 6.3 ± 0.5 using a Thermo Scientific Orion 8104BNUWP pH electrode connected to a Thermo Scientific Orion Star A211 pH

meter while for the buffered chloride solution the natural pH was maintained. Coupons were immersed in each of the exposure solutions and removed for analysis after exposure periods from two days to 30 months. Samples were analysed using a combination of Raman spectroscopy, infrared spectroscopy (FTIR), scanning electron microscopy (SEM), energy dispersive X-ray (EDX) spectroscopy, and focused ion beam milling (FIB).



Figure 2-1: (a) Magnified image of carbon steel coupons emplaced in the sample slots of a Teflon holder; (b) image of the Teflon sample holder placed in a modified 2 L beaker.

2.2. ELECTROCHEMICAL TECHNIQUES

2.2.1. Corrosion Potential (E_{CORR})

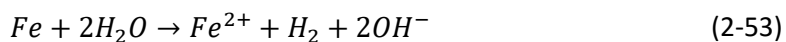
The corrosion potential (E_{CORR}) is the potential measured when the oxidation of a material is coupled, in the absence of an applied potential, to a supporting reduction reaction. Figure 2-2 shows the Butler-Volmer relationships for the two electrochemical reactions involved in a corrosion reaction, in the illustrated case, the corrosion of Fe. At the equilibrium potential for the Fe dissolution/deposition reaction ($E^e_{\text{Fe}/\text{Fe}^{2+}}$) both the forward and reverse reactions are occurring at the same rate (i.e. the system is at a reversible equilibrium):



A similar reversible equilibrium is established at the equilibrium potential of the water reduction/ H_2 oxidation reaction ($E^e_{\text{H}_2\text{O}/\text{H}_2}$):



For the corrosion of the Fe metal to occur, the anodic dissolution of Fe must combine with the cathodic reduction of water yielding the overall corrosion reaction:



This coupling can only occur when the anodic and cathodic currents for the two half reactions are equal. Therefore, there is only a single potential at which these half reactions can couple. This potential is the corrosion potential (E_{CORR}). Each of the reactions has polarized the other away from its equilibrium potential by an amount which is dependent on the slope of the respective current-potential relationships.

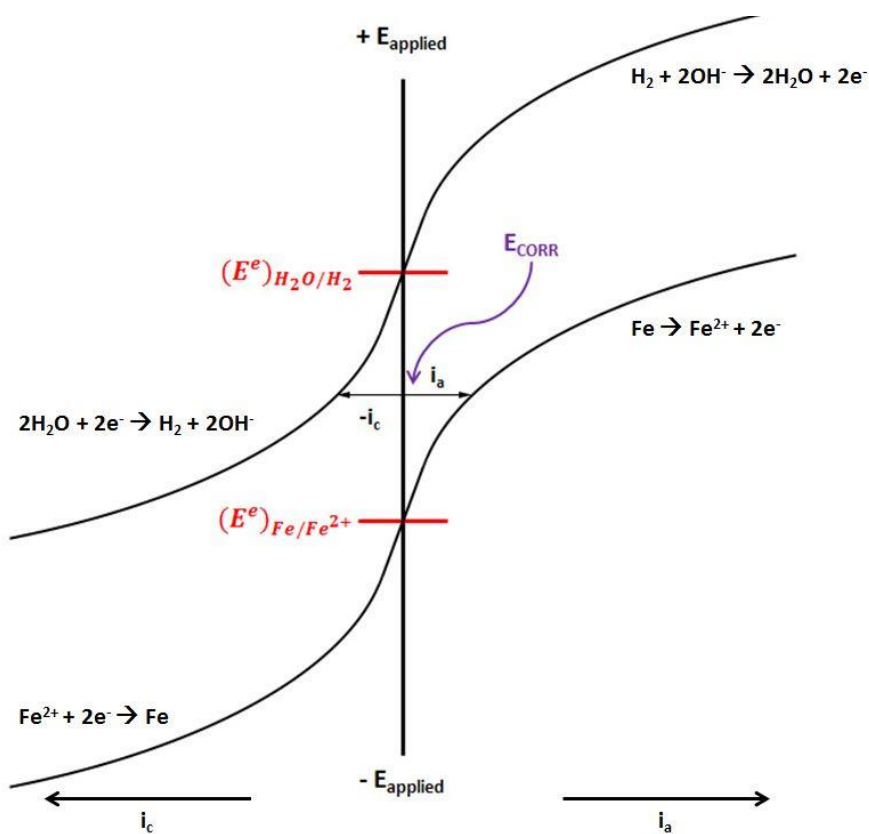


Figure 2-2: Current-potential (Butler-Volmer) relationships for the Fe dissolution/deposition and water reduction/H₂ oxidation reactions illustrating their coupling at the E_{CORR} .

2.2.2. Linear Polarization Resistance (LPR) Measurements

2.2.2.1. Basic Principles of LPR

Linear polarization resistance (LPR) is an electrochemical technique which measures the interfacial polarization resistance (R_p). Figure 2-3 illustrates that, for small overpotentials ($\eta = E_{CORR} \pm E_{applied}$), the slope of the current-potential relationship for a corrosion process is approximately linear and can be expressed by Ohm's Law:

$$\frac{\Delta E}{\Delta I} = R_p \quad (2-54)$$

where R_p represents the polarization resistance which is the ratio of the applied potential to the corresponding current response. For small overpotentials from E_{CORR} , the measured current can be described by:

$$i = i_{CORR} \left[e^{\frac{2.303(E-E_{CORR})}{\beta_a}} - e^{\frac{2.303(E-E_{CORR})}{\beta_c}} \right] \quad (2-55)$$

where i_{corr} is the corrosion current and β_a and β_c are the Tafel slopes of the anodic and cathodic reactions.

Approximating the exponential terms with the first two terms of a power expansion series and simplifying yields:

$$i = i_{CORR} \left[\left(1 + \frac{2.303(E - E_{CORR})}{\beta_a} \right) - \left(1 - \frac{2.303(E - E_{CORR})}{\beta_c} \right) \right] \quad (2-56)$$

$$i = i_{CORR} \left[\left(1 + \frac{2.303\Delta E}{\beta_a} \right) - \left(1 - \frac{2.303\Delta E}{\beta_c} \right) \right] \quad (2-57)$$

$$\beta_a \beta_c * \frac{i}{i_{CORR}} = \left[\frac{2.303\Delta E}{\beta_a} + \frac{2.303\Delta E}{\beta_c} \right] * \beta_a \beta_c \quad (2-58)$$

$$\frac{\beta_a \beta_c i}{i_{CORR}} = 2.303\Delta E \beta_c + 2.303\Delta E \beta_a \quad (2-59)$$

which can be rearranged to yield:

$$\frac{\Delta E}{i} = R_p = \frac{\beta_a \beta_c}{2.303 i_{CORR} (\beta_a + \beta_c)} \quad (2-60)$$

As shown in equation 2-60, known as the Stern-Geary equation, the linear slope of the polarization curve yields the R_p which is shown to be inversely proportional to i_{CORR} and subsequently the corrosion rate [1]. If the values of the Tafel constants are known, the R_p value can also be used to calculate the value of the corrosion current density (i_{CORR}) which can then be related to the corrosion rate of the system.

For this technique to be valid, we assume that corrosion damage is uniform, there is a single anodic and cathodic reaction, the Tafel constants are known, the resistance of the solution is negligible and the value of E_{CORR} is stable [2].

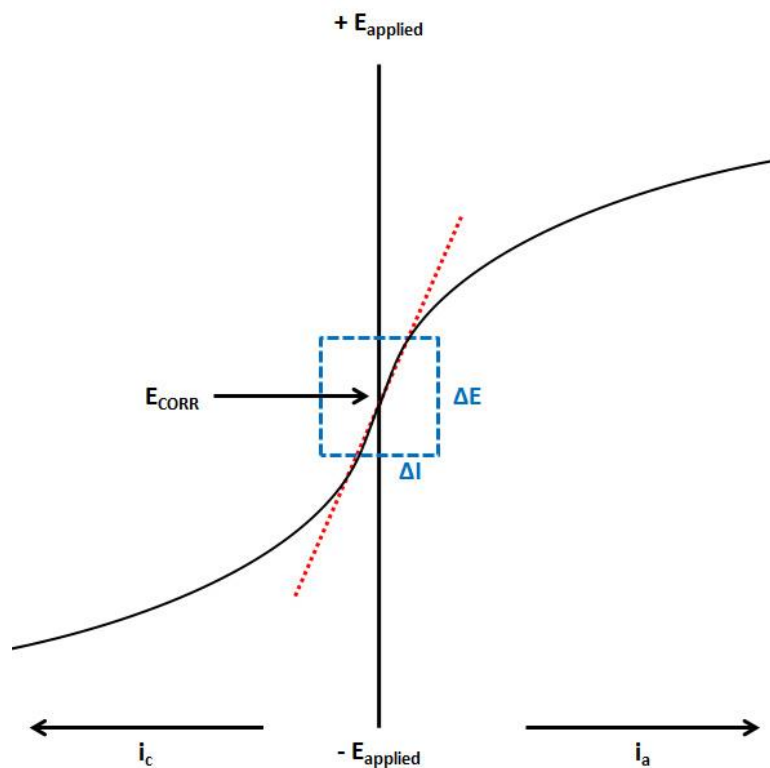


Figure 2-3: Current-potential relationship for a corrosion process demonstrating the linearization for small overpotentials from E_{CORR} used in polarization resistance measurements.

2.2.2.2. *LPR Experimental Details*

LPR measurements were performed between E_{CORR} measurements at various intervals (i.e. every 6 or 8 hours) during long term corrosion experiments. LPR measurements were executed by scanning the potential ± 10 mV from E_{CORR} at a scan rate of 0.1667 mV/s. The R_p values were then determined from the linear slope of the potential-current relationship.

2.2.3. **Cyclic Voltammetry**

2.2.3.1. *Basic Principles of Cyclic Voltammetry*

Voltammetry is an electrochemical method which follows the current response as a function of a potential applied to the working electrode [3]. Cyclic voltammetry is a potentiodynamic technique which employs a triangular potential waveform, Figure 2-4, to determine the electrochemical reactivity of a system [4]. To generate the cyclic voltammogram (CV), a linear potential ramp is applied between t_0 and t_1 , the switching potential. The ramp is then reversed to bring the potential back to the initial value at t_2 [3]. The potential range scanned should cover the standard or equilibrium potential for the reaction of interest (i.e. the E^e for the dissolution of Fe in the present case). Depending on the rate of the reaction under study, a suitable scan rate is chosen.

For a reversible reaction involving soluble species, such as the one illustrated in Figure 2-5, the chemical species under study experiences an anodic oxidation on the forward scan and a cathodic reduction on the reverse scan (with the direction of the scan indicated by the red arrows). The peak current values are proportional to the concentrations of the species being oxidized and reduced and the separation between the potentials at which the peaks occur can be calculated theoretically.

For an irreversible reaction, peaks become broader and more separated. If the reaction is totally irreversible, the peak on the return cathodic scan is no longer seen. For reactions involving the oxidation and dissolution of a metal, more complex curves are observed due to the formation of oxide films and deposits. Depending on the properties of the films and deposits formed no current may be observed on the reverse scan [3].

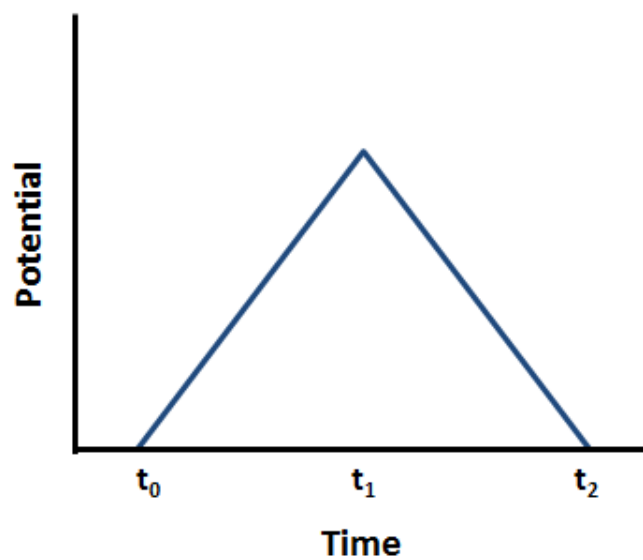


Figure 2-4: Potential-time profile used to generate a CV in which the potential is increased from t_0 to the switching potential at t_1 and then back to the initial potential at t_2 .

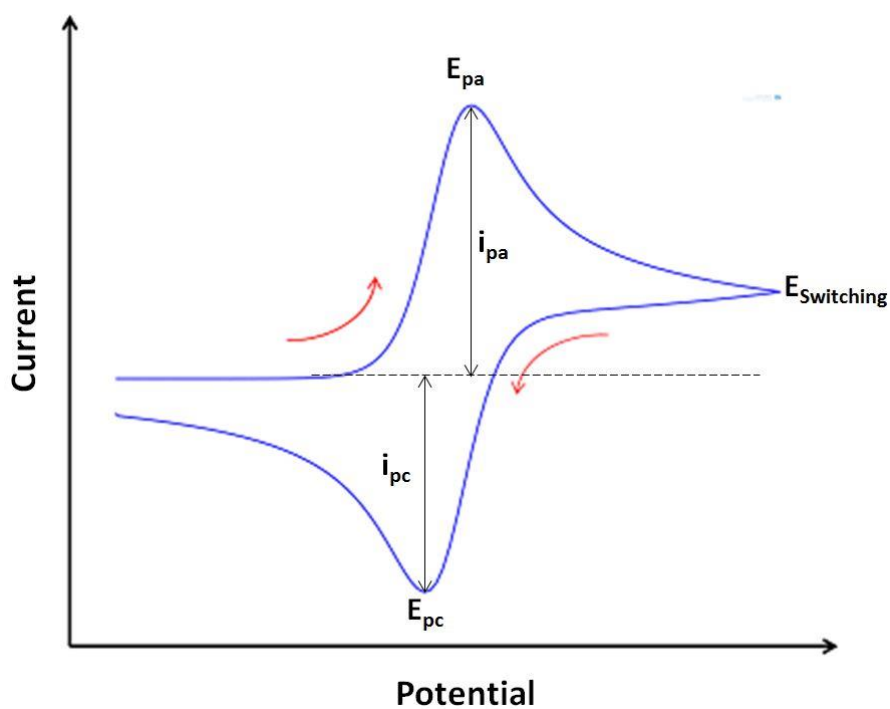


Figure 2-5: Schematic of a typical CV recorded for a reversible electrochemical reaction involving soluble species.

2.2.3.2. *Cyclic Voltammetry Experimental Details*

Prior to each CV the electrode was cathodically cleaned at -1.3 V for two minutes to reduce any air formed oxide followed by three minutes at -1.1 V to allow H₂ bubbles, formed by the reduction of water at -1.3 V, to detach from the surface. The electrode potential was then scanned from -1.1 V to a pre-determined anodic limit and back again. In some experiments several scans were performed to various anodic potential limits. The potential range chosen depended on the specific reactions being investigated. In the case of experiments performed in this work the anodic limit was chosen to capture passive film formation and breakdown processes. Measurements for benchtop experiments were performed at a scan rate of 5 mV/s with a current value recorded either every mV or half mV. Measurements in the anaerobic chamber were performed at a scan rate of 1 mV/s with a current recorded every mV.

2.2.4. **Electrochemical Impedance Spectroscopy (EIS)**

2.2.4.1. *Basic Principles of EIS*

Electrochemical impedance spectroscopy (EIS) is used in corrosion science to determine both interfacial and materials parameters related to the corrosion processes occurring and to determine the properties of oxide films and corrosion product deposits which may be formed [2, 5]. As with any other spectroscopic technique, EIS is based upon an observed response to an applied excitation to the system under study. EIS involves a potential excitation applied to the working electrode in the form of a sine wave followed by the measurement of the ensuing sinusoidal current response, Figure 2-6. From the response the impedance can be obtained, and parameters such as resistances and capacitances may be calculated. Figure 2-7 shows a Nyquist plot which can be used to determine the values of the system resistances for the film (R_{film}) and solution (R_s). Bode plots, Figure 2-8, show the relationship between the resistance and capacitance values and frequency. In order to interpret their significance, EIS spectra are commonly interpreted in terms of an electrical equivalent circuit used to represent the properties of the interface. Figure 2-9 shows an example of an equivalent circuit for the impedance of a corrosion film controlled by the transfer of charge carriers across the film and includes the film capacitance (C_{film}) and resistance (R_{film}).

2.2.4.2. EIS Experimental Details

EIS measurements were performed every 48 hours following a series of E_{CORR} and R_p measurements in simulated groundwater solutions under anaerobic conditions. EIS experiments were conducted using a Solartron Analytical Modulab potentiostat/FRA running Modulab XM ECS software. A sinusoidal potential perturbation of ± 10 mV was applied around E_{CORR} . The corresponding current response was measured over a frequency range from 10^5 Hz to 10^{-3} Hz with 11 data points recorded per decade. Kramers-Kronig transformations were applied to all EIS data to confirm their validity.

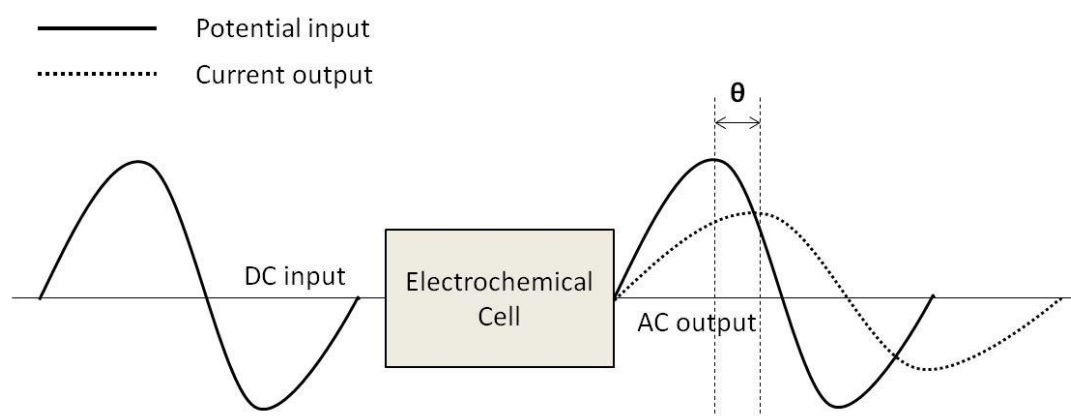


Figure 2-6: Illustrative representation of the sinusoidal potential excitation used in EIS and the corresponding sinusoidal current response. The phase shift is given by ϑ .

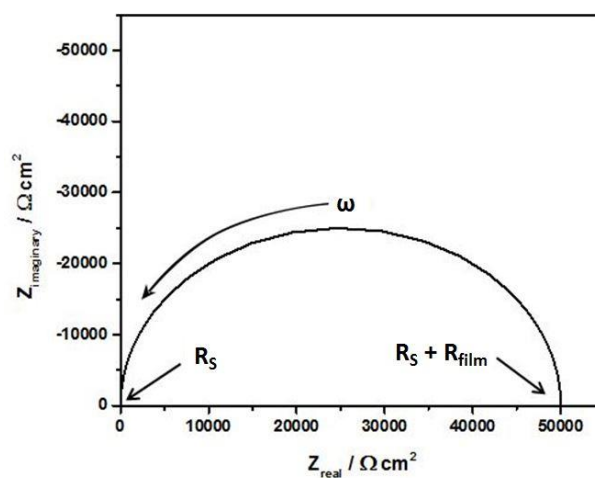


Figure 2-7: Graphical representation of a typical Nyquist plot.

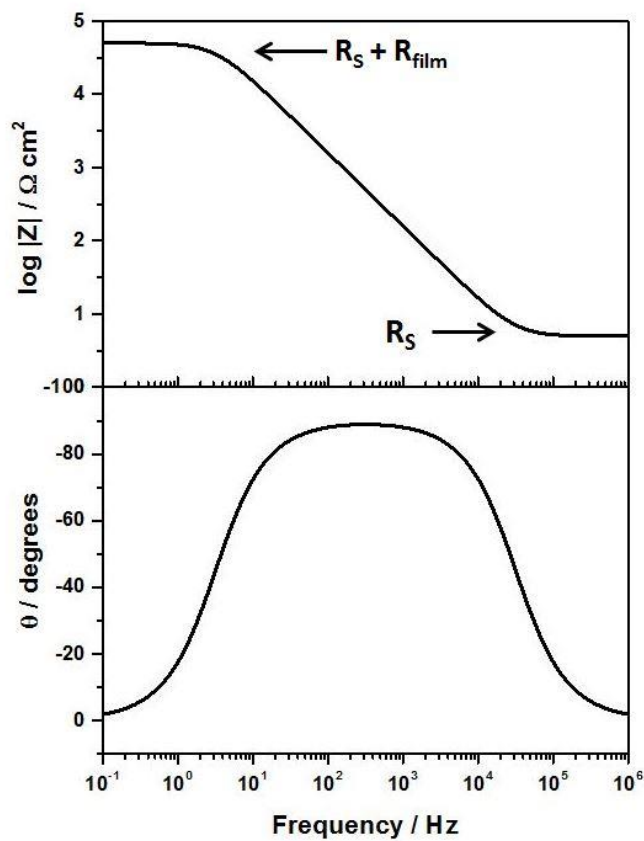


Figure 2-8: Graphical representation of Bode plots of $\log |Z|$ and θ against the log of the frequency.

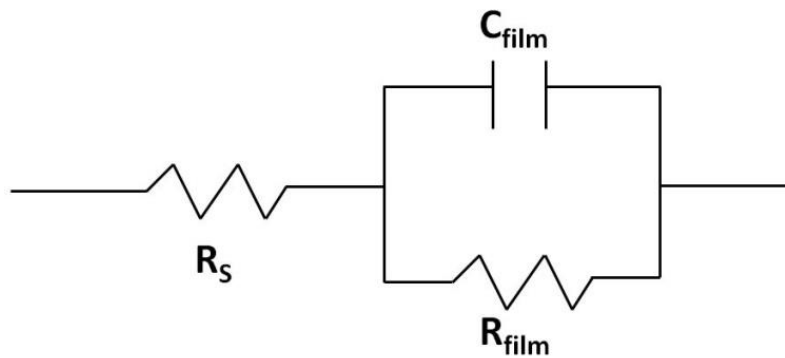


Figure 2-9: Equivalent circuit representative of a passive metal covered with an oxide film.

2.3. SURFACE ANALYTICAL TECHNIQUES

2.3.1. Scanning Electron Microscopy (SEM)

2.3.1.1. *Basic Principles of SEM*

Information on the physical nature of a sample surface can be obtained through optical microscopy. However, the resolution is limited by diffraction effects to roughly the wavelength of the white light being used. Scanning electron microscopy (SEM) can be used to obtain more detailed image resolution. This enhanced resolution is achieved due to the much shorter wavelength of the electron which minimizes diffraction effects. A standard SEM instrumental arrangement is shown in Figure 2-10 [6]. A beam of electrons (200 eV – 30 keV) is thermionically produced from an electron gun, usually fitted with a W filament. This beam of electrons is then accelerated through a series of condenser and objective lenses which act to reduce the diameter of the beam. It is the objective lens that largely determines the spatial resolution of the instrument which can never be better than the incident beam diameter. Typical SEM beam diameters are on the order of 10 nm but the use of a field emission source can reduce the diameter to 1 nm [7]. The SEM micrograph is created by scanning the electron beam horizontally along the sample surface in perpendicular directions. Just above the objective lens are two deflection coils connected in series which generate a magnetic field, supplied by a sawtooth-wave generator operating at a line frequency in the *y*-direction which deflects the electron beam in the *x*-direction. A second sawtooth-wave generator generates the slower *y*-scan. The overall procedure is known as rastering and leads to sequential beam coverage over a rectangular area of the sample. The size of the rastered area of the sample surface is what gives rise to the magnification of the SEM rather than the strength of the objective lens as in light microscopy [7].

The electron beam penetrates the sample surface producing secondary electrons (SE), backscattered electrons (BSE), X-rays and Auger electrons. SEs are the most commonly used to produce SEM images and are generated from inelastic collisions between the primary electrons and the electrons in the K-orbital of an atom. Inelastic scattering reduces the kinetic energy of the primary electrons by repeated random scattering or absorption. The depth at which the electrons come to rest within the solid is known as the penetration depth and the volume of the

sample containing most of these scattered electrons is the interaction volume. Figure 2-11 illustrates the interaction volume based on incident beam energy [7].

Because most SEs start with relatively low energies, the average distance they tend to travel within a solid is very small. As such, many SEs do not have enough energy to escape the solid. Those which do escape the solid typically come from very shallow depths, known as the escape depth, causing the technique to be surface sensitive. Features which are at higher positions on the sample will appear brighter in the SE image due to the increased probability of the SEs reaching the detector, leading to the topographical contrast of the image [7].

The most common SE detector is the Everhart-Thornley detector which uses a positive bias to attract the SEs which are then accelerated toward a scintillator, converting the electrons to photons before they pass through a photomultiplier tube which amplifies the signal.

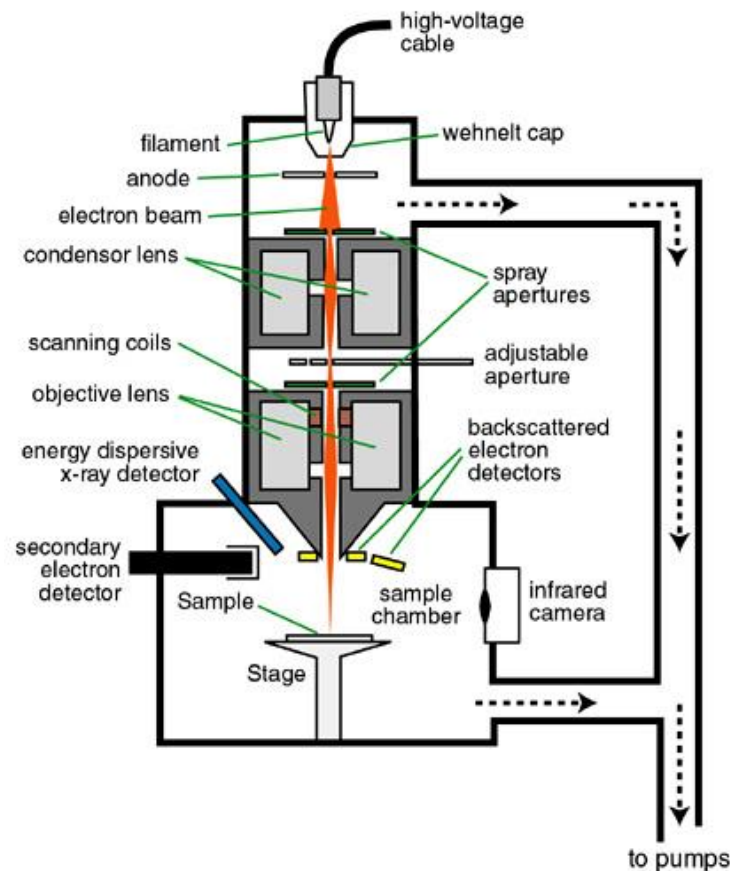


Figure 2-10: General schematic for an SEM instrumental arrangement [6].

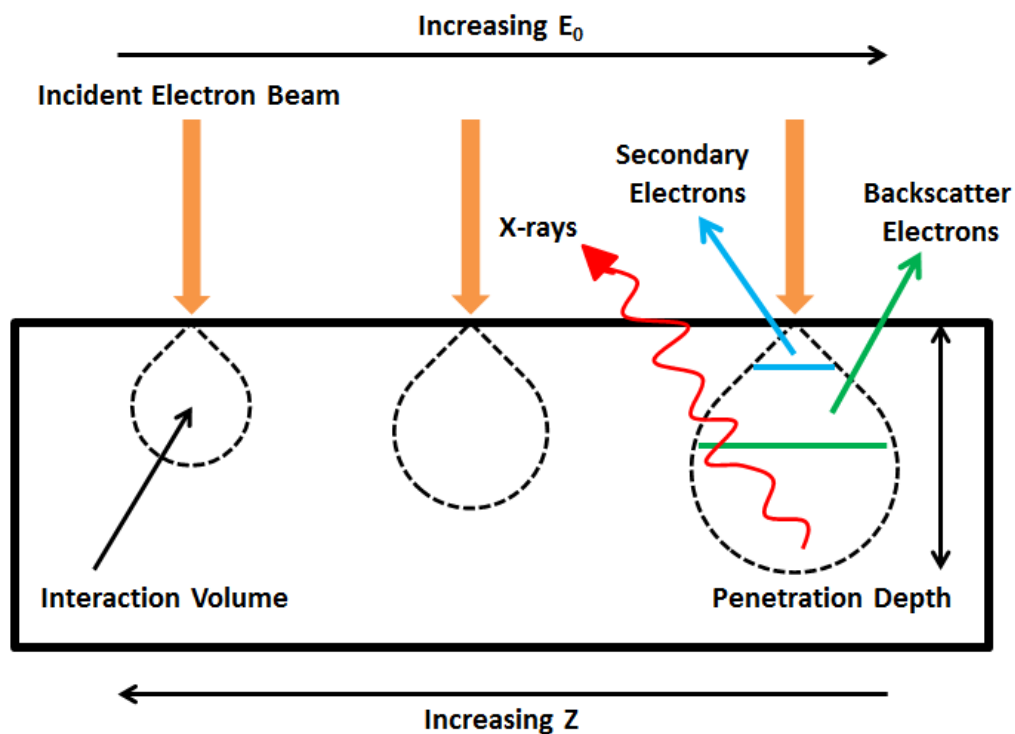


Figure 2-11: Excitation volume caused by an incident electron beam showing the regions of signal generation, and the effects of increasing the incident energy (E_0) and atomic number (Z).

2.3.1.2. SEM Experimental Details

SEM was used to image the electrode surface to determine the morphology of the corrosion films formed after electrochemical or corrosion experiments. Depending on the experiment, either a Hitachi S-4500 (Hitachi, Japan) Field Emission SEM or LEO (Zeiss) 1540XB FIB/SEM was used. Unmounted samples were adhered to the sample stage either via a small vice-grip (LEO 1540XB) or by carbon stickers (Hitachi S-4500). Mounted samples were electrically connected to the stage by Cu tape which was used to cover the epoxy resin and reduce charging. Areas of interest on the sample surface were imaged at accelerating voltages of 1 keV (LEO 1540XB) or 5 keV (Hitachi S-4500). SE mode was used to image all samples at various magnifications (250 – 25,000X). SEM images presented within this thesis are representative of the entirety of the sample surface.

2.3.2. Energy Dispersive X-Ray (EDX) Spectroscopy

2.3.2.1. *Basic Principles of EDX*

In addition to the SEs used in SEM to image a sample surface, characteristic X-rays are generated from deeper within the interaction volume produced by the incident beam, Figure 2-11. These X-rays are analyzed using Energy Dispersive X-ray (EDX) Spectroscopy and yield a quantitative elemental analysis of a sample. A small fraction of the electrons from the incident beam in the SEM can in-elastically excite electrons within the inner shell of atoms on the sample surface. Some of the kinetic energy of the incident electron is transferred to this inner-shell (usually the K-shell) electron causing it to be ejected. The vacancy left in the inner shell can then be filled by an outer shell electron, Figure 2-12. The excess energy due to this de-excitation process is released in the form of a photon whose energy is given by the difference in binding energies between the upper and lower orbital levels. Because the x-ray photon is characteristic of the binding energy differences of the orbital levels and of the atomic structure of the element, the elemental composition of the sample can be measured. This element specificity is related to the atomic number (Z) of the element as shown in Figure 2-11. As the atomic number is increased, the interaction volume of the electrons within the sample is subsequently decreased. Repeated scanning of a selected area on the sample can generate an EDX map of the elemental locations and, based on the signal intensity, quantitative measurements of the elemental composition are possible [7].

Spectrum generation requires the separation of the x-ray signal either by energy (EDX) or wavelength (WDX). In EDX the x-ray emission signal is sorted via an energy dispersive x-ray detector. There are several advantages to distinguishing via x-ray energies over wavelengths. Firstly, the speed of data acquisition is much greater since a wide range of energies can be measured simultaneously. Second, since the detector can be placed very close to the specimen, a large percentage of the emitted x-rays can be analyzed whereas a wavelength dispersive detector requires excess space for crystal movement. Finally, the cost of an EDX detector is much lower than that of a WDX detector. The EDX detector is equipped with a protective Be, or more recently diamond or boron nitride, window and a semiconductor diode fabricated from a Si(Li) crystal [7].

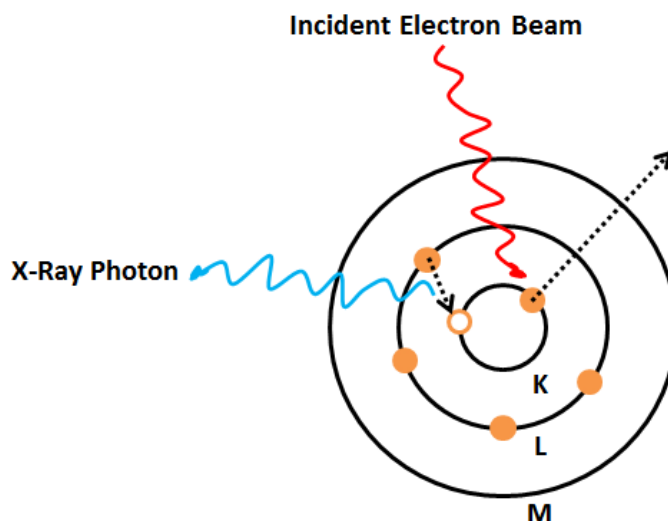


Figure 2-12: Schematic showing the creation of an electron hole due to an incident electron beam and the subsequent X-Ray photon released due to an outer shell electron filling the inner shell hole.

2.3.2.2. EDX Experimental Details

EDX elemental maps of sample surfaces and cross-sections were produced using a LEO (Zeiss) 1540XB FIB/SEM. All electrodes were mounted on the SEM stage as described in the SEM analysis. The sample was tilted to an angle of 54° to facilitate x-ray collection by the detector. A beam voltage of 10 keV was generally used for x-ray excitation of the sample surface.

2.3.3. Focused Ion Beam (FIB) Milling

2.3.3.1. Basic Principles of FIB

Focused Ion Beam (FIB) instruments are complimentary to SEM systems and in addition to imaging are useful in milling, deposition, and implantation. The use of relatively heavy ions in the beam allows for fine milling of the sample surface to produce a cross-sectional view. The most common ion used in modern FIB instruments is Ga^+ generated through the use of a liquid-metal ion source (LMIS). Ga is an ideal candidate since its mass is heavy enough for milling without causing immediate surface damage, its low melting point allows for liquid phase storage during operation, its low volatility at the melting point conserves the supply of metal, and its low

vapour pressure allows it to be used in elemental form. Additionally, Ga is easily distinguishable from other elements and will therefore not interfere with elemental analyses [8].

Ga atoms are heated to a molten metal state where they flow to the tip of a W needle which is placed just above an extractor. The extractor is held at a higher voltage than the source which produces a large electric field and ionizes the liquid. The Ga^+ ions are then ejected and accelerated towards the sample surface through a series of electrostatic lenses and a beam-limiting aperture. The aperture acts to mitigate the beam current reaching the sample and thus controls the milling rate and image quality. Upon contact with the sample surface the Ga^+ ions can induce elastic collisions with surface atoms, leading to the ejection of neutral atoms or secondary ions from the outer layers of the material. This removal of surface species can penetrate into the sample, producing a large trench which can then be imaged in cross-section. Imaging in FIB systems, similar to SEM, can be achieved through the detection of SEs which are generated either through inelastic collisions from the incident beam or by recoil atoms from prior collisions. However, most dual beam FIB systems employ a secondary field emission electron beam for imaging purposes, as illustrated in Figure 2-13 [9].

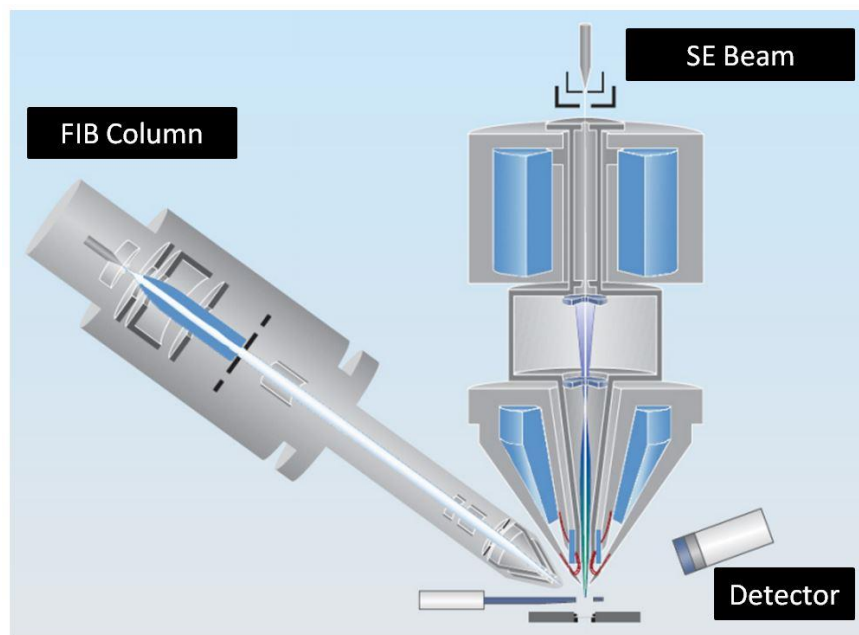


Figure 2-13: General schematic of a dual-beam FIB and SEM arrangement [10].

2.3.3.2. *FIB Experimental Details*

FIB was used in this research to cross-section samples to expose the oxide/metal interface which can be used to investigate oxide film/deposit thickness and morphology as well as to estimate the corrosion damage based on penetration depths into the base metal. FIB cuts were performed using a LEO (Zeiss) 1540XB FIB/SEM running in FIB mode with a gallium ion source. Cuts were performed with the sample tilted to an angle of 54°. Initial cutting was done at high beam currents (30 nA) to remove a trench of material ahead of the area of interest. Once close to the desired point of cross-section the beam was reduced to a current value of 1 nA to ensure a smooth polished surface for imaging. Sample preparations were performed as in the case of SEM analysis.

2.3.4. **Vibrational Spectroscopies**

In this study, both Raman spectroscopy and Infrared (IR) spectroscopy were used to identify corrosion product deposits.

2.3.4.1. *Basic Principles of Raman Spectroscopy*

Figure 2-14 shows a schematic of a Raman microscope, built from a standard optical microscope, by adding an excitation laser, a monochromator, and a sensitive detector such as a charge-coupled device (CCD) or photomultiplier tube (PMT).

Raman spectroscopy irradiates a sample with a monochromatic incident laser beam in either the visible, near infrared, or the ultra-violet regions of the spectrum while observing the scattered light in a perpendicular orientation. The excitation of a molecule involves a virtual state as the excitation wavelength is sufficiently far from the nearest absorption band [4]. The resultant scattered light is of two types: Rayleigh scattering and Raman scattering. While the Rayleigh scattering signal is strong, it represents an oscillating dipole radiating at the same frequency as the incident beam and does not provide significant information about the structure of the molecular states. Raman scattering (ca. 10^{-5} % of the incident beam intensity) [11] occurs when the scattered light is shifted in energy from the incident beam. Raman shifted photons of lower energy than the incident beam give rise to Stokes lines while shifted photons of higher energy give rise to anti-Stokes lines, Figure 2-15.

From the Maxwell-Boltzmann distribution law, the population of molecules occupying the $v = 0$ state in Figure 2-15 is much larger than the population in the $v = 1$ state. As such, the Stokes lines will be of greater intensity than the anti-Stokes lines under the same conditions making it customary to measure only the Stokes side of the spectrum [11]. A plot of the intensity of the shifted light versus the Raman shift can be used to identify chemical species by comparison to reference spectra available in the literature or through the use of digital databases. Figure 2-16 illustrates typical experimental and reference Raman spectra for magnetite (Fe_3O_4).

For the vibrational mode of a molecule to be Raman active it must experience a change in polarizability during the vibration. When placed in an electric field molecules suffer distortions due to the attraction of the positively charged nucleus towards the negative pole of the field and the attraction of the electrons to the positive pole. Charge separation within the molecule produces an induced dipole moment. However, in molecules the induced dipole moment and the electric field are vectors in the x, y, and z directions. This can be represented as a matrix known as the polarizability tensor:

$$\begin{bmatrix} P_x \\ P_y \\ P_z \end{bmatrix} = \begin{bmatrix} \alpha_{xx} & \alpha_{xy} & \alpha_{xz} \\ \alpha_{yx} & \alpha_{yy} & \alpha_{yz} \\ \alpha_{zx} & \alpha_{zy} & \alpha_{zz} \end{bmatrix} \begin{bmatrix} E_x \\ E_y \\ E_z \end{bmatrix} \quad (2-61)$$

where P is the dipole moment, α is the polarizability, and E is the field strength of the radiation. If one of the components of the polarizability tensor is changed during the vibration, the vibration is considered to be Raman active. For molecules with a center of symmetry the mutual exclusion principle applies in which symmetric vibrations are Raman active while anti-symmetric vibrations are IR active [11].

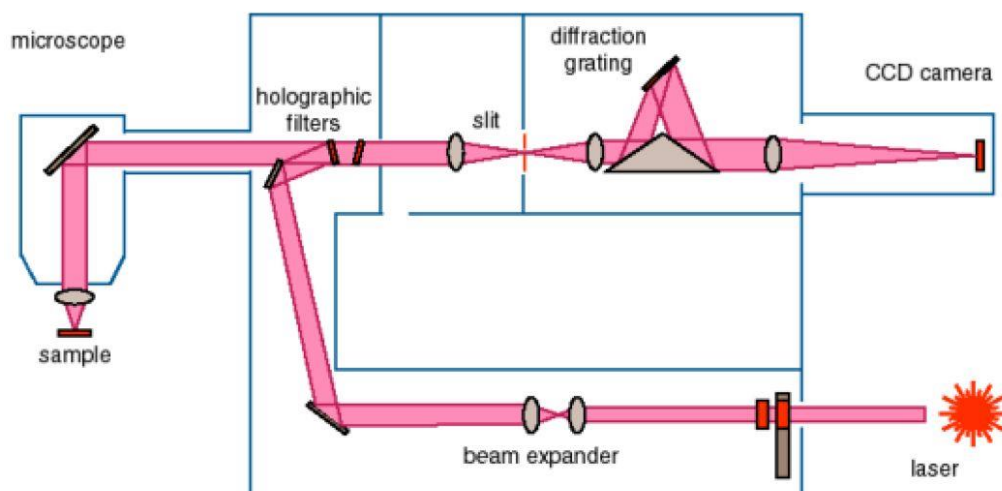


Figure 2-14: Schematic of a Renishaw Raman microscope system [12, 13].

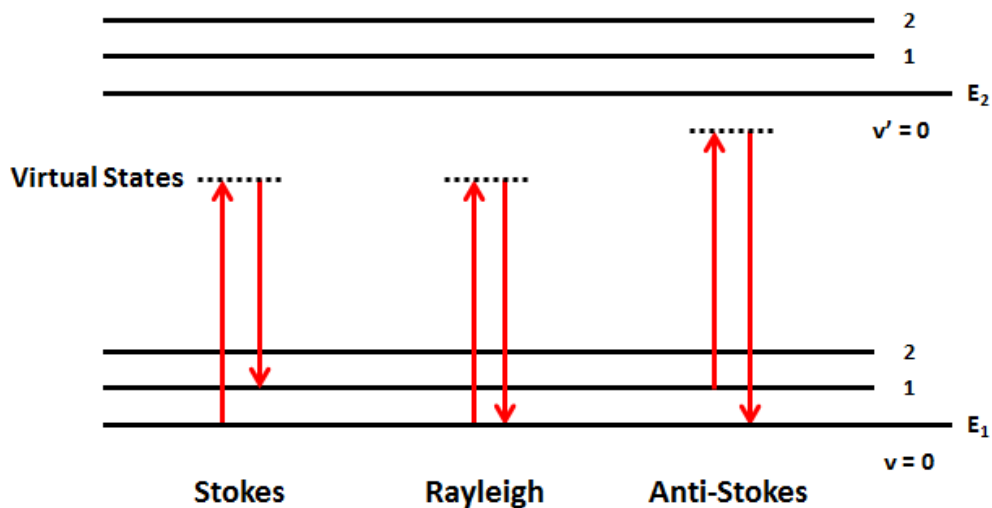


Figure 2-15: Energy level diagram showing the electron transitions for Rayleigh scattering and Stokes and Anti-Stokes Raman shifts. E_1 and E_2 represent the first and second discrete energy levels. The ground state is given by $v=0$ and $v=1$, and 2 represent the first and second vibrational excited states within the molecule.

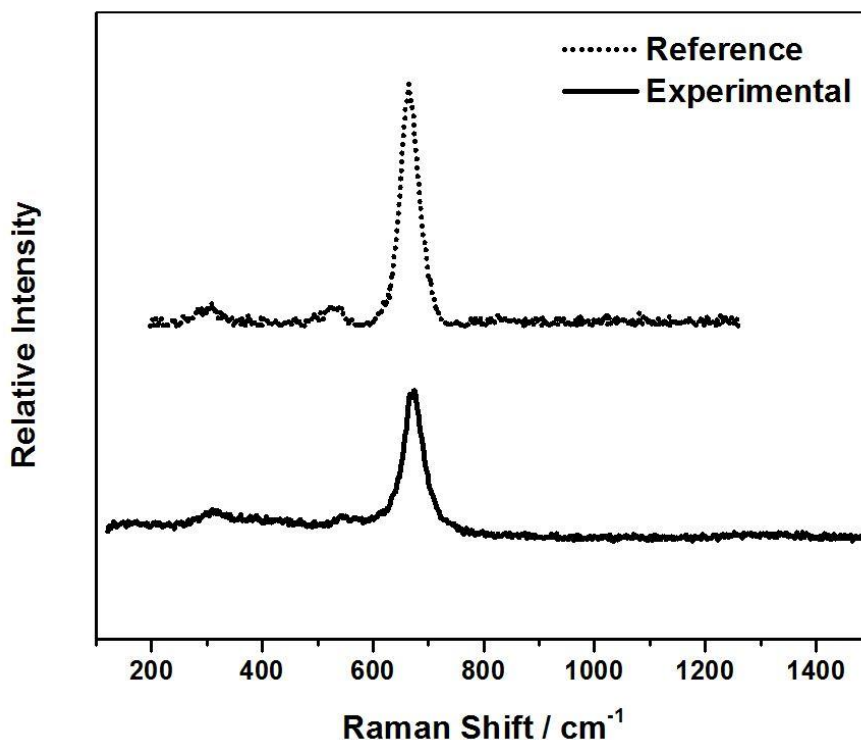


Figure 2-16: Comparison of a reference spectrum for magnetite (Fe_3O_4) to an experimentally collected Fe_3O_4 spectrum.

2.3.4.2. Basic Principles of Fourier Transform Infrared (FTIR) Spectroscopy

IR spectroscopy relies on the same type of quantized vibrational changes associated with Raman scattering. As such, the IR spectrum is frequently similar to that of the Raman spectrum for the same species. In IR spectroscopy an incident beam of IR radiation is used to excite the naturally occurring vibrations within the molecule. The relative positions of atoms, even in solids, are not fixed but change due to constant vibrations about the molecular bonds. These vibrations are broadly classified as either stretching, the continuous change in interatomic distance between two atoms, or bending vibrations, caused by a change in the angle between bonds [4]. If the frequency of the molecular vibration exactly matches that of the incident radiation, absorption will occur, inducing a change in the amplitude of the vibration. This absorption (or transmittance) of the radiation is then plotted versus wavenumber (cm^{-1}) to form the IR spectrum. Since each material is a different combination of atoms, no two compounds will produce the same IR spectrum which makes this technique useful for the identification of unknown samples.

FTIR employs an optical device called an interferometer which produces a signal incorporating all of the IR frequencies. Most interferometers use a beamsplitter which divides the incident IR beam into two optical beams. The first beam reflects off a mirror which is fixed in place while the second beam reflects off a second mirror which is moved in small increments from the beamsplitter. When the two beams recombine at the beamsplitter, the path of one beam is at a fixed length while the other has changed as the mirror moved. This process allows the simultaneous collection of all of the IR frequencies in a very short period of time. In order to convert this interferogram to a wavenumber spectrum, the frequencies are decoded via a Fourier transformation. Additional advantages of FTIR instrumentation include: increased sensitivity, mechanical simplicity, and the ability for internal calibration [4]. Figure 2-17 shows an experimentally obtained FTIR spectrum for $\text{Fe}_2(\text{OH})_2\text{CO}_3$ (chukanovite).

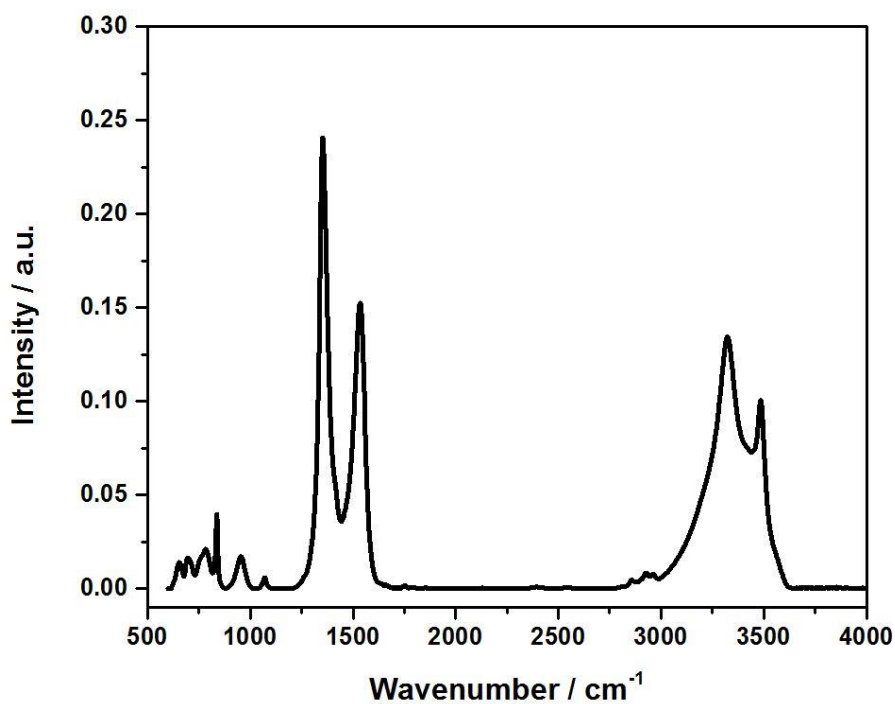


Figure 2-17: Example of an experimental FTIR spectrum obtained for a chukanovite ($\text{Fe}_2(\text{OH})_2\text{CO}_3$) corrosion product.

2.3.4.3. *Raman vs. IR Spectroscopy*

While both Raman and IR provide information about the vibrational frequencies of molecules, there are advantages and disadvantages to each. Due to the differences in selection rules for each technique, some vibrations are only Raman-active while others are IR-active. As such, Raman and IR are often used in conjunction as complimentary techniques. Raman, however, provides some significant advantages over conventional IR techniques. Since water molecules are weak Raman scatterers, it is possible to collect Raman spectra of samples in aqueous solution. This is particularly advantageous in the in-situ analysis of corroding samples over an extended period of time. Similarly, Raman spectra can also be collected on samples which may be air-sensitive or hygroscopic through the use of sealed glass vessels. Unlike IR, the glass does not absorb the Raman radiation. The laser source in Raman also provides an advantage due to the reduced spot size that can be analyzed, which is useful when only small quantities of sample are available or when the sample surface is highly heterogeneous, a common occurrence in corroded samples. Finally, a region covering 4,000 to 50 cm^{-1} can be scanned in a single recording with Raman. IR, however, requires a change of the gratings, beam splitters, filters, and detectors to cover the same spectral range [11].

Disadvantages of using Raman over IR include: (i) the requirement of a strong laser source to observe weak Raman scattering which may cause localized heating and photodecomposition effects; (ii) irradiation by the laser source can cause significant fluorescence in certain compounds; and (iii) a Raman system is more expensive than a conventional IR system [11].

2.3.4.4. *Raman Experimental Details*

Raman spectroscopy was used in order to identify the corrosion products formed on electrode surfaces during electrochemical and corrosion experiments. Samples were excited using a Renishaw 2000 Raman spectrometer equipped with a 50 mW HeNe laser at a wavelength of 632.8 nm. The laser beam was focused using an optical microscope with a 50X objective lens. The Raman spectrometer was calibrated at room temperature daily using a Si crystal standard. GRAMS 386 Raman software was used both to collect and manipulate the spectra. Each spectrum was measured for an exposure time of 60 seconds over the range of 2000 to 120 cm^{-1} at laser powers of either 10 or 25%. Several representative spectra were recorded over each sample surface.

2.3.4.5. FTIR Experimental Details

FTIR was used to confirm the identity of chukanovite ($\text{Fe}_2(\text{OH})_2\text{CO}_3$) on the sample surfaces due to its Raman inactivity. Samples were analyzed with a Bruker-Hyperion 2000 FTIR spectrometer in reflectance mode. Each spectrum was collected via the average of 32 scans over a gold background. Three or four spectra were collected from different areas for each sample.

2.4. REFERENCES

- [1] M. Stern and A. L. Geary "Electrochemical polarization I. A theoretical analysis of the shape of polarization curves" *Journal of the Electrochemical Society* 104 (1) **(1957)** 56-63
- [2] R. G. Kelly, J. R. Scully, D. W. Shoesmith and R. G. Buchheit "Electrochemical techniques in corrosion science and engineering" Marcel Dekker Inc. , New York, **(2003)**
- [3] D. C. Harris "Quantitative chemical analysis" 7th Edition, W. H. Freeman and Company, New York, **(2007)**
- [4] D. A. Skoog, F. J. Holler and S. R. Crouch "Principles of instrumental analysis" 6th Edition, Thomson Brooks/Cole, Belmont, CA, **(2007)**
- [5] M. E. Orazem and B. Tribollet "Electrochemical impedance spectroscopy" John Wiley & Sons, Inc., New Jersey, **(2008)**
- [6] J. H. Wittke, "Instrumentation" **(2008)** <http://nau.edu/CEFNS/Labs/Electron-Microprobe/GLG-510-Class-Notes/Instrumentation/> (Accessed January 8, 2016)
- [7] R. F. Egerton "Physical principles of electron microscopy : an introduction to TEM, SEM, and AEM" Springer, New York, **(2005)**
- [8] N. Yao "Focused ion beam systems: Basics and applications" Cambridge University Press, New York, **(2007)**
- [9] P. R. Munroe "The application of focused ion beam microscopy in the material sciences" *Materials Characterization* 60 (1) **(2009)** 2-13
- [10] "Detecting secondary electrons or secondary ions with the SESI detector" <https://www.zeiss.com/content/dam/Microscopy/Products/electron-microscopes/upgradesEM/pdf/upgradeinfo-sesi-detector.pdf> (Accessed January 8, 2016)
- [11] J. R. Ferraro and K. Nakamoto "Introductory Raman spectroscopy" Academic Press Inc., San Diego, **(1994)**
- [12] DSI, "Renishaw 2000 raman imaging microscope" **(2013)** <https://fas.dsi.a-star.edu.sg/equipments/raman.aspx> (Accessed October 9, 2015)
- [13] M. Razdan "Electrochemical and surface compositional studies on uranium dioxide" PhD Thesis, Department of Chemistry, University of Western Ontario, **(2013)**

Chapter 3

Interactions between Carbon Steel and UO₂ Corrosion Fronts inside a Failed Nuclear Waste Container

Shannon L.W. Hill, Nazhen Liu, Ziqiang Qin, Dmitriy Zagidulin, David W. Shoesmith

Department of Chemistry and Surface Science Western, The University of Western Ontario, London, ON, Canada

3.1. INTRODUCTION

A by-product of the use of nuclear energy is the generation of spent fuel. As of 2014, roughly 2.51 million bundles of used CANDU fuel are being stored at Canadian reactor sites [1]. In Canada the plan is to seal the spent nuclear fuel in metallic containers and emplace them in a deep geologic repository (DGR) [2]. This approach is based on multiple barriers with the primary barrier being a carbon steel vessel with an outer corrosion resistant Cu coating [3]. While copper is thermodynamically stable under anoxic conditions, and should undergo minimal corrosion [4, 5], the consequences of container failure must be considered.

Within a failed container, two corrosion fronts will be established; one on the fuel surface and a second on the inner surface of the steel vessel (Figure 3-1), on the conservative assumption that the Zircaloy fuel cladding does not act as a barrier. While the groundwaters entering the container will be anoxic after the initial emplacement period, radioactive decay processes in the fuel will cause water radiolysis with the radiolytic oxidants leading to fuel corrosion [6]. The dominant oxidant will be H₂O₂ due to alpha-radiolysis [7-9]. The H₂O₂ can either cause fuel corrosion, decompose, or be transported away from the surface.

The second corrosion front on the surface of the steel will lead to the production of soluble Fe²⁺ and H₂ as well as a surface layer of magnetite (which is not expected to protect the steel). The model recently developed by Wu et al. [9] shows that corrosion of the fuel will be strongly influenced by the interaction of radiolytic oxidants with the products of steel corrosion. The Fe²⁺ will react with the radiolytic H₂O₂ via the Fenton reaction,



with model calculations indicating that [Fe²⁺] in the range 0.1 μM to 1.0 μM will consume 67% to 90% of the radiolytic H₂O₂. However, the dominant species controlling fuel corrosion was found

to be H_2 , which calculations suggested could completely suppress fuel corrosion when present at μM levels.

For Fe^{2+} and H_2 to control redox conditions inside a failed container it is imperative that the steel vessel remain in the active condition. A possible mechanism by which the steel could be passivated and Fe^{2+}/H_2 production suppressed, is passivation of the steel by reaction with radiolytic H_2O_2 transported via the groundwater in the container. In this chapter, we investigate the corrosion of carbon steel in H_2O_2 -containing solutions under both deaerated conditions, when traces of dissolved O_2 could be present in the solution and under anaerobic conditions, when dissolved O_2 levels would be expected to be ~ 0.1 ppb. The results of this study are then compared to model calculations, to assess whether or not steel passivation is a possibility.

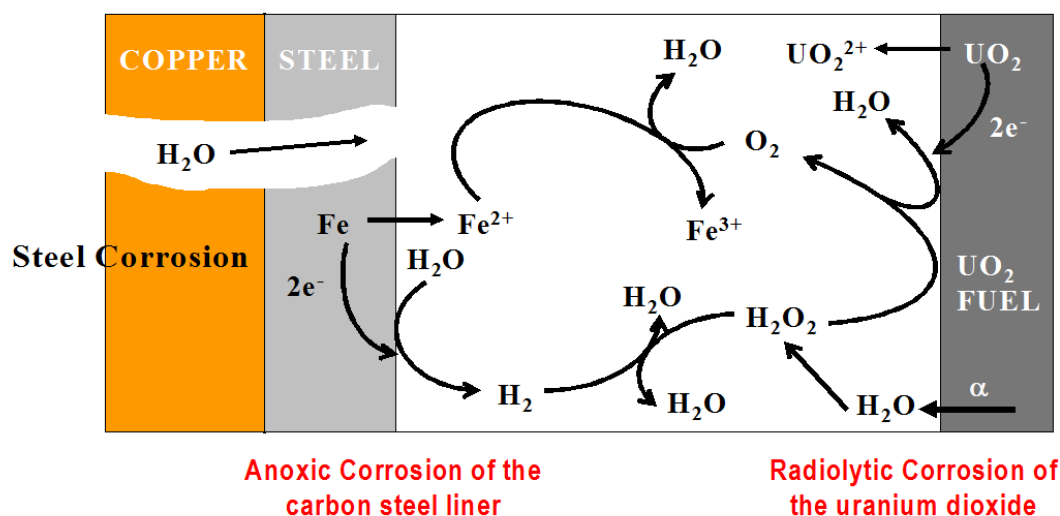


Figure 3-1: Interactions of the steel and UO_2 corrosion products and radiolytically produced oxidants within a failed spent nuclear fuel container.

3.2. EXPERIMENTAL DETAILS

3.2.1. Materials and Electrode Preparations

Electrodes were fabricated using A516 Gr 70 carbon steel (0.23 C; 1.11 Mn; 0.07 P; 0.03 S; 0.26 Si; 0.01 Cu; 0.01 Ni; 0.02 Cr; 0.004 Mo; 0.036 Al; 0.019 V; 0.003 O [wt.%], balance Fe). For the experiment performed under deaerated conditions on the bench-top, the electrode was a rectangular rod 6.5 cm in length with a 1 cm height and width. For the experiment performed in an anaerobic chamber, the electrode was a circular coupon (1.0 cm diameter and 0.5 cm

thickness) emplaced in a high-performance epoxy resin with a single exposed flat face (0.7854 cm^2). The connection between the electrode and the stainless steel rod used to connect the electrode to external measuring circuits was covered first with laboratory film (Parafilm), and then with several layers of Teflon tape to prevent exposure of the connection to the electrolyte. The electrodes were wet polished with a series of SiC papers (Presi) to a final 1200 grit finish and rinsed in type I water (conductivity of $18.2 \text{ M}\Omega\cdot\text{cm}$) before emplacement either directly into the electrolyte solution or into an anaerobic chamber in preparation for electrolyte exposure.

3.2.2. Electrochemical Cell and Equipment

Experiments were conducted in a three-compartment glass electrochemical cell equipped with a Pt counter electrode and a saturated calomel reference electrode (SCE; 0.241 V vs. SHE). All potentials are reported on the SCE scale. In the deaerated bench-top experiment, the cell was housed within a grounded Faraday cage to minimize interference from external noise. For the anaerobic experiment, the cell was placed in an anaerobic chamber to avoid the influx of atmospheric O_2 . For the deaerated bench-top experiment a Solartron 1480 multistat running CorrWare software was used to control applied potentials and to record current responses. For the experiment performed in the anaerobic chamber, a Solartron Analytical Modulab was used with raw data converted and analyzed using CorrView software.

3.2.3. Experimental Solutions

Experiments were performed in a solution containing 0.1 M NaCl , $0.1 \text{ M Na}_2\text{SO}_4$ and $0.01 \text{ M NaHCO}_3/\text{Na}_2\text{CO}_3$ set to a pH of 8.9 ± 0.5 (i.e., within the pH range of 7-10 expected for groundwaters) [10]. In the bench-top deaerated experiment, the solution was continuously sparged with UHP Ar beginning one hour prior to measurements. In the anaerobic chamber experiment, ultra-high purity water was sparged with UHP Ar at a high flow rate for one hour prior to being sealed and transferred into the anaerobic chamber. The flask was sealed with the entire volume of the flask filled with water to avoid trapped air. Once inside the chamber no additional Ar sparging was necessary.

3.2.4. Experimental Procedure

Electrodes were cathodically cleaned at a potential of -1.3 V for three minutes to reduce air-formed surface oxides. The potential was then held at -1.1 V to avoid further H_2 production

while H₂ bubbles were removed from the surface. Throughout an experiment the corrosion potential (E_{CORR}) was monitored continuously and the polarization resistance (R_p) measured using the linear polarization resistance (LPR) technique every 3 to 6 hours for the deaerated and anaerobic cases. The R_p is calculated from the linear relationship between current and potential observed by scanning the potential ± 10 mV from the E_{CORR} at a scan rate of 0.1667 mV/s.

Prior to the first addition of H₂O₂, the steel was allowed to corrode and E_{CORR} monitored to ensure similar behaviour in both experiments. Subsequently, small amounts of H₂O₂ were added to achieve concentrations in the range 0.1 to 20 μM , values expected to be conservatively large compared to anticipated concentrations within a failed container. The experiments were terminated when either passivation occurred or further additions of H₂O₂ had no apparent influence on E_{CORR} and R_p .

3.2.5. Surface Analysis

To identify the iron corrosion products formed, a Renishaw 2000 Raman spectrometer with a 632.8 nm laser line, using an optical microscope with a 50X magnification objective lens, running GRAMS 386 software was used. To identify the film morphology, SEM was performed using a Hitachi S-4500 Field Emission SEM for the deaerated experiment and a LEO (Zeiss) 1540XB FIB/SEM for the anaerobic experiment.

3.2.6. Computational Modelling

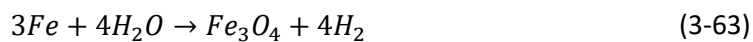
The mathematical model is numerically solved using COMSOL Multiphysics (version 4.3.1.151, COMSOL Inc.) a commercial simulation package based on the finite element model. The model was simulated using the diluted species transportation module of the COMSOL software.

3.3. RESULTS AND DISCUSSION

3.3.1. Electrochemical Analysis

Figure 3-2 and Figure 3-3 show the E_{CORR} and R_p values recorded under deaerated and anaerobic exposure conditions over periods of 35 and 66 days, respectively. The red stars indicate the time the LPR measurements were made immediately after a H₂O₂ addition. In both experiments, the value of E_{CORR} is < -0.800 V prior to H₂O₂ addition confirming that corrosion is proceeding

under anoxic conditions by reaction of the steel with water. Under these conditions, the steel would be expected to form a magnetite layer



accompanied by dissolution as Fe^{2+} , the latter being a process accelerated by the anion content of the solution, for example $\text{HCO}_3^-/\text{CO}_3^{2-}$, which is known to form soluble complexes such as FeHCO_3^+ , $\text{Fe}(\text{CO}_3)_2^{2-}$, and $\text{Fe}(\text{HCO}_3)_2$. The increases in R_p values in both environments are consistent with the thickening of a surface Fe_3O_4 layer. This initial film growth appears to occur slightly differently in the two experiments, the R_p value increasing to a substantially higher value in the anaerobic compared to the deaerated solution (Figure 3-2 and Figure 3-3). However, even prior to the addition of H_2O_2 , R_p begins to decrease again in the anaerobic experiment, Figure 3-3. This may indicate the initially formed Fe_3O_4 film is restructured, possibly developing some porosity.

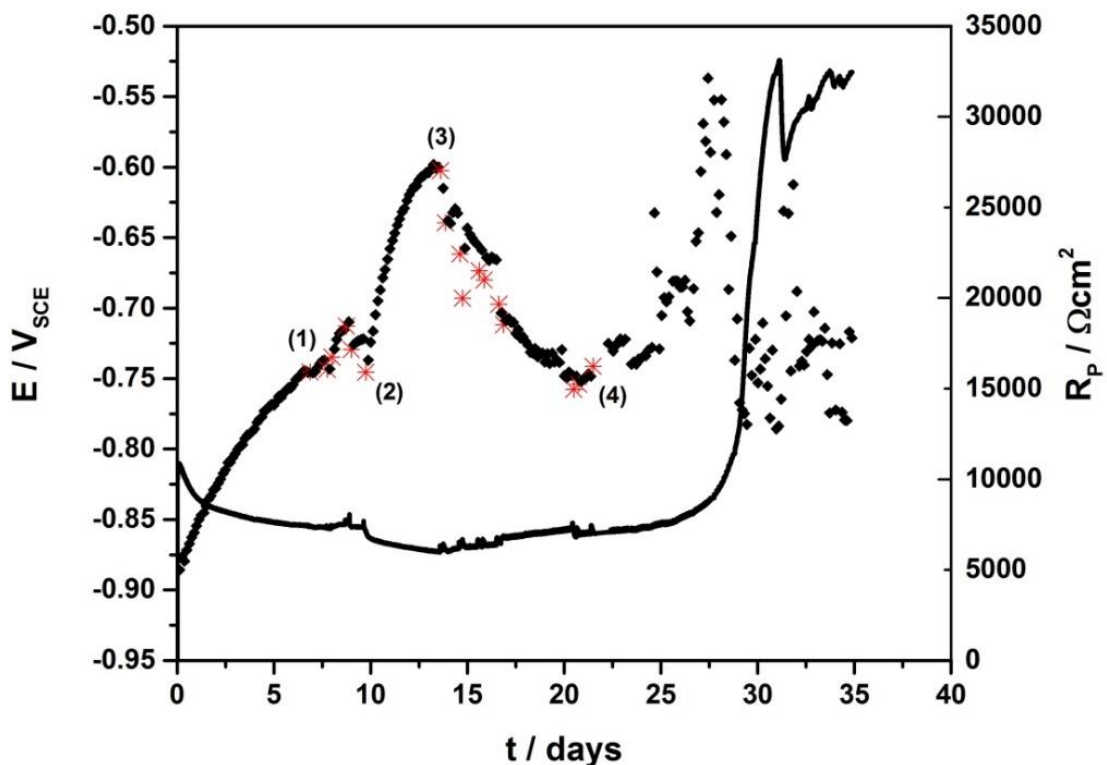


Figure 3-2: Corrosion potential (E_{CORR}) under deaerated conditions. Points indicate the R_p values, with the red points showing R_p values recorded after an addition of H_2O_2 .

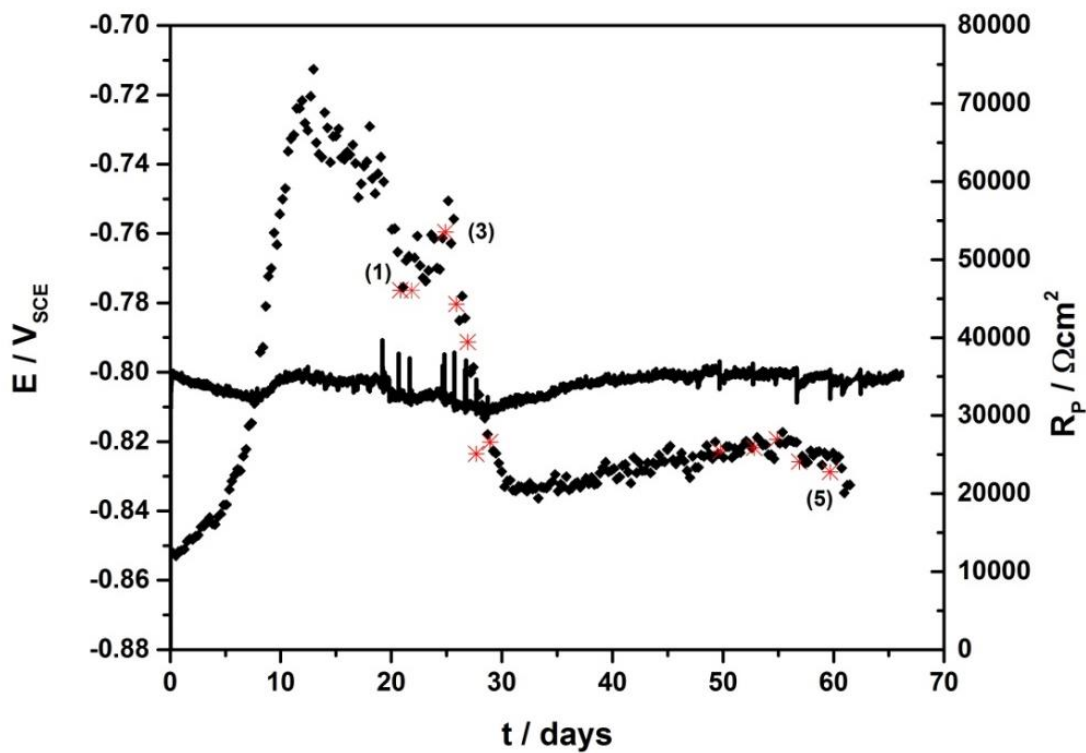


Figure 3-3: Corrosion potential (E_{CORR}) under anaerobic conditions ($[O_2] \sim 0.1$ ppb). Points indicate R_p values, with the red points showing R_p values recorded after the addition of H_2O_2 .

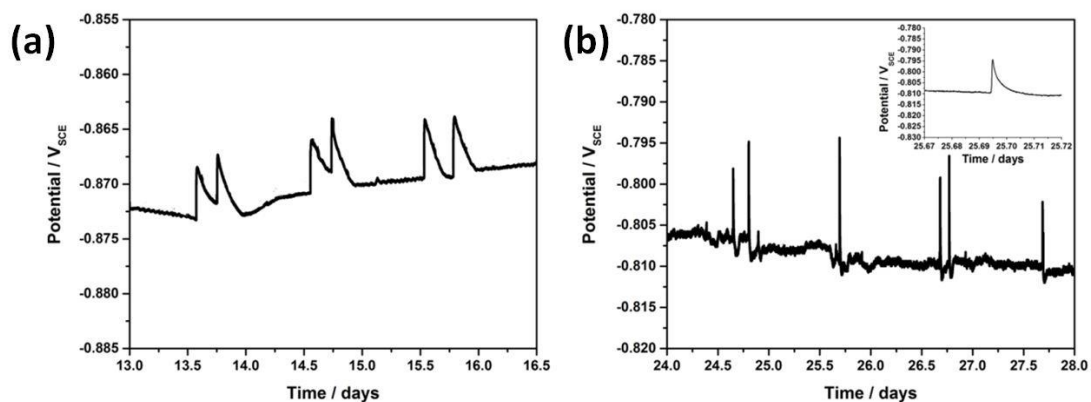


Figure 3-4: Metastable transients in E_{CORR} recorded under (a) deaerated and (b) anaerobic corrosion conditions.

On first adding H_2O_2 (at (1) in both experiments, Figure 3-2 and Figure 3-3) the E_{CORR} responds but only transitorily, eventually recovering to the value prior to the addition. This response is seen as positive-going spikes in the potential, and is more noticeable for the anaerobic experiment (Figure 3-3). Minor changes in R_p are also observed but are less readily discernible. Further additions of H_2O_2 to the deaerated experiment (indicated by the red stars in Figure 3-2) again show only transitory changes in E_{CORR} but also temporary decreases in R_p confirming the surface is reactive in the presence of H_2O_2 . Increasing $[H_2O_2]$ to $5.2 \mu M$ after 10 days ((2) in Figure 3-2) led to a significant increase in R_p but only a small decrease in E_{CORR} . The most likely reason for the increase in R_p is an accelerated growth of the Fe_3O_4 surface layer or a decrease in its porosity. On increasing the $[H_2O_2]$ to $\geq 6.1 \mu M$ ((3) in Figure 3-2) the E_{CORR} begins to increase slightly accompanied by successive decreases in R_p as the $[H_2O_2]$ is increased. Figure 3-4(a) shows that metastable transients occur during this period as R_p decreases. The positive surge in E_{CORR} followed by a slower recovery to the original value would be consistent with enhanced anodic dissolution occurring at fracture sites in the surface film followed by their subsequent repair as the film is either reformed or corrosion product is deposited within the breakdown site. While Figure 3-4(a) indicates that two spikes in E_{CORR} occur in sequence this is not always the case. One explanation for the behaviour shown is that the initial film breakdown stimulates an adjacent second breakdown. Figure 3-4(b) shows similar behaviour but the transients are of shorter duration. Whether or not steel corrosion is accompanied by H_2O_2 decomposition,



as might be expected on a conductive and probably catalytic Fe_3O_4 surface, cannot be discerned in these experiments.

After 22 days at a total added $[H_2O_2]$ of $16.1 \mu M$ ((4) in Figure 3-2) the slight increase in E_{CORR} is accompanied by a doubling of R_p . This is rapidly followed by a major and irreversible transition in E_{CORR} to a value in the region of $-0.550 V$. This transition is accompanied by a substantial decrease in R_p . During and after this transition R_p becomes erratic and no longer a reliable indication of the corrosion rate. Similar coincidental behaviour in E_{CORR} and R_p on carbon steel has been observed previously under similar deaerated conditions [11, 12]. The increase in R_p during the early stages of the transition can be interpreted as an attempt by the steel to passivate and the subsequent decrease as the transition progresses to completion to the

formation of localized corrosion sites; i.e., pitting. Under these conditions the R_p values reflect the presence of these actively corroding locations and are no longer a reliable indication of the general corrosion behaviour of the steel.

Despite the considerably higher R_p values the steel electrode exposed in the anaerobic experiment shows a similar decrease in R_p without any significant increase in E_{CORR} , as the $[H_2O_2]$ is increased, Figure 3-3 (12 to 30 days). However, further increases in $[H_2O_2]$ to a final concentration of $6.0 \mu M$ ((5) in Figure 3-3) did not stimulate the transition observed in the deaerated experiment, with E_{CORR} achieving a steady-state value of ~ -0.800 V after 65 days.

Based on a comparison of the two experiments and previous observations, the transition to a passive state undergoing localized corrosion observed in the deaerated experiment can be attributed to the slow passivation of the steel surface caused by the low background concentration of dissolved O_2 present in this experiment. The alternative source of O_2 , H_2O_2 decomposition by equation 1-3, is present in both experiments, but apparently not in sufficient quantities to induce passivation.

3.3.2. Surface Analysis of Steel in the Deaerated Solution

Figure 3-5 shows the SEM micrographs recorded on the steel surface after the 35 day exposure to the deaerated solution. The low magnification micrograph (Figure 3-5 (a)) shows that the surface is covered with a uniformly distributed compact film with areas apparently covered with a thin deposit. A number of individual larger crystals (or deposits) are also visible. The compact film is thin enough that the polishing lines of the initially prepared steel are still discernable. Figure 3-5(b) shows that the thin deposit is comprised of hexagonal crystals grown at fractures/faults in the compact layer. This morphology is consistent with the observation of potential transients, Figure 3-4(a), indicating periodic breakdown of the compact layer followed by their repair due to the subsequent deposition of corrosion product. Several well-formed hexagonal crystals (Figure 3-5 (c)), on the order of $5-15 \mu m$ in size, were also dispersed over the sample surface.

Figure 3-6 shows the ex-situ Raman analyses for both the general surface regions and the large hexagonal crystals (Figure 3-5 (c)). Spectra (a) and (b) recorded on the general surface indicate the presence of green rust (GR) which is a frequently observed corrosion product on iron surfaces when traces of dissolved O_2 are present [13] as would be the case in the deaerated

experiment. GRs are layered double-hydroxide (LDH) compounds isostructural to pyroaurite ($\text{Mg}_6\text{Fe}_2(\text{OH})_{16}\text{CO}_3$) consisting of HCP sheets of $\text{Fe}^{(II)}(\text{OH})_6$ octahedra where some $\text{Fe}^{(II)}$ has been replaced by $\text{Fe}^{(III)}$. The substitution of $\text{Fe}^{(III)}$ into the layers lends a positive charge to the structure which is then balanced by anions located between the $\text{Fe}(\text{OH})_2$ sheets [14-16]. The most commonly found anions within the GR structure are chloride (green rust I) and sulphate (green rust II). The small bands, Figure 3-6(a) and (b), from ca. $200\text{-}250\text{ cm}^{-1}$ (ref. $219\text{-}221\text{ cm}^{-1}$) [17] suggest that the coordinating anion of the green rust formed in this deaerated experiment is chloride rather than carbonate or sulphate, indicating an idealised structure for the $\text{GR}(\text{Cl}^-)$ of $[\text{Fe}_3^{(II)}\text{Fe}^{(III)}(\text{OH})_8][\text{Cl}\cdot 2\text{H}_2\text{O}]$ [18, 19]. The bands at 433 and 516 cm^{-1} (ref. 434 and 510 cm^{-1}) [17] are assigned to the $\text{Fe}^{2+}\text{-OH}$ and $\text{Fe}^{3+}\text{-OH}$ stretching modes of the green rust structure [17]. From the Raman data, the hexagonal plates seen within Figure 3-5(b) can be assigned to the $\text{GR}(\text{Cl}^-)$ corrosion product. Several others have also reported GR to have a hexagonal platelet structure [13, 20].

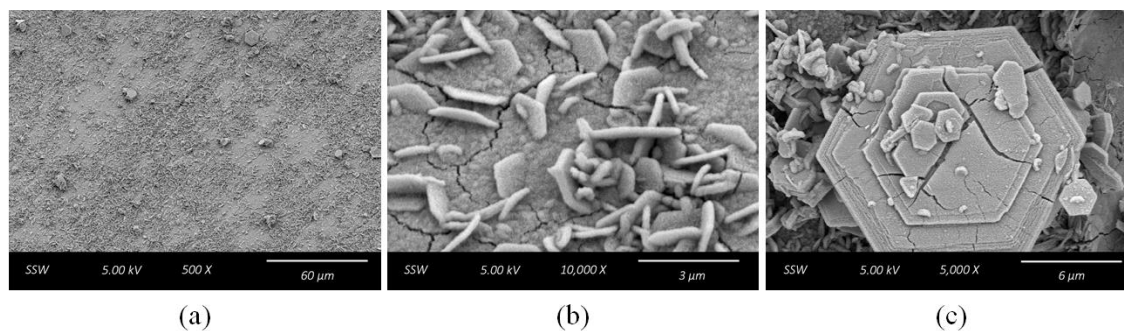


Figure 3-5: SEM micrographs showing the morphology of the corrosion film and deposits on the steel surface after corrosion under deaerated conditions.

Raman analysis of the large hexagonal crystals (line 6(c)) seen in Figure 3-5(c) suggests they are composed of ferrihydrite based on Raman bands at 359 , 512 and 706 cm^{-1} (ref. 370 , 510 and 710 cm^{-1}) [21]. The band centered at 1370 cm^{-1} (ref. 1340 cm^{-1}) may originate from the ferrihydrite as observed by Mazzetti and Thistlethwaite [21]. Two forms of ferrihydrite are reported, 2-line and 6-line, so named because their XRD patterns show 2 or 6-8 reflections as the structural order increases [13]. The lack of asymmetry in the peak at 706 cm^{-1} and the greater intensity of the band at 359 cm^{-1} to that of the 512 cm^{-1} suggests that the form of ferrihydrite formed during the corrosion process was the 6-line form [21]. The structure seen within Figure 3-5(c) for the SEM micrograph showing a highly ordered hexagonal crystal is also in

line with the formation of a more structurally ordered ferrihydrite. Ferrihydrite ($\text{Fe}_{10}\text{O}_4(\text{OH})_2$) has been shown to form in atmospheric corrosion conditions [22, 23] and is a metastable precursor to phases such as hematite ($\alpha\text{-Fe}_2\text{O}_3$).

The absence of a Raman signal for Fe_3O_4 (expected at 667 cm^{-1}) is at first surprising since one would have expected the compact film to be dominantly this phase. This suggests either the compact film is amorphous or has been converted to GR by H_2O_2 or the traces of dissolved O_2 present in this experiment. This latter explanation would support our conclusion that the general surface is at least partially passivated as indicated by the major transition in E_{CORR} , Figure 3.2.

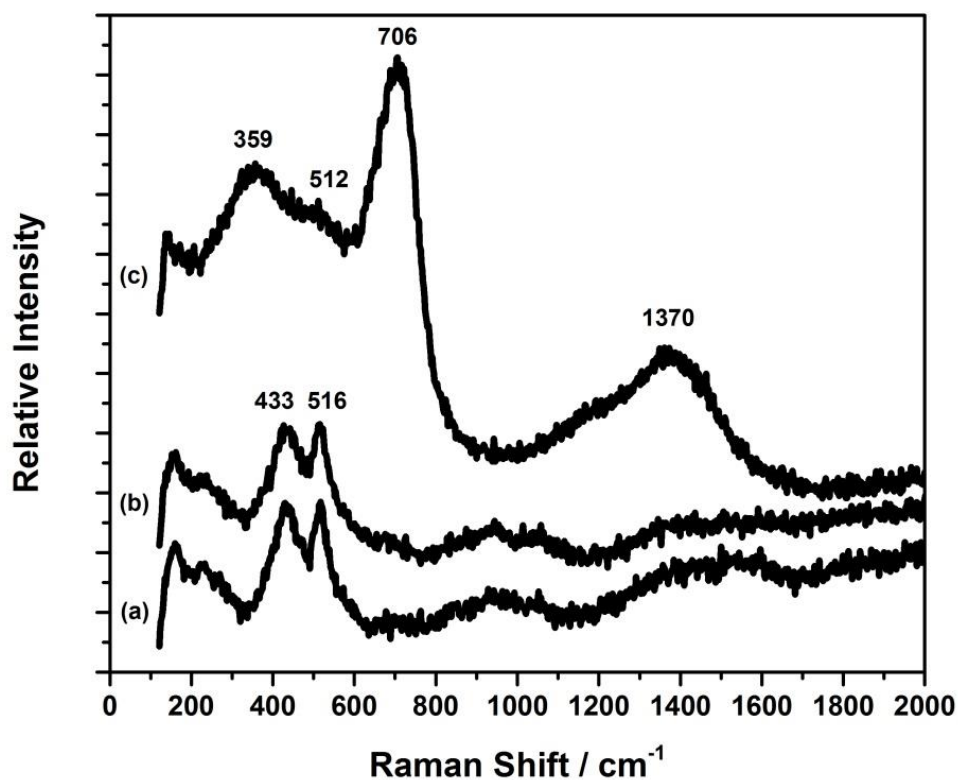


Figure 3-6: Raman spectra (a-c) recorded at various locations on the steel after corrosion under deaerated conditions (Figure 3-2).

3.3.3. Surface Analysis of Steel in the Anaerobic Solution

Figure 3-7 shows the SEM micrographs recorded on the steel surface after 66 days of exposure within the anaerobic experiment. The film appears to be thin and compact as evidenced by the visible polishing lines (Figure 3-7(a)). The cracking of the film was likely induced by the vacuum exposure of both the anaerobic chamber and that of the SEM itself. Figure 3-7(b) shows that the film is composed of a fine crystalline film interspersed with smooth hexagonal crystals. One small region of the surface was shown to be covered in a thicker and highly irregularly shaped crystalline corrosion product (Figure 3-7(c)).

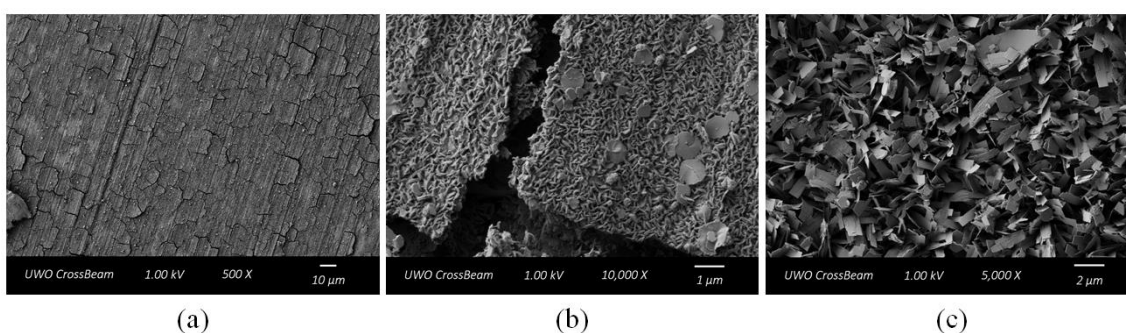


Figure 3-7: SEM micrographs showing the morphology of the corrosion film and deposits on the steel surface after corrosion under anaerobic conditions.

Figure 3-8 shows the ex situ Raman spectra recorded at several locations across the surface. The band at 667 cm^{-1} (ref. 667 cm^{-1}) [24] in line (a) is assigned to the strongest A_{1g} mode of Fe_3O_4 [24]. Formation of Fe_3O_4 confirms the anoxic corrosion of the steel under anaerobic conditions. Two bands centered between 1300 and 1600 cm^{-1} within line (a) are attributed to Fe_3C residues left behind from the dissolution of the α -Fe in the pearlite grain structure of the steel [24]. Evidence of Fe_3C residues of pearlite indicates the presence of areas covered only by a thin Fe_3O_4 film, which would further suggest that the surface of the steel coupon has not been passivated by the addition of the H_2O_2 . The large fluorescence in the spectrum, Figure 3-8(a), is due to electronic excitations of the underlying Fe metal [11].

Spectra (b) and (c) show bands at 330 , 420 and 730 cm^{-1} which could indicate the formation of either akaganeite ($\beta\text{-FeO}(\text{OH})_{1-x}\text{Cl}_x$) [25] which is known to form under chloride containing aqueous conditions [26, 27], or maghemite (ref. 350 , 505 , 660 and 710 cm^{-1}) [28]. Réguer et al. reported strong Raman bands at 310 , 390 , and 720 cm^{-1} in conjunction with less intense bands

at 490, 540, and 610 cm^{-1} for akaganeite [27]. Rémazeilles et al. reported broad bands at 308, 390, 418 and 722 cm^{-1} [26]. The large discrepancy in the assignment of Raman bands for β -FeOOH may be due to the various chloride contents possible within the structure which has been shown to alter the Raman spectra [27]. The absence of the distinct peak at 310 cm^{-1} for akaganeite and the band at 660 cm^{-1} for maghemite makes the structure elucidation precarious. All iron oxides present a main peak in the region of 650-700 cm^{-1} , except in the case of hematite, goethite, and lepidocrocite [28]. As such, the classification of many iron oxides requires examination of the shape and broadness of the peaks in this region. In our case, the breadth of the peak in this region, as well as the relatively low intensity of the spectrum makes it hard to definitively state its compositions. There is good possibility that spectra (b) and (c) may be caused either by a very poorly crystalline iron species or a mixture of several iron oxide/oxyhydroxide species.

The Raman band at 1072 cm^{-1} (ref.1070-1072 cm^{-1} , Figure 3-8(d)) is due to the ν_1 C—O symmetric stretching of a coordinated CO_3^{2-} species [29, 30]. However, the lack of any other Raman bands in the spectrum suggests that while the CO_3^{2-} component of the film is seen, the remainder of the corrosion product structure is not Raman active. The highly crystalline morphology seen in the SEM micrograph in Figure 3-7(c) is similar to that seen in our own work (subsequent Chapters), on specimens not exposed to H_2O_2 , which also displayed the characteristic C—O stretching Raman band at 1072 cm^{-1} . FTIR analysis of these samples confirmed the formation of chukanovite ($\text{Fe}_2(\text{OH})_2\text{CO}_3$). Pandarinathan et al. also showed the same structural morphology for chukanovite formed during the corrosion of sand-deposited carbon steel in CO_2 saturated brines at 80°C [31].

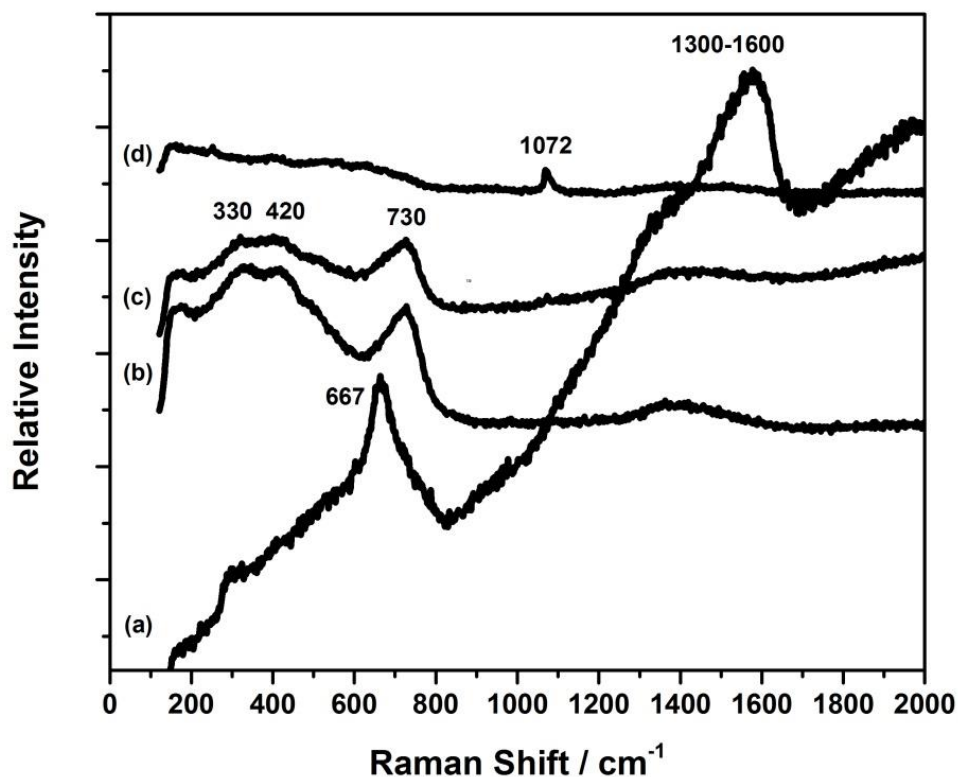


Figure 3-8: Raman spectra (a-d) recorded at various locations on the steel after corrosion under anaerobic conditions (Figure 3-3).

3.3.4. Computational Modelling

A model developed previously to determine fuel corrosion rates [9] was adapted to include the possibility of the reaction of H_2O_2 with the inner surface of the steel vessel. This model takes into account the consumption of H_2O_2 by the corrosion of the fuel, decomposition catalyzed by the fuel surface, and by reaction with soluble Fe^{2+} from the corroding steel vessel in the Fenton reaction (equation 3-62). The expected long term corrosion rate of the steel is expected to be around $0.1 \mu\text{m/a}$ [32] with corrosion proceeding on a magnetite-covered surface. The model was used to investigate the $[\text{H}_2\text{O}_2]$ expected on the inside surface of the steel container.

Figure 3-9(a) shows the $[\text{H}_2\text{O}_2]$ profile between the fuel surface, at which it is produced (0 mm on the plot), and the steel surface set at a distance of 1 mm from the fuel surface. Such a separation is conservatively close and minimizes the transport range for H_2O_2 between the two

surfaces. After 500 s the $[H_2O_2]$ at the fuel surface is calculated to be 4.05×10^{-10} M. Figure 3-9(b) shows that the $[H_2O_2]$ at the steel surface becomes negligibly small after ~ 8000 s of radiolytic H_2O_2 production at the fuel surface. The variability in calculated values is due to the “noise” encountered in the numerical calculations at such low values.

Since the corrosion rate of the steel is uncertain, the sensitivity of the model to various parameters and reactions was evaluated. As expected, increasing the distance between the fuel and steel surfaces to more realistic separations leads to a decrease in $[H_2O_2]$ at the steel surface. Figure 3-10 shows the influence of steel corrosion rate on the predicted $[H_2O_2]$ at the steel surface. An increase in corrosion rate from $0.1 \mu\text{m/a}$ to $1.0 \mu\text{m/a}$ leads to a decrease in this concentration. This can be attributed to the increase in $[Fe^{2+}]$ and $[H_2]$ both of which increase the consumption rate of H_2O_2 . For H_2 this is by reaction with H_2O_2 catalyzed on the noble metal particles in the spent fuel and for Fe^{2+} by reaction with H_2O_2 in the Fenton reaction. Additional calculations show that the key reaction consuming H_2O_2 and preventing its transport to the steel surface is the Fenton reaction (equation 3-62). For the $[H_2O_2]$ at the steel surface to approach the micro-molar level this reaction would have to not occur, which is extremely unlikely.

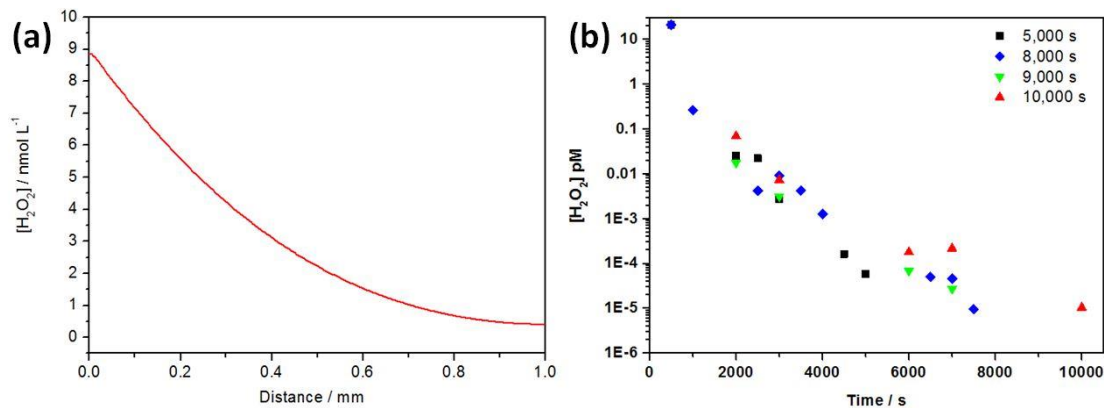


Figure 3-9: (a) $[H_2O_2]$ profile from the UO_2 surface (0.0 mm) to the surface of the carbon steel (1.0 mm) after 500 s; (b) plot of $[H_2O_2]$ at the carbon steel surface as a function of the period of α -radiolysis at the fuel surface (surface separation, 1 mm). The different coloured points are for a series of simulations using different time intervals in the calculation with slight variations being produced due to the fact the calculated values are for a boundary parameter (a discontinuity in the calculation).

Based on these calculations we can conclude that it is highly unlikely that H_2O_2 concentrations will reach the micro-molar levels at which an influence on steel corrosion would become significant, which, as discussed above, would be in the 1 to 10 μM range. Even for concentrations in this range there is no experimental indication that exposure to H_2O_2 would lead to passivation of the steel and suppression of the production of the redox scavengers, Fe^{2+} and H_2 .

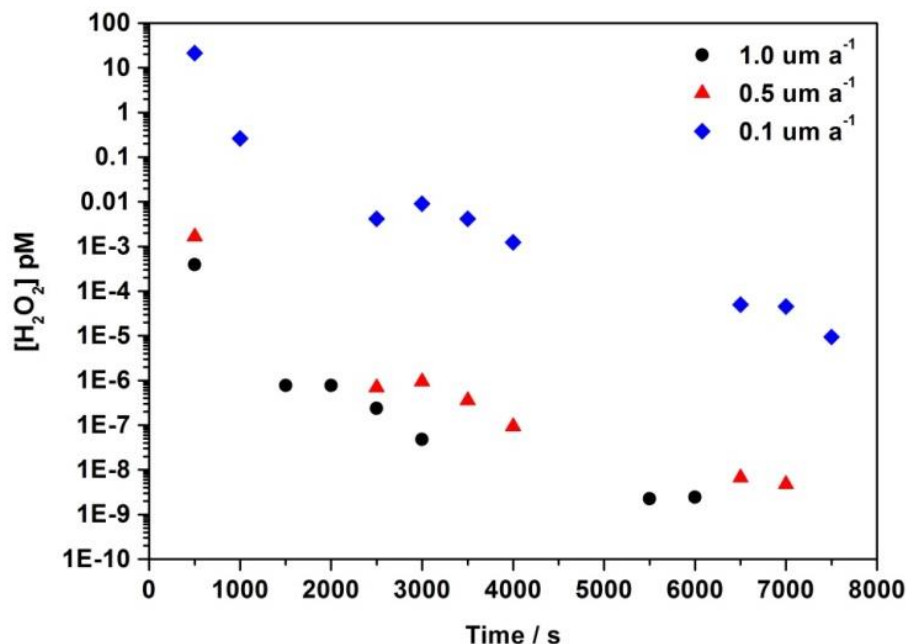


Figure 3-10: The influence of the steel corrosion rate on the $[\text{H}_2\text{O}_2]$ at the steel surface as a function of the period of α -radiolysis at the fuel surface (surface separation, 1 mm).

3.4. CONCLUSIONS

The influence of H_2O_2 on the corrosion of carbon steel has been investigated under deaerated conditions, when traces of dissolved O_2 could be present, and under anaerobic conditions, when the $[\text{O}_2]$ would be expected to be at the ppb level.

Under anaerobic conditions active steel corrosion, producing Fe^{2+} and H_2 was maintained up to $[\text{H}_2\text{O}_2] = 6 \mu\text{M}$. For deaerated conditions, passivation leading to pitting occurred for added $[\text{H}_2\text{O}_2] \geq 10$ to $15 \mu\text{M}$. However, this was attributable to the presence of traces of dissolved O_2 despite the continuous Ar sparging.

The presence of non-passivating Fe^{III}-containing corrosion products confirmed the interaction of H₂O₂ with the steel.

Model calculations indicate that [H₂O₂] > 10⁻⁹ M are effectively unachievable at the steel surface.

Based on these results it can be concluded that active steel corrosion will be maintained inside a failed waste container, and that the soluble corrosion products will be available to suppress fuel corrosion and radionuclide release.

3.5. REFERENCES

- [1] M. Garamszeghy "Nuclear fuel waste projections in Canada - 2014 update" Nuclear Waste Management Organization Report No. NWMO TR-2014-16 **(2014)**
- [2] J. McMurry, D. A. Dixon, J. D. Garroni, B. M. Ikeda, S. Stroes-Gascoyne, P. Baumgartner and T. W. Melnyk "Evolution of a Canadian deep geological repository: Base scenario" Ontario Power Generation Report No. 06819-REP-01200-10092-R00 **(2003)**
- [3] P. G. Keech, P. Vo, S. Ramamurthy, J. Chen, R. Jacklin and D. W. Shoesmith "Design and development of copper coatings for long term storage of used nuclear fuel" *Corrosion Engineering Science and Technology* 49 (6) **(2014)** 425-430
- [4] F. King and M. Kolar "A numerical model for the corrosion of copper nuclear fuel waste containers" *Scientific Basis for Nuclear Waste Management xix*, 412, Boston, MA, **(1996)** 555-562
- [5] F. King and M. Kolar "The copper container corrosion model used in AECL's second case study" Ontario Power Generation Report No. 06819-REP-01200-10041-R00 **(2000)**
- [6] L. Wu and D. W. Shoesmith "An electrochemical study of H₂O₂ oxidation and decomposition on simulated nuclear fuel (SIMFUEL)" *Electrochimica Acta* 137 **(2014)** 83-90
- [7] D. W. Shoesmith "Used fuel and uranium dioxide dissolution studies - A review" Nuclear Waste Management Organization Report No. NWMO TR-2007-03 **(2007)**
- [8] D. W. Shoesmith "Fuel corrosion processes under waste disposal conditions" *Journal of Nuclear Materials* 282 (1) **(2000)** 1-31
- [9] L. D. Wu, Z. Qin and D. W. Shoesmith "An improved model for the corrosion of used nuclear fuel inside a failed waste container under permanent disposal conditions" *Corrosion Science* 84 **(2014)** 85-95
- [10] J. McMurry "Reference water compositions for a deep geological repository in the Canadian Shield" Ontario Power Generation Report No. 06819-REP-01200-10135-R01 **(2004)**
- [11] B. W. A. Sherar, P. G. Keech, Z. Qin, F. King and D. W. Shoesmith "Nominally anaerobic corrosion of carbon steel in near-neutral pH saline environments" *Corrosion* 66 (4) **(2010)** 045001-1-045001-11
- [12] B. W. A. Sherar, P. G. Keech and D. W. Shoesmith "Carbon steel corrosion under anaerobic-aerobic cycling conditions in near-neutral pH saline solutions - Part 1: Long term corrosion behaviour" *Corrosion Science* 53 (11) **(2011)** 3636-3642
- [13] R. M. Cornell and U. Schwertmann "The iron oxides: Structure, properties, reactions, occurrences, and uses" Wiley-VCH GmbH & Co. KGaA, Weinheim, Germany, **(2003)**

- [14] G. W. Brindley, D. L. Bish and A. L. Mackay "Green rust: A Pyroaurite type structure" *Nature* 263 (5575) **(1976)** 353
- [15] R. M. Taylor and R. M. Mckenzie "The influence of aluminum on iron-oxides. VI. The formation of Fe(II)-Al(III) hydroxy-chlorides, -sulfates, and -carbonates as new members of the pyroaurite group and their significance in soils" *Clays and Clay Minerals* 28 (3) **(1980)** 179-187
- [16] P. Refait and J. M. R. Genin "Mechanisms of oxidation of Ni(II)-Fe(II) hydroxides in chloride-containing aqueous media: Role of the pyroaurite-type Ni-Fe hydroxychlorides" *Clay Minerals* 32 (4) **(1997)** 597-613
- [17] S. Simard, M. Odziemkowski, D. E. Irish, L. Brossard and H. Menard "In situ micro-Raman spectroscopy to investigate pitting corrosion product of 1024 mild steel in phosphate and bicarbonate solutions containing chloride and sulfate ions" *Journal of Applied Electrochemistry* 31 (8) **(2001)** 913-920
- [18] P. H. Refait, M. Abdelmoula and J. M. R. Genin "Mechanisms of formation and structure of green rust one in aqueous corrosion of iron in the presence of chloride ions" *Corrosion Science* 40 (9) **(1998)** 1547-1560
- [19] P. Refait and J. M. R. Genin "The oxidation of ferrous hydroxide in chloride-containing aqueous media and Pourbaix diagrams of green rust one" *Corrosion Science* 34 (5) **(1993)** 797-819
- [20] P. Refait, J. A. Bourdoiseau, M. Jeannin, D. D. Nguyen, A. Romaine and R. Sabot "Electrochemical formation of carbonated corrosion products on carbon steel in deaerated solutions" *Electrochimica Acta* 79 **(2012)** 210-217
- [21] L. Mazzetti and P. J. Thistlethwaite "Raman spectra and thermal transformations of ferrihydrite and schwertmannite" *Journal of Raman Spectroscopy* 33 (2) **(2002)** 104-111
- [22] J. L. Jambor and J. E. Dutrizac "Occurrence and constitution of natural and synthetic ferrihydrite, a widespread iron oxyhydroxide" *Chemical Reviews* 98 (7) **(1998)** 2549-2585
- [23] S. Music, M. Gotic and S. Popovic "X-Ray-diffraction and Fourier transform-infrared analysis of the rust formed by corrosion of steel in aqueous solutions" *Journal of Materials Science* 28 (21) **(1993)** 5744-5752
- [24] C. T. Lee, M. S. Odziemkowski and D. W. Shoesmith "An in situ Raman-electrochemical investigation of carbon steel corrosion in $\text{Na}_2\text{CO}_3/\text{NaHCO}_3$, Na_2SO_4 , and NaCl solutions" *Journal of the Electrochemical Society* 153 (2) **(2006)** B33-B41
- [25] J. Monnier, D. Vantelon, S. Reguer and P. Dillmann "X-ray absorption spectroscopy study of the various forms of phosphorus in ancient iron samples" *Journal of Analytical Atomic Spectrometry* 26 (5) **(2011)** 885-891
- [26] C. Remazeilles and P. Refait "On the formation of beta-FeOOH (akaganeite) in chloride-containing environments" *Corrosion Science* 49 (2) **(2007)** 844-857
- [27] S. Reguer, D. Neff, L. Bellot-Gurlet and P. Dillmann "Deterioration of iron archaeological artefacts: Micro-Raman investigation on Cl-containing corrosion products" *Journal of Raman Spectroscopy* 38 (4) **(2007)** 389-397
- [28] N. Boucherit, A. H. L. Goff and S. Joiret "Raman studies of corrosion films grown on Fe and Fe-Mo in pitting conditions" *Corrosion Science* 32 (5-6) **(1991)** 497-507
- [29] M. Saheb, D. Neff, L. Bellot-Gurlet and P. Dillmann "Raman study of a deuterated iron hydroxycarbonate to assess long-term corrosion mechanisms in anoxic soils" *Journal of Raman Spectroscopy* 42 (5) **(2011)** 1100-1108
- [30] R. L. Frost, M. C. Hales and B. J. Reddy "Aurichalcite - An SEM and Raman spectroscopic study" *Polyhedron* 26 (13) **(2007)** 3291-3300

- [31] V. Pandarinathan, K. Lepkova and W. van Bronswijk "Chukanovite ($\text{Fe}_2(\text{OH})_2\text{CO}_3$) identified as a corrosion product at sand-deposited carbon steel in CO_2 -saturated brine" *Corrosion Science* 85 (2014) 26-32
- [32] F. King "Corrosion of carbon steel under anaerobic conditions in a repository for SF and HLW in opalinus clay" Nagra Report No. 08-12 (2008)

Chapter 4

The Effects of Groundwater Anions on the Corrosion of A516 Gr70 Carbon Steel

4.1. INTRODUCTION

In the anoxic environment anticipated in deep geological repositories for spent nuclear fuel, carbon steel containers are expected to corrode anaerobically. The corrosion behaviour, including the corrosion rate and the composition of the corrosion products, has been shown to have a complex dependence on temperature, pH, redox conditions, immersion time, and the chemistry of the groundwater [1-8]. While a variety of groundwater species such as Ca^{2+} , Mg^{2+} , Cl^- , SO_4^{2-} , CO_3^{2-} , and SiO_3^{2-} are known to affect carbon steel corrosion, the nature and content of anions have a strong influence on the electrochemical behaviour and nature of the corrosion product deposits [2, 5, 6, 8].

The groundwater in a Canadian nuclear repository could contain high levels of Cl^- , an anion known to be highly aggressive in the corrosion of carbon steel [9]. Due to the clay based bentonite backfill material used in the repository, the groundwaters contacting the carbon steel container will be near neutral or slightly alkaline (pH 8.4) and may contain fairly high levels of carbonate. Consequently, it is possible that the corrosion products formed on the container could contain carbonates such as FeCO_3 (siderite), carbonated green rusts, and $\text{Fe}_2(\text{OH})_2\text{CO}_3$ (chukanovite) [7, 8]. Refait et al. [8] suggest that the nature of the corrosion products formed in CO_3^{2-} containing environments will be controlled mainly by the interfacial ratios of $[\text{CO}_3^{2-}]/[\text{Fe}^{2+}]$ and $[\text{OH}^-]/[\text{Fe}^{3+}]$. In addition, SO_4^{2-} has been shown to be an aggressive anion increasing the anodic dissolution rates and pitting sensitivity of carbon steel [1, 2, 5, 6, 10-14].

Several researchers have attempted to rank the aggressiveness of various anions on carbon steel corrosion. Vyskocil [15] claimed that the aggressiveness of anions in neutral solutions decreased in the order $\text{F}^- > \text{SO}_4^{2-} > \text{Cl}^- > \text{Br}^- > \text{I}^-$. King and Davidson [16] suggested that the corrosion rate decreased with decreasing complexation; i.e., $\text{P}_2\text{O}_7^{4-} > \text{PO}_4^{3-} > \text{Cl}^- > \text{SO}_4^{2-} > \text{ClO}_4^-$. Kolotyrkin [17] distinguished anions based on their aggressive (Cl^- , Br^- , I^-) or non-aggressive (SO_4^{2-} , ClO_4^- , CO_3^{2-} , NO_3^- , CrO_4^{2-}) tendency. Tamura et al. [18] suggested that the corrosion rate decreased in the order $\text{ClO}_4^- > \text{NO}_3^- > \text{Cl}^- > \text{SiO}_4^{2-} > \text{Br}^- > \text{I}^- > \text{SO}_4^{2-}$, and Tanaka et al. [19] found that the influence of anions on the formation of artificial rust particles decreased in the order

$\text{SO}_4^{2-} \geq \text{Cl}^- > \text{NO}_3^-$. The differences between these studies can be ascribed to the various anion concentrations and differences in pH and temperature used.

The objective of the research described in this chapter is to explore the effect of common groundwater anions on the electrochemical and corrosion behaviour of A516 Gr70 carbon steel, with a primary focus on the effects of Cl^- , $\text{HCO}_3^-/\text{CO}_3^{2-}$ and SO_4^{2-} , with an emphasis on highly concentrated Cl^- solutions. A combination of electrochemical techniques were employed to characterize the corrosion behaviour under deaerated conditions and Raman spectroscopy and scanning electron microscopy (SEM) techniques were used to study the identity and morphology of the corrosion products.

4.2. EXPERIMENTAL DETAILS

4.2.1. Materials and Electrode Preparations

Electrodes were fabricated as circular coupons (1.0 cm diameter) from a 0.5 cm thick plate of A516 Gr 70 carbon steel (0.23 C; 1.11 Mn; 0.07 P; 0.03 S; 0.26 Si; 0.01 Cu; 0.01 Ni; 0.02 Cr; 0.004 Mo; 0.036 Al; 0.019 V; 0.003 O [wt.%], balance Fe). Each electrode was set in a high-performance epoxy resin such that only a single face was exposed (0.7854 cm^2). Connection to external measuring circuits was achieved with a stainless steel rod first covered with Parafilm and then with several layers of Teflon tape to avoid exposure to the electrolyte. Each electrode was wet polished with 180, 600, 800, 1000, and 1200 grit SiC papers (Presi), and rinsed in type 1 water (conductivity $18.2 \text{ M}\Omega\cdot\text{cm}$) before being placed in the solution.

4.2.2. Electrochemical Cell and Equipment

Experiments were conducted in a three-compartment glass electrochemical cell. A Pt foil connected to a Pt wire was used as the counter electrode and a saturated calomel electrode (SCE; 0.241 V vs. SHE) as the reference electrode. All potentials are reported on the SCE scale. The electrochemical cell was housed within a grounded Faraday cage to minimize interference from external noise sources. Corrosion potentials (E_{CORR}), polarization resistance (R_p) measurements, and cyclic voltammograms were recorded using a Solartron 1480 multistat running CorrWare software.

4.2.3. Experimental Procedure

Prior to E_{CORR} /LPR experiments, electrodes were cathodically cleaned at -1.3 V for three minutes to reduce any air formed surface oxides, and the potential held at -1.1 V for seven minutes to remove H_2 bubbles from the sample surface. R_p values were determined at six hour intervals via linear polarization resistance (LPR) measurements by scanning the potential over the range $E_{\text{CORR}} \pm 10$ mV at a scan rate of 0.1667 mV/s. E_{CORR} experiments were run for a period of ~14-15 days.

Prior to cyclic voltammetry (CV) experiments, electrodes were cathodically cleaned at -1.3 V and -1.1 V for two and three minutes, respectively. The potential was then scanned from -1.1 V to various anodic limits at a scan rate of 5 mV/s.

4.2.4. Experimental Solutions

Experiments were performed in a series of solutions containing only Cl^- or a combination of 5.0 M Cl^- with various concentrations of $\text{HCO}_3^-/\text{CO}_3^{2-}$ or SO_4^{2-} . The highly concentrated (5.0 M) Cl^- solutions were used to mimic the high salinity of the sedimentary groundwaters at the repository depth. In comparison, the concentration of Cl^- in seawater is only approximately 0.6 M. The pH was set to 8.9 ± 0.5 to simulate the expected pH range of the groundwater (pH 7-10). Before starting the experiment each solution was continuously sparged at a high flow rate with ultra-high purity Ar for at least one hour. Ar sparging was continued throughout the experiment at a reduced flow rate to maintain minimal levels of dissolved O_2 within the solution.

4.2.5. Surface Analysis

Iron corrosion products were identified using a Renishaw 2000 Raman spectrometer equipped with a 632.8 nm laser line and an optical microscope with a 50X magnification objective lens. GRAMS 386 Raman software was used for the collection and fitting of spectra. SEM was used to determine the morphology of corroded surfaces using either a Hitachi S-4500 Field Emission SEM or LEO (Zeiss) 1540XB FIB/SEM.

4.3. RESULTS

4.3.1. Effects of Chloride

4.3.1.1. E_{CORR} and R_p Measurements

Figure 4-1 shows the E_{CORR} values recorded on the steel coupons, over exposure periods of 6-15 days, to deaerated solutions containing $[Cl^-]$ of 0.01, 1.00, and 5.00 M. The dashed horizontal lines represent the equilibrium potentials (E^e) for the transformation of metallic iron to Fe_3O_4 (-0.851 V) and the oxidation of $Fe(OH)_2$ to α - Fe_2O_3 (-0.755 V) calculated from the Nernst equation at a pH of 8.9. The equilibrium for the oxidation of $Fe(OH)_2$ to α - Fe_2O_3 was chosen as it represents the lowest potential at which an Fe^{III} oxide can be thermodynamically expected. Subsequently, this equilibrium will be designated $Fe^{II} ox \rightleftharpoons Fe^{III} ox$, since, as will be shown, a wide range of Fe^{III} oxides and oxyhydroxides can form. Figure 4-2 shows the R_p values recorded during the E_{CORR} experiments.

It is evident from Figure 4-1 that the E_{CORR} values for the two lower $[Cl^-]$ experiments are lower than the values recorded in 5.0 M. For the two lower $[Cl^-]$, the E_{CORR} values suggest that the surface oxide may be predominantly Fe_3O_4 with little conversion to Fe^{III} oxides. Figure 4-2 shows the R_p values recorded in the $[Cl^-]=0.01$ solution remain approximately constant at $20 \text{ k}\Omega\text{cm}^2$, indicating a relatively high constant corrosion rate, while the E_{CORR} values are slightly erratic, suggesting minor corrosion events occur on the electrode surface. For $[Cl^-]=1.00$ M, R_p decreases slightly from $30 \text{ k}\Omega\text{cm}^2$ to $20 \text{ k}\Omega\text{cm}^2$ over the duration of the experiment as E_{CORR} rises from -0.820 V to -0.795 V. This combination of an increasing corrosion rate ($\propto R_p^{-1}$) and E_{CORR} suggests a slight acceleration of the cathodic reaction, likely caused by H_2O reduction on a surface oxide layer expected to be Fe_3O_4 .

For the three experiments in $[Cl^-]=5.00$ M solutions, E_{CORR} initially ranges between -0.780 V and -0.760 V. These values approach the $(E^e)_{Fe^{II} ox/Fe^{III} ox}$ boundary. Over the first 2 days of exposure, the R_p values are similar in all three experiments suggesting similar corrosion behaviour. For experiments #2 and #3 R_p increases in a similar manner over the first six days. The increase in the E_{CORR} compared to the low $[Cl^-]$ solutions could reflect slight differences in the dissolved $[O_2]$ of the solution. However, the more positive E_{CORR} values are accompanied by a significant increase in the R_p values, suggesting a less reactive surface. One possibility is that the

high $[\text{Cl}^-]$ leads to Cl^- adsorption and an accelerated conversion of Fe^{II} to Fe^{III} in the oxide surface. The steady increase in R_p in experiment #2 suggests a slow passivation of the steel surface, consistent with a slow oxidation due to reaction with O_2 . After 11 days E_{CORR} increases by $\sim 15\text{-}20$ mV to a value close to the $(E^e)_{\text{Fe}^{\text{II}} \text{ ox}/\text{Fe}^{\text{III}} \text{ ox}}$ boundary leading to a marked increase in R_p . This behaviour is consistent with the suppression of the anodic reaction by the formation of an insulating Fe^{III} oxide. Subsequently, around ~ 13 days both E_{CORR} and R_p decrease, indicating a slight reactivation of the anodic reaction most likely caused by the local breakdown of the passivating Fe^{III} oxide. The small decrease in R_p suggests any breakdown locations were only moderately active or few in number. This apparent passive film breakdown and onset of localized corrosion occurs when E_{CORR} reaches the equilibrium line for the $\text{Fe}^{\text{II}} \text{ ox}/\text{Fe}^{\text{III}} \text{ ox}$ transformation.

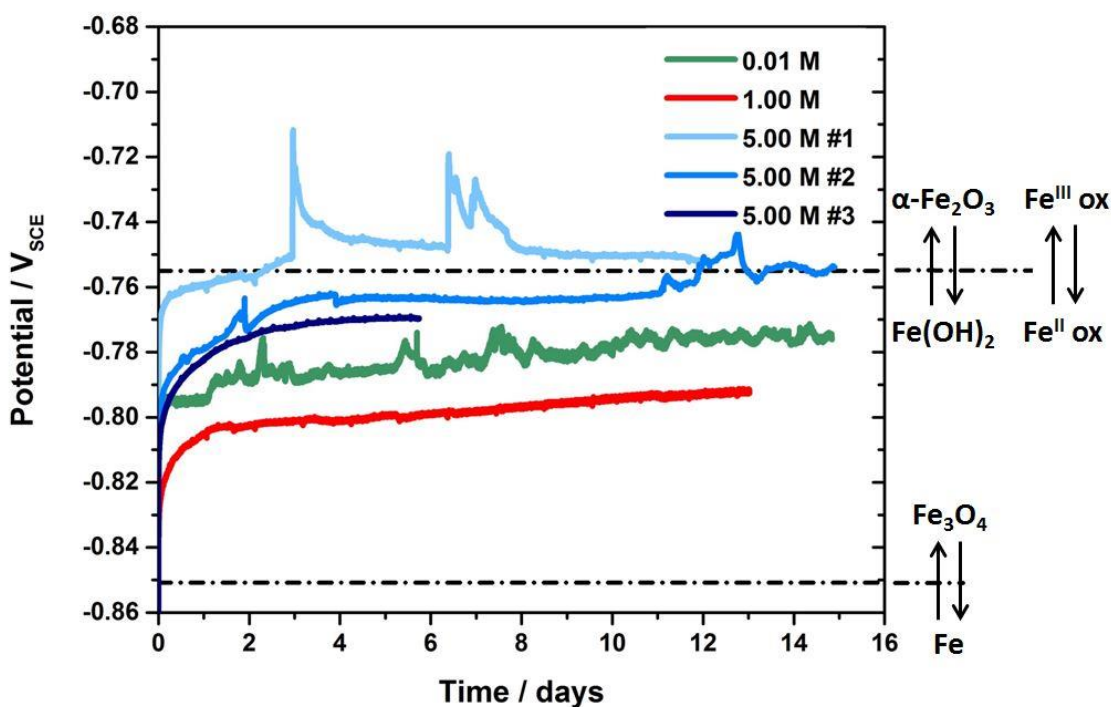


Figure 4-1: Corrosion potentials (E_{CORR}) measured in solutions containing various $[\text{Cl}^-]$. Dashed lines represent the thermodynamic boundaries for the oxidation of Fe to Fe_3O_4 and $\text{Fe}(\text{OH})_2$ to $\alpha\text{-Fe}_2\text{O}_3$. The latter equilibrium is subsequently designated $\text{Fe}^{\text{II}} \text{ ox}/\text{Fe}^{\text{III}} \text{ ox}$.

In experiment #1, E_{CORR} increased more rapidly to values more positive than $(E^e)_{\text{Fe}^{II} \text{ ox}/\text{Fe}^{III} \text{ ox}}$. Over this initial 3 day period R_p values are close to those observed in the other two experiments in 5.0 M Cl^- solution. However, after ~ 3 days, a major E_{CORR} transient is observed leading to a significant decrease in R_p . Similar major events occur after ~ 6 and 7 days, Figure 4-3, each with sudden increases in E_{CORR} accompanied by a decrease in R_p (increase in corrosion rate) suggesting a breakdown of the Fe^{III} passivating oxide, formed as E_{CORR} increased to and exceeded $(E^e)_{\text{Fe}^{II} \text{ ox}/\text{Fe}^{III} \text{ ox}}$, leading to high corrosion rates at local breakdown sites. The subsequent decrease in E_{CORR} is not accompanied by a change in R_p (e.g., over the time period 3 to 6 days) consistent with the maintenance of a high localized corrosion rate in response to the evolution of conditions within the breakdown site(s). The subsequent events occurring after 6.5 and 7 days (lines (b) and (c), Figure 4-3) lead to further minor decreases in R_p confirming the onset of localized corrosion at sites which do not subsequently repair. The magnitude and number of such events in experiment #1 compared to experiment #2 and the much lower R_p values indicate highly active localized corrosion in the first case.

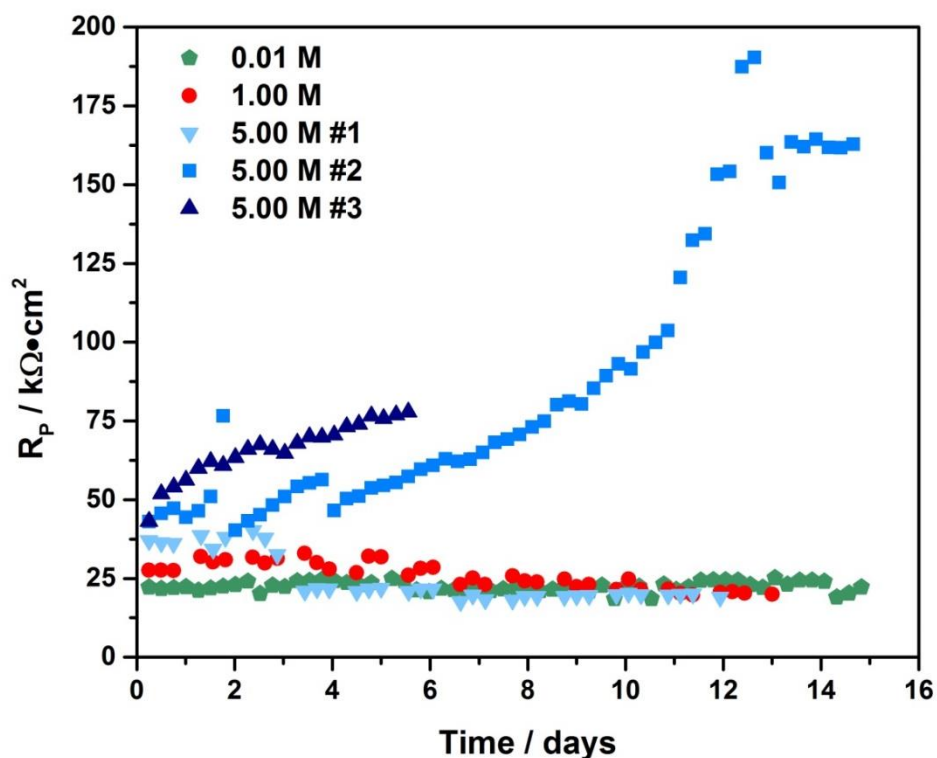


Figure 4-2: Polarization resistance (R_p) measurements for solutions containing various $[\text{Cl}^-]$ as given in Figure 4-1.

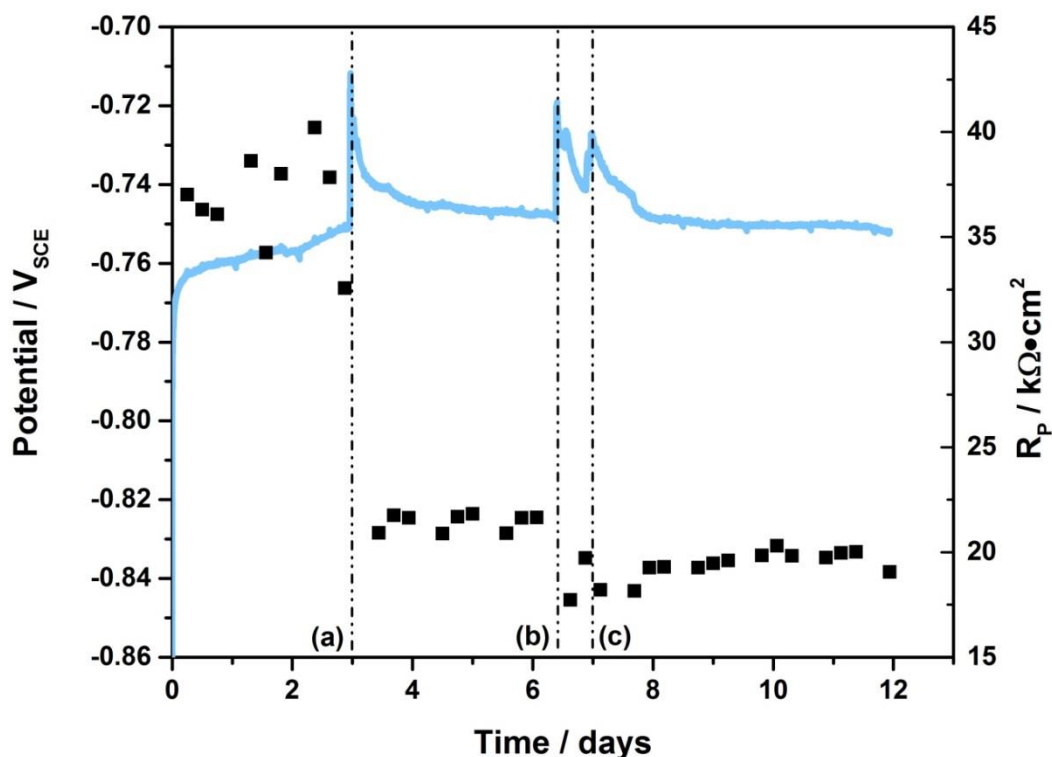


Figure 4-3: Corrosion potential (E_{CORR}) and polarization resistance (R_p) measurements recorded in the $[Cl^-]=5.00$ M (#1) solution.

4.3.1.2. Raman Spectroscopy

Figure 4-4(a) shows Raman spectra recorded on various locations on the steel surface after exposure to the $[Cl^-]=0.01$ M solution. Spectrum (1), recorded on the corrosion product deposit, suggests the presence of green rust (GR), with minor bands at 425 and 506 cm^{-1} assigned to the $Fe^{2+}-OH$ and $Fe^{3+}-OH$ stretching modes of the green rust structure [20-26]. Since Cl^- is the only anion present, the coordinating interlayer anion of the GR will be either Cl^- , with the idealized structure $[Fe_3^II Fe^III(OH^-)_8]^+[Cl \cdot nH_2O]^-$, or OH^- with the structure $[Fe_{(1-x)}^II Fe_x^III(OH^-)_2]^{x+}[xOH^- \cdot (1-x)H_2O]^{x-}$ [27-29]. Differentiating between the two is difficult since both exhibit Raman bands in the $200-250$ cm^{-1} region. The presence of minor amounts of GR can be attributed to a slight ingress of O_2 into the electrochemical cell from the surrounding air environment.

The Raman band at 673 cm^{-1} in spectra (2) and (3) is attributed to the A_{1g} mode of Fe_3O_4 [3, 20, 23, 24, 26, 30-37]. The formation of Fe_3O_4 indicates the dominance of anoxic corrosion via H_2O reduction, confirming that only traces of dissolved O_2 were present in this experiment, consistent with the measured E_{CORR} (Figure 4-1) which was well below the $(E^e)_{\text{Fe}^{\text{II}}\text{ ox}/\text{Fe}^{\text{III}}\text{ ox}}$ boundary, making Fe_3O_4 the expected phase. The large intensity and the sharpness of the peaks indicate the Fe_3O_4 film is crystalline and relatively thick. The absence of Fe^{III} oxides indicates that the Cl^- catalyzed oxidation of the Fe^{II} film is minimal at this low $[\text{Cl}^-]$, at least after only 15 days of exposure.

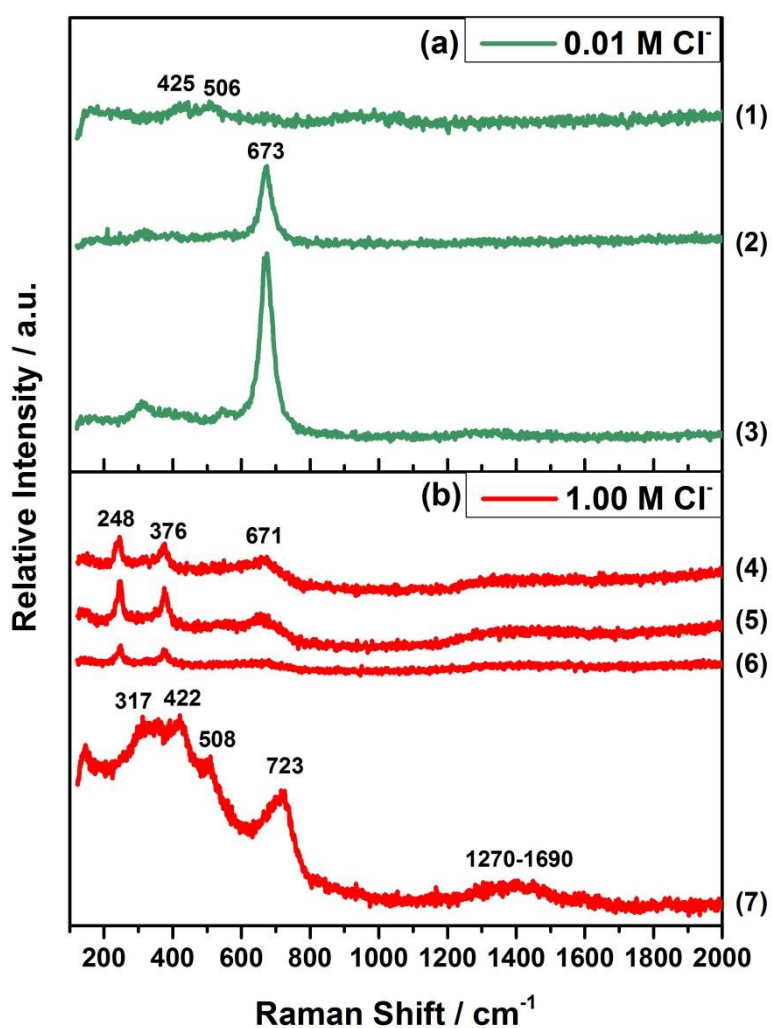


Figure 4-4: Ex-situ Raman spectra (1-7) recorded at various locations on the steel surface after exposure to (a) $[\text{Cl}^-] = 0.01\text{ M}$ and (b) $[\text{Cl}^-] = 1.00\text{ M}$.

Figure 4-4(b) shows the Raman spectra recorded on various locations on the steel surface exposed to the $[Cl^-]=1.00$ M solution. The peaks located at 248 and 376 cm^{-1} (spectra 4-6) confirm the presence of lepidocrocite (γ -FeOOH) [20, 22, 26, 30, 34, 38-42], with the peak at 671 cm^{-1} (spectra 4, 5) attributed to Fe_3O_4 . The presence of both γ -FeOOH and Fe_3O_4 suggests a surface partially oxidized by reaction with dissolved O_2 , but not passivated, as expected given the low E_{CORR} and small R_p values. It is possible that the oxidation of Fe^{II} to Fe^{III} in the surface of the corrosion product film occurs more rapidly at this higher $[Cl^-]$. Spectrum (7) shows peaks at 317, 422, 508, and 723 cm^{-1} attributable to akaganeite (β -FeOOH) which is known to form on archaeological artefacts corroded in Cl^- containing soils [31]. However, maghemite (γ - Fe_2O_3) also exhibits broad peaks at 350, 500, and 700 cm^{-1} [22, 30, 32, 43]. Given the relatively high $[Cl^-]$, β -FeOOH appears to be the most likely phase. The broad bands at low Raman shifts and the presence of a broad band in the region of 1270 to 1690 cm^{-1} (attributable to carbonaceous residues at a corroded site) indicate this was a slightly more corroded location covered with a poorly crystalline deposit.

Figure 4-5 shows the Raman spectra recorded on the coupons corroded in each of the three $[Cl^-]=5.00$ M solutions. All three spectra recorded after experiment #1 exhibit peaks at 243 and 378 cm^{-1} indicating the formation of γ -FeOOH, Figure 4-5(a). The band at 659 cm^{-1} in (1) could be due to either γ -FeOOH or Fe_3O_4 . While the accepted location for the main band of Fe_3O_4 is closer to 670 cm^{-1} , several studies have seen this characteristic Fe_3O_4 peak at Raman shifts as low as 661 cm^{-1} [30, 35, 40]. However, the clear presence of bands for γ -FeOOH in all three spectra suggests the band at 659 cm^{-1} can also be attributed to γ -FeOOH. The broad peaks at 726 and 722 cm^{-1} in spectra (2) and (3) are more difficult to assign since β -FeOOH (720 cm^{-1}) [22, 31, 44, 45], γ - Fe_2O_3 (700-710 cm^{-1}) [22, 30, 32, 43], and ferrihydrite (680 cm^{-1} to 720 cm^{-1}) [20, 25, 26, 35, 46] all have peaks in this region. Given the high $[Cl^-]$ and the minor peak at ~ 300 cm^{-1} [31, 44, 45] (spectrum 3) β -FeOOH seems the most probable phase. The two broad peaks between 1270-1700 cm^{-1} can be attributed to Fe_3C residues after dissolution of α -Fe from pearlite grains in the steel [3, 33], and suggests that spectrum (3) was recorded on a more heavily corroded location on the surface. The universal presence of γ -FeOOH and β -FeOOH is consistent with the presence of an Fe^{III} surface layer expected at the positive value of E_{CORR} measured in this solution (Figure 4-1). The positive E_{CORR} and major localized events, leading to low R_p values, observed in this experiment are consistent with the general surface coverage by Fe^{III} oxide/hydroxide.

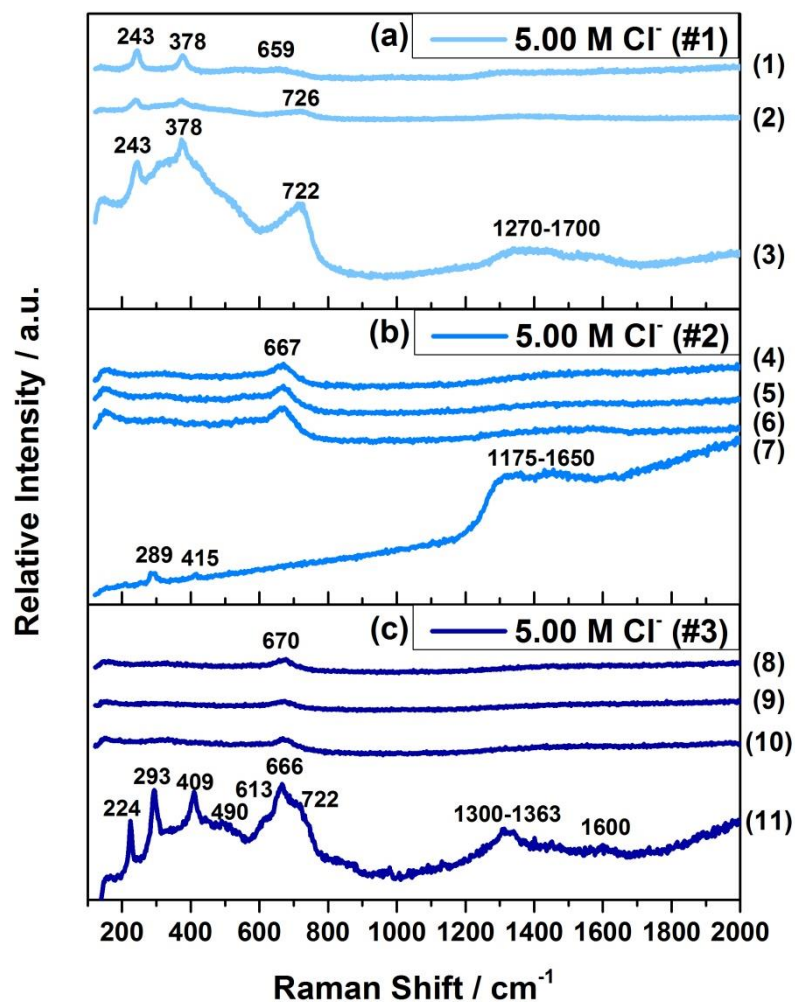


Figure 4-5: Ex-situ Raman spectra (1-11) recorded at various locations on the steel surface after exposure to $[Cl^-]=5.00$ M environments.

Spectra (4), (5), and (6) recorded after exposure to $[Cl^-]=5.00$ M (#2), Figure 4-5(b), were recorded on areas of the surface covered by a uniform corrosion film; i.e. not exhibiting significant deposits. The Raman band at 667 cm^{-1} and the very broad weak band in the 1300 to 1600 cm^{-1} region indicate a thin layer of Fe_3O_4 over a slightly corroded surface. Also, the suggestion of bands in the 200 to 400 cm^{-1} range would be consistent with oxidation of the outer layers of this Fe_3O_4 layer to an Fe^{III} state as expected at the positive E_{CORR} achieved. The peaks at 289 and 415 cm^{-1} in spectrum (7), recorded on a location covered by a deposit (suggesting localized corrosion) are difficult to assign, although only Fe^{III} oxides generally exhibit Raman bands in this spectral region. Raman bands located at 410 and 425 cm^{-1} have been

assigned to $\text{Fe}(\text{OH})_2$ [22], which is known to form as a precursor to other iron oxides. While the deposit cannot be identified, the Fe_3C signature in the region $1175\text{-}1650\text{ cm}^{-1}$ suggests more extensive corrosion at this location than observed at locations (4) to (6). The background fluorescence can be attributed to electronic excitation of the exposed metal surface. The apparent dominance of Fe_3O_4 with a slightly oxidized surface indicates that the large increase in the R_p , Figure 4-2, can be attributed to a slow passivation process to produce a thin layer difficult to detect by Raman spectroscopy. The spectra recorded on the surface of the specimen exposed in experiment #3, Figure 4-5(c), show similar peaks to those observed in both experiments #1 and #2 with large areas of the surface covered by a thin Fe_3O_4 film, possibly with a slightly oxidized surface (spectra 8 to 10), and some areas more heavily corroded and covered by Fe^{III} oxyhydroxide deposits (spectrum (11)).

Table 4-1: Summary of corrosion products identified by Raman spectroscopy in the range of chloride environments investigated

Oxide Phase	0.01 M	1.00 M	5.00 M (#1)	5.00 M (#2)	5.00 M (#3)
Fe_3O_4					
GR					
$\beta\text{-FeOOH}$					
$\gamma\text{-FeOOH}$					
$\alpha\text{-Fe}_2\text{O}_3$					
$\gamma\text{-Fe}_2\text{O}_3$					

4.3.1.3. Scanning Electron Microscopy on surfaces and cross-sections prepared by Focused Ion Beam Milling

Figure 4-6 shows SEM micrographs recorded on the steel surface after 15 days exposure in $[\text{Cl}^-]=0.01\text{ M}$. The low magnification image indicates the surface is relatively uncorroded, Figure 4-6(a), but higher magnification indicates corrosion has occurred on a minor scale, Figure 4-6(c). Corrosion is non-uniform with partially detached layers and a scattered deposit. The micrographs do not reveal deposits with a morphology indicating the presence $\text{GR}(\text{Cl}^-)$ (observed in the Raman spectra) suggesting only minimal amounts are present. Also, very little evidence of localized corrosion is observed despite the fluctuations in E_{CORR} and to a lesser degree R_p . This is

consistent with the Raman evidence, Figure 4-4(a), and indicates the surface is generally covered by only a thin surface layer of Fe_3O_4 .

SEM micrographs after 13 days exposure to the $[\text{Cl}^-]=1.00\text{ M}$ solution are shown in Figure 4-7. The visibility of polishing lines, Figure 4-7(a), confirms only a very thin surface film is present. This is confirmed by FIB cross-sections cut through these locations (Figure 4-8) and consistent with the low value of E_{CORR} , Figure 4-1. The fine structure of the general surface is shown in Figure 4-7(b), and is likely a mix of Fe_3O_4 and $\gamma\text{-FeOOH}$ based on the Raman analyses, consistent with some surface oxidation due to the presence of traces of dissolved O_2 . Figure 4-7(c) shows the morphology of small deposits seen in several locations. Cross-sectional analysis through one of these deposits is shown in Figure 4-9. The magnified image, Figure 4-9(b), shows that the deposit is porous, possibly exposing the base metal, but that no significant localized corrosion has occurred. The Raman spectrum (7 in Figure 4-4(b)) confirms such locations are more heavily corroded and covered with deposited akaganeite, $\beta\text{-FeOOH}$.

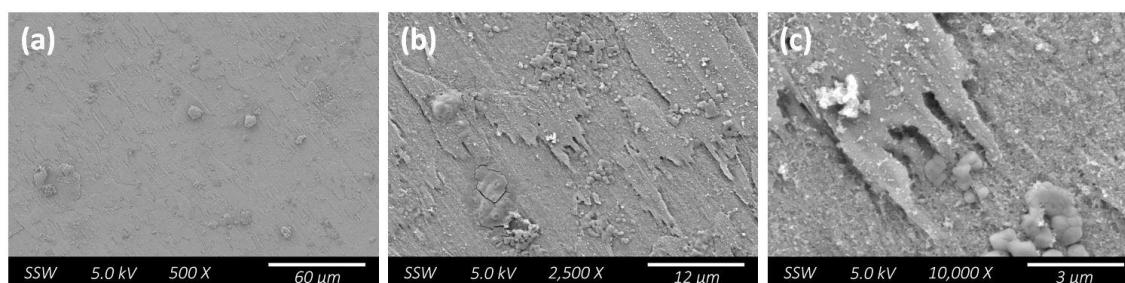


Figure 4-6: SEM micrographs showing the morphology of the corrosion product after exposure to the solution containing $[\text{Cl}^-]=0.01\text{ M}$.

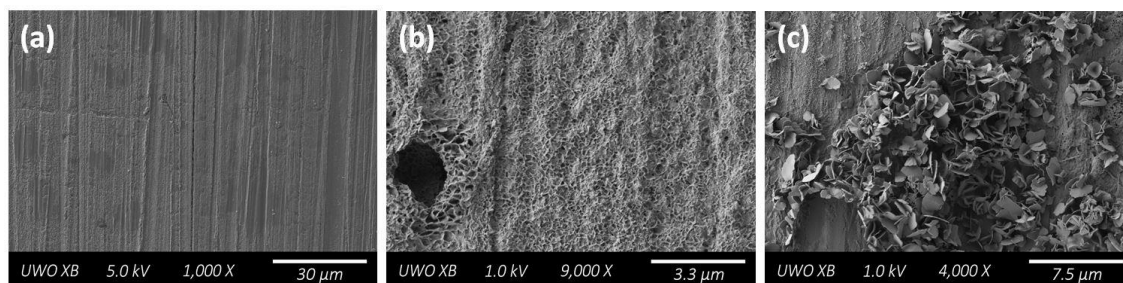


Figure 4-7: SEM micrographs showing the morphology of the corrosion product after exposure to the solution containing $[\text{Cl}^-]=1.00\text{ M}$.

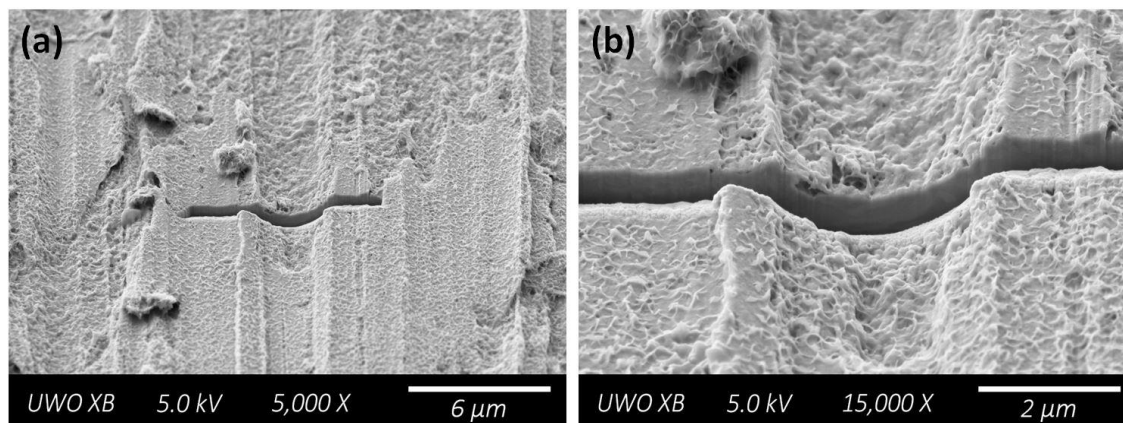


Figure 4-8: FIB cross-sections for the general corrosion film on the steel exposed to $[Cl^-]=1.00\text{ M}$.

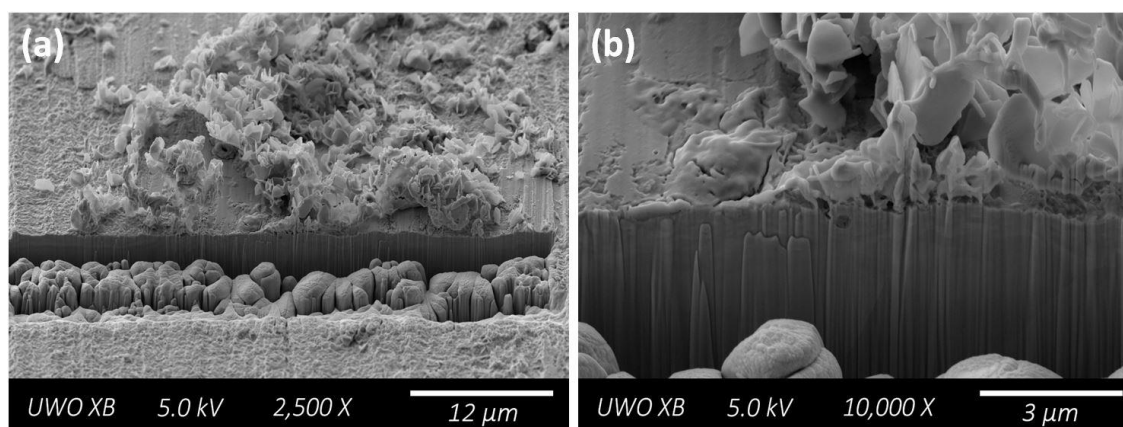


Figure 4-9: FIB cross-sections for corrosion deposits formed on the steel surface exposed to $[Cl^-]=1.00\text{ M}$.

Figure 4-10 shows the SEM micrographs recorded after exposure to $[Cl^-]=5.00\text{ M}$ (#1). These images are consistent with the electrochemical observations which show a positive E_{CORR} and a number of potential transients indicating either individually large or a large number of localized corrosion sites on a generally passive surface, Figure 4-10(a). The clear visibility of the polishing lines confirms the general surface is passivated by a thin film. The accumulation of corrosion product seen at local sites, Figure 4-10(b), and a FIB cross-section through such a deposit, Figure 4-11(a), confirms that the deposits are located over shallow pits on the steel surface which the low R_p values (Figure 4-2) show remain active over the ensuing exposure period. Figure 4-11(b) and (c) show additional FIB cross-sections through a second active location with the

backscattered electron image, Figure 4-11(c), more clearly outlining the interface between the base metal and deposited corrosion product. Again, pitting beneath such a deposit is shallow.

Figure 4-12 shows the SEM micrographs recorded after 15 days of exposure to the $[Cl^-]=5.00\text{ M}$ (#2) environment. The surface is generally featureless, Figure 4-12(a), with some minor localized corrosion events which are much less frequent than in experiment #1. This is consistent with the noiseless E_{CORR} and steady increase in R_p prior to the minor breakdown events which occur after ~ 11 days of exposure (Figure 4-1 and Figure 4-2). The strong Raman signal for residual Fe_3C , spectrum (7) in Figure 4-5, is most likely recorded on such a region. Figure 4-12(b) shows the morphology of the general surface film, seen as darker regions in Figure 4-12(a), which Raman analysis indicates is Fe_3O_4 . The observation of Fe_3O_4 coupled with an E_{CORR} which approaches the $(E^e)_{Fe^{II} ox/Fe^{III} ox}$ boundary indicates oxidation of the outer surface of the Fe_3O_4 consistent with the large R_p values recorded. The relatively small drop in the R_p compared to that recorded in $[Cl^-]=5.00\text{ M}$ (#1) can be attributed to the much smaller density of film breakdown locations and their limited propagation which is confirmed by the absence of the large events shown to occur in experiment (#1). It is possible this is due to a lower O_2 concentration in this experiment. SEM micrographs recorded in the shorter experiment (#3) in $[Cl^-]=5.00\text{ M}$ (Figure 4-13) exhibit similar features to those observed in the $[Cl^-]=1.00\text{ M}$ experiment which are comprised of a thin layer which the Raman analysis suggests is Fe_3O_4 , Figure 4-13(b), and a fine corrosion deposit, Figure 4-13(c), which appears to be a mixture of $\alpha\text{-Fe}_2\text{O}_3$ and $\gamma\text{-Fe}_2\text{O}_3$. The yellow/orange colour of the deposit supports this phase assignment.

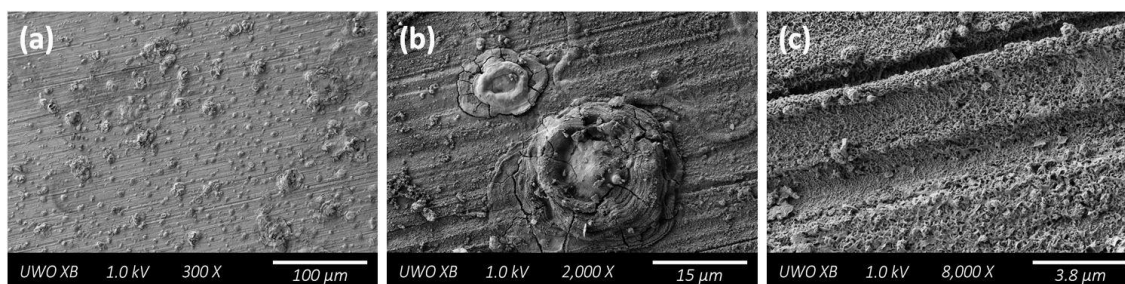


Figure 4-10: SEM micrographs showing the morphology of the corrosion product after exposure to the $[Cl^-]=5.00\text{ M}$ (#1) solution.

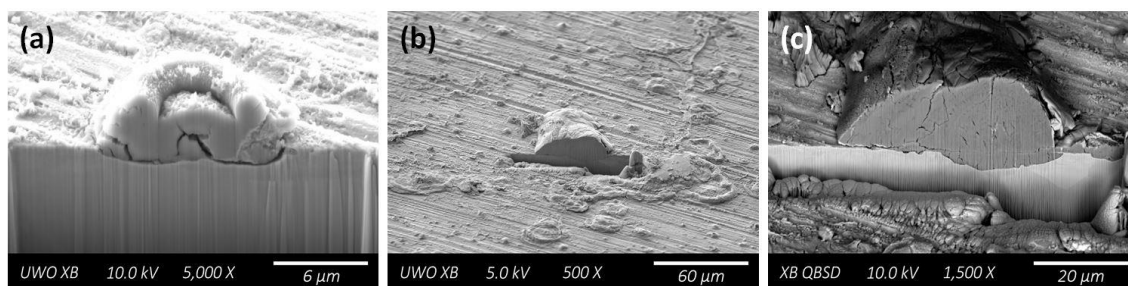


Figure 4-11: FIB cross-sections through corrosion deposit accumulations on the steel exposed to $[Cl^-]=5.00\text{ M}$ (#1).

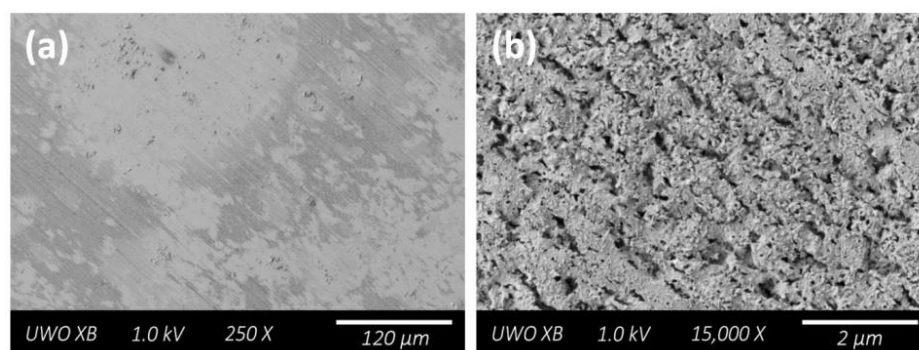


Figure 4-12: SEM micrographs showing the corrosion product morphology after exposure to $[Cl^-]=5.00\text{ M}$ (#2).

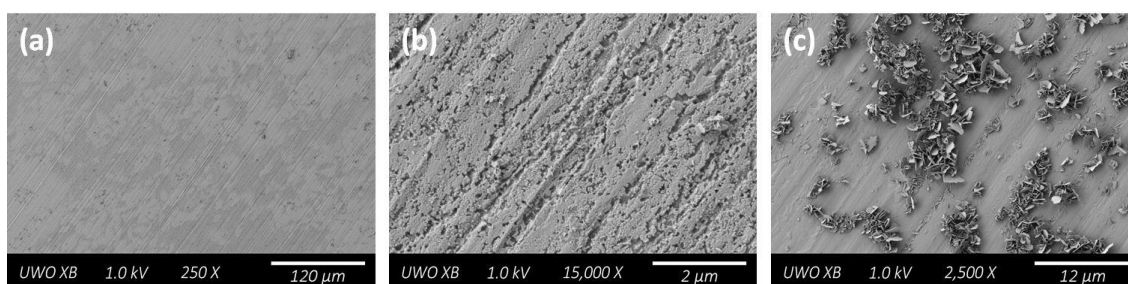


Figure 4-13: SEM micrographs showing the corrosion product morphology after exposure to $[Cl^-]=5.00\text{ M}$ (#3).

4.3.1.4. Cyclic Voltammetry

Figure 4-14(a) shows a series of CVs recorded to increasing anodic limits in the $[Cl^-]=0.01$ M solution. Since the linear increase in current with potential indicates an ohmic effect due to low solution conductivity the experiment was repeated at an increased ionic strength by adding 0.10 M $NaClO_4$, Figure 4-14(b). The vertical lines indicate the range of E_{CORR} values measured in the corrosion experiment, Figure 4-1, and show E_{CORR} was located at the base of the active dissolution region. The current increases at more positive potentials and shows no tendency to passivate confirming that, under voltammetric conditions, active dissolution occurs. The low R_p values, Figure 4-2, confirm that passivation did not occur in this experiment.

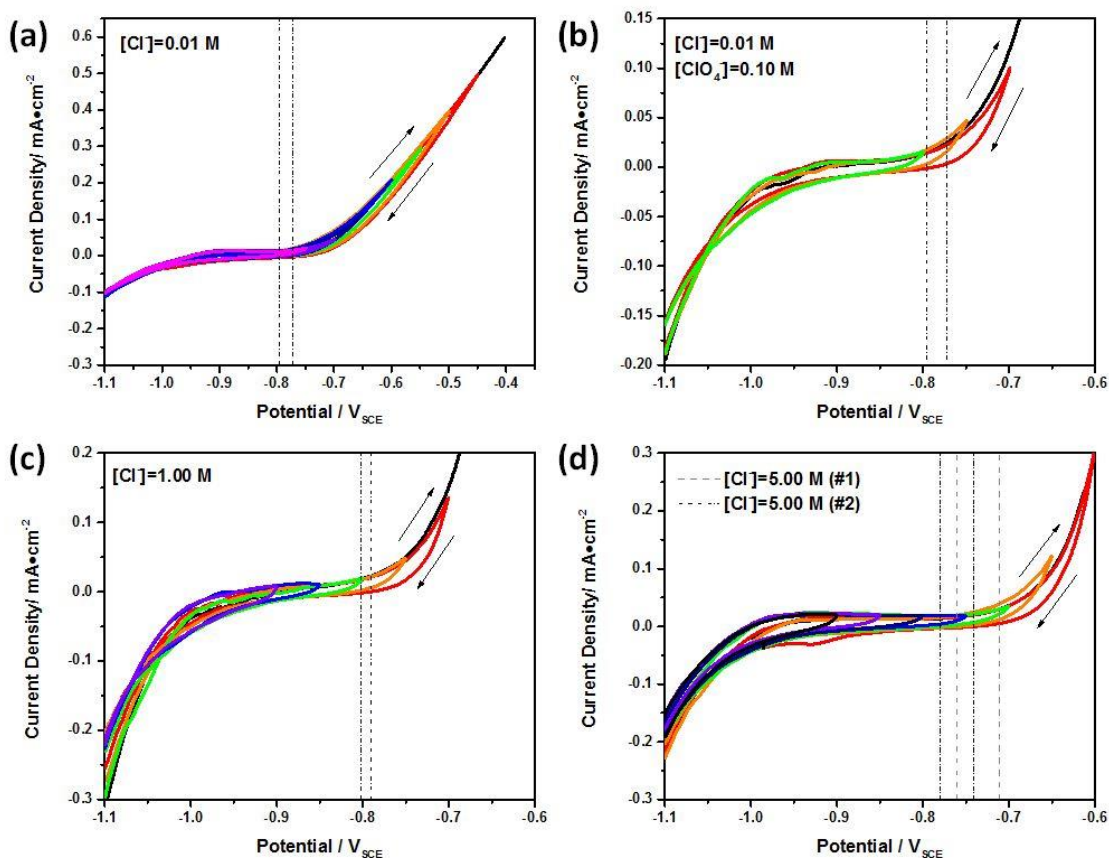


Figure 4-14: Cyclic voltammograms recorded to increasing anodic limits on steel coupons exposed to (a) $[Cl^-]=0.01$ M; (b) $[Cl^-]=0.01$ M & $[ClO_4^-]=0.10$ M; (c) $[Cl^-]=1.00$ M; and (d) $[Cl^-]=5.00$ M. Dashed vertical lines represent the range of E_{CORR} measured during the corrosion experiments.

For $[\text{Cl}^-]=1.00\text{ M}$, (Figure 4-14(c)) E_{CORR} values are again at the foot of the active dissolution curve, while for $[\text{Cl}^-]=5.00\text{ M}$, Figure 4-14(d), the onset of active dissolution is significantly suppressed. This is best appreciated by comparing the anodic currents at -0.7 V for the three Cl^- solutions. For 0.01 M and 0.1 M the current is approximately the same, but for 5.00 M it is considerably lower. This shift of active dissolution to more positive potentials is consistent with the claim that, in the corrosion experiments the surface can be initially stabilized against active dissolution by the catalyzed oxidation of the surface by traces of O_2 when $[\text{Cl}^-]$ is high. A surface stabilized in this manner would then be more susceptible to the breakdown processes observed at this $[\text{Cl}^-]$. These results are consistent with previous work performed by Lee et al. [4] which showed that Cl^- was able to suppress the anodic reaction of Fe to Fe^{2+} .

4.3.2. Effects of Carbonate

4.3.2.1. E_{CORR} and R_p Measurements

Since specimens exposed to $[\text{Cl}^-]=5.00\text{ M}$ exhibited the highest E_{CORR} values and are the most likely to exhibit localized corrosion, the influence of $[\text{HCO}_3^-/\text{CO}_3^{2-}]$ was examined at this $[\text{Cl}^-]$. The observation of shallow pits clearly indicated pit initiation occurred in the concentrated Cl^- solution in the absence of any buffer capacity. Hydrolysis of Fe^{2+} produced by active dissolution at local sites would lead to the increase in local acidity required to maintain active propagation providing some O_2 remained available. Here, the influence of added $\text{HCO}_3^-/\text{CO}_3^{2-}$ on the pitting process is investigated.

Figure 4-15 shows E_{CORR} values recorded over an 11-13 day exposure period to deaerated 5.00 M Cl^- solutions containing two different $\text{HCO}_3^-/\text{CO}_3^{2-}$ concentrations. The dashed horizontal lines show the E^e for the oxidation of Fe to Fe_3O_4 (-0.851 V) and the $(E^e)_{\text{Fe}^{II}\text{ ox}/\text{Fe}^{III}\text{ ox}}$ boundary (-0.755 V). When $[\text{HCO}_3^-/\text{CO}_3^{2-}]_{\text{T}}=0.001\text{ M}$, E_{CORR} initially achieves a value in the range of -0.760 V , as observed in $[\text{Cl}^-]=5.00\text{ M}$ (Figure 4-1), suggesting the formation of a surface oxide with a high Fe^{III} content. Both E_{CORR} and R_p (Figure 4-16) values follow the same trend as observed in the absence of $\text{HCO}_3^-/\text{CO}_3^{2-}$ (Figure 4-1 and Figure 4-2), with R_p increasing as E_{CORR} increases, consistent with a slow passivation of the surface by traces of dissolved O_2 . The transients in E_{CORR} indicate many attempts to initiate localized corrosion sites which lead to erratic R_p values. However, the establishment of stable active locations leading to a permanent decrease in R_p , as observed in the absence of $\text{HCO}_3^-/\text{CO}_3^{2-}$, (Figure 4-1 and Figure 4-2) is not observed. This could

be attributed to the ability of the $\text{HCO}_3^-/\text{CO}_3^{2-}$ to buffer, at least partially, the attempted increase in acidity caused by Fe^{2+} hydrolysis at breakdown sites, which allows repassivation to occur.

For both experiments at the higher $[\text{HCO}_3^-/\text{CO}_3^{2-}]_{\text{T}}=0.01$ M, E_{CORR} and R_p behave almost identically, lower steady values of E_{CORR} being observed and only a slow increase in R_p occurring. As expected at lower E_{CORR} values, local film breakdown events were not observed. While E_{CORR} remains steady over the course of the experiments, the R_p values are seen to rise slowly indicating a slow reaction with O_2 which could eventually lead to passivation. The lower values of R_p compared to those observed at the lower $[\text{HCO}_3^-/\text{CO}_3^{2-}]_{\text{T}}$ indicate that the passivation of the surface either did not occur or did not progress to the same extent. This, along with the lower E_{CORR} , suggests the surface film is likely Fe_3O_4 rather than an Fe^{III} oxide.

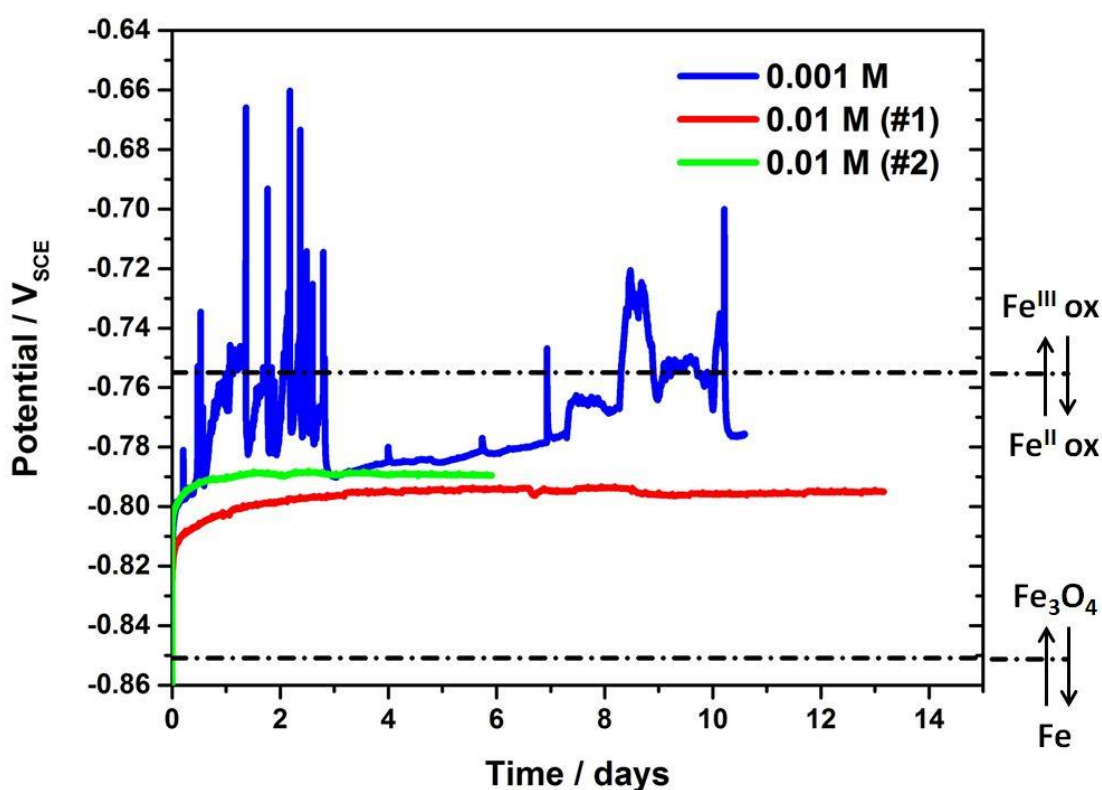


Figure 4-15: Corrosion potentials (E_{CORR}) for solutions in $[\text{Cl}^-]=5.00$ M containing $\text{HCO}_3^-/\text{CO}_3^{2-}$ at concentrations of 0.001 M and 0.01 M. Dashed horizontal lines represent the thermodynamic boundaries for the oxidation of Fe to Fe_3O_4 and $\text{Fe}(\text{OH})_2$ to $\alpha\text{-Fe}_2\text{O}_3$.

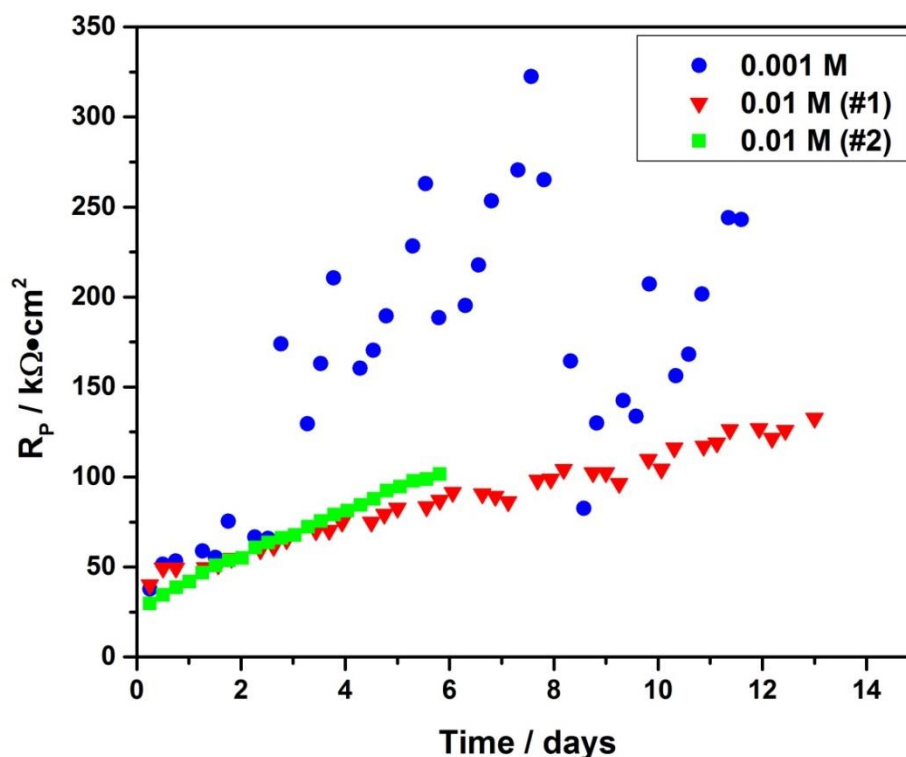


Figure 4-16: Polarization resistance (R_p) measurements for solutions containing $[Cl^-]=5.00\text{ M}$ and HCO_3^-/CO_3^{2-} at concentrations of 0.001 M and 0.01 M as given in Figure 4-15.

Figure 4-17 and Figure 4-18 show the E_{CORR} and R_p values measured in $[HCO_3^-/CO_3^{2-}]_T=0.10\text{ M}$. The transient behaviour of E_{CORR} , designated by the dashed vertical lines in both Figure 4-17 and Figure 4-18, can be attributed to unintended variations in dissolved O_2 content in the system. Within the various time periods shown both E_{CORR} and R_p increase as the glass frit in the tip of the gas sparging tube became clogged with precipitate formed in the extremely concentrated solution. This allowed the slow ingress of O_2 . The dashed lines show the times at which the tube was replaced and Ar-sparging re-established which lead to a decrease in both E_{CORR} and R_p . These excursions are consistent with changes in the kinetics of the anodic reaction; i.e., the corrosion rate decreases (R_p increases) as E_{CORR} increases, indicating the slow leakage of O_2 into the cell leading to oxidation of the surface to Fe^{III} and partial passivation. On re-establishing Ar-sparging the process is reversed and the corrosion rate increases as E_{CORR} is decreased. The increase in corrosion rate on depletion of O_2 indicates a loss of passivity (only partially established in this case) and the adoption of H_2O reduction as the cathodic reaction. This, and

the low E_{CORR} values (<-0.80 V) maintained under Ar-sparged conditions, indicate that at a high $[HCO_3^-/CO_3^{2-}]_T$ active dissolution conditions are maintained by the ability of HCO_3^-/CO_3^{2-} to complex Fe^{2+} .

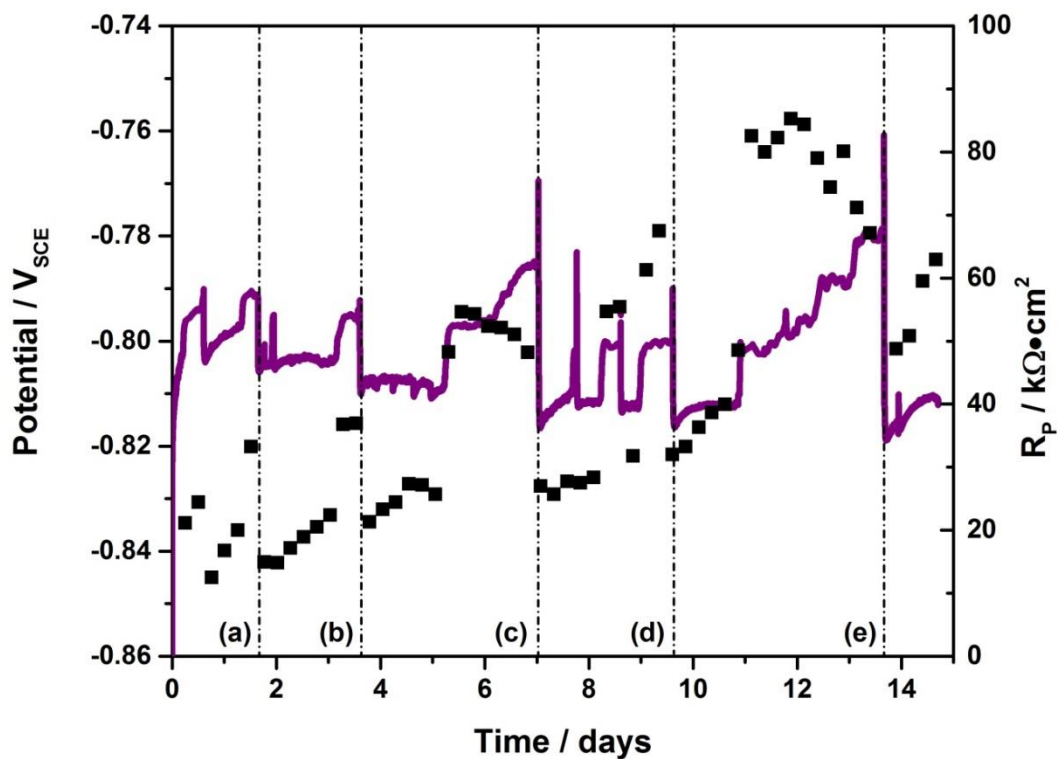


Figure 4-17: Corrosion potential (E_{CORR}) (solid line) and polarization resistance (R_p) (points) values recorded in $[Cl^-]=5.00$ M and $[HCO_3^-/CO_3^{2-}]=0.10$ M (#1). The dashed vertical lines indicate points at which the Ar sparging system needed to be replaced due to precipitate build-up.

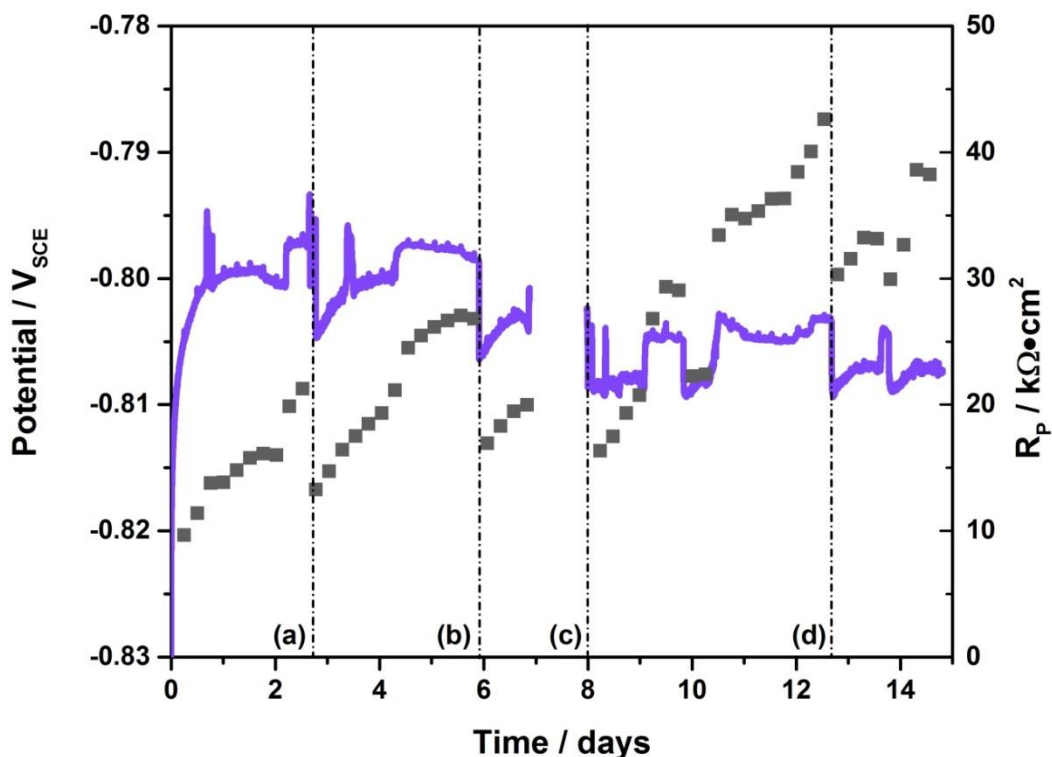


Figure 4-18: Corrosion potential (E_{CORR}) (solid line) and polarization resistance (R_p) (points) values recorded in $[Cl^-]=5.00\text{ M}$ and $[HCO_3^-/CO_3^{2-}]=0.10\text{ M}$ (#2). The dashed vertical lines indicate points at which the Ar sparging system needed to be replaced due to precipitate build-up

4.3.2.2. Raman and Infrared Spectroscopies

Figure 4-19(a) shows Raman spectra recorded on various surface locations after exposure to the $[HCO_3^-/CO_3^{2-}]_T=0.001\text{ M}$ solution. Spectra (1), (2), and (3) indicate the presence of green rust (GR), with the bands at 427 and 510 cm^{-1} assigned to the $Fe^{2+}-OH$ and $Fe^{3+}-OH$ stretching modes of the green rust structure. The composition of the solution suggests the coordinating anion in the GR interlayers could be OH^- , Cl^- , or CO_3^{2-} . Both CO_3^{2-} and Cl^- anions have been reported to generate peaks around $\sim 220\text{ cm}^{-1}$ [21, 24], and either of these anions may be incorporated within the GR structure, although it has been noted that GR has a preference for incorporating CO_3^{2-} . The Raman band located at 674 cm^{-1} in each of the four spectra for $[HCO_3^-/CO_3^{2-}]_T=0.001\text{ M}$ is attributed to the A_{1g} mode of Fe_3O_4 while the band at 300 cm^{-1} in spectrum (4) is attributed to a t_{2g} mode of Fe_3O_4 [30, 32, 36]. The Raman band located at 405 cm^{-1} remains

unassigned. Despite E_{CORR} approaching the $(E^e)_{\text{Fe}^{\text{II}}_{\text{ox}}/\text{Fe}^{\text{III}}_{\text{ox}}}$ boundary when the outer surface might be expected to be oxidized to Fe^{III} , this is not supported by the Raman data.

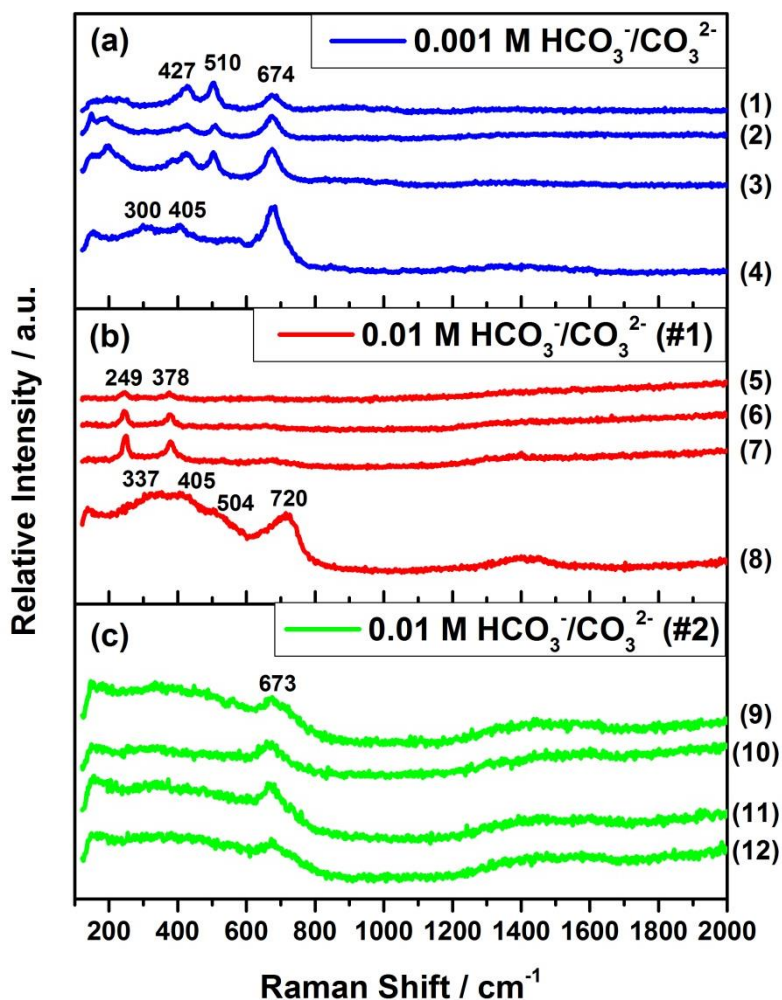


Figure 4-19: Ex-situ Raman spectra (1-12) recorded at various locations on the steel surface after exposure to 5.0 M Cl^- solutions containing (a) $[\text{HCO}_3^-/\text{CO}_3^{2-}] = 0.001$ M; and (b-c) $[\text{HCO}_3^-/\text{CO}_3^{2-}] = 0.01$ M.

Figure 4-19(b) shows the Raman spectra recorded on various locations on the surface after exposure to the $[\text{HCO}_3^-/\text{CO}_3^{2-}]_{\text{T}} = 0.01$ M (#1) solution. The Raman bands located at 249 and 378 cm^{-1} in spectra (5), (6), and (7) indicate the presence of $\gamma\text{-FeOOH}$. Given the value of E_{CORR} this suggests some surface oxidation has occurred. The Raman bands seen in spectrum (8) are difficult to assign but the general shape and the position of the bands are consistent with the

spectra observed at locations which have experienced localized corrosion to yield a poorly crystalline Fe^{III} deposit (peaks in the range < 800 cm⁻¹) over a more extensively corroded location (peaks within the region 1200-1700 cm⁻¹), Figure 4-4(b) and Figure 4-5(a) and (c).

The single Raman band seen at 673 cm⁻¹ in Figure 4-19(c) for [HCO₃⁻/CO₃²⁻]_T=0.01 M (#2) shows Fe₃O₄ is the dominant phase which is not unexpected at the low values of E_{CORR} measured in this experiment, Figure 4-15. The single peak in each of the spectra indicates that the surface is uniformly covered in Fe₃O₄. The relatively low intensity of the broad bands suggests the film is very thin, which is not unexpected after a 6 day exposure period.

Figure 4-20(a) shows the Raman spectra recorded on various locations after exposure to the [HCO₃⁻/CO₃²⁻]_T=0.10 M (#1) solution. The band at 663 cm⁻¹ (spectrum (3)) can be attributed Fe₃O₄, which is not unexpected since the E_{CORR} in the electrochemical experiment was low. The bands located at 380 and 722 cm⁻¹ are more difficult to assign but are attributable to Fe^{III} phases. Their breadth and the broad band located in the region 1200-1700 cm⁻¹ indicates a deposit-covered corroded location. The Raman band at 1070 cm⁻¹ is attributed to the ν₁ C–O symmetric stretching of a coordinated CO₃²⁻ species [20, 47, 48]. For spectra (1) and (2) there is no other detectable Raman bands suggesting that while the CO₃²⁻ component of the film is clearly seen, the remainder of the structure is not Raman active. Figure 4-21 shows two FTIR spectra recorded at different locations on the sample surface. While the corrosion deposit in these regions may not be fully Raman active, the clear IR active spectra indicate the presence of chukanovite (Fe₂(OH)₂CO₃) [49, 50]. The peaks at ~780 cm⁻¹, ~840 cm⁻¹ and ~950 cm⁻¹ can be attributed to the ν₄ in-plane bending of CO₃²⁻, the ν₂ out of plane bending of CO₃²⁻, and the δ-OH bending mode, respectively. The peaks centered over 1350-1520 cm⁻¹ are due to C–O stretching while those in the range 3300-3475 cm⁻¹ are due to O–H stretching. Both the Raman and FTIR analyses show the surface of the coupon exposed to [HCO₃⁻/CO₃²⁻]_T=0.10 M (#1) is largely covered by a film of Fe₂(OH)₂CO₃ with a small amount of detectable Fe₃O₄ and possibly an Fe^{III} oxide such as β-FeOOH or γ-Fe₂O₃.

The Raman spectra recorded on various locations on the steel coupon exposed to [HCO₃⁻/CO₃²⁻]_T=0.10 M (#2) are shown in Figure 4-20(b), the Raman band at 674 cm⁻¹ confirming presence of Fe₃O₄. Despite the similarity in E_{CORR} and R_p values in experiments #1 and #2 (Figure 4.21 and Figure 4.22) no Fe₂(OH)₂CO₃ is observed in experiment #2, suggesting the iron carbonate phase is precipitated only after extensive exposure. The two Raman bands seen within spectrum (7) at

326 and 425 cm^{-1} are not readily assigned. Table 4-2 summarizes the surface species detected by Raman spectroscopy on the steel coupons corroded in each of the $\text{HCO}_3^-/\text{CO}_3^{2-}$ exposure environments.

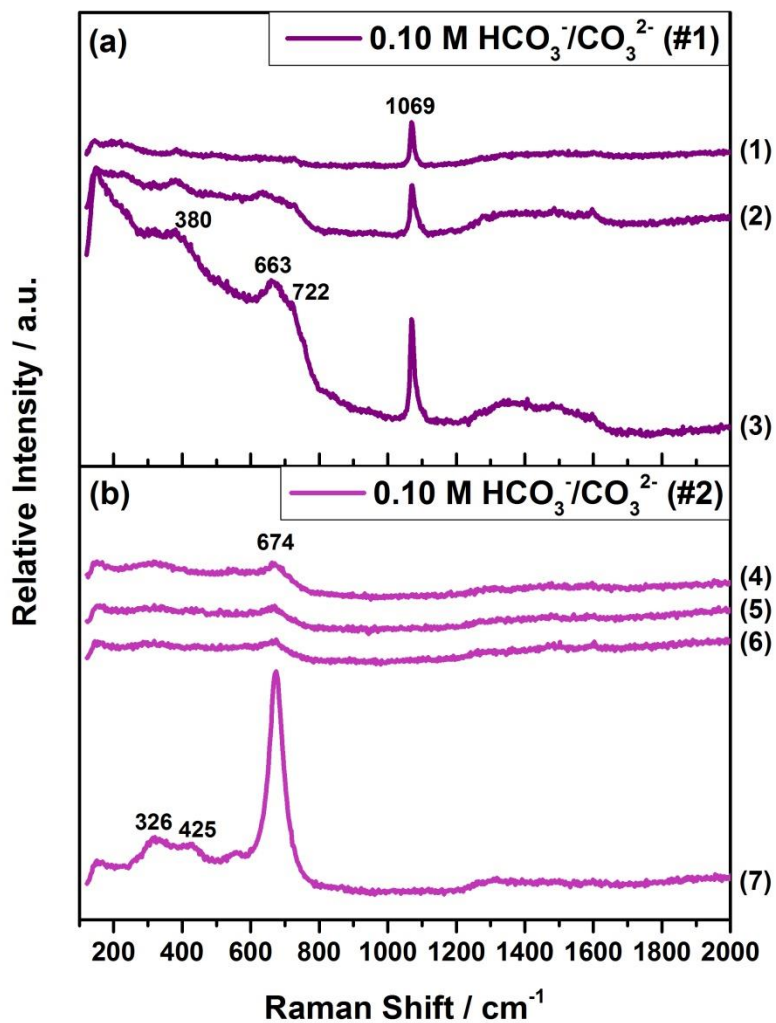


Figure 4-20: Ex-situ Raman spectra (1-7) recorded at various locations on the steel surface after exposure to 5.0 M Cl^- solutions containing $[\text{HCO}_3^-/\text{CO}_3^{2-}]=0.10$ M.

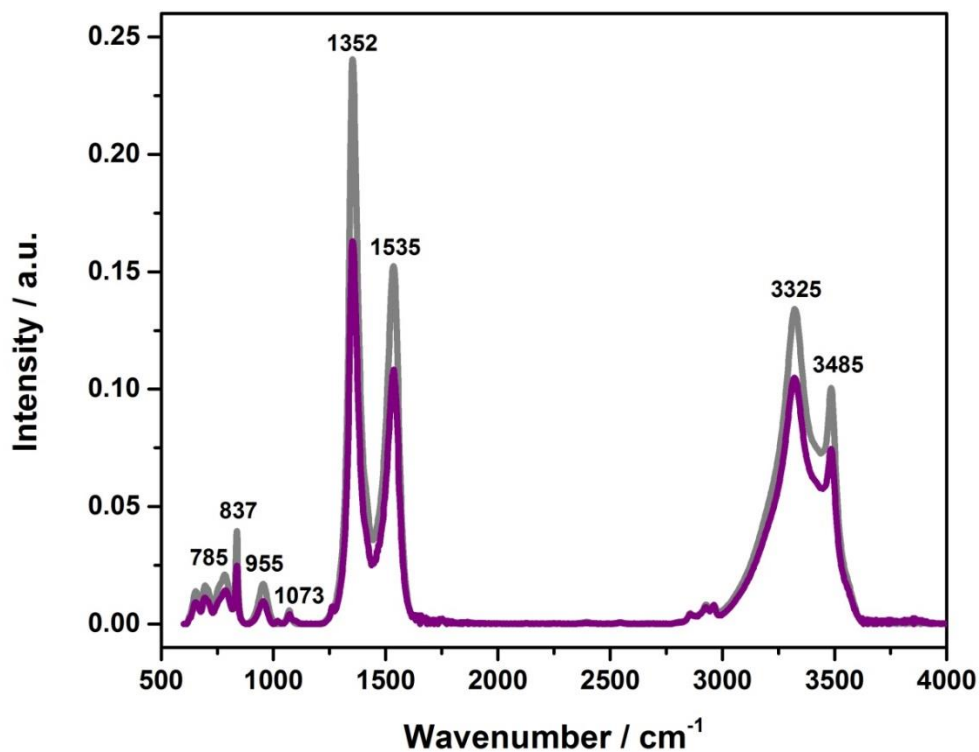


Figure 4-21: Ex-situ FTIR spectra recorded at two locations on the steel surface after exposure to a 5.0 M Cl⁻ solution with [HCO₃⁻/CO₃²⁻]=0.10 M (#1).

Table 4-2: Summary of corrosion products identified by Raman spectroscopy for HCO₃⁻/CO₃²⁻ containing exposure environments.

Oxide Phase	0.001 M	0.01 M (#1)	0.01 M (#2)	0.10 M (#1)	0.10 M (#2)
Fe ₃ O ₄					
GR					
β-FeOOH					
γ-FeOOH					
Fe ₂ (OH) ₂ CO ₃					

4.3.2.3. Scanning Electron Microscopy

Figure 4-22 shows the SEM micrographs recorded after 11 days of exposure in the $[\text{HCO}_3^-/\text{CO}_3^{2-}]_{\text{T}}=0.001$ M solution. The surface is covered by deposits suggesting the occurrence of many localized corrosion events, Figure 4-22(a), consistent with the erratic values of E_{CORR} . The large values of R_p indicate that such locations repassivated due to the formation of Fe^{III} oxide/hydroxide deposits, Figure 4-22(b-c), assigned as GR by Raman analyses. The thin platelets, Figure 4-22(d-f) are deposited on relatively uncorroded areas of the surface which Raman analyses show is Fe_3O_4 .

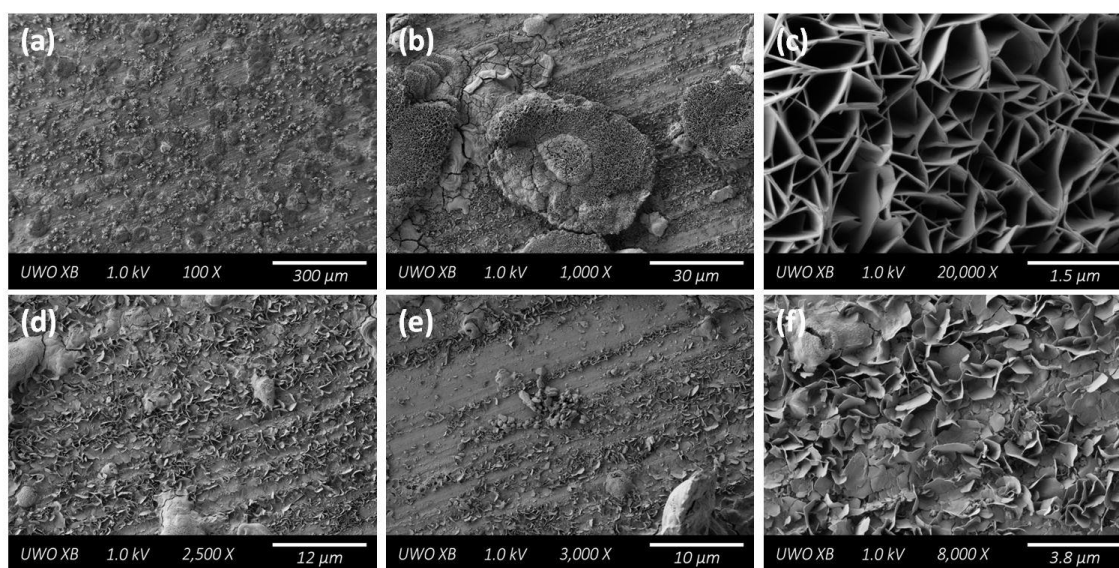


Figure 4-22: SEM micrographs showing the corrosion product morphology after exposure to a 5.0 M Cl⁻ solution containing $[\text{HCO}_3^-/\text{CO}_3^{2-}]_{\text{T}}=0.001$ M.

The SEM micrographs recorded on the steel surface after 13 days exposure to the $[\text{HCO}_3^-/\text{CO}_3^{2-}]_{\text{T}}=0.01$ M (#1) exposure environment, Figure 4-23, show only the presence of a thin surface film with no deposits indicating pitting as expected given E_{CORR} was low (-0.800 V) and exhibited no breakdown transients. The fine structured minor deposit appears to be $\gamma\text{-FeOOH}$, Figure 4-23(c). SEM images recorded after exposure to the $[\text{HCO}_3^-/\text{CO}_3^{2-}]_{\text{T}}=0.01$ M (#2) solution show similar features, but fewer deposited crystals consistent with the Raman analyses indicating the dominant presence of Fe_3O_4 .

SEM micrographs recorded on the steel surface after 15 days exposure to the $[\text{HCO}_3^-/\text{CO}_3^{2-}]_{\text{T}} = 0.10 \text{ M}$ (#1) solution are shown in Figure 4-24. Most of the surface is covered with a thin featureless film, Figure 4-24(a), with patches of thin platelets shown in more detail in Figure 4-24(b). The thin featureless area is consistent with the presence of Fe_3O_4 , as indicated by the Raman analyses. The thin platelets, Figure 4-24(b), show the morphology expected for the $\text{Fe}_2(\text{OH})_2\text{CO}_3$ detected by FTIR [50-53]. In these experiments, the periodic loss of Ar-sparging lead to localized corrosion sites generally covered by $\text{Fe}_2(\text{OH})_2\text{CO}_3$ showing that at such a high $[\text{HCO}_3^-/\text{CO}_3^{2-}]$ dissolution occurred mainly as Fe^{2+} which redeposited rather than being further oxidized to produce Fe^{III} compounds. Although not shown, similar surface features were observed in the second experiment at this $[\text{HCO}_3^-/\text{CO}_3^{2-}]$.

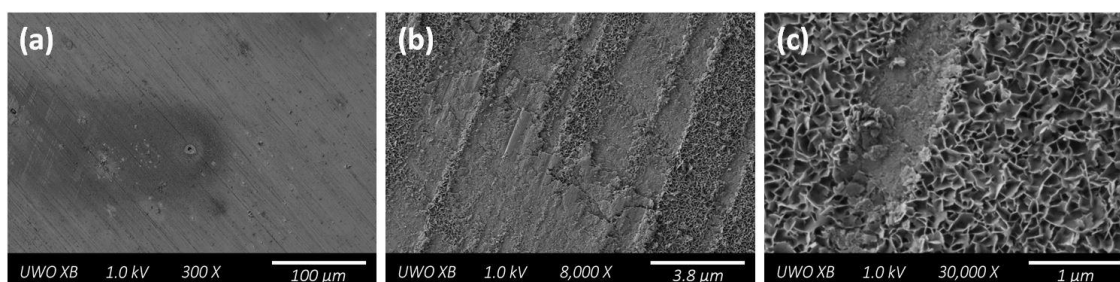


Figure 4-23: SEM micrographs showing the corrosion product morphology after exposure to a 5.0 M Cl⁻ solution containing $[\text{HCO}_3^-/\text{CO}_3^{2-}] = 0.01 \text{ M}$ (#1).

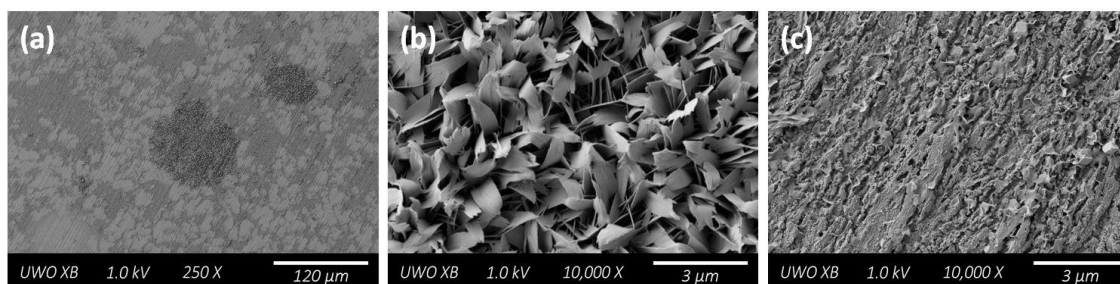


Figure 4-24: SEM micrographs showing the corrosion product morphology after exposure to a 5.0 M Cl⁻ solution containing $[\text{HCO}_3^-/\text{CO}_3^{2-}] = 0.10 \text{ M}$ (#1).

4.3.2.4. Cyclic Voltammetry

Figure 4-25(a) shows CVs recorded in 5.00 M NaCl solutions containing 0.01 M and 0.20 M $[\text{HCO}_3^-/\text{CO}_3^{2-}]$. A number of features are clear:

- (i) The current for the cathodic reaction is higher at the higher $[\text{HCO}_3^-/\text{CO}_3^{2-}]$ which can be attributed to the reduction of protons supplied by the dissociation of HCO_3^- .
- (ii) The anodic current in the region of the peak is increased, confirming that dissolution as Fe^{2+} is accelerated by carbonate complexation as $\text{Fe}(\text{CO}_3)_2^{2-}$.
- (iii) The current on the reverse scan is revived in the potential range within which the anodic peak occurs at the higher $[\text{HCO}_3^-/\text{CO}_3^{2-}]$ indicating that the formation of a passive oxide is inhibited by $\text{HCO}_3^-/\text{CO}_3^{2-}$.

Figure 4-25(b) shows the anodic peak currents recorded at -0.700 V (indicated by the vertical line in (a)) as a function of $[\text{HCO}_3^-/\text{CO}_3^{2-}]$ in 1.00 M and 5.00 M NaCl solutions. In both cases an increase in $[\text{HCO}_3^-/\text{CO}_3^{2-}]_T$ causes an increase in anodic current although the influence of $\text{HCO}_3^-/\text{CO}_3^{2-}$ is suppressed at the higher $[\text{Cl}^-]$.

Figure 4-25(c) shows the anodic polarization scans recorded in 5.00 M Cl^- extended until a sharp increase in current indicated passive film breakdown. Figure 4-25(d) shows the breakdown potentials as a function of $[\text{HCO}_3^-/\text{CO}_3^{2-}]$ for both $[\text{Cl}^-]$. The values of the breakdown potentials were obtained by extrapolating the linear region of the active dissolution current back to the potential axis. For both $[\text{Cl}^-]$ the breakdown potential increases with $[\text{HCO}_3^-/\text{CO}_3^{2-}]$, and for $[\text{HCO}_3^-/\text{CO}_3^{2-}] > 0.05$ M are more positive at the lower $[\text{Cl}^-]$; i.e., film breakdown is suppressed by $\text{HCO}_3^-/\text{CO}_3^{2-}$ but less so at the higher $[\text{Cl}^-]$. It is noteworthy that this is the opposite of what was observed in exposure environments containing only Cl^- when the onset of active dissolution was delayed at higher $[\text{Cl}^-]$.

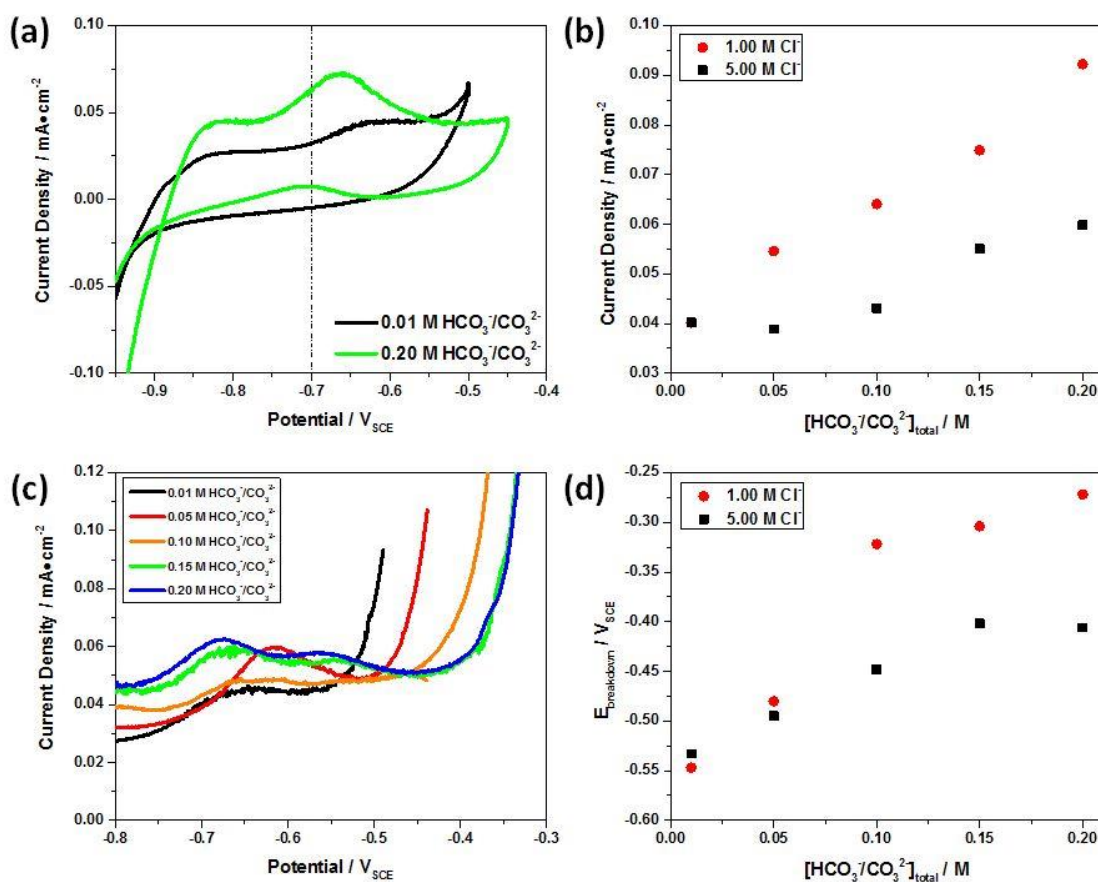


Figure 4-25: (a) Cyclic voltammograms starting at a potential of -1.1 V recorded on steel in a $[Cl^-]=5.00$ M solution containing either 0.01 M or 0.20 M HCO_3^-/CO_3^{2-} ; (b) anodic currents at -0.7 V as a function of $[HCO_3^-/CO_3^{2-}]$; (c) anodic polarization scans starting at a potential of -1.1 V recorded up to the onset of film breakdown in a $[Cl^-]=5.00$ M solution containing increasing $[HCO_3^-/CO_3^{2-}]$; (d) breakdown potentials as a function of $[HCO_3^-/CO_3^{2-}]$.

4.3.3. Effects of Sulphate

4.3.3.1. E_{CORR} and R_p Measurements

Figure 4-26 shows the E_{CORR} values recorded over exposure periods from 11-35 days in deaerated 5.00 M Cl^- solutions containing $[SO_4^{2-}]$ ranging from 0.001 M to 0.50 M. The dashed horizontal line shows the E^e for the oxidation of $Fe^{II} ox$ to $Fe^{III} ox$ (-0.755 V). Figure 4-27 shows the corresponding R_p values. At $[SO_4^{2-}] = 0.001$ M, E_{CORR} (~ -0.770 V) and R_p values are similar to those recorded in $[Cl^-] = 5.00$ M (#2 and #3), Figure 4-1 and Figure 4-2. In experiments in which E_{CORR} increases to $> (E^e)_{Fe^{II} ox/Fe^{III} ox}$ R_p increases to values indicating passive conditions. Once the E^e is exceeded a high density of metastable transients is observed, indicating localized corrosion events. Despite these events the R_p values, while becoming erratic, do not decrease to < 100 $k\Omega cm^2$ indicating transient localized corrosion not the establishment of stable propagating pits. Similar behaviour is observed at the other $[SO_4^{2-}]$. If E_{CORR} increased to values close to or exceeding $(E^e)_{Fe^{II} ox/Fe^{III} ox}$, R_p increases to values indicating passivity and localized initiation/repassivation events are observed. If E_{CORR} does not increase to such positive values then R_p remains < 100 $k\Omega cm^2$ and localized corrosion events are avoided. This behaviour can be contrasted with that observed in HCO_3^-/CO_3^{2-} solutions in which E_{CORR} remains lower and localized events are less frequent, Figure 4-15 and Figure 4-16. It is also clear that the trends in E_{CORR} and R_p are not determined by the $[SO_4^{2-}]$ suggesting that the dominant influence on E_{CORR}/R_p are traces of dissolved O_2 which determine the extent of surface oxidation and, hence, whether or not passivation occurs.

4.3.3.2. Raman Spectroscopy

Figure 4-28(a) shows the Raman spectra recorded on various locations after exposure to $[SO_4^{2-}] = 0.001$ M. The absence of significant Raman bands in (1) suggests the presence of an undetectably thin or amorphous deposit. Spectra (2) and (3), recorded at locations with visible corrosion deposits, exhibit the bands in the range 1200-1500 cm^{-1} which indicate the presence of amorphous carbon residue left behind after dissolution of α -Fe from a pearlite matrix. The absence of peaks in the range 700 cm^{-1} to < 200 cm^{-1} indicate these corroded locations are not associated with identifiable deposits, although optical analysis showed a corrosion product was present. This is consistent with the E_{CORR}/R_p measurements which indicate the occurrence of only metastable local events which would result in only minor corrosion product deposits.

Raman spectra recorded on various locations after exposure to $[\text{SO}_4^{2-}] = 0.01 \text{ M}$, Figure 4-28(b), show Fe_3O_4 (667 cm^{-1}) to be present as expected since E_{CORR} did not increase to the $(E^e)_{\text{Fe}^{\text{II}} \text{ ox} / \text{Fe}^{\text{III}} \text{ ox}}$ boundary and R_p values remained low. The very shallow band between 1200 and 1700 cm^{-1} indicates this Fe_3O_4 film allows some corrosion of the underlying steel.

The optical image in Figure 4-29 shows both dark and yellow/orange regions are present on the steel surface after exposure to $[\text{SO}_4^{2-}] = 0.10 \text{ M}$ (#1). Raman spectra ((1) and (2)) recorded on the yellow/orange deposit, Figure 4-30(a), show the bands at 247 and 376 cm^{-1} associated with $\gamma\text{-FeOOH}$. The small broad peak at $\sim 660 \text{ cm}^{-1}$ may indicate a poorly crystalline or thin layer of Fe_3O_4 in the black areas. The presence of areas of Fe^{III} oxides/hydroxides on a generally uncorroded surface is consistent with the positive E_{CORR} values and the proliferation of metastable events at long exposure times.

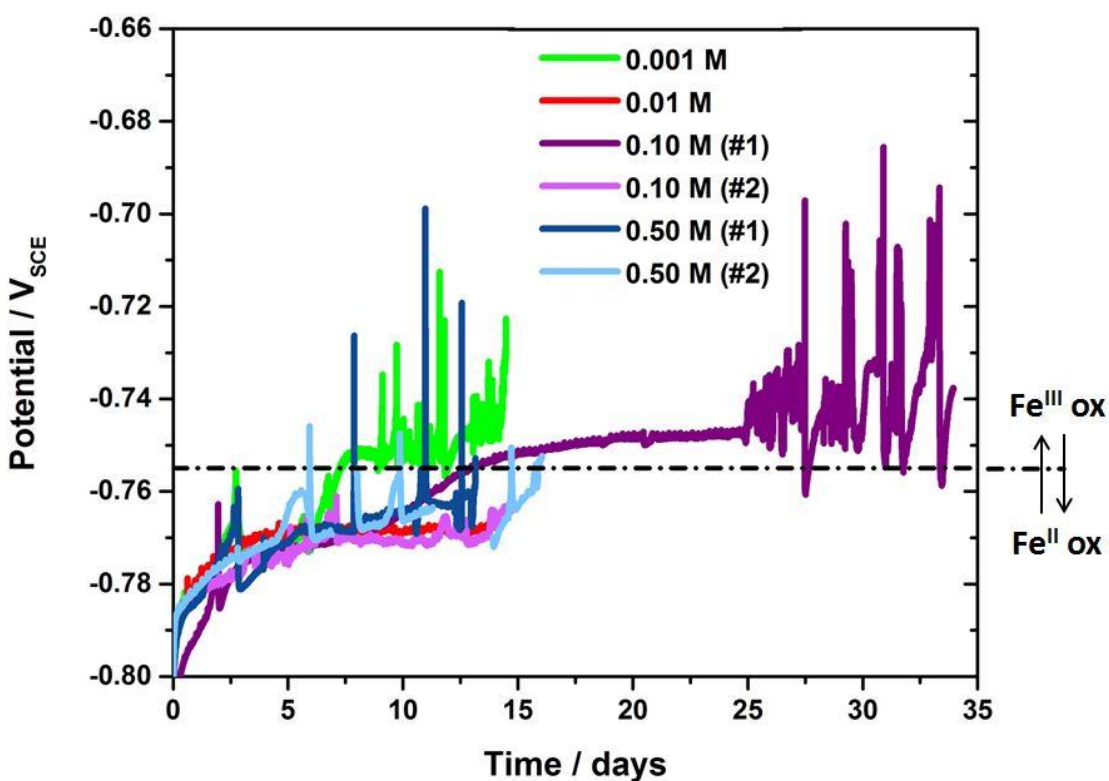


Figure 4-26: Corrosion potentials (E_{CORR}) for solutions containing 5.00 M Cl^- and various concentrations of SO_4^{2-} . The dashed horizontal line represents the thermodynamic boundary for the transformation of $\text{Fe}(\text{OH})_2$ to $\alpha\text{-Fe}_2\text{O}_3$.

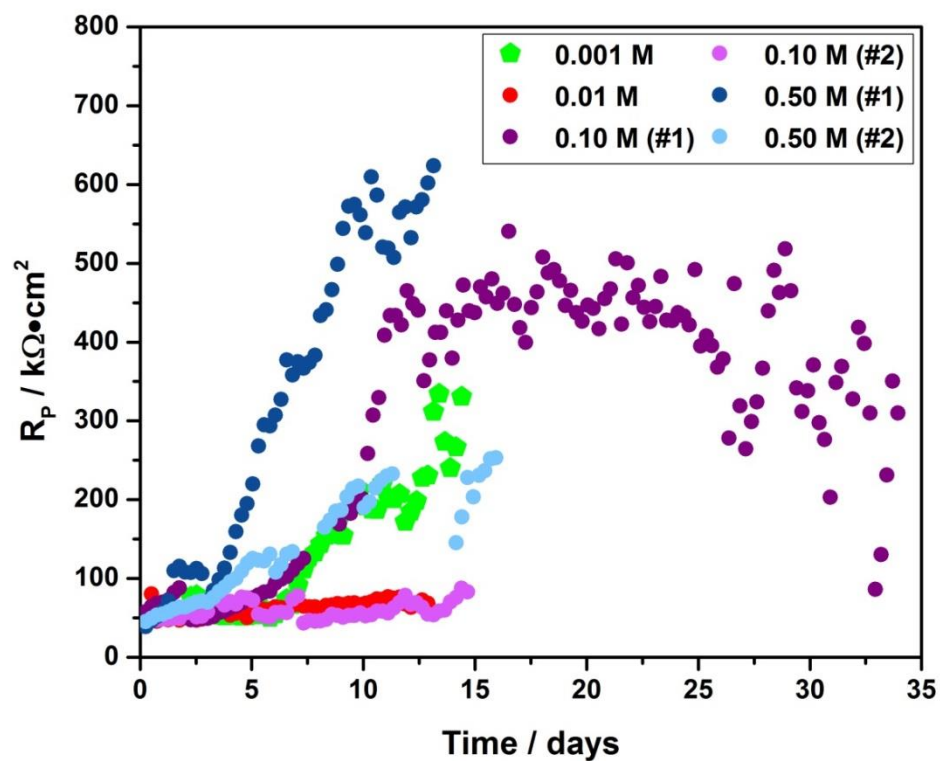


Figure 4-27: Polarization resistance (R_p) measurements for solutions containing 5.00 M Cl⁻ and various concentrations of SO_4^{2-} as given in Figure 4-26.

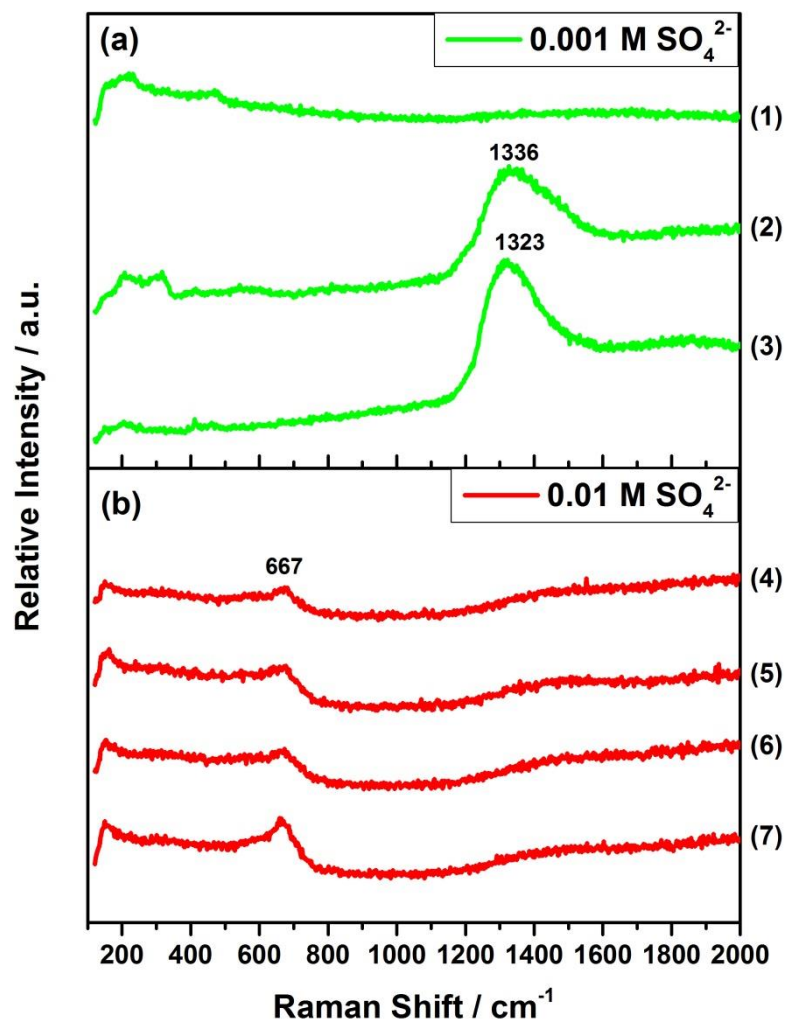


Figure 4-28: Ex-situ Raman spectra (1-7) recorded at various locations on the steel surface after exposure to 5.0 M Cl⁻ solutions with (a) [SO₄²⁻]=0.001 M; (b) [SO₄²⁻]=0.01 M.

In the second shorter experiment in 0.10 M SO₄²⁻ (#2), E_{CORR} remained well below $(E^e)_{\text{Fe}^{\text{II}}_{\text{ox}}/\text{Fe}^{\text{III}}_{\text{ox}}}$ and localized corrosion events were avoided, Figure 4-26. The Raman spectra, Figure 4-30(b), indicated a Fe₃O₄ covered surface as expected, although the enhanced intensity in the region 200 to 600 cm⁻¹ suggests the presence of some Fe^{III} oxyhydroxides.

The optical image in Figure 4-31 shows a generally uncorroded surface with a number of small locations which are probably pits after exposure to the [SO₄²⁻]=0.50 M (#1) solution. Spectra (1-3), Figure 4-32(a), were recorded on the lightly corroded areas of the surface. The Raman bands located at 432 and 508 cm⁻¹ are characteristic of the Fe²⁺-OH and Fe³⁺-OH stretching modes of GR, and given the solution composition ([Cl⁻]=5.00 M and [SO₄²⁻]=0.50 M) the interlayer anion

will be either Cl^- or SO_4^{2-} . The faint Raman band at 982 cm^{-1} suggests $\text{GR}(\text{SO}_4^{2-})$ in this experiment. Spectrum (4) was recorded on a more obviously corroded location confirmed by the strong, but broad, peak at 1324 cm^{-1} indicating the presence of residual Fe_3C from corroded pearlite grains. The peaks in the range $\sim 250\text{ cm}^{-1}$ to 350 cm^{-1} can be attributed to Fe^{III} oxyhydroxides (most likely α - and γ - FeOOH) which would be expected to accumulate at such locations. The absence of Fe_3O_4 (i.e., a peak at 667 cm^{-1}) confirms this spectrum was recorded on a more corroded location.

Similar behaviour was observed after exposure to $[\text{SO}_4^{2-}]=0.50\text{ M}$ (#2) although in this experiment a peak attributable to Fe_3O_4 ($\sim 666\text{ cm}^{-1}$) was observed, Figure 4-32(b). The blue hued locations in Figure 4-31 appear to be γ - FeOOH . Table 4-3 summarizes the iron oxide phases formed in SO_4^{2-} containing exposure environments.

Table 4-3: Summary of corrosion products identified by Raman spectroscopy for SO_4^{2-} containing exposure environments.

Oxide Phase	0.001 M	0.01 M	0.10 M (#1)	0.10 M (#2)	0.50 M (#1)	0.50 M (#2)
Fe_3O_4						
GR						
α - FeOOH						
γ - FeOOH						

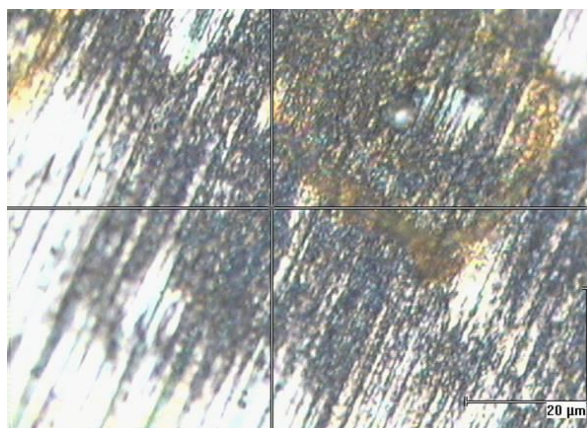


Figure 4-29: Raman optical image recorded on the steel surface exposed to a 5.0 M Cl^- solution containing $[\text{SO}_4^{2-}]=0.10\text{ M}$ (#1). Crosshairs indicate location of Raman spectra collection.

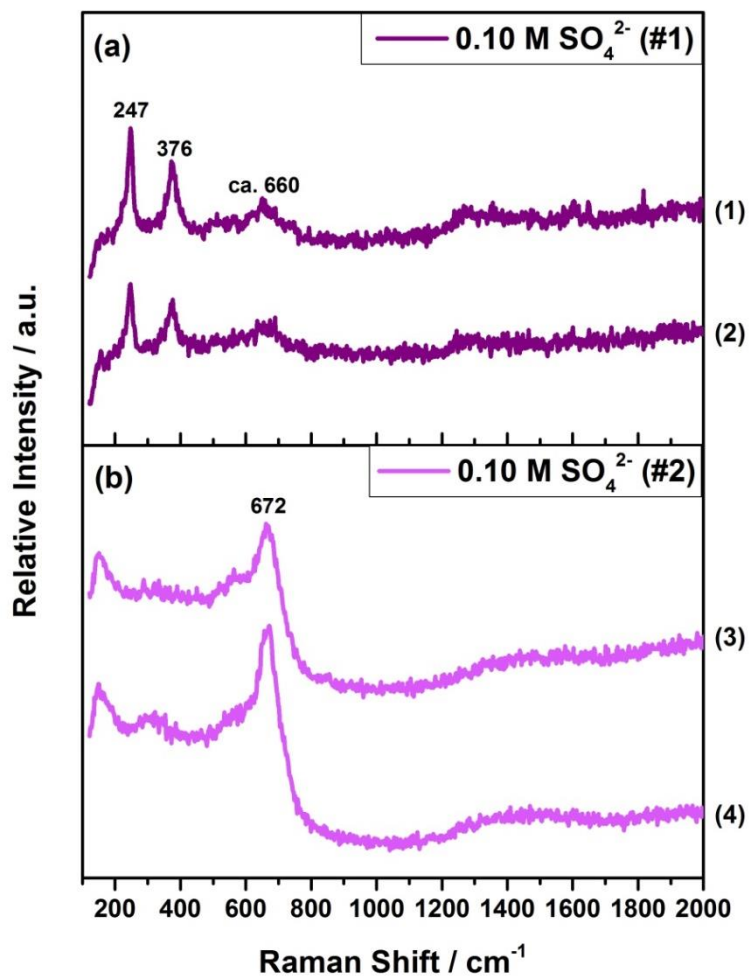


Figure 4-30: Ex-situ Raman spectra (1-4) recorded at various locations on the steel surface after exposure to 5.0 M Cl⁻ solutions containing [SO₄²⁻]=0.10 M.

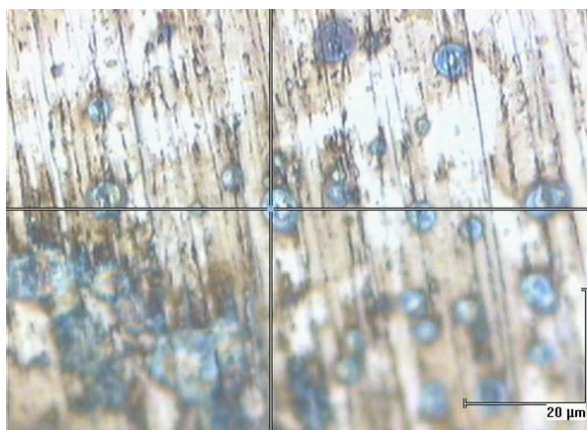


Figure 4-31: Raman optical image recorded on the steel surface exposed to a 5.0 M Cl⁻ solution containing [SO₄²⁻]=0.50 M (#1). Crosshairs indicate location of Raman spectra collection.

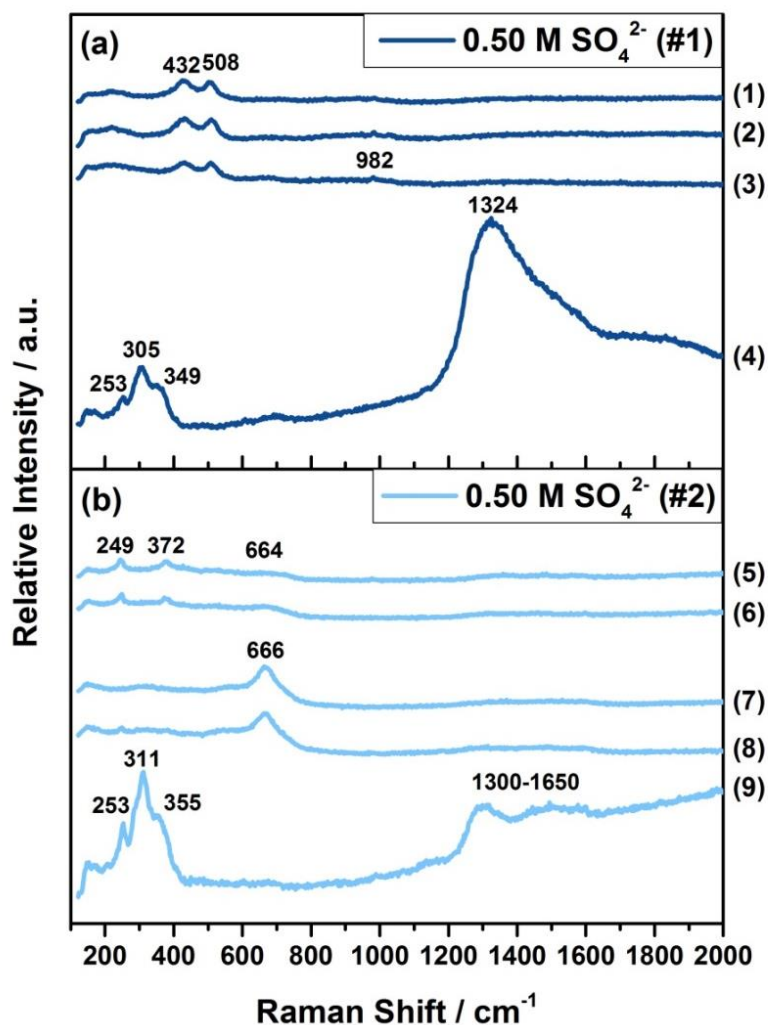


Figure 4-32: Ex-situ Raman spectra (1-9) recorded at various locations on the steel surface after exposure to 5.0 M Cl⁻ solutions containing [SO₄²⁻]=0.50 M.

4.3.3.3. Scanning Electron Microscopy

The surface features are similar to those observed in other solutions. If E_{CORR} remains low (-0.770 V), R_p does not increase to very high values, and metastable film breakdown events are avoided and corrosion occurs generally with some areas covered with very thin crystalline deposits as shown for [SO₄²⁻]=0.01 M in Figure 4-33. The optical images and the accompanying Raman analyses indicate corrosion is not extensive and probably occurs most readily on the pearlite grains. In the experiments in which the E_{CORR} becomes very positive and metastable events are observed, minor breakdown sites are observed on the surface (not shown).

4.3.3.4. Cyclic Voltammetry

Figure 4-34 shows two CVs recorded at a high and a low $[\text{SO}_4^{2-}]$ in highly concentrated chloride solutions of $[\text{Cl}^-]=5.00$ M. Figure 4-34(b) shows the currents recorded at -0.700 V taken from the voltammograms and shows there is no significant dependence of the anodic dissolution current on $[\text{SO}_4^{2-}]$ at this potential. For comparison, the influence of $[\text{HCO}_3^-/\text{CO}_3^{2-}]_{\text{T}}$ on the current at this potential is also shown. The clear influence on the anodic dissolution due to $\text{HCO}_3^-/\text{CO}_3^{2-}$ is not observed for SO_4^{2-} . The anodic polarization scans for each $[\text{SO}_4^{2-}]$ in $[\text{Cl}^-]=5.00$ M, Figure 4-34(c), show there is no measurable effect of the SO_4^{2-} on the breakdown potential. Figure 4-34(d) compares the breakdown potentials in SO_4^{2-} and $\text{HCO}_3^-/\text{CO}_3^{2-}$ solutions, and shows SO_4^{2-} is more effective than $\text{HCO}_3^-/\text{CO}_3^{2-}$ in suppressing breakdown.

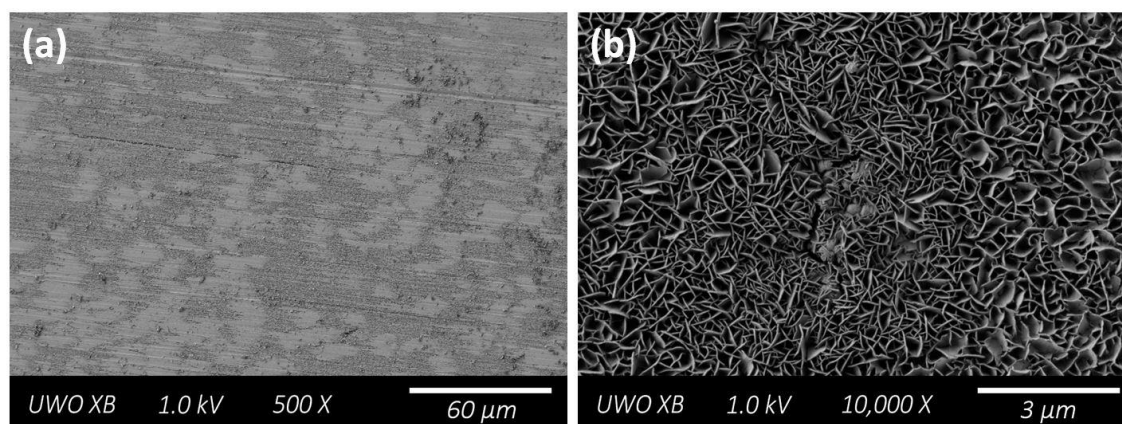


Figure 4-33: SEM micrographs showing the corrosion product morphology after exposure to a 5.0 M Cl^- solution containing $[\text{SO}_4^{2-}]=0.01$ M.

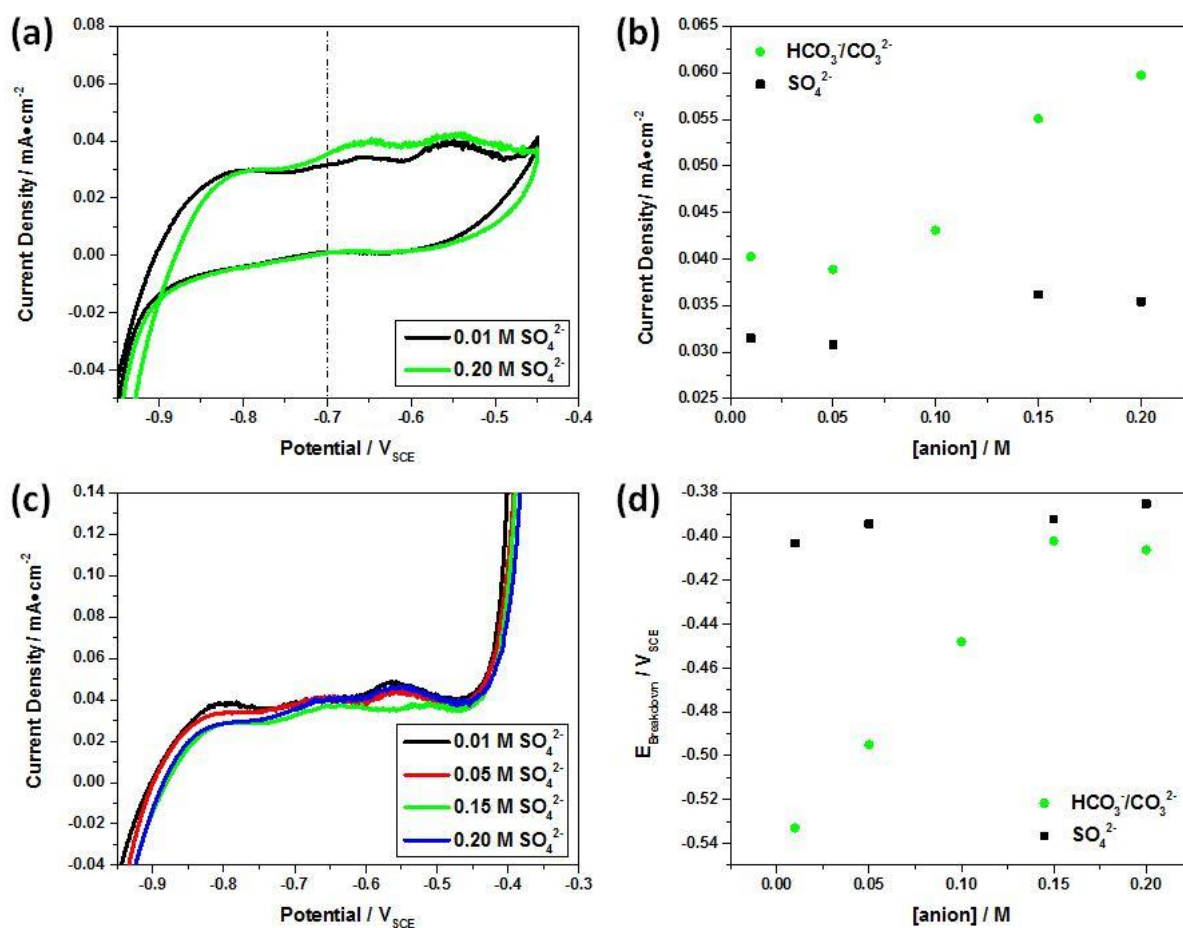


Figure 4-34: (a) cyclic voltammograms recorded for steel exposed to a [Cl⁻]=5.00 M solution containing 0.01 M or 0.20 M SO₄²⁻; (b) anodic dissolution currents measured at -0.7 V as a function of anion concentration; (c) anodic polarization scans recorded up to the onset of film breakdown in a [Cl⁻]=5.00 M solution containing increasing [SO₄²⁻]; (d) breakdown potentials as a function of [SO₄²⁻] and [HCO₃⁻/CO₃²⁻].

4.4. DISCUSSION

4.4.1. Effects of Chloride

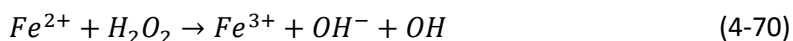
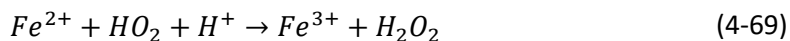
Electrochemical data showed that as the $[Cl^-]$ was increased the values of E_{CORR} and R_p generally increased. The exception to this observation was the E_{CORR} value for $[Cl^-]=0.01$ M which was more positive than for the $[Cl^-]=1.00$ M solution. However, cyclic voltammetry measurements revealed that the electrochemistry of this solution was distorted by the low ionic strength in such a low $[Cl^-]$ solution. The value of E_{CORR} in this solution may reflect this. The tendency for Cl^- to cause an increase in both E_{CORR} and R_p suggests that the Cl^- is able to induce passivation of the surface by formation of Fe^{III} oxides. This hypothesis is supported by published studies [16, 18, 54-62]. Based on the mechanism proposed by Weiss [63], Kurimura et al. [56] proposed that the oxidation of Fe^{2+} to Fe^{3+} could be catalyzed by chelation,



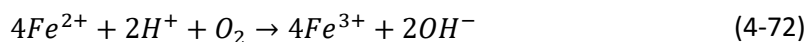
where X^- represents the chelating species which can be regenerated via the following equilibrium process:



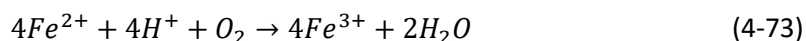
The highly reactive O_2^- species produced from the chelation step can then go on to oxidize a further three Fe^{2+} ions to Fe^{3+} .



The overall reaction for the oxidation of Fe^{2+} catalyzed by chelation is then given by:

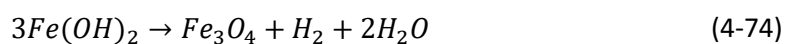


or,



Kurimura et al. [56] state that the acceleration of the oxidation process is due to the stabilization of the oxidized form by chelation. If this is the case, the oxidation rate of Fe^{2+} will depend on the complexing affinity of the chelating anion for the Fe^{3+} state. Acceleration of the oxidation of Fe^{2+} has been shown to increase with increasing $[Cl^-]$ [54-59]. Previous work by Ulrich and Anson suggests that this acceleration due to chelation could be facilitated by a ligand bridging mechanism of adsorbed Cl^- as observed for the oxidation of Cr^{2+} to Cr^{3+} [64]. In the present case the catalysis appears to be a slow surface reaction with an initially formed $Fe(OH)_2$, or more likely Fe_3O_4 , surface layer being slowly oxidized on the outer surface to an undefined Fe^{III} state. Isostructurally, it is easy to convert Fe_3O_4 to γ - Fe_2O_3 suggesting this is the most likely product of the Cl^- catalyzed oxidation. Any Fe^{III} formed in this manner would be extremely insoluble allowing the surface to be slowly passivated as oxidation proceeds.

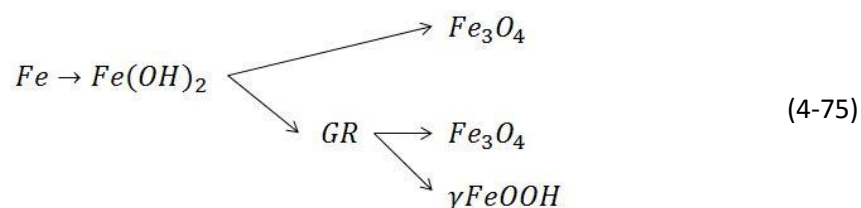
Consistent with the need for a high $[Cl^-]$ in order to convert the outer layer of Fe_3O_4 to Fe^{III} oxide, only Fe_3O_4 and traces of GR are observed after corrosion in the 0.01 M Cl^- solution and both E_{CORR} and R_p remain low. It is commonly accepted that the first product of the anaerobic corrosion of iron is $Fe(OH)_2$, which, due to its low thermodynamic stability, is subsequently converted to magnetite via the Schikorr reaction [3, 7, 23]:



The presence of both Fe_3O_4 and GR after corrosion in a low Cl^- solution suggests a number of possible mechanisms. The GR could have formed by reaction of this $Fe(OH)_2$ with traces of O_2 . Then, since GR is metastable with respect to Fe_3O_4 at pH values > 5 , Fe_3O_4 could have formed as a conversion product of GR via dehydration and oxidation [65] rather than directly via reaction 4-74, although formation via both routes would be possible.

Increasing the Cl^- content of the exposure solution would lead to an excess of intercalated Cl^- ions within the structure of $GR(Cl^-)$, and to maintain electroneutrality, a number of Fe^{2+} ions, equal in number to that of the incorporated Cl^- anions, would be oxidized to Fe^{3+} . This increase in the $[Cl^-]/[Fe]$ ratio leads to γ - $FeOOH$ formation at the expense of Fe_3O_4 as observed previously [27, 59, 65-68]. Taylor [69] suggested that the effect of the Cl^- was due to preferential adsorption of Cl^- over OH^- on the electrode surface which hindered the elimination of water by

condensation of neighbouring OH^- anions to form the Fe-O-Fe bonds required for Fe_3O_4 formation. As such, the Cl^- content of the exposure environment leads to a competition between the formation of Fe_3O_4 at low $[\text{Cl}^-]$ and $\gamma\text{-FeOOH}$ at higher $[\text{Cl}^-]$.



This evolution in composition is evident in the corrosion products as the $[\text{Cl}^-]$ is increased. When $[\text{Cl}^-]=1.00$ M, the presence of both Fe_3O_4 and $\gamma\text{-FeOOH}$ shows a turning point in the ability of the Cl^- to catalyze Fe^{2+} to Fe^{3+} possibly via the transformation of GR. However, the simultaneous presence of Fe_3O_4 indicates its formation persists either via direct anaerobic corrosion or via GR conversion. Each of the $[\text{Cl}^-]=5.00$ M experiments exhibits small differences in the corrosion products. For $[\text{Cl}^-]=5.00$ M (#2) only Fe_3O_4 and residual Fe_3C were identified. This would suggest that the O_2 level in this solution was too low for surface oxidation despite the high $[\text{Cl}^-]$. The identification of Fe_3C indicated that while the electrochemistry and SEM suggested the surface had passivated, there remains open areas in the corrosion product where the film is only partially protective. For $[\text{Cl}^-]=5.00$ M (#3), Fe_3O_4 remained the dominant corrosion product, whereas for $[\text{Cl}^-]=5.00$ M (#1), $\gamma\text{-FeOOH}$ was the dominant corrosion product. This would indicate that the trace levels of O_2 present combined with the high $[\text{Cl}^-]$ were sufficient to drive the Cl^- induced catalysis of Fe^{II} oxidation to Fe^{III} via transformation of GR to $\gamma\text{-FeOOH}$.

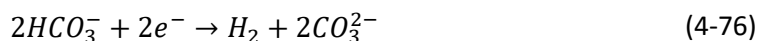
The presence of $\beta\text{-FeOOH}$ could also be attributed to the increased $[\text{Cl}^-]$ ($[\text{Cl}^-]=1.00$ M and 5.00 M (#1)), since an increase in the Cl^- intercalation in the GR precursor has been shown to cause preferential oxidation to $\beta\text{-FeOOH}$ [27]. However, the appearance of the $\beta\text{-FeOOH}$ as a corrosion product is always accompanied by the presence of Fe_3C indicating that $\beta\text{-FeOOH}$ is formed at regions of higher activity. Under the conditions (high $[\text{Cl}^-]$; traces of O_2) when surface passivation does occur and pit initiation is observed, the breakdown sites accumulate deposits which are generally Fe^{III} oxyhydroxides although the composition is difficult to determine since the Raman peaks are commonly broad indicating poor crystallinity. The extent of propagation at these locations will be limited by the availability of dissolved O_2 .

Thus, the difference between the repeated experiments in 5.0 M Cl⁻ (#1 and #2) appears to be a difference in available O₂. In #1 E_{CORR} rapidly approaches $(E^e)_{Fe^{II} ox / Fe^{III} ox}$ leading to the early onset of film breakdown events. Once initiated, R_p falls to a low value which is then sustained indefinitely, indicating the presence of sufficient O₂ to maintain propagation. By contrast, in #2, E_{CORR} increases more slowly and breakdown events take a substantial period of time to occur and are considerably smaller and limited, the R_p value decreasing only marginally. This indicates a much lower O₂ concentration.

These results indicate a dual role for Cl⁻ when present at high concentration. In the presence of dissolved O₂ it can catalyze surface oxidation leading to passivity. However, once passivity is achieved it can lead to the initiation of breakdown sites, the expected influence of Cl⁻ on passive oxide films.

4.4.2. Effects of Carbonate

From the cyclic voltammetry data, two important trends can be noted. First, as the [HCO₃⁻/CO₃²⁻]_T increases an increase in both the cathodic and anodic dissolution current is observed. The acceleration of the cathodic reaction is due to the additional H⁺ supplied by the dissolution of HCO₃⁻. In addition, it is possible that the HCO₃⁻ may in fact act as a secondary cathodic reaction.



The acceleration of anodic dissolution in the presence of HCO₃⁻/CO₃²⁻ has been reported previously and is attributed to the stabilization of the dissolved Fe²⁺ via complexation as FeHCO₃⁺ and Fe(HCO₃)₂ at the pH in this experiment [3, 4, 8, 70-74]. This acceleration is more marked at lower [Cl⁻] suggesting a competition between the influence of Cl⁻ in accelerating Fe^{II} oxidation to Fe^{III} and that of HCO₃⁻/CO₃²⁻ to stabilize and dissolve Fe²⁺. In the most concentrated HCO₃⁻/CO₃²⁻ solution the difficulties in maintaining the Ar-purge gas flow lead to fluctuations in E_{CORR} and R_p attributable to changes in the anodic reaction kinetics. These responses indicate that the slow oxidation of the Fe₃O₄ surface is reversible at least in the early stages when the extent of oxidation to Fe^{III} is minor and the surface is not passivated. The ability to reverse the oxidation process suggests that Fe^{III} in the oxide surface can be reduced to the more soluble Fe²⁺ state, a process which could be driven by reaction with soluble Fe²⁺ [75] or by galvanic coupling

of the reductive dissolution of the Fe^{III} oxide with the corrosion of the substrate steel surface [76, 77].

Secondly, an increase in the [HCO₃⁻/CO₃²⁻] increased the anodic breakdown potential to more positive values. This competition between the two anions can be attributed to one of two possible effects: (i) the anions compete for adsorption sites on the oxide surface with Cl⁻ more likely to be adsorbed at lower [HCO₃⁻/CO₃²⁻] leading to breakdown and pit initiation [4, 72, 78]; (ii) if film breakdown is to lead to pit propagation local acidity, due to hydrolysis of dissolved Fe²⁺, must be achieved and maintained. In carbonate solutions this acidity could be neutralized. At the pH (8.9) employed in these experiments, HCO₃⁻ would be the dominant species, the pKa for the equilibrium



being ~10.3, and the equilibrium



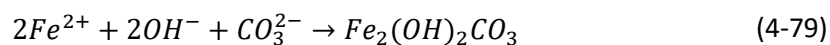
being ~6.35.

At [HCO₃⁻/CO₃²⁻]=0.001 M, the positive E_{CORR} indicates the high Cl⁻ content has the dominant influence on surface chemistry, confirmed by the nature of the corrosion products, the mixture of Fe₃O₄ and GR being similar to that observed when only Cl⁻ was present. This indicates that the [HCO₃⁻/CO₃²⁻] is too small to stabilize Fe²⁺ species and that the Cl⁻ causes preferential stabilization of Fe³⁺ [3, 4, 72]. This is consistent with the occurrence of localized corrosion events. However, the small [HCO₃⁻/CO₃²⁻] appears to be sufficient to inhibit the transformation from metastable to stable pitting by buffering the pH at these breakdown sites allowing repassivation to occur.

When [HCO₃⁻/CO₃²⁻] is increased to 0.01 M the lower E_{CORR} and R_p values show Cl⁻ no longer dominates the surface chemistry, possibly due to its replacement on the surface by HCO₃⁻/CO₃²⁻, which would stabilize the formation of soluble Fe²⁺ and prevent Cl⁻ induced oxidation. Raman analyses showed Fe₃O₄ to be the generally observed corrosion product, consistent with this assignment, although the observation of γ-FeOOH and β-FeOOH, confirms that traces of dissolved O₂ still dominated the nature of the corrosion products. At the highest [HCO₃⁻/CO₃²⁻] (0.10 M) the low E_{CORR} and R_p values and the observation of Fe₃O₄ and Fe₂(OH)₂CO₃ as the

dominant corrosion products confirms that the surface chemistry is $\text{HCO}_3^-/\text{CO}_3^{2-}$ dominated not Cl^- dominated.

$\text{Fe}_2(\text{OH})_2\text{CO}_3$ has been observed as a corrosion product in O_2 -poor environments [8, 47, 52, 79-86] and is found as a large component of the rust layers on archaeological artefacts recovered from anoxic, water saturated soils [47, 50, 81, 87, 88]. $\text{Fe}_2(\text{OH})_2\text{CO}_3$ is known to form competitively and together with siderite (FeCO_3) [47, 81, 87, 89]. Azoulay et al. [89] propose that $\text{Fe}_2(\text{OH})_2\text{CO}_3$ can form via direct precipitation from solution or in the conversion of $\text{Fe}(\text{OH})_2$:



Analysis of the Pourbaix diagram, Figure 4-35, shows that $\text{Fe}_2(\text{OH})_2\text{CO}_3$ is expected in neutral to slightly alkaline conditions, and its oxidation to $\alpha\text{-FeOOH}$, while possible, would require oxidizing conditions not expected in our experiments. Of more interest is the fact that $\text{Fe}_2(\text{OH})_2\text{CO}_3$ is thermodynamically metastable with respect to FeCO_3 and would be expected to transform to FeCO_3 over an extended exposure period. Our experiments are of relatively short duration and it is possible that over a longer exposure period $\text{Fe}_2(\text{OH})_2\text{CO}_3$ would transform to FeCO_3 [8, 78, 89]. This is consistent with the observation of inner $\text{Fe}_2(\text{OH})_2\text{CO}_3$ and outer FeCO_3 corrosion layers observed on archaeological artefacts exposed to anoxic groundwaters containing $\text{HCO}_3^-/\text{CO}_3^{2-}$ [8, 47, 50, 81, 88, 89].

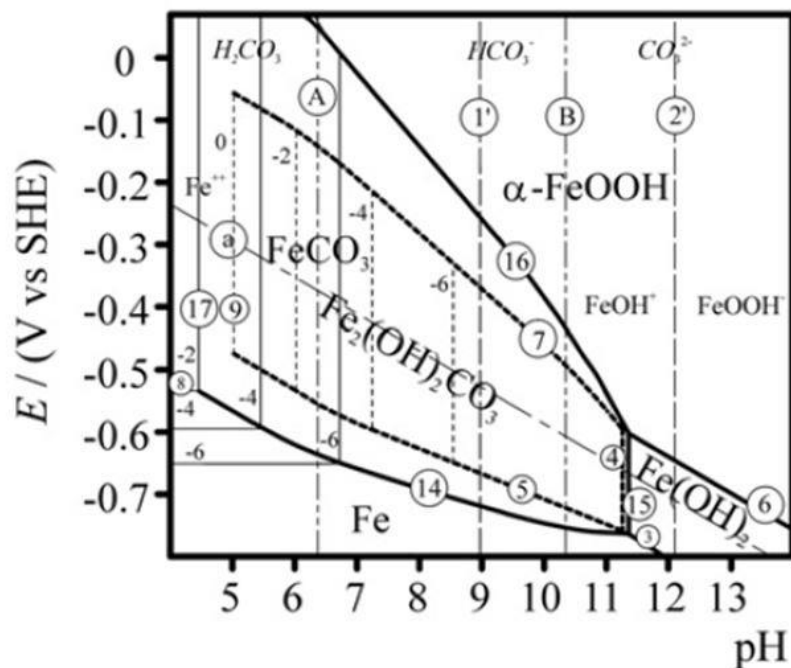


Figure 4-35: Pourbaix diagram of iron in carbonate containing aqueous media at 25°C for equilibria involving $\text{Fe}_2(\text{OH})_2\text{CO}_3$ (dotted lines) and FeCO_3 (solid lines) [89].

4.4.3. Effects of Sulphate

The considerably more positive E_{CORR} and larger R_p values obtained when SO_4^{2-} as opposed to $\text{HCO}_3^-/\text{CO}_3^{2-}$ is present shows SO_4^{2-} does not stabilize Fe^{2+} and does not, therefore, inhibit the Cl^- catalyzed oxidation of the surface by traces of dissolved O_2 . As a consequence, film breakdown processes are frequent leading to the expected Raman signature for such locations, peaks in the 200 to 600 cm^{-1} range and broad bands in the 1200 to 1700 cm^{-1} range indicating the presence of Fe^{III} oxyhydroxides over a carbonaceous residue left behind by corrosion of pearlite grains. Irrespective of the $[\text{SO}_4^{2-}]$ such pitted locations do not propagate extensively which reflects both the limited amount of available O_2 and the inability of SO_4^{2-} to accelerate anodic dissolution of the steel. This latter point is demonstrated in the CVs which show no significant effect of this anion on the anodic dissolution current.

The breakdown potentials determined in CVs, Figure 4-34(d), show SO_4^{2-} is much more effective than $\text{HCO}_3^-/\text{CO}_3^{2-}$ in retarding film breakdown. Since the pK_a for the $\text{HSO}_4^-/\text{SO}_4^{2-}$ dissociation

equilibrium is 1.92, this cannot be attributed to the ability of SO_4^{2-} to buffer the acidity which accompanies the development of pits. This would suggest that SO_4^{2-} can displace Cl^- from the Fe^{III} oxide surface at sufficiently positive potentials, thereby stabilizing the oxide against breakdown. By contrast, $\text{HCO}_3^-/\text{CO}_3^{2-}$ appears unable to do this except at significantly higher concentrations. A possibility is that at low $[\text{HCO}_3^-/\text{CO}_3^{2-}]$ any ability of the ion to suppress breakdown is counterbalanced by its ability to stabilize the Fe^{2+} state once breakdown occurs.

4.5. SUMMARY AND CONCLUSIONS

The electrochemical behaviour as well as the corrosion products formed on carbon steel is dependent on the anion content of the exposure environment as well as the levels of dissolved O_2 .

An increase in $[\text{Cl}^-]$ led to an increase in E_{CORR} and R_p which suggested a less reactive surface state explained by the ability of Cl^- to induce passivation by the stabilization of Fe^{III} oxides in the presence of traces of O_2 . The catalysis of this oxidation appears to be a slow reaction with the outer surface of Fe_3O_4 and is dependent on the availability of dissolved O_2 . When passivation does occur (high $[\text{Cl}^-]$; traces of O_2) pitting can occur with an accumulation of Fe^{III} oxyhydroxides leading to partial passivation of breakdown sites. At high concentrations, Cl^- exerts a dual role first catalyzing surface oxidation leading to passivity, and then causing the initiation of breakdown sites on the passivated surface. The presence of Cl^- also influences the final corrosion product with low $[\text{Cl}^-]$ favouring the formation of Fe_3O_4 while high $[\text{Cl}^-]$ promotes the formation of $\gamma\text{-FeOOH}$.

The addition of $[\text{HCO}_3^-/\text{CO}_3^{2-}]$ accelerates the anodic dissolution of Fe^{2+} by stabilization of soluble complexes such as FeHCO_3^+ and $\text{Fe}(\text{HCO}_3)_2$. This leads to a competition between the stabilization of Fe^{2+} by $\text{HCO}_3^-/\text{CO}_3^{2-}$ and the oxidation to Fe^{III} oxides catalyzed by Cl^- . An increase in $[\text{HCO}_3^-/\text{CO}_3^{2-}]$ also shifted the breakdown potential to more positive values due to the ability of the $\text{HCO}_3^-/\text{CO}_3^{2-}$ to buffer local acidity and prevent pit propagation. Even at low $[\text{HCO}_3^-/\text{CO}_3^{2-}]$ (0.001 M), $\text{HCO}_3^-/\text{CO}_3^{2-}$ can buffer the pH at breakdown sites allowing repassivation to occur.

The increased values of E_{CORR} and R_p in the presence of SO_4^{2-} indicate this anion does not prevent the Cl^- catalyzed oxidation to Fe^{III} oxide in the presence of traces of O_2 . Passivation of the surface in this manner causes more frequent breakdown processes but their propagation appears limited due to the inability of SO_4^{2-} to promote Fe^{2+} dissolution. Additionally, SO_4^{2-} was shown to

have a more pronounced effect on the film breakdown potential than $\text{HCO}_3^-/\text{CO}_3^{2-}$, suggesting it may be more strongly adsorbed on the Fe^{III} oxide surface.

4.6. REFERENCES

- [1] K. Azumi and M. Seo "Corrosion behavior of titanium-clad carbon steel in weakly alkaline solutions" *Corrosion Science* 45 (2) (2003) 413-426
- [2] Y. Benamor, L. Bousselmi, H. Takenouti and E. Triki "Influence of sulphate ions on corrosion mechanism of carbon steel in calcareous media" *Corrosion Engineering Science and Technology* 40 (2) (2005) 129-136
- [3] C. T. Lee, M. S. Odziemkowski and D. W. Shoesmith "An in situ Raman-electrochemical investigation of carbon steel corrosion in $\text{Na}_2\text{CO}_3/\text{NaHCO}_3$, Na_2SO_4 , and NaCl solutions" *Journal of the Electrochemical Society* 153 (2) (2006) B33-B41
- [4] C. T. Lee, Z. Qin, M. Odziemkowski and D. W. Shoesmith "The influence of groundwater anions on the impedance behaviour of carbon steel corroding under anoxic conditions" *Electrochimica Acta* 51 (8-9) (2006) 1558-1568
- [5] M. M. El-Naggar "Effects of Cl^- , NO_3^- and SO_4^{2-} anions on the anodic behavior of carbon steel in deaerated 0.50 M NaHCO_3 solutions" *Applied Surface Science* 252 (18) (2006) 6179-6194
- [6] E. M. Rus, I. Baldea and C. Calin "OLT-35 low carbon steel corrosion in presence of sulfate ions" *Studia Universitatis Babeş-Bolyai Chimia* 52 (3) (2007) 137-146
- [7] N. R. Smart "Corrosion behavior of carbon steel radioactive waste packages: A summary review of Swedish and U.K. research (reprinted from proceedings of the CORROSION/2008 research topical symposium)" *Corrosion* 65 (3) (2009) 195-212
- [8] P. Refait, J. A. Bourdoiseau, M. Jeannin, D. D. Nguyen, A. Romaine and R. Sabot "Electrochemical formation of carbonated corrosion products on carbon steel in deaerated solutions" *Electrochimica Acta* 79 (2012) 210-217
- [9] R. Crowe, K. Birch, J. Freire-Canosa, J. Chen, D. Doyle, F. Garisto, P. Gierszewski, M. Gobien, C. Hatton, N. Hunt, S. Hirschorn, M. Hobbs, M. Jensen, P. G. Keech, L. Kennell, E. Kremer, P. Maak, J. McKelvie, C. Medri, M. Mielcarek, A. Murchison, A. Parmenter, R. Ross, E. Sykes and T. Yang "Technical program for long-term management of Canada's used nuclear fuel - annual report 2014" Nuclear Waste Management Organization Report No. NWMO TR-2015-01 (2015)
- [10] G. Vatankhah, M. Drogowska, H. Menard and L. Brossard "Electrodissolution of iron in sodium sulfate and sodium bicarbonate solutions at pH 8" *Journal of Applied Electrochemistry* 28 (2) (1998) 173-183
- [11] M. S. Rahman, S. Divi, D. Chandra and J. Daemen "Effect of different salts on the corrosion properties of friction type A607 steel rock bolt in simulated concentrated water" *Tunnelling and Underground Space Technology* 23 (6) (2008) 665-673
- [12] P. Smith, S. Roy, D. Swailes, S. Maxwell, D. Page and J. Lawson "A model for the corrosion of steel subjected to synthetic produced water containing sulfate, chloride and hydrogen sulfide" *Chemical Engineering Science* 66 (23) (2011) 5775-5790
- [13] K. Premllal, J. H. Potgieter and S. Sanja "Laser surface treatment to inhibit observed corrosion of reinforcing steel in sulphate: Alkaline media" *Anti-Corrosion Methods and Materials* 58 (5) (2011) 267-284
- [14] Z. Zhu, X. Jiao, X. Tang and H. Lu "Effects of SO_4^{2-} concentration on corrosion behaviour of carbon steels" *Anti-Corrosion Methods and Materials* 62 (5) (2015) 322-326

- [15] A. Vyskocil "Corrosion of iron - the kinetic problem" *Chemicke Listy Pro Vedu a Prumysl* 41 (5) (1947) 107-114
- [16] J. King and N. Davidson "Kinetics of the ferrous iron-oxygen reaction in acidic phosphate-pyrophosphate solutions" *Journal of the American Chemical Society* 80 (7) (1958) 1542-1545
- [17] J. M. Kolotyrkin "Pitting corrosion of metals" *Corrosion* 19 (8) (1963) 261t-268t
- [18] H. Tamura, K. Goto and M. Nagayama "Effect of anions on oxygenation of ferrous ion in neutral solutions" *Journal of Inorganic & Nuclear Chemistry* 38 (1) (1976) 113-117
- [19] H. Tanaka, N. Hatanaka, M. Muguruma, T. Ishikawa and T. Nakayama "Influence of anions on the formation of artificial steel rust particles prepared from aqueous Fe(III) solution" *Corrosion Science* 66 (2013) 136-141
- [20] P. Refait, M. Reffass, J. Landoulsi, R. Sabot and M. Jeannin "Role of phosphate species during the formation and transformation of the Fe(II-III) hydroxycarbonate green rust" *Colloids and Surfaces A: Physicochemical and Engineering Aspects* 299 (1-3) (2007) 29-37
- [21] S. Simard, M. Odziemkowski, D. E. Irish, L. Brossard and H. Menard "In situ micro-Raman spectroscopy to investigate pitting corrosion product of 1024 mild steel in phosphate and bicarbonate solutions containing chloride and sulfate ions" *Journal of Applied Electrochemistry* 31 (8) (2001) 913-920
- [22] N. Boucherit, A. H. L. Goff and S. Joiret "Raman studies of corrosion films grown on Fe and Fe-Mo in pitting conditions" *Corrosion Science* 32 (5-6) (1991) 497-507
- [23] M. S. Odziemkowski, T. T. Schuhmacher, R. W. Gillham and E. J. Reardon "Mechanism of oxide film formation on iron in simulating groundwater solutions: Raman spectroscopic studies" *Corrosion Science* 40 (2-3) (1998) 371-389
- [24] P. Refait, M. Reffass, J. Landoulsi, R. Sabot and M. Jeannin "Role of nitrite species during the formation and transformation of the Fe(II-III) hydroxycarbonate green rust" *Colloids and Surfaces A: Physicochemical and Engineering Aspects* 459 (2014) 225-232
- [25] L. Legrand, G. Sagon, S. Lecomte, A. Chausse and R. Messina "A Raman and infrared study of a new carbonate green rust obtained by electrochemical way" *Corrosion Science* 43 (9) (2001) 1739-1749
- [26] R. Sabot, M. Jeannin, M. Gadouleau, Q. Guo, E. Sicre and P. Refait "Influence of lactate ions on the formation of rust" *Corrosion Science* 49 (3) (2007) 1610-1624
- [27] P. Refait and J. M. R. Genin "The mechanisms of oxidation of ferrous hydroxychloride beta-Fe₂(OH)₃Cl in aqueous solution: The formation of akaganeite vs goethite" *Corrosion Science* 39 (3) (1997) 539-553
- [28] P. H. Refait, M. Abdelmoula and J. M. R. Genin "Mechanisms of formation and structure of green rust one in aqueous corrosion of iron in the presence of chloride ions" *Corrosion Science* 40 (9) (1998) 1547-1560
- [29] J. M. R. Genin, P. Refait, G. Bourrie, M. Abdelmoula and F. Trolard "Structure and stability of the Fe(II)-Fe(III) green rust "fougerite" mineral and its potential for reducing pollutants in soil solutions" *Applied Geochemistry* 16 (5) (2001) 559-570
- [30] D. de Faria, S. Silva and M. de Oliveira "Raman microspectroscopy of some iron oxides and oxyhydroxides" *Journal of Raman Spectroscopy* 28 (11) (1997) 873-878
- [31] D. Neff, P. Dillmann, L. Bellot-Gurlet and G. Beranger "Corrosion of iron archaeological artefacts in soil: Characterisation of the corrosion system" *Corrosion Science* 47 (2) (2005) 515-535
- [32] I. Chamritski and G. Burns "Infrared- and Raman-active phonons of magnetite, maghemite, and hematite: A computer simulation and spectroscopic study" *Journal of Physical Chemistry B* 109 (11) (2005) 4965-4968

- [33] L. J. Simpson and C. A. Melendres "Surface-enhanced Raman spectroelectrochemical studies of corrosion films on iron in aqueous carbonate solution" *Journal of the Electrochemical Society* 143 (7) (1996) 2146-2152
- [34] K. Yazdanfar, X. Zhang, P. G. Keech, D. W. Shoesmith and J. C. Wren "Film conversion and breakdown processes on carbon steel in the presence of halides" *Corrosion Science* 52 (4) (2010) 1297-1304
- [35] M. Hanesch "Raman spectroscopy of iron oxides and (oxy)hydroxides at low laser power and possible applications in environmental magnetic studies" *Geophysical Journal International* 177 (3) (2009) 941-948
- [36] D. Neff, S. Reguer, L. Bellot-Gurlet, P. Dillmann and R. Bertholon "Structural characterization of corrosion products on archaeological iron: An integrated analytical approach to establish corrosion forms" *Journal of Raman Spectroscopy* 35 (8-9) (2004) 739-745
- [37] S. Savoye, L. Legrand, G. Sagon, S. Lecomte, A. Chausse, R. Messina and P. Toulhoat "Experimental investigations on iron corrosion products formed in bicarbonate/carbonate containing solutions at 90 degrees C" *Corrosion Science* 43 (11) (2001) 2049-2064
- [38] M. Bouchard and D. C. Smith "Catalogue of 45 reference Raman spectra of minerals concerning research in art history or archaeology, especially on corroded metals and coloured glass" *Spectrochimica Acta Part A Molecular and Biomolecular Spectroscopy* 59 (10) (2003) 2247-2266
- [39] C. Johnston "In-situ laser Raman microprobe spectroscopy of corroding iron electrode surfaces" *Vibrational Spectroscopy* 1 (1) (1990) 87-96
- [40] R. J. Thibeau, C. W. Brown and R. H. Heidersbach "Raman spectra of possible corrosion products of iron" *Applied Spectroscopy* 32 (6) (1978) 532-535
- [41] M. Criado, S. Martinez-Ramirez, S. Fajardo, P. P. Gomez and J. M. Bastidas "Corrosion rate and corrosion product characterisation using Raman spectroscopy for steel embedded in chloride polluted fly ash mortar" *Materials and Corrosion* 64 (5) (2013) 372-380
- [42] S. J. Oh, D. C. Cook and H. E. Townsend "Characterization of iron oxides commonly formed as corrosion products on steel" *Hyperfine Interactions* 112 (1) (1998) 59-65
- [43] G. V. M. Jacintho, P. Corio and J. C. Rubim "Surface-enhanced Raman spectra of magnetic nanoparticles adsorbed on a silver electrode" *Journal of Electroanalytical Chemistry* 603 (1) (2007) 27-34
- [44] S. Reguer, D. Neff, L. Bellot-Gurlet and P. Dillmann "Deterioration of iron archaeological artefacts: Micro-Raman investigation on Cl-containing corrosion products" *Journal of Raman Spectroscopy* 38 (4) (2007) 389-397
- [45] C. Remazeilles and P. Refait "On the formation of beta-FeOOH (akaganeite) in chloride-containing environments" *Corrosion Science* 49 (2) (2007) 844-857
- [46] L. Mazzetti and P. J. Thistlethwaite "Raman spectra and thermal transformations of ferrihydrite and schwertmannite" *Journal of Raman Spectroscopy* 33 (2) (2002) 104-111
- [47] M. Saheb, D. Neff, L. Bellot-Gurlet and P. Dillmann "Raman study of a deuterated iron hydroxycarbonate to assess long-term corrosion mechanisms in anoxic soils" *Journal of Raman Spectroscopy* 42 (5) (2011) 1100-1108
- [48] R. L. Frost, M. C. Hales and B. J. Reddy "Aurichalcite - An SEM and Raman spectroscopic study" *Polyhedron* 26 (13) (2007) 3291-3300

- [49] I. V. Pekov, N. Perchiazzi, S. Merlino, N. Vyacheslav, M. Merlini and A. E. Zadov "Chukanovite, $\text{Fe}_2(\text{CO}_3)(\text{OH})_2$, a new mineral from the weathered iron meteorite Dronino" *European Journal of Mineralogy* 19 (6) (2007) 891-898
- [50] C. Remazeilles and P. Refait "Fe(II) hydroxycarbonate $\text{Fe}_2(\text{OH})_2\text{CO}_3$ (Chukanovite) as iron corrosion product: Synthesis and study by Fourier transform infrared spectroscopy" *Polyhedron* 28 (4) (2009) 749-756
- [51] V. E. Erdos and H. Altorfer "Ein dem Malachit ahnliches basisches Eisenkarbonat als Korrosionsprodukt von Stahl" *Materials and Corrosion-Werkstoffe Und Korrosion* 27 (5) (1976) 304-312
- [52] V. Pandarinathan, K. Lepkova and W. van Bronswijk "Chukanovite ($\text{Fe}_2(\text{OH})_2\text{CO}_3$) identified as a corrosion product at sand-deposited carbon steel in CO_2 -saturated brine" *Corrosion Science* 85 (2014) 26-32
- [53] K. Dideriksen, C. Frandsen, N. Bovet, A. F. Wallace, O. Sel, T. Arbour, A. Navrotsky, J. J. De Yoreo and J. F. Banfield "Formation and transformation of a short range ordered iron carbonate precursor" *Geochimica et Cosmochimica Acta* 164 (2015) 94-109
- [54] A. M. Posner "The kinetics of autoxidation of ferrous ions in concentrated HCl solutions" *Transactions of the Faraday Society* 49 (4) (1953) 382-388
- [55] W. Stumm and G. F. Lee "Oxygenation of ferrous iron" *Industrial and Engineering Chemistry* 53 (2) (1961) 143-146
- [56] Y. Kurimura, R. Ochiai and N. Matsuura "Oxygen oxidation of ferrous ions induced by chelation" *Bulletin of the Chemical Society of Japan* 41 (10) (1968) 2234-2239
- [57] R. P. Colborn and M. J. Nicol "Investigation into the kinetics and mechanism of oxidation of iron (II) by oxygen in aqueous chloride solutions" *Journal of the Southern African Institute of Mining and Metallurgy* 73 (9) (1973) 281-289
- [58] K. Porsch and A. Kappler "Fe" oxidation by molecular O_2 during HCl extraction" *Environmental Chemistry* 8 (2) (2011) 190-197
- [59] P. Refait and J. M. R. Genin "The oxidation of ferrous hydroxide in chloride-containing aqueous-media and Pourbaix diagrams of green rust one" *Corrosion Science* 34 (5) (1993) 797-819
- [60] F. M. Al-Kharafi, B. G. Ateya and R. M. Abdallah "Electrochemical behaviour of low carbon steel in concentrated carbonate chloride brines" *Journal of Applied Electrochemistry* 32 (12) (2002) 1363-1370
- [61] S. S. El-Egamy and W. A. Badaway "Passivity and passivity breakdown of 304 stainless steel in alkaline sodium sulphate solutions" *Journal of Applied Electrochemistry* 34 (11) (2004) 1153-1158
- [62] N. J. Laycock and R. C. Newman "Localised dissolution kinetics, salt films and pitting potentials" *Corrosion Science* 39 (10-11) (1997) 1771-1790
- [63] J. Weiss "The autoxidation of ferrous ions in aqueous solution" *Experientia* 9 (2) (1953) 61-62
- [64] J. J. Ulrich and F. C. Anson "Ligand bridging by halide in electrochemical oxidation of chromium(II) at mercury electrodes" *Inorganic Chemistry* 8 (2) (1969) 195-200
- [65] R. M. Taylor "Influence of chloride on the formation of iron-oxides from Fe(II) chloride. II. Effect of [Cl] on the formation of lepidocrocite and its crystallinity" *Clays and Clay Minerals* 32 (3) (1984) 175-180
- [66] U. Schwertmann and H. Fechter "The formation of green rust and its transformation to lepidocrocite" *Clay Minerals* 29 (1) (1994) 87-92

- [67] D. Rezel, P. Bauer and J. M. R. Genin "Superparamagnetic behavior and hyperfine interactions in ferrous hydroxide II and green rust I" *Hyperfine Interactions* 42 (1) **(1988)** 1075-1078
- [68] A. A. Olowe and J. M. R. Genin "The mechanism of oxidation of ferrous hydroxide in sulfated aqueous media: Importance of the initial ratio of the reactants" *Corrosion Science* 32 (9) **(1991)** 965-984
- [69] R. M. Taylor "Influence of chloride on the formation of iron-oxides from Fe(II) Chloride. I. Effect of [Cl]/[Fe] on the formation of magnetite" *Clays and Clay Minerals* 32 (3) **(1984)** 167-174
- [70] E. B. Castro, C. R. Valentini, C. A. Moina, J. R. Vilche and A. J. Arvia "The influence of ionic composition on the electrodisolution and passivation of iron electrodes in potassium carbonate-bicarbonate solutions in the 8.4-10.5 pH range at 25C" *Corrosion Science* 26 (10) **(1986)** 781-793
- [71] E. B. Castro, J. R. Vilche and A. J. Arvia "Iron dissolution and passivation in K₂CO₃-KHCO₃ solutions. Rotating-ring-disk electrode and XPS studies" *Corrosion Science* 32 (1) **(1991)** 37-50
- [72] B. W. A. Sherar, P. G. Keech, Z. Qin, F. King and D. W. Shoesmith "Nominally anaerobic corrosion of carbon steel in near-neutral pH saline environments" *Corrosion* 66 (4) **(2010)** 045001-1-045001-11
- [73] K. Videm and A. M. Koren "Corrosion, passivity, and pitting of carbon steel in aqueous-solutions of HCO₃⁻, CO₂, and Cl⁻" *Corrosion* 49 (9) **(1993)** 746-754
- [74] L. Legrand, S. Savoye, A. Chausse and R. Messina "Study of oxidation products formed on iron in solutions containing bicarbonate/carbonate" *Electrochimica Acta* 46 (1) **(2000)** 111-117
- [75] M. A. Blesa and H. A. Marinovich "Mechanism of dissolution of magnetite by oxalic acid-ferrous ion solutions" *Inorganic Chemistry* 26 (22) **(1987)** 3713-3717
- [76] A. Kuch "Investigations of the reduction and reoxidation kinetics of iron(III) oxide scales formed in waters" *Corrosion Science* 28 (3) **(1988)** 221-231
- [77] M. Stratmann, K. Bohnenkamp and H. J. Engell "An electrochemical study of phase-transitions in rust layers" *Corrosion Science* 23 (9) **(1983)** 969-985
- [78] M. Reffass, R. Sabot, C. Savall, M. Jeannin, J. Creus and P. Refait "Localised corrosion of carbon steel in NaHCO₃/NaCl electrolytes: Role of Fe(II)-containing compounds" *Corrosion Science* 48 (3) **(2006)** 709-726
- [79] J. H. Dong, T. Nishimura and T. Kodama "Corrosion behavior of carbon steel in bicarbonate (HCO₃) solutions" *Scientific Basis for Nuclear Waste Management XXV*, 713, Boston, MA, Materials Research Society, **(2002)** 105-112
- [80] S. Music, I. Nowik, M. Ristic, Z. Orehovec and S. Popovic "The effect of bicarbonate/carbonate ions on the formation of iron rust" *Croatica Chemica Acta* 77 (1-2) **(2004)** 141-151
- [81] M. Saheb, D. Neff, P. Dillmann, H. Matthiesen and E. Foy "Long-term corrosion behaviour of low-carbon steel in anoxic environment: Characterisation of archaeological artefacts" *Journal of Nuclear Materials* 379 (1-3) **(2008)** 118-123
- [82] M. L. Schlegel, C. Bataillon, C. Blanc, D. Pret and E. Foy "Anodic activation of iron corrosion in clay media under water-saturated conditions at 90 degrees C: Characterization of the corrosion interface" *Environmental Science & Technology* 44 (4) **(2010)** 1503-1508

- [83] A. Romaine, R. Sabot, M. Jeannin, S. Necib and P. Refait "Electrochemical synthesis and characterization of corrosion products on carbon steel under argillite layers in carbonated media at 80 degrees C" *Electrochimica Acta* 114 (2013) 152-158
- [84] M. L. Schlegel, C. Bataillon, F. Brucker, C. Blanc, D. Pret, E. Foy and M. Chorro "Corrosion of metal iron in contact with anoxic clay at 90 degrees C: Characterization of the corrosion products after two years of interaction" *Applied Geochemistry* 51 (2014) 1-14
- [85] M. Ko, B. Ingham, N. Laycock and D. E. Williams "In situ synchrotron X-ray diffraction study of the effect of chromium additions to the steel and solution on CO₂ corrosion of pipeline steels" *Corrosion Science* 80 (2014) 237-246
- [86] M. Ko, B. Ingham, N. Laycock and D. E. Williams "In situ synchrotron X-ray diffraction study of the effect of microstructure and boundary layer conditions on CO₂ corrosion of pipeline steels" *Corrosion Science* 90 (2015) 192-201
- [87] M. Saheb, D. Neff, P. Dillmann, H. Matthiesen, E. Foy and L. Bellot-Gurlet "Multisecular corrosion behaviour of low carbon steel in anoxic soils: Characterisation of corrosion system on archaeological artefacts" *Materials and Corrosion* 60 (2) (2009) 99-105
- [88] Y. Leon, M. Saheb, E. Drouet, D. Neff, E. Foy, E. Leroy, J. J. Dynes and P. Dillmann "Interfacial layer on archaeological mild steel corroded in carbonated anoxic environments studied with coupled micro and nano probes" *Corrosion Science* 88 (2014) 23-35
- [89] I. Azoulay, C. Remazeilles and P. Refait "Determination of standard Gibbs free energy of formation of chukanovite and Pourbaix diagrams of iron in carbonated media" *Corrosion Science* 58 (2012) 229-236

Chapter 5

The Electrochemical Behaviour of A516 Gr70 Carbon Steel Exposed to Anoxic Simulated Groundwater Environments

5.1. INTRODUCTION

Sedimentary clay environments have been chosen as a potential site for the use of single-walled carbon steel containers for the disposal of high level nuclear waste in Canada. The emplacement of the container within sedimentary clays provides an additional barrier to the release of radionuclides should container failure occur. However, the composition of groundwaters in sedimentary clay environments may differ between individual locations. As such, it is prudent to determine the effects of various groundwater compositions on the corrosion of the steel container. Specifically, the effects of $[\text{Cl}^-]$ and $[\text{HCO}_3^-/\text{CO}_3^{2-}]$ are of top priority since Cl^- and $\text{HCO}_3^-/\text{CO}_3^{2-}$ have been shown to influence the corrosion behaviour of the steel as well as the identity of the corrosion products formed.

Since the design life of a container in a Deep Geologic Repository (DGR) is very long, it is important to determine the corrosion behaviour of steel over extended periods of time under conditions which simulate the groundwater environment. Archaeological artefacts have commonly been used to determine the behaviour of iron over extended periods of time (up to 450 years). However, the groundwaters in which these objects were corroded may not closely simulate those of the DGR sedimentary clay environment. In this and the subsequent chapter, results of a study of the corrosion behaviour of A516 Gr70 carbon steel over extended periods of time are presented. The electrochemical results, recorded over a period of 60 days, are complimentary to the results of exposure experiments conducted over a 30 month time scale presented in Chapter 6.

The objective of the research described in this chapter is to explore the effects of $[\text{Cl}^-]$ and $\text{HCO}_3^-/\text{CO}_3^{2-}$ buffering on the electrochemical behaviour of A516 Gr70 carbon steel as well as the composition and morphology of the corrosion deposits formed over a 60 day exposure period. In addition, experiments were conducted in a simulated groundwater solution comparable to those expected within sedimentary clay repository environments. A combination of electrochemical techniques was employed to monitor the corrosion behaviour of the steel while

Raman and FTIR spectroscopy and scanning electron microscopy were used to identify the corrosion product deposits and determine their morphology.

5.2. EXPERIMENTAL DETAILS

5.2.1. Materials and Electrode Preparations

Electrodes were fabricated using A516 Gr70 carbon steel (0.23 C; 1.11 Mn; 0.07 P; 0.03 S; 0.26 Si; 0.01 Cu; 0.01 Ni; 0.02 Cr; 0.004 Mo; 0.036 Al; 0.019 V; 0.003 O [wt.%], balance Fe) in the form of circular coupons 1.0 cm in diameter and 0.5 cm in height. Each electrode was fixed in a high-performance epoxy resin (Hysol EE 4190) with a single face (surface area = 0.7854 cm²) exposed. Each coupon was wet polished with 180, 600, 800 and 1000 grit SiC papers (Presi). A stainless steel rod was connected to the back of the electrode to facilitate connection to external measuring circuits. The steel rod and connection were sealed with laboratory film (Parafilm) and several layers of Teflon tape to avoid exposure to the electrolyte. The electrodes were then transferred into an anaerobic chamber and further polished with 1200 grit SiC paper to remove any air-formed oxides and rinsed with deaerated type 1 water prior to emplacement in the experimental solution.

5.2.2. Electrochemical Cell and Equipment

All experiments were conducted in a standard three-electrode, three-compartment glass cell. The main chamber of the cell was separated from the two side compartments by glass frits. The reference electrode was a commercial saturated calomel electrode (SCE, Fisher Scientific) placed in one side compartment of the cell and connected to the main chamber via a Luggin capillary, the tip of which was positioned just below the surface of the working electrode. All potentials are reported against the SCE scale (+0.241 V vs. SHE). A Pt sheet welded to a Pt wire housed in the second side compartment of the cell acted as the counter electrode. The electrochemical cell was placed in an anaerobic chamber to avoid any influx of atmospheric O₂. Corrosion potential (E_{CORR}), polarization resistance (R_p) and electrochemical impedance spectroscopy (EIS) measurements were recorded using a Solartron Analytical Modulab running Modulab XM ECS software.

5.2.3. Experimental Procedure

E_{CORR} measurements were performed over a period of 47-60 days to monitor the corrosion behaviour of the steel coupons in a series of four solutions. R_p measurements were taken at 8 hour intervals using the linear polarization resistance (LPR) technique using a ± 10 mV change from E_{CORR} . Electrochemical impedance spectroscopy (EIS) measurements were made every 48 hours using a potential perturbation of $E_{\text{CORR}} \pm 10$ mV over the frequency range of 10^5 to 10^{-3} Hz with a data collection rate of 11 points per decade.

5.2.4. Experimental Solutions

A series of three exposure solutions were used to investigate the effects of $[\text{Cl}^-]$ and buffering by $\text{HCO}_3^-/\text{CO}_3^{2-}$, Table 5-1. Additionally, a simulated groundwater solution mimicking the composition of Canadian sedimentary clay groundwater (given in Table 5-2) was also used. The pH of solutions (i), (ii), and (iv) were set to 6.3 ± 0.5 to mimic the expected pH range of sedimentary groundwaters at the repository level. The pH of solution (iii) was allowed to maintain its naturally buffered pH value of 8.85. Before preparing each solution, type 1 water was deaerated on the benchtop using ultra-high purity Ar at a high flow rate for at least 90 minutes prior to being sealed and transferred to the anaerobic chamber. The flask was sealed such that the entire volume was filled with deaerated Type 1 water to avoid any trapped air. Final preparation of the solution was completed within the anaerobic chamber where no additional measures were required to ensure anoxic conditions.

Table 5-1: Chemical composition of solutions (i-iii) containing Cl^- and $\text{HCO}_3^-/\text{CO}_3^{2-}$.

Exposure Solution	$[\text{Cl}^-]$ (M)	$[\text{HCO}_3^-]$ (M)	$[\text{CO}_3^{2-}]$ (M)
(i)	0.10	0.002213	0.00
(ii)	4.77	0.002213	0.00
(iii)	4.77	0.05	0.05

Table 5-2: Chemical composition of solution (iv) representing the expected composition of sedimentary clay groundwater in the Canadian Shield.

Cation	Concentration (M)	Anion	Concentration (M)
Ca ²⁺	0.811	Br ⁻	0.021
K ⁺	0.320	Cl ⁻	4.758
Mg ²⁺	0.337	HCO ₃ ⁻	0.002
Na ⁺	2.175	SO ₄ ²⁻	0.019
Sr ²⁺	0.014		

5.2.5. Surface Analysis

Iron corrosion products formed on the coupon surfaces were identified using Raman and/or infrared spectroscopy. Raman analyses were conducted using a Renishaw 2000 Raman spectrometer equipped with a 632.8 nm laser line and an optical microscope with a 50X magnification objective lens. GRAMS 386 Raman software was used for the collection and manipulation of spectra. FTIR analysis was performed using a Bruker-Hyperion 2000 FTIR spectrometer in reflectance mode. Each spectrum was collected via the average of 32 scans on a gold background. Visualization of the corrosion product morphology was determined using either a Hitachi S-4500 Field Emission SEM or LEO (Zeiss) 1540XB FIB/SEM crossbeam system.

5.3. RESULTS

5.3.1. E_{CORR} and R_p Measurements

Figure 5-1 shows the E_{CORR} values recorded on electrodes exposed for 47-60 days under anoxic conditions in solutions (i-iv) while Figure 5-2 shows the corresponding R_p values. The dashed horizontal line in Figure 5-1 represents the equilibrium potential for the oxidation of metallic Fe to Fe²⁺ (-0.859 V) calculated from the Nernst equation for an [Fe²⁺]=10⁻⁶ M. E_{CORR} for solution (i) decreases over the first 35 days of exposure from -0.773 V to -0.789 V, while R_p increases from 4 kΩcm² to 72 kΩcm². This combination of a decrease in E_{CORR} and an increase in the R_p indicates a suppression of the cathodic reaction rate. The increase in R_p with time indicates the development of a corrosion-inhibiting oxide/hydroxide suggesting a blocking of both the anodic and cathodic reactions with the dominant influence being on the cathodic reaction. Since anoxic conditions are maintained in the anaerobic chamber, a Fe₃O₄ film would be expected. Beyond 35

days, E_{CORR} continues to decrease marginally accompanied by a minor increase in R_p to a final value of $113 \text{ k}\Omega\text{cm}^2$, consistent with a slowly increasing suppression of the cathodic reaction.

In solution (ii) E_{CORR} is considerably more positive (-0.745 V to -0.739 V) and effectively constant over the 47 day exposure. The R_p values are lower and do not increase with time in contrast to the behaviour at the lower $[\text{Cl}^-]$. The lower R_p values coupled with a considerably higher E_{CORR} suggest a more rapid corrosion rate on a thinner Fe_3O_4 film, as indicated by the $87 \text{ k}\Omega\text{cm}^2$ difference in the steady-state R_p values, Figure 5-2. This indicates the surface remains more active in solution (ii) with the higher $[\text{Cl}^-]$. This suggests an opposite effect of a high $[\text{Cl}^-]$ on the corrosion rate under anoxic conditions (this Chapter) than when traces of dissolved O_2 are present (Chapter 4). There is no indication of localized events in either solution.

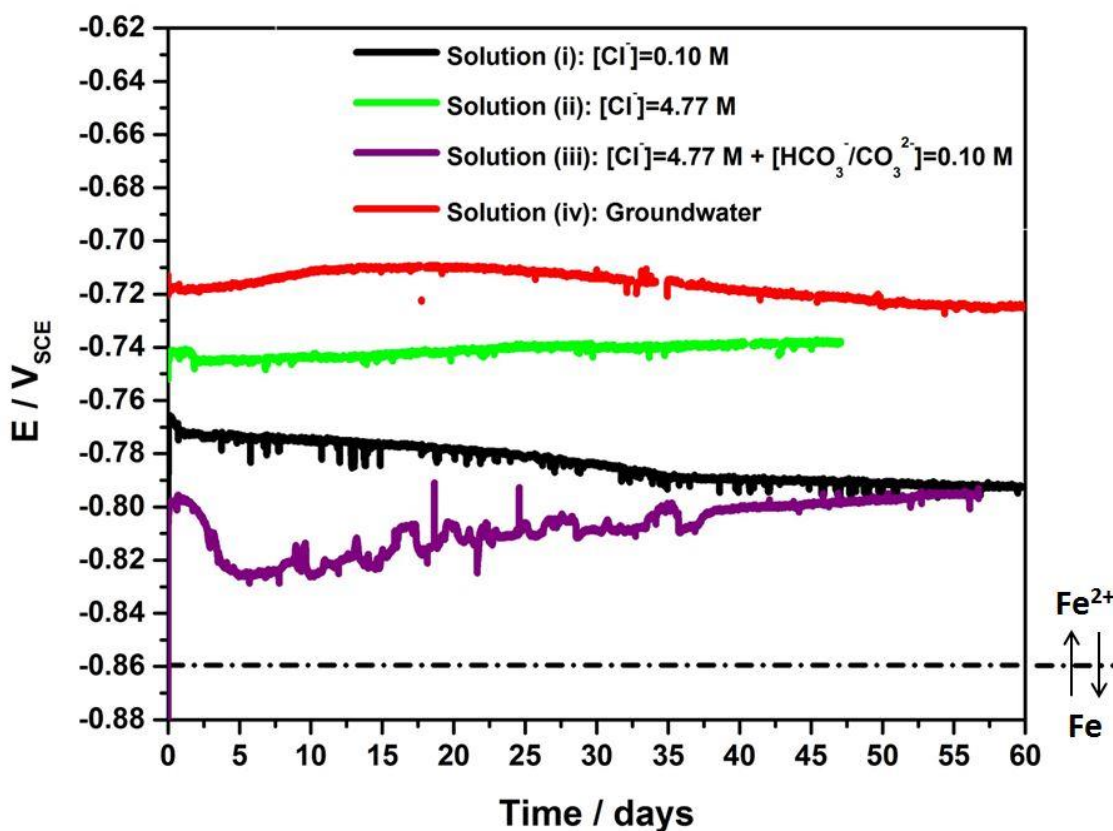


Figure 5-1: Corrosion potential (E_{CORR}) measurements recorded on steel exposed to solutions (i) to (iv) (Table 5-1 and Table 5-2).

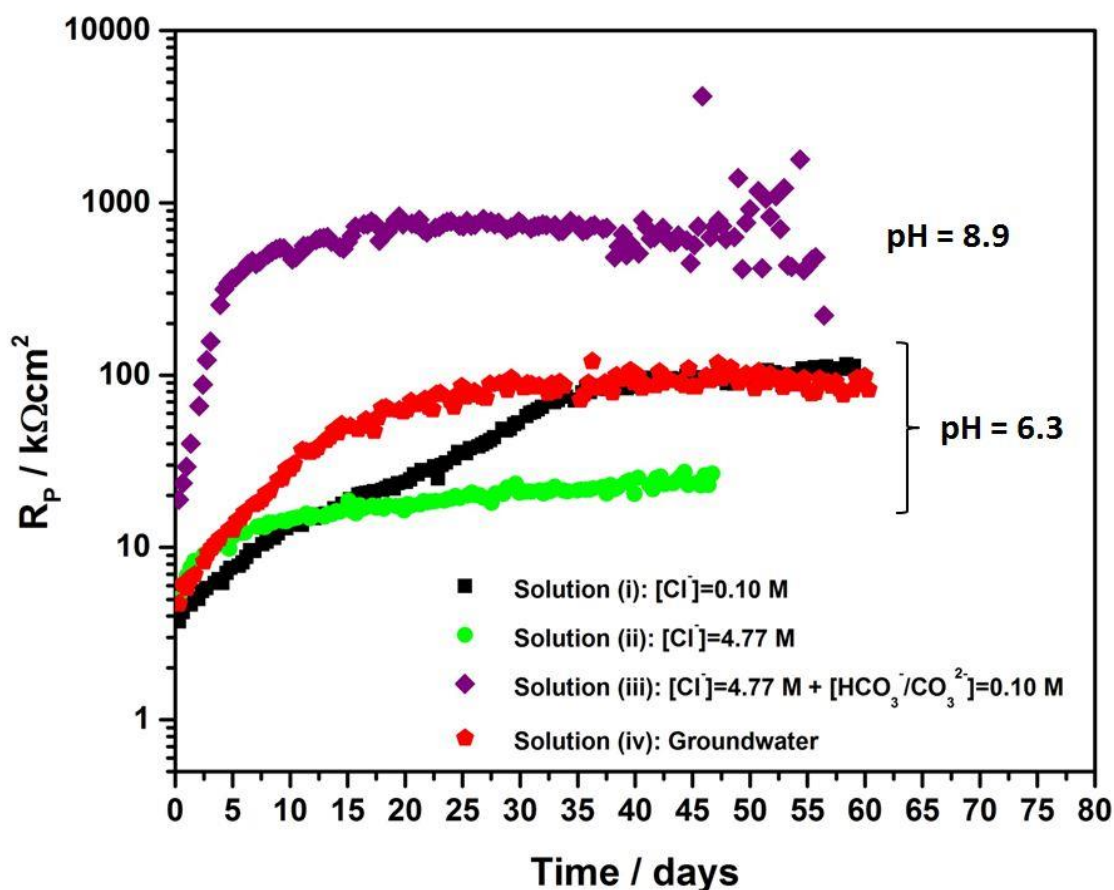


Figure 5-2: Polarization resistance (R_p) measurements recorded on steel exposed to solutions (i) to (iv) (Table 5-1 and Table 5-2).

When 0.10 M HCO_3^-/CO_3^{2-} is added to the high $[Cl^-]$ solution a significant decrease in E_{CORR} is observed, Figure 5-1, consistent with the findings of Chapter 4, which showed that an increase in $[HCO_3^-/CO_3^{2-}]$ led to a decrease in E_{CORR} . Over the first 10 days, E_{CORR} decreases to $\sim -0.825 V$ accompanied by a steep increase in R_p from 19 $k\Omega cm^2$ to 470 $k\Omega cm^2$. In the high $Cl^- + HCO_3^-/CO_3^{2-}$ solution the initial fall in E_{CORR} accompanied by a large increase in R_p (decrease in corrosion rate) suggests a large decrease in the rate of the cathodic reaction. If active conditions prevailed then this would be unexpected. The most likely explanation is that this initial period involves the galvanically coupled reduction of surface Fe^{III} oxide to anodic dissolution of the substrate steel. That this is observable in this experiment but not in the others may reflect the differences in pH, the removal of surface oxide requiring a longer time at this higher pH. Closer inspection of the E_{CORR}/R_p behaviour in the other experiments show a similar effect is observed

but of much shorter duration. For the duration of the experiment, E_{CORR} steadily increases (-0.795 V) while R_p remains effectively constant at a value of $1100 \text{ k}\Omega\text{cm}^2$. However, while increasing slightly, E_{CORR} experiences fluctuations on the order of 10-20 mV over the exposure period of 5 to 35 days. These fluctuations, and the accompanying changes in R_p , are shown in more detail in Figure 5-3. Both parameters show concurrent increases and decreases indicating fluctuations in the rate of the anodic reaction. At such a low E_{CORR} this could indicate the periodic and localized interruption of Fe_3O_4 formation by CO_3^{2-} catalyzed Fe^{2+} dissolution. A possibility is that this reflects the dissolution of Fe_3O_4 and the deposition of FeCO_3 (as discussed below). The observation of very high R_p values with a very low E_{CORR} is different to the behaviour observed when traces of dissolved O_2 are present (Chapter 4) when large R_p values are generally associated with more positive E_{CORR} values, a combination taken to indicate slow passivation of the steel surface.

The value of E_{CORR} in the simulated groundwater solution initially increases slightly over the first 15-20 days of exposure accompanied by an increase in R_p from $4 \text{ k}\Omega\text{cm}^2$ to $50 \text{ k}\Omega\text{cm}^2$. Given the similar $[\text{Cl}^-]$ and the absence of a significant $[\text{HCO}_3^-/\text{CO}_3^{2-}]_T$, the E_{CORR} values in solutions (ii) and (iv) would be expected to be similar. However, from Figure 5-1, E_{CORR} in the simulated groundwater experiment (solution (iv)) was much higher. This increase in E_{CORR} , coupled with a lower corrosion rate (higher R_p value), indicates that the dominant influence on the corrosion rate is the suppression of the anodic reaction. The CO_3^{2-} and SO_4^{2-} concentrations are low in the groundwater and would not be expected to significantly increase the corrosion rate. Also, in the absence of traces of dissolved O_2 the formation of passivating Fe^{III} phases would not be expected. Beyond 20 days E_{CORR} decreases to a final value of -0.725 V while the R_p remains unchanged. The constant R_p value suggests the steel has achieved steady-state corrosion, which is similar to that observed in solution (i). However, this constant corrosion rate is achieved ~ 10 days earlier in the simulated groundwater solution (iv), indicating a more rapid suppression of the rate by corrosion.

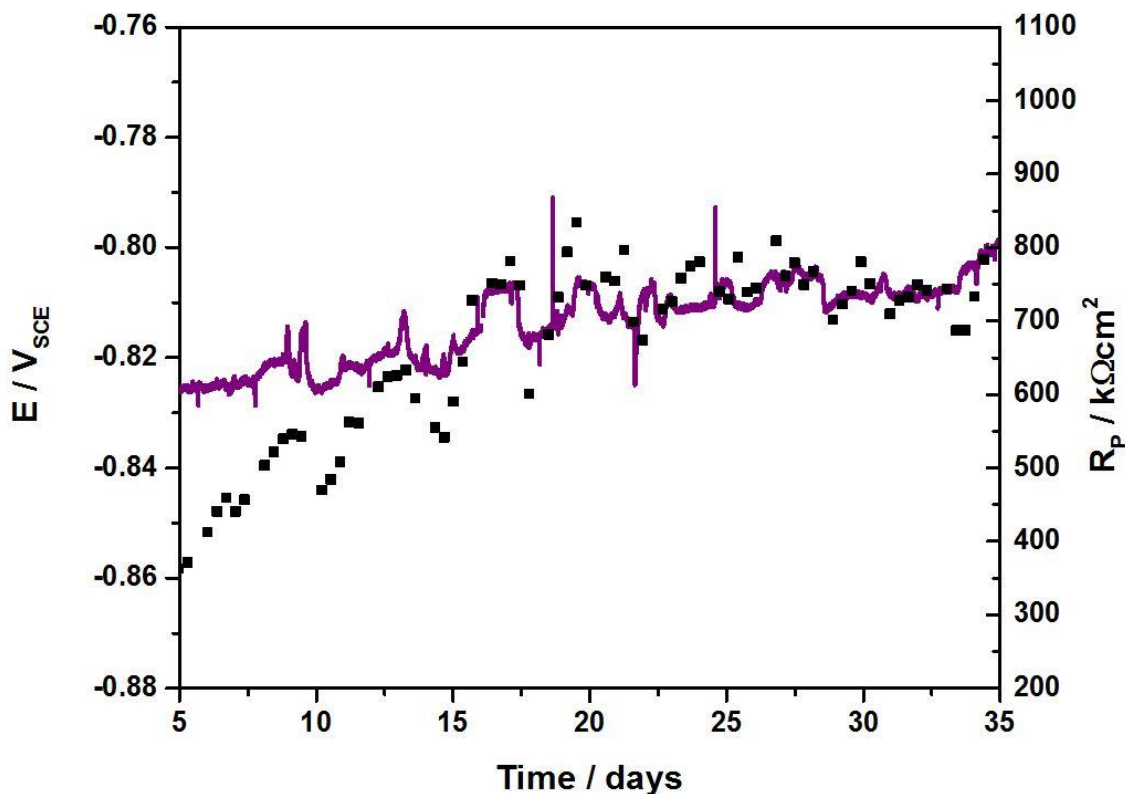


Figure 5-3: Corrosion potential (E_{CORR}) (solid line) and polarization resistance (R_p) (points) measurements for steel exposed to solution (iii) (Table 5-1) over a period of 5-35 days showing simultaneous fluctuations in the values of both E_{CORR} and R_p .

5.3.2. Electrochemical Impedance Spectroscopy

Figure 5-4 shows the impedance data collected on the steel electrode exposed to solution (i). The Bode plots, Figure 5-4(a-b), show what appears to be a single time constant response with the absolute impedance increasing over time in the low frequency range. A single time constant circuit, Figure 5-5, was used to fit the spectra. A constant phase element (CPE) was used to account for the non-ideality of the capacitive response of the film, $(R_p)_{EIS}$ is the polarization resistance, and R_s the solution resistance. Figure 5-4(c) shows the data plotted in the Nyquist form. Figure 5-4(d) shows the expanded Nyquist spectra recorded over the first 9 days of exposure. An additional feature is visible in the low frequency range, as shown in the inset, Figure 5-4(e). This behaviour suggests that multiple surface states, leading to an inductive effect, are observed in the early period of exposure, when E_{CORR} is increasing. This is most likely attributable to active corrosion of the steel surface during the early stages. Figure 5-4(f)

compares the values of $(R_p)_{EIS}$, obtained by fitting the spectra, to the polarization resistance (R_p) values (from Figure 5-2). The similarity between $(R_p)_{EIS}$ and R_p shows the two sets of measurements are consistent. Also shown in Figure 5-4(f) are the capacitances (C) obtained by using the Brug method for converting the CPE, deemed appropriate since the exponent of the CPE was between 0.8 and 0.83. The Brug conversion was used since frequency dispersion due to a general roughening of the surface was most likely to produce non-ideality in the capacitance. The calculated capacitance increased from 65 to 95 $\mu\text{F}/\text{cm}^2$ over the 60 day exposure period. Such a value suggests the interfacial capacitance can be attributed to the double layer on a rough surface. The values are too high to be attributed to a passive film, which is not unexpected since the $(R_p)_{EIS}$ values are relatively low. The slight increase in the value of the capacitance over the exposure period is consistent with an on-going roughening of the surface.

Figure 5-6(a) and (b) present the Bode plots measured over the 47 day exposure period in solution (ii) which show an increase in absolute impedance over the low frequency range. The Nyquist plot, Figure 5-6(c), indicates a single time constant response, and the equivalent circuit in Figure 5-5 was again used to fit the spectra, yielding $(R_p)_{EIS}$ values consistent with the R_p values (from Figure 5-2), Figure 5-6(d). Also given in Figure 5-6(d) are the capacitance values, extracted from the CPE, using a Brug conversion. The values of the CPE exponent ranged between 0.84 and 0.89, which are significantly larger than those observed for solution (i), suggesting a more ideal capacitance. As for solution (i), the capacitance values increased over the exposure period from 60 $\mu\text{F}/\text{cm}^2$ to 120 $\mu\text{F}/\text{cm}^2$, consistent with a double layer capacitance measured on an increasingly rough surface. While the absolute values of the double layer capacitance will change with the concentrations of the different solutions (i.e., increasing $[\text{Cl}^-]$), we wouldn't expect these variations to have a large effect on the capacitance values and their comparisons.

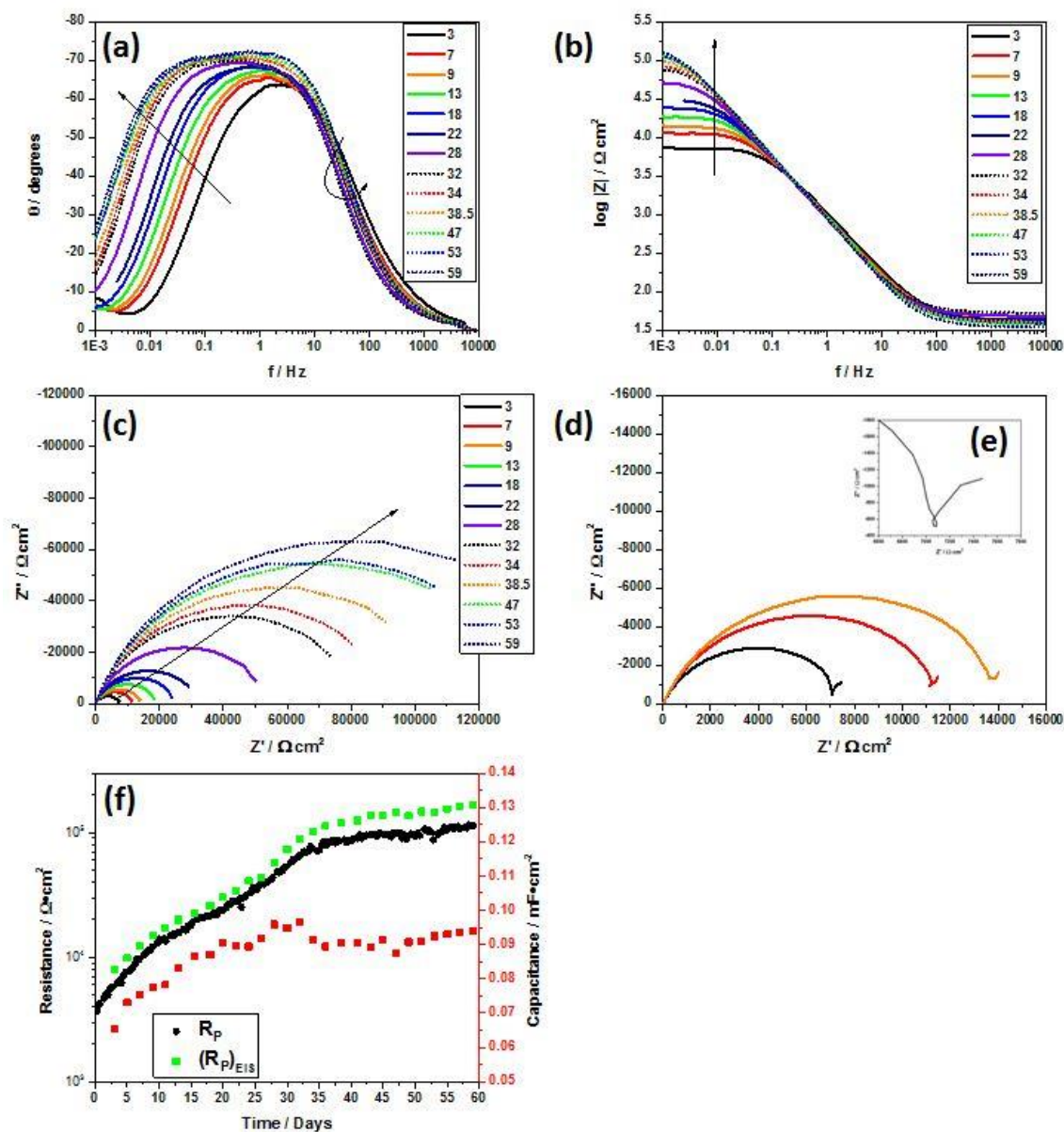


Figure 5-4: EIS data for steel exposed to solution (i) (Table 5-1) showing (a) and (b) Bode plots; (c) Nyquist plots; (d) the first three Nyquist plots on a larger scale; (e) the low frequency plot for the spectra taken after 3 days (black); (f) a comparison of R_p (from LPR) and $(R_p)_{EIS}$ (from fitted EIS plots) and the capacitance (C) (from the fitted EIS plots). Inset legends show the exposure time, in days, at the time of the EIS measurement.

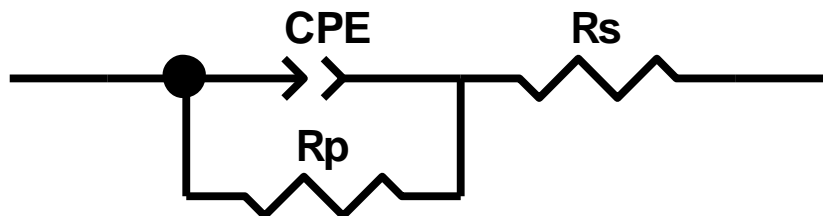


Figure 5-5: One time-constant equivalent circuit used to fit impedance spectra for solutions (i) to (iv) consisting of a constant phase element representative of the film capacitance (CPE), a polarization resistance $(R_p)_{EIS}$, and the solution resistance (R_s) .

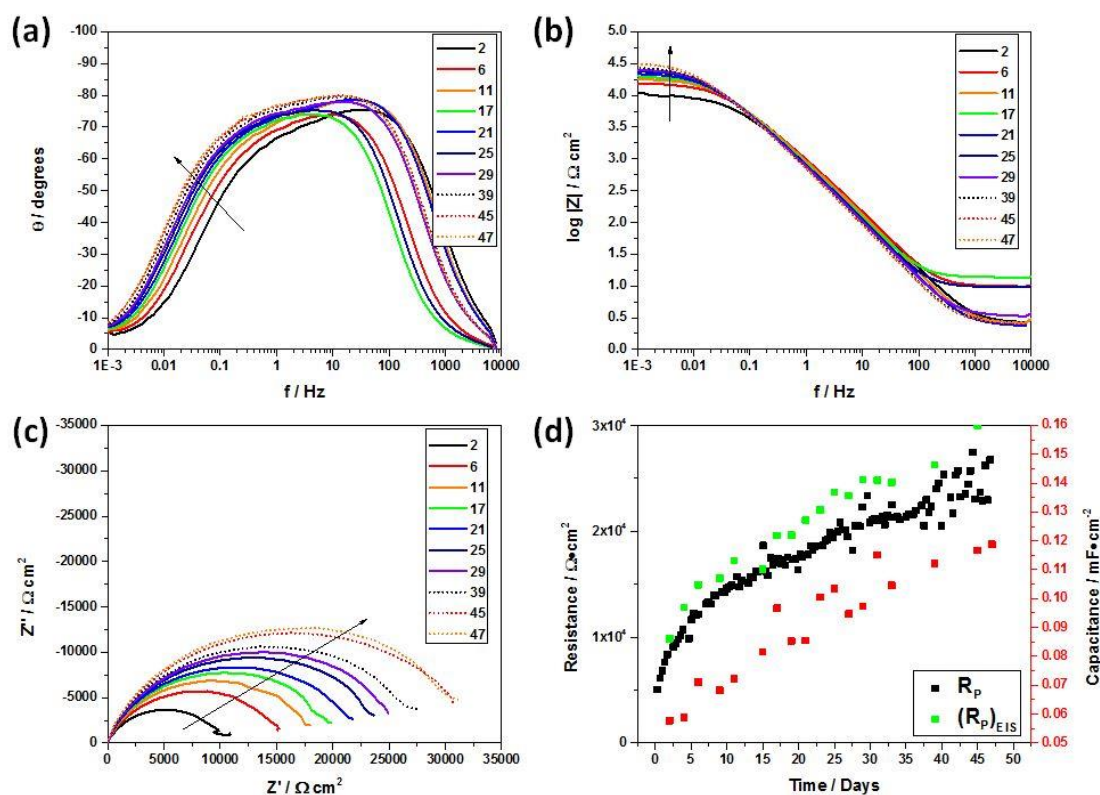


Figure 5-6: EIS data for steel exposed to solution (ii) (Table 5-1) showing (a) and (b) Bode plots; (c) Nyquist plots; (d) a comparison of R_p (from LPR) and $(R_p)_{EIS}$ (from fitted EIS plots) and the capacitance (C) (from the fitted EIS plots). Inset legends show the exposure time, in days, at the time of the EIS measurement.

Figure 5-7(a-b) shows the Bode plots obtained over a 60 day period of exposure to solution (iii). The phase angle plot, Figure 5-7(a), suggests the possibility of two time constants, the phase angle remaining constant at high frequency (100 Hz) but increasing at low frequency as observed in solutions (i) and (ii). This would suggest it may be possible to separate the charge transfer resistance at high frequencies from the film resistance at low frequency. However, while fitting to a two time constant circuit yielded a visually better fit, it also led to large errors associated with the calculated values. Consequently, the single time constant equivalent circuit, Figure 5-5, was again used to fit the spectra, although it should be noted that the low frequency data suggests features not accounted for in the equivalent circuit. Figure 5-7(d) shows the $(R_p)_{EIS}$

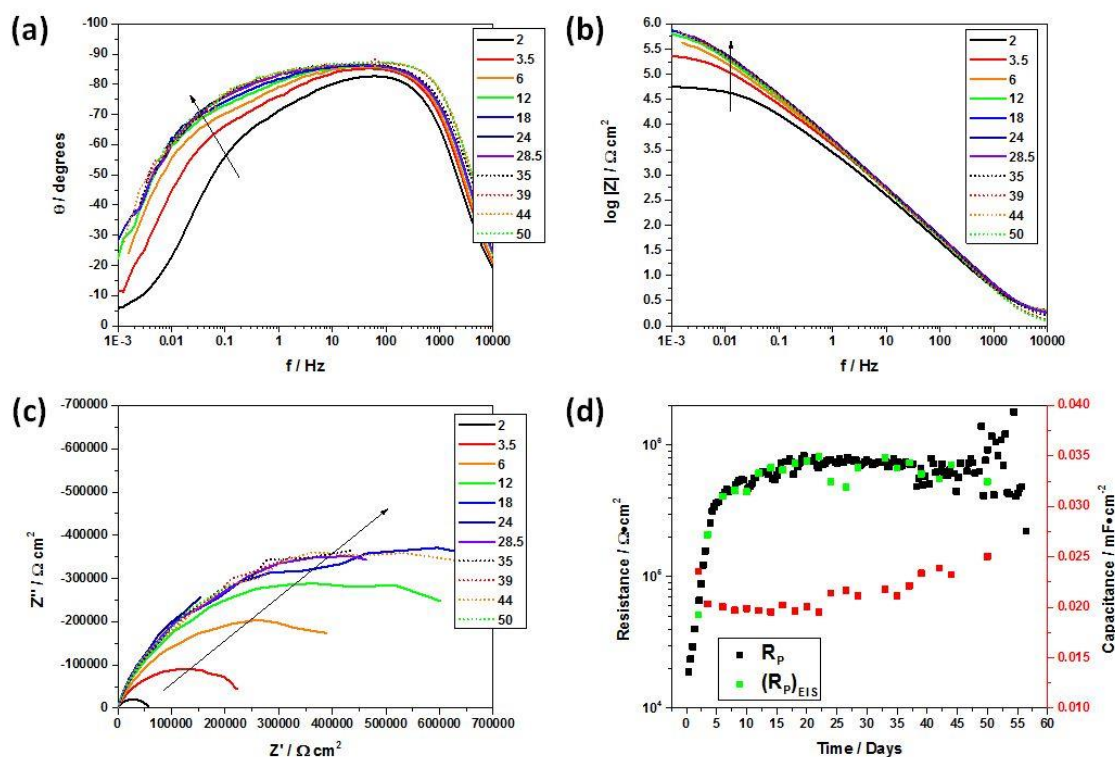


Figure 5-7: EIS data for steel exposed to solution (iii) (Table 5-1) showing (a) and (b) Bode plots; (c) Nyquist plots; (d) a comparison of R_p (from LPR) and $(R_p)_{EIS}$ (from fitted EIS plots) and the capacitance (C) (from the fitted EIS plots). Inset legends show the exposure time, in days, at the time of the EIS measurement.

values are consistent with the R_p values. The capacitance values obtained as described above are presented in Figure 5-7(d). The CPE exponent was in the range 0.88 to 0.95, which was significantly higher than in the other solutions, indicating very little frequency dispersion and a much more uniform surface than observed for the more active conditions present in solutions (i) and (ii). The capacitance values increase only slightly from 20 to 25 $\mu\text{F}/\text{cm}^2$ over the duration of the experiment. These low capacitances are consistent with a film-free surface and suggest the surface remains un-roughened by significant corrosion, consistent with the considerably reduced corrosion rate. This may reflect the influence of the increased pH in this solution.

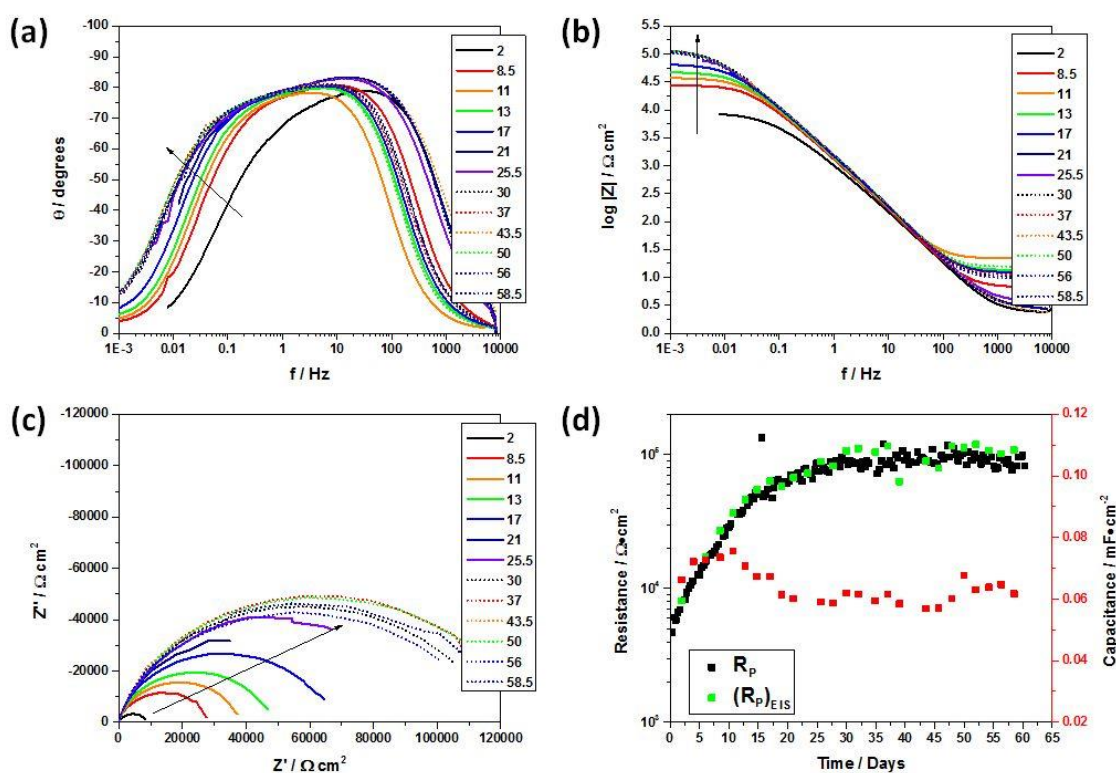


Figure 5-8: EIS data for steel exposed to solution (iv) (Table 5-2) showing (a) and (b) Bode plots; (c) Nyquist plots; (d) a comparison of R_p (from LPR) and $(R_p)_{\text{EIS}}$ (from fitted EIS plots) and the capacitance (C) (from the fitted EIS plots). Inset legends show the exposure time, in days, at the time of the EIS measurement.

Figure 5-8(a-b) show the Bode plots obtained over 59 days of exposure to the simulated groundwater solution (iv). The spectra were fitted to the single time constant circuit, and the $(R_p)_{\text{EIS}}$ values were identical to the R_p values. Capacitance values for the surface film are given in Figure 5-8(d). The CPE exponent values remain constant for the duration of the exposure at

~ 0.91 indicating a uniform surface and little frequency dispersion. The calculated capacitance values were also constant, suggesting a uniform surface, between 60 and 70 $\mu\text{F}/\text{cm}^2$. While larger than observed in solutions (i) and (ii), their consistency indicates no increase in surface roughness with exposure time.

5.3.3. Surface Analyses

Figure 5-9 shows SEM micrographs recorded after 60 days of exposure to solution (i). Figure 5-9(a) shows a low magnification image, representative of the steel surface, which appears to be generally roughened and possibly covered with a very thin but uniform corrosion film. The general roughening of the surface is consistent with the slow increase in capacitance which suggested an on-going roughening of the sample surface. Figure 5-9(b) and (c) suggest that any film present, if at all, is extremely thin. Figure 5-9(d) shows a large area exhibiting a different morphology found to form on some regions of the sample surface. Closer examination, Figure 5-9(e), shows this patch is composed of thin and irregularly spaced plate-like crystals consistent with the morphology of $\text{Fe}_2(\text{OH})_2\text{CO}_3$, as discussed in Chapter 4, for samples exposed to a solution containing $\text{HCO}_3^-/\text{CO}_3^{2-}$. Figure 5-9(f) shows a second location within this deposit which appears to be covered with a thicker and more dense deposit. Figure 5-9(g) is a low magnification image which shows four such locally corroded regions (observed as dark circles) which are on the order of 12-15 μm in diameter and exhibit a film morphology consistent with $\text{Fe}_2(\text{OH})_2\text{CO}_3$, Figure 5-9(h) and (i). The demarcation between these patches and the general surface suggests, while not pits, these areas experienced enhanced dissolution.

The Raman spectra recorded on the steel surface exposed to solution (i) are shown in Figure 5-10. The single band at 1069 cm^{-1} in each spectrum can be attributed to the ν_1 C–O symmetric stretching of a coordinated CO_3^{2-} species [1-3]. The lack of any other visible features within the spectra suggests that the CO_3^{2-} containing species is not Raman active. The FTIR spectra recorded on three different locations on the surface, Figure 5-11, confirm the presence of $\text{Fe}_2(\text{OH})_2\text{CO}_3$ [4, 5]. The prominent peaks at 1364 and 1527 cm^{-1} are due to C–O stretching while those at 3319 and 3482 cm^{-1} are due to O–H stretching. The peaks at 770 cm^{-1} and 835 cm^{-1} are attributed to the ν_4 in-plane and ν_2 out-of-plane bending of CO_2^{2-} while the peak at 951 cm^{-1} is due to the δ -OH bending mode. The FTIR spectra indicate that the crystalline film observed in Figure 5-9(d-f) and in the small circles in Figure 5-9(g-i) is $\text{Fe}_2(\text{OH})_2\text{CO}_3$. The absence of a Raman band at 667 cm^{-1} , indicating the presence of Fe_3O_4 [1, 6-15], would suggest either the active

metal surface is exposed or any surface film present is too thin to be detected by Raman spectroscopy. In addition, the absence of a Raman signature between 1200 and 1700 cm^{-1} , indicating the presence of residual Fe_3C from corroded pearlite grains, confirms that the extent of corrosion is minimal.

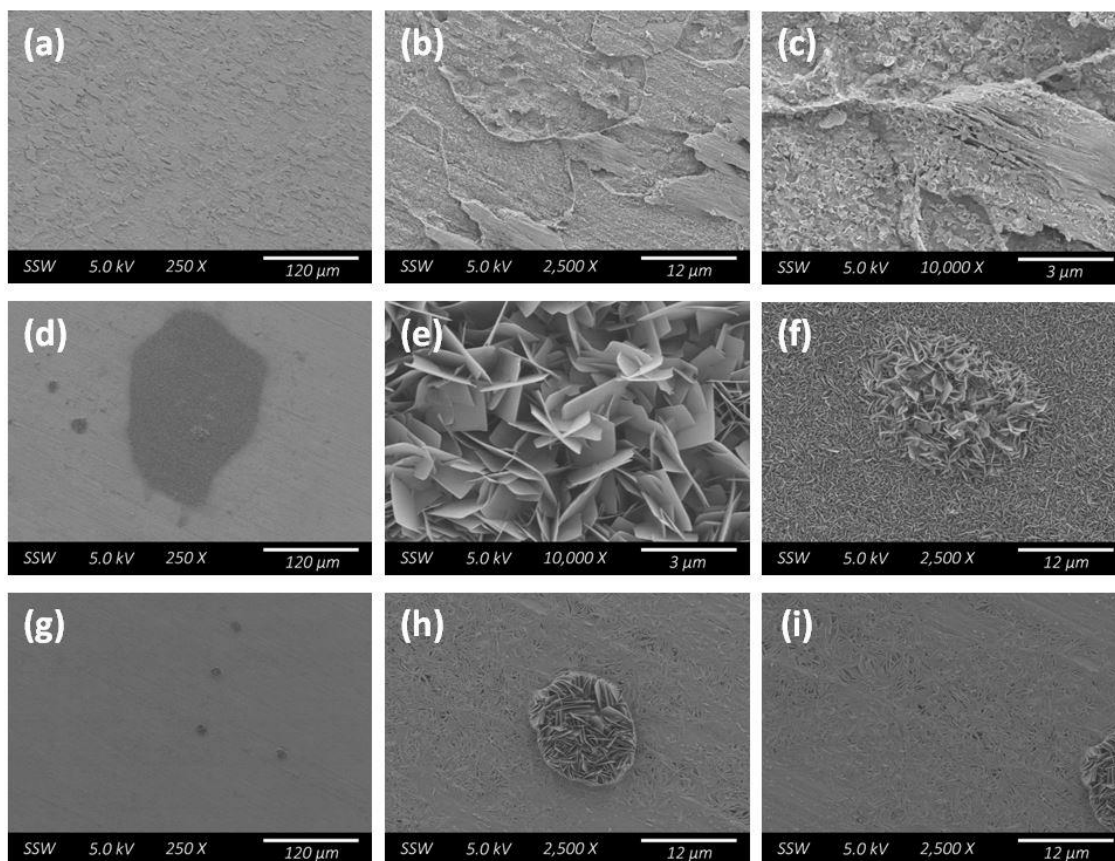


Figure 5-9: SEM micrographs of the corrosion product formed after 60 days of exposure to solution (i) (Table 5-1) for (a-c) the general steel surface; (d-f) patches of crystalline $\text{Fe}_2(\text{OH})_2\text{CO}_3$; and (g-i) additional locations showing distribution (g) and the morphology ((h) and (i)) of the crystalline patches.

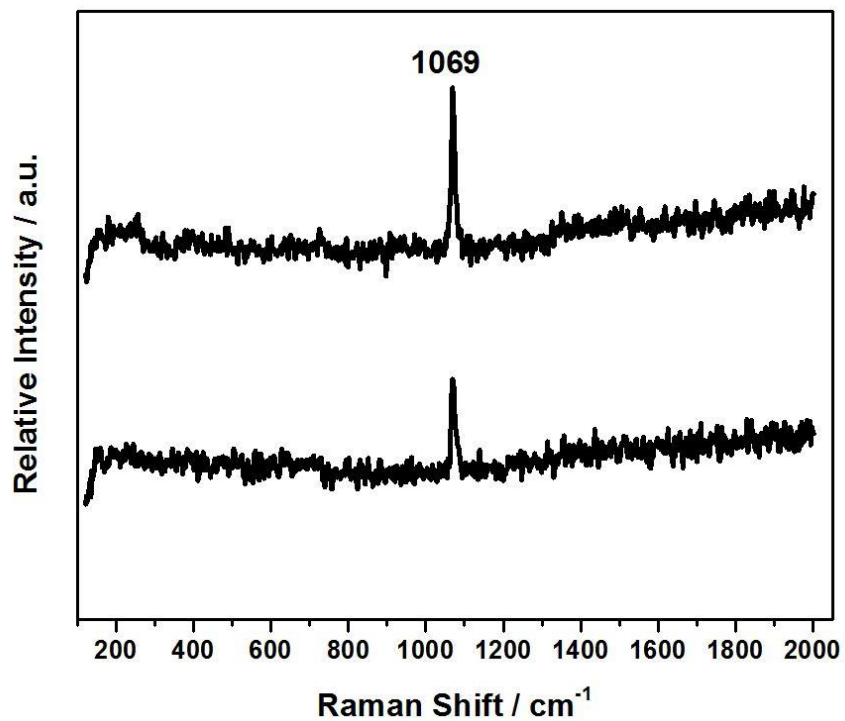


Figure 5-10: Ex-situ Raman spectra recorded on the steel coupon after 60 days of exposure to solution (i) (Table 5-1).

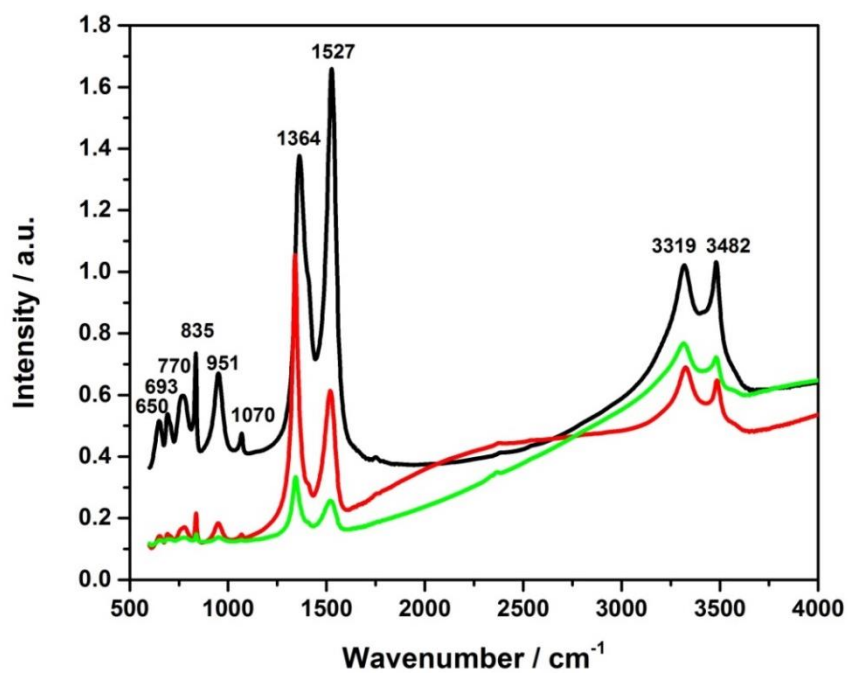


Figure 5-11: Ex-situ FTIR spectra recorded on three locations of the steel after 60 days of exposure to solution (i) (Table 5-1).

Figure 5-12 shows the Raman spectra recorded on the surface exposed to solution (ii) (Table 5-1) for 47 days. Each of the three spectra recorded are featureless with no discernable Raman bands. Figure 5-13(a,d,g) shows the SEM micrographs, recorded at low magnification across the sample surface, confirming the steel has been corroded lightly in a uniform manner across the entire surface, consistent with the slow active corrosion process indicated by the positive E_{CORR} values and higher corrosion rates, compared to solution (i), indicated by the R_p values. Furthermore, the general corrosion morphology confirms that the increase in capacitance over the duration of the exposure period can be attributed to a general roughening of the sample surface caused by active corrosion. The SEM images show a surface which is generally uniformly covered with some areas covered with a very thin layer of crystalline corrosion product. The thin nature of the corrosion product, if one is present, would explain why no Raman bands were seen in Figure 5-12.

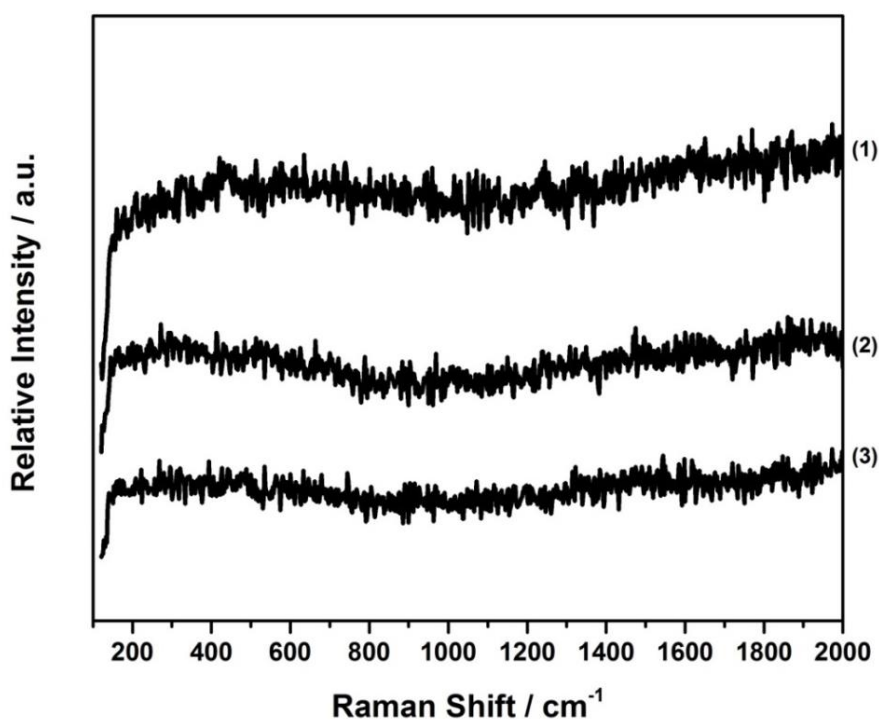


Figure 5-12: Ex-situ Raman spectra (1-3) recorded at various locations on the steel coupon after 47 days of exposure to solution (ii) (Table 5-1).

Figure 5-14 shows the SEM micrographs recorded on the steel surface exposed to solution (iii) (Table 5-1) for 57 days. As observed for carbonate-containing solution (i), several regions of the sample surface were covered with dark patches of corrosion product, Figure 5-14(a), with magnified images, Figure 5-14(b-c), showing a morphology consistent with the presence of $\text{Fe}_2(\text{OH})_2\text{CO}_3$. The Raman spectra, Figure 5-15, and FTIR spectra, Figure 5-16, confirm the presence of $\text{Fe}_2(\text{OH})_2\text{CO}_3$ as observed in solution (i).

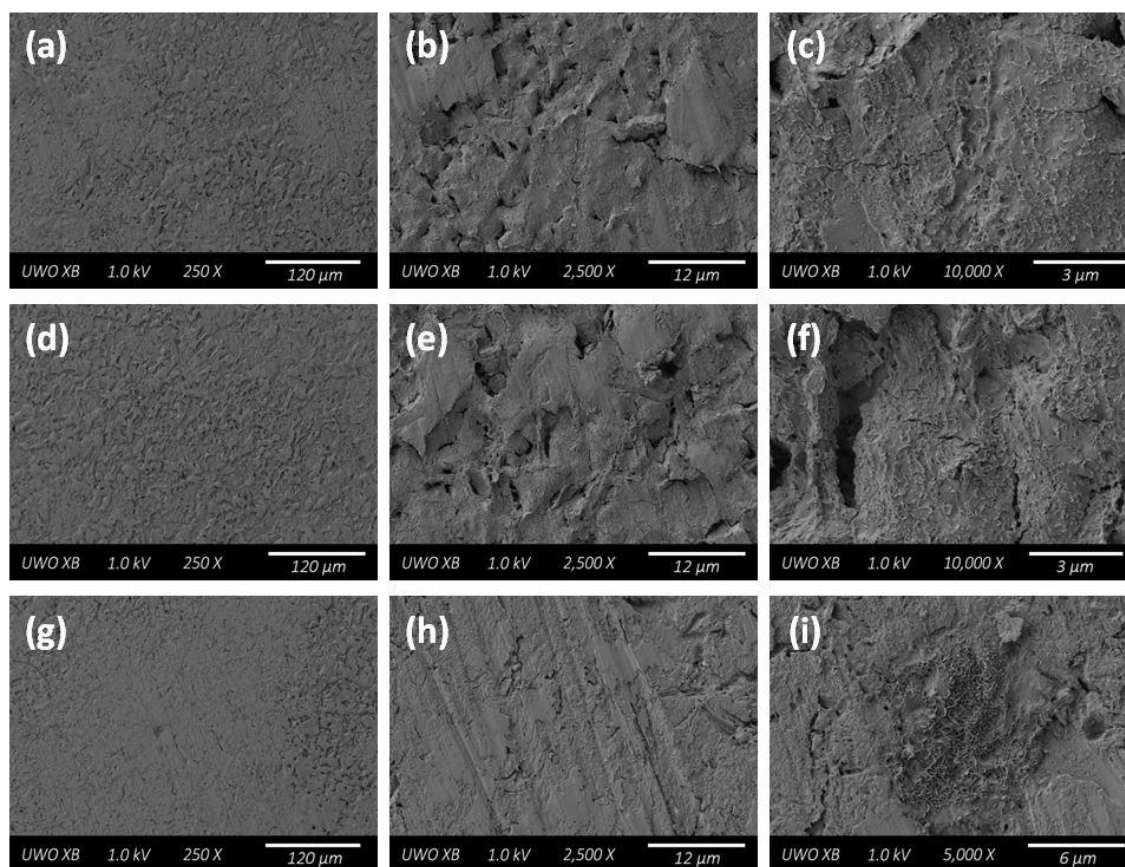


Figure 5-13: SEM micrographs recorded on three locations on the surface after 47 days of exposure to solution (ii) (Table 5-1).

Figure 5-14(d-f) shows that limited amounts of corrosion product are present with areas thinly covered by crystals consistent with the structure of $\text{Fe}_2(\text{OH})_2\text{CO}_3$. Figure 5-14(g-h) shows a location with a corrosion product of different morphology consisting of small clumps of multi-faceted cubic crystals. While there was no evidence for FeCO_3 (siderite) in the Raman or FTIR spectra, this morphology has been associated with siderite. The presence of siderite would not be unexpected at the high $[\text{HCO}_3^-/\text{CO}_3^{2-}]=0.10$ M in this solution. Whether or not the surface is covered with any oxide (presumably Fe_3O_4) is uncertain since this phase is not detected by Raman spectroscopy.

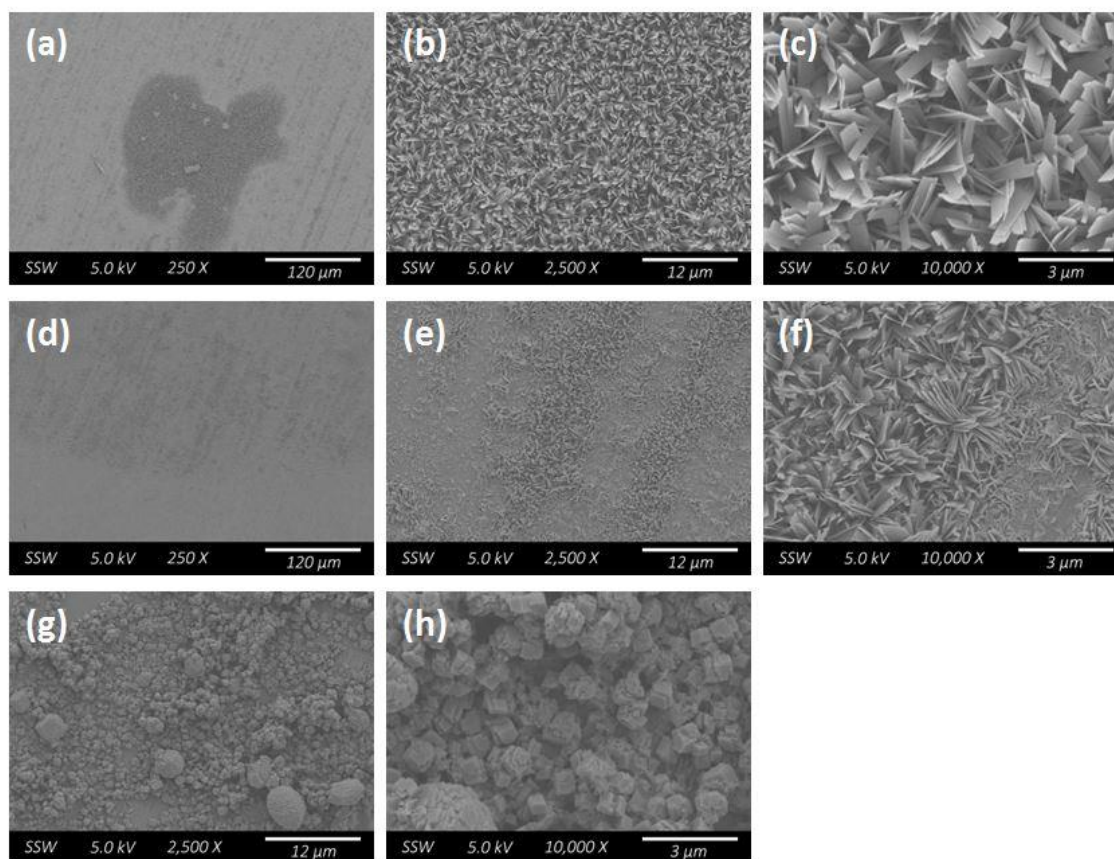


Figure 5-14: SEM micrographs recorded on the steel surface after 57 days of exposure to solution (iii) (Table 5-1) showing: (a-c) a large patch of $\text{Fe}_2(\text{OH})_2\text{CO}_3$; (d-f) the uneven distribution of $\text{Fe}_2(\text{OH})_2\text{CO}_3$ on the steel surface; (g-h) a location covered by small multi-faceted cubic crystals.

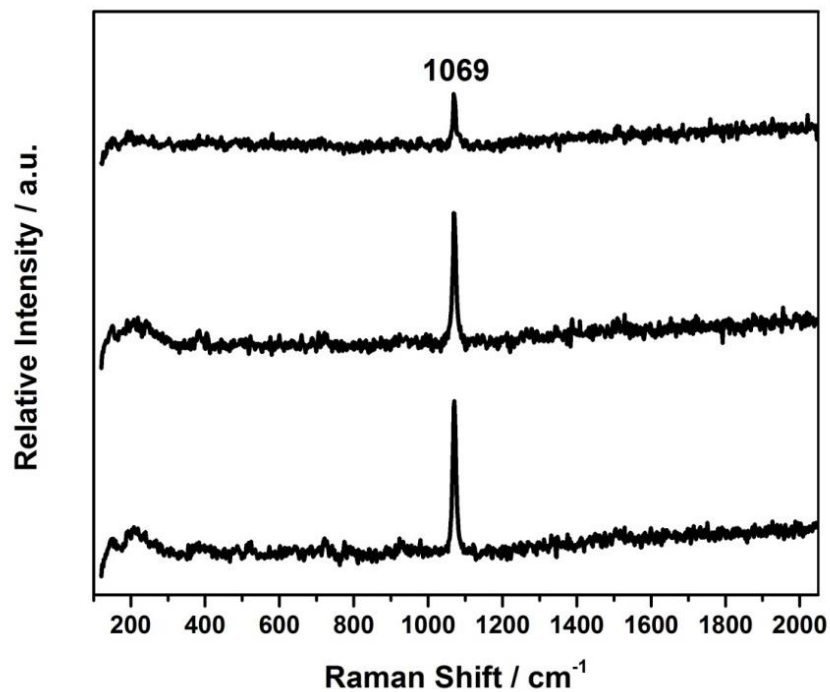


Figure 5-15: Ex-situ Raman spectra recorded on the steel coupon after 57 days of exposure to solution (iii) (Table 5-1).

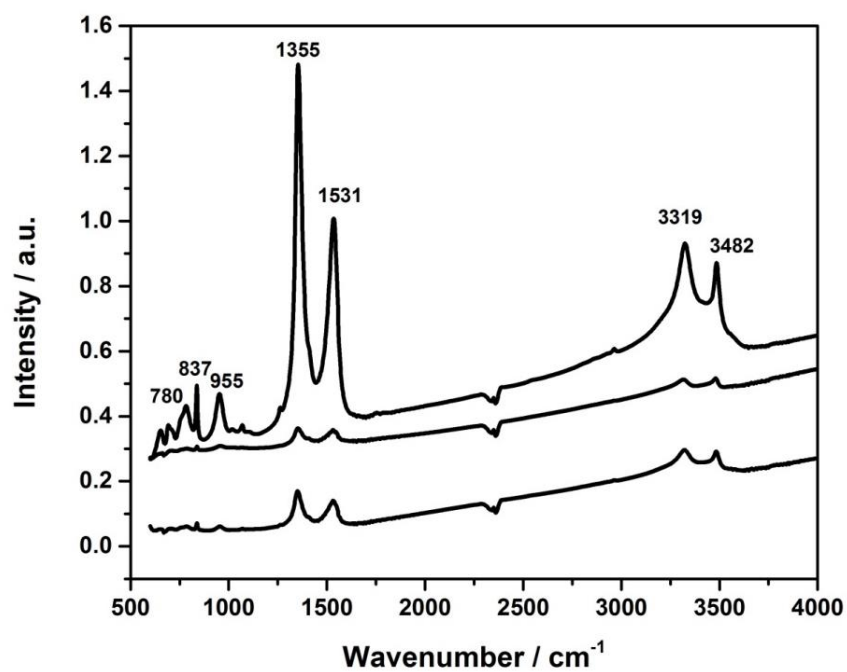


Figure 5-16: Ex-situ FTIR spectra recorded on the steel coupon after 57 days exposure to solution (iii) (Table 5-1).

Figure 5-17 shows the SEM micrographs of the steel surface exposed for 60 days in the simulated groundwater solution (iv) (Table 5-2). Some areas of the surface are covered by loosely adhered crystalline deposits, Figure 5-17(a), while Figure 5-17(b-c) shows the morphology of the underlying surface product. Figure 5-17(d-i) show two additional regions on the surface with denser coverages by crystals but with the same underlying corrosion morphology. Figure 5-17(g) shows a region of the surface extensively covered by a deposit, comprising well-formed disc-shaped or spherical star-shaped crystals, Figure 5-17(h-i).

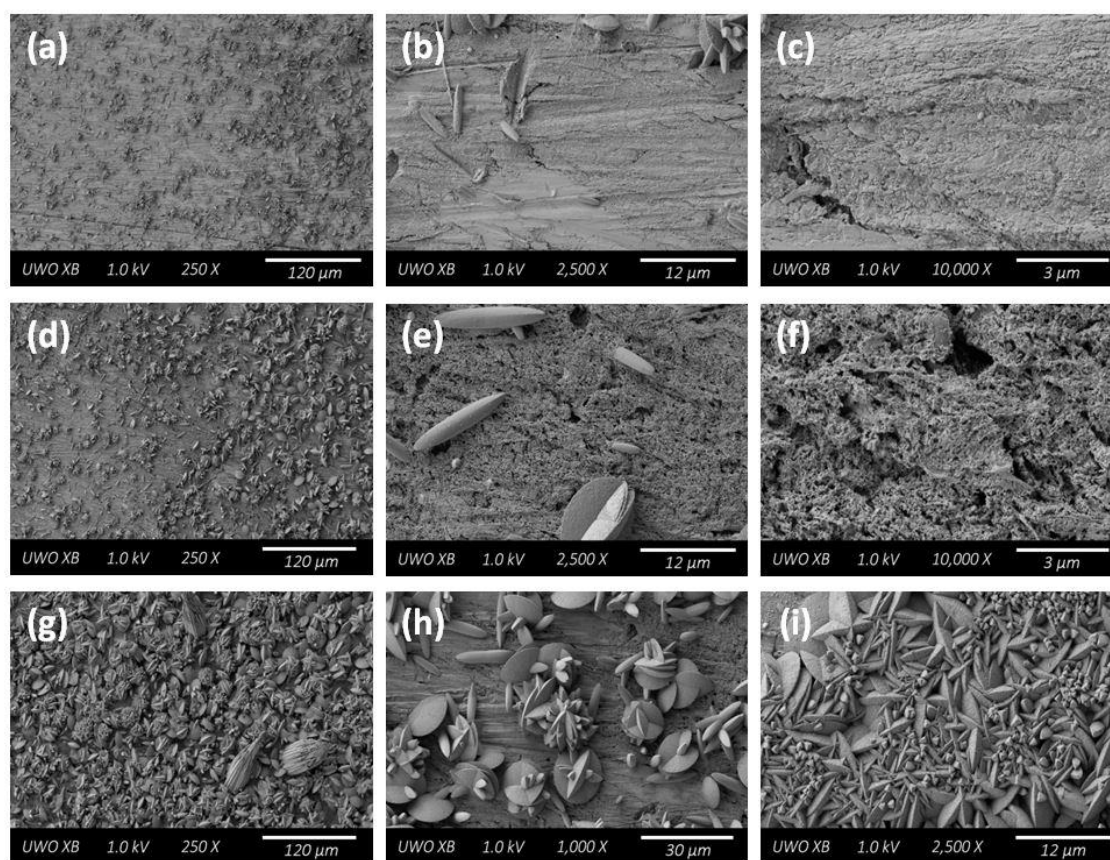


Figure 5-17: SEM micrographs recorded on the steel surface after 60 days of exposure to solution (iv) (Table 5-2) showing: (a-f) two regions on the sample surface with different coverages by deposits but exhibiting the same underlying morphology; (g) a region covered by a more dense crystal layer with the morphology of the disc-shaped and spherical star-shaped crystals shown in (h) and (i).

Figure 5-18 shows Raman spectra recorded on several locations. Spectrum (5) was recorded at a location covered with deposited crystals, identified as vaterite, a rare polymorph of CaCO_3 . Vaterite exhibits either a doublet or triplet for the ν_1 symmetric stretching found between 1073 and 1091 cm^{-1} , with the strongest band at 1091 cm^{-1} [16], whereas aragonite or calcite (the other two polymorphs of CaCO_3) exhibit a single sharp peak at 1085 cm^{-1} [16]. The additional Raman bands in the ν_1 stretching region (1073 - 1091 cm^{-1}) as well as the strength of the band at 1091 cm^{-1} suggests the formation of vaterite. This assignment is confirmed by the doublet at 714 and 753 cm^{-1} which corresponds to the ν_4 in-plane bending mode of the molecular CO_3^{2-} , and the peaks centered around 205 - 371 cm^{-1} which correspond to the translational and rotational lattice modes. It is likely that the crystals begin growing with the disc-like morphology but when growth is particularly rapid, twinning of adjacent crystals occurs leading to the star-shaped crystal structures.

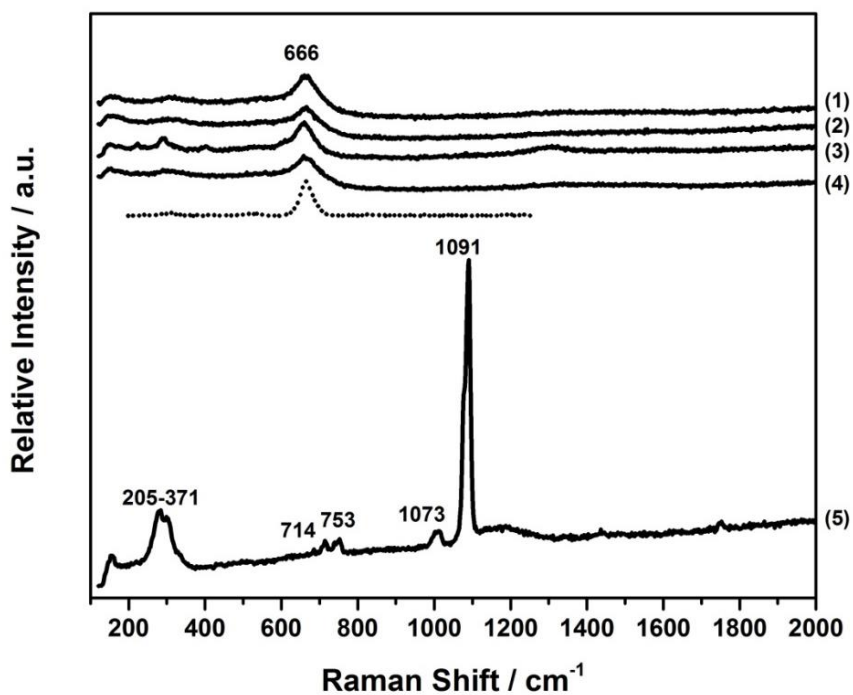


Figure 5-18: Raman spectra (1-5) recorded at various locations on the steel coupon after 60 days of exposure to solution (iv) (Table 5-2). Dotted spectrum represents the reference spectrum of Fe_3O_4 .

The morphology of the surface film underneath the growing vaterite crystals can be seen for two locations in Figure 5-17(b-c) and (e-f). While differing in roughness, the general morphology at each location is the same. Raman spectra (1-4) recorded on such locations, Figure 5-18, show a single band located at 667 cm^{-1} which can be attributed to Fe_3O_4 . It is noteworthy that a Fe_3O_4 film is identifiable after exposure to this solution but not after exposure to solution (ii) (Figure 5-1) which also had a high $[\text{Cl}^-]$ and low pH (6.3 ± 0.5). This may reflect the very positive E_{CORR} observed in solution (iv) which is close to the equilibrium potential, $(E^e)_{\text{Fe}_3\text{O}_4/\text{Fe}}$, at this potential ($\sim -0.700\text{ V}$). It is possible the presence of this surface film accounts for the higher R_p values (lower corrosion rate) measured in the simulated groundwater.

5.4. DISCUSSION

The influence of $[\text{Cl}^-]$ on the corrosion rate is to increase it, with an increase in $[\text{Cl}^-]$ leading to an increase in E_{CORR} accompanied by an increase in corrosion rate (decrease in R_p). At the low $[\text{Cl}^-]$ the morphology of the corroded surface is clearly visible and illustrates the general nature of the corrosion process. The narrow strips outlining the grain features are not likely residual iron carbide along grain boundaries. Magnification of an apparently less corroded grain shows the residual lamellar structure left behind as the $\alpha\text{-Fe}$ is preferentially dissolved from pearlite grains leaving a residue of Fe_3C . The more heavily attacked grains are $\alpha\text{-Fe}$ grains. Clearly if any oxide film is present it is extremely thin. At the high $[\text{Cl}^-]$ the corrosion rate is substantially higher, consistent with the larger and increasing capacitance values which indicate the development of a rougher surface; this is confirmed by the SEM images. In both cases Raman analyses detect no oxide films.

The combination of an increase in E_{CORR} and the corrosion rate at the higher $[\text{Cl}^-]$ indicates that the increase can be attributed to an acceleration of the cathodic reaction. The R_p values show that initially the corrosion rates in the two solutions ((i) $[\text{Cl}^-]=0.10\text{ M}$; (ii) $[\text{Cl}^-]=4.77\text{ M}$) are effectively the same and only deviate for exposure times ≥ 20 days. It is over this period that surface roughness increases markedly at the higher $[\text{Cl}^-]$, but achieves a steady-state at the lower $[\text{Cl}^-]$. The slight decrease in E_{CORR} and accompanying increase in R_p over the exposure period 30 to 60 days suggests a slight suppression of the cathodic kinetics. Presently, the explanation of this effect of Cl^- is uncertain but possibly explained by surface roughening which could lead to a greater exposure of Fe_3C , the most likely location of the cathodic reaction. However, this is not supported by the Raman analyses which show no significant band in the

region 1200 to 1700 cm^{-1} and the SEM images which show a general surface roughening rather than any locations where the residual bands of Fe_3C are clearly visible due to the preferential anodic dissolution of the α -Fe bands within pearlite grains. This is in contrast to bench top experiments (Chapter 4) when traces of O_2 are available when such residues were commonly observed. This suggests that when H_2O is the oxidant the cathodic reaction is more uniformly distributed. By contrast, when O_2 supports corrosion, the Fe_3C strips within the pearlite grains act as preferential cathodes leading to the preferential dissolution of the α -Fe within these grains.

At the lower $[\text{Cl}^-]$ distinct patches of chukanovite ($\text{Fe}_2(\text{OH})_2\text{CO}_3$) are present, consistent with dissolution as Fe^{2+} and re-deposition in the carbonate-containing solution. The distinct separation between the generally corroded surface and the more heavily corroded patches covered with $\text{Fe}_2(\text{OH})_2\text{CO}_3$ suggests the exposed surface is at least partially protected despite an inability to detect any oxide by Raman spectroscopy. At the higher $[\text{Cl}^-]$ similar, but less well defined, patches of crystalline material are observed but Raman does not detect any $\text{Fe}_2(\text{OH})_2\text{CO}_3$. The absence of Fe_3O_4 , or its presence as a thin layer only, would be consistent with the high solubility of Fe^{2+} at $\text{pH} = 6.3$ [17].

While chukanovite ($\text{Fe}_2(\text{OH})_2\text{CO}_3$) is known to form in anoxic environments [5, 18-20], it was unexpected due to the low (0.002213 M) $[\text{HCO}_3^-]$ in comparison to $[\text{Cl}^-]$ in these solutions. The effect of Cl^- not HCO_3^- would be expected to dominate as observed in experiments conducted in the presence of trace O_2 (Chapter 4), in which the formation of $\text{Fe}_2(\text{OH})_2\text{CO}_3$ in high $[\text{Cl}^-]$ solutions was not observed until the $[\text{HCO}_3^-/\text{CO}_3^{2-}]$ reached 0.10 M. This is consistent with reports that at low $[\text{CO}_3^{2-}]$ the main corrosion product expected is Fe_3O_4 with $\text{Fe}_2(\text{OH})_2\text{CO}_3$ becoming the main product in solutions with moderate $[\text{CO}_3^{2-}]$ [21]. Refait et al. [21] showed that the nature of the corrosion products formed in carbonated media is dependent on the interfacial concentration ratios of CO_3^{2-} to Fe^{2+} and OH^- to Fe^{2+} , with the ideal conditions for $\text{Fe}_2(\text{OH})_2\text{CO}_3$ over Fe_3O_4 formation being $[\text{OH}^-]/[\text{Fe}^{2+}]=1$ and $[\text{CO}_3^{2-}]/[\text{Fe}^{2+}]=0.5$.

Since the present experiments were conducted at a pH of 6.3 ± 0.5 two competing phenomena could control the formation of corrosion products on the surface. First, the relatively low pH would be expected to inhibit the formation of $\text{Fe}_2(\text{OH})_2\text{CO}_3$ due to a low $[\text{OH}^-]/[\text{Fe}^{2+}]$ ratio, it being well known that $\text{Fe}_2(\text{OH})_2\text{CO}_3$ generally forms in neutral to slightly alkaline solutions [19, 22-25]. However, at the relatively low pH the solubility of the Fe^{2+} is high and it is possible the

increased interfacial $[\text{Fe}^{2+}]$ led to the solubility product being exceeded allowing $\text{Fe}_2(\text{OH})_2\text{CO}_3$ formation even at such low $[\text{HCO}_3^-]$. This suggests the dominant effect controlling the formation of $\text{Fe}_2(\text{OH})_2\text{CO}_3$ is the $[\text{Fe}^{2+}]$. Several authors have reported that the formation of $\text{Fe}_2(\text{OH})_2\text{CO}_3$ is driven by an excess supply of Fe^{2+} rather than simple precipitation kinetics [5, 12, 19, 22, 23]. In addition, it has been reported that the rate of Fe_3O_4 formation in anoxic solutions is slow, which would also favour $\text{Fe}_2(\text{OH})_2\text{CO}_3$ formation at low $[\text{HCO}_3^-]$ [12].

In the simulated groundwater solution (iv) the increase in both E_{CORR} and R_p over the first 15-20 days suggests the anodic reaction is suppressed, after which the corrosion rate remained constant. By comparison to solution (ii), which has the same $[\text{Cl}^-]$ and $[\text{HCO}_3^-]$, the value of E_{CORR} was more positive and R_p higher, indicating that the additional groundwater ions in solution (iv) influenced the corrosion rate. This suggests that the vaterite (CaCO_3) deposit is at least partially protective. The rapid initial increase in R_p over the first 20 days may reflect the formation of Fe_3O_4 and accumulation of vaterite. While vaterite may be a rare polymorph of CaCO_3 , several authors have claimed that the growth of calcareous corrosion deposits is protective on steel [26-30].

The difference in corrosion behaviour in the pH=8.9 solution (iii) compared to those conducted in the other three solutions clearly demonstrates the important influence of pH. The observation of a lower E_{CORR} is to be expected based on thermodynamics. However, the differences in R_p values indicate a significant difference in corrosion kinetics, the rate being decreased markedly, consistent with the low and constant capacitance values. It has been reported that the corrosion layers formed in carbonated media are passivating in nature which could explain the high R_p values. However, the expected layer of Fe_3O_4 is not detected with Raman and FTIR analyses which showed $\text{Fe}_2(\text{OH})_2\text{CO}_3$ as the only identifiable corrosion product. SEM images confirmed the presence of large amounts of $\text{Fe}_2(\text{OH})_2\text{CO}_3$ forming in non-uniform patches across the surface. Despite this, studies of iron archaeological artefacts show dense layers of Fe_3O_4 tend to form in contact with the metal surface followed by the formation of iron carbonates (FeCO_3 and $\text{Fe}_2(\text{OH})_2\text{CO}_3$) at the Fe_3O_4 /solution interface [18, 22, 31]. Electrochemical studies in simulated soils indicate the presence of a compact and non-porous corrosion product layer at the metal interface most likely responsible for the corrosion kinetics [32-34]. Synchrotron XRD and XPS studies of passive films formed over short durations in neutral to slightly alkaline borate buffer solutions indicate this dense interfacial layer was composed of a

spinel-type iron oxide intermediate in composition between Fe_3O_4 and $\gamma\text{-Fe}_2\text{O}_3$ [33]. Synchrotron STXM studies on an archaeological iron nail exposed to anoxic, carbonated soil for a period of >450 years [34] confirmed the presence of a 100 nm interfacial layer at the metal interface, which X-ray absorption spectra indicated was predominantly composed of a mixture of Fe_3O_4 and $\gamma\text{-Fe}_2\text{O}_3$ in proportions of roughly 1/3 and 2/3 respectively. A thin $\text{Fe}_3\text{O}_4/\gamma\text{-Fe}_2\text{O}_3$ spinel layer in contact with the metal surface has been identified passive [18, 31, 34].

The presence of a thin $\text{Fe}^{\text{II}}/\text{Fe}^{\text{III}}$ spinel oxide at the metal interface combined with the outer $\text{Fe}_2(\text{OH})_2\text{CO}_3$ layer could explain the relatively low resistivities of these corrosion layers observed with macroscopic techniques. The low resistivity of both Fe_3O_4 ($\rho=3 \times 10^{-3} \Omega\text{m}$) and $\gamma\text{-Fe}_2\text{O}_3$ ($\rho=5 \times 10^{-3} \Omega\text{m}$) allows for the formation of a conductive network in what would otherwise be an insulating matrix of carbonates [34]. The constant corrosion rate observed after 10 days can then be attributed to the growth of an interfacial Fe_3O_4 barrier layer. The noise associated with the E_{CORR} and R_p values indicate variations in the kinetics of the anodic reaction suggesting any thin Fe_3O_4 barrier layer present is unstable, and the ensuing Fe^{2+} dissolution could then account for the precipitation or growth of $\text{Fe}_2(\text{OH})_2\text{CO}_3$ [34]. While the outer $\text{Fe}_2(\text{OH})_2\text{CO}_3$ layer may play a role in corrosion protection by slowing the transport of dissolved ions to and from the metal, it has also been shown to be highly porous and cracked which allows water to maintain contact with the metal through a network of micro- and nano-pores leading to a slow and constant corrosion process [18, 34]. This could explain why the sample surface has not yet been completely covered by the $\text{Fe}_2(\text{OH})_2\text{CO}_3$ film even after a period of 60 days exposure.

The results obtained in solution (iii) with a $\text{pH}=8.9$ can be compared to those presented in Chapter 4 for experiments conducted in solutions with the same $[\text{Cl}^-]$, with and without added $\text{HCO}_3^-/\text{CO}_3^{2-}$, and in the presence of traces of dissolved O_2 . In a solution containing only Cl^- , high R_p values (75 to 160 $\text{k}\Omega \text{cm}^2$) were accompanied by E_{CORR} values in the range of -0.75 V to -0.77 V indicating passivation of the steel surface. As a consequence, local film breakdown leading to shallow pitting occurred and the localization of corrosion within these pits lead to low R_p values ($\sim 20 \text{ k}\Omega \text{cm}^2$) providing a sufficient supply of dissolved O_2 was maintained. When $\text{HCO}_3^-/\text{CO}_3^{2-}$ was added, E_{CORR} was significantly reduced and the R_p values remained low (20 to 80 $\text{k}\Omega \text{cm}^2$).

5.5. SUMMARY AND CONCLUSIONS

The effects of $[\text{Cl}^-]$, and $\text{HCO}_3^-/\text{CO}_3^{2-}$ on the corrosion behaviour and corrosion product identity and morphology were investigated. The results were compared to those obtained in a simulated sedimentary groundwater.

The increase in $[\text{Cl}^-]$ caused an increase in the corrosion rate of the steel and a shift from a general and uniform corrosion of the surface at low $[\text{Cl}^-]$ to more aggressive and non-uniform corrosion at high $[\text{Cl}^-]$ leading to an increased roughness of the sample surface. At the higher $[\text{Cl}^-]$ an acceleration of the cathodic kinetics was observed possibly due to the exposure of Fe_3C in the pearlite grains during the roughening of the sample surface, leading to an increased surface area on which the cathodic reaction could occur.

Even in a solution with low $[\text{HCO}_3^-]$ (solution (i)), chukanovite ($\text{Fe}_2(\text{OH})_2\text{CO}_3$) was formed in non-uniform patches on the steel surface. While generally expected to form in slightly alkaline conditions, it was shown that the interfacial $[\text{Fe}^{2+}]$ was most likely the main factor leading to $\text{Fe}_2(\text{OH})_2\text{CO}_3$ deposition. Increased dissolution of the steel led to an increased interfacial $[\text{Fe}^{2+}]$ which was then able to combine with available HCO_3^- in the bulk solution leading to the precipitation of $\text{Fe}_2(\text{OH})_2\text{CO}_3$.

Addition of anticipated groundwater ions for a sedimentary clay environment (solution (iv)) caused an initial suppression of the anodic kinetics followed by a constant corrosion rate. The difference in behaviour between solution (iv) and solution (ii) with comparable $[\text{Cl}^-]$ and $[\text{HCO}_3^-]$ showed that the groundwater ions influence the steel corrosion rate. The initial increase in R_p likely reflects the formation of the Fe_3O_4 film and a deposited layer of vaterite (CaCO_3), the latter offering partial protection to the steel surface.

The addition of 0.10 M $\text{HCO}_3^-/\text{CO}_3^{2-}$ to buffer the pH to 8.85 leads to a significant decrease in corrosion rate. While not observed by Raman spectroscopy, Fe_3O_4 formation would be expected to reduce the corrosion rate while the outer layer of $\text{Fe}_2(\text{OH})_2\text{CO}_3$ observed would provide additional protection of the surface. Growth of such a barrier layer would explain the constant corrosion rate observed after 10 days of exposure. The subsequent noise observed in the E_{CORR} and R_p values is then attributed to the unstable nature of this Fe_3O_4 layer with its dissolution leading to the precipitation of $\text{Fe}_2(\text{OH})_2\text{CO}_3$.

5.6. REFERENCES

- [1] P. Refait, M. Reffass, J. Landoulsi, R. Sabot and M. Jeannin "Role of phosphate species during the formation and transformation of the Fe(II-III) hydroxycarbonate green rust" *Colloids and Surfaces A: Physicochemical and Engineering Aspects* 299 (1-3) **(2007)** 29-37
- [2] M. Saheb, D. Neff, L. Bellot-Gurlet and P. Dillmann "Raman study of a deuterated iron hydroxycarbonate to assess long-term corrosion mechanisms in anoxic soils" *Journal of Raman Spectroscopy* 42 (5) **(2011)** 1100-1108
- [3] R. L. Frost, M. C. Hales and B. J. Reddy "Aurichalcite - An SEM and Raman spectroscopic study" *Polyhedron* 26 (13) **(2007)** 3291-3300
- [4] I. V. Pekov, N. Perchiazzi, S. Merlini, V. N. Kalachev, M. Merlini and A. E. Zadov "Chukanovite, $\text{Fe}_2(\text{CO}_3)(\text{OH})_2$, a new mineral from the weathered iron meteorite Dronino" *European Journal of Mineralogy* 19 **(2007)** 891-898
- [5] C. Remazeilles and P. Refait "Fe(II) hydroxycarbonate $\text{Fe}_2(\text{OH})_2\text{CO}_3$ (Chukanovite) as iron corrosion product: Synthesis and study by Fourier transform infrared spectroscopy" *Polyhedron* 28 (4) **(2009)** 749-756
- [6] C. T. Lee, M. S. Odziemkowski and D. W. Shoesmith "An in situ Raman-electrochemical investigation of carbon steel corrosion in $\text{Na}_2\text{CO}_3/\text{NaHCO}_3$, Na_2SO_4 , and NaCl solutions" *Journal of the Electrochemical Society* 153 (2) **(2006)** B33-B41
- [7] D. de Faria, S. Silva and M. de Oliveira "Raman microspectroscopy of some iron oxides and oxyhydroxides" *Journal of Raman Spectroscopy* 28 (11) **(1997)** 873-878
- [8] D. Neff, P. Dillmann, L. Bellot-Gurlet and G. Beranger "Corrosion of iron archaeological artefacts in soil: Characterisation of the corrosion system" *Corrosion Science* 47 (2) **(2005)** 515-535
- [9] M. S. Odziemkowski, T. T. Schuhmacher, R. W. Gillham and E. J. Reardon "Mechanism of oxide film formation on iron in simulating groundwater solutions: Raman spectroscopic studies" *Corrosion Science* 40 (2-3) **(1998)** 371-389
- [10] M. Hanesch "Raman spectroscopy of iron oxides and (oxy)hydroxides at low laser power and possible applications in environmental magnetic studies" *Geophysical Journal International* 177 (3) **(2009)** 941-948
- [11] D. Neff, S. Reguer, L. Bellot-Gurlet, P. Dillmann and R. Bertholon "Structural characterization of corrosion products on archaeological iron: An integrated analytical approach to establish corrosion forms" *Journal of Raman Spectroscopy* 35 (8-9) **(2004)** 739-745
- [12] S. Savoye, L. Legrand, G. Sagon, S. Lecomte, A. Chausse, R. Messina and P. Toulhoat "Experimental investigations on iron corrosion products formed in bicarbonate/carbonate containing solutions at 90 degrees C" *Corrosion Science* 43 (11) **(2001)** 2049-2064
- [13] K. Yazdanfar, X. Zhang, P. G. Keech, D. W. Shoesmith and J. C. Wren "Film conversion and breakdown processes on carbon steel in the presence of halides" *Corrosion Science* 52 (4) **(2010)** 1297-1304
- [14] I. Chamritski and G. Burns "Infrared- and Raman-active phonons of magnetite, maghemite, and hematite: A computer simulation and spectroscopic study" *Journal of Physical Chemistry B* 109 (11) **(2005)** 4965-4968
- [15] L. J. Simpson and C. A. Melendres "Surface-enhanced Raman spectroelectrochemical studies of corrosion films on iron in aqueous carbonate solution" *Journal of the Electrochemical Society* 143 (7) **(1996)** 2146-2152

- [16] U. Wehrmeister, A. L. Soldati, D. E. Jacob, T. Hager and W. Hofmeister "Raman spectroscopy of synthetic, geological and biological vaterite: A Raman spectroscopic study" *Journal of Raman Spectroscopy* 41 (2) (2010) 193-201
- [17] M. Stratmann, K. Bohnenkamp and H. J. Engell "An electrochemical study of phase-transitions in rust layers" *Corrosion Science* 23 (9) (1983) 969-985
- [18] M. Saheb, P. Berger, L. Raimbault, D. Neff and P. Dillmann "Investigation of iron long-term corrosion mechanisms in anoxic media using deuterium tracing" *Journal of Nuclear Materials* 423 (1-3) (2012) 61-66
- [19] I. Azoulay, C. Remazeilles and P. Refait "Determination of standard Gibbs free energy of formation of chukanovite and Pourbaix diagrams of iron in carbonated media" *Corrosion Science* 58 (2012) 229-236
- [20] I. Azoulay, C. Remazeilles and P. Refait "Corrosion of steel in carbonated media: The oxidation processes of chukanovite ($\text{Fe}_2(\text{OH})_2\text{CO}_3$)" *Corrosion Science* 85 (2014) 101-108
- [21] P. Refait, J. A. Bourdoiseau, M. Jeannin, D. D. Nguyen, A. Romaine and R. Sabot "Electrochemical formation of carbonated corrosion products on carbon steel in deaerated solutions" *Electrochimica Acta* 79 (2012) 210-217
- [22] M. L. Schlegel, C. Bataillon, C. Blanc, D. Pret and E. Foy "Anodic activation of iron corrosion in clay media under water-saturated conditions at 90 degrees C: Characterization of the corrosion interface" *Environmental Science & Technology* 44 (4) (2010) 1503-1508
- [23] V. Pandarinathan, K. Lepkova and W. van Bronswijk "Chukanovite ($\text{Fe}_2(\text{OH})_2\text{CO}_3$) identified as a corrosion product at sand-deposited carbon steel in CO_2 -saturated brine" *Corrosion Science* 85 (2014) 26-32
- [24] M. L. Schlegel, C. Bataillon, F. Brucker, C. Blanc, D. Pret, E. Foy and M. Chorro "Corrosion of metal iron in contact with anoxic clay at 90 degrees C: Characterization of the corrosion products after two years of interaction" *Applied Geochemistry* 51 (2014) 1-14
- [25] M. Ko, B. Ingham, N. Laycock and D. E. Williams "In situ synchrotron X-ray diffraction study of the effect of microstructure and boundary layer conditions on CO_2 corrosion of pipeline steels" *Corrosion Science* 90 (2015) 192-201
- [26] Y. Ben Amor, L. Bouselmi, B. Tribollet and E. Triki "Study of the effect of magnesium concentration on the deposit of allotropic forms of calcium carbonate and related carbon steel interface behavior" *Electrochimica Acta* 55 (16) (2010) 4820-4826
- [27] F. G. Liu, S. R. Wu and C. S. Lu "Characterisation of calcareous deposits on freely corroding low carbon steel in artificial sea water" *Corrosion Engineering Science and Technology* 46 (5) (2011) 611-617
- [28] J. Marin-Cruz, R. Cabrera-Sierra, M. A. Pech-Canul and I. Gonzalez "Characterization of different allotropic forms of calcium carbonate scales on carbon steel by electrochemical impedance spectroscopy" *Journal of Applied Electrochemistry* 34 (3) (2004) 337-343
- [29] H. Moller "The influence of Mg^{2+} on the formation of calcareous deposits on a freely corroding low carbon steel in seawater" *Corrosion Science* 49 (4) (2007) 1992-2001
- [30] G. S. Vasyliiev, Y. S. Gerasimenko, S. K. Poznyak and L. S. Tsybulskaya "A study of the anticorrosion properties of carbonate deposits to protect low-carbon steel from the action of tap water" *Russian Journal of Applied Chemistry* 87 (4) (2014) 450-455
- [31] A. Romaine, R. Sabot, M. Jeannin, S. Necib and P. Refait "Electrochemical synthesis and characterization of corrosion products on carbon steel under argillite layers in carbonated media at 80 degrees C" *Electrochimica Acta* 114 (2013) 152-158

- [32] C. Bataillon, C. Musy and M. Roy "Corrosion of waste supercontainers - Case of a supercontainer made of weakly alloyed steel" *Journal De Physique Iv* 11 (Pr1) **(2001)** 267-274
- [33] C. Bataillon, F. Bouchon, C. Chainais-Hillairet, C. Desgranges, E. Hoarau, F. Martin, S. Perrin, M. Tupin and J. Talandier "Corrosion modelling of iron based alloy in nuclear waste repository" *Electrochimica Acta* 55 (15) **(2010)** 4451-4467
- [34] A. Michelin, E. Drouet, E. Foy, J. J. Dynes, D. Neff and P. Dillmann "Investigation at the nanometre scale on the corrosion mechanisms of archaeological ferrous artefacts by STXM" *Journal of Analytical Atomic Spectrometry* 28 (1) **(2013)** 59-66

Chapter 6

Long Term Analysis of the Corrosion Product Identities and Morphologies Formed on A516 Gr70 Carbon Steel Exposed to Anoxic Simulated Groundwater Environments

6.1. INTRODUCTION

While electrochemical monitoring of steel coupons exposed to simulated groundwater solutions may provide some insight into the corrosion behaviour of steel waste containers (Chapters 4 and 5), there are limitations to the length of such experiments. As such, the experiments described in this chapter were designed to follow the corrosion process over an extended period of time, up to 30 months. The experiments were designed to mimic the conditions expected in a DGR environment, although the bentonite backfill material was not included. Experiments were conducted under anaerobic conditions in solutions which varied in $[Cl^-]$ and pH and in a simulated groundwater solution for exposure periods up to 30 months. Specimens were exposed to an initial period of air exposure prior to emplacement in the solutions to simulate the initial state of the container when first emplaced. Samples removed from experiments were analyzed using techniques such as Raman spectroscopy, FTIR spectroscopy, scanning electron microscopy and focused ion beam milling.

6.2. EXPERIMENTAL DETAILS

6.2.1. Materials and Electrode Preparations

A total of 64 steel coupons were fabricated using A516 Gr70 carbon steel (0.23 C; 1.11 Mn; 0.07 P; 0.03 S; 0.26 Si; 0.01 Cu; 0.01 Ni; 0.02 Cr; 0.004 Mo; 0.036 Al; 0.019 V; 0.003 O [wt.%], balance Fe). Each coupon was cut from a 0.5 cm thick plate with the dimensions 1 cm x 1 cm. Each coupon was polished on all six sides with 180, 600, 800, 1000, and 1200 grit SiC papers (Presi), and then rinsed with methanol and Type 1 water to remove any organic contaminants. Prior to exposure, each coupon was placed on a Teflon sample holder and left exposed to air for a period of one week. This was done to simulate the air formed oxide that would be present when a disposal container is first emplaced in a DGR.

6.2.2. Experimental Setup

Four exposure environments were tested to determine the effects of groundwater composition on the corrosion process, with 16 specimens being exposed to each environment. Steel coupons

were placed in 2 L beakers fitted with an air tight lid. The lids were fabricated from Teflon and fitted with an O-ring seal. A small (1 mm) hole was drilled in the top of the lid to allow any H₂ gas formed during the corrosion process to be vented. Figure 6-1 shows schematics of the sample holder. Sixteen separate sample compartments were machined so that all sides of each coupon would be exposed to the solution. Two small ledges were left to prevent coupons from falling to the bottom of the beaker. The four small, circular, holes drilled into the Teflon plate allowed legs to be added so that the holder was held ~0.5 cm from the bottom of the beaker. Figure 6-2 shows the 16 coupons on the Teflon holder which was placed in a 2 L beaker. This holder was then transferred into an anaerobic chamber, and the solution poured into the beakers which were then sealed with the Teflon lids. The solutions were allowed to adopt the ambient temperature of the anaerobic chamber which fell between 24 and 26°C. Samples were removed periodically over a period of 30 months and analyzed using a series of surface analysis techniques to track the progress of the corrosion process. Table 6-1 lists the removal schedule for the steel coupons from each of the four exposure environments.

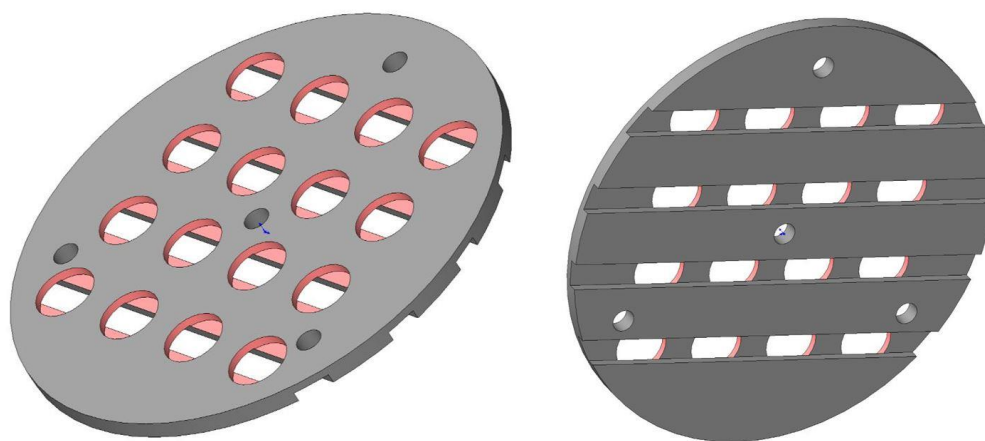


Figure 6-1: Schematic showing the top and bottom views of the Teflon sample holder used to support 16 steel coupons in each of 4 exposure solutions.

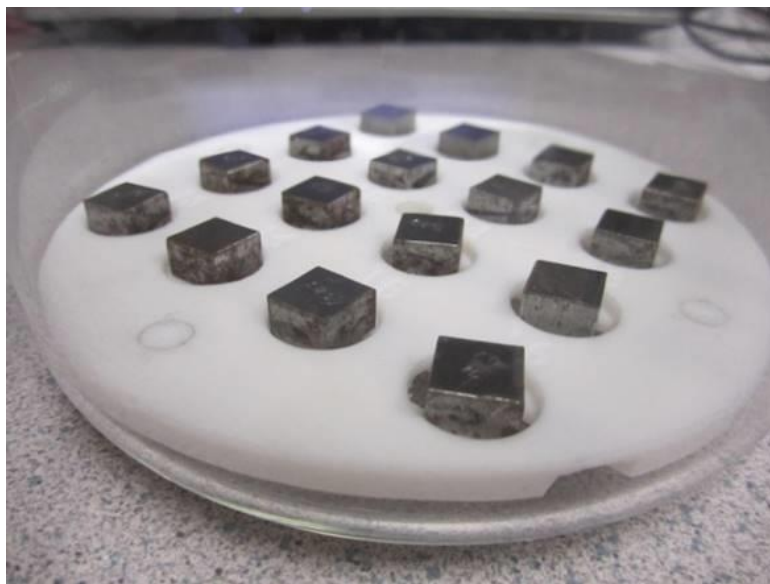


Figure 6-2: Steel coupons emplaced on a Teflon holder which was subsequently placed in a modified 2 L beaker. The coupons shown had not been polished and are shown to demonstrate the experimental set-up.

Table 6-1: Removal times for steel coupons exposed to a series of four exposure environments.

Removal Times	
2 days	4 months
4 days	6 months
1 week	9 months
2 weeks	12 months
4 weeks	18 months
6 weeks	24 months
2 months	30 months

6.2.3. Experimental Solutions

Table 6-2 and Table 6-3 list the chemical compositions of the four solutions. Solutions (i) and (ii) were used to investigate the effects of $[Cl^-]$ while solution (iii) included HCO_3^-/CO_3^{2-} which was shown to have a significant effect on steel corrosion, Chapter 4. Solution (iv) simulated the high ionic concentration of the groundwater anticipated in sedimentary clays. The pH of solutions (i), (ii), and (iv) were set to 6.3 ± 0.5 to mimic that expected in groundwaters at the repository level. The pH of solution (iii) was maintained at its natural level (initially 8.85) set by HCO_3^-/CO_3^{2-} buffering. Type 1 water was deaerated using ultra-high purity Ar gas at a high flow rate for at

least 90 minutes prior to being sealed and transferred to the anaerobic chamber. The flask used for transfer was filled to capacity and sealed with a glass stopper and Parafilm to ensure no trapped air was present in the solution flask during the transfer process. Final preparation of each solution was carried out within the anaerobic chamber. No additional measures were required to maintain the anoxic conditions of each solution.

Table 6-2: Chemical compositions of exposure solutions (i) to (iii).

Exposure Solution	[Cl ⁻] (M)	[HCO ₃ ⁻] (M)	[CO ₃ ²⁻] (M)
(i)	0.10	0.002213	0.00
(ii)	4.77	0.002213	0.00
(iii)	4.77	0.05	0.05

Table 6-3: Chemical composition of solution (iv) made up to simulate sedimentary clay groundwater in the Canadian Shield.

Cation	Concentration (M)	Anion	Concentration (M)
Ca ²⁺	0.811	Br ⁻	0.021
K ⁺	0.320	Cl ⁻	4.758
Mg ²⁺	0.337	HCO ₃ ⁻	0.002
Na ⁺	2.175	SO ₄ ²⁻	0.019
Sr ²⁺	0.014		

6.2.4. Surface Analysis

The corrosion products formed on coupon surfaces were identified using either Raman or infrared spectroscopy. Raman analyses were conducted using a Renishaw 2000 Raman spectrometer equipped with a 632.8 nm laser line and an optical microscope with a 50X magnification objective lens. Collection and manipulation of the spectra, including their deconvolution, was performed using GRAMS 386 Raman software. Prior to deconvolution, each spectrum was baseline corrected using multiple points with the level and zero function of the Raman software. The overlapping peak of interest (representing Fe₃O₄ and γ-Fe₂O₃) was deconvoluted between 550 and 900 cm⁻¹ by fitting the sample spectra to a reference spectrum for γ-Fe₂O₃.

A Bruker-Hyperion 2000 FTIR spectrometer was used under reflectance mode for FTIR analyses. Each spectrum was collected as an average of 32 scans. Gold was used to collect the background

spectrum. The general morphology of the corrosion product was determined using either a Hitachi S-4500 Field Emission SEM or LEO (Zeiss) 1540XB FIB/SEM cross beam system. Cross-sectional analyses were performed using the LEO (Zeiss) 1540XB FIB system equipped with a Ga ion gun to profile and to observe the corroded steel interface.

6.3. RESULTS

The results presented in this chapter are a selection of the data collected for each of the four exposure solutions. All of the Raman and SEM data collected, but not presented in this chapter, can be found in Appendix A.

6.3.1. Solution (i): Low Chloride Concentration

6.3.1.1. Raman Spectroscopy

From the observations in the previous chapters, the Raman spectra can be generally divided into three regions, Figure 6-3, which can aid in the classification of the corrosion products. The characteristic peak for Fe_3O_4 (667 cm^{-1}) is found in region (1) (600 to 800 cm^{-1}), but commonly overlaps with the main peak for the structurally similar $\gamma\text{-Fe}_2\text{O}_3$ (700 cm^{-1} , broad). In this study the combined peak in this region is deconvoluted to determine the individual fractions of these phases present on the corroded surface. Region (2) (200 to 570 cm^{-1}) is generally characteristic of Fe^{III} containing oxides and oxyhydroxides ($\gamma\text{-Fe}_2\text{O}_3$, $\alpha\text{-FeOOH}$, $\gamma\text{-FeOOH}$). When poorly crystalline and/or present simultaneously it is often difficult to distinguish the nature of the phase present by analysis of peaks in this region. Also, bands for GR as well as the t_{2g} and e_{1g} modes of Fe_3O_4 can also be present in this region. Finally, region (3) (1200 to 1700 cm^{-1}) generally contains broad peaks which indicate a more extensively corroded surface, the peaks indicating the presence of carbonaceous residue at corroded pearlite locations. However, $\gamma\text{-Fe}_2\text{O}_3$ can also exhibit broad peaks in this region. In support of this classification, reference spectra for commonly observed oxides and oxyhydroxides are presented in Appendix A.

Figure 6-4(a) through Figure 6-9(a) show the Raman spectra recorded on various surface locations on specimens exposed to solution (i) for increasing periods of time. After exposure for 4 days, the Raman spectra all appear similar with a broad peak centered at 672 cm^{-1} as well as a significant shoulder in the region of 720 cm^{-1} , indicating the presence of both Fe_3O_4 [1-10] and $\gamma\text{-Fe}_2\text{O}_3$ [3, 7, 11, 12]. The presence of $\gamma\text{-Fe}_2\text{O}_3$ could also be responsible for the shallow broad

peaks observed in region (2) (γ -Fe₂O₃, Appendix A) and the broad peak (spectra (4), (6), and (7)) in the region 1300-1660 cm⁻¹ (region (3)) indicating the presence of carbonaceous residue (Fe₃C) on lightly corroded pearlite grains [1, 8].

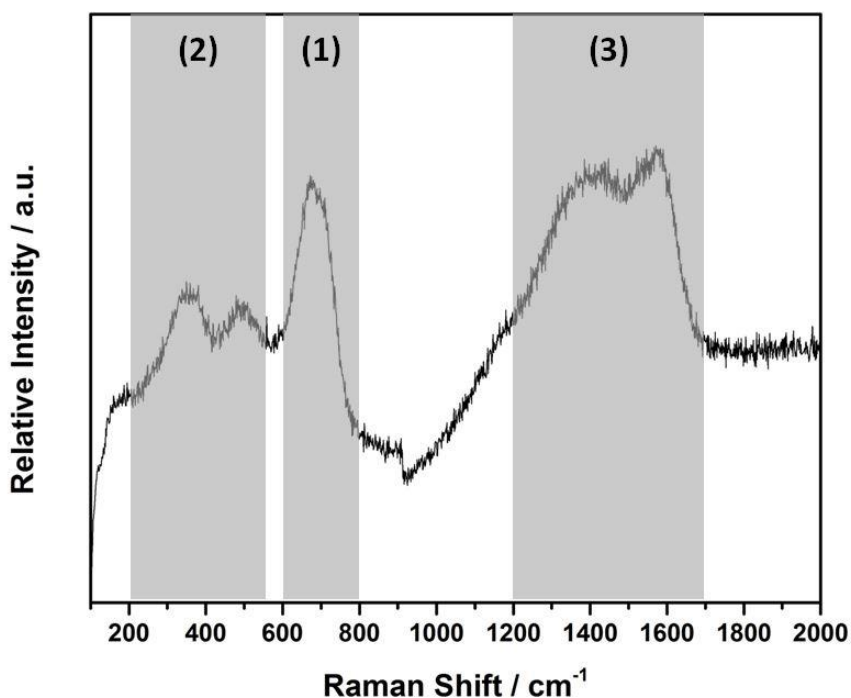


Figure 6-3: Sample Raman spectrum highlighting the three regions in which characteristic features aiding in the identification of corrosion products can be found.

Figure 6-4(b) through Figure 6-9(b) show deconvolutions of the spectra within region (1) (Figure 6-3) into the main contributing peaks for Fe₃O₄ (672 cm⁻¹) and γ -Fe₂O₃ (705 cm⁻¹). However, it should be noted that both Fe₃O₄ and γ -Fe₂O₃ contain bands at these locations. The gray band observed in the deconvolution is an artefact required by the Raman software to obtain an appropriate fit and is not assigned to any Fe oxide or oxyhydroxide species. While several spectra were collected across the specimen surface, only the spectrum closest to the specimen average is shown. The deconvolution was accomplished by fitting the experimental spectra to a reference spectrum for γ -Fe₂O₃ which, like Fe₃O₄, exhibits peaks at both of these locations. The Fe₃O₄ reference peak ratio (Fe₃O₄: γ -Fe₂O₃; 8.2) was obtained by fitting a reference Fe₃O₄ spectrum to the γ -Fe₂O₃ spectrum. From the deconvolution in Figure 6-4(b) it can be seen that the peak area for both Fe₃O₄ and γ -Fe₂O₃ are similar after 4 days of exposure. Such a peak ratio, nearing unity, is indicative of a γ -Fe₂O₃ dominated film.

Over the first 12 months of exposure the spectra appear very similar, Figure 6-4(a) to Figure 6-8(a). While the peak positions remain similar, the deconvoluted spectra, Figure 6-4(b) to Figure 6-8(b), show a subtle progression in which the peak for Fe_3O_4 becomes dominant over time. Some locations ((6), (7) after 14 days; (7), (8) after 252 days) appear more corroded than others with significant peak intensities in region (3) indicating Fe_3C residues on corroded pearlite grains. Following 604 days of exposure substantial changes in the Raman spectra were observed, Figure 6-9. The broad band in region (3) (1200 to 1700 cm^{-1}) is more intense and better defined peaks are observed in region (2), suggesting a more corroded surface which may have Fe^{III} oxide or oxyhydroxides phases present, although Fe_3O_4 can exhibit peaks in region (2). That a slightly more oxidized surface is present is suggested by the prominence of the shoulder on the Fe_3O_4 peak in region (1) when the bands in region (2) and (3) are more developed. While, to our knowledge, no ingress of O_2 occurred over the exposure period from 365 to 604 days, such a change in composition would be explained by the introduction of traces of O_2 causing the oxidation of the outer surface of Fe_3O_4 to the isostructural $\gamma\text{-Fe}_2\text{O}_3$.

To determine the ratio of Fe_3O_4 to $\gamma\text{-Fe}_2\text{O}_3$ the areas under the two peaks separated by deconvolution (as exhibited in Figure 6-4(b) to Figure 6-9(b)) were plotted as a ratio in Figure 6-10. The horizontal dashed lines indicate the ratios expected if only either $\gamma\text{-Fe}_2\text{O}_3$ or Fe_3O_4 were present. The ratio after 4 days of exposure indicates a dominantly $\gamma\text{-Fe}_2\text{O}_3$ film, consistent with the presence of an air-formed oxide. Over the subsequent 14 days of exposure the ratio increases to a value of 3.2 indicating a decrease in $\gamma\text{-Fe}_2\text{O}_3$ and/or an increase in the amount of Fe_3O_4 present on the surface. As shown by a comparison of Figure 6-4 and Figure 6-5, an increase in the area of the Fe_3O_4 peak as well as a decrease in the peak area for the $\gamma\text{-Fe}_2\text{O}_3$ is clear. This change in composition is most likely due to the reductive dissolution of $\gamma\text{-Fe}_2\text{O}_3$ caused by galvanic coupling to the anodically corroding steel leading to Fe_3O_4 . Such a process is consistent with the presence of peaks in region (3) indicative of the presence of some more extensively corroded regions. The area ratio remains constant up to an exposure time of 56 days, Figure 6-10. The error bars associated with the calculated ratio beyond 56 days of exposure become unacceptably large. This could be due either to the difficulty in accurately deconvoluting the spectra or the non-homogeneity of the surface composition. For longer exposure periods (up to 365 days), the area ratio increases to an average value of 5.74 suggesting a clear dominance of Fe_3O_4 . After 365 days the spectra, Figure 6-8(a), no longer show any evidence for carbonaceous residues (assumed to be Fe_3C of pearlite grains) suggesting that

the surface has become completely covered by the Fe_3O_4 corrosion product. Over the subsequent exposure period (365 to 604 days) the ratio appears to increase to the reference value for Fe_3O_4 but the deconvolution process becomes unreliable as indicated by extremely large error bars. This ratio is not considered meaningful and is not shown in Figure 6-10.

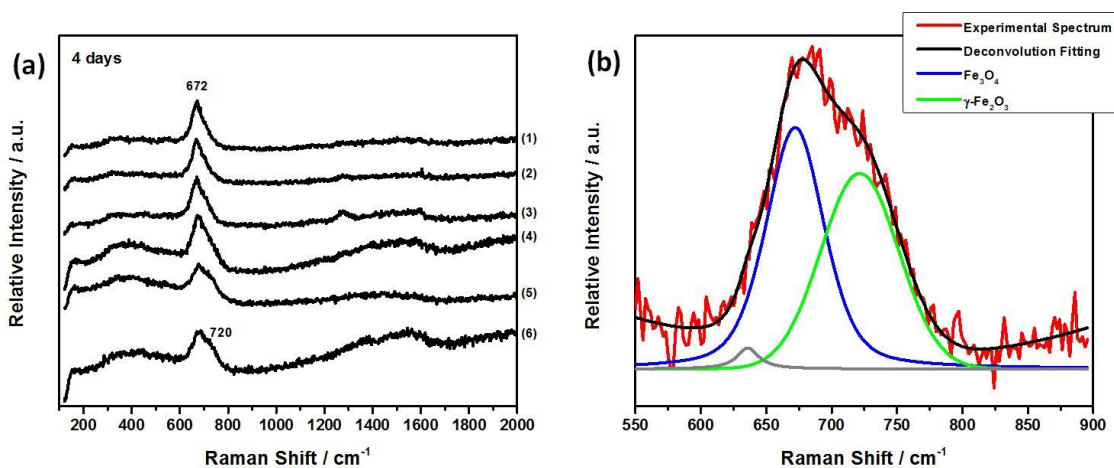


Figure 6-4: (a) Raman spectra (1-6) recorded at various locations on a steel specimen after 4 days of exposure to solution (i); (b) deconvolution of the spectrum closest to the sample average.

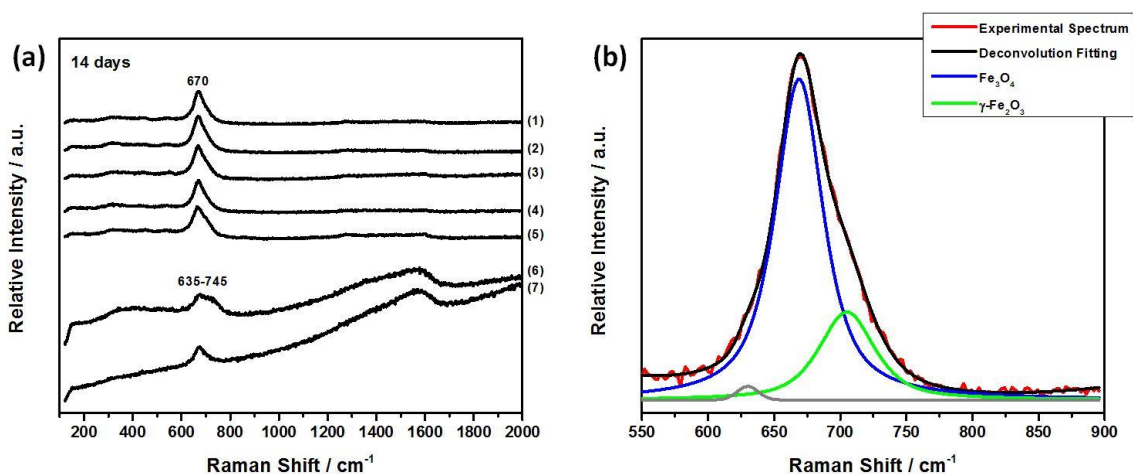


Figure 6-5: (a) Raman spectra (1-7) recorded at various locations on a steel specimen after 14 days of exposure to solution (i); (b) deconvolution of the spectrum closest to the sample average.

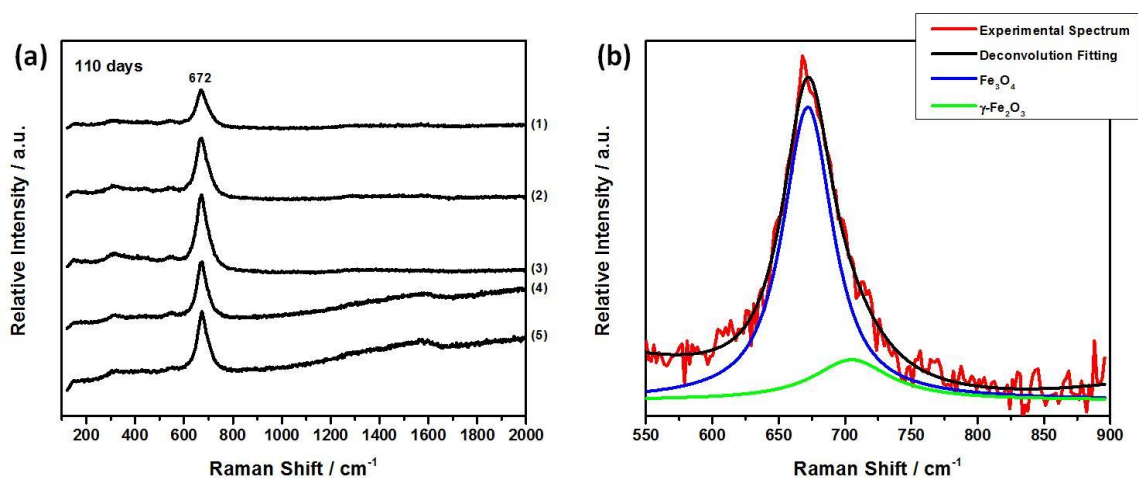


Figure 6-6: (a) Raman spectra (1-5) recorded at various locations on a steel specimen after 110 days exposure to solution (i); (b) deconvolution of the spectrum closest to the sample average.

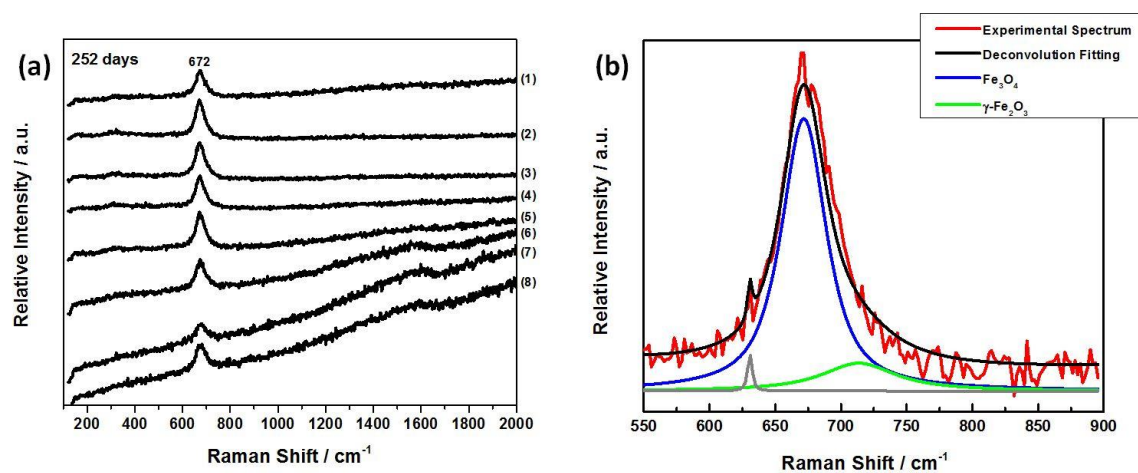


Figure 6-7: (a) Raman spectra (1-8) recorded at various locations on a steel specimen after 252 days exposure to solution (i); (b) deconvolution of the spectrum closest to the sample average.

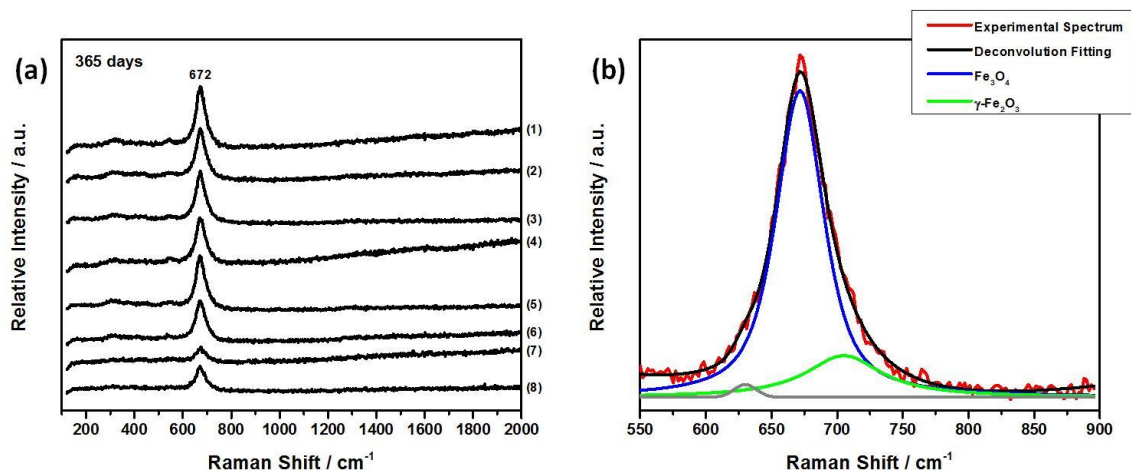


Figure 6-8: (a) Raman spectra (1-8) recorded at various locations on a steel specimen after 365 days exposure to solution (i); (b) deconvolution of the spectrum closest to the sample average.

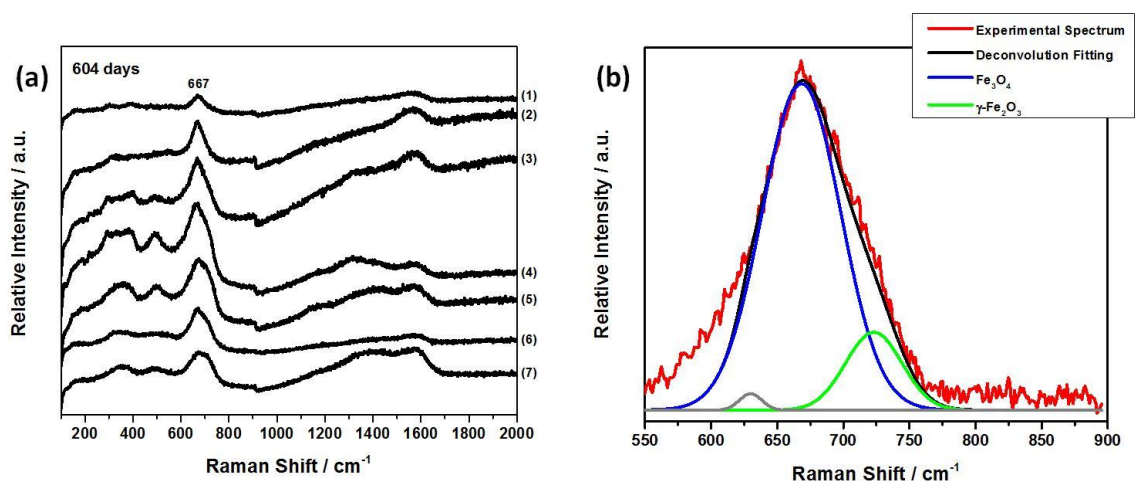


Figure 6-9: (a) Raman spectra (1-7) recorded at various locations on a steel specimen after 604 days exposure to solution (i); (b) deconvolution of the spectrum closest to the sample average.

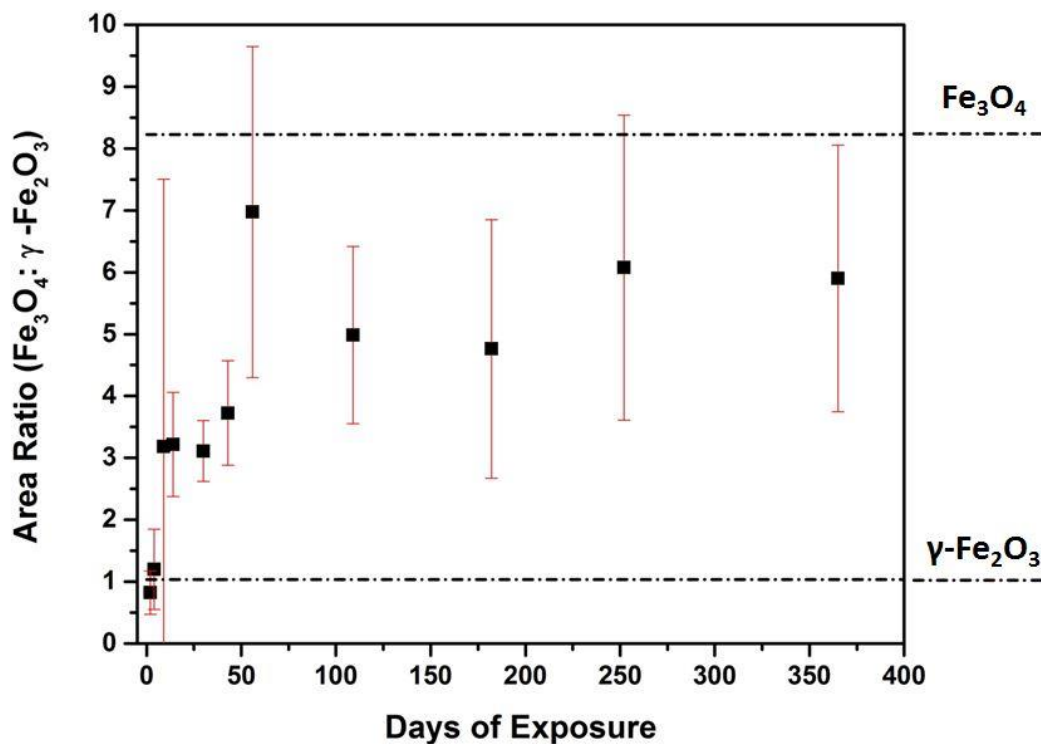


Figure 6-10: Evolution of the area ratio for the Fe_3O_4 (672 cm^{-1}) and $\gamma\text{-Fe}_2\text{O}_3$ (705 cm^{-1}) Raman peaks after exposure to solution (i), calculated from the deconvoluted spectra.

6.3.1.2. Scanning Electron Microscopy

Figure 6-11 shows, that after 4 days of exposure to solution (i), the surface was covered by patches of corrosion products with the distribution possibly reflecting more heavily corroded pearlite grains. Examination of the surface in between these deposits suggests a general roughening as well as the initial stages of Fe_3O_4 formation, Figure 6-11(c), consistent with the onset of an anodic corrosion process. The crystalline platelets comprising the film morphology are consistent with the presence of a Fe^{III} oxide, Figure 6-11(d-i), present due to corrosion in humid air prior to immersion in the solution. This would be consistent with the Raman spectra which showed that the surface film is dominated by $\gamma\text{-Fe}_2\text{O}_3$ with little Fe_3O_4 formed over this short exposure period.

After 14 days of exposure these patches of $\gamma\text{-Fe}_2\text{O}_3$ are less prominent, Figure 6-12. The general morphology of the surface film, Figure 6-12(c) and (f), suggests the crystals have dissolved into

the bulk solution. This is again consistent with the Raman spectra which showed a change in the $\text{Fe}_3\text{O}_4/\gamma\text{-Fe}_2\text{O}_3$ phase ratio in favour of Fe_3O_4 . The area of the surface shown in Figure 6-12(g-i) looks more corroded than the general surface. The general surface morphology is similar to that observed in the short experiments discussed in Chapter 4. The Raman analyses recorded on the specimen exposed for 110 days suggest Fe_3O_4 is the dominant corrosion product, Figure 6-6, while Figure 6-13 shows that the platelets initially present have disappeared. The sample surface appears to be uniformly corroded, Figure 6-13(c) and (f). Higher magnifications, Figure 6-13(h-i), show regions with the layered morphology indicating residual Fe_3C at corroded pearlite locations after preferential dissolution of the $\alpha\text{-Fe}$ in the pearlite grain.

Continued exposure up to 252 days (Figure 6-14) shows little change in the morphology of the damaged surface with a slight increase in the extent of corrosion product build-up, Figure 6-14(c) and (f). Figure 6-14(f) shows preferential corrosion of the pearlite grain structures. Figure 6-14(g) to (i) show some regions of localized damage are present. After 365 days of exposure the morphology of the damaged surface remains the same confirming that, in general, only slow anoxic corrosion is occurring, consistent with the Raman analyses indicating Fe_3O_4 is the dominant corrosion product. After 604 days of exposure the surface is considerably rougher, Figure 6-16(c, f), consistent with the stronger Raman bands (region 3) for carbonaceous residue. Also, the presence of a more ubiquitous deposit suggests some deposition of corrosion product from solution. This is likely to be Fe^{III} oxide or oxyhydroxides since Fe^{2+} would be considerably more soluble than Fe^{3+} at the pH of this solution. It is possible even traces of O_2 in the chamber could account for this and the Raman observations that Fe^{III} oxides are present.

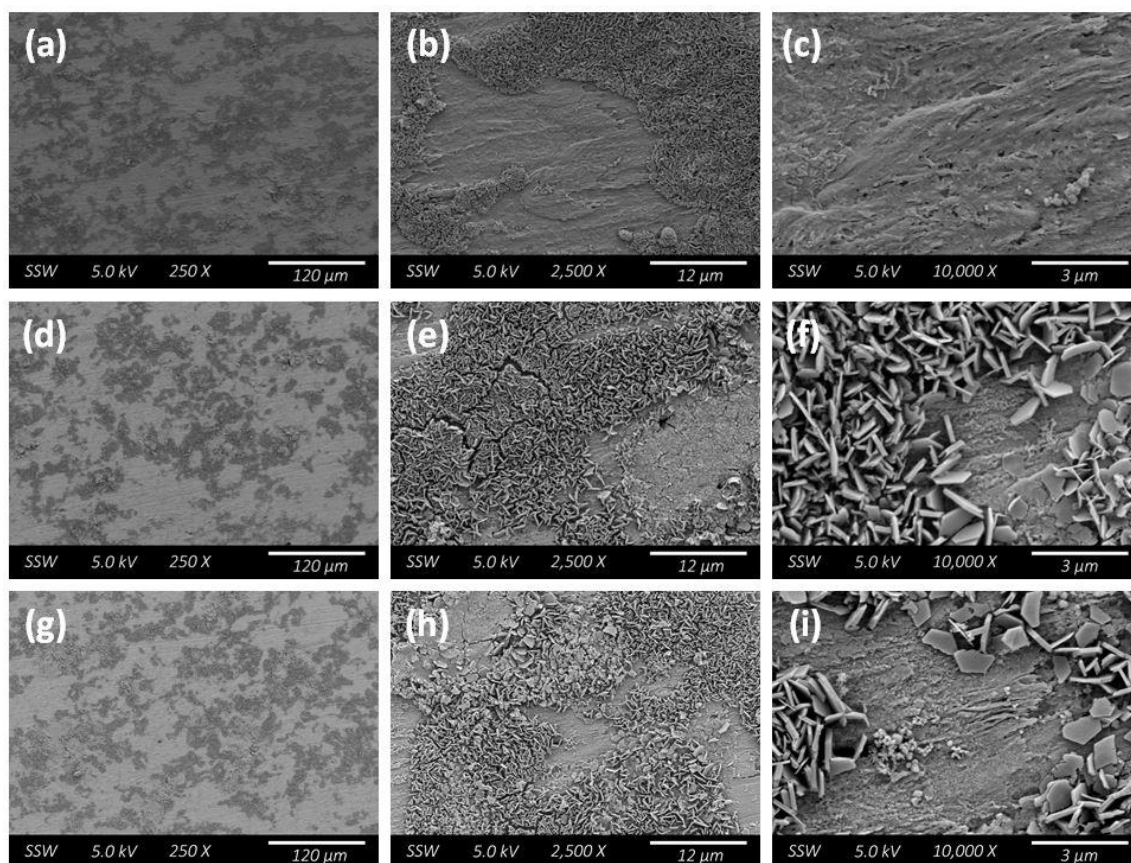


Figure 6-11: SEM micrographs recorded on three locations of a specimen surface (a-c), (d-f), and (g-h) after 4 days of exposure to solution (i) showing the distributions of crystalline $\gamma\text{-Fe}_2\text{O}_3$ and the general surface morphology.

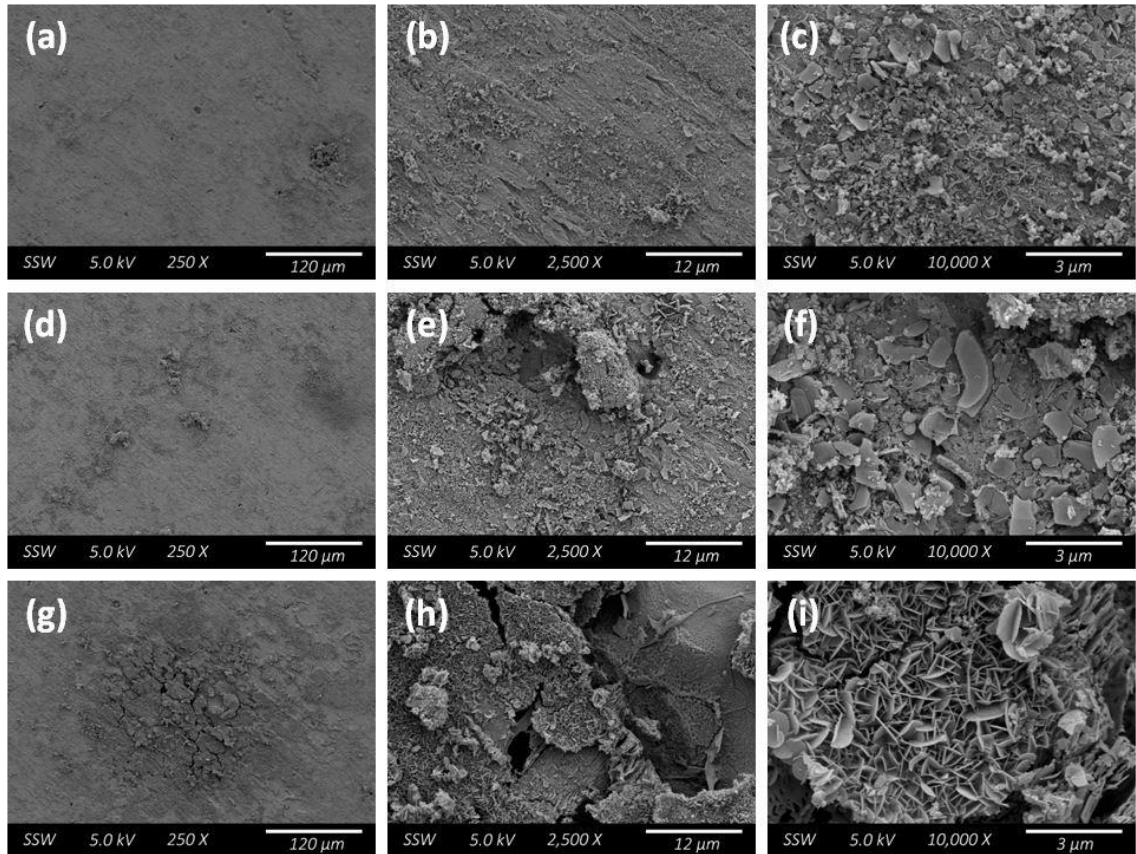


Figure 6-12: SEM micrographs recorded on a specimen surface after 14 days of exposure to solution (i) showing: (a-f) the general surface morphology; (g-i) a region exhibiting a higher degree of corrosion damage.

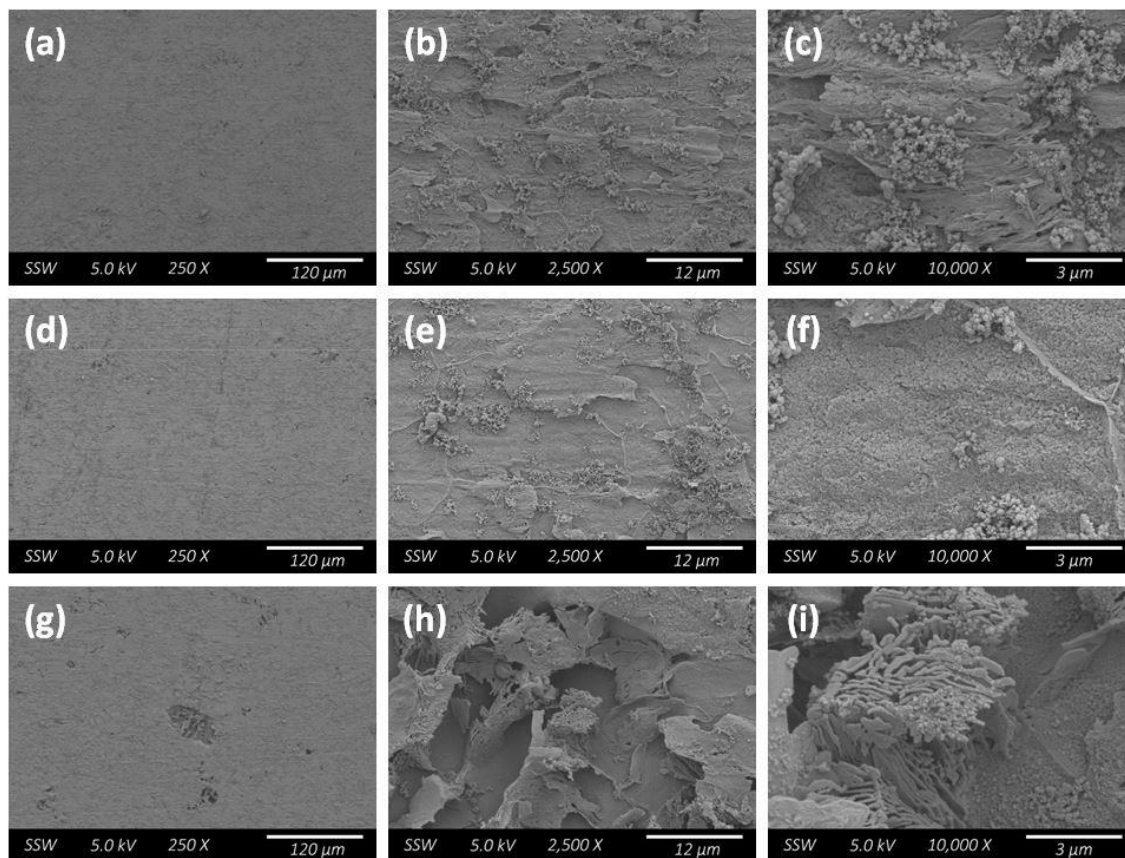


Figure 6-13: SEM micrographs recorded on a specimen surface after 110 days of exposure to solution (i) showing: (a-f) the general surface morphology; (g-i) a layered morphology consistent with the remnants of Fe_3C from ferrite dissolution of pearlite grains.

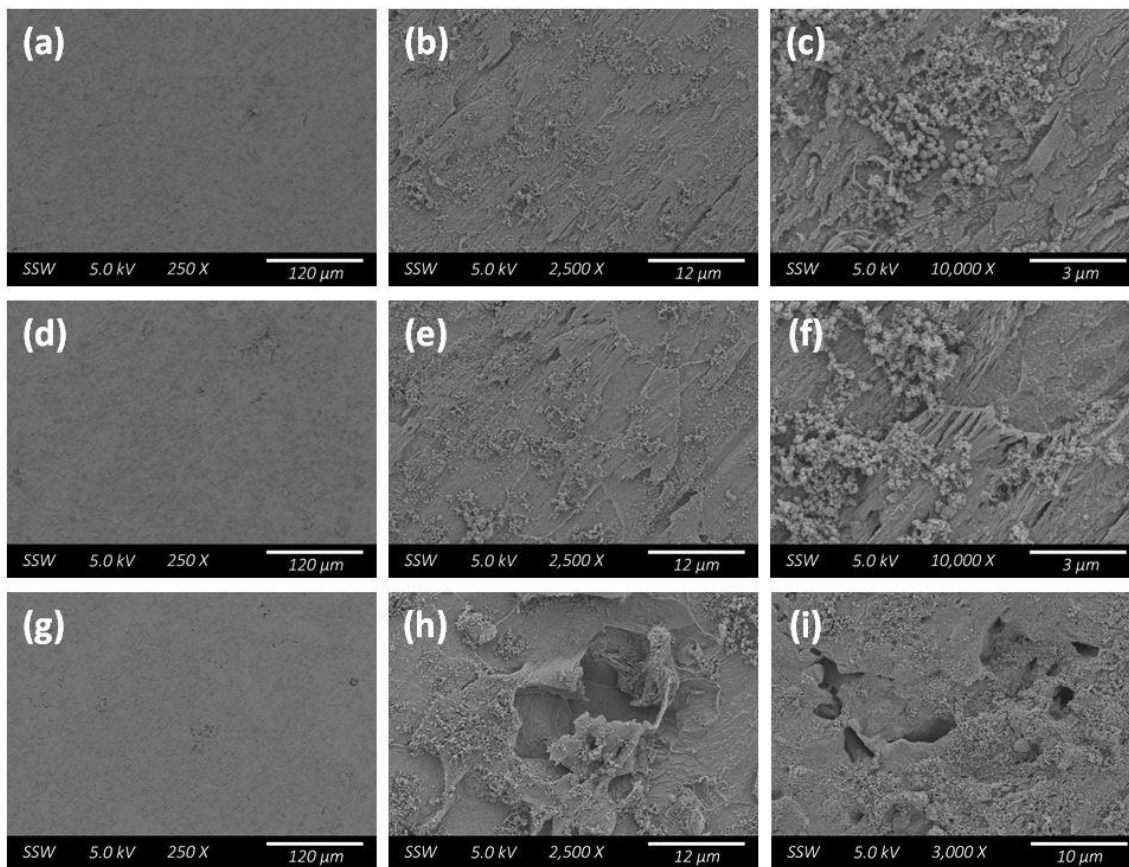


Figure 6-14: SEM micrographs recorded on a specimen surface after 252 days of exposure to solution (i) showing: (a-e) the general surface morphology; (f) the preferential corrosion of ferrite in pearlite grains; (g-i) a region of localized damage.

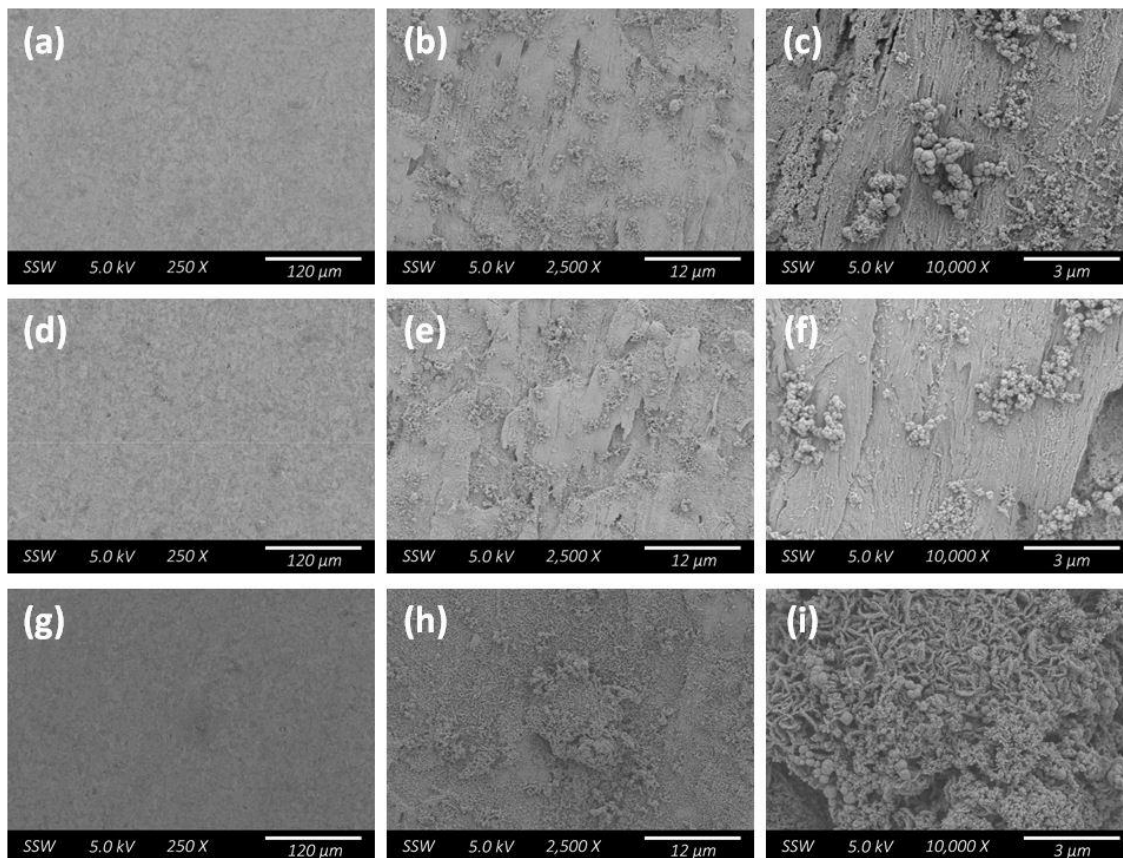


Figure 6-15: SEM micrographs recorded on a specimen surface after 365 days of exposure to solution (i) showing: (a-f) the general surface morphology; (g-i) a region exhibiting a more significant corrosion deposit.

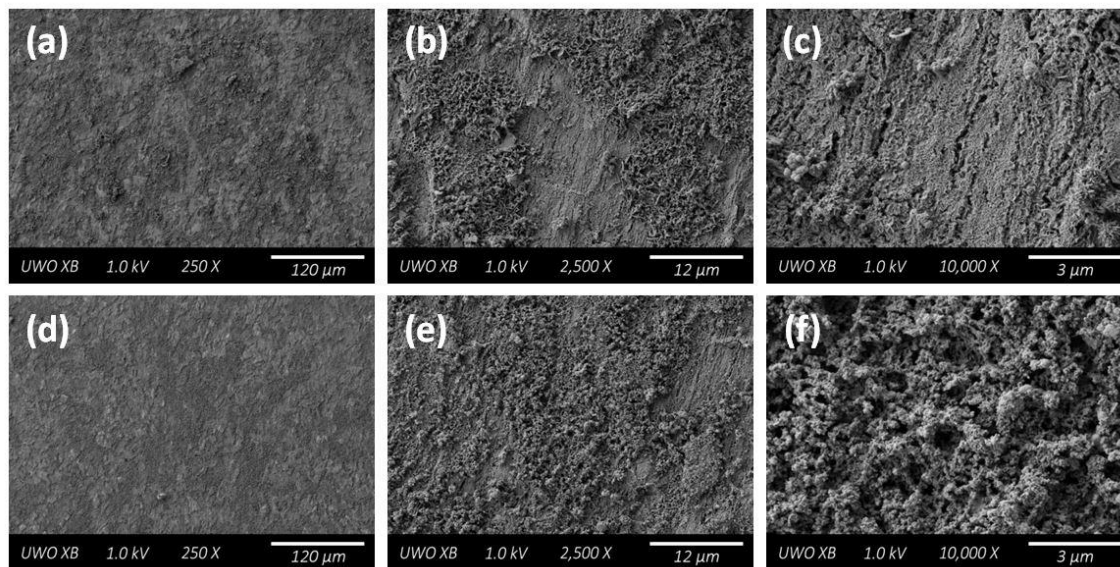


Figure 6-16: SEM micrographs recorded on a specimen surface after 604 days of exposure to solution (i) showing: (a-c) the increased roughening of the specimen surface; (d-f) the increase in corrosion product coverage.

6.3.1.3. *Focused Ion Beam Milling*

Figure 6-17 shows FIB cross-sections for three locations ((a-c), (d-e), and (g-f)) on the specimen exposed to solution (i) for 252 days. The corrosion product is very thin and in some locations porous. Figure 6-17(c) and (f) clearly show the residual Fe_3C bands after corrosion of $\alpha\text{-Fe}$ lamellae bands from pearlite grains. This is particularly obvious in Figure 6-14(f). Even at apparently more heavily corroded locations, penetration of corrosion into the steel is generally uniform. In some locations, Figure 6-17(g-i), corrosion appears to create void space underneath surface oxide layers.

FIB cross-sections taken on the specimen exposed for 540 days show locations, Figure 6-18(a), which appear to have undergone shallow localized corrosion. The backscatter image in Figure 6-18(b) shows the film on the general surface is very thin. Figure 6-18(c) confirms that shallow pitting had occurred at this location. Figure 6-18(d-f) shows the cross-section of a location which appears to have undergone significant localized damage. The backscattered image, Figure 6-18(f), highlights the corrosion product (dark)/base metal (light) interface. In some regions, the damage appears to penetrate more than $10\ \mu\text{m}$ into the base metal. Although confirming evidence is lacking, it is possible these are boundaries between pearlite and $\alpha\text{-Fe}$ grains within which the Fe_3C acts as a local cathode for the anodic dissolution of the adjacent $\alpha\text{-Fe}$.

Figure 6-19 shows the FIB cross-sections for the final sample exposed for 604 days. Even after this extended period, the film on the generally corroded surface remains extremely thin. The deposits are clearly porous and often undermined by corrosion. Figure 6-19(c) shows the preferential dissolution of the $\alpha\text{-Fe}$ from pearlite grains leaving behind the lamellae of Fe_3C . Additionally, the angled crevasse on the left side of this image may be the preferentially corroded boundary between a pearlite and $\alpha\text{-Fe}$ grain. It is possible that Figure 6-19(g-i) shows a cross-section taken at one of the locations similar to that seen in Figure 6-16(g-h). It is likely that the undermining corrosion occurs at $\alpha\text{-Fe}$ /pearlite boundaries and could suggest the cathodic reaction is supported on pearlite grains. The porous nature of the corrosion product is most likely maintained by the formation of H_2 by H_2O reduction at the metal surface.

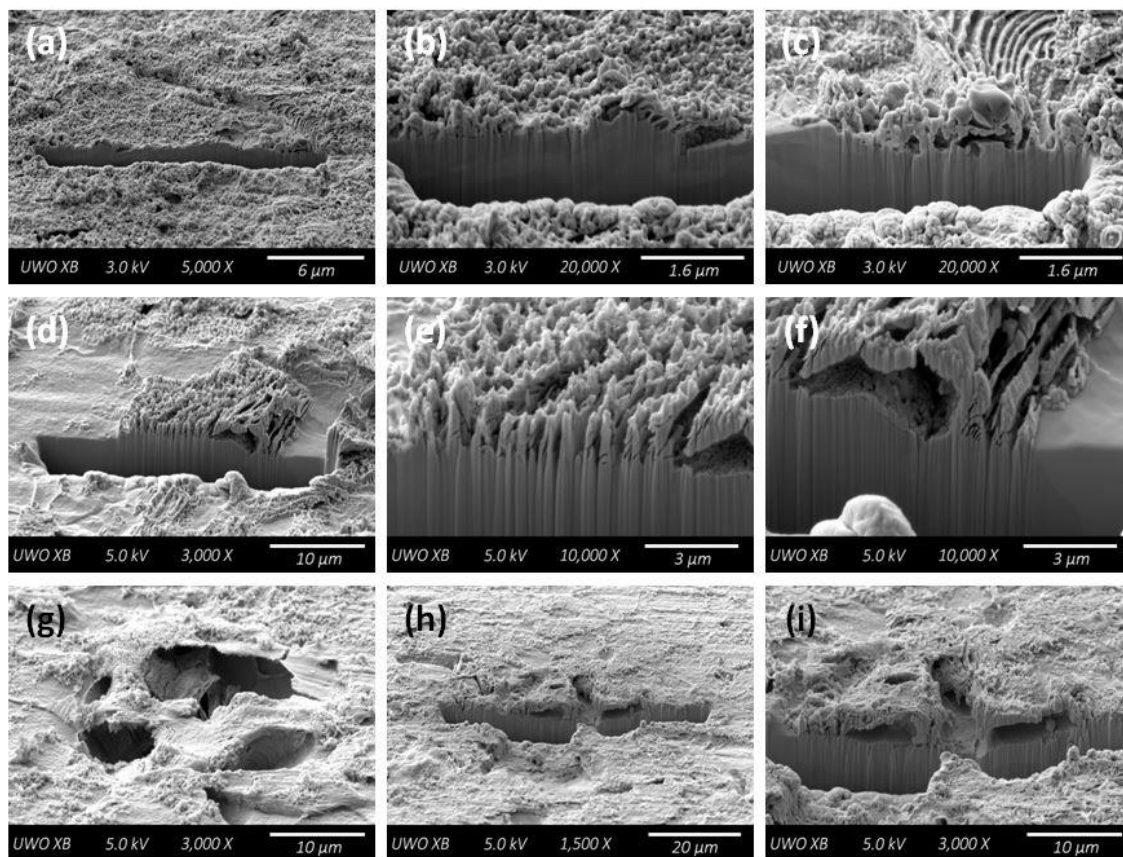


Figure 6-17: FIB cross-section micrographs recorded on a specimen surface after 252 days of exposure to solution (i) showing: (a-b) and (d-e) the thin nature of the corrosion film; (c) and (f) the residual bands of Fe_3C left behind after preferential dissolution of the $\alpha\text{-Fe}$ in the pearlite grains; (g-i) a region exhibiting void spaces created by corrosion under the surface oxide layer.

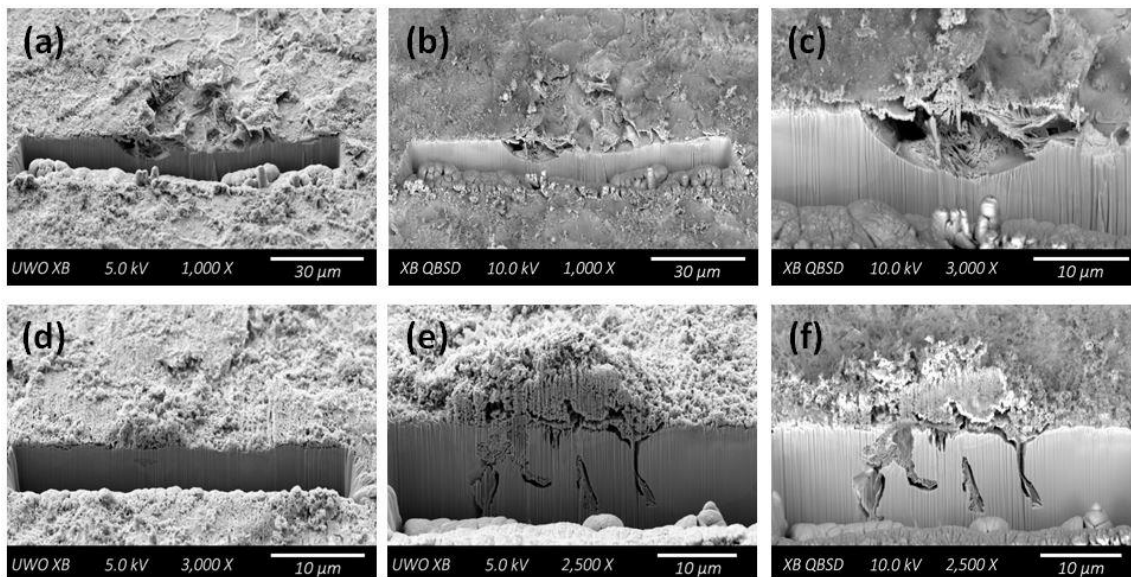


Figure 6-18: FIB cross-section micrographs recorded on a specimen surface after 540 days of exposure to solution (i) showing: (a-b) a region of shallow localized corrosion; (c) the formation of a localized pit; (d-f) a region which has undergone significant localized damage. Backscatter images in (b), (c), and (f) highlight the interface between the base metal (bright) and the oxide film (dark).

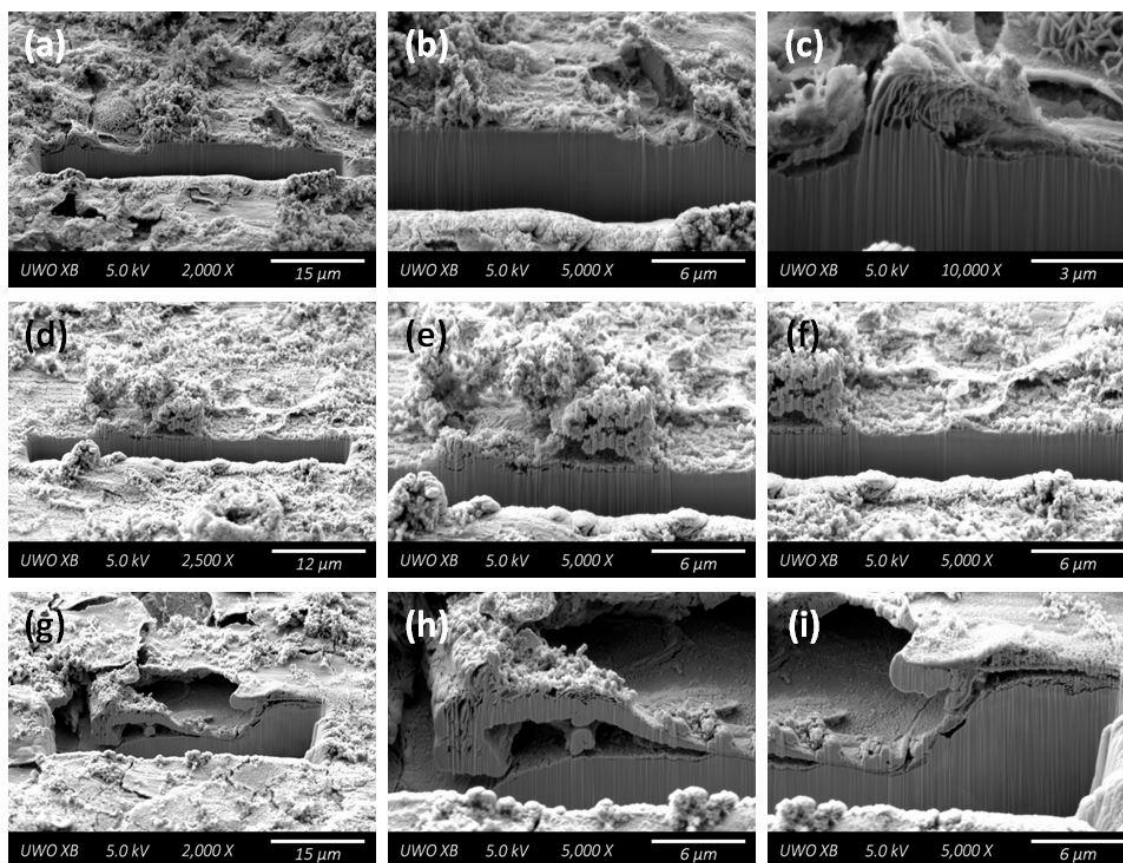


Figure 6-19: FIB cross-section micrographs recorded on a specimen surface after 604 days of exposure to solution (i) showing: (a-f) the thin nature of the corrosion film; (c) lamellae of Fe_3C left after the preferential dissolution of $\alpha\text{-Fe}$ from the pearlite grains; (g-i) a region exhibiting void spaces created by corrosion under the surface oxide layer.

6.3.2. Solution (ii): High Chloride Concentration

6.3.2.1. Raman Spectroscopy

Figure 6-20(a) through Figure 6-25 show the Raman spectra recorded on various locations of the specimens exposed to solution (ii) for increasing periods of time. After 4 days the spectra are similar to those recorded in solution (i) after the same exposure period, Figure 6-20(a). The peak in region (1) (600 to 800 cm^{-1}) indicates the presence of both Fe_3O_4 and $\gamma\text{-Fe}_2\text{O}_3$. When the shoulder at 720 cm^{-1} (indicative of the presence of $\gamma\text{-Fe}_2\text{O}_3$) is prominent in region (1), broad peaks in region (2) confirm the presence of Fe^{III} oxides, in particular $\gamma\text{-Fe}_2\text{O}_3$. In addition, these two features are accompanied by the broad bands in region (3) which indicates sites dominated by $\gamma\text{-Fe}_2\text{O}_3$ are more heavily corroded than those covered by Fe_3O_4 . The deconvolutions of the spectra closest to the sample average are shown in Figure 6-20(b) through Figure 6-24(b), and Figure 6-26 shows the evolution of the peak area ratios over the exposure period. The ratios show that over the first 110 days of exposure, $\gamma\text{-Fe}_2\text{O}_3$ is replaced by Fe_3O_4 , as was seen in solution (i). This is confirmed by the Raman spectra (Figure 6-21) which show a single peak at 672 cm^{-1} combined with the disappearance of the broad peaks in regions (2) and (3), consistent with the reductive dissolution of the $\gamma\text{-Fe}_2\text{O}_3$ coupled to the anodic oxidation of the steel (to Fe^{2+} and Fe_3O_4) as proposed for the early exposure period in solution (i).

After a period of 182 days, an unscheduled power outage caused a failure of the anaerobic chamber and a subsequent influx of O_2 into the sample environment. Comparison of the Raman spectra in Figure 6-21(a) and Figure 6-22(a) (i.e., for exposure periods not including and including the O_2 influx) shows the reformation of $\gamma\text{-Fe}_2\text{O}_3$ indicated by the shoulder in region (1) and the reintroduction of broad peaks in regions (2) and (3). This is confirmed by the observed decrease in the Raman peak area ratio recorded on specimens extracted immediately after the O_2 incursion. After 548 days however, the dominant phase is again Fe_3O_4 with the bands in regions (2) and (3), indicating a more heavily corroded surface, absent, Figure 6-23. This indicates that the O_2 incursion produced Fe^{III} oxides which were subsequently cathodically reduced by coupling to Fe dissolution and Fe_3O_4 formation. After 716 days the Raman features in regions (2) and (3) indicating the presence of Fe^{III} species are again present, suggesting a possible second O_2 incursion, Figure 6-24. Figure 6-25 shows the Raman spectra recorded after the full exposure period of 910 days. The peak in region (1) is at 672 cm^{-1} and there is no indication of a shoulder suggesting the presence of $\gamma\text{-Fe}_2\text{O}_3$. In addition, two of the three shallow

peaks in region 200 to 600 cm^{-1} can be attributed to Fe_3O_4 since the bands for Fe_3C in region (3) are no longer visible. The third minor peak is not attributable to any iron oxide or oxyhydroxide. These spectra indicate the surface is comprehensively covered by Fe_3O_4 .

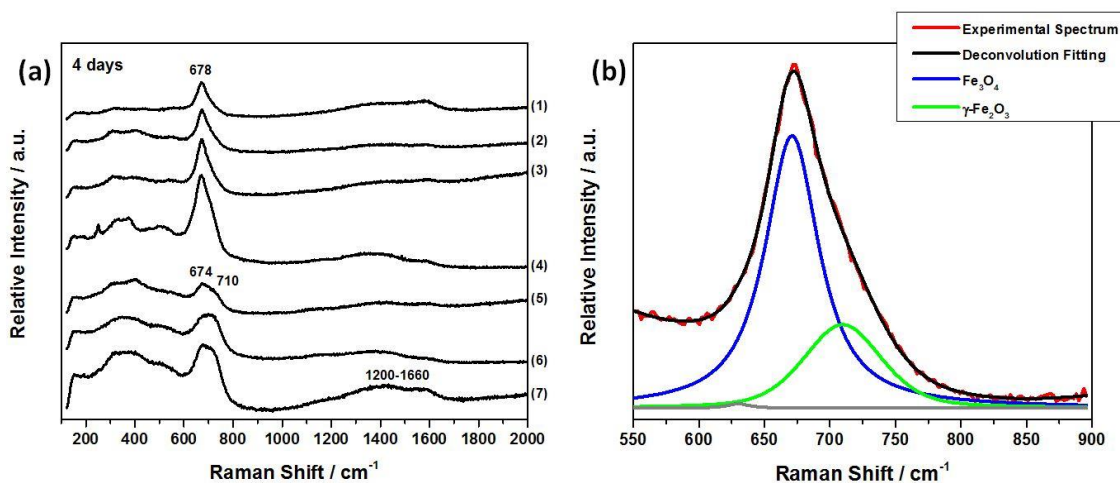


Figure 6-20: (a) Raman spectra (1-7) recorded at various locations on a steel specimen after 4 days exposure to solution (ii); (b) deconvolution of the spectrum closest to the sample average.

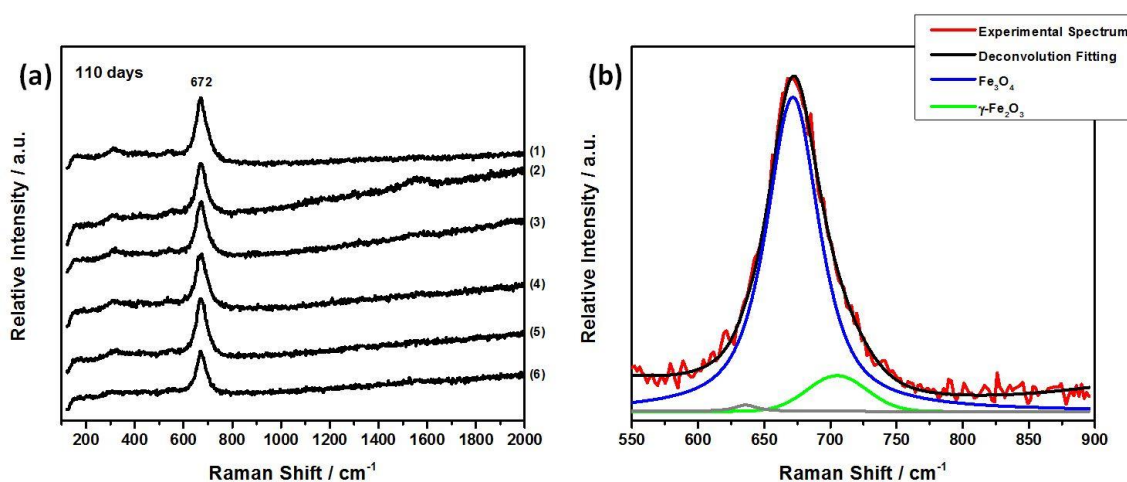


Figure 6-21: (a) Raman spectra (1-6) recorded at various locations on a steel specimen after 110 days exposure to solution (ii); (b) deconvolution of the spectrum closest to the sample average.

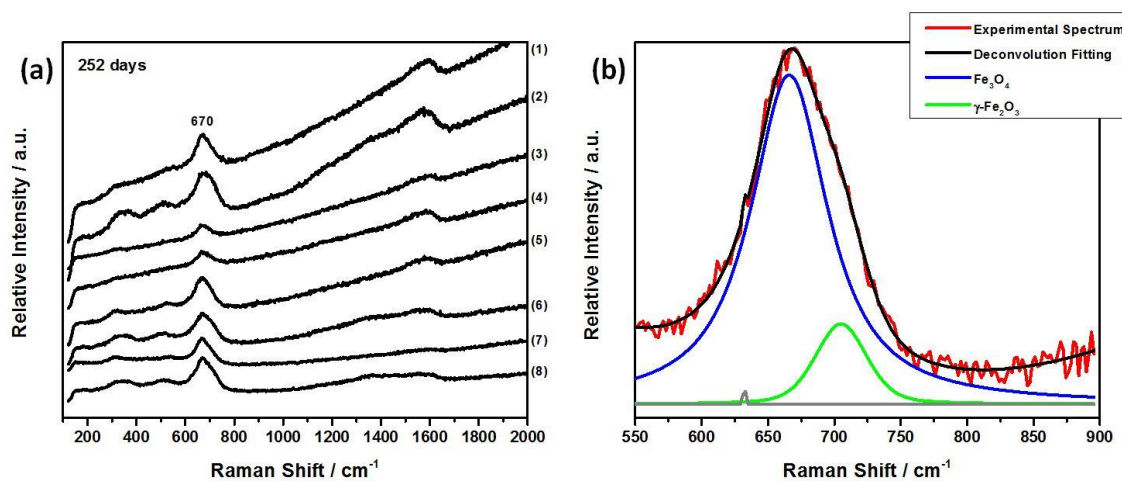


Figure 6-22: (a) Raman spectra (1-8) recorded at various locations on a steel specimen after 252 days exposure to solution (ii); (b) deconvolution of the spectrum closest to the sample average.

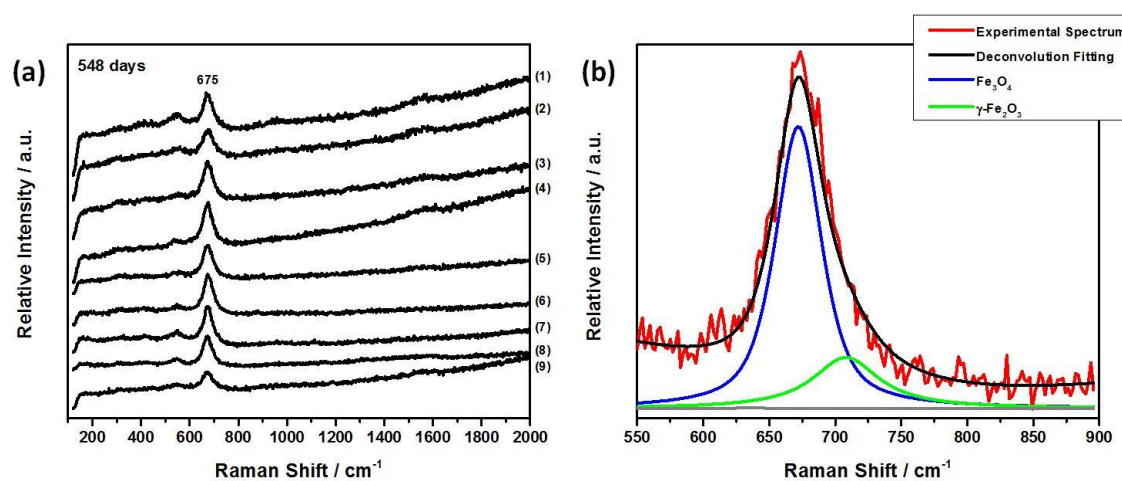


Figure 6-23: (a) Raman spectra (1-9) recorded at various locations on a steel specimen after 548 days exposure to solution (ii); (b) deconvolution of the spectrum closest to the sample average.

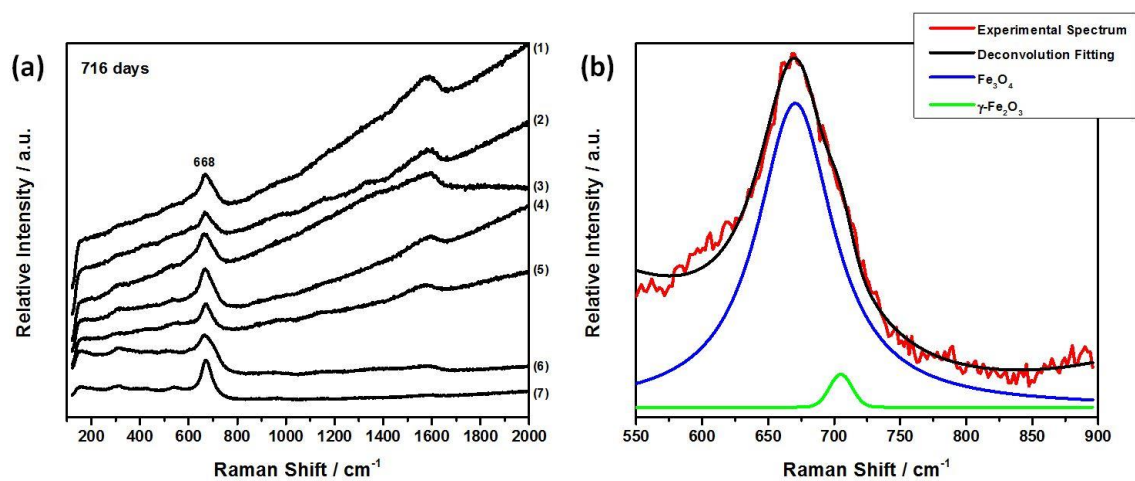


Figure 6-24: (a) Raman spectra (1-7) recorded at various locations on a steel specimen after 716 days exposure to solution (ii); (b) deconvolution of the spectrum closest to the sample average.

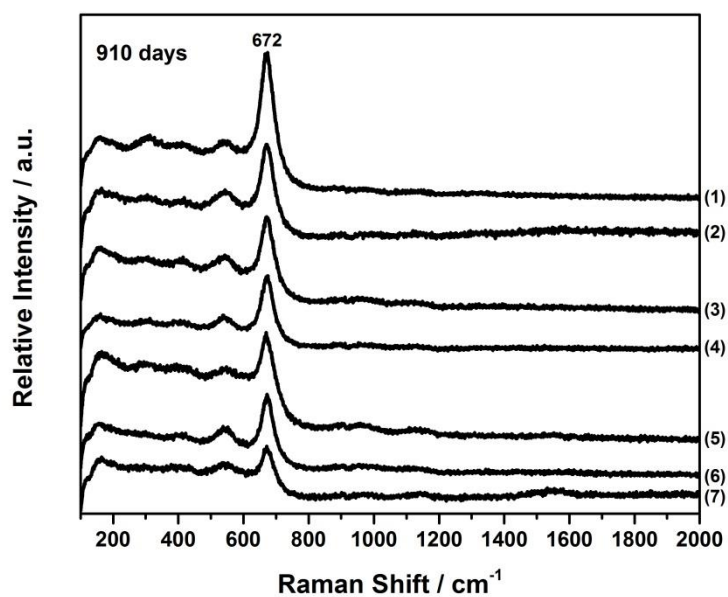


Figure 6-25: Raman spectra (1-7) recorded at various locations on a steel specimen after 910 days exposure to solution (ii).

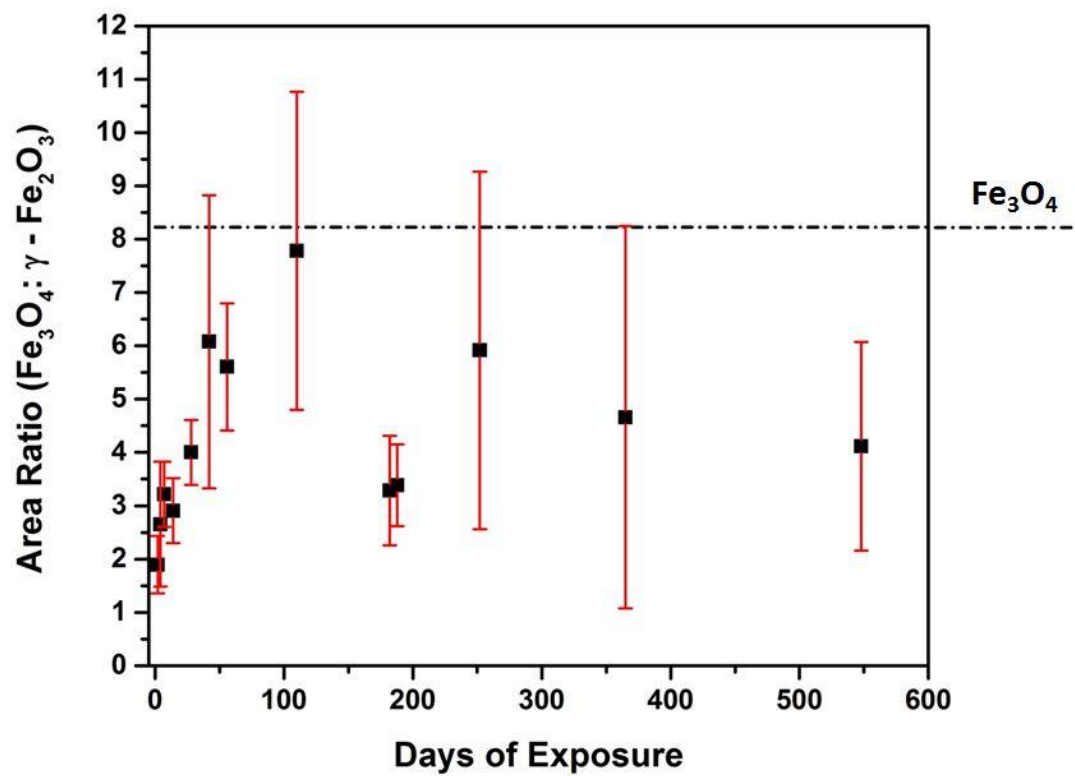


Figure 6-26: Evolution of the area ratio for the Fe_3O_4 (672 cm^{-1}) and $\gamma\text{-Fe}_2\text{O}_3$ (705 cm^{-1}) Raman peaks after exposure to solution (ii), calculated from the deconvoluted spectra.

6.3.2.2. Scanning Electron Microscopy

Figure 6-27 shows the SEM micrographs recorded after 4 days of exposure to solution (ii). The low magnification images show a slightly corroded surface. While there are fewer patches of corrosion product deposit compared to the number on the specimen extracted after a similar exposure period in solution (i) this surface probably reflects the surface prior to immersion. The early stages of corrosion of pearlite features can be seen in Figure 6-27(c). The area ratio calculated from deconvoluted Raman spectra confirms the presence of both Fe_3O_4 and $\gamma\text{-Fe}_2\text{O}_3$. Figure 6-27(g-h) show some areas of the surface are more heavily corroded.

After a period of 110 days exposure a visible compact film covered with a scattered deposit is observed. The underlying corrosion film, Figure 6-28(b-c) and (e-f), appears compact with some regions exhibiting platelet structures. The cracked pattern can be attributed to dehydration on removing the specimen from the anaerobic chamber as well as in the chamber of the SEM. Figure 6-28(h) shows the morphology of the overlying corrosion deposits. The corrosion product deposits on the order of 15-30 μm in diameter, Figure 6-28(i), indicate some localized corrosion has occurred, a process that would require the presence of traces of O_2 .

Following the O_2 incursion after roughly six months of exposure a change in the morphology of the corrosion product was observed, Figure 6-29. While the morphology does appear to remain consistent with those seen previously, the underlying corrosion film appears to have lost some structural definition, becoming more amorphous in nature, Figure 6-29(a-f). Since the Raman data suggested formation of $\gamma\text{-Fe}_2\text{O}_3$ it is possible that is what constitutes the deposit, Figure 6-29(h-i). After 548 days exposure, the morphology of the corrosion product has not changed but there appears to be more of it, Figure 6-30. The scattered deposit appears to be in the form of particulates $\leq 1 \mu\text{m}$ in diameter, Figure 6-30. Similar features are observed after 716 days, Figure 6-31. It is likely these particulates were formed by oxidation of dissolved Fe^{2+} to the highly insoluble Fe^{3+} state when the solution absorbed O_2 during the loss of atmospheric control in the anaerobic chamber. The presence of dissolved O_2 would also lead to a thickening of the general corrosion layer. After the full exposure period of 910 days, the extent of deposition has increased suggesting the surface is slowly accumulating Fe^{III} oxide deposited from the solution, Figure 6-32, with the Raman analysis suggesting the deposit is amorphous or has been converted to Fe_3O_4 by galvanic coupling to the corroding steel.

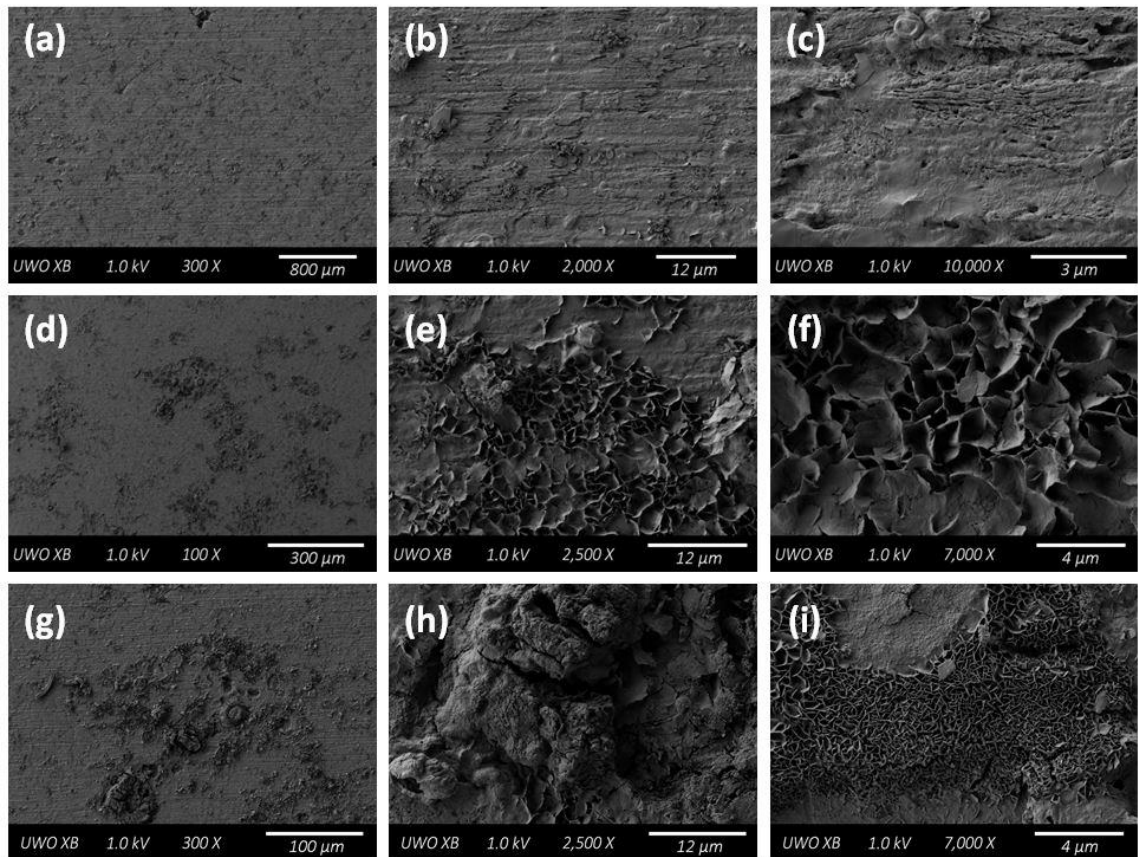


Figure 6-27: SEM micrographs recorded on a specimen surface after 4 days of exposure to solution (ii) showing a lightly corroded surface with (c) early stages of visible pearlite corrosion; (d-f) a region of crystalline corrosion product; (g-i) a more heavily corroded location.

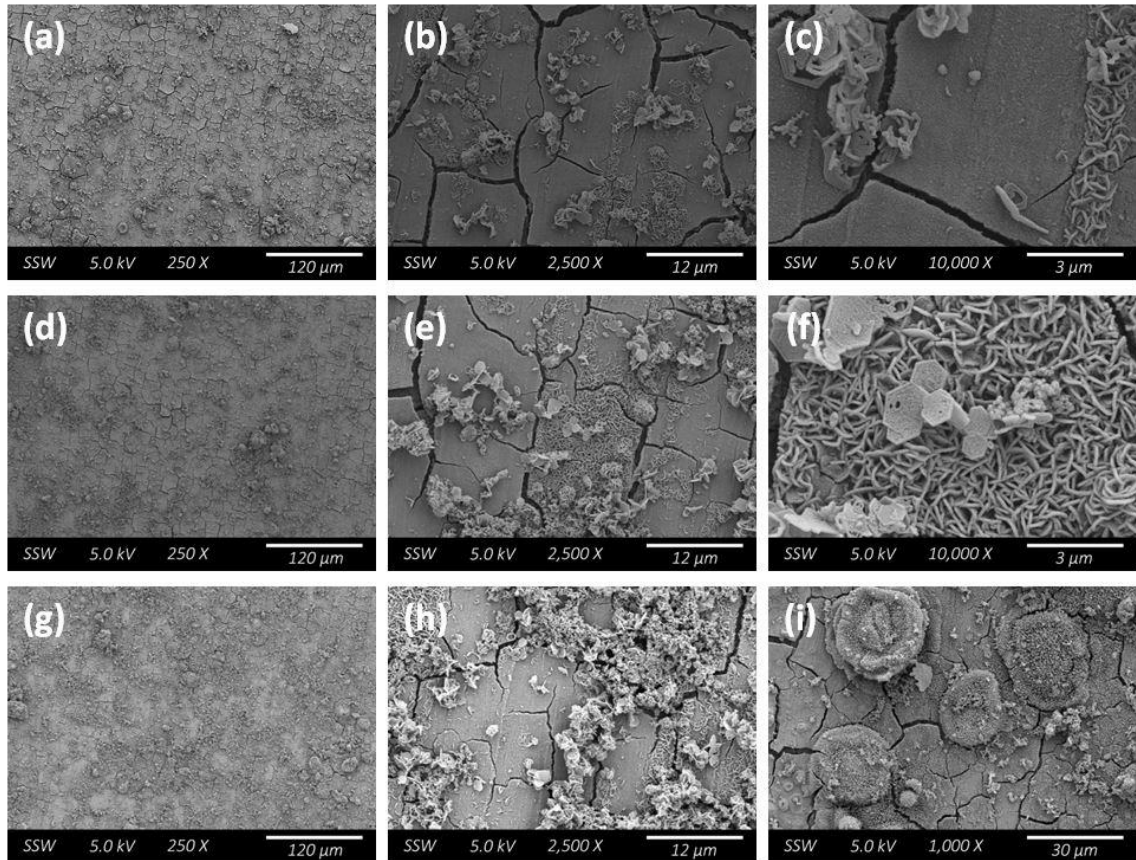


Figure 6-28: SEM micrographs recorded on a specimen surface after 110 days of exposure to solution (ii) showing: (a-f) regions of the general surface with a compact underlying film with interspersed platelet structures; (g-h) regions with overlying corrosion product deposits; (i) localized corrosion products on the order of 15-30 μm .

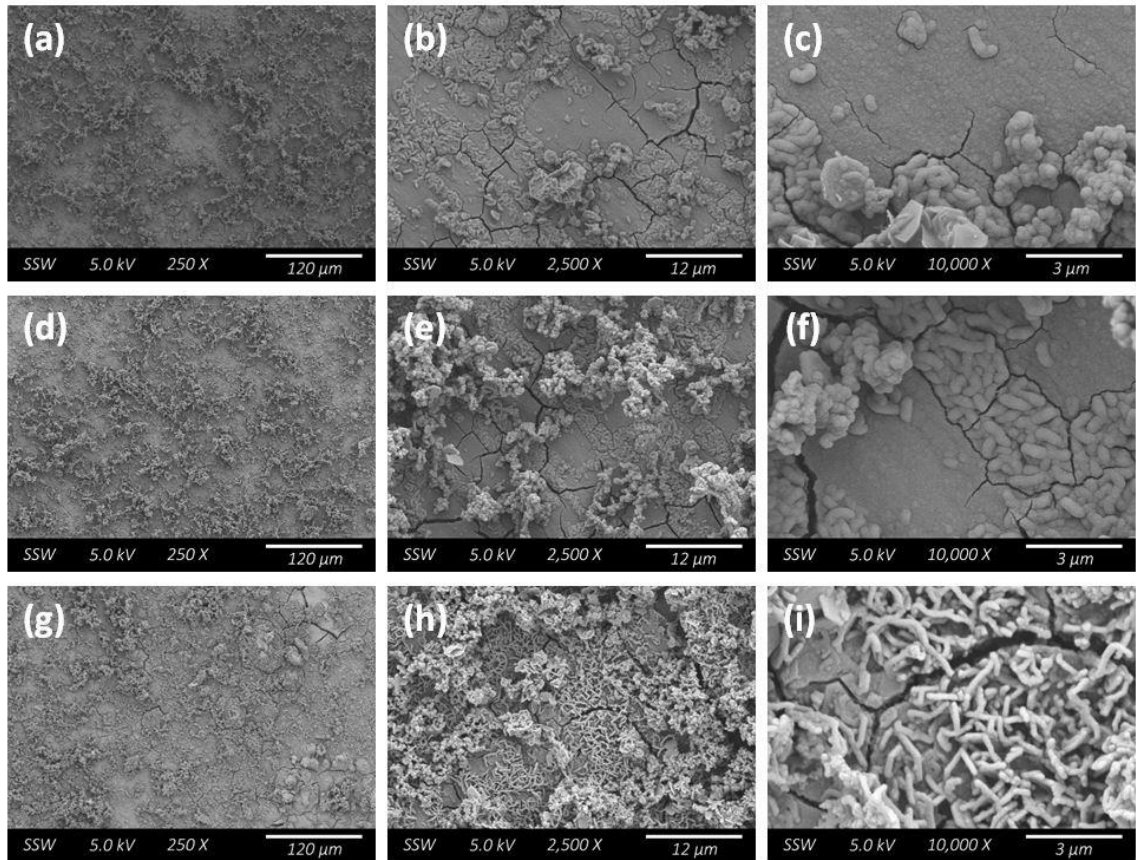


Figure 6-29: SEM micrographs recorded on a specimen surface after 252 days of exposure to solution (ii) showing: (a-f) the general surface and underlying corrosion layer; (g-i) corrosion product deposits, possible $\gamma\text{-Fe}_2\text{O}_3$.

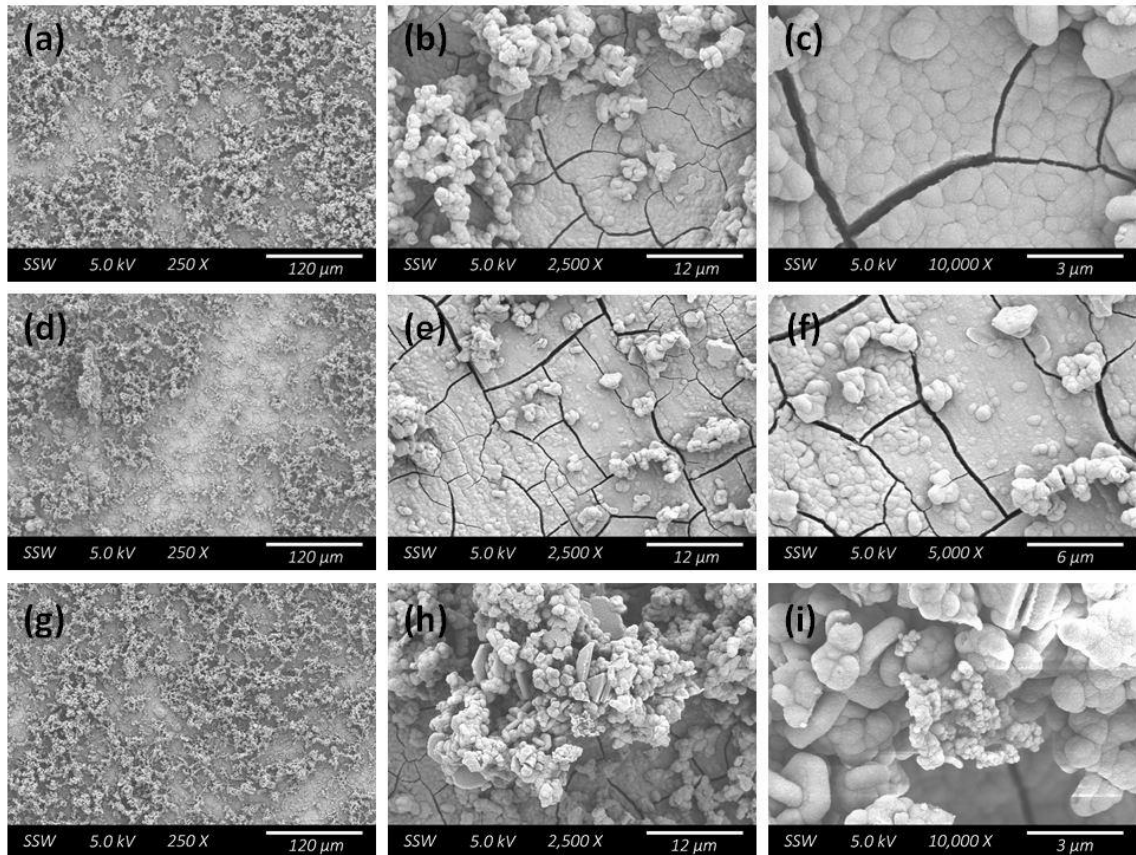


Figure 6-30: SEM micrographs recorded on a specimen surface after 548 days of exposure to solution (ii) showing: (a-f) the general surface with increasing levels of corrosion product deposits; (g-i) the morphology of the overlying corrosion product deposits.

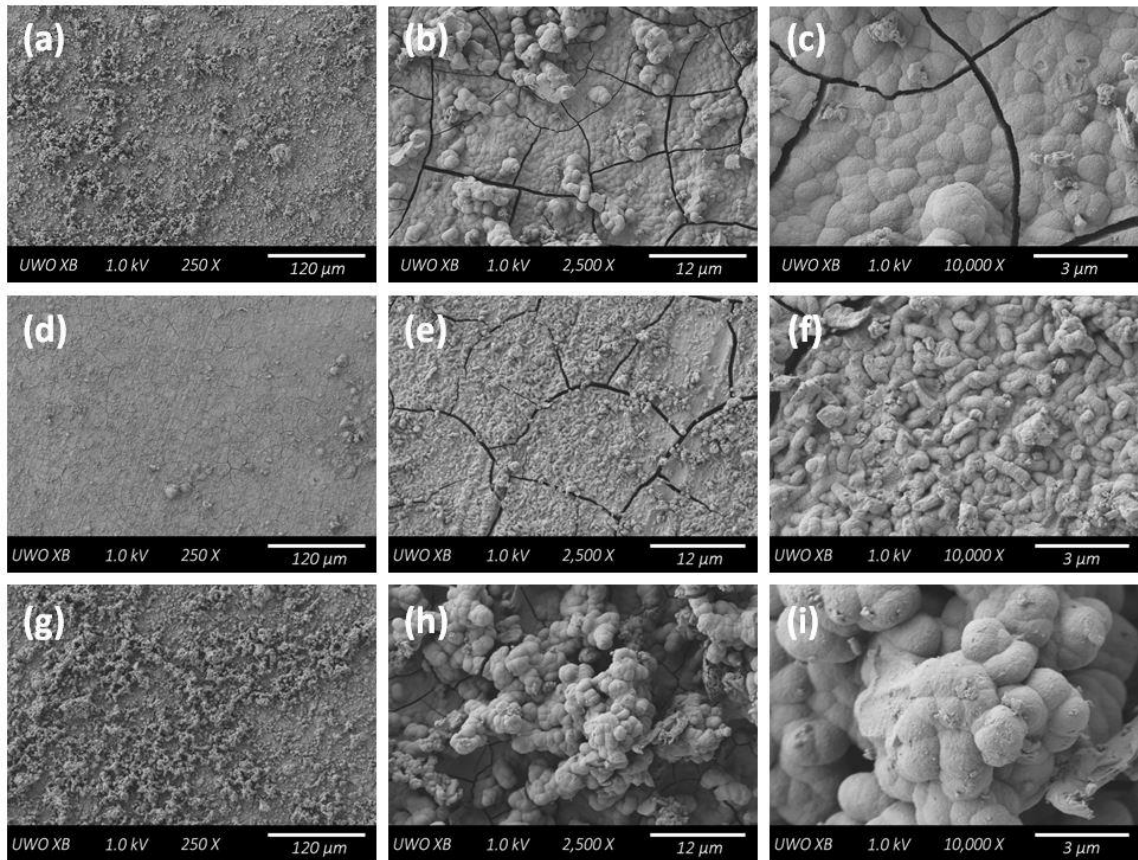


Figure 6-31: SEM micrographs recorded on a specimen surface after 716 days of exposure to solution (ii) showing: (a-f) regions with a visible underlying corrosion layer; (g-i) a region exhibiting extensive overlying corrosion product deposits.

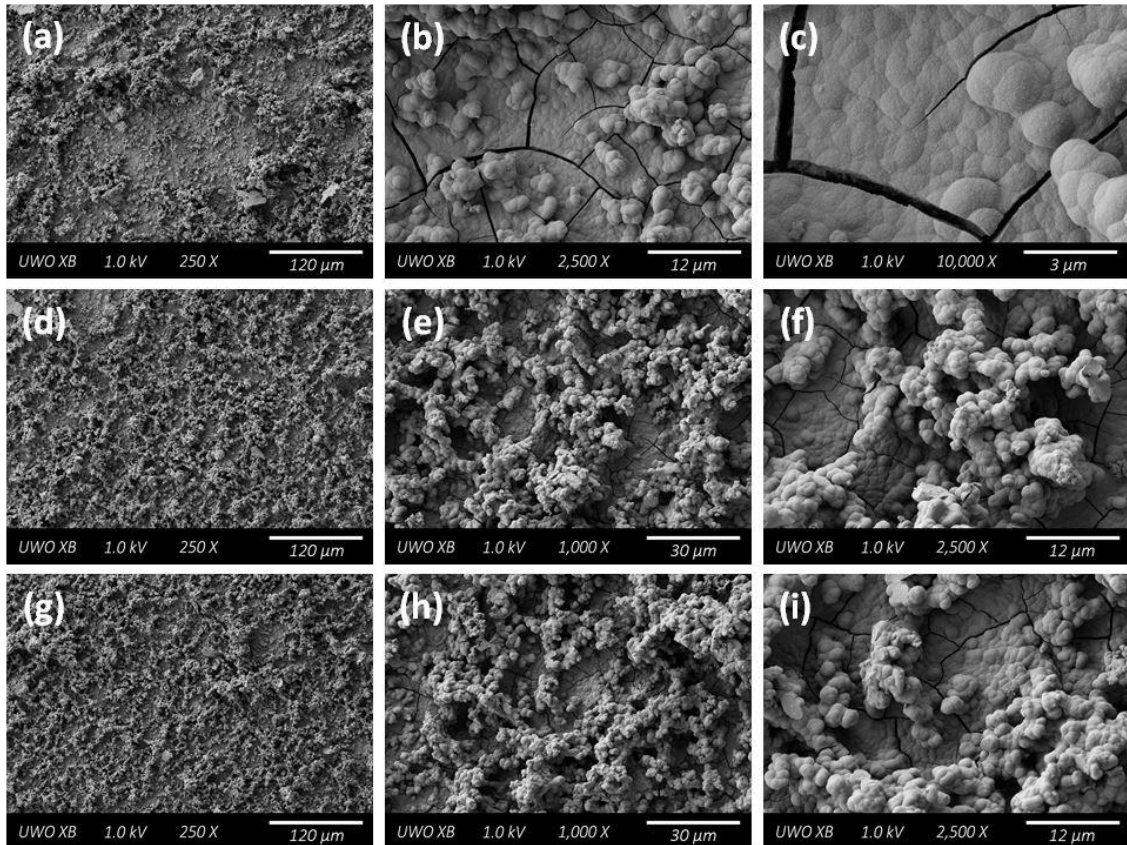


Figure 6-32: SEM micrographs recorded on a specimen surface after 910 days of exposure to solution (ii) showing: (a-c) the general underlying corrosion film; (d-i) the increasing extent of surface coverage by corrosion product deposits.

6.3.2.3. *Focused Ion Beam Milling*

Figure 6-33(a-c) shows a FIB cross-section of a specimen after 252 days of exposure for the area shown in Figure 6-29(f). The use of the backscatter detector highlights the interface between the base metal (bright) and the oxide film (dark), Figure 6-33(b). From the cross-section it can be seen that the penetration under a compact film is minor, whereas regions covered with a more textured film experience more extensive penetration. This is clear in Figure 6-33(d-f) which shows a cross-section cut through one of the overlying corrosion product deposits. The corrosion product film to the side of the deposit is very thin while the location directly under the deposit experienced more significant penetration. The EDX map shown in Figure 6-33(f) highlights the interface of the metal (blue) and the oxide film (pink). Although not clear in these images it is possible the extent of corrosion, and hence corrosion product deposition, is dictated by the grain structure of the steel. Figure 6-33(g-i) shows a cross-section through a large corrosion deposit on the sample surface. It is clear that the corrosion deposit is thickest over the more extensively corroded area confirming the porosity of the deposit at this location.

Figure 6-34 shows FIB cross-sections for three locations on the sample removed after 548 days of exposure to solution (ii). By comparison to the images in Figure 6-33, the cross-sections show that the corrosion product has thickened from $\leq 1 \mu\text{m}$ to as thick as $\sim 3 \mu\text{m}$ in some places over the additional 296 days of exposure. Figure 6-34(e) shows bright bands within the oxide structure. While first noted after the 252 day exposure period, Figure 6-33(h), the bands are much more extensive and clearly much larger and more resolved. An EDX map for Fe and C recorded on this location, Figure 6-34(f), shows that the bright bands are residual Fe_3C while the dark bands are Fe oxide. This confirms that the $\alpha\text{-Fe}$ lamellae in the pearlite grains have been converted to oxide. It would also appear that the locations covered by thicker deposits and experiencing deeper metal penetration coincide with the pearlite structure, Figure 6-34(b) and (e). Figure 6-34(g-i) shows a cross-section cut through a large corrosion deposit, which is porous and non-protective in nature and located over a region of localized corrosion. Again, Fe_3C is seen in the oxide, Figure 6-34(h).

Figure 6-35 shows FIB cross-sections cut on a specimen exposed for the full 910 day exposure period. The compact film on the steel surface has achieved a thickness in the range of $\sim 3\text{-}5 \mu\text{m}$ and is generally uniform and in most locations appears protective. Locations which have undergone deeper penetration are clearly spreading laterally across the surface rather than

developing into deep pits. The accumulation of an outer layer of deposited particles can be clearly seen.

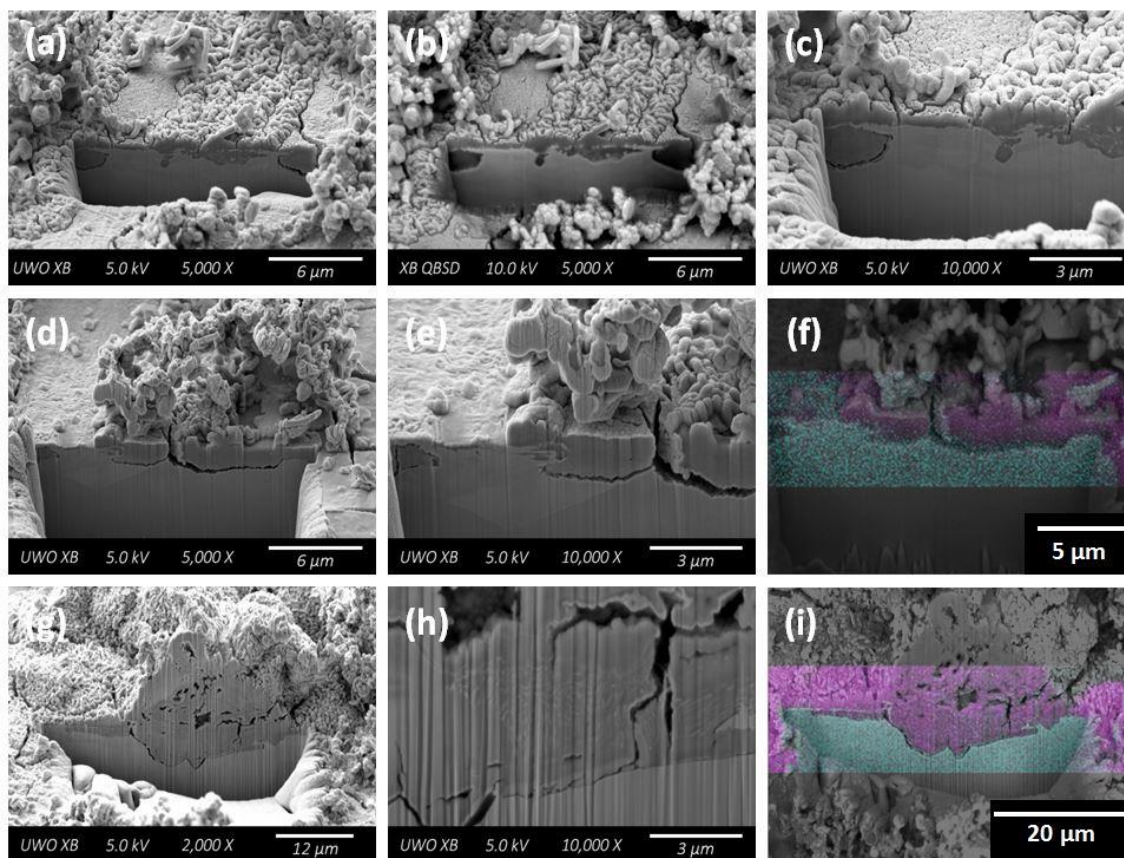


Figure 6-33: FIB cross-section micrographs recorded on a specimen surface after 252 days of exposure to solution (ii) showing: (a-c) that penetration beneath the compact film is minor; (d-f) a cut through an overlying deposit which has experienced more extensive penetration; (g-i) a cut through a large corrosion deposit at a location which has experienced more extensive corrosion. The backscatter image in (b) highlights the interface between the base metal (bright) and the oxide film (dark). EDX maps (f and i) further highlight the interface by mapping of elemental oxygen (pink) and iron (blue).

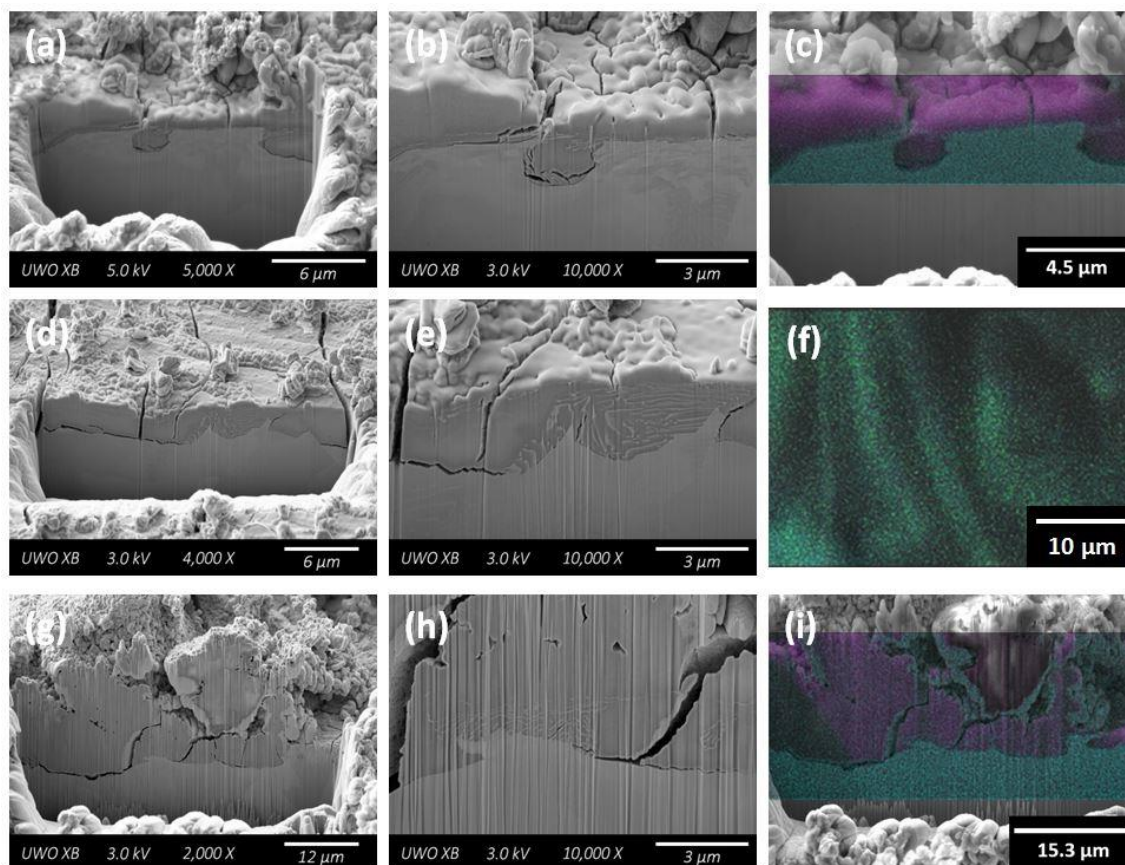


Figure 6-34: FIB cross-section micrographs recorded on a specimen surface after 548 days of exposure to solution (ii) showing: (a-f) a thickening of the film to $\sim 3 \mu\text{m}$ with more penetrating damage beneath thicker regions; (e) bright bands within the oxide structure, which the EDX map (f) for iron (blue) and carbon (green), shows are residual Fe_3C bands of the pearlite grains; (g-i) a cut through a large deposit which appears porous and non-protective. The EDX maps (c,i) highlight the interface between the base metal and the oxide film by mapping of elemental oxygen (pink) and iron (blue).

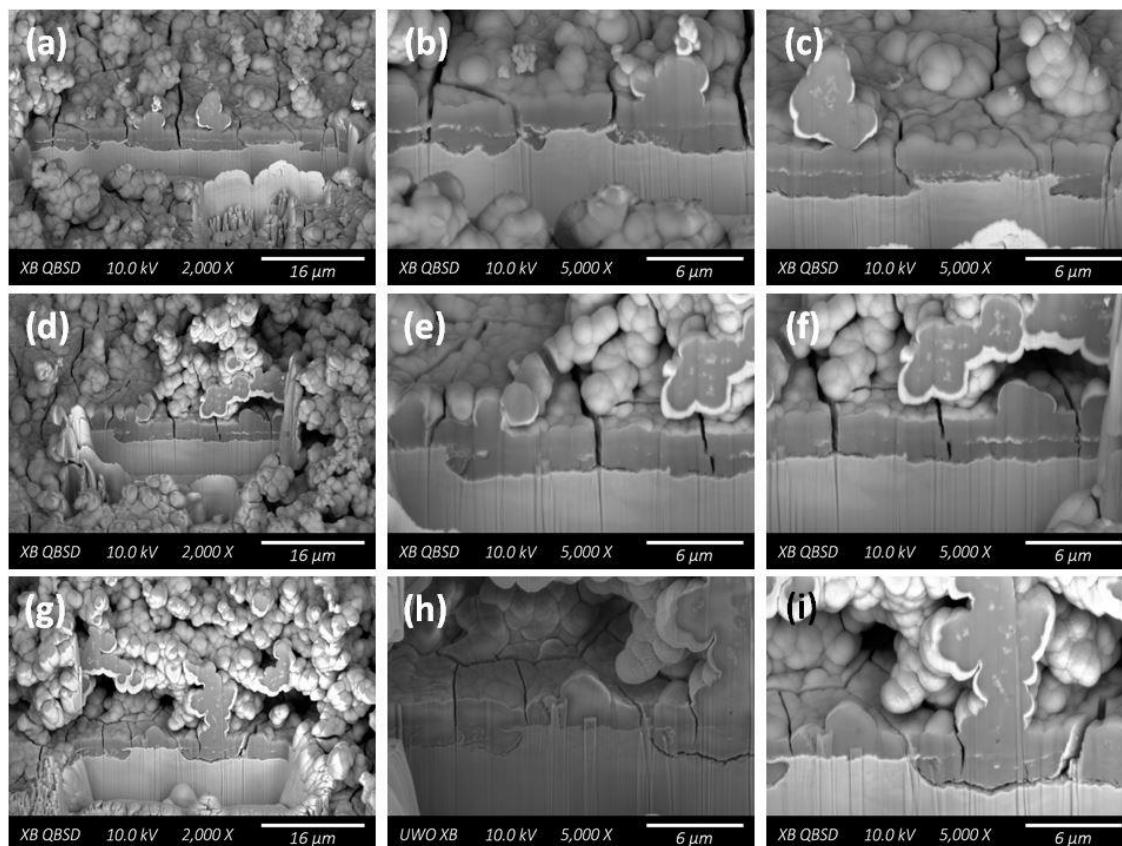


Figure 6-35: FIB cross-section micrographs recorded on a specimen surface after 910 days of exposure to solution (ii) showing: (a-c) a $\sim 3\text{-}5\ \mu\text{m}$ thick corrosion layer which appears generally uniform and protective; (d-i) regions showing deeper penetration which has spread laterally rather than developing as deep pits. The backscatter images ((b-c), (e-f), (i)) highlight the interface between the base metal (bright) and the oxide film (dark).

6.3.3. Solution (iii): Buffered, High Chloride Concentration

6.3.3.1. Raman and Infrared Spectroscopies

The evolution of the corrosion product compositions formed in solution (iii) can be seen in Figure 6-36 through Figure 6-41. Figure 6-36 shows the Raman spectra recorded on a steel coupon after 4 days of exposure. As observed in the other solutions, most locations analyzed exhibit the features expected after a period of humid air corrosion; a peak at 672 cm^{-1} with a shoulder at 720 cm^{-1} (region (1)); a broad featureless band between 200 and 570 cm^{-1} (region (2)); and a broad band in the region 1200 to 1700 cm^{-1} (region (3)). Again, as observed in the other solutions the prominence of the shoulder at 720 cm^{-1} coincides with the intensity in region (2) and the presence of the broad band in region (3) consistent with the presence of corroded locations on the steel surface prior to first immersion. For location (4), Raman bands located at 437 cm^{-1} and 512 cm^{-1} can be attributed to the $\text{Fe}^{2+}\text{-OH}$ and $\text{Fe}^{3+}\text{-OH}$ stretching modes of green rust (GR) [2, 6, 12-15] suggesting its rapid formation at some locations. Given the high $[\text{Cl}^-]$ it is likely that the coordinating interlayer anion of the GR is Cl^- with a structure of $[\text{Fe}_3^{\text{II}}\text{Fe}^{\text{III}}(\text{OH})_8]^{+}[\text{Cl} \cdot n\text{H}_2\text{O}]^{-}$ [16-18]. Spectrum (5) shows a single band at 1088 cm^{-1} which can be attributed to the ν_1 C–O symmetric stretching of a coordinated CO_3^{2-} species [2, 19-21]. It has been reported that the reference Raman band of siderite (FeCO_3) is 1089 cm^{-1} [19] while chukanovite ($\text{Fe}_2(\text{OH})_2\text{CO}_3$) has a reference band at 1070 cm^{-1} [20]. The band in spectrum (5) appears at 1088 cm^{-1} suggesting the formation of FeCO_3 . However, the multiple species present on the sample surface may cause some shifting of the Raman bands, and the previously observed formation of $\text{Fe}_2(\text{OH})_2\text{CO}_3$ in a $\text{HCO}_3^-/\text{CO}_3^{2-}$ solution (Chapter 5) suggests that the formation of $\text{Fe}_2(\text{OH})_2\text{CO}_3$ is likely. Interestingly, when the peak at 1088 cm^{-1} is present the peak in region (1) is minor and regions (2) and (3) are effectively absent, suggesting the carbonate containing phase masks the underlying surface phases.

The masking is apparently confirmed by the Raman spectra recorded after 14 days exposure, Figure 6-37(a), which show the peak in region (1) is generally visible in the absence of the peak at 1073 cm^{-1} and vice-versa. As observed over the shorter exposure period, the formation of GR persists. The band found at $1071/1073\text{ cm}^{-1}$ in spectra (1) and (3-5) is consistent with the coordinated CO_3^{2-} anion of $\text{Fe}_2(\text{OH})_2\text{CO}_3$ [22, 23], whose presence is confirmed by the FTIR spectra presented in Figure 6-37(b).

After an exposure time of 109 days, the only visible Raman bands are those at 1082 cm^{-1} , Figure 6-38(a), which the FTIR spectra, Figure 6-38(b), confirm is $\text{Fe}_2(\text{OH})_2\text{CO}_3$. The absence of Raman bands for any other species suggests that the $\text{Fe}_2(\text{OH})_2\text{CO}_3$ corrosion product has become ubiquitous and is thick enough to totally obscure any other corrosion product. $\text{Fe}_2(\text{OH})_2\text{CO}_3$ remains the only corrosion product visible in both the Raman and FTIR spectra after 252 days, Figure 6-39. After 365 days a Raman band for Fe_3O_4 at 670 cm^{-1} is observed at location (6), Figure 6-40, suggesting formation of a Fe_3O_4 sublayer has occurred. The presence of Raman bands at both 1069 and 1085 cm^{-1} suggests both $\text{Fe}_2(\text{OH})_2\text{CO}_3$ and FeCO_3 are present. As outlined in Chapter 4, $\text{Fe}_2(\text{OH})_2\text{CO}_3$ is thermodynamically metastable with respect to FeCO_3 and its conversion over extended periods of time would not be unexpected [24-26]. This phenomenon is observed in archaeological artefacts which have developed inner $\text{Fe}_2(\text{OH})_2\text{CO}_3$ and outer FeCO_3 corrosion layers after exposure to anoxic groundwaters containing $\text{HCO}_3^-/\text{CO}_3^{2-}$ [20, 23, 24, 26-28]. After a final exposure period of 639 days, the Raman spectra show broad peaks at $552\text{-}544\text{ cm}^{-1}$ which may be due to the presence of Fe_3O_4 , Figure 6-41(a). This is consistent with the observation of Fe_3O_4 after 365 days. However, the band at 552 cm^{-1} is not the main band of Fe_3O_4 suggesting that the corrosion product may be highly amorphous or not attributable to Fe_3O_4 . The sharp Raman band at 1071 cm^{-1} along with the FTIR spectra show that $\text{Fe}_2(\text{OH})_2\text{CO}_3$ remains the dominant corrosion product found on the surface, Figure 6-41(b). This emergence of Fe_3O_4 over a long exposure period indicates its on-going formation throughout the exposure period.

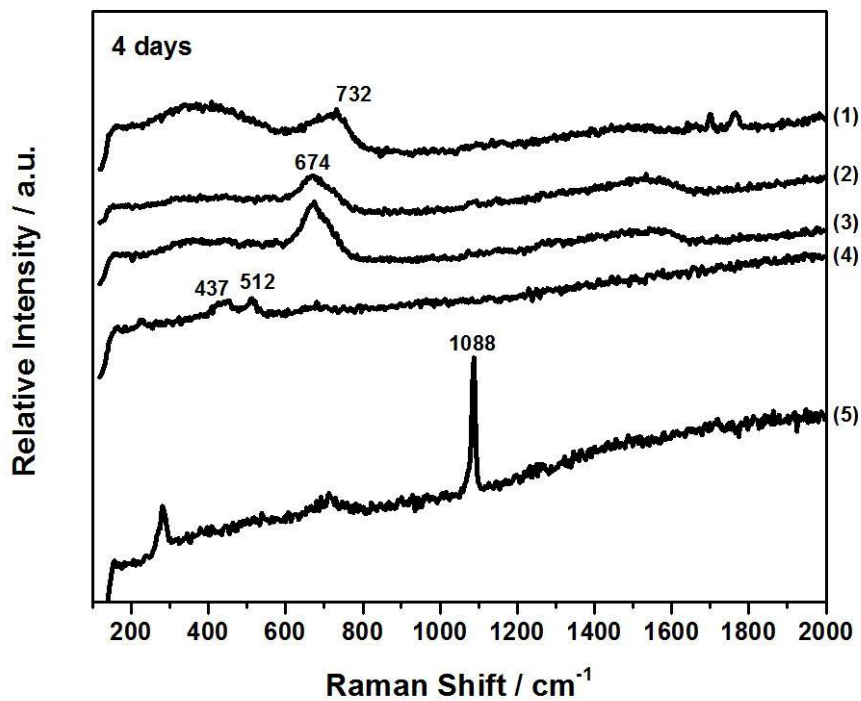


Figure 6-36: Raman spectra (1-5) recorded at various locations on a steel specimen after 4 days of exposure to solution (iii).

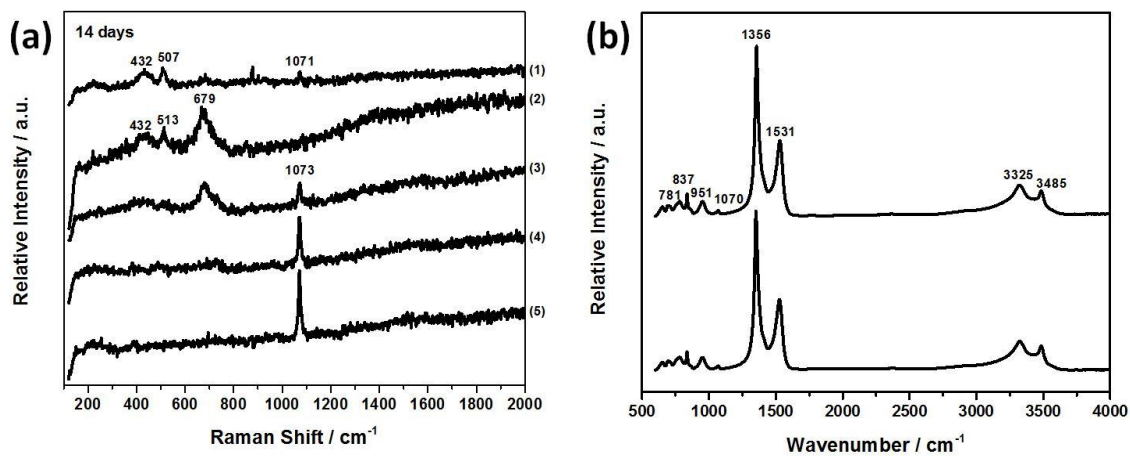


Figure 6-37: (a) Raman spectra (1-5) and (b) FTIR spectra recorded at various locations on a steel specimen after 14 days of exposure to solution (iii).

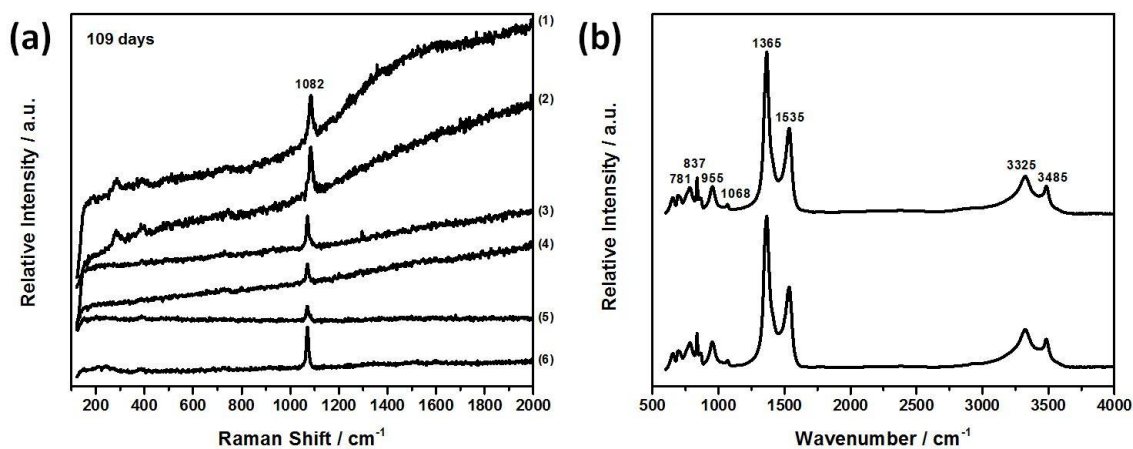


Figure 6-38: (a) Raman spectra (1-6) and (b) FTIR spectra recorded at various locations on a steel specimen after 109 days of exposure to solution (iii).

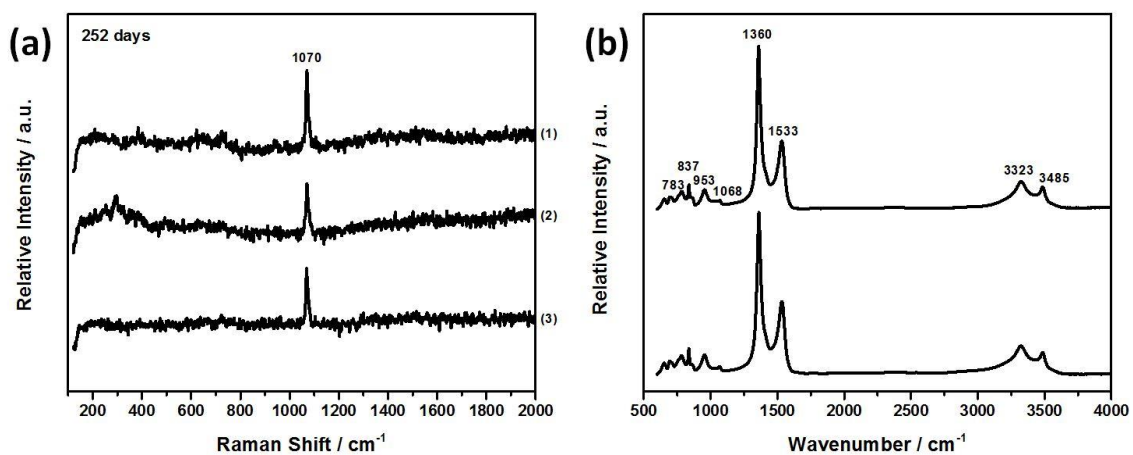


Figure 6-39: (a) Raman spectra (1-3) and (b) FTIR spectra recorded at various locations on a steel specimen after 252 days of exposure to solution (iii).

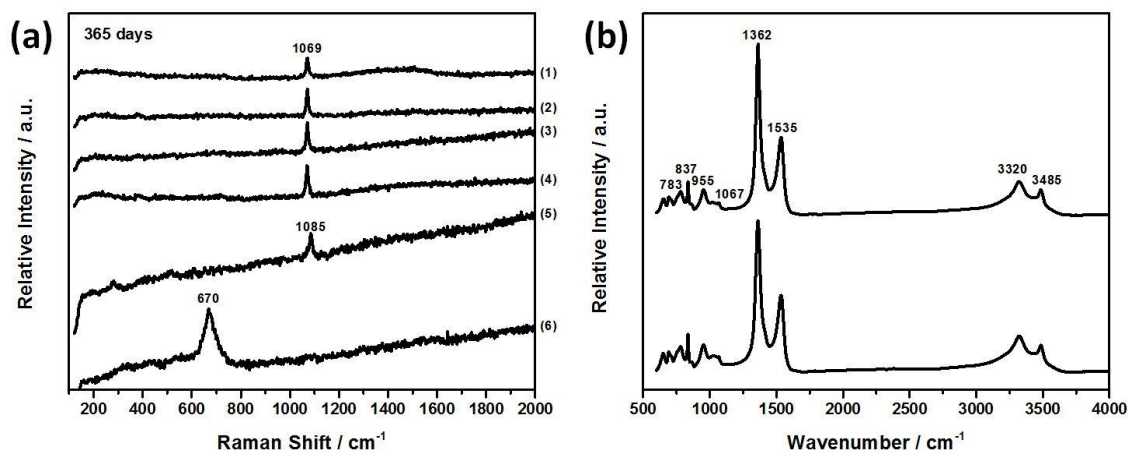


Figure 6-40: (a) Raman spectra (1-6) and (b) FTIR spectra recorded at various locations on a steel specimen after 365 days of exposure to solution (iii).

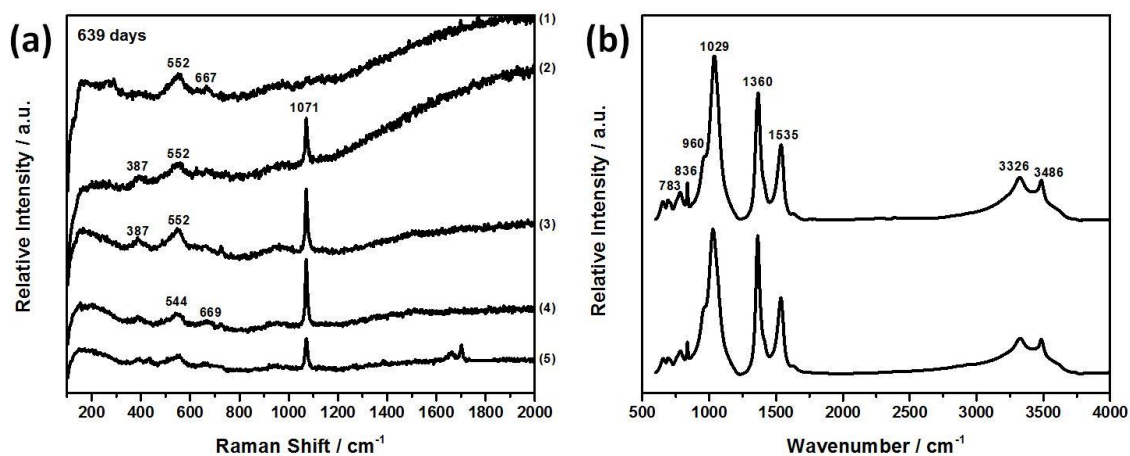


Figure 6-41: (a) Raman spectra (1-5) and (b) FTIR spectra recorded at various locations on a steel specimen after 639 days of exposure to solution (iii).

6.3.3.2. Scanning Electron Microscopy

Figure 6-42 shows the SEM images recorded on the surface of a specimen removed after 4 days of exposure to solution (iii). Figure 6-42(a-c) shows the surface is completely covered by an oxide with the needle-like acicular morphology expected for $\text{Fe}_2(\text{OH})_2\text{CO}_3$ consistent with the Raman spectra. Several locations across the surface also displayed large localized corrosion product deposits (60-100 μm in diameter), Figure 6-42(d-f) and (g-i), suggesting the formation of these deposits may be due to pitting. The morphology of these deposits is different to that of the surrounding $\text{Fe}_2(\text{OH})_2\text{CO}_3$, and could correspond to the GR or $\gamma\text{-Fe}_2\text{O}_3$ observed in the Raman spectra. After a 14 day exposure, the morphology of the corrosion products remains unchanged, Figure 6-43. Figure 6-43(c) and (e-f) show large hexagonal crystals which are observed on the $\text{Fe}_2(\text{OH})_2\text{CO}_3$ surface layer. The structure is likely to be the GR which was identified in the Raman analyses. Evidence for small locally corroded sites remains, but they are not as obvious as those observed in the first few days, Figure 6-43(g-i).

After 109 days, a deposit with a different morphology emerges in the $\text{Fe}_2(\text{OH})_2\text{CO}_3$ crystals. This is most obvious in Figure 6-44(c). The multi-faceted cubes suggest the formation of FeCO_3 . Since $\text{Fe}_2(\text{OH})_2\text{CO}_3$ is thermodynamically metastable with respect to FeCO_3 this may indicate the slow transformation of $\text{Fe}_2(\text{OH})_2\text{CO}_3$ into FeCO_3 .

After 252 days of exposure these cubic structures become more regular and denser, supporting the claim that they are FeCO_3 crystals formed from the transformation of $\text{Fe}_2(\text{OH})_2\text{CO}_3$, Figure 6-45. The remainder of the surface remains covered in a coherent layer of $\text{Fe}_2(\text{OH})_2\text{CO}_3$ as suggested by the Raman and FTIR analyses as well as hexagonal crystals (Figure 6-45(e) and (g)) which may indicate the continued presence of GR. After 365 days the surface remains covered with $\text{Fe}_2(\text{OH})_2\text{CO}_3$ but an additional morphology is observed. Small amorphous deposits are visible, Figure 6-46(c), on top of the $\text{Fe}_2(\text{OH})_2\text{CO}_3$ deposit. In addition, Figure 6-46(d-f) and (g-h) show the localized corrosion deposits remain. It is possible, and in effect most likely, these features were present throughout the total exposure period. The morphology within deposits at these locations appears to be a mixture of $\text{Fe}_2(\text{OH})_2\text{CO}_3$ and FeCO_3 .

After a final exposure period of 639 days the surface remains covered in $\text{Fe}_2(\text{OH})_2\text{CO}_3$ but the small deposits are more numerous in number, Figure 6-47(a-c). In addition, localized corrosion deposits, Figure 6-47(d-i), remain frequent across the surface. The morphology of such features

appears less crystalline and may account for the additional features seen in the Raman spectra which cannot be attributed to $\text{Fe}_2(\text{OH})_2\text{CO}_3$.

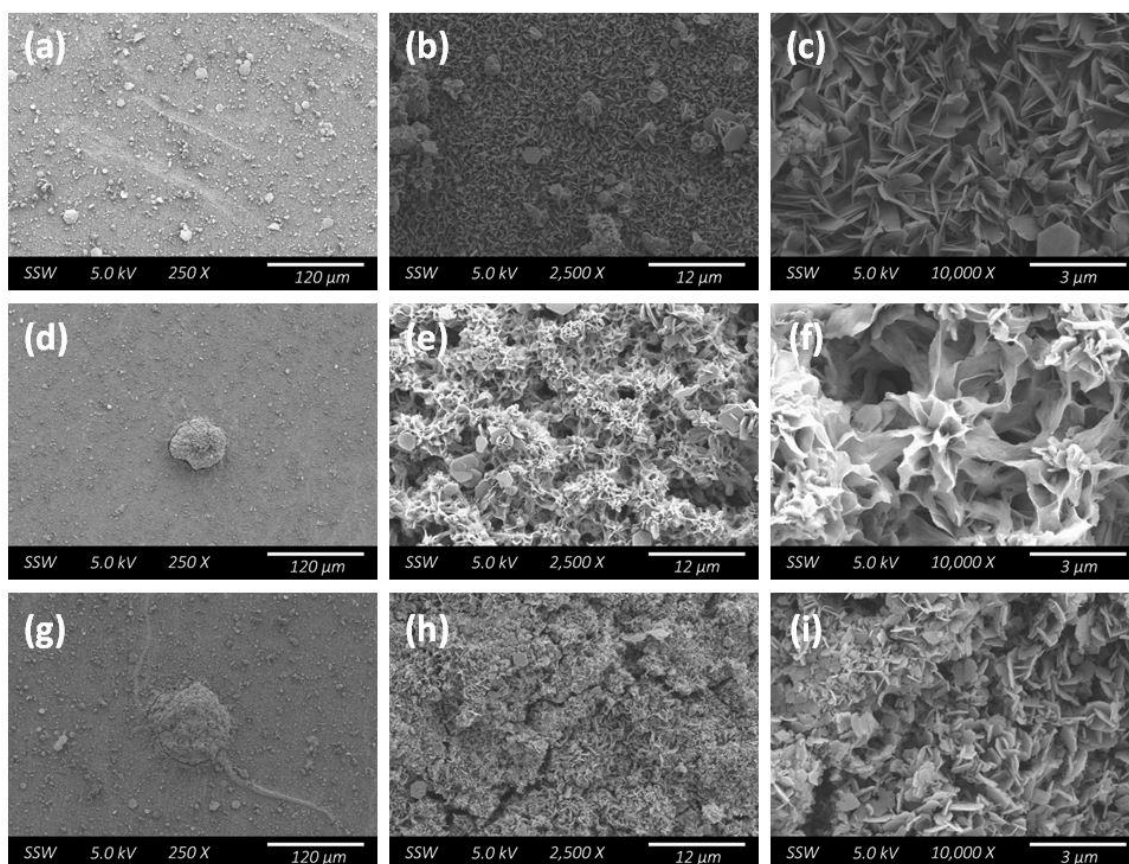


Figure 6-42: SEM micrographs recorded on a steel specimen after 4 days of exposure to solution (iii) showing: (a-c) needle-like acicular crystals expected of $\text{Fe}_2(\text{OH})_2\text{CO}_3$; (d-i) large localized corrosion products 60-100 μm in diameter.

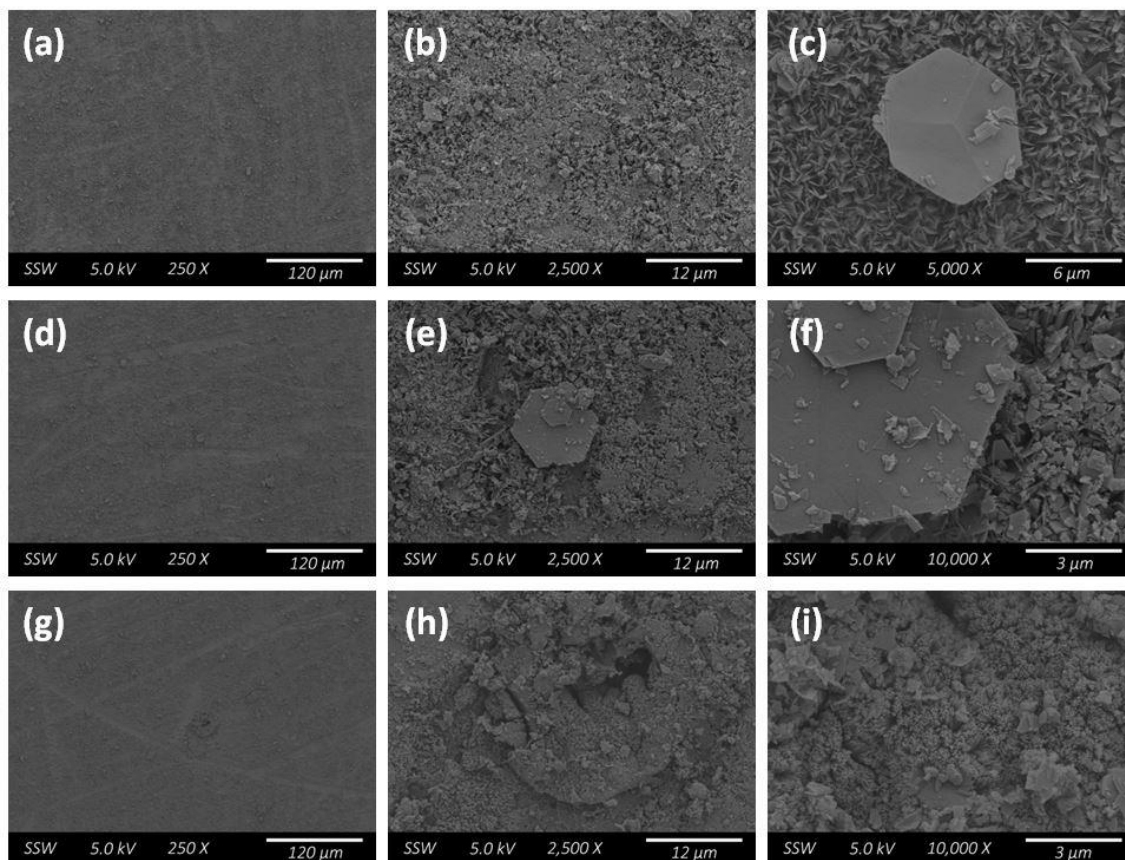


Figure 6-43: SEM micrographs recorded on a steel specimen after 14 days of exposure to solution (iii) showing that the morphology of the corrosion product has remained unchanged but that small hexagonal crystals (c, e-f) appear across the surface and evidence for small locally corroded sites (g-i).

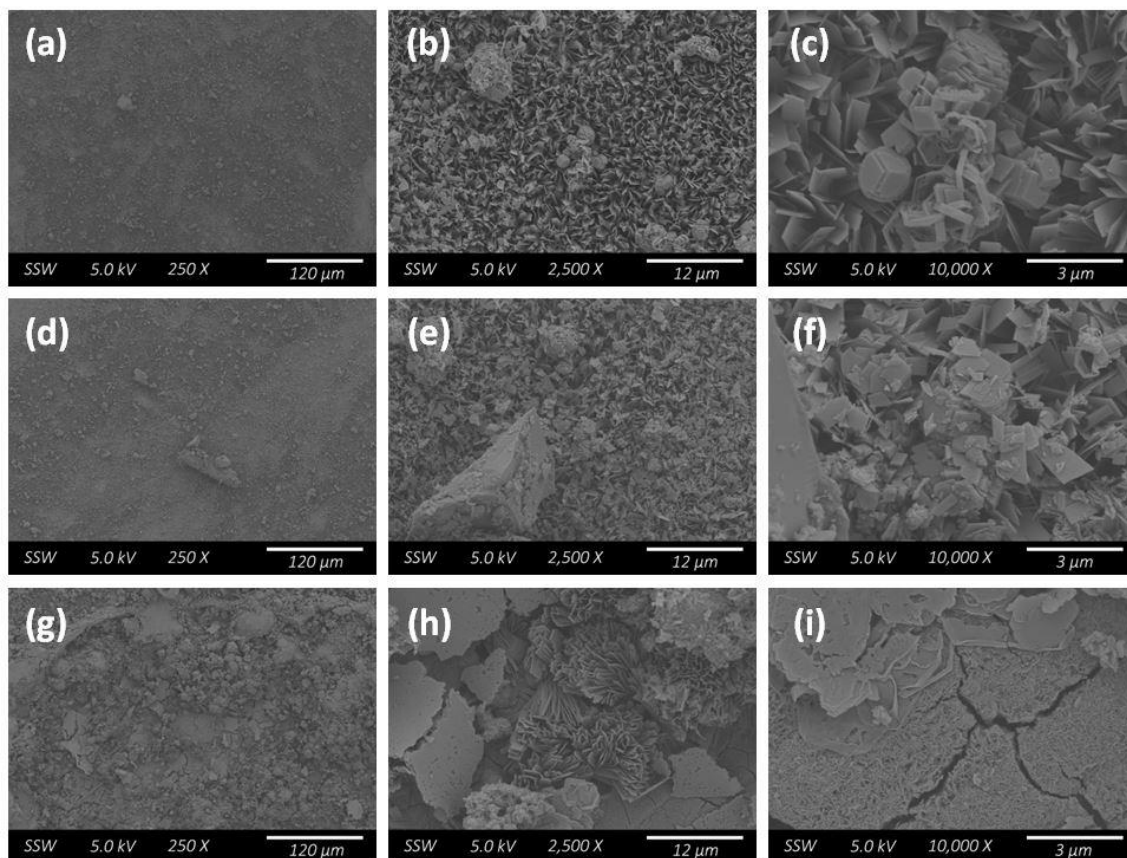


Figure 6-44: SEM micrographs recorded on a steel specimen after 109 days of exposure to solution (iii) showing the emergence of a different morphology of cubic structure best observed in (c) which suggests the formation of FeCO_3 .

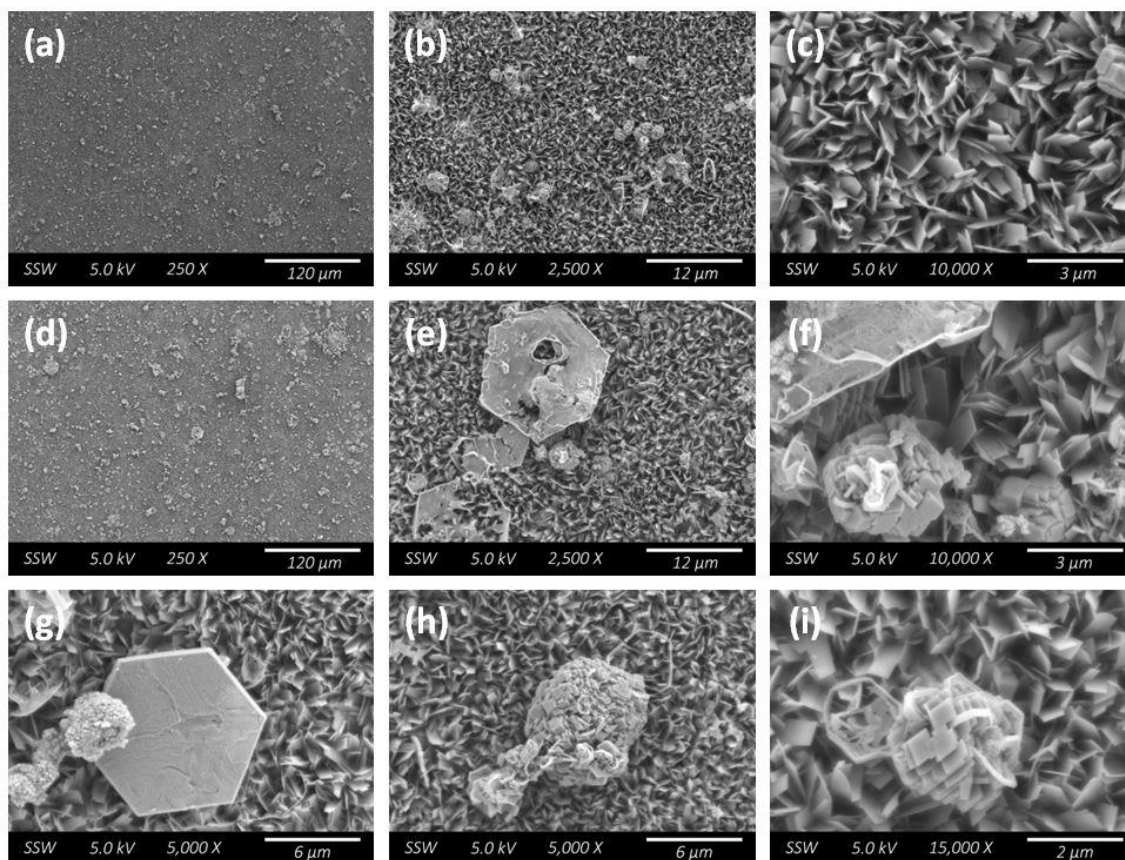


Figure 6-45: SEM micrographs recorded on a steel specimen after 252 days of exposure to solution (iii) showing a general $\text{Fe}_2(\text{OH})_2\text{CO}_3$ film with an increase in the density of the cubic structure, supporting FeCO_3 formation as well as hexagonal crystals in (e) and (g) which may indicate the presence of GR.

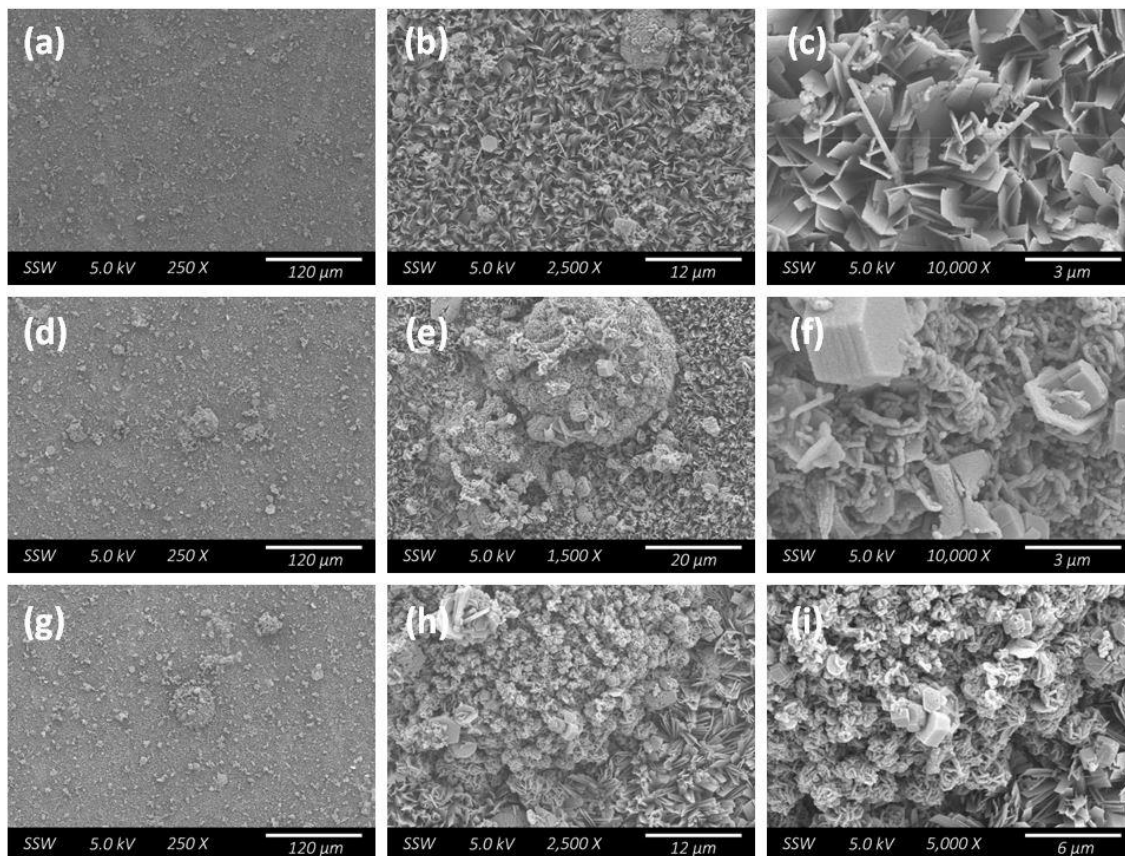


Figure 6-46: SEM micrographs recorded on a steel specimen after 365 days of exposure to solution (iii) showing: (a-c) the dominance of $\text{Fe}_2(\text{OH})_2\text{CO}_3$ with small amorphous deposits (c) visible on top of the $\text{Fe}_2(\text{OH})_2\text{CO}_3$ deposit; (d-i) two regions of localized corrosion deposits.

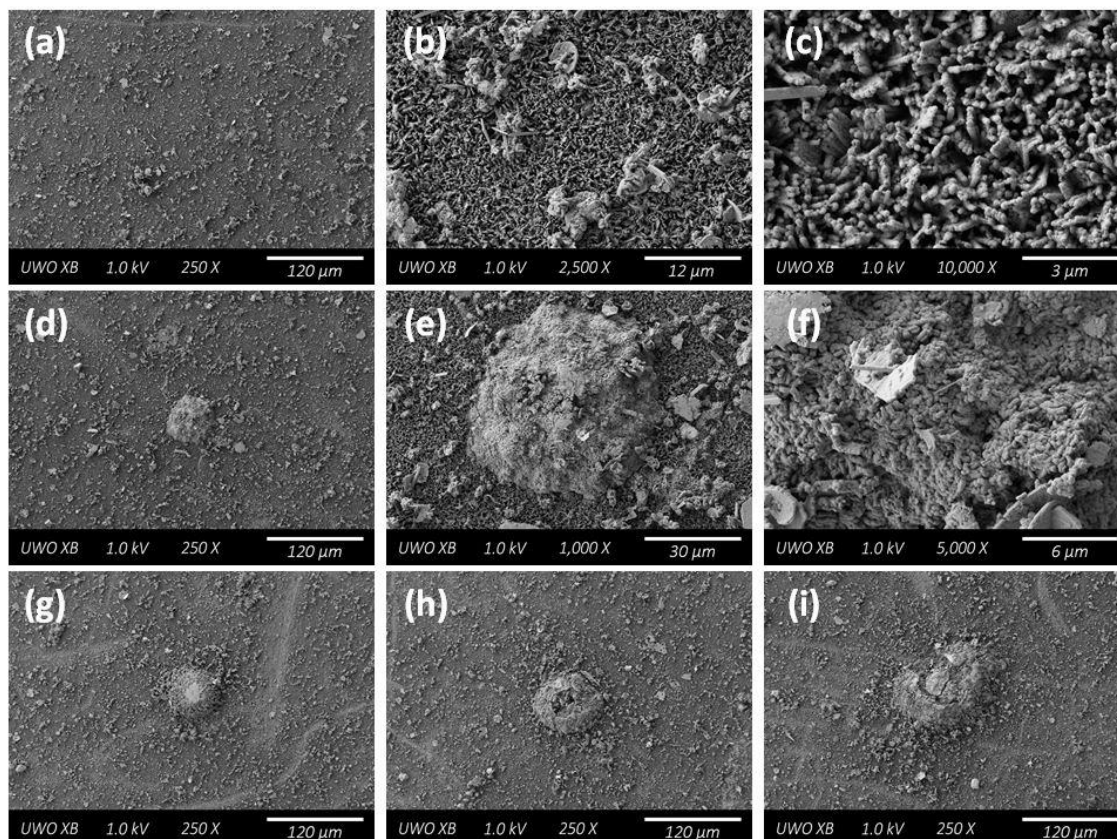


Figure 6-47: SEM micrographs recorded on a steel specimen after 639 days of exposure to solution (iii) showing: (a-c) a $\text{Fe}_2(\text{OH})_2\text{CO}_3$ film with more numerous small deposits; (d-f) a region with a localized corrosion deposit; (g-i) the size distribution of additional localized corrosion deposits.

6.3.3.3. *Focused Ion Beam Milling*

Figure 6-48 shows cross-sectional images for three locations after 252 days of exposure. Figure 6-48(a-b) shows a cross-section cut through the $\text{Fe}_2(\text{OH})_2\text{CO}_3$ film formed ubiquitously across the surface. The film is grown from Fe^{2+} dissolved at that location, the crystals being directly attached to the substrate. This is confirmed in the backscatter image, Figure 6-48(b), which highlights the location of the metal/oxide interface. Growth of a porous film directly from the base metal suggests, at least in the short term, that a corrosion inhibiting film is not forming as observed in solutions (i) and (ii). In addition, the damage to the metal surface is uniform across the cross-section indicating these are locations of general corrosion.

However, cross-sectional analyses of the isolated deposits show they are located over regions of enhanced localized corrosion. At these locations the deposit is highly porous, Figure 6-48(c-d), and not protective. A similar feature is shown in Figure 6-48(e-f), and suggests $\text{Fe}_2(\text{OH})_2\text{CO}_3$ has reformed at the metal/oxide interface underneath the original deposit.

Figure 6-49 shows the FIB cross-sections of three locations on the sample surface after 546 days of exposure. Cross-sectioning of the large deposit shown in Figure 6-49(a-c) indicates that this is a more active location on the steel surface. However, the backscatter image shows only shallow penetration into the metal, Figure 6-49(c). The thickness of the deposit over such a shallow penetration indicates it is porous and unprotective. In contrast, the deposit shown in Figure 6-49(d-f) shows a significant penetration into the sample surface indicating an active pitting corrosion process had occurred. The bright region seen in the center of Figure 6-49(f) is more than likely due to back deposited Ga from the milling process rather than a location of uncorroded steel. Cross-sectional analysis of the general $\text{Fe}_2(\text{OH})_2\text{CO}_3$ surface film shows the thickness of the film has remained unchanged and confirms that the corrosion process has not accelerated and the $\text{Fe}_2(\text{OH})_2\text{CO}_3$ film is likely protective, Figure 6-49(g-h).

Figure 6-50 shows the FIB cross-sections for two locations after 639 days of exposure. Cross-sectioning of a large deposit (Figure 6-47(a-c)) shows the film to be porous suggesting this site remained active. Beneath the deposit, damage has penetrated $\sim 8 \mu\text{m}$ into the steel while the surrounding areas show little penetration. A cross-section through the general surface film, Figure 6-50(d-f), shows little damage to the base metal. While the $\text{Fe}_2(\text{OH})_2\text{CO}_3$ deposit looks

unprotective it is possible that the growth of a Fe_3O_4 layer (detected by Raman spectroscopy) on the steel surface is providing corrosion protection.

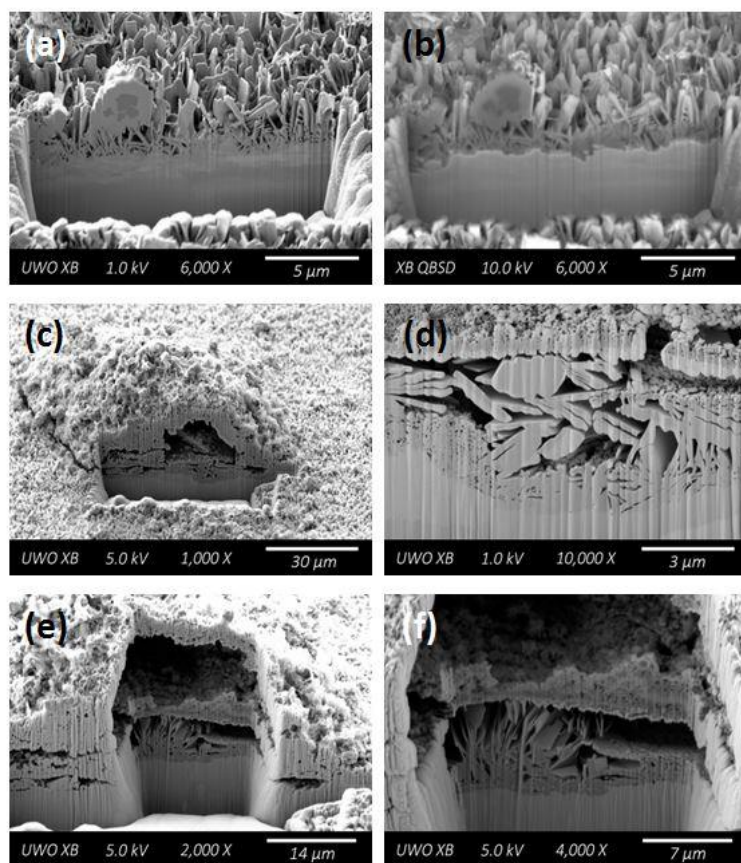


Figure 6-48: FIB cross-section micrographs recorded on a steel specimen after 252 days of exposure to solution (iii) showing: (a-b) the general $\text{Fe}_2(\text{OH})_2\text{CO}_3$ film in which the crystals are attached directly to the substrate which is confirmed by the backscatter image (b); (c-d) a cut through a region of isolated deposit showing that they are located over regions of active localized corrosion; (e-f) a cut through a region of active corrosion suggesting $\text{Fe}_2(\text{OH})_2\text{CO}_3$ has reformed at the metal/oxide interface under the original deposit.

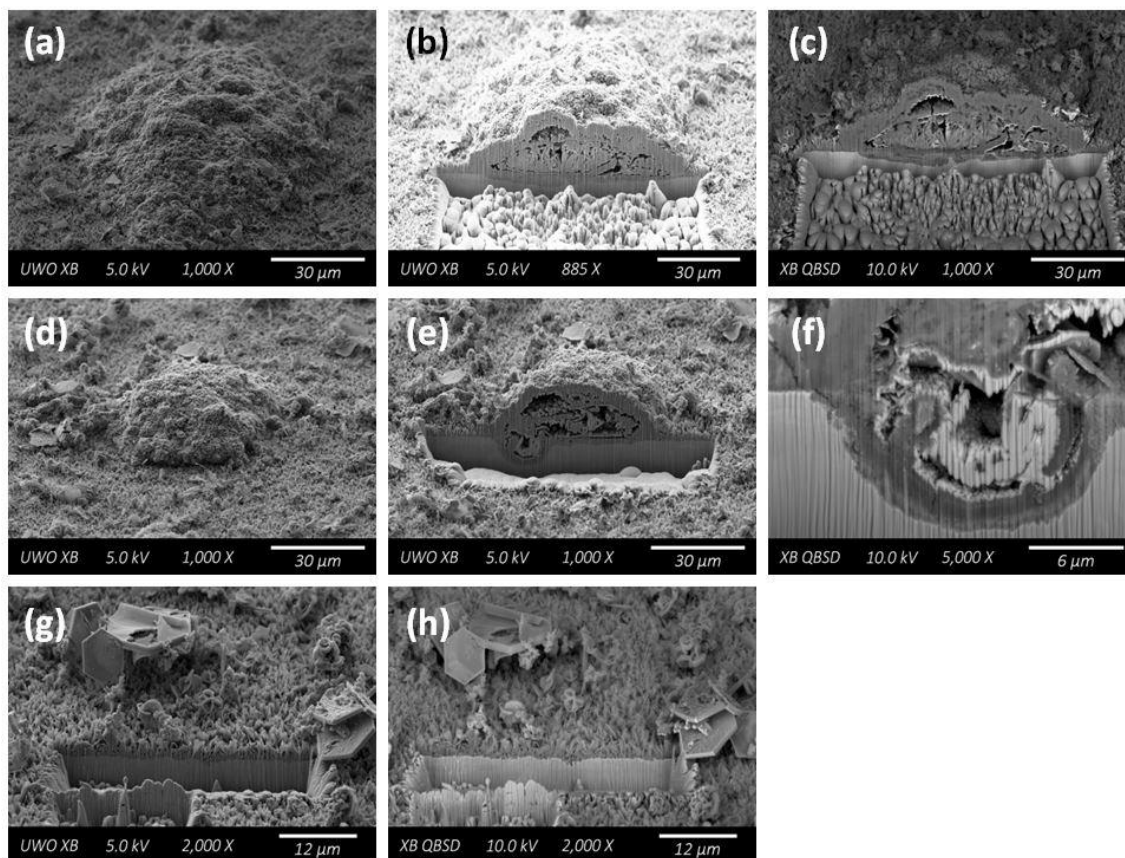


Figure 6-49: FIB cross-section micrographs recorded on a steel specimen after 546 days of exposure to solution (iii) showing: (a-c) a cut through a localized deposit indicating a more active location with shallow penetration shown in the backscatter image (c); (d-f) a cut through a region with significant penetration indicating an active pitting process had occurred; (g-h) a cut through the general $\text{Fe}_2(\text{OH})_2\text{CO}_3$ film showing that its thickness has remained unchanged.

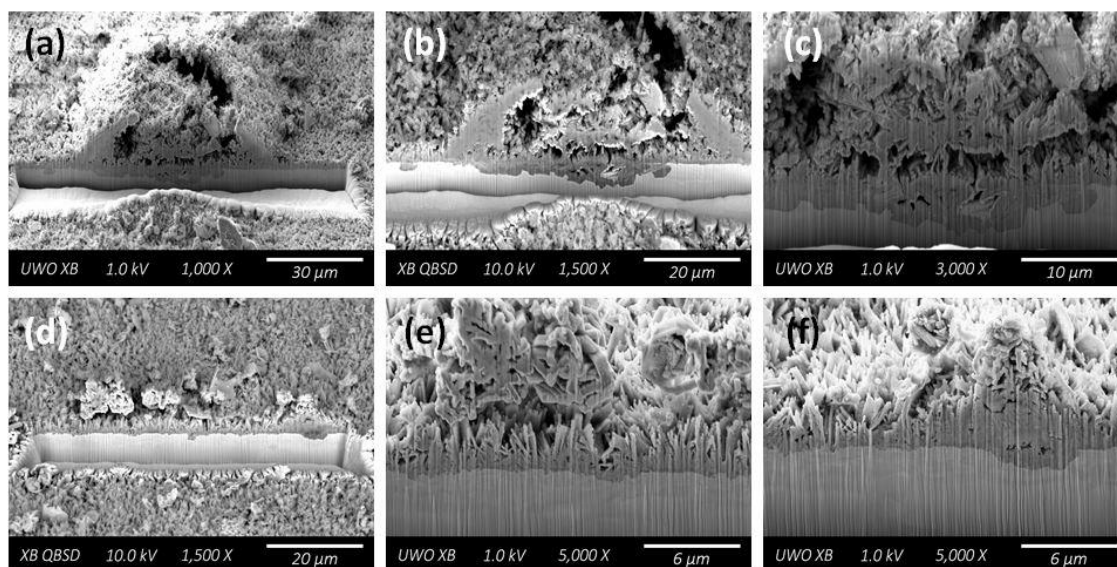


Figure 6-50: FIB cross-section micrographs recorded on a steel specimen after 639 days of exposure to solution (iii) showing: (a-c) a cut through a large deposit showing the film at this location to be porous and suggesting this site remained active; (d-f) a cut through the general $\text{Fe}_2(\text{OH})_2\text{CO}_3$ covered surface which shows little penetration into the metal. The backscatter images in (b), and (d) highlight the interface between the base metal (bright) and oxide film (dark).

6.3.4. Solution (iv): Simulated Groundwater Solution

6.3.4.1. Raman Spectroscopy

Figure 6-51 shows the Raman spectra recorded on the specimen exposed for 5 days to solution (iv). The minor Raman bands found at 426 and 502 cm^{-1} in spectrum (1) are attributable to GR, but the lack of any other Raman bands makes determination of the coordinating interlayer anion difficult. It is possible that, due to the complex nature of the simulated groundwater solution, any one of OH^- , Cl^- , CO_3^{2-} , and SO_4^{2-} could contribute to the GR structure. Spectrum (2) is consistent with Raman spectra observed for CaSO_4 (gypsum) [29]. The internal modes of the SO_4^{2-} anion can be assigned to Raman bands at 415 and 494 cm^{-1} for the ν_2 out-of-plane bending mode, the bands at 619 and 670 cm^{-1} to the ν_4 in-plane bending mode, 1008 cm^{-1} to the ν_1 symmetric stretching, and 1136 cm^{-1} to the ν_3 asymmetric stretching. The very small peak at 1008 cm^{-1} in spectrum (3) confirms the formation of CaSO_4 , with the remaining Raman bands indicating the formation of the CaCO_3 polymorph, aragonite [5, 30]. Previously, in Chapter 5, it was shown that a steel coupon exposed to a similar simulated groundwater solution for 60 days was covered with vaterite, another polymorph of CaCO_3 . Since the Raman spectra for each polymorph (including calcite) differ it is possible to distinguish between them. While the Raman bands located at 152 and 1085 cm^{-1} in spectrum (3) could be attributed to aragonite or calcite, the bands at 206 cm^{-1} and 704 cm^{-1} confirm the formation of aragonite. The bands at 152 and 206 cm^{-1} are attributed to the rotational and translational lattice modes of the CaCO_3 structure while the bands at 704 and 1085 cm^{-1} are due to the ν_4 in-plane bending and ν_1 symmetric stretching, respectively. Spectrum (4) indicates a mixture of both CaSO_4 (Raman bands 415, 494, 619, 670, 1008, and 1136 cm^{-1}) and aragonite (Raman bands 208 and 1084 cm^{-1}) is present. The persistence of minor peaks for GR in most of the spectra indicates that the surface is not fully protected by the CaSO_4 and CaCO_3 deposits over this early exposure period.

After an exposure period of 42 days the Raman spectra confirm the presence of GR (432 and 511 cm^{-1}) and the non-uniform presence of CaSO_4 and CaCO_3 , Figure 6-52. However, the addition of a band at 672 cm^{-1} in spectra (3) and (4) indicates formation of Fe_3O_4 , and the peaks at 1135 and 1600 cm^{-1} in spectrum (4) show the residual Fe_3C from corroded pearlite grains is just detectable.

After an exposure period of 110 days, Figure 6-53, Fe_3O_4 (676 cm^{-1}) becomes detectable at many locations while the bands for GR are no longer observed. Spectrum (3) shows that when CaSO_4 and CaCO_3 are not present (no bands at 1010 and 1084 cm^{-1}) the underlying corroded surface is visible (peaks at 1347 and 1604 cm^{-1} in region (3)). Spectra (4-6) indicate that when CaSO_4 and CaCO_3 are dominant on the surface the corrosion products on the underlying steel surface cannot be detected. The decrease in the relative peak height (1010 cm^{-1} for CaSO_4) to that for CaCO_3 (1084 cm^{-1}) suggests an on-going formation of CaCO_3 or a redissolution of CaSO_4 .

After a period of 728 days exposure, Figure 6-54, Raman bands for CaSO_4 and CaCO_3 are no longer present. Instead spectra (1-5) all exhibit Raman bands at 533 - 550 cm^{-1} and 668 - 679 cm^{-1} , consistent with the presence of Fe_3O_4 [3, 5, 7]. However, the broadness and relatively low intensity of the peaks suggest that the Fe_3O_4 is neither highly crystalline nor very thick contrary to what might be expected after such a prolonged exposure period. This observation suggests continued coverage of the surface by CaSO_4 and CaCO_3 crystals may have hindered steel corrosion leading to the growth of the Fe_3O_4 film. After the full 910 day exposure period, Figure 6-55, the surface is free of any CaSO_4 or CaCO_3 deposits. The very weak and broad band at 549 cm^{-1} can be attributed to poorly crystalline Fe_3O_4 , suggesting its growth has been severely hindered by the early presence of $\text{CaSO}_4/\text{CaCO}_3$. The peaks at 1300 - 1400 cm^{-1} and 1615 cm^{-1} , attributable to residual Fe_3C on corroded pearlite grains, confirm observable corrosion has occurred.

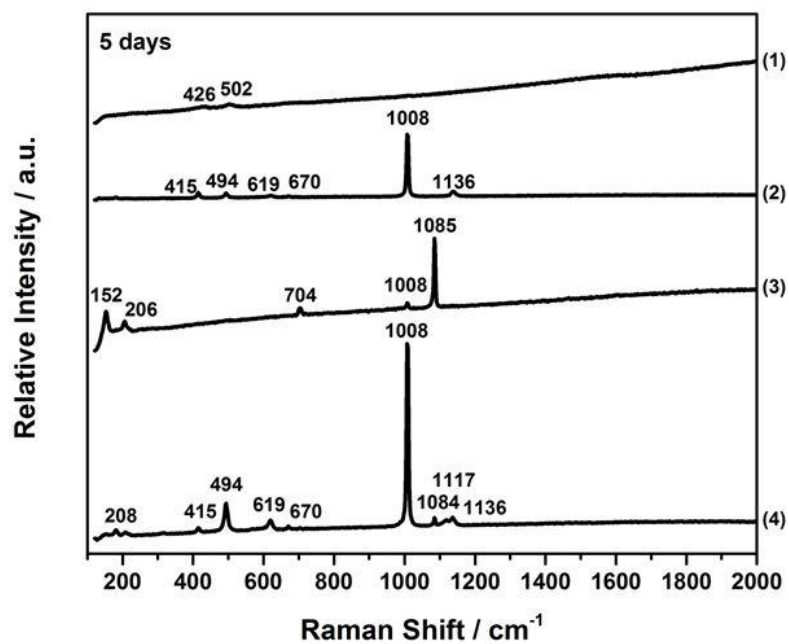


Figure 6-51: Raman spectra (1-4) recorded at various locations on a steel specimen after 5 days of exposure to solution (iv).

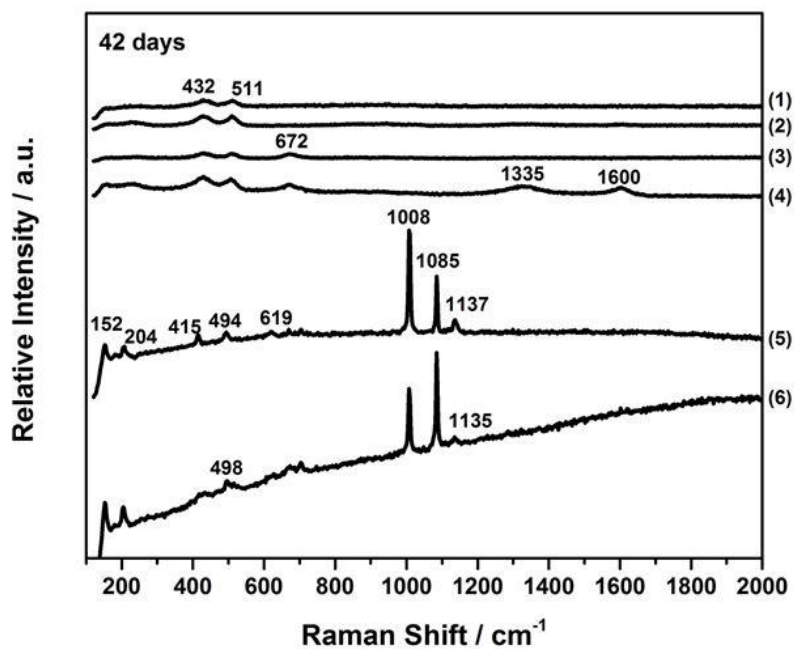


Figure 6-52: Raman spectra (1-6) recorded at various locations on a steel specimen after 42 days of exposure to solution (iv).

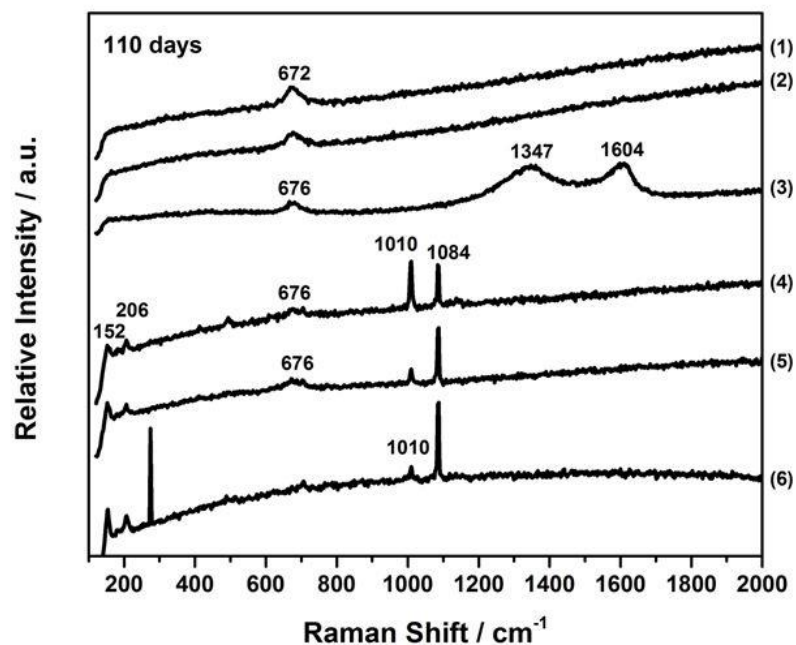


Figure 6-53: Raman spectra (1-6) recorded at various locations on a steel specimen after 110 days of exposure to solution (iv).

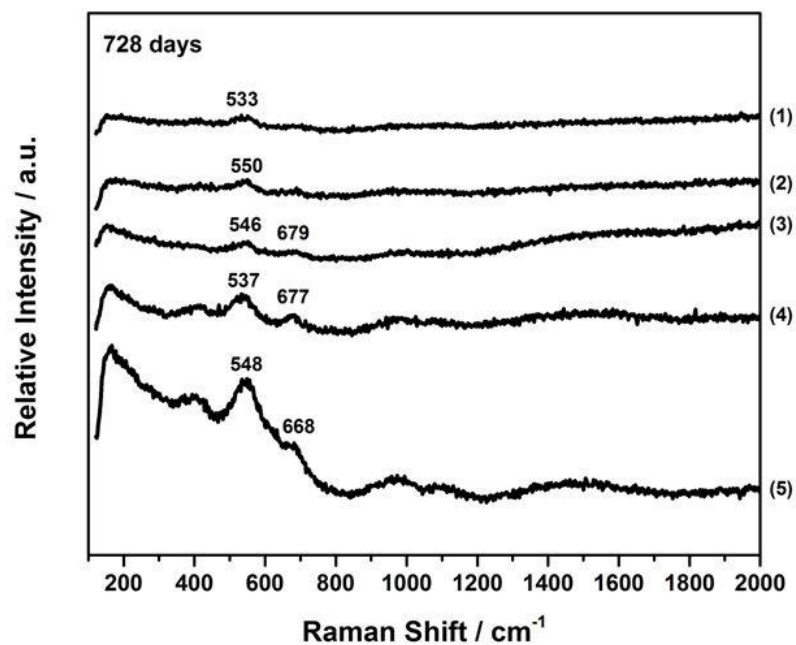


Figure 6-54: Raman spectra (1-5) recorded at various locations on a steel specimen after 728 days of exposure to solution (iv).

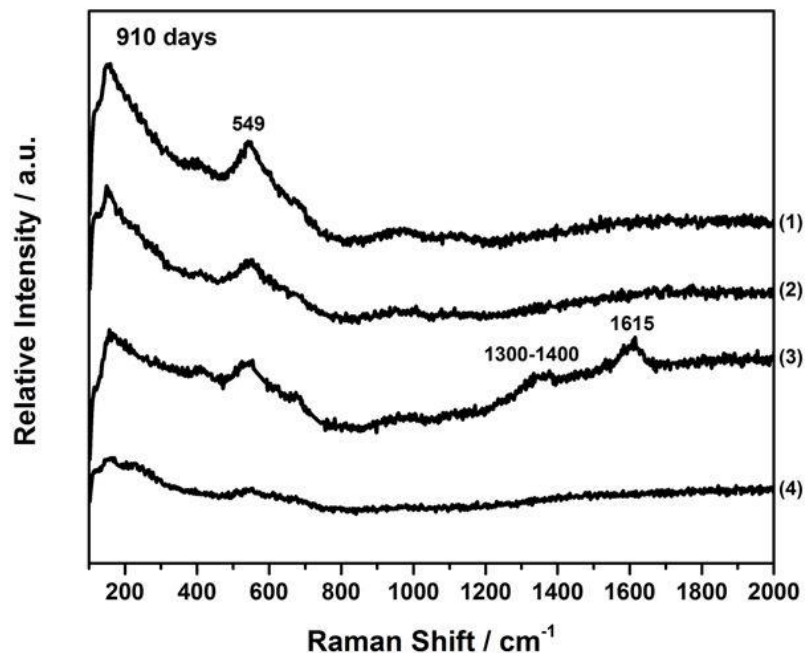


Figure 6-55: Raman spectra (1-4) recorded at various locations on a steel specimen after 910 days of exposure to solution (iv).

6.3.4.2. Scanning Electron Microscopy

Figure 6-56(a-c) shows the extent of coverage by the CaSO_4 and CaCO_3 after an exposure period of only 5 days. The fine morphology of the crystal structures can be seen in Figure 6-56(d-f). The long rectangular crystals are the expected structure for CaSO_4 and the star-shaped crystals are the expected structure of aragonite. The finely detailed spheres, Figure 6-56(f), are likely a polymorph of CaCO_3 associated with the aragonite crystals seen growing in close proximity. Alternatively, they could be calcite, or possibly vaterite, the latter having been seen in electrochemical experiments performed in a similar solution in Chapter 5. Figure 6-56(g-i) shows an area of exposed steel which exhibits the surface roughening seen on the surfaces corroded in the Cl^- only solutions. The emerging crystalline corrosion product seen in Figure 6-56(i) is likely the GR identified by Raman analysis.

After 42 days the underlying metal surface is almost completely obscured by the CaSO_4 and CaCO_3 crystals, Figure 6-57. After 56 days this coverage persists, Figure 6-58, but some regions

of the steel surface are visible and appear corroded, Figure 6-58(b-c), exhibiting a roughness similar to that observed on a specimen corroded in a similar solution (solution (iv)) in Chapter 5, on which Fe_3O_4 was observed under a deposit of vaterite crystals.

After 728 days the surface is clear of $\text{CaSO}_4/\text{CaCO}_3$ crystals which have redissolved, Figure 6-59. The visible surface shows a coherent oxide layer (Figure 6-59(a-c) and (d-f)), and a significant corrosion product deposit (Figure 6-59(g-i)). The morphology of the general film, as well as the deposits, resembles those seen for the Fe_3O_4 film formed over an extended period of time in solution (ii) containing a similar $[\text{Cl}^-]$. The apparently amorphous nature of the film would explain the broad and low intensity Raman bands observed for Fe_3O_4 . Figure 6-60 shows that after the full exposure period of 910 days the corrosion product morphology remains unchanged. An apparently thick and protective layer of Fe_3O_4 remains with a scattered deposit spread across the surface. The similarity of the composition and morphology of the films grown over extended time periods in both solution (ii) and (iv) confirm that, regardless of the crystal coverage, the corrosion behaviour is similar in the two concentrated Cl^- solutions and that the additional groundwater ions of solution (iv) do not play a strong role in the corrosion product identity and morphology.

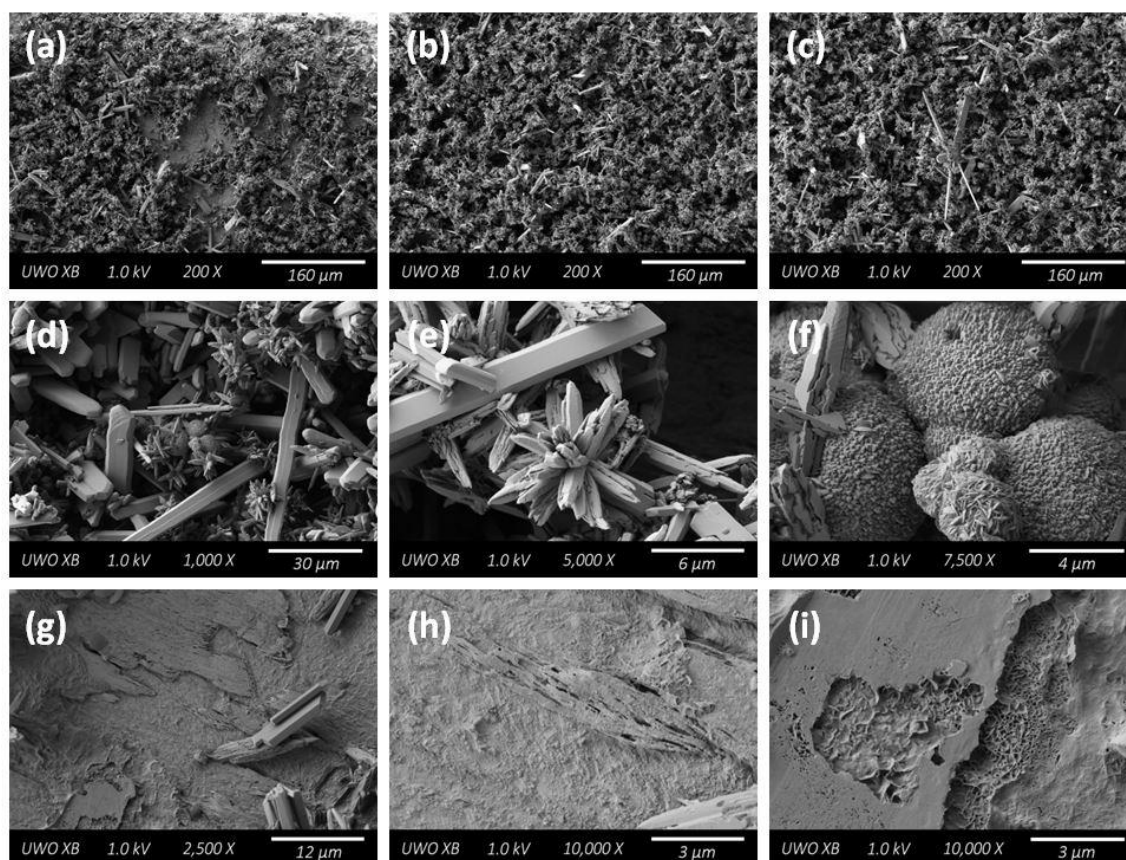


Figure 6-56: SEM micrographs recorded on a steel specimen after 5 days of exposure to solution (iv) showing: (a-c) the extend of CaSO_4 and CaCO_3 crystal coverage; (d-f) the fine crystal morphology with the long rectangular crystals the expected structure of CaSO_4 and the star-shaped crystals the expected structure of CaCO_3 (aragonite); (g-i) a region of the exposed steel exhibiting a roughening of the surface.

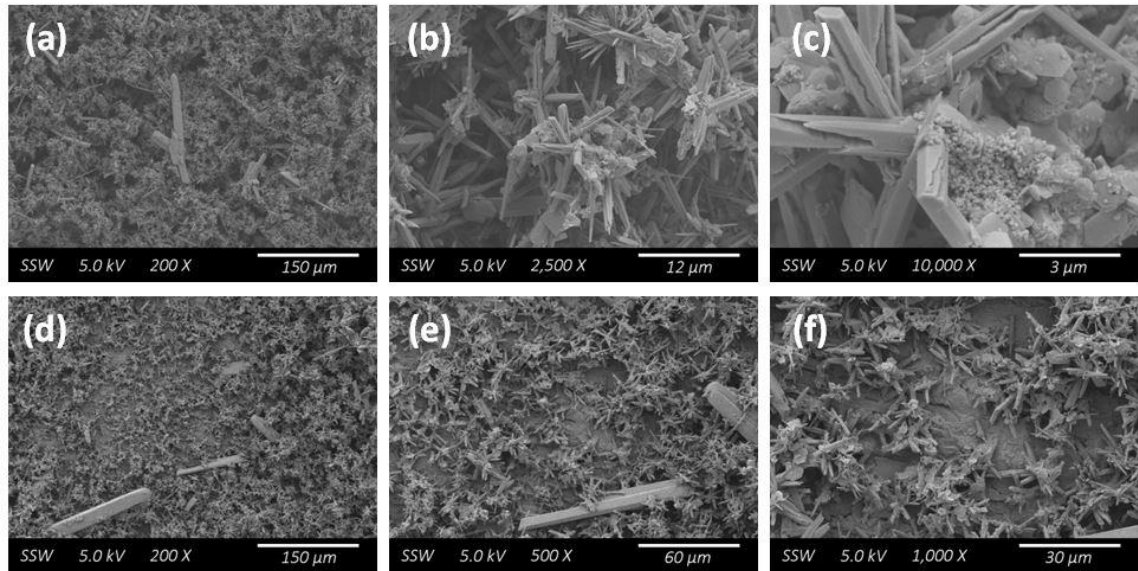


Figure 6-57: SEM micrographs recorded on a steel specimen after 42 days of exposure to solution (iv) showing that the underlying steel surface is almost completely obscured by the CaSO_4 and CaCO_3 crystals.

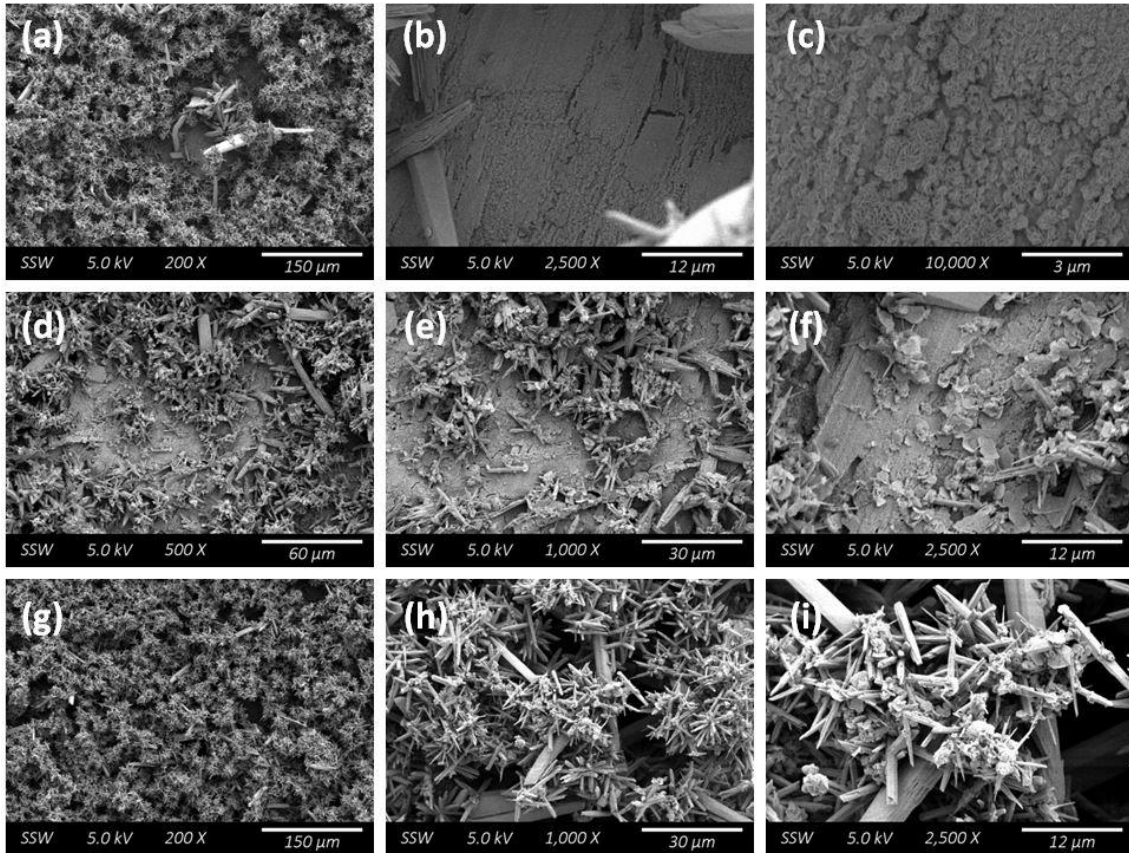


Figure 6-58: SEM micrographs recorded on a steel specimen after 56 days of exposure to solution (iv) showing that the crystal coverage continues while regions of visible surface (b-c) appear roughened.

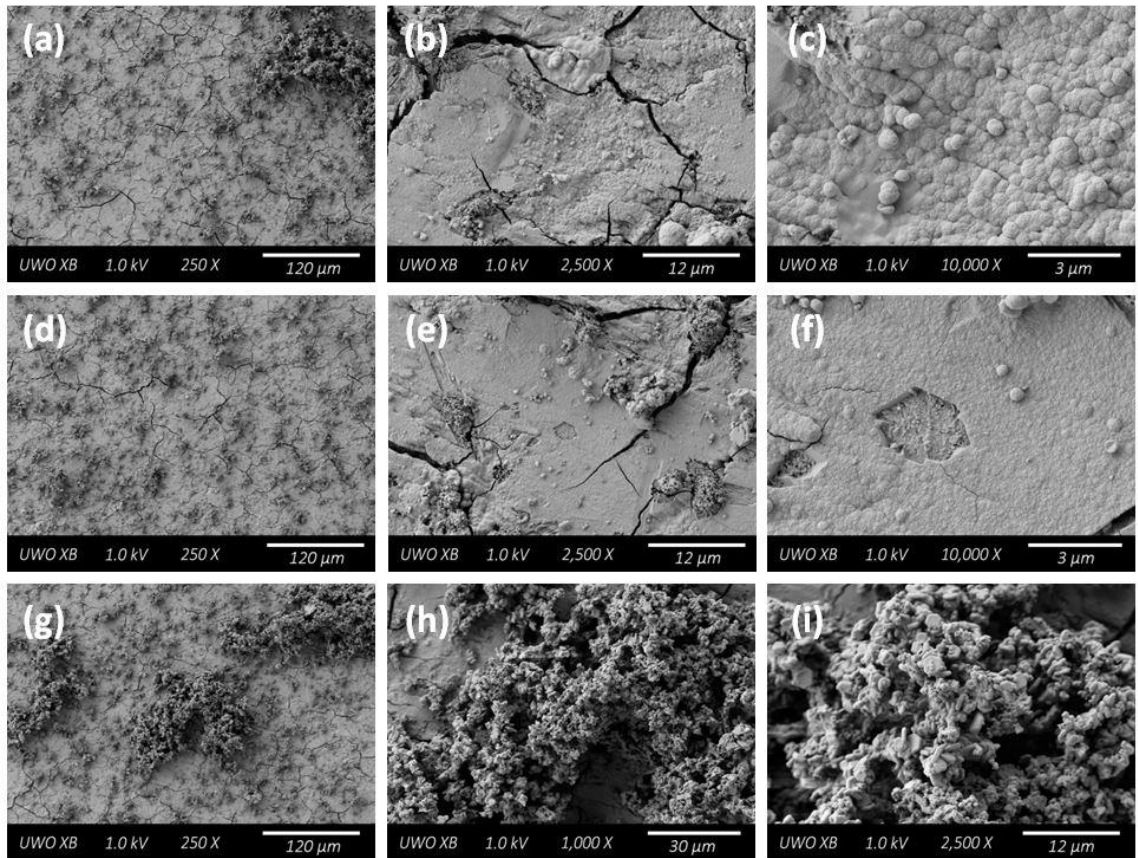


Figure 6-59: SEM micrographs recorded on a steel specimen after 728 days of exposure to solution (iv) showing: (a-f) the visible surface which exhibits a coherent oxide layer; (g-i) a region with a significant corrosion product deposit.

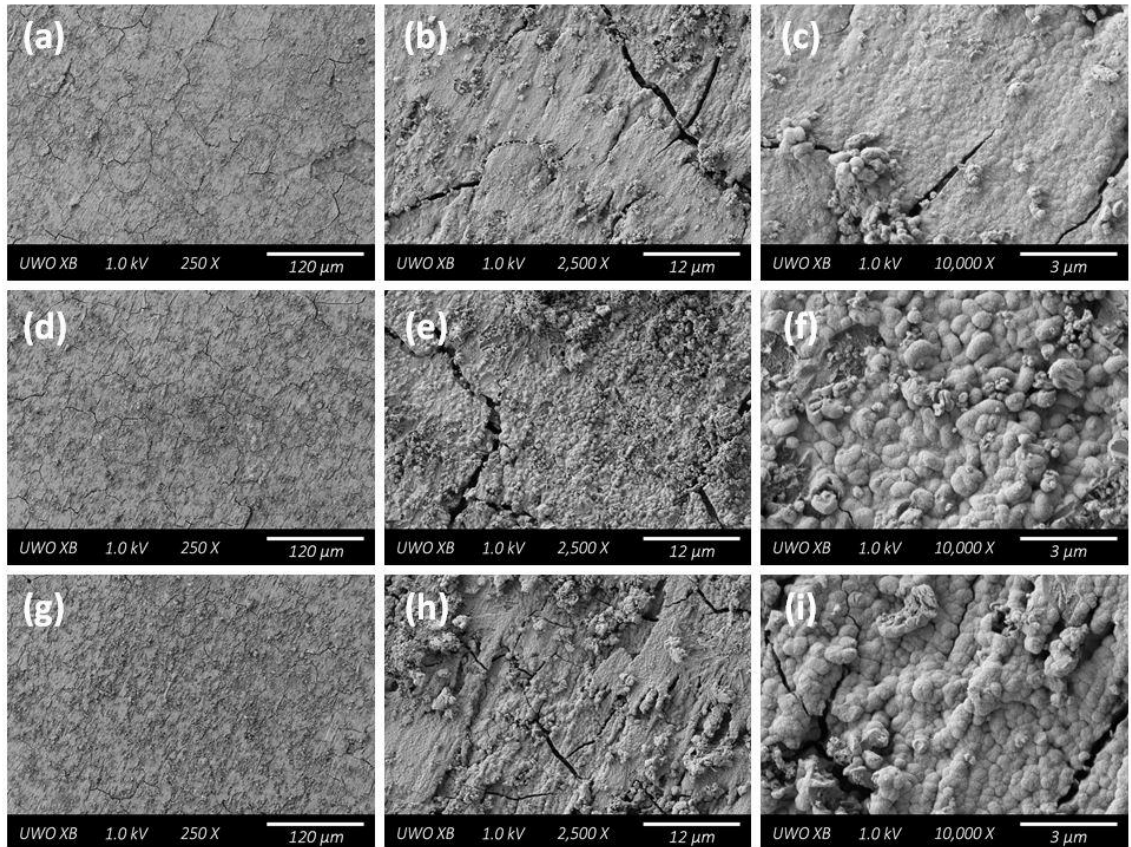


Figure 6-60: SEM micrographs recorded on a steel specimen after 910 days of exposure to solution (iv) showing an apparently thick protective layer of Fe_3O_4 with scattered corrosion deposits.

6.3.4.3. *Focused Ion Beam Milling*

Due to the coverage of the steel surface by the CaSO_4 and CaCO_3 crystals, the cutting of FIB cross-sections was not possible for samples extracted prior to 728 days of exposure. Figure 6-61 shows the FIB cross-sections for two locations on the steel surface after 728 days. Cross-sectioning through both the deposit (Figure 6-61(a-c)) and the more generally covered surface (Figure 6-61(d-f)) showed that no significantly greater penetration into the steel occurred under the deposit but some regions of the general surface appeared to be more extensively corroded than others. This is in contrast to samples removed at a similar time interval from solution (ii) (with a similar $[\text{Cl}^-]$) in which the corrosion across the general surface was more-or-less uniform. However, the characteristic bands of Fe_3C left behind by the corrosion of the pearlite structure can be seen within the oxide film, Figure 6-61(e-f).

Figure 6-62 shows the FIB cross-sections after the full exposure period of 910 days. The cross-sections show considerable void space appears between the corrosion product deposit and the steel substrate. Backscatter images, Figure 6-62(b) and (d), highlight the separation between the oxide film and base metal. The depth of penetration appears similar to that on the sample exposed for 728 days. The delamination of the film from the steel may be due to the drying out process when the specimen was extracted from the solution. Comparison of images of these specimens to those for specimens exposed to solution (ii) indicates more extensive corrosion occurred in the absence of the groundwater species. This may be due to protection of the steel due to the deposition of CaSO_4 and CaCO_3 . Only after the crystals have redissolved was active corrosion of the base metal visible.

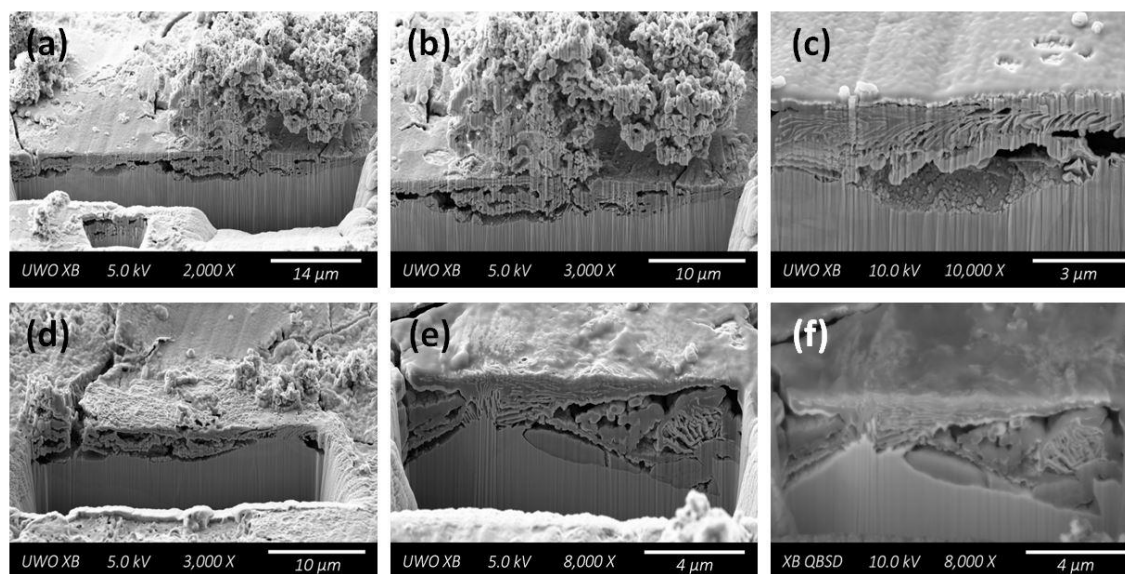


Figure 6-61: FIB cross-section micrographs recorded on a steel specimen after 728 days of exposure to solution (iv) showing: (a-c) a cut through a localized deposit showing some undercutting of the substrate; (d-f) a cut through a general corroded region showing no significant penetration into the steel. The backscatter image in (f) highlights the interface between the base metal (bright) and oxide film (dark).

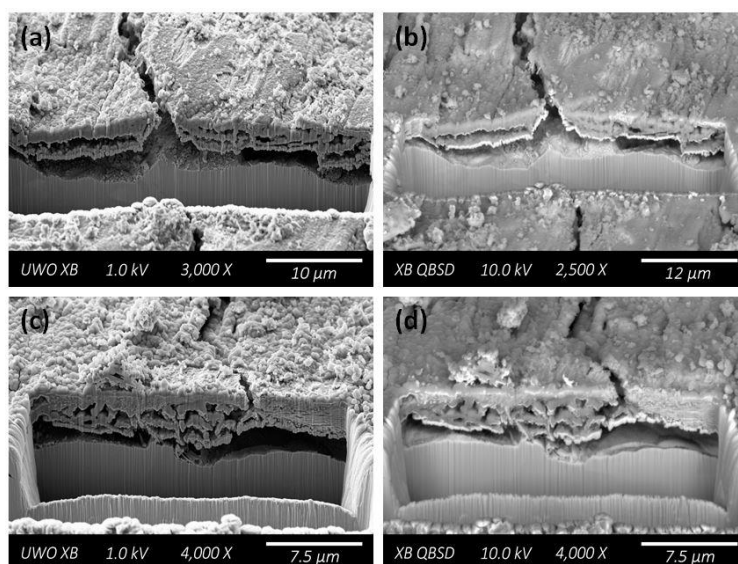
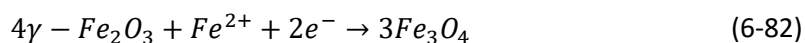


Figure 6-62: FIB cross-section micrographs recorded on a steel specimen after 910 days of exposure to solution (iv) showing regions exhibiting considerable void space between the product and substrate. Backscatter images (b, d) highlight the separation of the oxide film (dark) and the base metal (bright).

6.4. DISCUSSION

In the solutions dominated by Cl^- the evolution of the corrosion process can be directly observed since the additional anions present in the other solutions do not obscure the changes on the surface due to corrosion. Due to the prior exposure of the specimens to a humid laboratory atmosphere the surfaces are already visibly corroded prior to first immersion. The dominant surface corrosion layer is $\gamma\text{-Fe}_2\text{O}_3$ and some areas of the surface, possibly those associated with pearlite grains, are already visibly more corroded than others.

Over the first ~ 50 days this $\gamma\text{-Fe}_2\text{O}_3$ disappears most likely via its reduction driven by galvanic coupling to the corroding steel substrate. This would be consistent with the claims of Stratmann et al. [31] who proposed that in anoxic environments, such as periods of high water content in the pore structure of rusts formed during wet/dry cycling, the dissolution of iron metal is balanced by the reduction of Fe^{III} oxides within the rust layers. In our experiments this reductive dissolution of the Fe^{III} oxides could occur in the acidic conditions (6.3 ± 0.5) used which, according to Stratmann et al. [31] would lead to the reduction of $\gamma\text{-Fe}_2\text{O}_3$ to Fe_3O_4 via the following mechanism:



At the pH used in our experiments the solubility of Fe^{2+} would be high, which would kinetically favour reaction 6-82. In addition, this is facilitated by the similarity in crystal structures of the two oxides. Both exhibit inverse spinel structures in which the O^{2-} sub-lattices are almost identical, the only difference being the slightly different octahedral and tetrahedral holes occupied by the $\text{Fe}^{2+}/\text{Fe}^{3+}$ cations [31, 32].

After ~ 100 days, Fe_3O_4 is the dominant surface phase and appears to be present as a uniformly distributed film. Also, only minor amounts of deposited oxide are observed over moderate exposure periods (up to ~ 250 days) but a significant deposit accumulates over extended exposure periods. These observations are not unexpected since the Fe^{2+} solubility is quite high at pH 6.3.

Corrosion appears to be preferentially located at pearlite grains, the cross-sectional analysis of the samples exposed for extended periods of time (252 to 910 days) showing the remnants of

Fe₃C bands from the original pearlite structure of the steel coupon. This was particularly evident as bright bands within the darker oxide layer as shown in the cross-section in Figure 6-34(e). EDX mapping of this location showed a coincidence in the signals for both elemental Fe and C, confirming the presence of Fe₃C inside the surrounding Fe₃O₄ film, Figure 6-34(f). Several authors have stated that the Fe₃C of the pearlite structure has a lower overpotential for the cathodic reaction than the surrounding α -Fe and could, therefore, support microgalvanic coupling by accelerating the cathodic reaction leading to the preferential dissolution of the α -Fe in the pearlite grains [33-37]. The conversion of α -Fe lamellae to Fe₃O₄ leads eventually to the Fe₃C bands being entrapped within the oxide. While this process is most evident in Figure 6-34(e-f), it can be seen within most of the FIB cross-sections suggesting that this process has occurred uniformly at pearlite grains across the entire sample surface.

Some authors have suggested that exposure of Fe₃C causes an acceleration in the corrosion rate in this manner [35, 36]. However, this acceleration may only be temporary since, as claimed by others [37], the corrosion rate would eventually be suppressed by the accumulation of Fe₃O₄ within the reduced Fe₃C lamellae. However, bands within the already conductive Fe₃O₄ facilitate the coupling of these locations as cathodes supporting corrosion of α -Fe grains [36]. The observation of some apparent intergranular corrosion between grains may support this claim. This intergranular effect was most apparent in Figure 6-19(c) and may be involved in the creation of the void space beneath the corrosion product layer, Figure 6-19(g-i).

The early behaviour in the dilute (solution (i)) and concentrated (solution (ii)) chloride solutions is effectively the same. This is not unexpected under anoxic conditions, the results in Chapter 4 showing that this difference in [Cl⁻] was only important when traces of dissolved O₂ were present when a Cl⁻ catalyzed passivation of the surface could occur at the higher concentration. However, the O₂ incursion which occurred after 182 days in the high [Cl⁻] solution did lead to a change in behaviour between the two solutions. As expected, oxidation to γ -Fe₂O₃, and possibly other Fe oxyhydroxides, was observed. Subsequently, the consequences of this change in redox conditions were observable over the following 718 days. The final general corrosion product layer was thicker than in the low [Cl⁻] solution. This can be attributed partially to the extended exposure period but also to the increase in overall extent of corrosion due to the availability of an increased O₂ inventory. However, while the Raman analyses show oxidation to γ -Fe₂O₃ occurs as a consequence of the presence of O₂, it also shows that eventually Fe₃O₄ is re-established as

the dominant corrosion product. This can be attributed to the microgalvanic coupling of $\gamma\text{-Fe}_2\text{O}_3$ reduction to Fe_3O_4 to Fe dissolution as described above. Unfortunately, the deconvolution of the Raman spectra in region (1) becomes too unreliable to demonstrate the effectiveness of this conversion. The slow accumulation of deposited particulates can also be attributed to the temporary establishment of more oxidizing conditions which lead to the oxidation of soluble Fe^{2+} and the deposition of the considerably less soluble Fe^{3+} .

In the presence of $\text{HCO}_3^-/\text{CO}_3^{2-}$ (solution (iii)) the surface rapidly becomes covered by $\text{Fe}_2(\text{OH})_2\text{CO}_3$, although the formation of GR is observed after short exposure periods. It is possible that the formation of GR can be attributed to trace levels of O_2 in the solution and catalysis of the oxidation of Fe^{2+} to Fe^{3+} reaction at the high $[\text{Cl}^-]$ [38-48]. Since GR is metastable with respect to Fe_3O_4 , especially as conditions become more anoxic, Fe_3O_4 is probably partially formed as a conversion product of the GR dehydration and oxidation [1, 49] accounting for its disappearance beyond short exposure periods.

While $\text{Fe}_2(\text{OH})_2\text{CO}_3$ was expected to form, based on the observation that it was formed in shorter (60 days) experiments as described in Chapter 5, its formation in this experiment was considerably faster. The freshly polished steel coupon exposed to solution (iii) (Chapter 5) only slowly grew an interfacial layer of Fe_3O_4 followed by the slow accumulation of an outer $\text{Fe}_2(\text{OH})_2\text{CO}_3$ layer. For the specimens described in this chapter the surface was already partially covered with a thin $\gamma\text{-Fe}_2\text{O}_3$ layer formed by humid air exposure prior to immersion. It is likely that the high $[\text{Fe}^{2+}]$, caused by the conversion of this oxide to Fe_3O_4 coupled to dissolution in the presence of $[\text{HCO}_3^-/\text{CO}_3^{2-}]$ at a pH >8.9, promoted the formation of $\text{Fe}_2(\text{OH})_2\text{CO}_3$ over other iron carbonates such as FeCO_3 [23, 24, 26, 50-53]. ICP-OES analysis of the solution after a period of roughly 252 days showed no detectable traces of dissolved iron in the solution. This indicates that the available Fe^{2+} is rapidly converted to $\text{Fe}_2(\text{OH})_2\text{CO}_3$.

The combination of an inner Fe_3O_4 interfacial layer on the metal surface with an outer $\text{Fe}_2(\text{OH})_2\text{CO}_3$ layer would offer an explanation of the corrosion kinetics and the growth of the film over the full 639 day period. Thin interfacial layers of $\text{Fe}_3\text{O}_4/\gamma\text{-Fe}_2\text{O}_3$ are well known to control the kinetics of iron corrosion [54, 55], and it has been suggested that the protective nature of a $\text{Fe}_2(\text{OH})_2\text{CO}_3$ film can be attributed to the presence of a thin underlying spinel oxide layer [52, 54-56]. The SEM images and FIB cross-sections of samples exposed for the full 639 day exposure period indicated a constant corrosion rate since the corrosion product layer did not

thicken with exposure time, Figure 6-48(b) and Figure 6-49(h). This observation is consistent with published results [57] that showed a constant corrosion rate for iron in carbonated media due to the parallel growth and dissolution of an interfacial spinel layer on the metal surface.

The eventual formation of cubic and multi-faceted cubic crystals within the $\text{Fe}_2(\text{OH})_2\text{CO}_3$ film after 109 days exposure and their persistence for the duration of the experiment suggests the eventual conversion of $\text{Fe}_2(\text{OH})_2\text{CO}_3$ to FeCO_3 . The metastable nature of $\text{Fe}_2(\text{OH})_2\text{CO}_3$ with respect to FeCO_3 over extended periods of time is thought to be responsible for the formation of $\text{Fe}_2(\text{OH})_2\text{CO}_3$ and FeCO_3 strata on archaeological artefacts exposed to carbonated media [23, 24, 26, 53, 55]. The metastable nature of $\text{Fe}_2(\text{OH})_2\text{CO}_3$ with respect to FeCO_3 is illustrated by the Pourbaix diagram in Figure 6-63 [26]. FeCO_3 ingrowths in $\text{Fe}_2(\text{OH})_2\text{CO}_3$ corrosion products have previously been seen on multiple natural samples [22, 58].

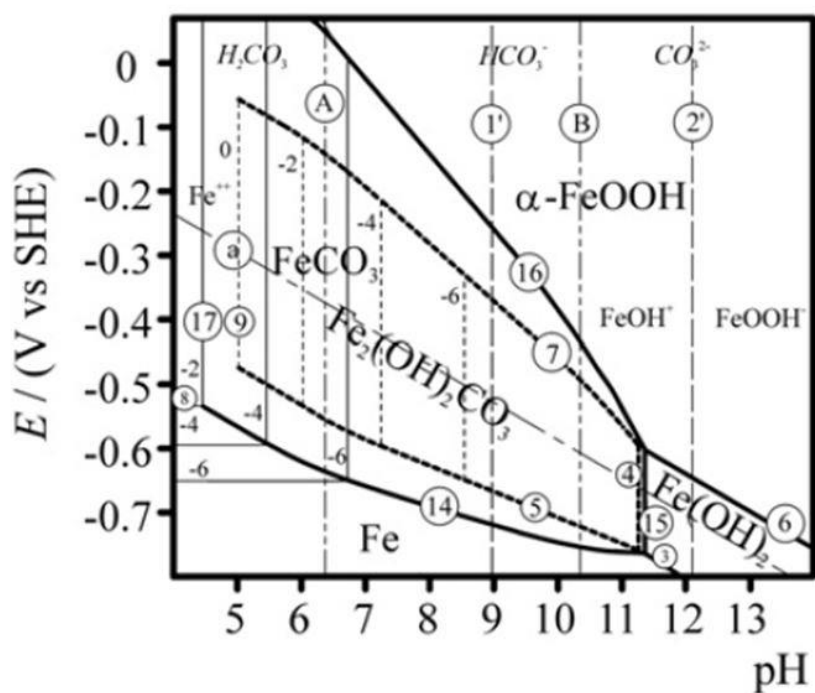


Figure 6-63: Pourbaix diagram of iron in carbonated aqueous media at 25°C for equilibria involving $\text{Fe}_2(\text{OH})_2\text{CO}_3$ (dotted lines) and FeCO_3 (solid lines) [26].

Pandarínathan et al. [53] have reported that defects within the corrosion layers, as well as mixed oxides of $\text{Fe}_2(\text{OH})_2\text{CO}_3$ and FeCO_3 , have the ability to induce localized corrosion and pitting processes, which could account for the localized corrosion events seen in Figure 6-48 to Figure 6-50, after 252, 546, and 639 days of exposure. Their voltammetric measurements on steel exposed to carbonated media under a simulated sand deposit showed a positive hysteresis in the reverse scan taken to indicate the development of the active locations shown to exist by SEM.

In the simulated groundwater solution the rapid formation of gypsum (CaSO_4) and aragonite (CaCO_3) deposits in as little as 2 days (Appendix A) obscures the early stages of any corrosion processes, although the presence of GR is detectable. The development of CaCO_3 deposits have been linked to reduced corrosion rates on steel surfaces due to their ability to act as a physical barrier blocking the surface from oxidizing species [59-63].

The composition of the exposure solution influences which of the polymorphs (calcite, aragonite, vaterite) will form and the nature of the steel surface affects the morphology and the rate of coverage [59, 61]. The development of aragonite over calcite is thought to increase the corrosion resistance of the base metal due to its better adhesion to the metal surface compared to calcite [63]. Previous authors have suggested that the presence of Mg^{2+} can promote the formation of aragonite over calcite in freely corroding systems [60-63]. Ben Amor et al. [61] suggest that aragonite may form exclusively when $[\text{Mg}^{2+}] \geq 0.27 \text{ M}$. The high $[\text{Mg}^{2+}]$ in the simulated groundwater (0.337 M) could then explain why the only polymorph to form on the sample surface was aragonite. At low $[\text{Mg}^{2+}]$ the Mg^{2+} ions are adsorbed onto the surface of calcite nuclei and block their further growth. At higher $[\text{Mg}^{2+}]$ the Mg^{2+} ions can be partially incorporated into the calcite crystal structure increasing its solubility and decreasing its ability to provide surface protection [63]. However, Mg^{2+} ions have no apparent effect on the growth of aragonite, and it is the hindrance of calcite formation which promotes the formation of aragonite. Moller [60] reported a reduction in steel corrosion rates in the presence of Mg^{2+} compared to rates measured in an identical solution without Mg^{2+} . This reduction in rate was attributed to aragonite formation promoted by Mg^{2+} leading to a more comprehensive coverage of the surface and a limitation of the diffusion of oxidants to the surface.

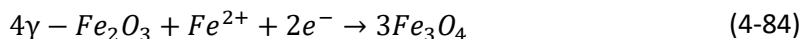
The high density of aragonite crystals grown in the simulated groundwater (solution (iv)) appear to impede, at least initially, the steel corrosion rate which would explain the difference in

corrosion product morphology and thickness after exposure to solutions (ii) and (iv), which differ only in the addition of the added groundwater ions such as Ca^{2+} and Mg^{2+} . However, while the crystal coverage may appear complete, EIS studies have shown corrosion could occur [61]. In our experiment this would explain the detection of GR and Fe_3O_4 over the initial 110 day exposure period and the continued growth of Fe_3O_4 until the conclusion of the exposure term at 910 days. That corrosion had occurred was confirmed by the Raman and SEM analyses once the CaSO_4 and CaCO_3 had redissolved.

6.5. SUMMARY AND CONCLUSIONS

The long-term corrosion behaviour of steel was investigated in solutions which varied in $[\text{Cl}^-]$ and pH as well as in a simulated sedimentary groundwater solution. These studies are meant to be complimentary to the electrochemical experiments outlined in Chapter 5.

The initial surface layer, present on first immersion, was shown to be $\gamma\text{-Fe}_2\text{O}_3$, formed as a result of humid air exposure prior to immersion. Over the first 100 days of exposure this film was reduced to Fe_3O_4 by galvanic coupling to the dissolution of the steel substrate,



with the high solubility of Fe^{2+} at the experimental pH kinetically promoting the conversion. Corrosion appeared to be preferentially located at pearlite grains with oxide accumulating in the Fe_3C bands as the $\alpha\text{-Fe}$ lamellae were converted to Fe_3O_4 . This preferential corrosion of pearlite can be attributed to the lower overpotential of Fe_3C lamellae for the cathodic reaction allowing them to act as preferential cathodes. However, this process may be suppressed over time by the slow accumulation of an Fe_3O_4 layer on the surface and within the Fe_3C lamellae.

While the corrosion in solutions (i) and (ii) was very similar in the initial stages, an incursion of O_2 caused a change in behaviour for solution (ii) which was shown to develop $\gamma\text{-Fe}_2\text{O}_3$ corrosion products as well as a generally thicker corrosion product layer. However, Fe_3O_4 was eventually established as the dominant corrosion product, confirming the microgalvanic coupling of $\gamma\text{-Fe}_2\text{O}_3$ reduction to Fe_3O_4 to Fe dissolution.

The addition of $\text{HCO}_3^-/\text{CO}_3^{2-}$ leading to an increase in pH to 8.85 led to the rapid formation of $\text{Fe}_2(\text{OH})_2\text{CO}_3$. The more rapid growth of this layer (in comparison to that in a similar solution (Chapter 5)) was attributed to the initial $\gamma\text{-Fe}_2\text{O}_3$ layer formed via humid air exposure prior to immersion. The high local $[\text{Fe}^{2+}]$ produced by the reduction of this layer to Fe_3O_4 promoted the rapid formation of $\text{Fe}_2(\text{OH})_2\text{CO}_3$. The reduction of $\gamma\text{-Fe}_2\text{O}_3$ leading to the formation of an interfacial layer of Fe_3O_4 combined with the outer layer of $\text{Fe}_2(\text{OH})_2\text{CO}_3$ was shown to slow the corrosion kinetics. The protective nature of $\text{Fe}_2(\text{OH})_2\text{CO}_3$ has often been attributed to a thin interfacial spinel oxide layer as seen in these experiments. However, the eventual thermodynamic transformation of $\text{Fe}_2(\text{OH})_2\text{CO}_3$ to FeCO_3 , consistent with the strata formed on archaeological artefacts, appeared to induce some localized corrosion/pitting processes observed in SEM/FIB images.

Addition of anticipated groundwater ions caused the formation of CaSO_4 and CaCO_3 crystals in as little as 2 days, which, consistent with the findings described in Chapter 5, were shown to impede the steel corrosion due to their ability to provide a physical barrier between oxidizing species and the steel surface. This crystal coverage explains the differences in morphology and thickness of the corrosion product layers grown in solutions (ii) and (iv) (which have similar $[\text{Cl}^-]$). However, corrosion was shown to occur after the dissolution of the crystals in the form of GR and Fe_3O_4 . In addition, the high Mg^{2+} content of the groundwater solution was shown to promote the formation of aragonite, a CaCO_3 polymorph known to cause a reduction in steel corrosion rates.

6.6. REFERENCES

- [1] C. T. Lee, M. S. Odziemkowski and D. W. Shoesmith "An in situ Raman-electrochemical investigation of carbon steel corrosion in $\text{Na}_2\text{CO}_3/\text{NaHCO}_3$, Na_2SO_4 , and NaCl solutions" *Journal of the Electrochemical Society* 153 (2) (2006) B33-B41
- [2] P. Refait, M. Reffass, J. Landoulsi, R. Sabot and M. Jeannin "Role of phosphate species during the formation and transformation of the Fe(II-III) hydroxycarbonate green rust" *Colloids and Surfaces A: Physicochemical and Engineering Aspects* 299 (1-3) (2007) 29-37
- [3] D. de Faria, S. Silva and M. de Oliveira "Raman microspectroscopy of some iron oxides and oxyhydroxides" *Journal of Raman Spectroscopy* 28 (11) (1997) 873-878
- [4] D. Neff, P. Dillmann, L. Bellot-Gurlet and G. Beranger "Corrosion of iron archaeological artefacts in soil: Characterisation of the corrosion system" *Corrosion Science* 47 (2) (2005) 515-535
- [5] M. S. Odziemkowski, T. T. Schuhmacher, R. W. Gillham and E. J. Reardon "Mechanism of oxide film formation on iron in simulating groundwater solutions: Raman spectroscopic studies" *Corrosion Science* 40 (2-3) (1998) 371-389

- [6] R. Sabot, M. Jeannin, M. Gadouleau, Q. Guo, E. Sicre and P. Refait "Influence of lactate ions on the formation of rust" *Corrosion Science* 49 (3) **(2007)** 1610-1624
- [7] I. Chamritski and G. Burns "Infrared- and Raman-active phonons of magnetite, maghemite, and hematite: A computer simulation and spectroscopic study" *Journal of Physical Chemistry B* 109 (11) **(2005)** 4965-4968
- [8] L. J. Simpson and C. A. Melendres "Surface-enhanced Raman spectroelectrochemical studies of corrosion films on iron in aqueous carbonate solution" *Journal of the Electrochemical Society* 143 (7) **(1996)** 2146-2152
- [9] M. Hanesch "Raman spectroscopy of iron oxides and (oxy)hydroxides at low laser power and possible applications in environmental magnetic studies" *Geophysical Journal International* 177 (3) **(2009)** 941-948
- [10] K. Yazdanfar, X. Zhang, P. G. Keech, D. W. Shoesmith and J. C. Wren "Film conversion and breakdown processes on carbon steel in the presence of halides" *Corrosion Science* 52 (4) **(2010)** 1297-1304
- [11] G. V. M. Jacintho, P. Corio and J. C. Rubim "Surface-enhanced Raman spectra of magnetic nanoparticles adsorbed on a silver electrode" *Journal of Electroanalytical Chemistry* 603 (1) **(2007)** 27-34
- [12] N. Boucherit, A. H. L. Goff and S. Joiret "Raman studies of corrosion films grown on Fe and Fe-Mo in pitting conditions" *Corrosion Science* 32 (5-6) **(1991)** 497-507
- [13] S. Simard, M. Odziemkowski, D. E. Irish, L. Brossard and H. Menard "In situ micro-Raman spectroscopy to investigate pitting corrosion product of 1024 mild steel in phosphate and bicarbonate solutions containing chloride and sulfate ions" *Journal of Applied Electrochemistry* 31 (8) **(2001)** 913-920
- [14] P. Refait, M. Reffass, J. Landoulsi, R. Sabot and M. Jeannin "Role of nitrite species during the formation and transformation of the Fe(II-III) hydroxycarbonate green rust" *Colloids and Surfaces A: Physicochemical and Engineering Aspects* 459 **(2014)** 225-232
- [15] L. Legrand, G. Sagon, S. Lecomte, A. Chausse and R. Messina "A Raman and infrared study of a new carbonate green rust obtained by electrochemical way" *Corrosion Science* 43 (9) **(2001)** 1739-1749
- [16] P. H. Refait, M. Abdelmoula and J. M. R. Genin "Mechanisms of formation and structure of green rust one in aqueous corrosion of iron in the presence of chloride ions" *Corrosion Science* 40 (9) **(1998)** 1547-1560
- [17] P. Refait and J. M. R. Genin "The mechanisms of oxidation of ferrous hydroxychloride beta-Fe₂(OH)₃Cl in aqueous solution: The formation of akaganeite vs goethite" *Corrosion Science* 39 (3) **(1997)** 539-553
- [18] J. M. R. Genin, P. Refait, G. Bourrie, M. Abdelmoula and F. Trolard "Structure and stability of the Fe(II)-Fe(III) green rust "fougerite" mineral and its potential for reducing pollutants in soil solutions" *Applied Geochemistry* 16 (5) **(2001)** 559-570
- [19] B. W. A. Sherar, P. G. Keech, Z. Qin, F. King and D. W. Shoesmith "Nominally anaerobic corrosion of carbon steel in near-neutral pH saline environments" *Corrosion* 66 (4) **(2010)** 045001-1-045001-11
- [20] M. Saheb, D. Neff, L. Bellot-Gurlet and P. Dillmann "Raman study of a deuterated iron hydroxycarbonate to assess long-term corrosion mechanisms in anoxic soils" *Journal of Raman Spectroscopy* 42 (5) **(2011)** 1100-1108
- [21] R. L. Frost, M. C. Hales and B. J. Reddy "Aurichalcite - An SEM and Raman spectroscopic study" *Polyhedron* 26 (13) **(2007)** 3291-3300

- [22] I. V. Pekov, N. Perchiazzi, S. Merlino, V. N. Kalachev, M. Merlini and A. E. Zadov "Chukanovite, $\text{Fe}_2(\text{CO}_3)(\text{OH})_2$, a new mineral from the weathered iron meteorite Dronino" *European Journal of Mineralogy* 19 (2007) 891-898
- [23] C. Remazeilles and P. Refait "Fe(II) hydroxycarbonate $\text{Fe}_2(\text{OH})_2\text{CO}_3$ (Chukanovite) as iron corrosion product: Synthesis and study by Fourier transform infrared spectroscopy" *Polyhedron* 28 (4) (2009) 749-756
- [24] P. Refait, J. A. Bourdoiseau, M. Jeannin, D. D. Nguyen, A. Romaine and R. Sabot "Electrochemical formation of carbonated corrosion products on carbon steel in deaerated solutions" *Electrochimica Acta* 79 (2012) 210-217
- [25] M. Reffass, R. Sabot, C. Savall, M. Jeannin, J. Creus and P. Refait "Localised corrosion of carbon steel in $\text{NaHCO}_3/\text{NaCl}$ electrolytes: Role of Fe(II)-containing compounds" *Corrosion Science* 48 (3) (2006) 709-726
- [26] I. Azoulay, C. Remazeilles and P. Refait "Determination of standard Gibbs free energy of formation of chukanovite and Pourbaix diagrams of iron in carbonated media" *Corrosion Science* 58 (2012) 229-236
- [27] M. Saheb, D. Neff, P. Dillmann, H. Matthiesen and E. Foy "Long term corrosion behavior of low-carbon steel in anoxic environment: Characterisation of archaeological artefacts" *Journal of Nuclear Materials* 379 (1-3) (2008) 118-123
- [28] Y. Leon, M. Saheb, E. Drouet, D. Neff, E. Foy, E. Leroy, J. J. Dynes and P. Dillmann "Interfacial layer on archaeological mild steel corroded in carbonated anoxic environments studied with coupled micro and nano probes" *Corrosion Science* 88 (2014) 23-35
- [29] J. Jehlicka, P. Vitek, H. G. M. Edwards, M. D. Hargreaves and T. Capoun "Fast detection of sulphate minerals (gypsum, anglesite, baryte) by a portable Raman spectrometer" *Journal of Raman Spectroscopy* 40 (8) (2009) 1082-1086
- [30] U. Wehrmeister, A. L. Soldati, D. E. Jacob, T. Hager and W. Hofmeister "Raman spectroscopy of synthetic, geological and biological vaterite: A Raman spectroscopic study" *Journal of Raman Spectroscopy* 41 (2) (2010) 193-201
- [31] M. Stratmann, K. Bohnenkamp and H. J. Engell "An electrochemical study of phase-transitions in rust layers" *Corrosion Science* 23 (9) (1983) 969-985
- [32] H. T. Hai, H. Kura, M. Takahashi and T. Ogawa "Facile synthesis of Fe_3O_4 nanoparticles by reduction phase transformation from $\gamma\text{-Fe}_2\text{O}_3$ nanoparticles in organic solvent" *Journal of Colloid and Interface Science* 341 (1) (2010) 194-199
- [33] M. B. Kermani and A. Morshed "Carbon dioxide corrosion in oil and gas production - A compendium" *Corrosion* 59 (8) (2003) 659-683
- [34] M. Ko, B. Ingham, N. Laycock and D. E. Williams "In situ synchrotron X-ray diffraction study of the effect of microstructure and boundary layer conditions on CO_2 corrosion of pipeline steels" *Corrosion Science* 90 (2015) 192-201
- [35] S. Netic and L. Lunde "Carbon-dioxide corrosion of carbon steel in two-phase flow" *Corrosion* 50 (9) (1994) 717-727
- [36] J. L. Crolet, N. Thevenot and S. Netic "Role of conductive corrosion products in the protectiveness of corrosion layers" *Corrosion* 54 (3) (1998) 194-203
- [37] C. A. Palacios and J. R. Shadley "Characteristics of corrosion scales on steels in a CO_2 -Saturated NaCl Brine" *Corrosion* 47 (2) (1991) 122-127
- [38] H. Tamura, K. Goto and M. Nagayama "Effect of anions on oxygenation of ferrous ion in neutral solutions" *Journal of Inorganic & Nuclear Chemistry* 38 (1) (1976) 113-117

- [39] J. King and N. Davidson "Kinetics of the ferrous iron-oxygen reaction in acidic phosphate-pyrophosphate solutions" *Journal of the American Chemical Society* 80 (7) (1958) 1542-1545
- [40] A. M. Posner "The kinetics of autoxidation of ferrous ions in concentrated HCl solutions" *Transactions of the Faraday Society* 49 (4) (1953) 382-388
- [41] W. Stumm and G. F. Lee "Oxygenation of ferrous iron" *Industrial and Engineering Chemistry* 53 (2) (1961) 143-146
- [42] Y. Kurimura, R. Ochiai and N. Matsuura "Oxygen oxidation of ferrous ions induced by chelation" *Bulletin of the Chemical Society of Japan* 41 (10) (1968) 2234-2239
- [43] R. P. Colborn and M. J. Nicol "Investigation into the kinetics and mechanism of oxidation of iron (II) by oxygen in aqueous chloride solutions" *Journal of the Southern African Institute of Mining and Metallurgy* 73 (9) (1973) 281-289
- [44] K. Porsch and A. Kappler "Fe^{II} oxidation by molecular O₂ during HCl extraction" *Environmental Chemistry* 8 (2) (2011) 190-197
- [45] P. Refait and J. M. R. Genin "The oxidation of ferrous hydroxide in chloride-containing aqueous media and Pourbaix diagrams of green rust one" *Corrosion Science* 34 (5) (1993) 797-819
- [46] F. M. Al-Kharafi, B. G. Ateya and R. M. Abdallah "Electrochemical behaviour of low carbon steel in concentrated carbonate chloride brines" *Journal of Applied Electrochemistry* 32 (12) (2002) 1363-1370
- [47] S. S. El-Egamy and W. A. Badaway "Passivity and passivity breakdown of 304 stainless steel in alkaline sodium sulphate solutions" *Journal of Applied Electrochemistry* 34 (11) (2004) 1153-1158
- [48] N. J. Laycock and R. C. Newman "Localised dissolution kinetics, salt films and pitting potentials" *Corrosion Science* 39 (10-11) (1997) 1771-1790
- [49] R. M. Taylor "Influence of chloride on the formation of iron-oxides from Fe(II) chloride. II. Effect of [Cl] on the formation of lepidocrocite and its crystallinity" *Clays and Clay Minerals* 32 (3) (1984) 175-180
- [50] M. L. Schlegel, C. Bataillon, C. Blanc, D. Pret and E. Foy "Anodic activation of iron corrosion in clay media under water-saturated conditions at 90 degrees C: Characterization of the corrosion interface" *Environmental Science & Technology* 44 (4) (2010) 1503-1508
- [51] S. Savoye, L. Legrand, G. Sagon, S. Lecomte, A. Chausse, R. Messina and P. Toulhoat "Experimental investigations on iron corrosion products formed in bicarbonate/carbonate containing solutions at 90 degrees C" *Corrosion Science* 43 (11) (2001) 2049-2064
- [52] M. L. Schlegel, C. Bataillon, F. Brucker, C. Blanc, D. Pret, E. Foy and M. Chorro "Corrosion of metal iron in contact with anoxic clay at 90 degrees C: Characterization of the corrosion products after two years of interaction" *Applied Geochemistry* 51 (2014) 1-14
- [53] V. Pandarinathan, K. Lepkova and W. van Bronswijk "Chukanovite (Fe₂(OH)₂CO₃) identified as a corrosion product at sand-deposited carbon steel in CO₂-saturated brine" *Corrosion Science* 85 (2014) 26-32
- [54] A. Michelin, E. Drouet, E. Foy, J. J. Dynes, D. Neff and P. Dillmann "Investigation at the nanometre scale on the corrosion mechanisms of archaeological ferrous artefacts by STXM" *Journal of Analytical Atomic Spectrometry* 28 (1) (2013) 59-66
- [55] A. Romaine, R. Sabot, M. Jeannin, S. Necib and P. Refait "Electrochemical synthesis and characterization of corrosion products on carbon steel under argillite layers in carbonated media at 80 degrees C" *Electrochimica Acta* 114 (2013) 152-158

- [56] M. Saheb, P. Berger, L. Raimbault, D. Neff and P. Dillmann "Investigation of iron long-term corrosion mechanisms in anoxic media using deuterium tracing" *Journal of Nuclear Materials* 423 (1-3) **(2012)** 61-66
- [57] M. Saheb, D. Neff, C. Bataillon, E. Foy and P. Dillmann "Copper tracing to determine the micrometric electronic properties of a thick ferrous corrosion layer formed in an anoxic medium" *Corrosion Science* 53 (6) **(2011)** 2201-2207
- [58] I. Azoulay, E. Conforto, P. Refait and C. Remazeilles "Study of ferrous corrosion products on iron archaeological objects by electron backscattered diffraction (EBSD)" *Applied Physics a-Materials Science & Processing* 110 (2) **(2013)** 379-388
- [59] J. Marin-Cruz, R. Cabrera-Sierra, M. A. Pech-Canul and I. Gonzalez "Characterization of different allotropic forms of calcium carbonate scales on carbon steel by electrochemical impedance spectroscopy" *Journal of Applied Electrochemistry* 34 (3) **(2004)** 337-343
- [60] H. Moller "The influence of Mg^{2+} on the formation of calcareous deposits on a freely corroding low carbon steel in seawater" *Corrosion Science* 49 (4) **(2007)** 1992-2001
- [61] Y. Ben Amor, L. Bouselmi, B. Tribollet and E. Triki "Study of the effect of magnesium concentration on the deposit of allotropic forms of calcium carbonate and related carbon steel interface behavior" *Electrochimica Acta* 55 (16) **(2010)** 4820-4826
- [62] F. G. Liu, S. R. Wu and C. S. Lu "Characterisation of calcareous deposits on freely corroding low carbon steel in artificial sea water" *Corrosion Engineering Science and Technology* 46 (5) **(2011)** 611-617
- [63] G. S. Vasyliiev, Y. S. Gerasimenko, S. K. Poznyak and L. S. Tsybul'skaya "A study of the anticorrosion properties of carbonate deposits to protect low-carbon steel from the action of tap water" *Russian Journal of Applied Chemistry* 87 (4) **(2014)** 450-455

Chapter 7

Conclusions and Future Research

7.1 CONCLUSIONS

The primary focus of this research was on the corrosion of A516 Gr70 steel under the environmental conditions anticipated in a nuclear waste repository. Various environmental features, such as anion content (Cl^- , $\text{HCO}_3^-/\text{CO}_3^{2-}$, and SO_4^{2-}), trace O_2 content, and pH were investigated. Also, the effects of H_2O_2 on the steel corrosion process were investigated to determine how corrosion of the inside of a container would be influenced by the radiolytic oxidants produced by the fuel waste form inside the container.

The influence of H_2O_2 on the corrosion of carbon steel was investigated under deaerated conditions, when traces of O_2 could be present, and under anaerobic conditions, when the $[\text{O}_2]$ would be expected to be at the ppb level. Under anaerobic conditions active steel corrosion, producing Fe^{2+} and H_2 was maintained up to an added $[\text{H}_2\text{O}_2]$ of 6 μM . For deaerated conditions, passivation leading to pitting occurred for added $[\text{H}_2\text{O}_2] \geq 10$ to 15 μM but was attributed to the presence of traces of dissolved O_2 despite continuous Ar-sparging. While passivation of the surface should not occur under anaerobic conditions, the presence of non-passivating Fe^{III} -containing corrosion products confirmed the interaction of the H_2O_2 with the steel. Model calculations showed that $[\text{H}_2\text{O}_2] > 10^{-9}$ M are effectively unachievable at the steel surface and therefore, it can be concluded that active steel corrosion will be maintained inside a failed waste container, and that the soluble corrosion products (Fe^{2+} and H_2) will be available to suppress fuel corrosion and radionuclide release.

The electrochemical behaviour as well as the corrosion products formed on carbon steel was shown to be dependent on the anion content of the exposure environment, specifically, Cl^- , $\text{HCO}_3^-/\text{CO}_3^{2-}$, and SO_4^{2-} . An increase in the $[\text{Cl}^-]$ led to an increase in E_{CORR} and R_p which suggested a less reactive surface state explained by the ability of Cl^- to induce passivation by the stabilization of Fe^{III} oxides in the presence of traces of dissolved O_2 . At high concentrations, Cl^- exerts a dual role first catalyzing surface oxidation leading to passivity, and then causing the initiation of breakdown sites on the passivated surface. The presence of Cl^- was also shown to influence the final corrosion products with low $[\text{Cl}^-]$ favouring the formation of Fe_3O_4 while high $[\text{Cl}^-]$ promotes the formation of $\gamma\text{-FeOOH}$.

The addition of $[\text{HCO}_3^-/\text{CO}_3^{2-}]$ was shown to accelerate the anodic dissolution of Fe^{2+} by stabilization of soluble complexes such as FeHCO_3^+ and $\text{Fe}(\text{HCO}_3)_2$. This led to a competition between the stabilization of Fe^{2+} by $\text{HCO}_3^-/\text{CO}_3^{2-}$ and the oxidation to Fe^{III} oxides catalyzed by Cl^- . An increase in $[\text{HCO}_3^-/\text{CO}_3^{2-}]$ also shifted the breakdown potential to more positive values due to the ability of the $\text{HCO}_3^-/\text{CO}_3^{2-}$ to buffer local acidity and prevent pit propagation. Even at low $[\text{HCO}_3^-/\text{CO}_3^{2-}]$ (0.001 M), $\text{HCO}_3^-/\text{CO}_3^{2-}$ can buffer the pH at breakdown sites allowing repassivation to occur.

The increased values of E_{CORR} and R_p in the presence of SO_4^{2-} indicated that this anion does not prevent the Cl^- catalyzed oxidation to Fe^{III} oxide in the presence of traces of O_2 . Passivation of the surface in this manner causes more frequent breakdown processes but their propagation appears limited due to the inability of SO_4^{2-} to promote Fe^{2+} dissolution. Additionally, SO_4^{2-} was shown to have a more pronounced effect on the film breakdown potential than $\text{HCO}_3^-/\text{CO}_3^{2-}$, suggesting it may be more strongly adsorbed on the Fe^{III} oxide surface.

Further electrochemical studies for periods of up to 60 days were performed in an anaerobic chamber to determine the behaviour of carbon steel corrosion over extended periods of time in the absence of traces of O_2 . These studies focused on the effects of $[\text{Cl}^-]$, $\text{HCO}_3^-/\text{CO}_3^{2-}$, and a simulated sedimentary clay groundwater solution. An increase in $[\text{Cl}^-]$ caused an increase in the corrosion rate of the steel, as indicated by an increased roughness of the steel surface. At the higher $[\text{Cl}^-]$ (4.77 M) an acceleration of the cathodic kinetics was observed which was attributed to the exposure of Fe_3C in the pearlite grains during corrosion, leading to an increased surface area on which the cathodic reaction could occur.

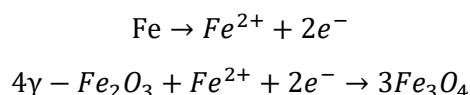
Even in a solution with low $[\text{HCO}_3^-]$ (0.002213 M; solution (i)), chukanovite ($\text{Fe}_2(\text{OH})_2\text{CO}_3$) was formed in non-uniform patches on the steel surface. While generally expected to form in slightly alkaline conditions, it was shown that the interfacial $[\text{Fe}^{2+}]$ was most likely the main factor leading to $\text{Fe}_2(\text{OH})_2\text{CO}_3$ deposition. Increased dissolution of the steel led to an increased interfacial $[\text{Fe}^{2+}]$ which was then able to combine with available HCO_3^- in the bulk solution leading to the precipitation of $\text{Fe}_2(\text{OH})_2\text{CO}_3$.

Addition of anticipated groundwater ions for a sedimentary clay environment (solution (iv)) caused an initial suppression of the anodic kinetics followed by a constant corrosion rate. The difference in behaviour between solution (iv) and solution (ii) with comparable $[\text{Cl}^-]$ and $[\text{HCO}_3^-]$

showed that the groundwater ions influence the steel corrosion rate. The initial increase in R_p likely reflects the formation of the Fe_3O_4 film and a deposited layer of vaterite ($CaCO_3$), the latter offering partial protection to the steel surface.

The addition of 0.10 M HCO_3^-/CO_3^{2-} to buffer the pH to 8.85 led to a significant decrease in the corrosion rate. While not observed by Raman spectroscopy, Fe_3O_4 formation would be expected to reduce the corrosion rate while the outer layer of $Fe_2(OH)_2CO_3$ observed would provide additional protection of the surface. Growth of such a barrier layer would explain the constant corrosion rate observed after 10 days of exposure. The subsequent noise observed in the E_{CORR} and R_p values is then attributed to the unstable nature of this Fe_3O_4 layer with its dissolution leading to the precipitation of $Fe_2(OH)_2CO_3$.

Complementary to electrochemical studies, a series of long-term exposure experiments were conducted, for exposure periods of up to 30 months, to determine the changes in corrosion product composition and morphology over extended corrosion periods. The initial surface layer, present on first immersion, was shown to be $\gamma-Fe_2O_3$, formed as a result of humid air exposure prior to immersion. Over the first 100 days of exposure this film was reduced to Fe_3O_4 by galvanic coupling to the dissolution of the steel substrate,



with the high solubility of Fe^{2+} at the experimental pH kinetically promoting the conversion. Corrosion appeared to be preferentially located at pearlite grains with oxide accumulating in the Fe_3C bands as the $\alpha-Fe$ lamellae were converted to Fe_3O_4 . This preferential corrosion of pearlite can be attributed to the lower overpotential of Fe_3C lamellae for the cathodic reaction allowing them to function as preferential cathodes. However, this process may be suppressed over time by the slow accumulation of an Fe_3O_4 layer on the surface and within the Fe_3C lamellae.

While the corrosion in solutions (i) and (ii) was very similar in the initial stages, an incursion of O_2 caused a change in behaviour for solution (ii) which was shown to develop $\gamma-Fe_2O_3$ corrosion products as well as a generally thicker corrosion product layer. However, Fe_3O_4 was eventually established as the dominant corrosion product, confirming the microgalvanic coupling of $\gamma-Fe_2O_3$ reduction to Fe_3O_4 to Fe dissolution.

The addition of $\text{HCO}_3^-/\text{CO}_3^{2-}$ leading to an increase in pH to 8.85 led to the rapid formation of $\text{Fe}_2(\text{OH})_2\text{CO}_3$. The more rapid growth of this layer (in comparison to that in a similar solution (Chapter 5)) was attributed to the initial $\gamma\text{-Fe}_2\text{O}_3$ layer formed via humid air exposure prior to immersion. The high local $[\text{Fe}^{2+}]$ produced by the reduction of this layer to Fe_3O_4 promoted the rapid formation of $\text{Fe}_2(\text{OH})_2\text{CO}_3$. The reduction of $\gamma\text{-Fe}_2\text{O}_3$ leading to the formation of an interfacial layer of Fe_3O_4 combined with the outer layer of $\text{Fe}_2(\text{OH})_2\text{CO}_3$ was shown to slow the corrosion kinetics. The protective nature of $\text{Fe}_2(\text{OH})_2\text{CO}_3$ has often been attributed to a thin interfacial spinel oxide layer as seen in these experiments. However, the eventual thermodynamic transformation of $\text{Fe}_2(\text{OH})_2\text{CO}_3$ to FeCO_3 , consistent with the strata formed on archaeological artefacts, appeared to induce some localized corrosion/pitting processes observed in SEM/FIB images.

Addition of anticipated groundwater ions caused the formation of CaSO_4 and CaCO_3 crystals in as little as 2 days, which, consistent with the findings described in Chapter 5, were shown to impede the steel corrosion due to their ability to provide a physical barrier between oxidizing species and the steel surface. This crystal coverage explains the differences in morphology and thickness of the corrosion product layers grown in solutions (ii) and (iv) (which have similar $[\text{Cl}^-]$). However, corrosion was shown to occur after the dissolution of the crystals in the form of GR and Fe_3O_4 . In addition, the high Mg^{2+} content of the groundwater solution was shown to promote the formation of aragonite, a CaCO_3 polymorph known to cause a reduction in steel corrosion rates.

7.2 CONSEQUENCES OF STEEL CONTAINER CORROSION

Based on the studies in this thesis, a number of conclusions can be made about the viability of a carbon steel waste container.

The results of Chapter 4 explored the effects of trace levels of O_2 on steel corrosion. Such conditions could arise after short periods of emplacement of a container in the repository if saturation of the clay surrounding the container occurs before the complete consumption of the initially trapped O_2 . Reaction with trace levels of O_2 could lead to passivation when the general corrosion rate would be very slow but minor amounts of pitting could occur. This only seems likely in very saline groundwaters if the pH is ≥ 9 . Under less alkaline conditions passivation leading to pitting should not occur.

If totally anoxic conditions prevail the Fe^{III} oxide initially present on the container surface on emplacement will reduce to Fe₃O₄ through galvanic coupling to steel dissolution leading to minor localized corrosion damage. Subsequently, corrosion will be general and in the absence of trace levels of O₂ no passivation/pitting would be expected. The slow accumulation of a Fe₃O₄ film would be expected.

Studies in simulated groundwater solutions showed that the presence of additional groundwater ions would promote the formation of calcareous deposits. These deposits would be partially protective but steel corrosion would continue slowly beneath them.

The results in Chapter 3 show that the radiolytic production of oxidants, in particular H₂O₂, inside a failed waste container will allow continued corrosion of the steel. The concentration of H₂O₂ that could reach the inner container wall should be negligible. Consequently, steel corrosion leading to the production of H₂O₂ scavengers (Fe²⁺ and H₂) will continue, leading to a suppression of radionuclide release from the fuel wasteform.

7.3 FUTURE RESEARCH

In this study, an attempt was made to determine the corrosion behaviour of A516 Gr70 carbon steel in a variety of sedimentary clay groundwater environments in both the presence and absence of trace levels of O₂.

The studies performed in the presence of H₂O₂ (Chapter 3) examine the consequences of container failure. However, the lack of repeat experiments under both the deaerated and anaerobic environments suggests that additional experiments for each would lend insight into their reproducibility. In addition, it would be beneficial to perform the anaerobic experiment under increased [H₂O₂] to confirm that while the H₂O₂ is seen to react with the steel surface, it is unable to induce passivation. This would confirm the results of the deaerated experiments which suggested the passivation was due to trace levels of O₂ within the solution.

Under anaerobic conditions, both short-term electrochemical (Chapter 5) and long-term surface analysis (Chapter 6) studies were performed. However, these studies did not present any quantitative results of the corrosion damage under these conditions. It would be beneficial to perform quantitative analysis on the film thicknesses and depths of corrosion penetration in each of the studied environments through the use of FIB cross-sectioning and statistical analysis.

In addition, it may prove beneficial to use mass loss measurements to convert the corrosion damage into a rate of penetration in order to determine the time at which failure of the container could occur.

In this study the corrosion behaviour was monitored under ambient conditions. However, during the initial stages of container corrosion the temperature of the repository may be as high as 80°C. As such, it would be beneficial to supplement the results found within this study with results of similar experiments performed at elevated temperatures more representative of the DGR environment. In addition, experiment may be performed under a range of temperature conditions from ambient to 80°C to study the evolution of the container corrosion behaviour as the DGR begins to cool over time.

When emplaced in a repository the container would be surrounded by compacted clay. This will lead to modification of the local exposure environment and introduce the possibility that corrosion will be affected by the ability of this clay to absorb dissolved Fe(II) species. A similar series of experiments to those presented in this thesis should be performed in the presence of compacted clay.

Appendix A

Supporting Raman Spectra and SEM images for the Long-Term Evolution of Carbon Steel
Corrosion under Anoxic Simulated Groundwater Environments

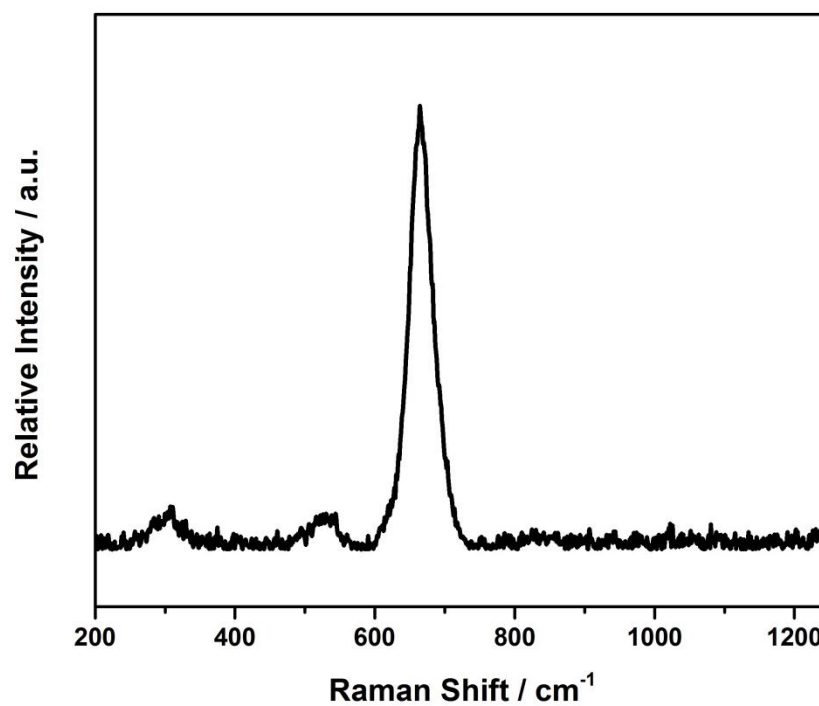
A.1. REFERENCE RAMAN SPECTRA

Figure A-1: Reference Raman spectrum for Fe₃O₄ (magnetite).

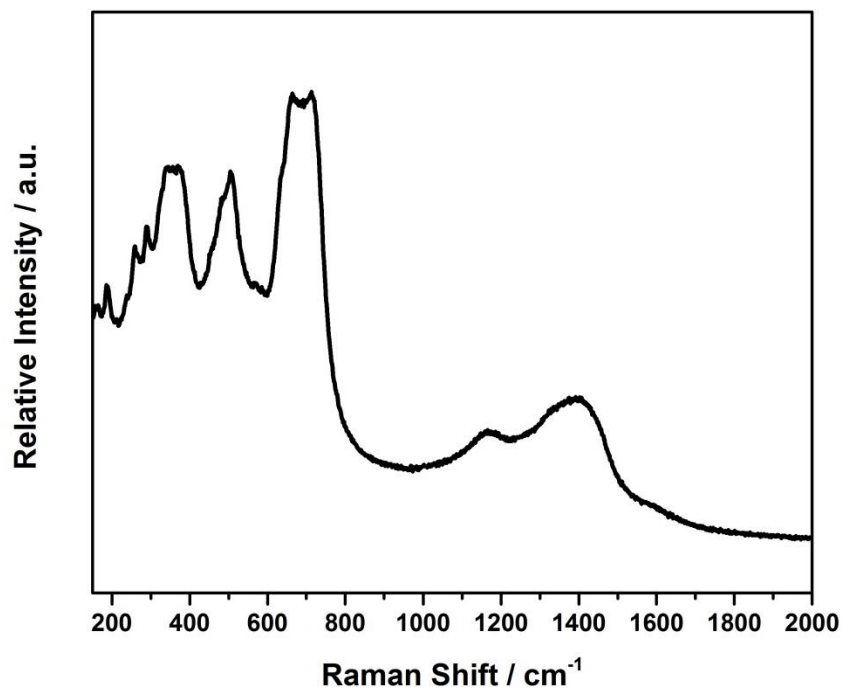


Figure A-2: Reference Raman spectrum for $\gamma\text{-Fe}_2\text{O}_3$ (maghemite).

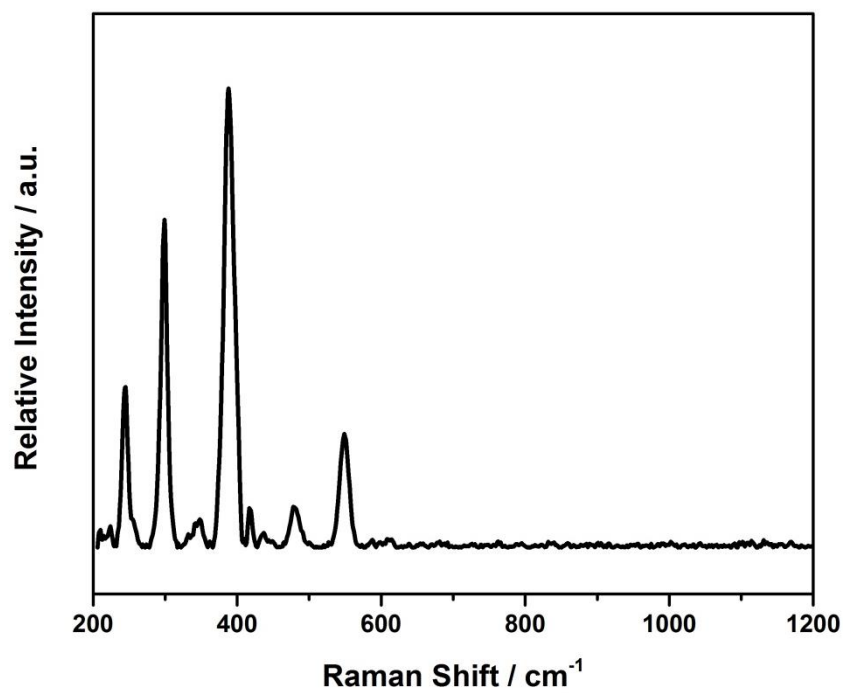


Figure A-3: Reference Raman spectrum for $\alpha\text{-FeOOH}$ (goethite).

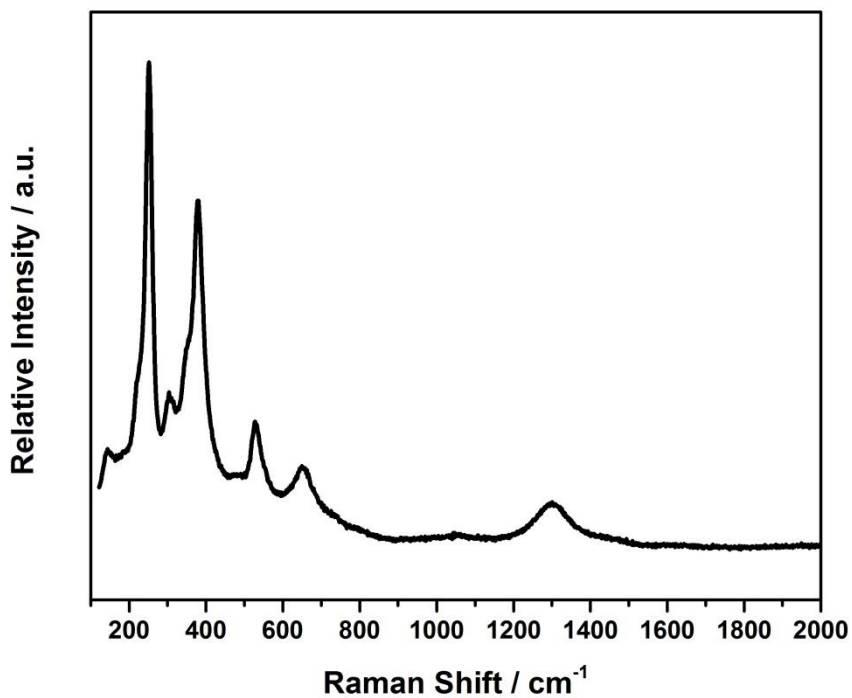


Figure A-4: Reference Raman spectrum for γ -FeOOH (lepidocrocite).

A.2. SOLUTION (I): LOW CHLORIDE CONCENTRATION

A.2.1. Raman Spectroscopy

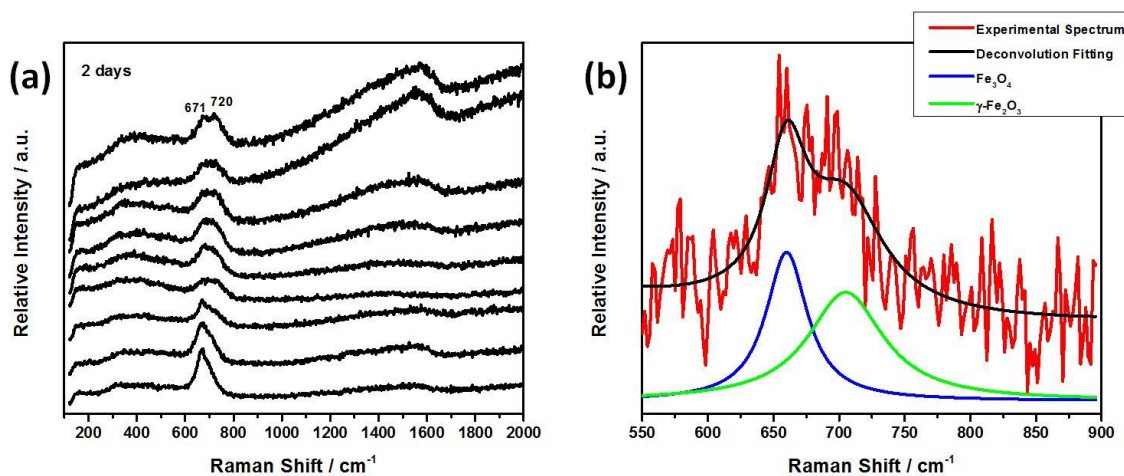


Figure A-5: (a) Raman spectra recorded at various locations on a steel specimen after 2 days of exposure to solution (i); (b) deconvolution of the spectrum closest to the sample average.

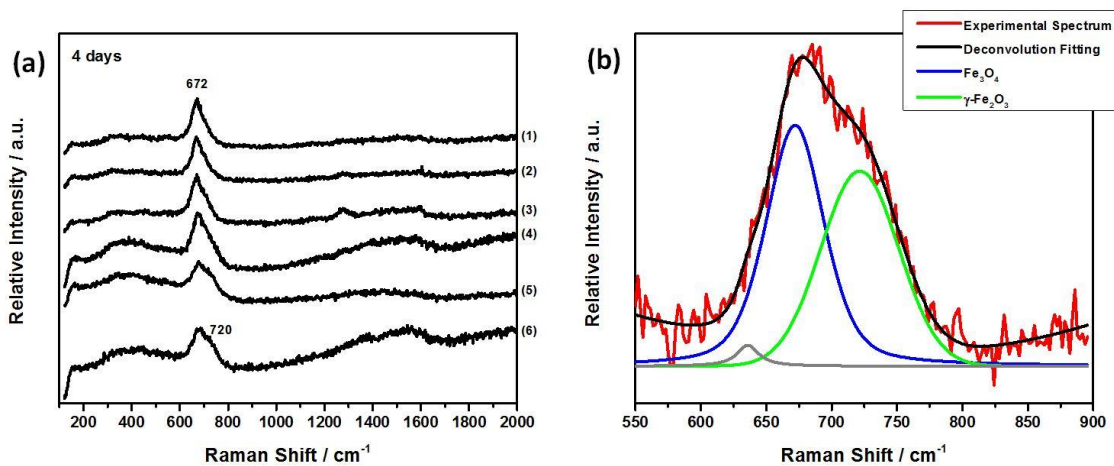


Figure A-6: (a) Raman spectra recorded at various locations on a steel specimen after 4 days of exposure to solution (i); (b) deconvolution of the spectrum closest to the sample average.

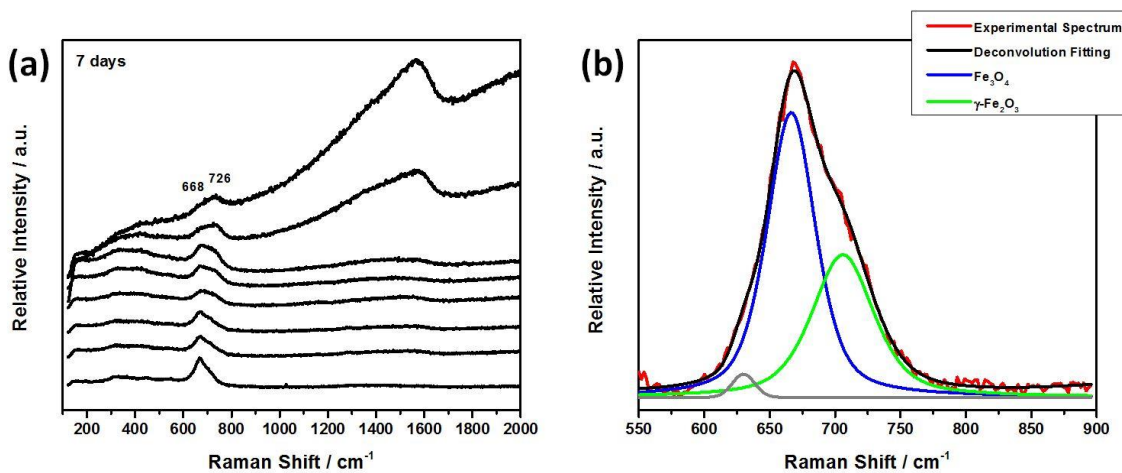


Figure A-7: (a) Raman spectra recorded at various locations on a steel specimen after 7 days of exposure to solution (i); (b) deconvolution of the spectrum closest to the sample average.

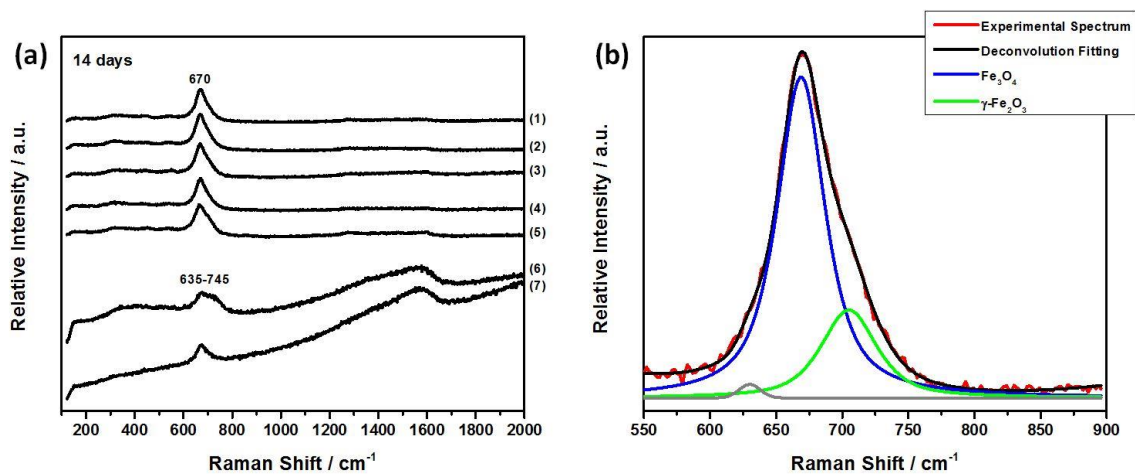


Figure A-8: (a) Raman spectra recorded at various locations on a steel specimen after 14 days of exposure to solution (i); (b) deconvolution of the spectrum closest to the sample average.

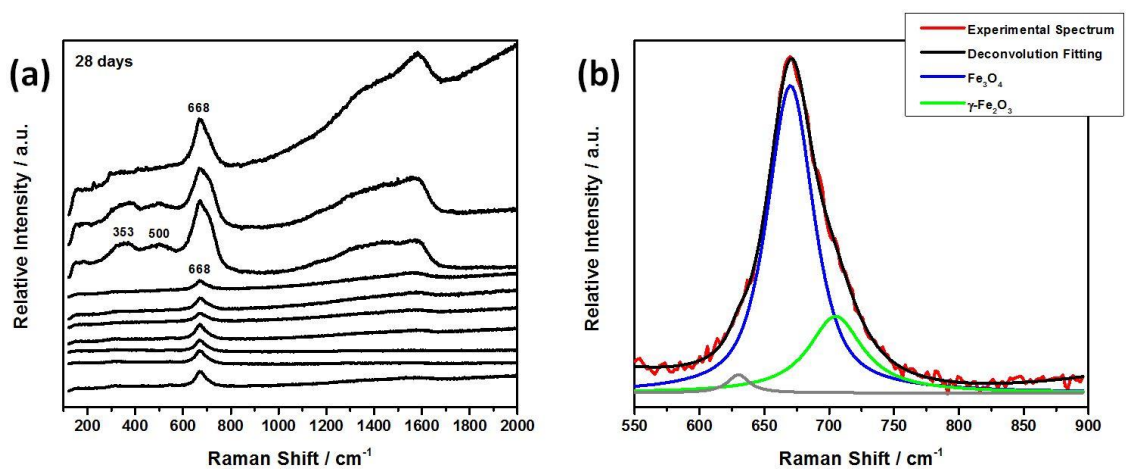


Figure A-9: (a) Raman spectra recorded at various locations on a steel specimen after 28 days of exposure to solution (i); (b) deconvolution of the spectrum closest to the sample average.

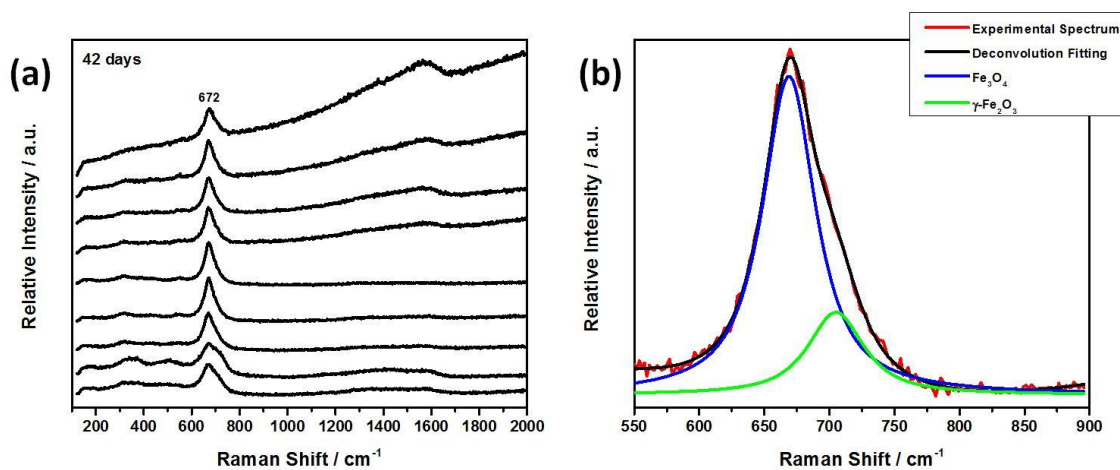


Figure A-10: (a) Raman spectra recorded at various locations on a steel specimen after 42 days of exposure to solution (i); (b) deconvolution of the spectrum closest to the sample average.

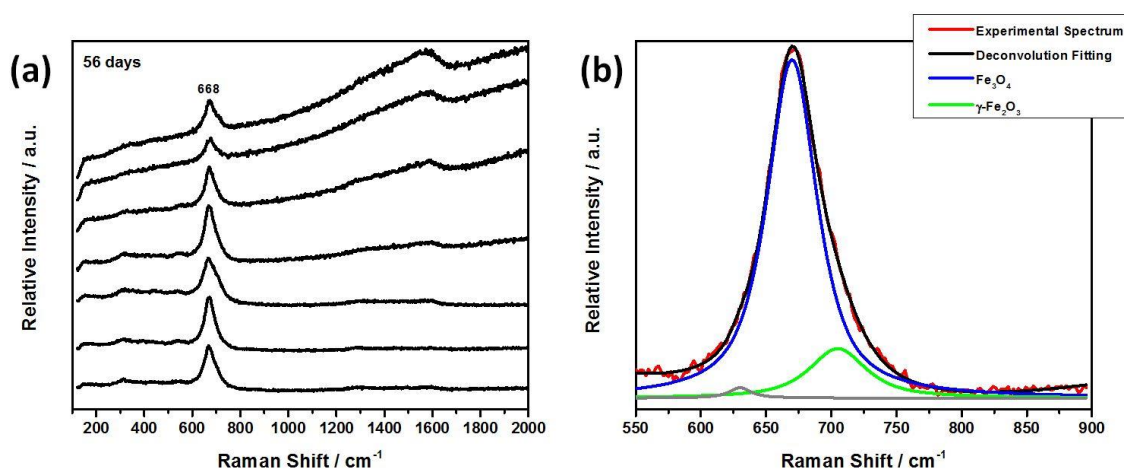


Figure A-11: (a) Raman spectra recorded at various locations on a steel specimen after 56 days of exposure to solution (i); (b) deconvolution of the spectrum closest to the sample average.

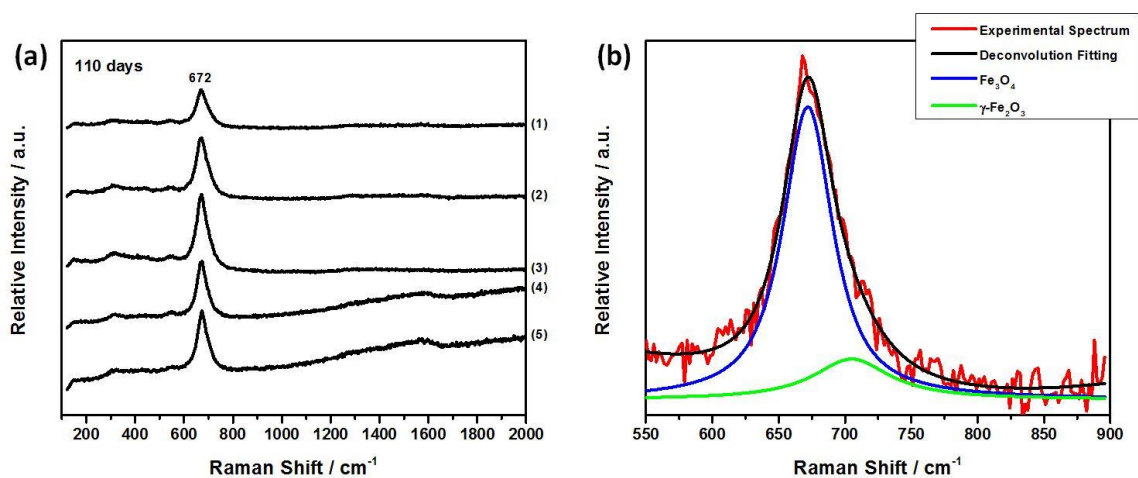


Figure A-12: (a) Raman spectra recorded at various locations on a steel specimen after 110 days of exposure to solution (i); (b) deconvolution of the spectrum closest to the sample average.

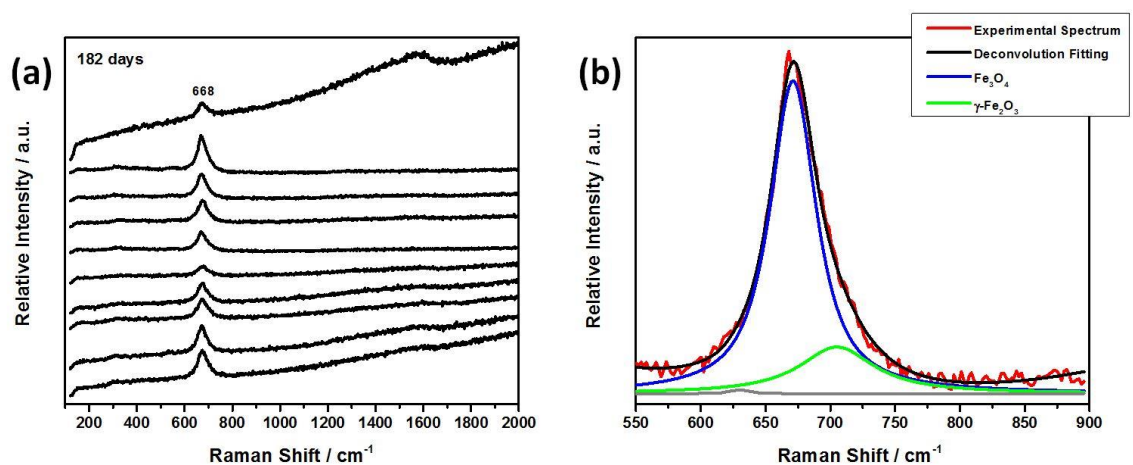


Figure A-13: (a) Raman spectra recorded at various locations on a steel specimen after 182 days of exposure to solution (i); (b) deconvolution of the spectrum closest to the sample average.

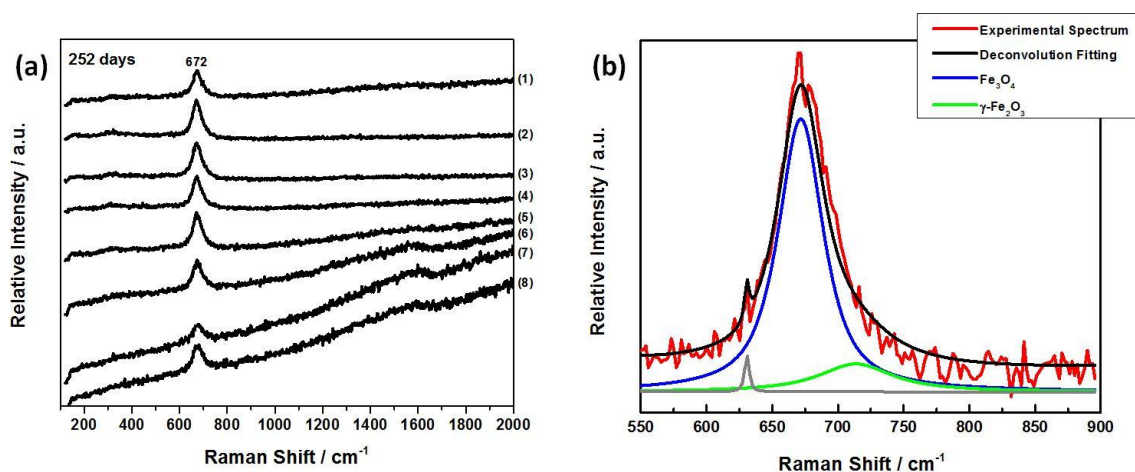


Figure A-14: (a) Raman spectra recorded at various locations on a steel specimen after 252 days of exposure to solution (i); (b) deconvolution of the spectrum closest to the sample average.

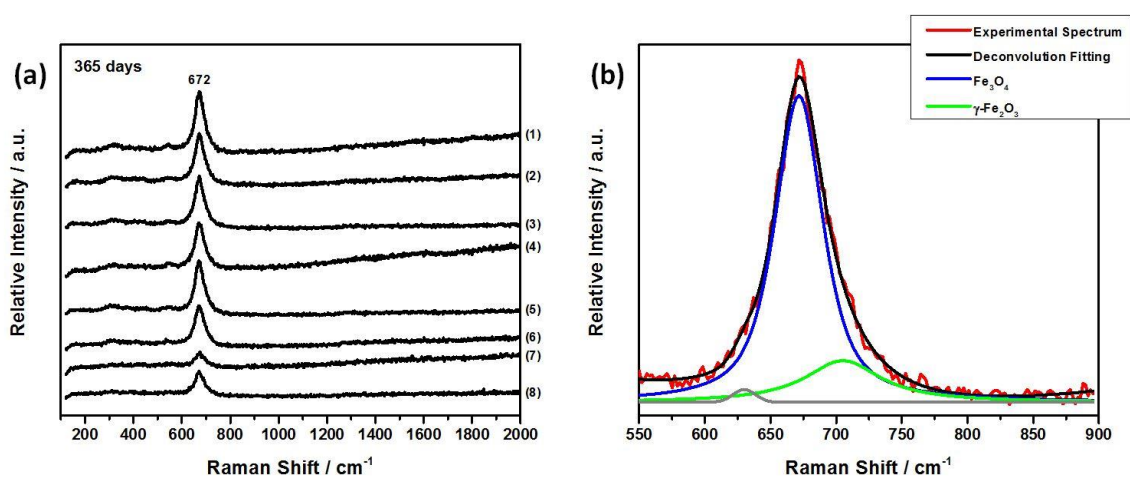


Figure A-15: (a) Raman spectra recorded at various locations on a steel specimen after 365 days of exposure to solution (i); (b) deconvolution of the spectrum closest to the sample average.

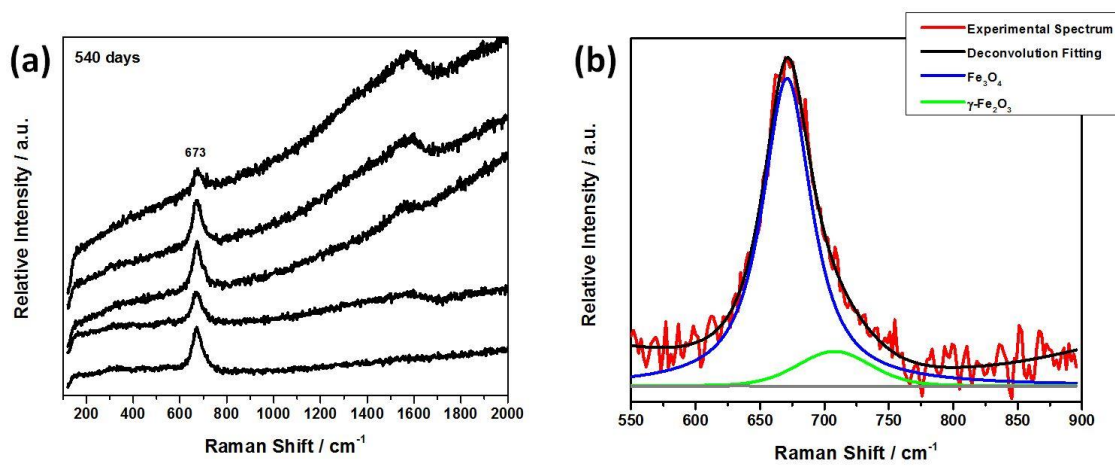


Figure A-16: (a) Raman spectra recorded at various locations on a steel specimen after 540 days of exposure to solution (i); (b) deconvolution of the spectrum closest to the sample average.

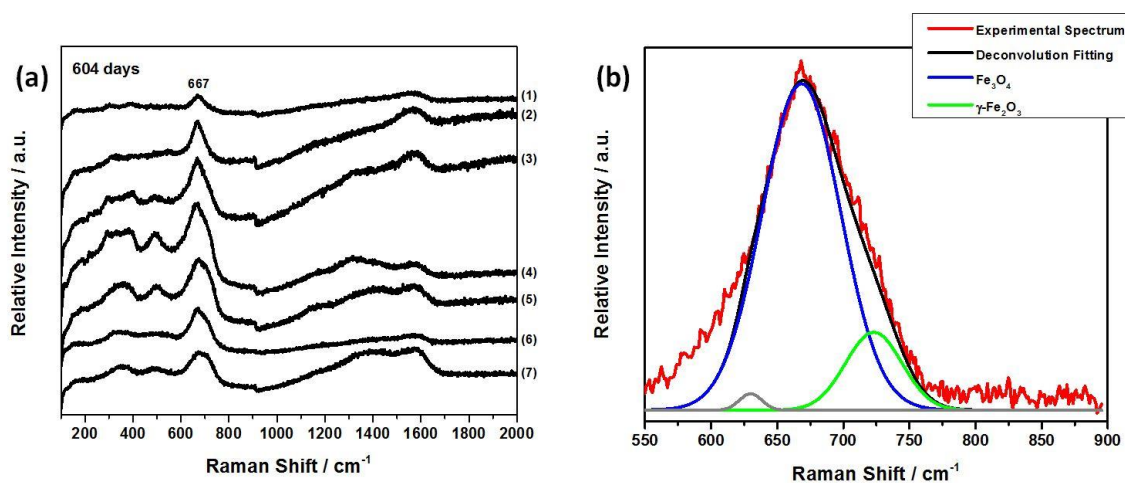


Figure A-17: (a) Raman spectra recorded at various locations on a steel specimen after 604 days of exposure to solution (i); (b) deconvolution of the spectrum closest to the sample average.

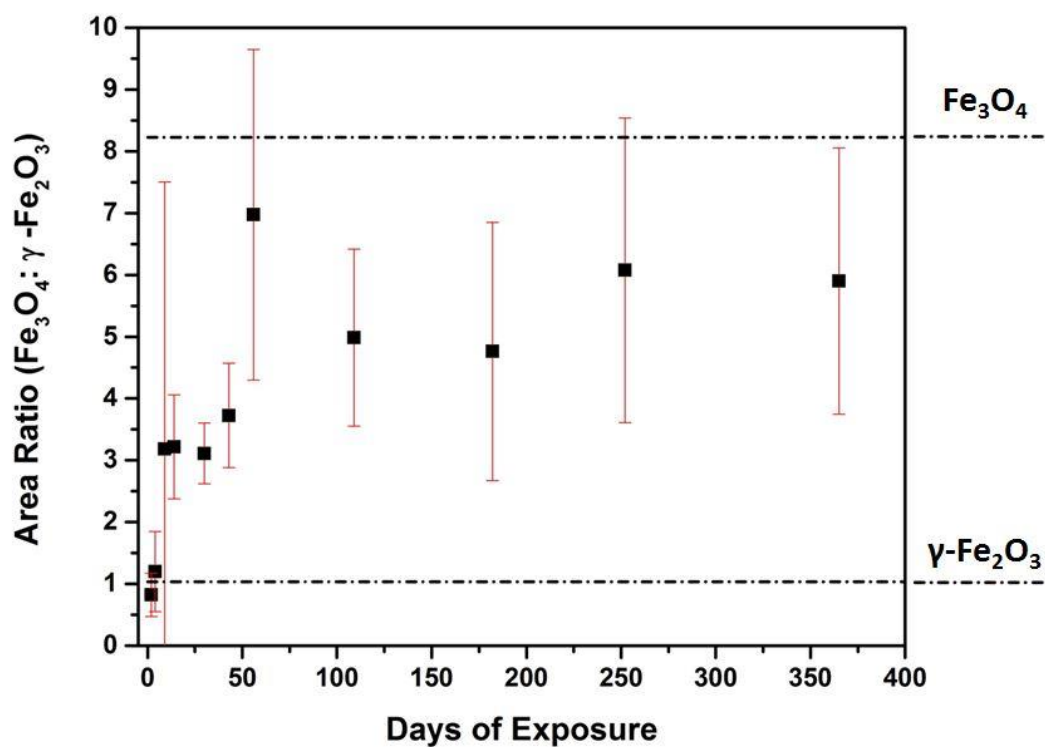


Figure A-18: Evolution of the area ratio between the Fe_3O_4 (672 cm^{-1}) and $\gamma\text{-Fe}_2\text{O}_3$ (705 cm^{-1}) Raman peaks after exposure to solution (i), calculated from the deconvoluted Raman spectra.

A.2.2. Scanning Electron Microscopy

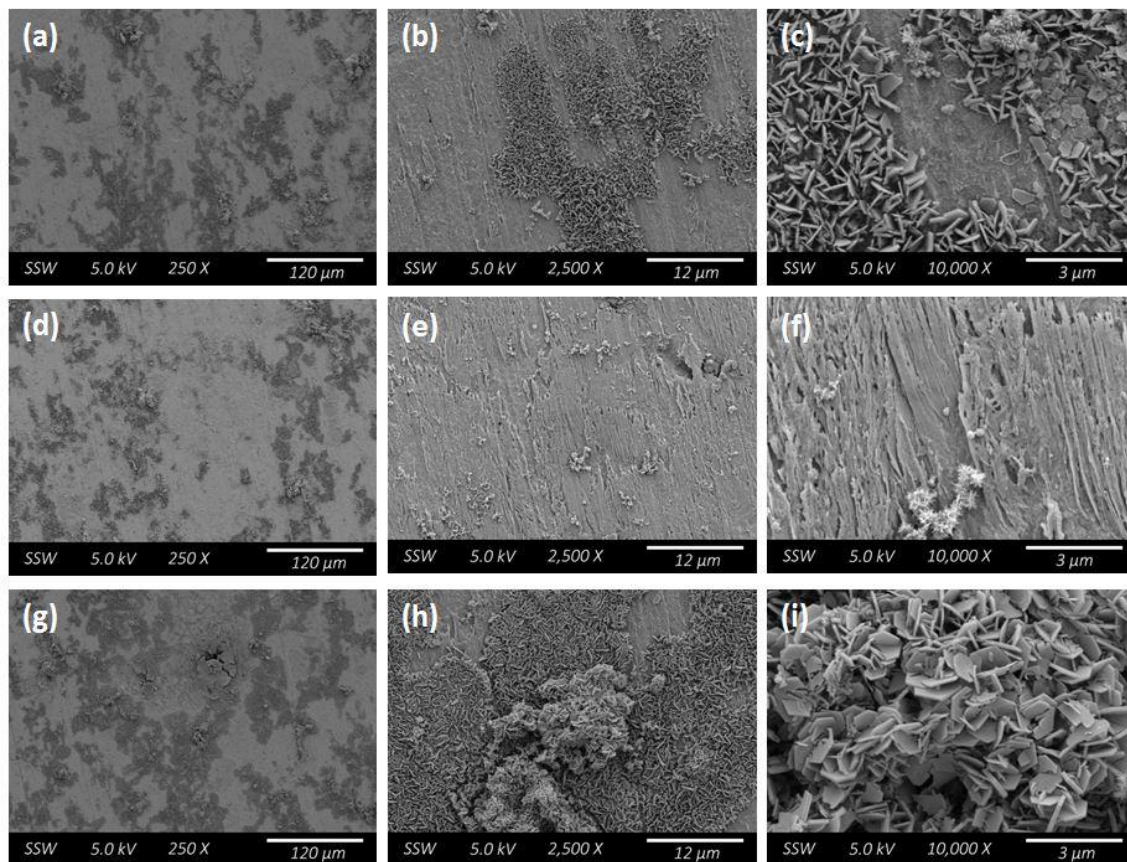


Figure A-19: SEM micrographs recorded on a specimen surface after 2 days of exposure to solution (i) showing: (a-c) the distribution of crystalline corrosion product; (d-f) the general surface morphology; (g-i) a region exhibiting a more significant degree of corrosion.

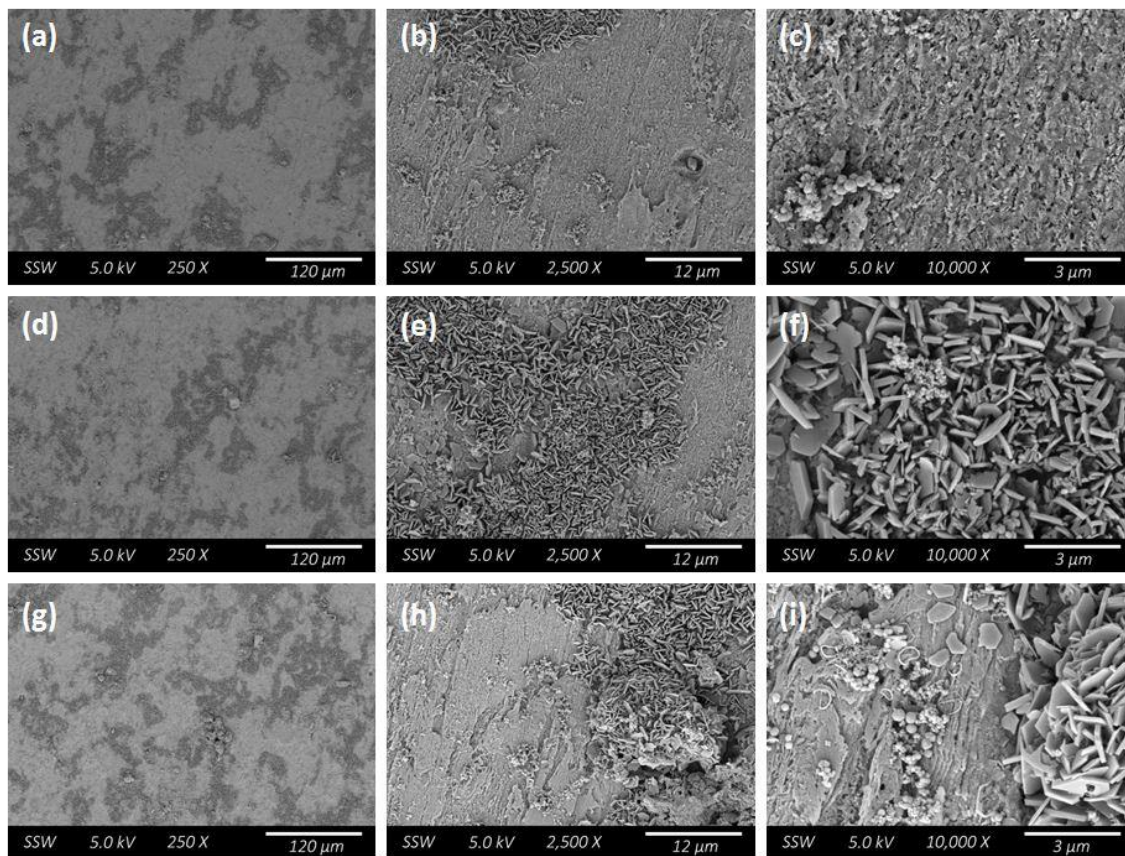


Figure A-20: SEM micrographs recorded on a specimen surface after 7 days of exposure to solution (i) showing: (a-c) the general surface morphology; (d-f) a region of crystalline corrosion product; (g-i) a region exhibiting a larger corrosion deposit and the surrounding surface morphology.

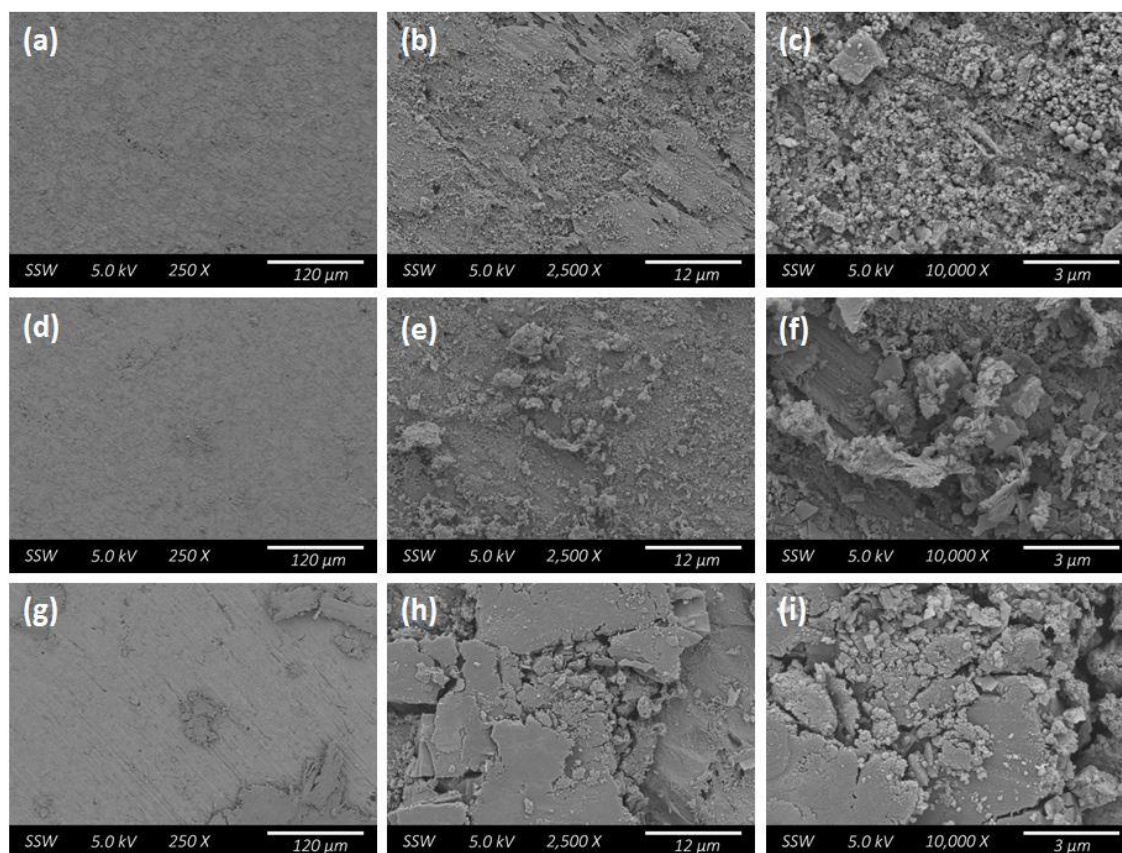


Figure A-21: SEM micrographs recorded on a specimen surface after 28 days of exposure to solution (i) showing: (a-c) the general surface morphology; (d-f) a region of minor corrosion product accumulation; (g-i) a region of heavier corrosion product accumulation.

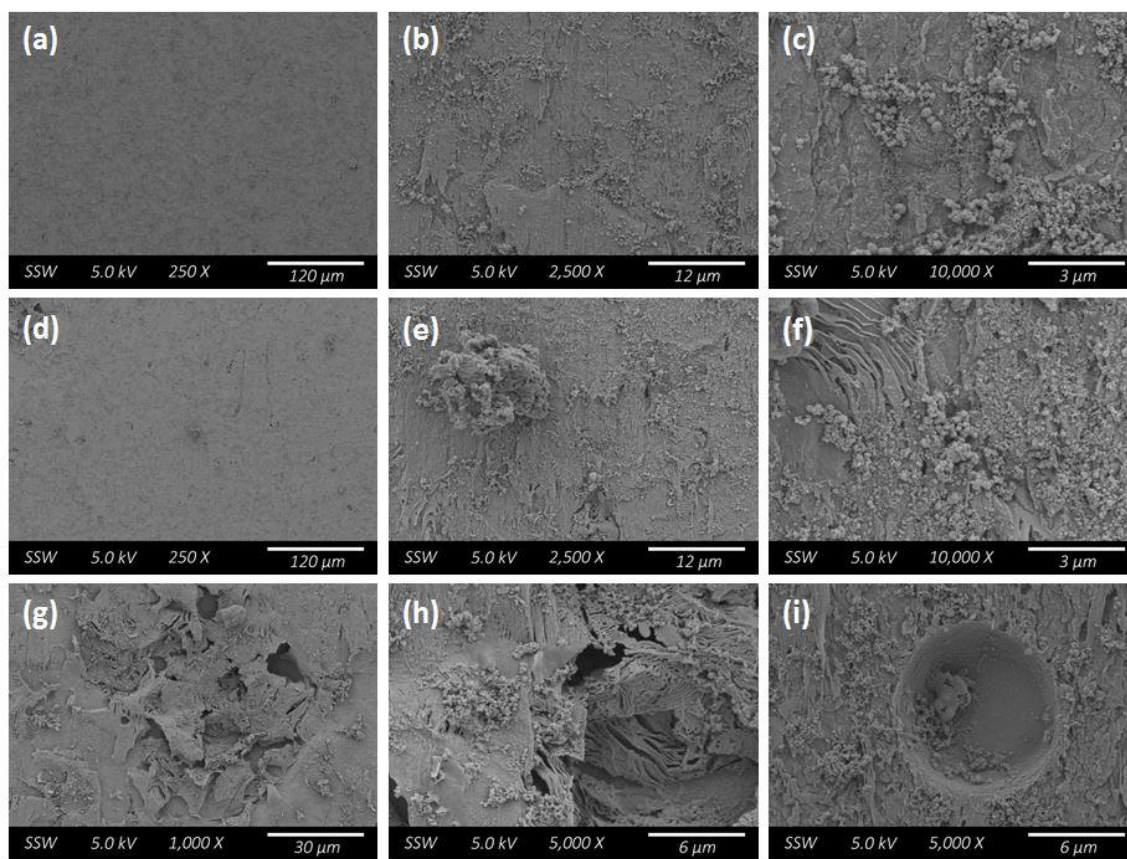


Figure A-22: SEM micrographs recorded on a specimen surface after 42 days of exposure to solution (i) showing: (a-c) the general surface morphology; (d-e) a location with deposited corrosion product; (f) a region exhibiting the characteristic lamella of Fe_3C left after the preferential dissolution of $\alpha\text{-Fe}$ from pearlite grains; (g-h) a region of localized damage; (i) a possible pitted location.

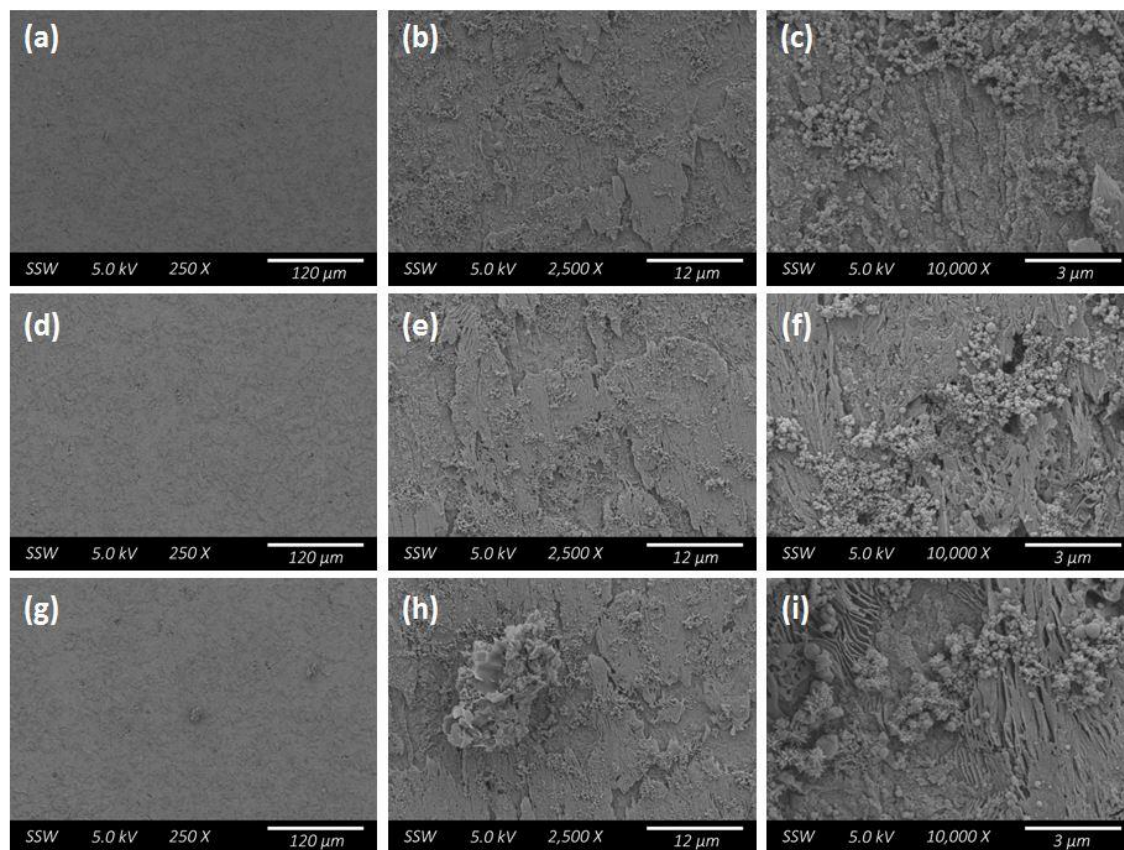


Figure A-23: SEM micrographs recorded on a specimen surface after 56 days of exposure to solution (i) showing: (a-f) the general surface morphology; (g-h) a region with a larger corrosion deposit; (i) a region exhibiting the characteristic lamella of Fe_3C left after the preferential dissolution of $\alpha\text{-Fe}$ from pearlite grains.

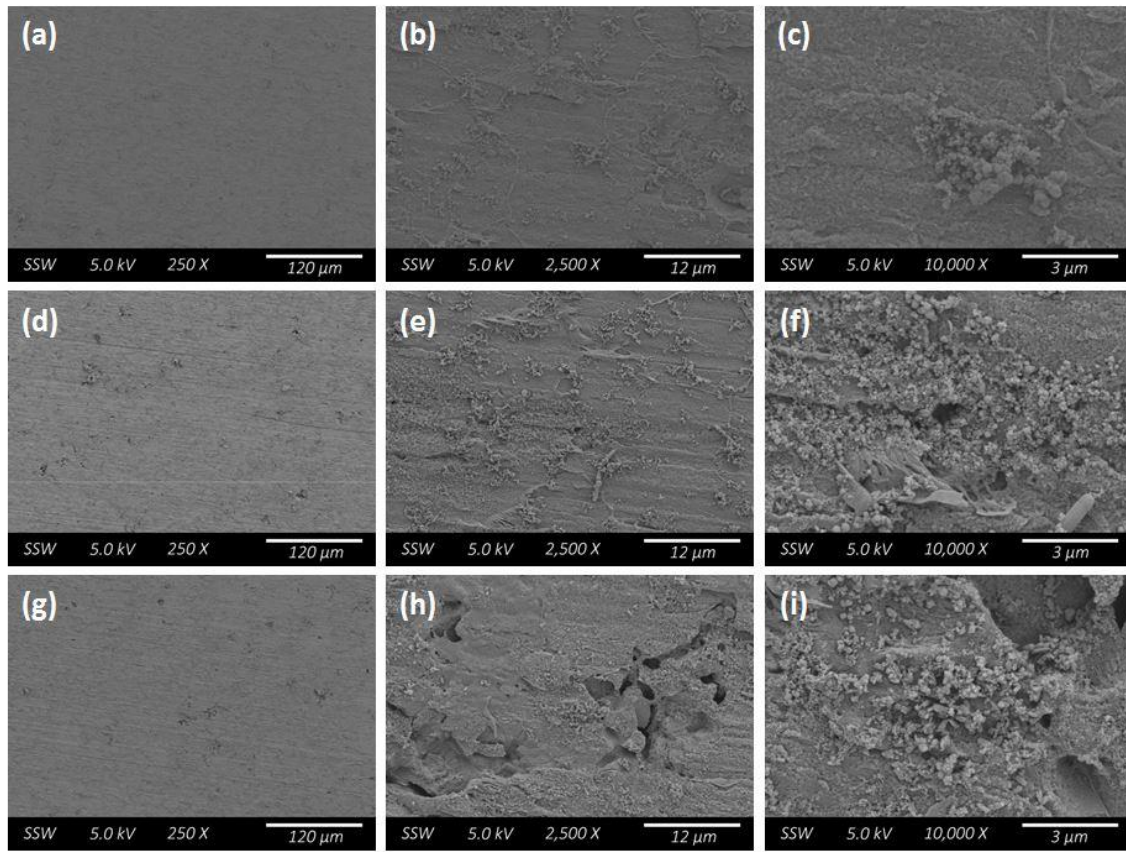


Figure A-24: SEM micrographs recorded on a specimen surface after 182 days of exposure to solution (i) showing: (a-f) the general surface morphology; (g-i) a region of localized corrosion damage.

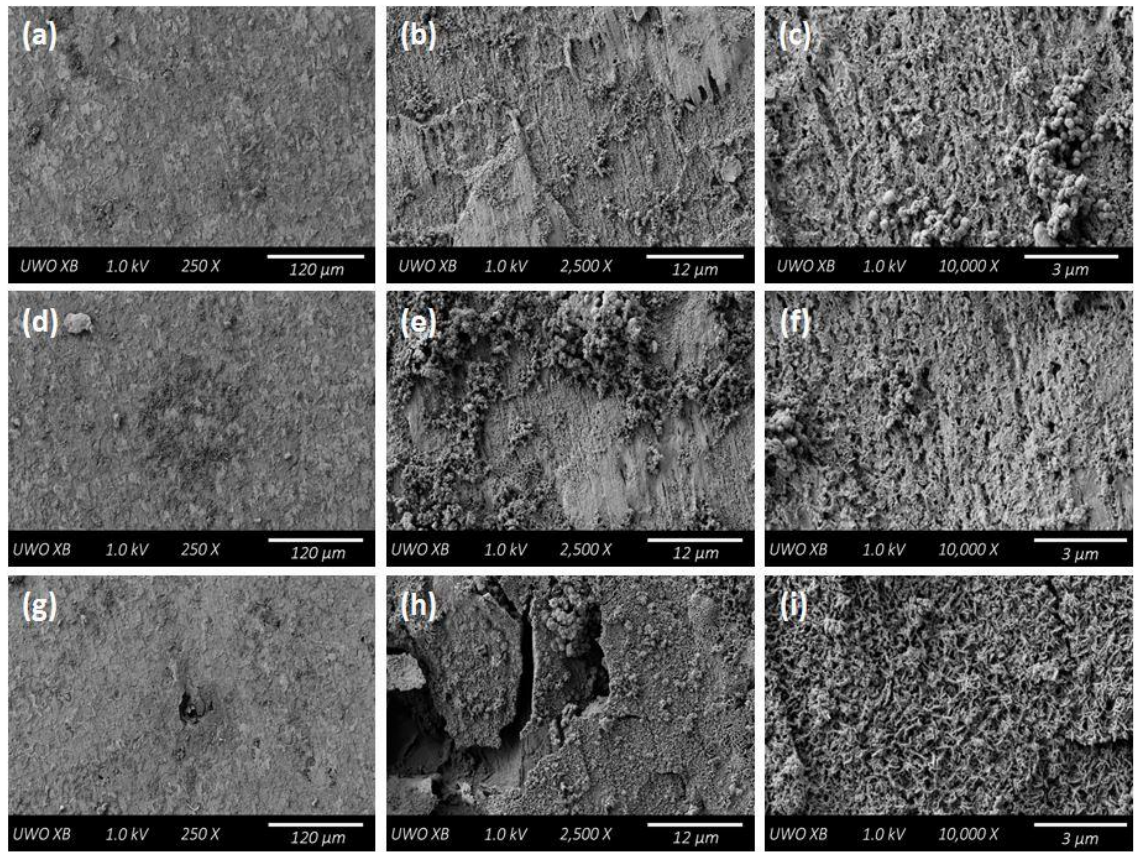


Figure A-25: SEM micrographs recorded on a specimen surface after 540 days of exposure to solution (i) showing: (a-c) the general surface morphology; (d-f) a region exhibiting additional corrosion deposits; (g-i) a region of localized corrosion damage.

A.3. SOLUTION (II): HIGH CHLORIDE CONCENTRATION

A.3.1. Raman Spectroscopy

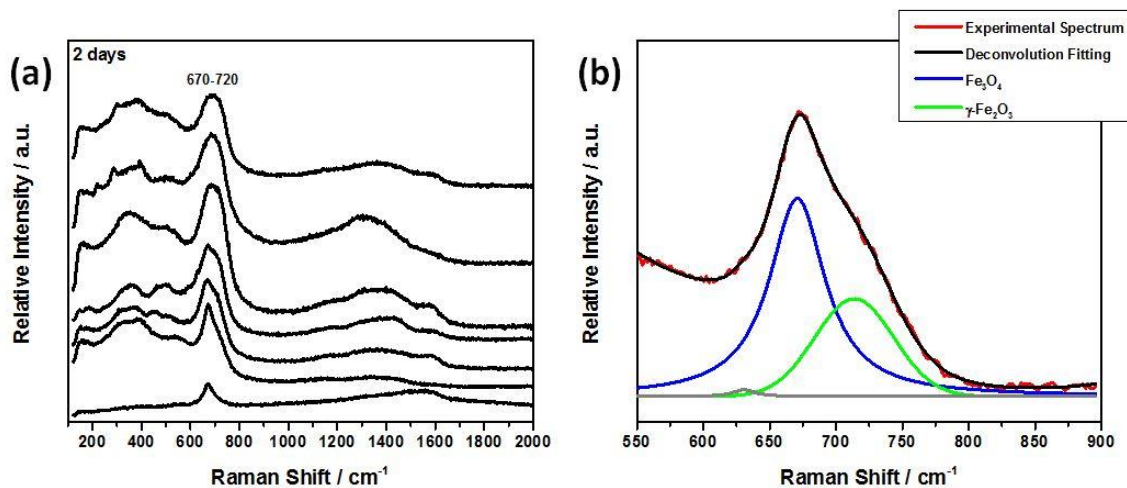


Figure A-26: (a) Raman spectra recorded at various locations on a steel specimen after 2 days of exposure to solution (ii); (b) deconvolution of the spectrum closest to the sample average.

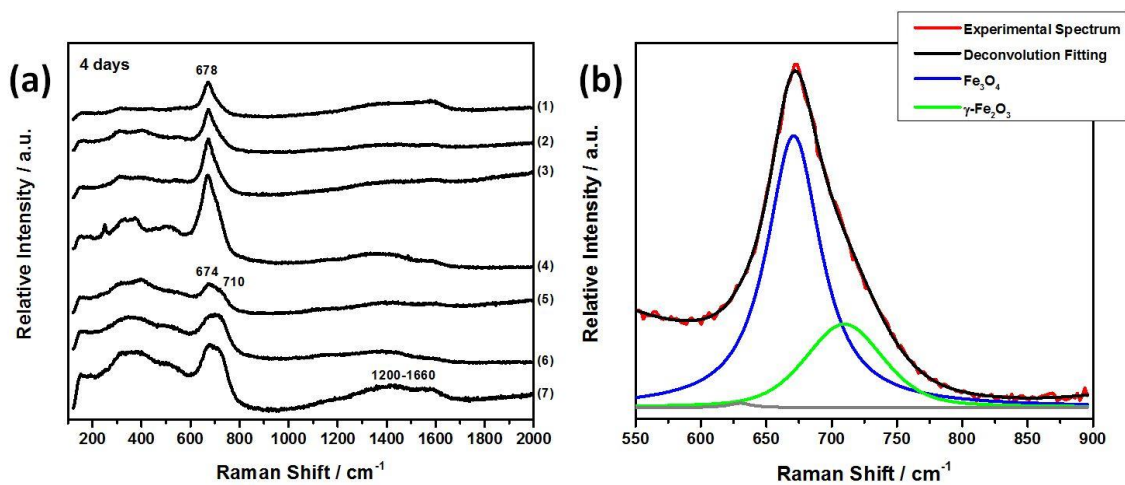


Figure A-27: (a) Raman spectra recorded at various locations on a steel specimen after 4 days of exposure to solution (ii); (b) deconvolution of the spectrum closest to the sample average.

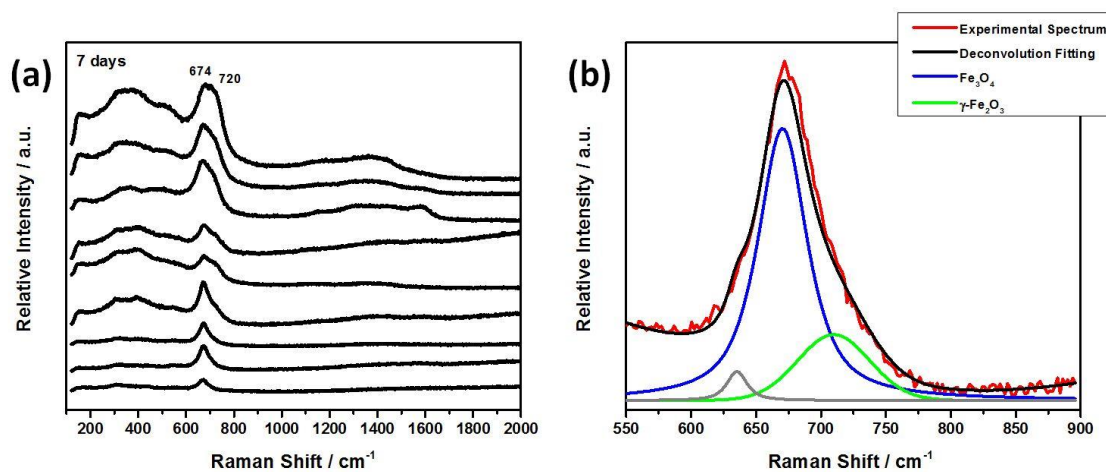


Figure A-28: (a) Raman spectra recorded at various locations on a steel specimen after 7 days of exposure to solution (ii); (b) deconvolution of the spectrum closest to the sample average.

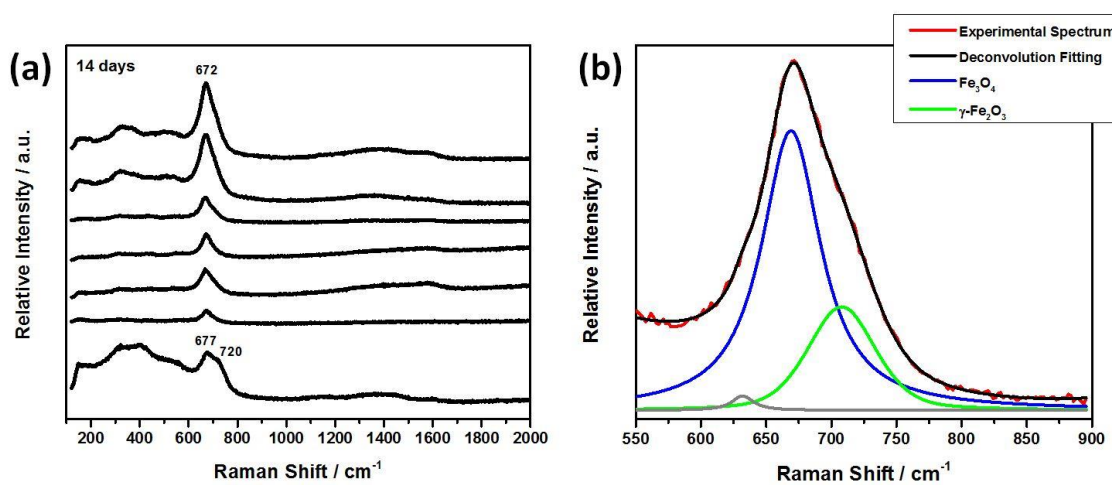


Figure A-29: (a) Raman spectra recorded at various locations on a steel specimen after 14 days of exposure to solution (ii); (b) deconvolution of the spectrum closest to the sample average.

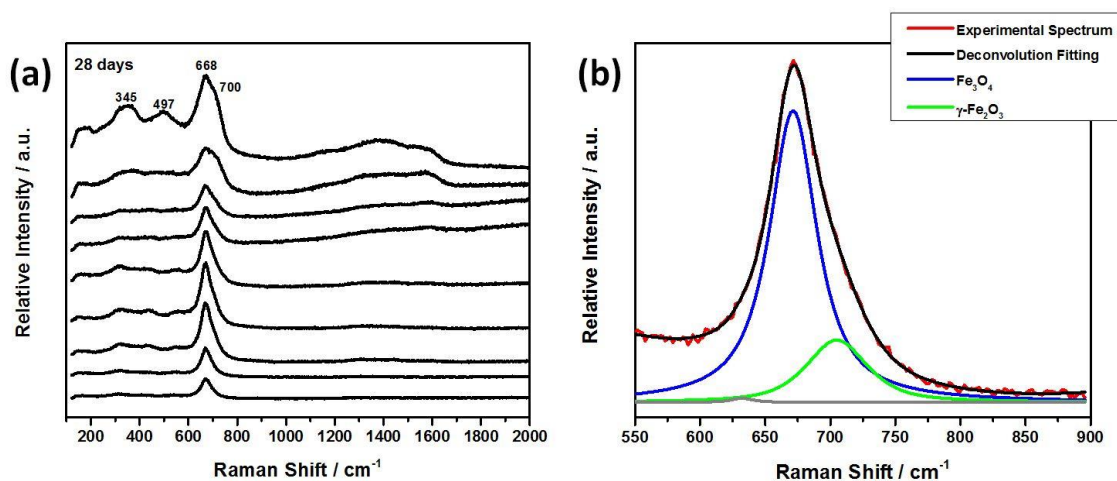


Figure A-30: (a) Raman spectra recorded at various locations on a steel specimen after 28 days of exposure to solution (ii); (b) deconvolution of the spectrum closest to the sample average.

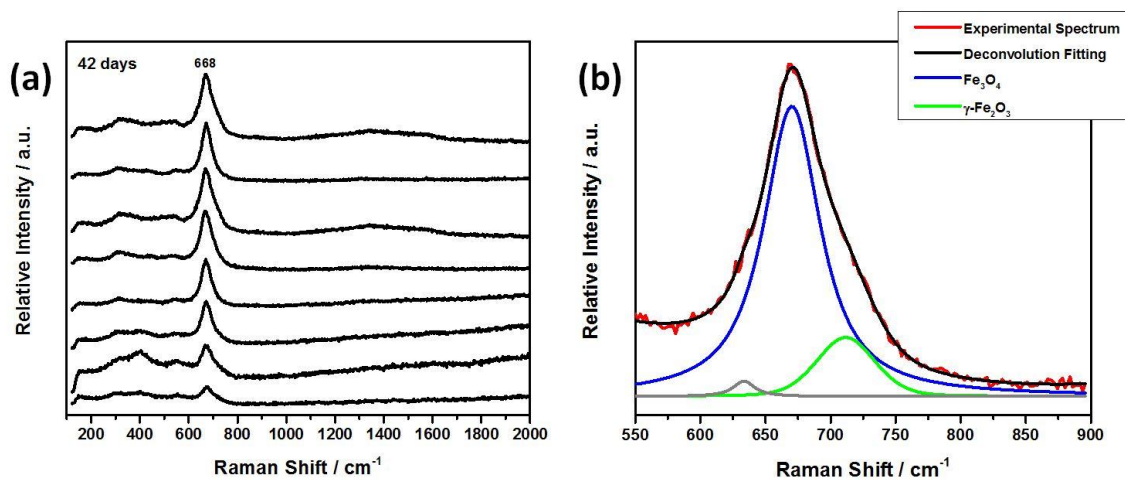


Figure A-31: (a) Raman spectra recorded at various locations on a steel specimen after 42 days of exposure to solution (ii); (b) deconvolution of the spectrum closest to the sample average.

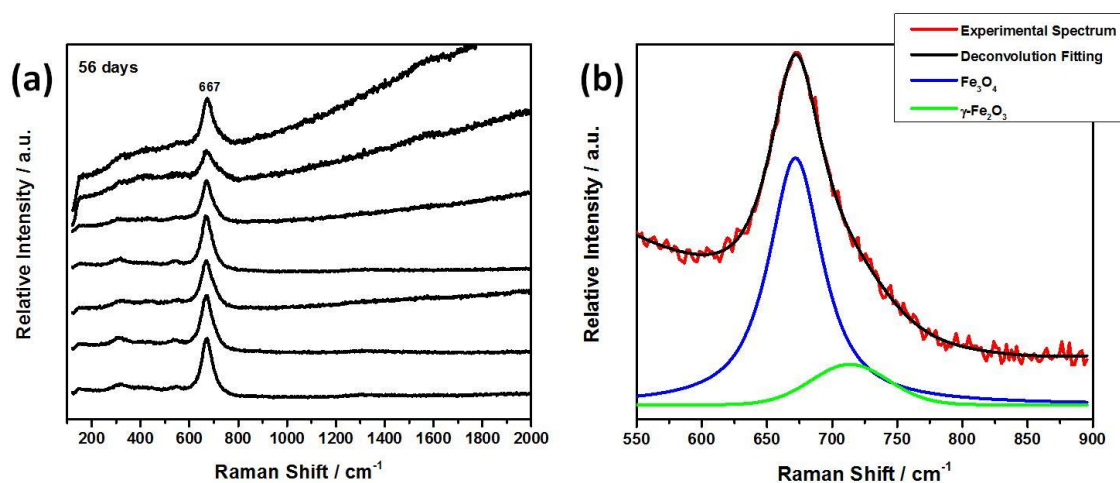


Figure A-32: (a) Raman spectra recorded at various locations on a steel specimen after 56 days of exposure to solution (ii); (b) deconvolution of the spectrum closest to the sample average.

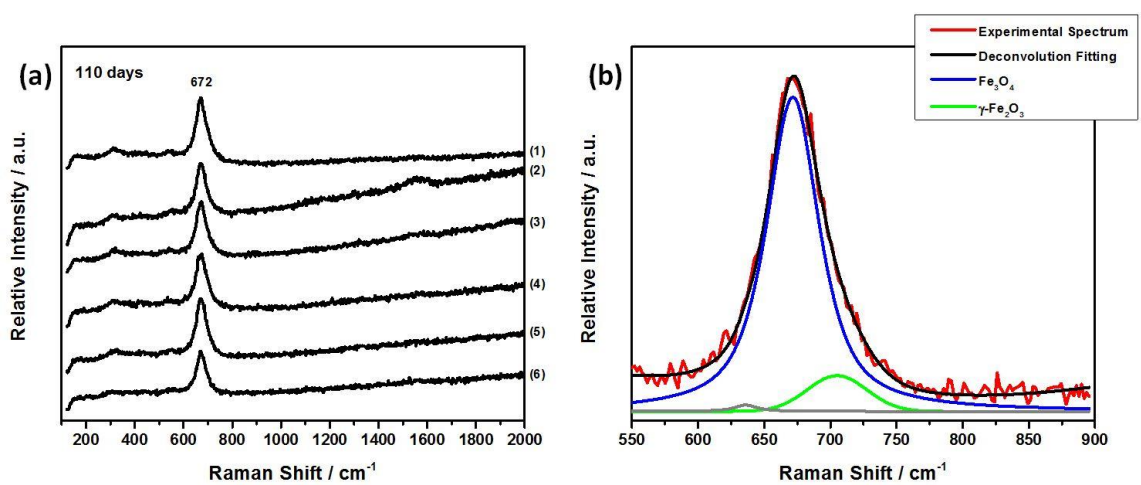


Figure A-33: (a) Raman spectra recorded at various locations on a steel specimen after 110 days of exposure to solution (ii); (b) deconvolution of the spectrum closest to the sample average.

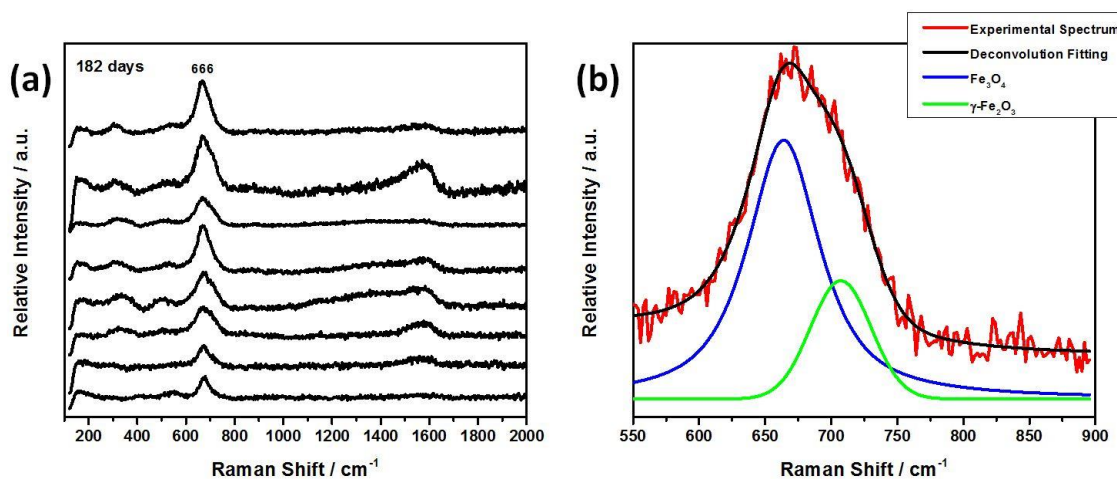


Figure A-34: (a) Raman spectra recorded at various locations on a steel specimen after 182 days of exposure to solution (ii); (b) deconvolution of the spectrum closest to the sample average.

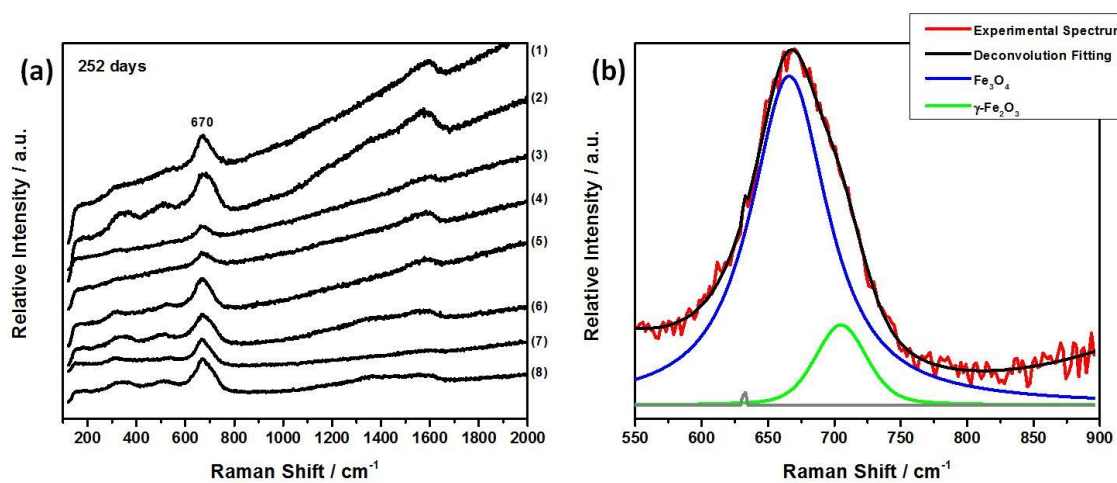


Figure A-35: (a) Raman spectra recorded at various locations on a steel specimen after 252 days of exposure to solution (ii); (b) deconvolution of the spectrum closest to the sample average.

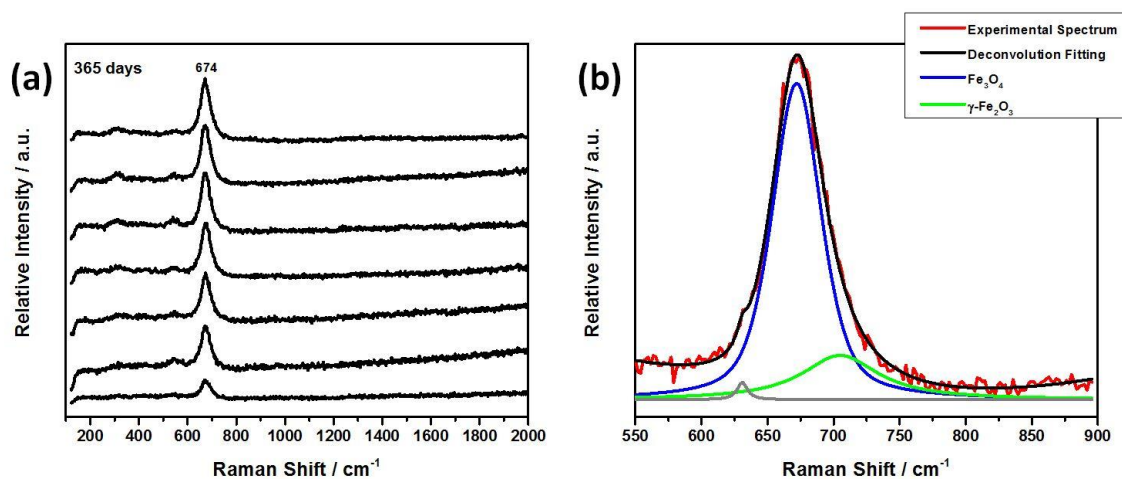


Figure A-36: (a) Raman spectra recorded at various locations on a steel specimen after 365 days of exposure to solution (ii); (b) deconvolution of the spectrum closest to the sample average.

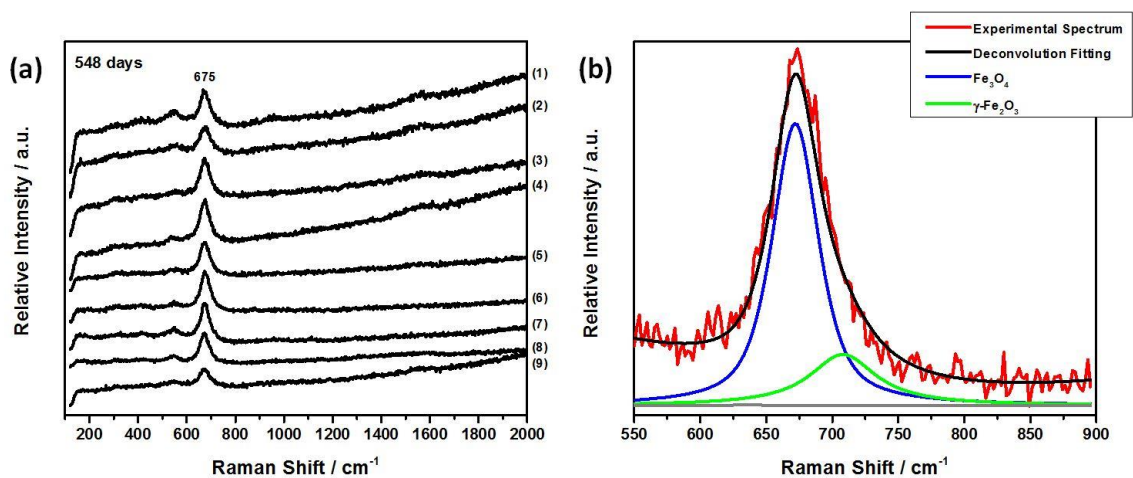


Figure A-37: (a) Raman spectra recorded at various locations on a steel specimen after 548 days of exposure to solution (ii); (b) deconvolution of the spectrum closest to the sample average.

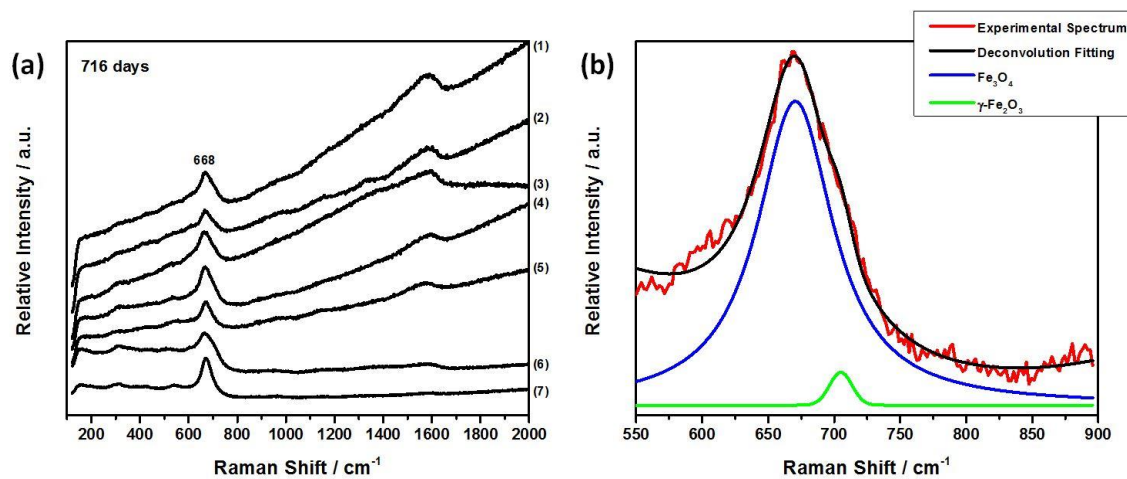


Figure A-38: (a) Raman spectra recorded at various locations on a steel specimen after 716 days of exposure to solution (ii); (b) deconvolution of the spectrum closest to the sample average.

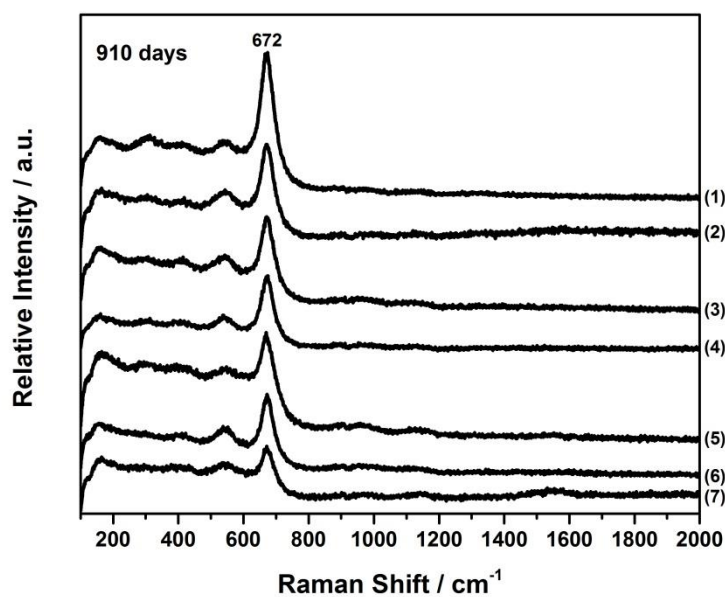


Figure A-39: Raman spectra recorded at various locations on a steel specimen after 910 days of exposure to solution (ii).

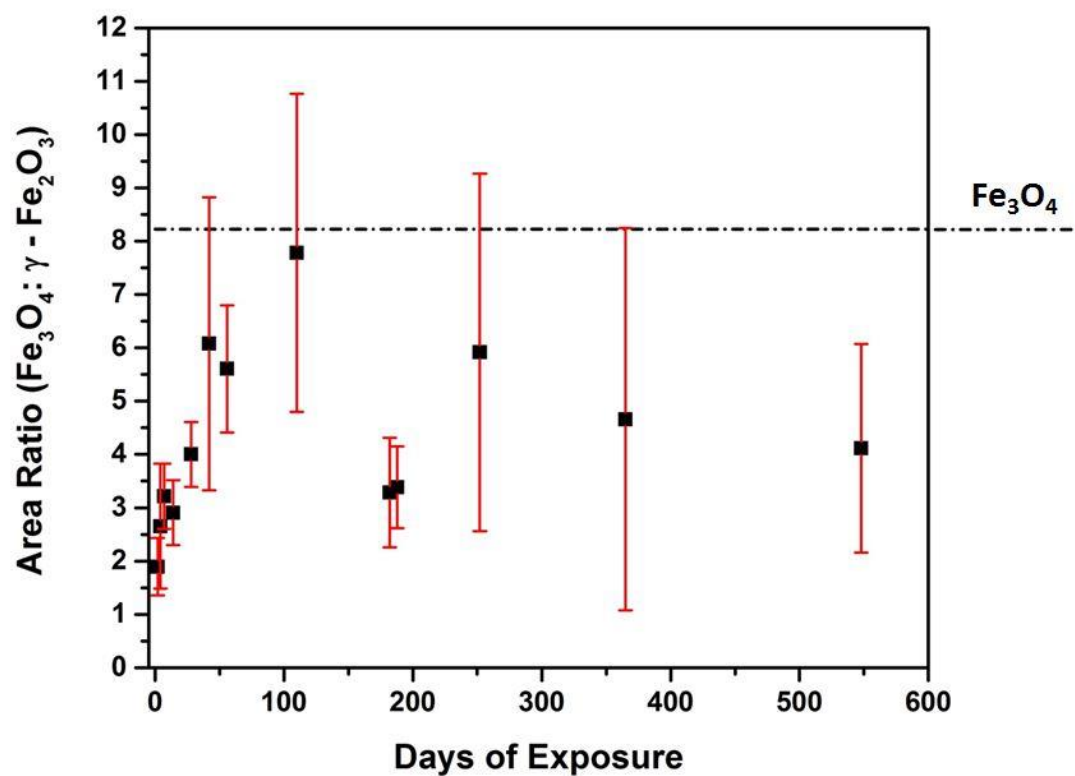


Figure A-40: Evolution of the area ratio between the Fe₃O₄ (672 cm⁻¹) and γ-Fe₂O₃ (705 cm⁻¹) Raman peaks after exposure to solution (ii), calculated from the deconvoluted spectra.

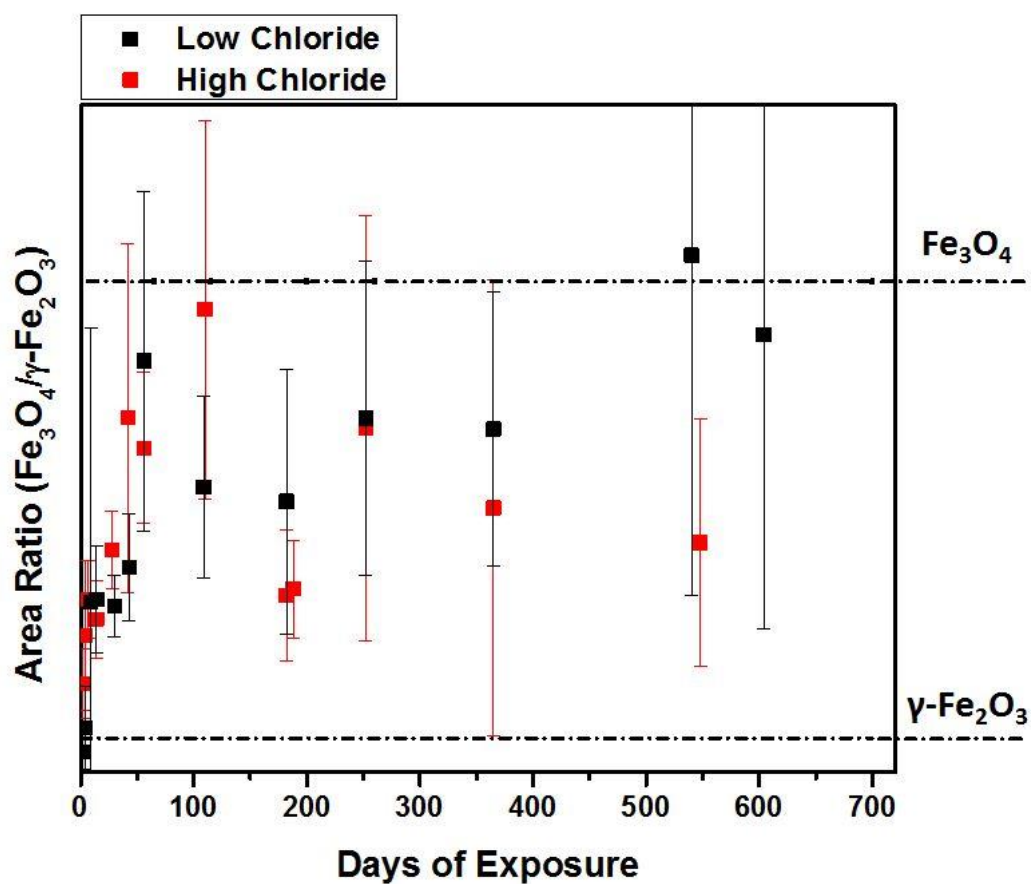


Figure A-41: Comparison of the evolution in the area ratio for the Fe_3O_4 (672 cm^{-1}) and $\gamma\text{-Fe}_2\text{O}_3$ (705 cm^{-1}) Raman peaks between solutions (i) and (ii), calculated from the deconvoluted Raman spectra.

A.3.2. Scanning Electron Microscopy

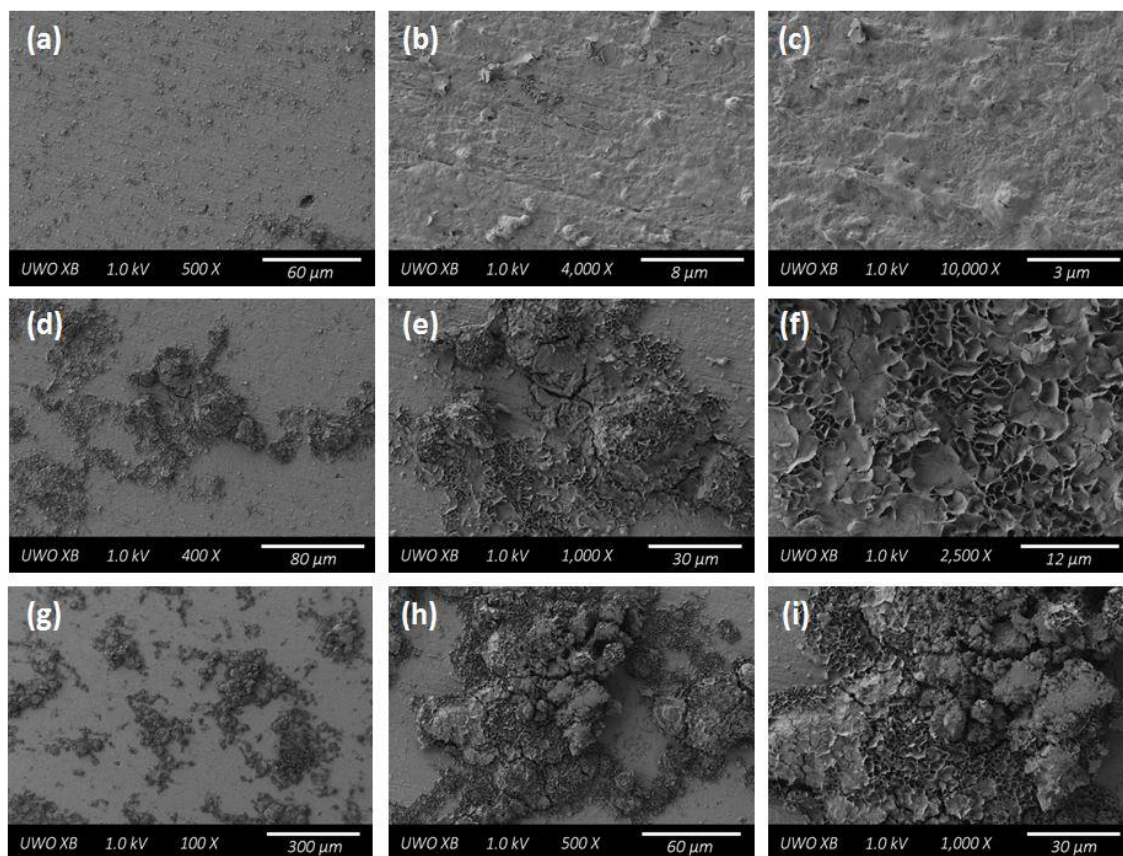


Figure A-42: SEM micrographs recorded on a specimen surface after 2 days of exposure to solution (ii) showing: (a-c) the general surface morphology; (d-f) a region of localized crystalline corrosion product; (g-i) the distribution and morphology of heavily corroded locations.

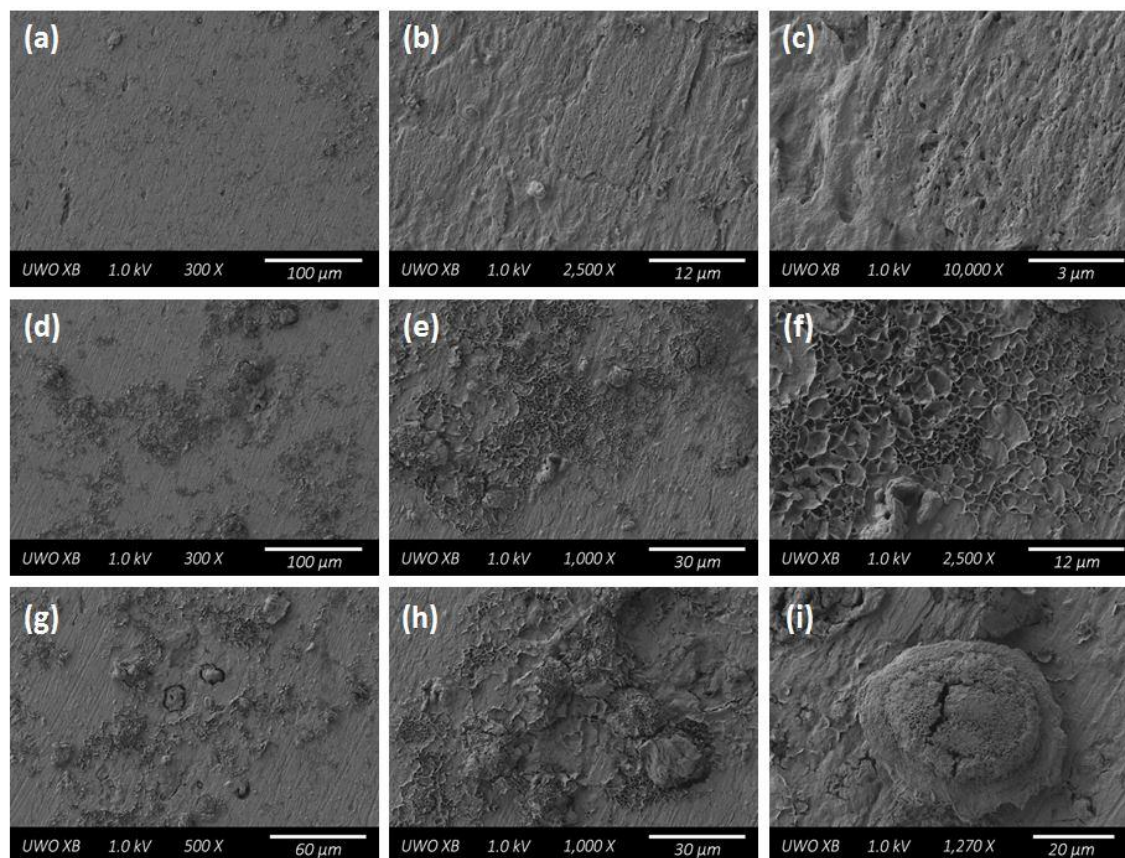


Figure A-43: SEM micrographs recorded on a specimen surface after 7 days of exposure to solution (ii) showing: (a-c) the general surface morphology; (d-f) a region with crystalline corrosion product; (g-h) a region exhibiting more extensive corrosion damage; (i) a location with a large localized corrosion product deposit.

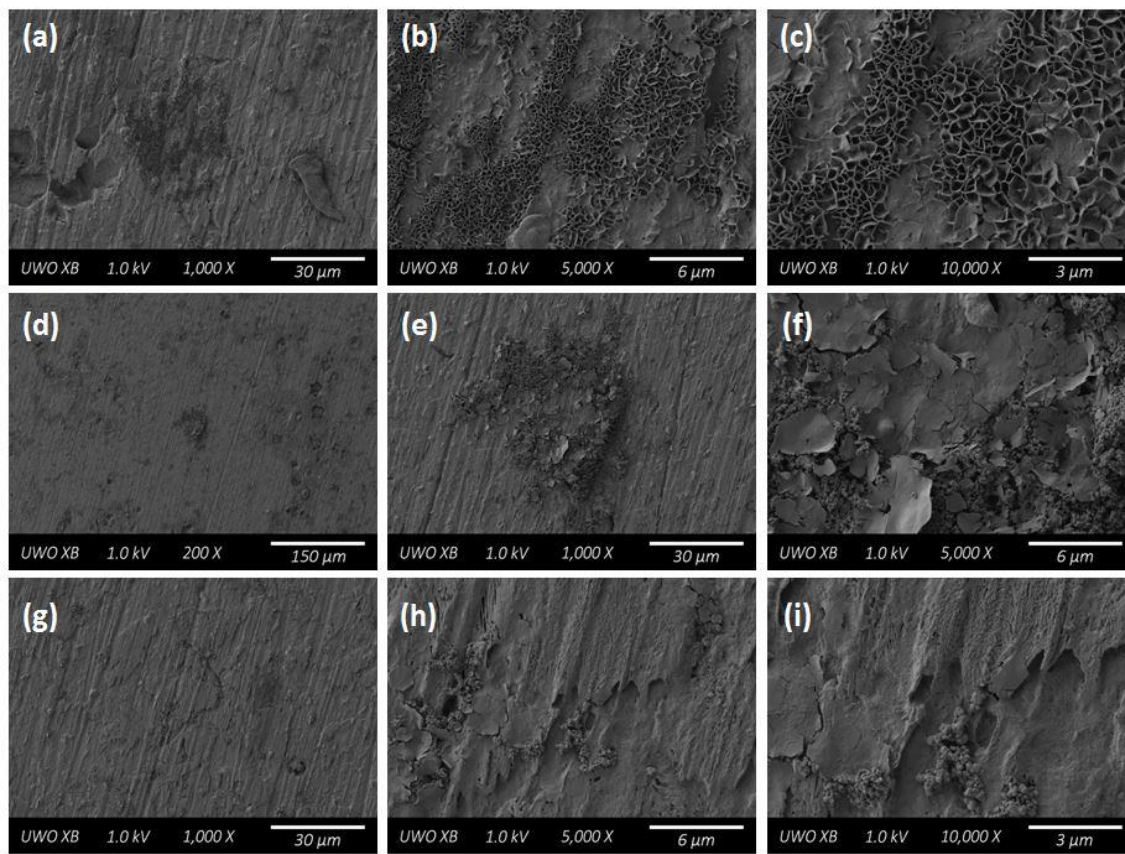


Figure A-44: SEM micrographs recorded on a specimen surface after 14 days of exposure to solution (ii) showing: (a-c) crystalline corrosion product; (d-f) a region of secondary corrosion product morphology; (g-i) the general surface morphology.

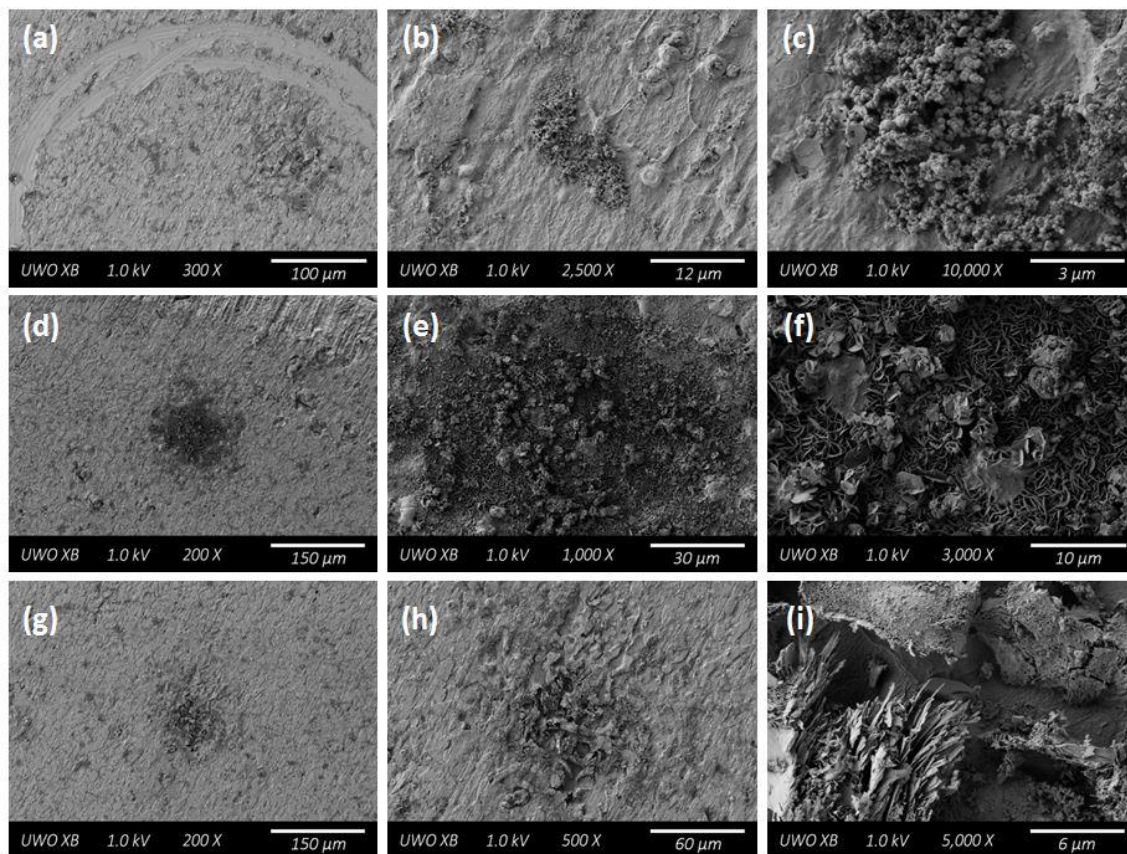


Figure A-45: SEM micrographs recorded on a specimen surface after 28 days of exposure to solution (ii) showing: (a-c) a region of general corrosion product deposit; (d-f) a more significantly corroded region with crystalline morphology; (g-i) a region of localized corrosion damage.

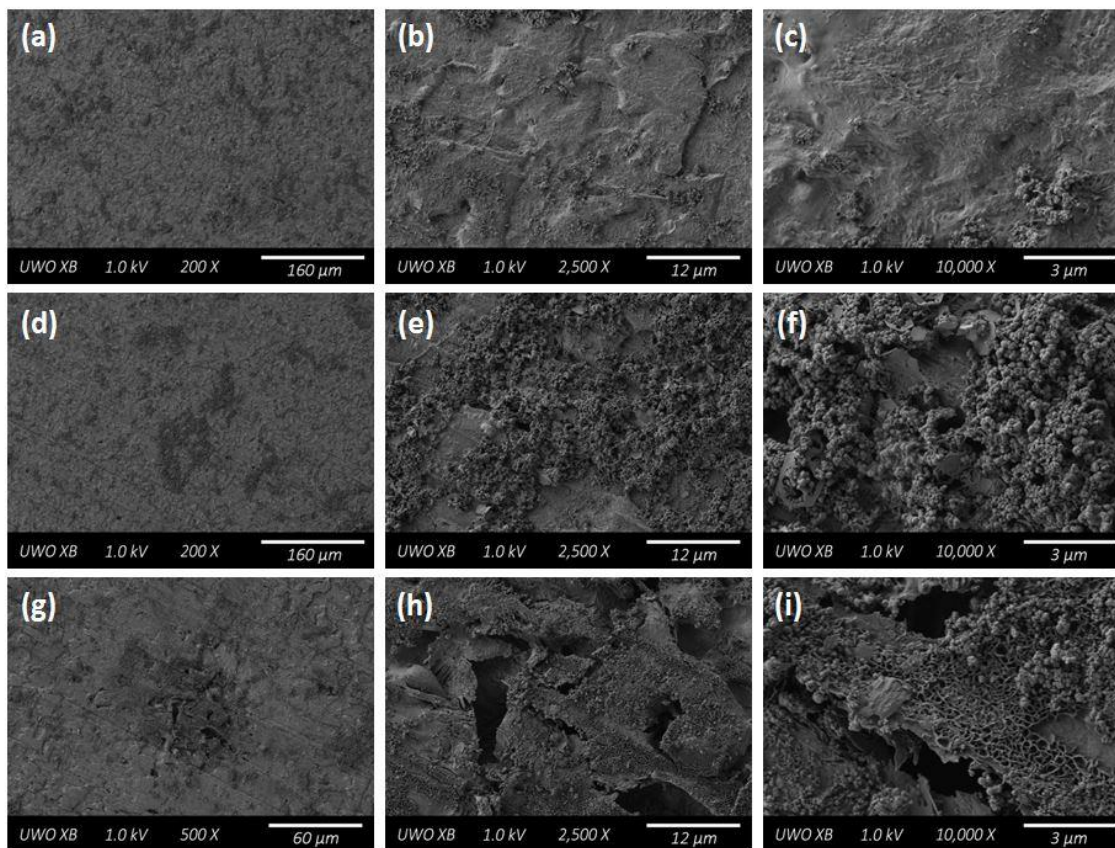


Figure A-46: SEM micrographs recorded on a specimen surface after 42 days of exposure to solution (ii) showing: (a-c) the general surface morphology; (d-f) a region of more significant corrosion product deposit; (g-i) a region of localized corrosion damage.

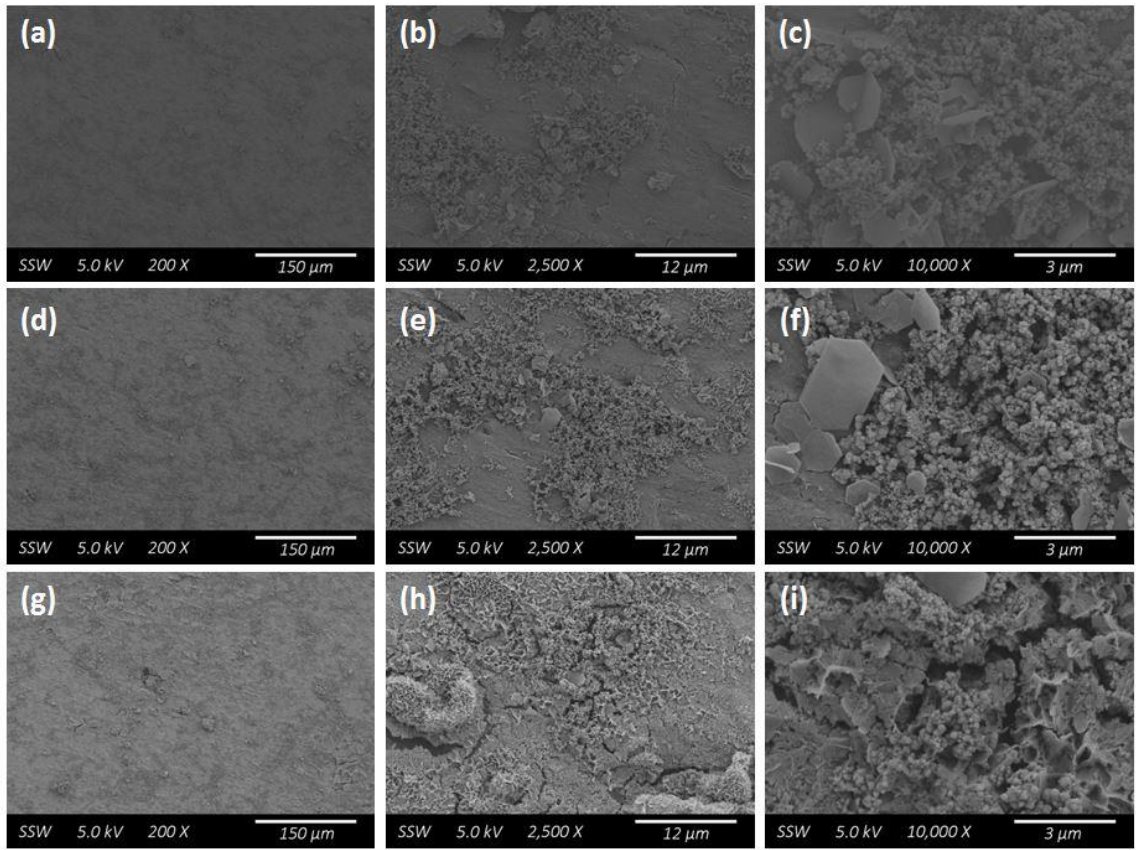


Figure A-47: SEM micrographs recorded on a specimen surface after 56 days of exposure to solution (ii) showing: (a-f) the general surface morphology; (g-i) a region of localized corrosion damage.

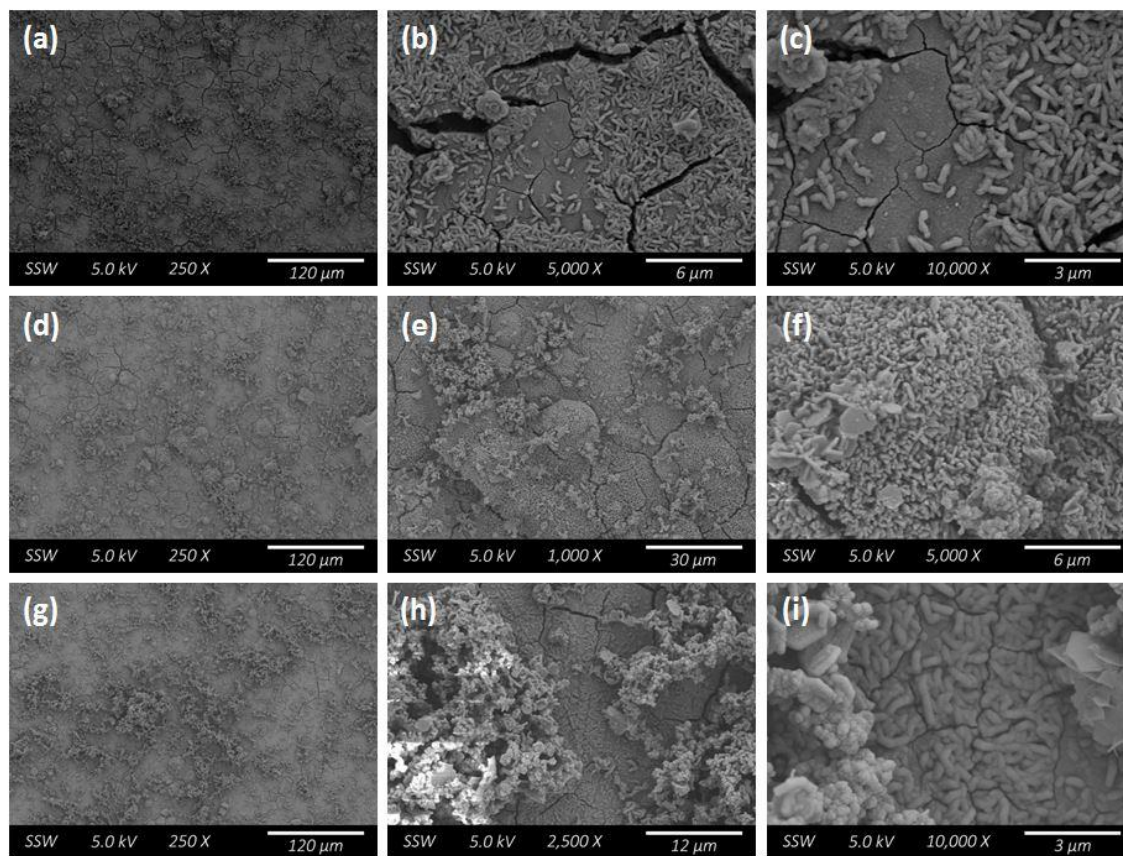


Figure A-48: SEM micrographs recorded on a specimen surface after 182 days of exposure to solution (ii) showing: (a-c) the general surface morphology; (d-f) a region of more significant corrosion damage; (g-h) a region exhibiting more significant corrosion product deposits; (i) the underlying general surface morphology beneath the corrosion product deposits.

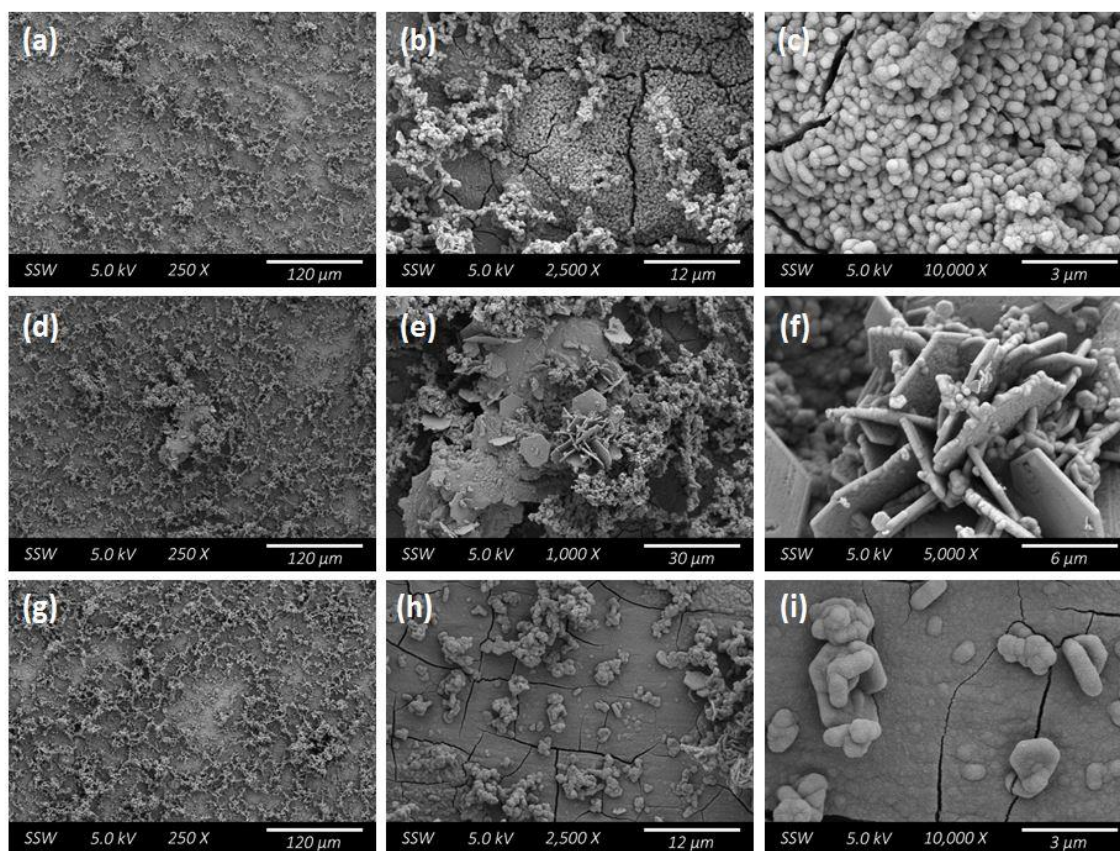


Figure A-49: SEM micrographs recorded on a specimen surface after 365 days of exposure to solution (ii) showing: (a-c) the general surface morphology; (d-f) a more significant crystalline corrosion product deposit; (g-i) a region of the general surface highlighting the smooth underlying corrosion product layer.

A.4. SOLUTION (III): BUFFERED, HIGH CHLORIDE CONCENTRATION

A.4.1. Raman Spectroscopy

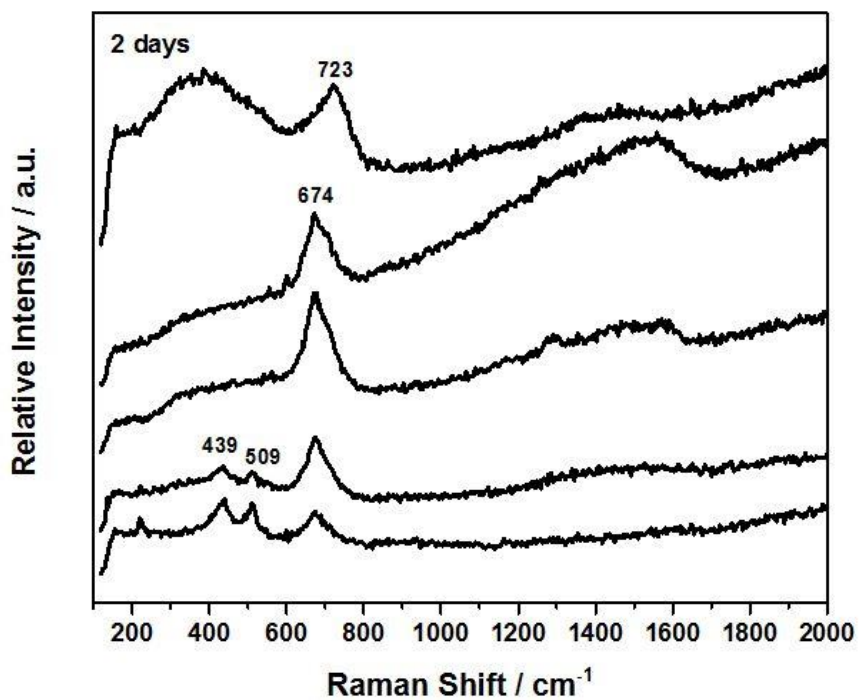


Figure A-50: Raman spectra recorded at various locations on a steel specimen after 2 days of exposure to solution (iii).

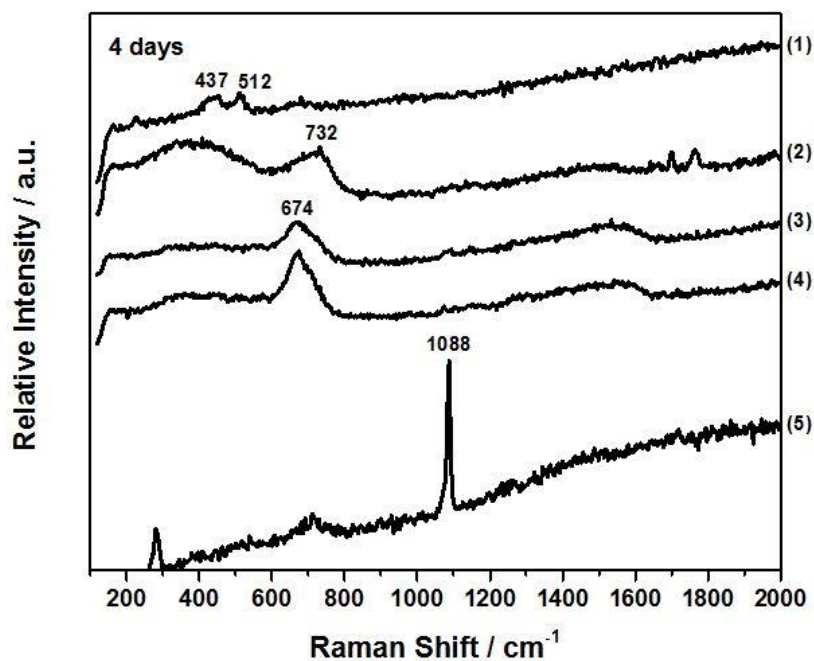


Figure A-51: Raman spectra recorded at various locations on a steel specimen after 4 days of exposure to solution (iii).

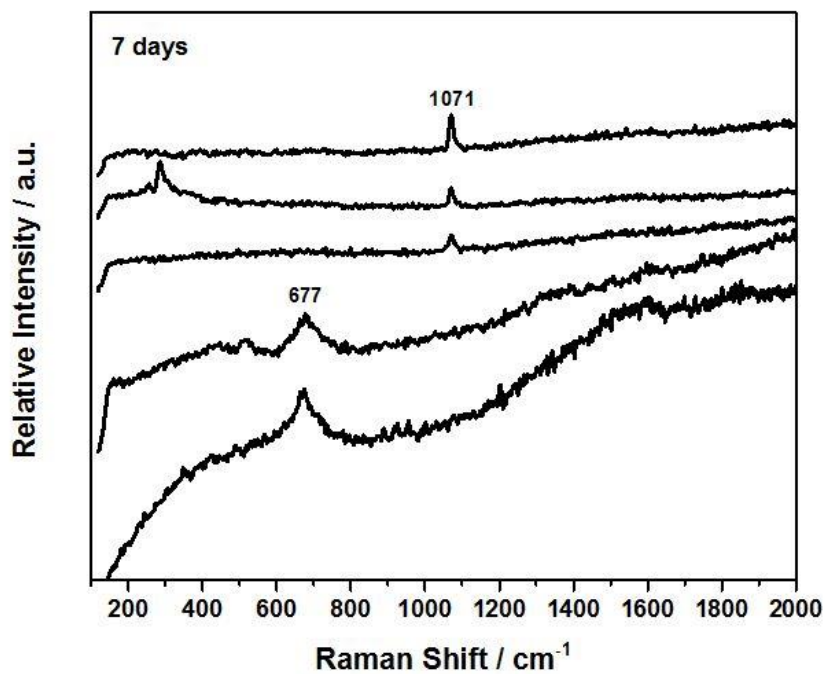


Figure A-52: Raman spectra recorded at various locations on a steel specimen after 7 days of exposure to solution (iii).

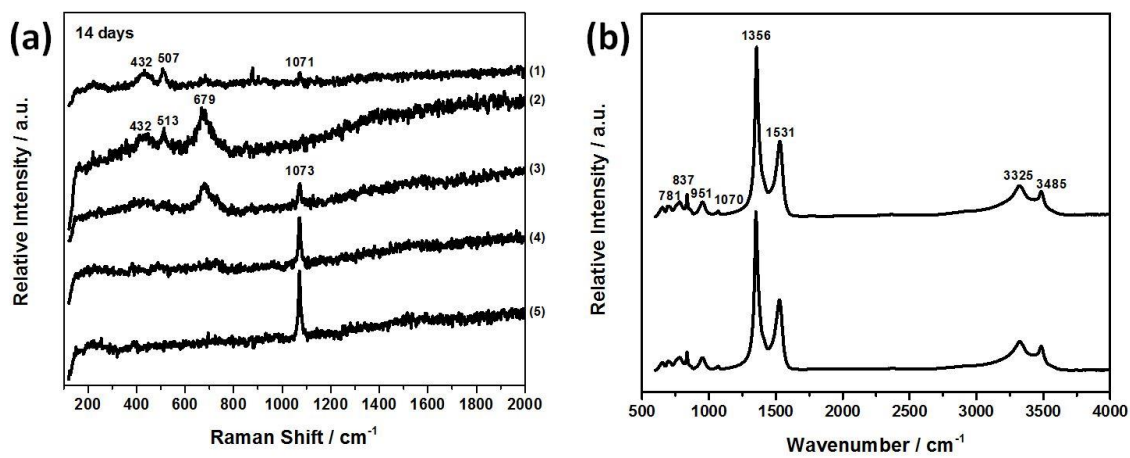


Figure A-53: (a) Raman and (b) FTIR spectra recorded at various locations on a steel specimen after 14 days of exposure to solution (iii).

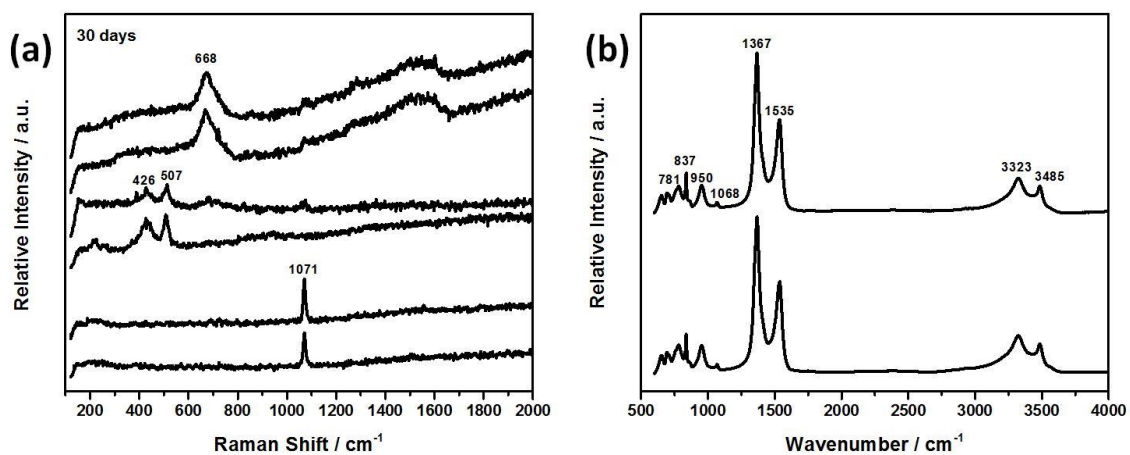


Figure A-54: (a) Raman and (b) FTIR spectra recorded at various locations on a steel specimen after 30 days of exposure to solution (iii).

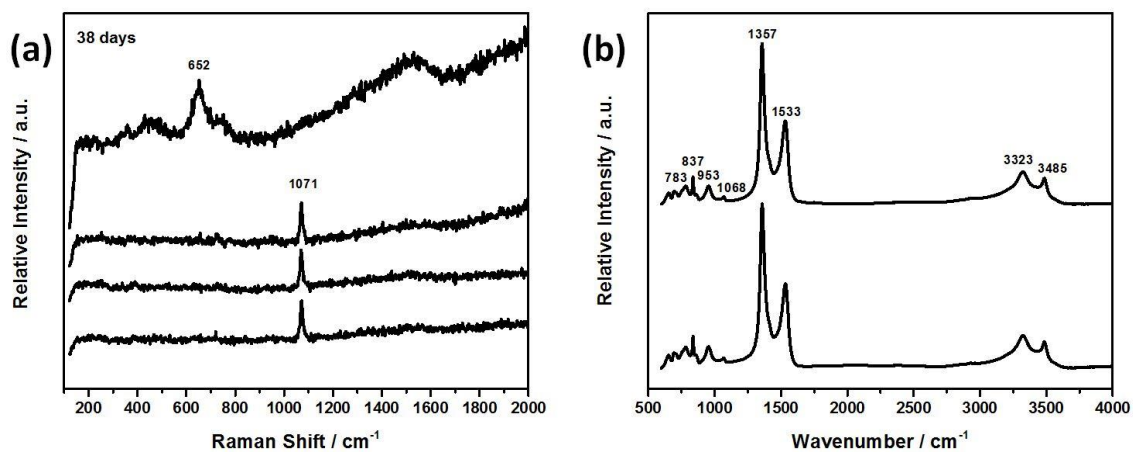


Figure A-55: (a) Raman and (b) FTIR spectra recorded at various locations on a steel specimen after 38 days of exposure to solution (iii).

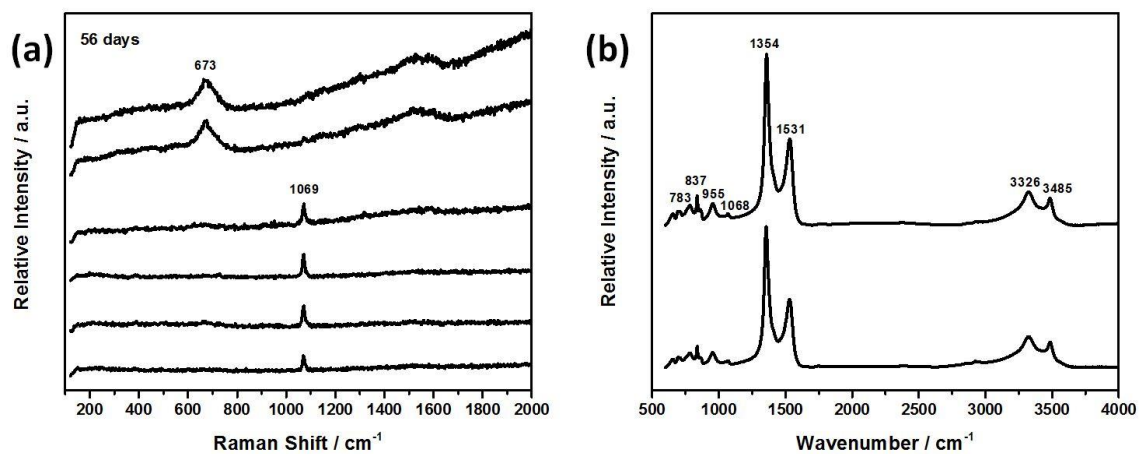


Figure A-56: (a) Raman and (b) FTIR spectra recorded at various locations on a steel specimen after 56 days of exposure to solution (iii).

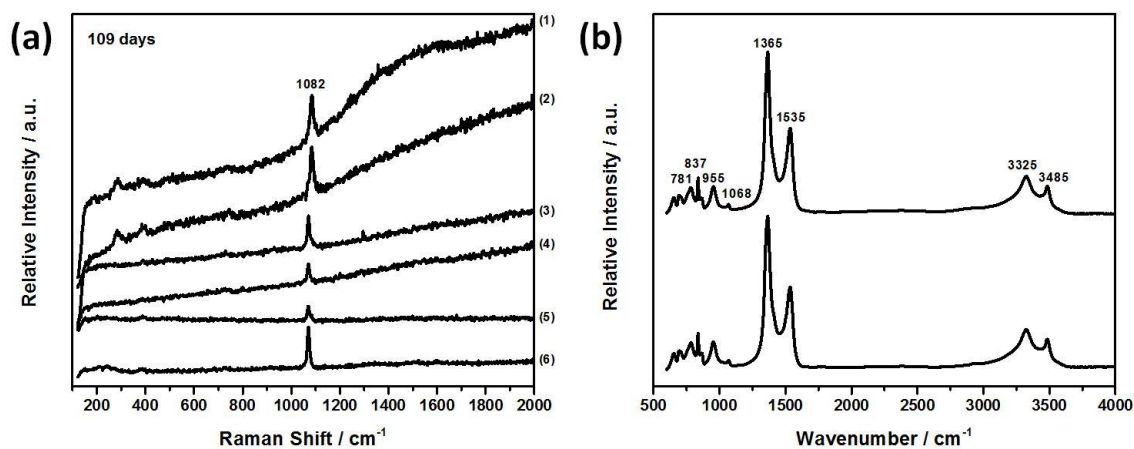


Figure A-57: (a) Raman and (b) FTIR spectra recorded at various locations on a steel specimen after 109 days of exposure to solution (iii).

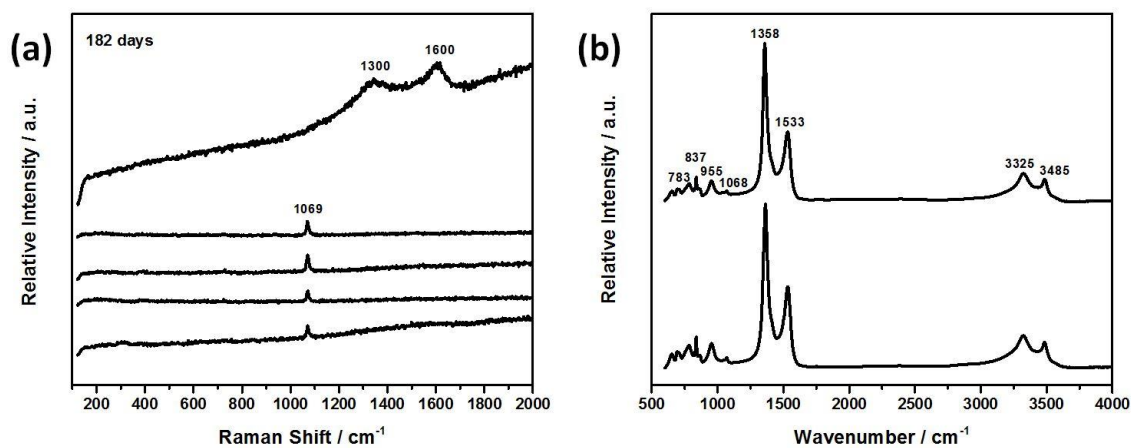


Figure A-58: (a) Raman and (b) FTIR spectra recorded at various locations on a steel specimen after 182 days of exposure to solution (iii).

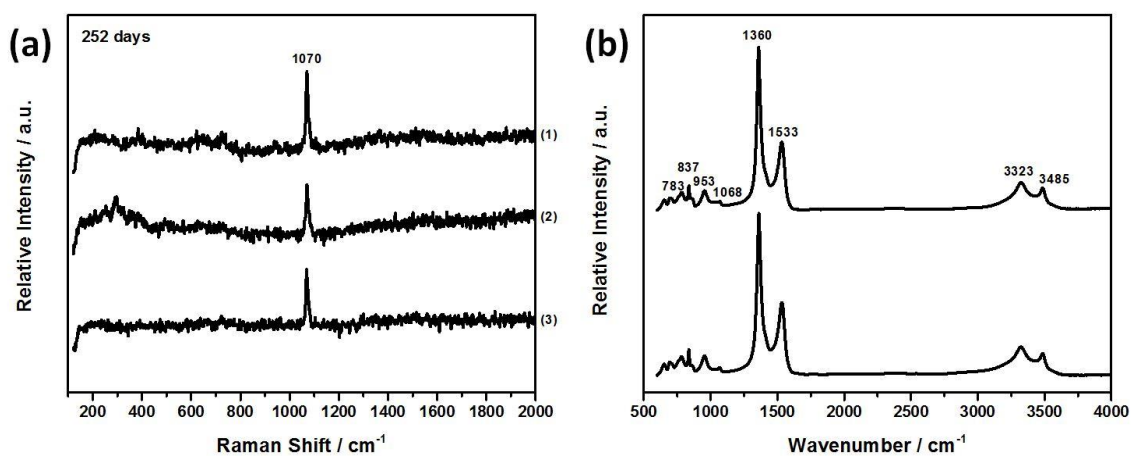


Figure A-59: (a) Raman and (b) FTIR spectra recorded at various locations on a steel specimen after 252 days of exposure to solution (iii).

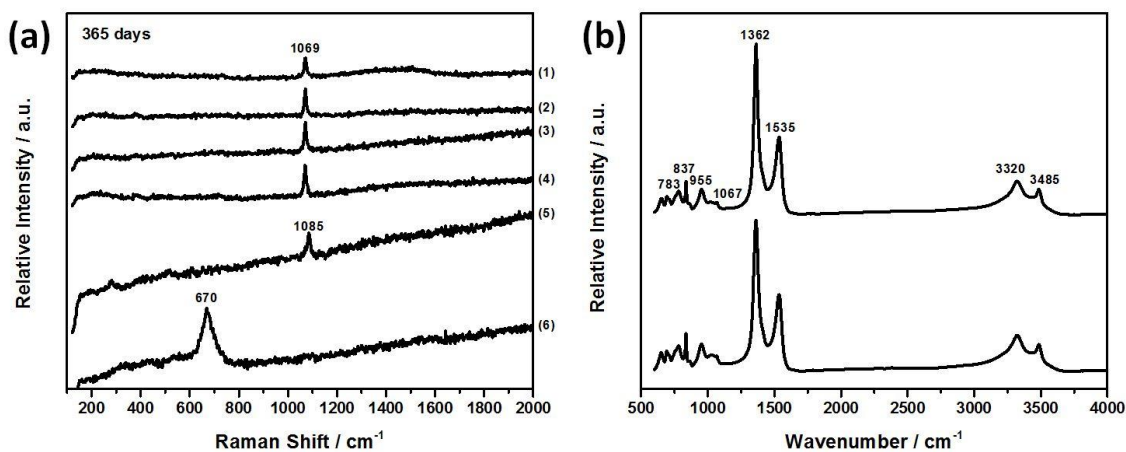


Figure A-60: (a) Raman and (b) FTIR spectra recorded at various locations on a steel specimen after 365 days of exposure to solution (iii).

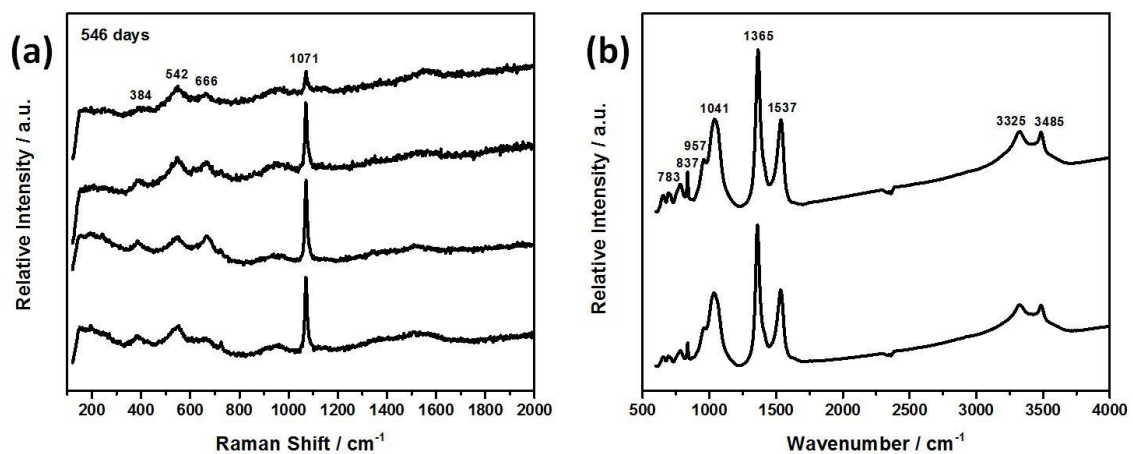


Figure A-61: (a) Raman and (b) FTIR spectra recorded at various locations on a steel specimen after 546 days of exposure to solution (iii).

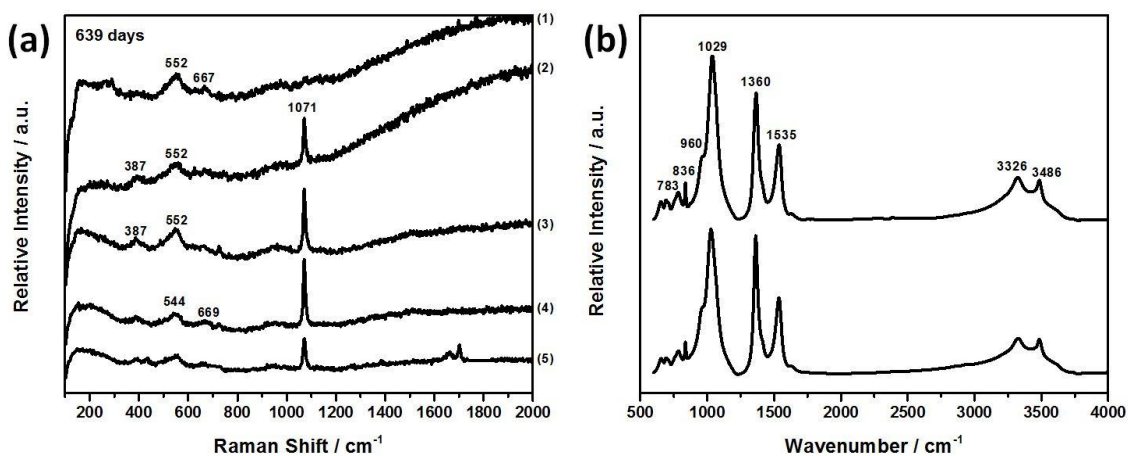


Figure A-62: (a) Raman and (b) FTIR spectra recorded at various locations on a steel specimen after 639 days of exposure to solution (iii).

A.4.2. Scanning Electron Microscopy

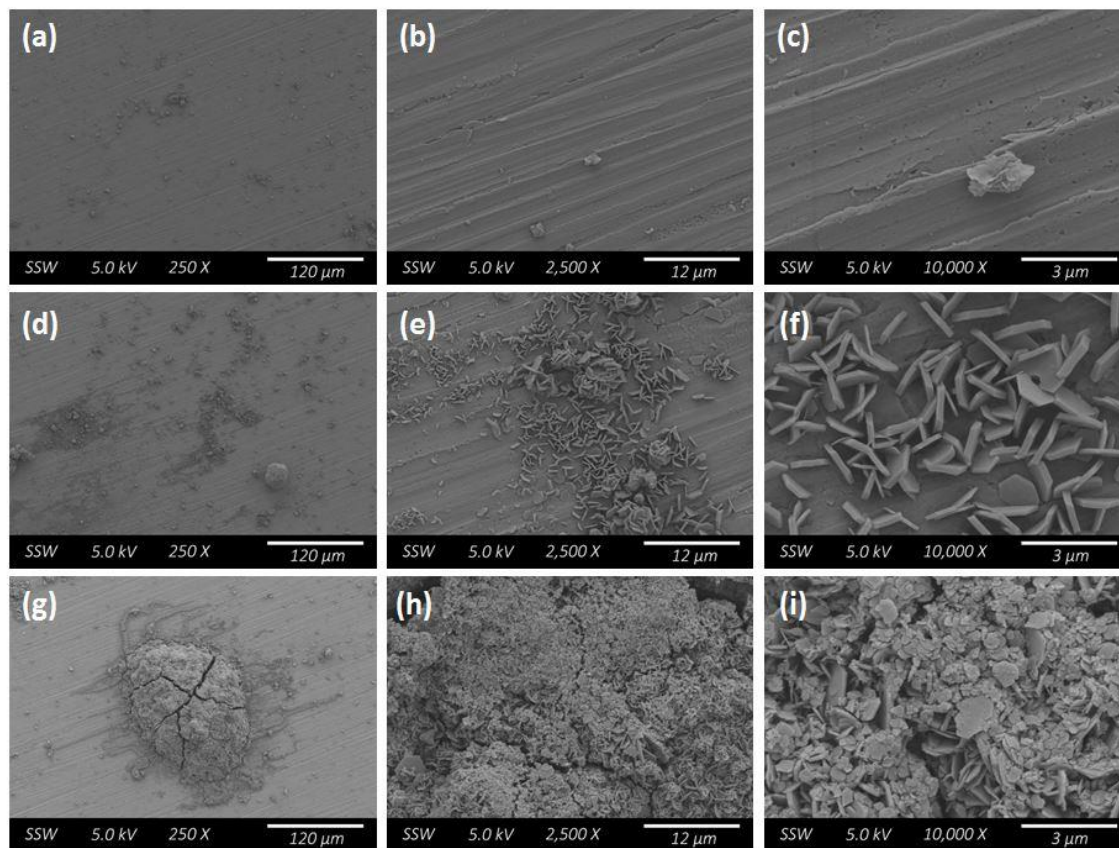


Figure A-63: SEM micrographs recorded on a specimen surface after 2 days of exposure to solution (iii) showing: (a-c) the general surface with no apparent corrosion product; (d-f) a region of crystalline corrosion product; (g-i) a region of localized corrosion product deposit.

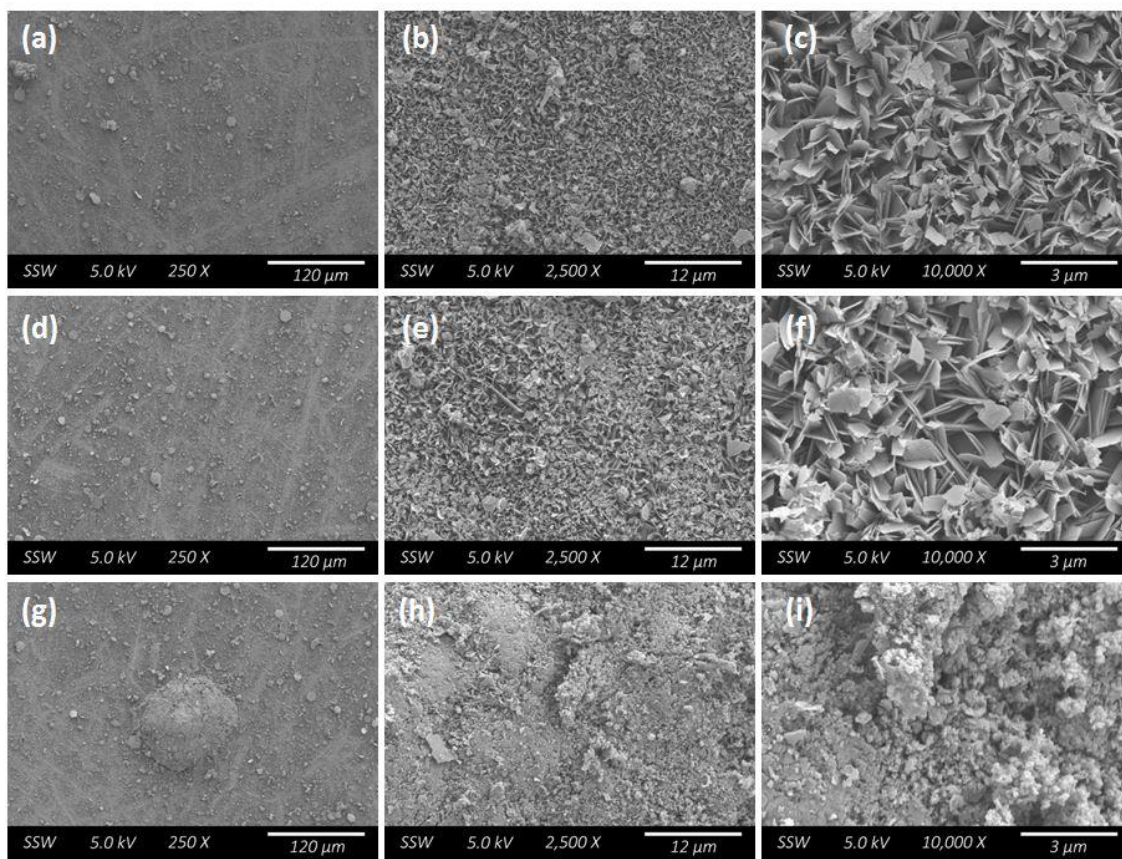


Figure A-64: SEM micrographs recorded on a specimen surface after 7 days of exposure to solution (iii) showing: (a-f) the general surface morphology, consistent with $\text{Fe}_2(\text{OH})_2\text{CO}_3$; (g-i) a region of localized corrosion product deposit.

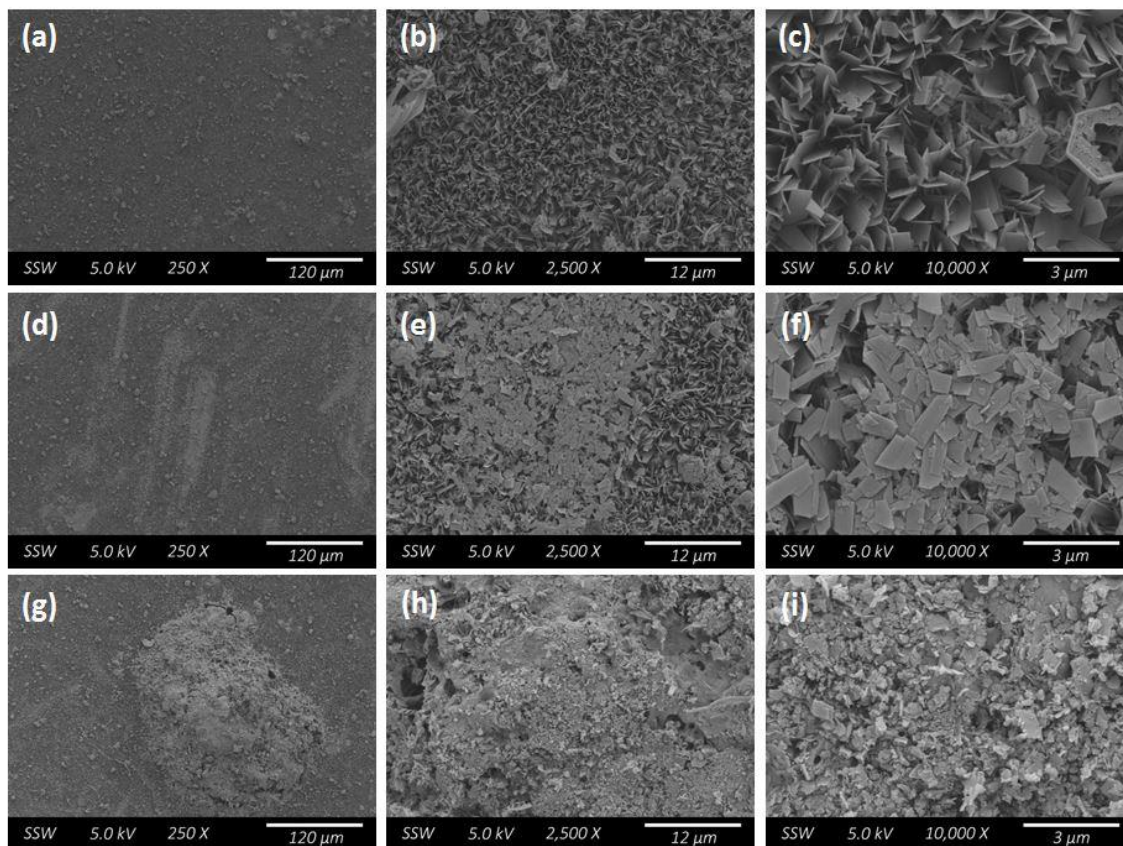


Figure A-65: SEM micrographs recorded on a specimen surface after 30 days of exposure to solution (iii) showing: (a-f) the general surface morphology, consistent with $\text{Fe}_2(\text{OH})_2\text{CO}_3$; (g-i) a region of localized corrosion product deposit.

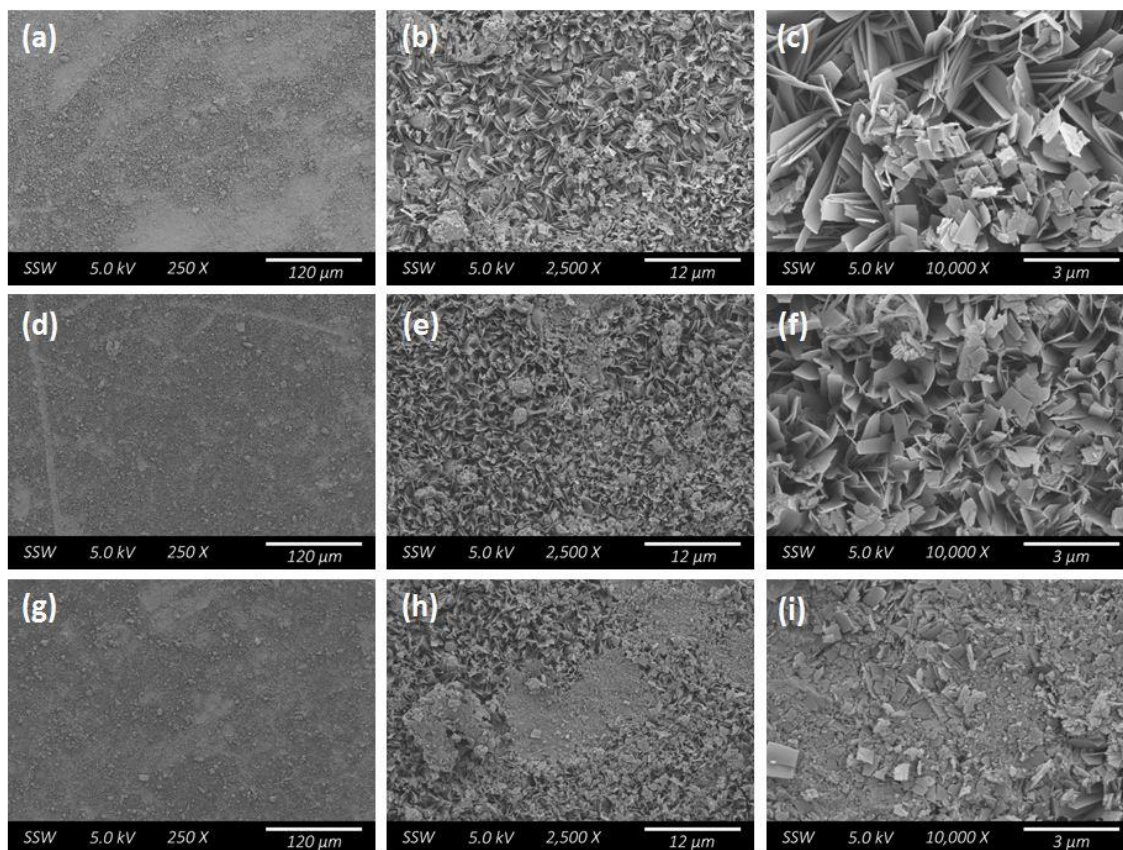


Figure A-66: SEM micrographs recorded on a specimen surface after 38 days of exposure to solution (iii) showing: (a-i) the general surface morphology, consistent with $\text{Fe}_2(\text{OH})_2\text{CO}_3$.

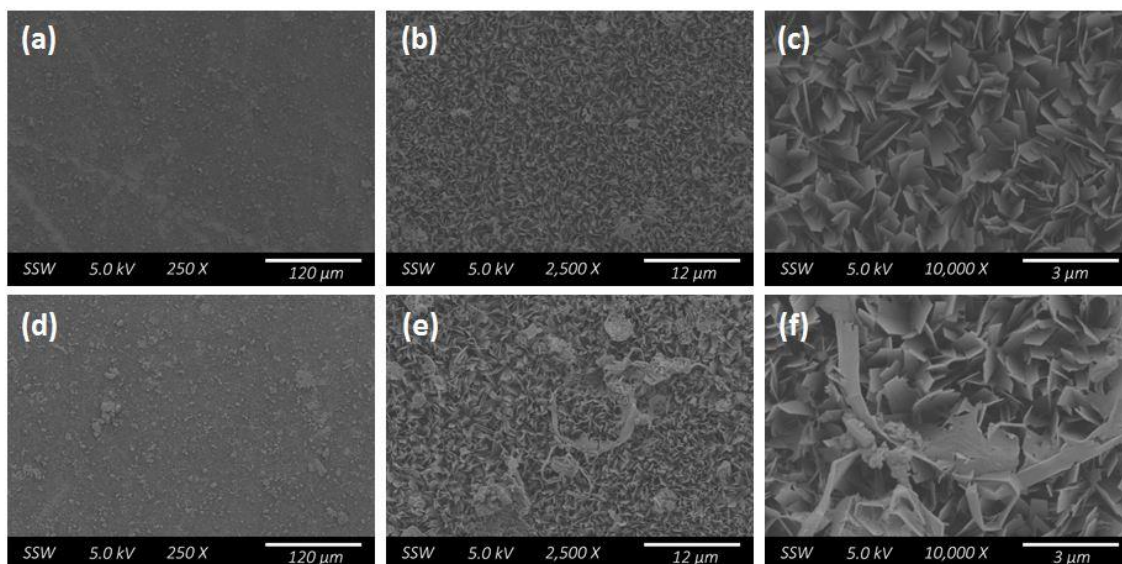


Figure A-67: SEM micrographs recorded on a specimen surface after 56 days of exposure to solution (iii) showing: (a-f) the general surface morphology, consistent with $\text{Fe}_2(\text{OH})_2\text{CO}_3$.

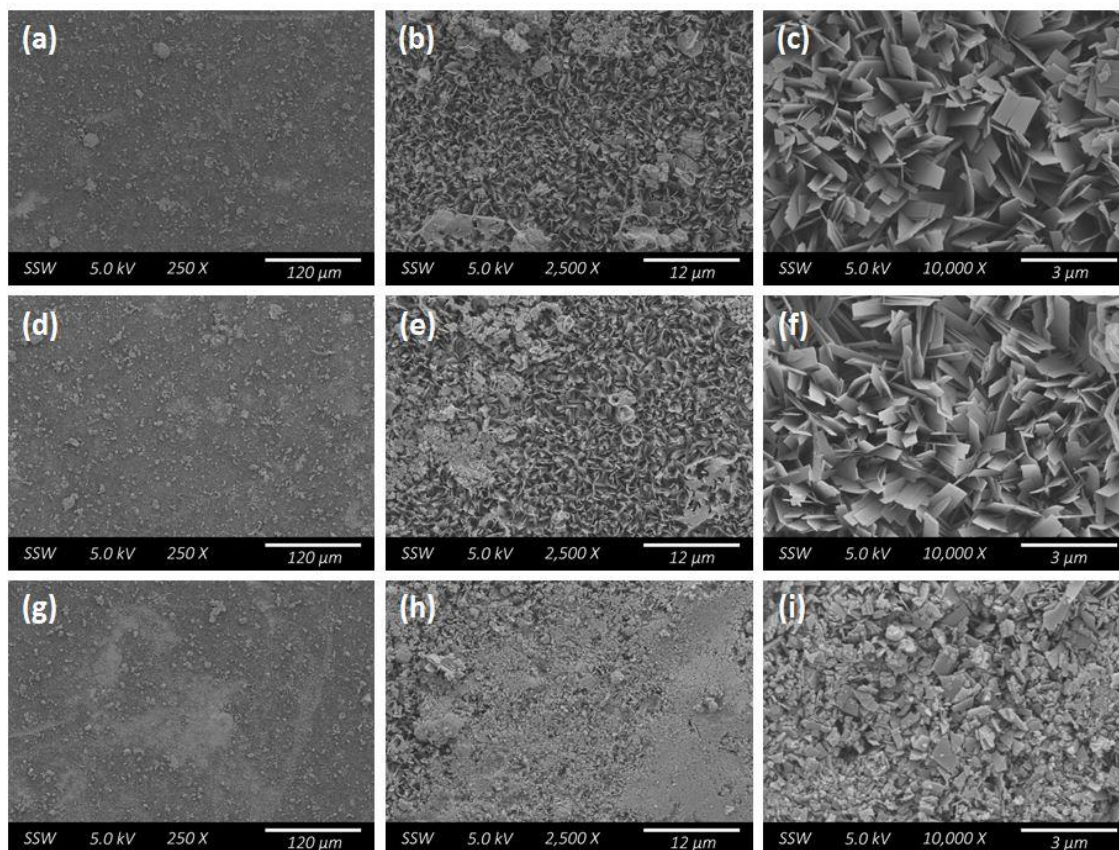


Figure A-68: SEM micrographs recorded on a specimen surface after 182 days of exposure to solution (iii) showing: (a-i) the general surface morphology, consistent with $\text{Fe}_2(\text{OH})_2\text{CO}_3$.

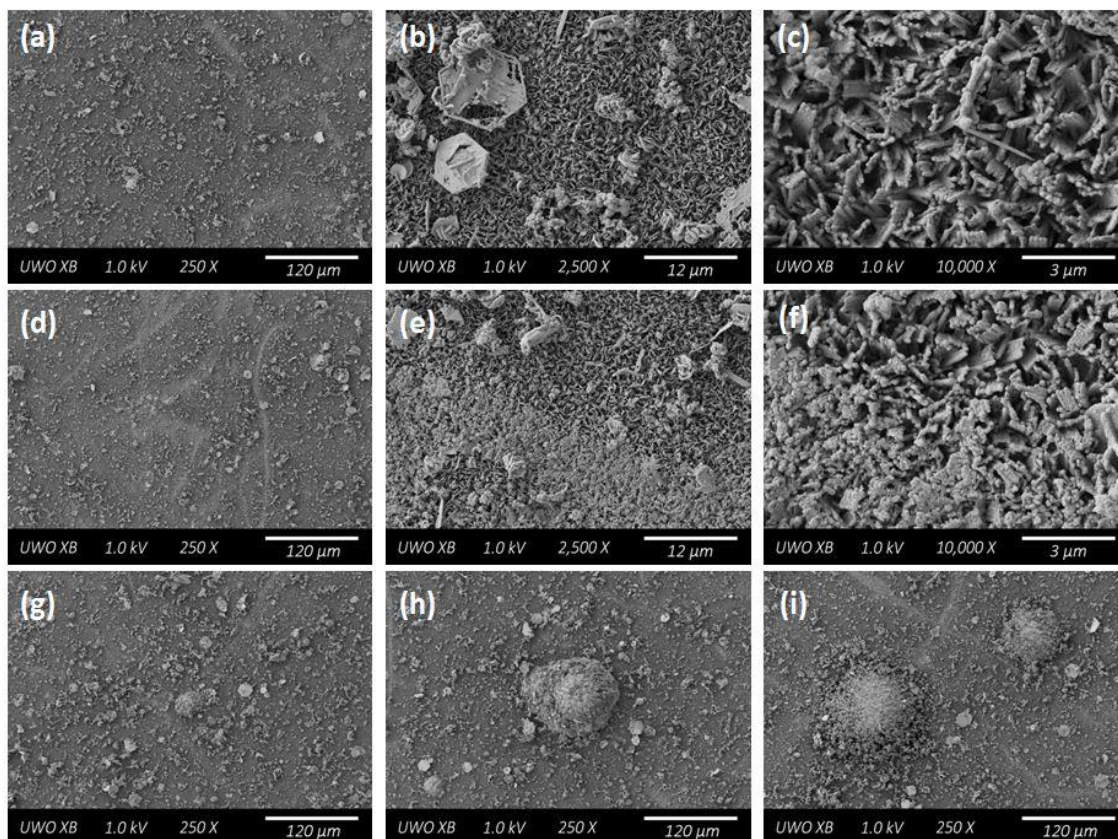


Figure A-69: SEM micrographs recorded on a specimen surface after 546 days of exposure to solution (iii) showing: (a-f) the general surface morphology, consistent with $\text{Fe}_2(\text{OH})_2\text{CO}_3$; (g-i) the size distribution of localized corrosion product deposits.

A.5. SOLUTION (IV): SIMULATED GROUNDWATER SOLUTION

A.5.1. Raman Spectroscopy

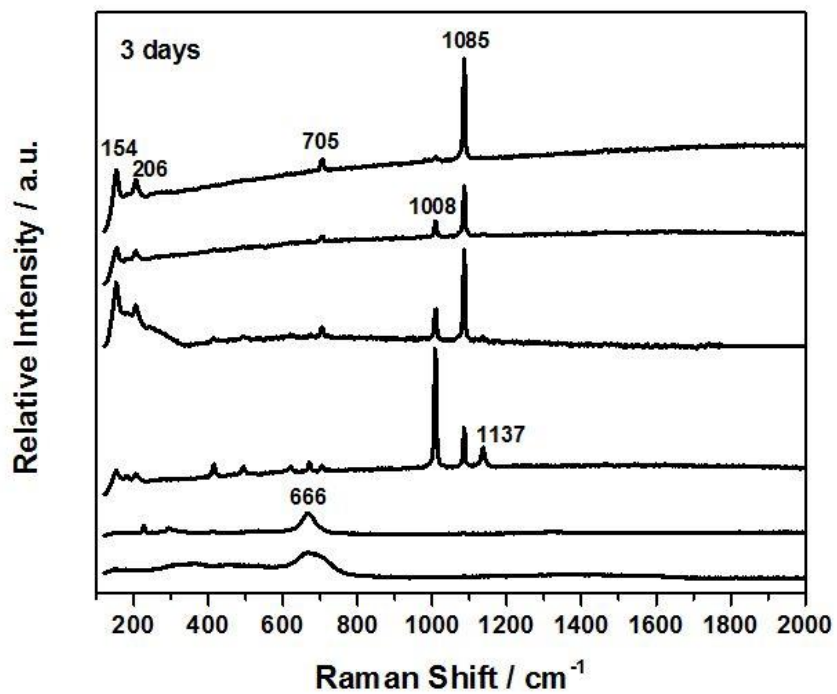


Figure A-70: Raman spectra recorded at various locations on a steel specimen after 3 days of exposure to solution (iv).

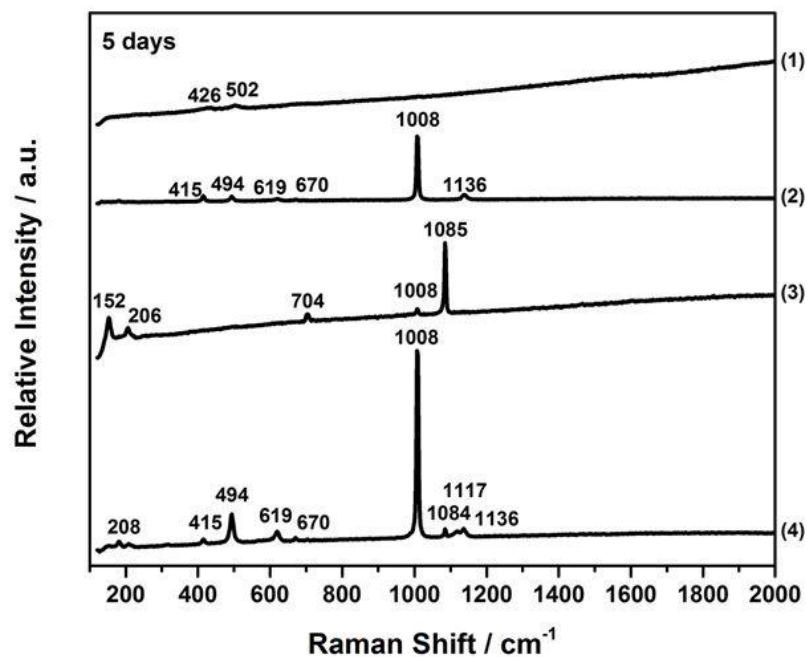


Figure A-71: Raman spectra recorded at various locations on a steel specimen after 5 days of exposure to solution (iv).

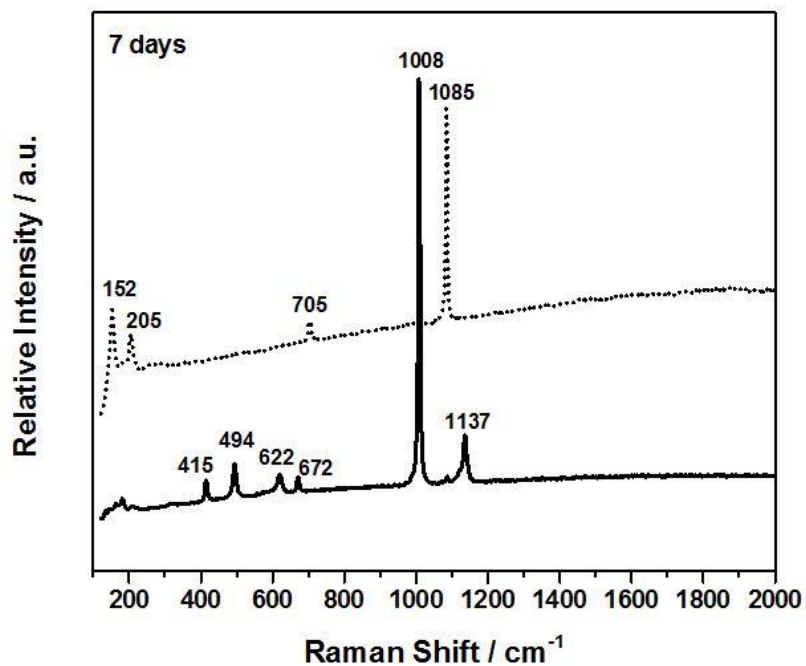


Figure A-72: Raman spectra recorded at various locations on a steel specimen after 7 days of exposure to solution (iv).

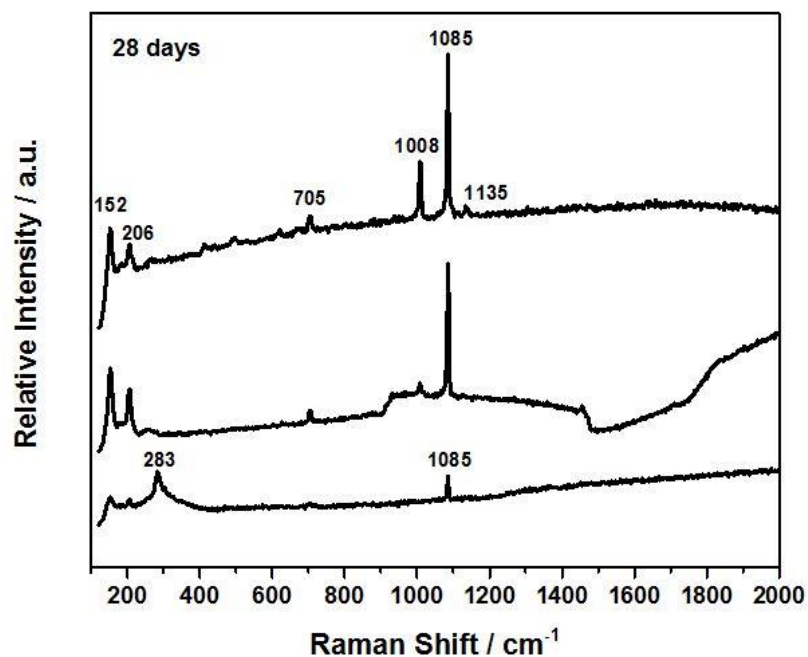


Figure A-73: Raman spectra recorded at various locations on a steel specimen after 28 days of exposure to solution (iv).

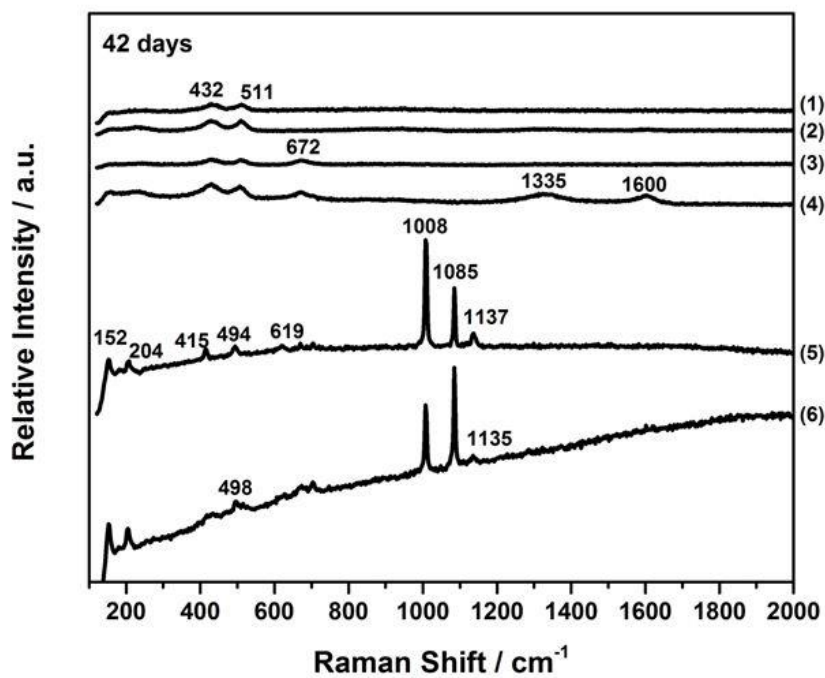


Figure A-74: Raman spectra recorded at various locations on a steel specimen after 42 days of exposure to solution (iv).

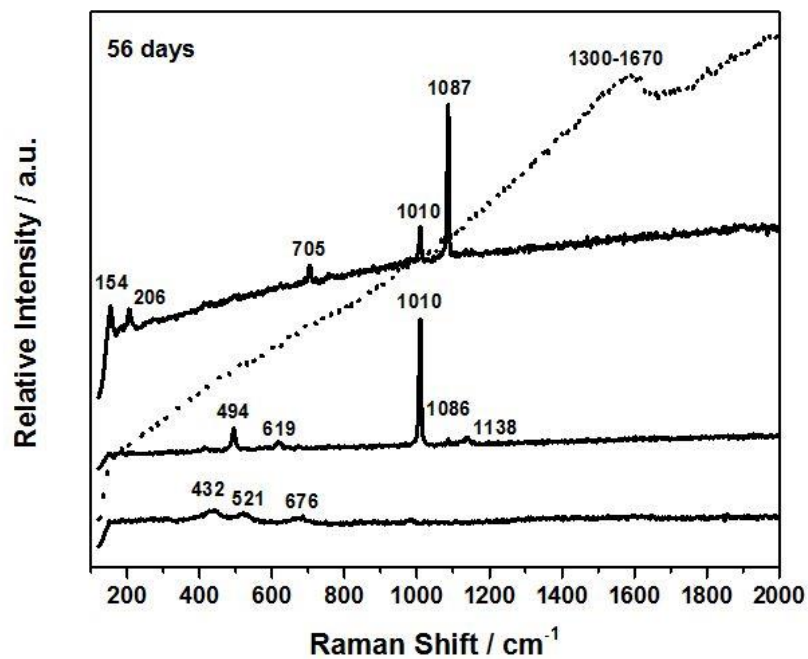


Figure A-75: Raman spectra recorded at various locations on a steel specimen after 56 days of exposure to solution (iv).

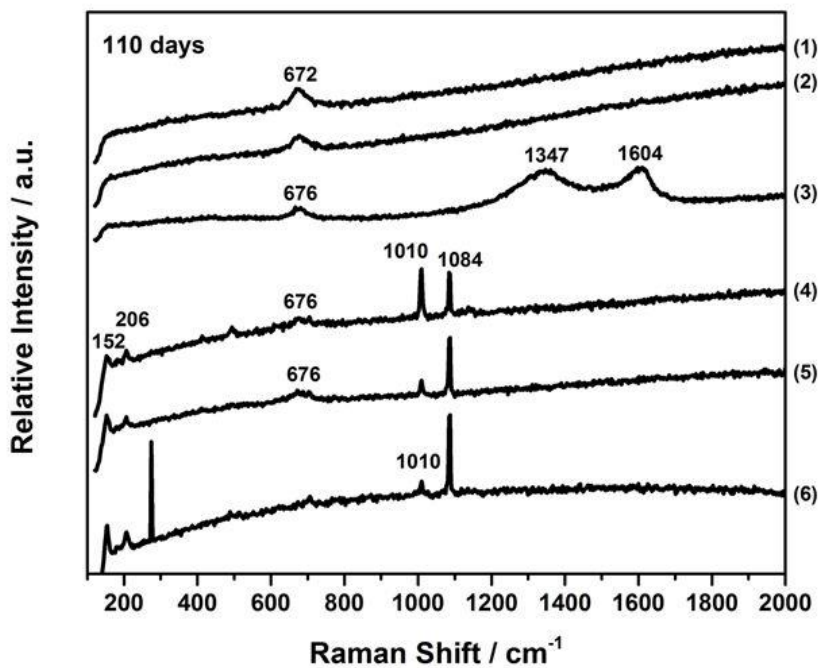


Figure A-76: Raman spectra recorded at various locations on a steel specimen after 110 days of exposure to solution (iv).

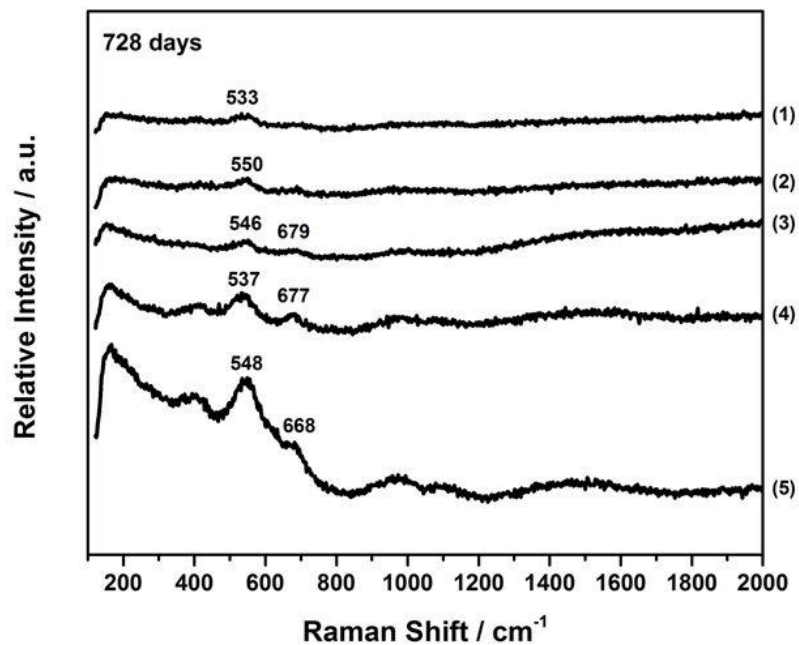


Figure A-77: Raman spectra recorded at various locations on a steel specimen after 728 days of exposure to solution (iv).

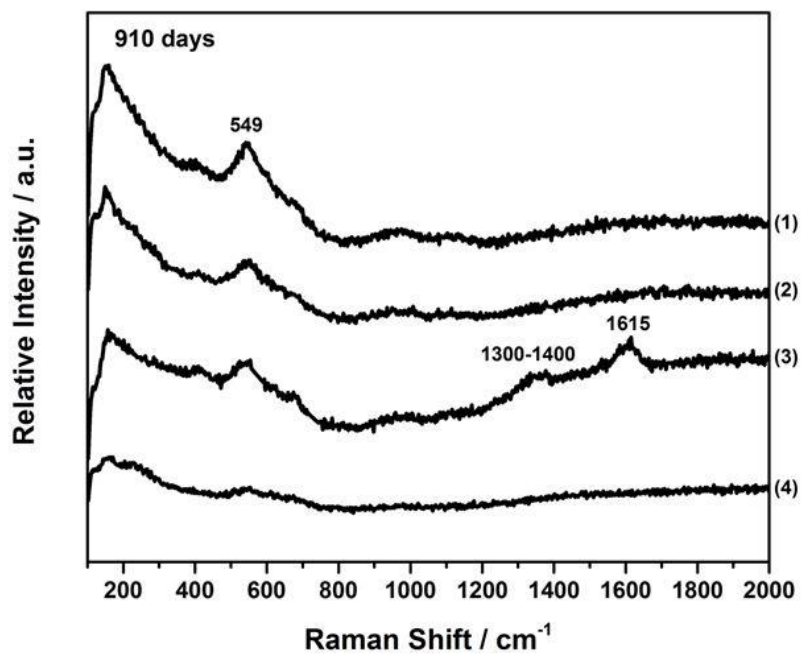


Figure A-78: Raman spectra recorded at various locations on a steel specimen after 910 days of exposure to solution (iv).

A.5.2. Scanning Electron Microscopy

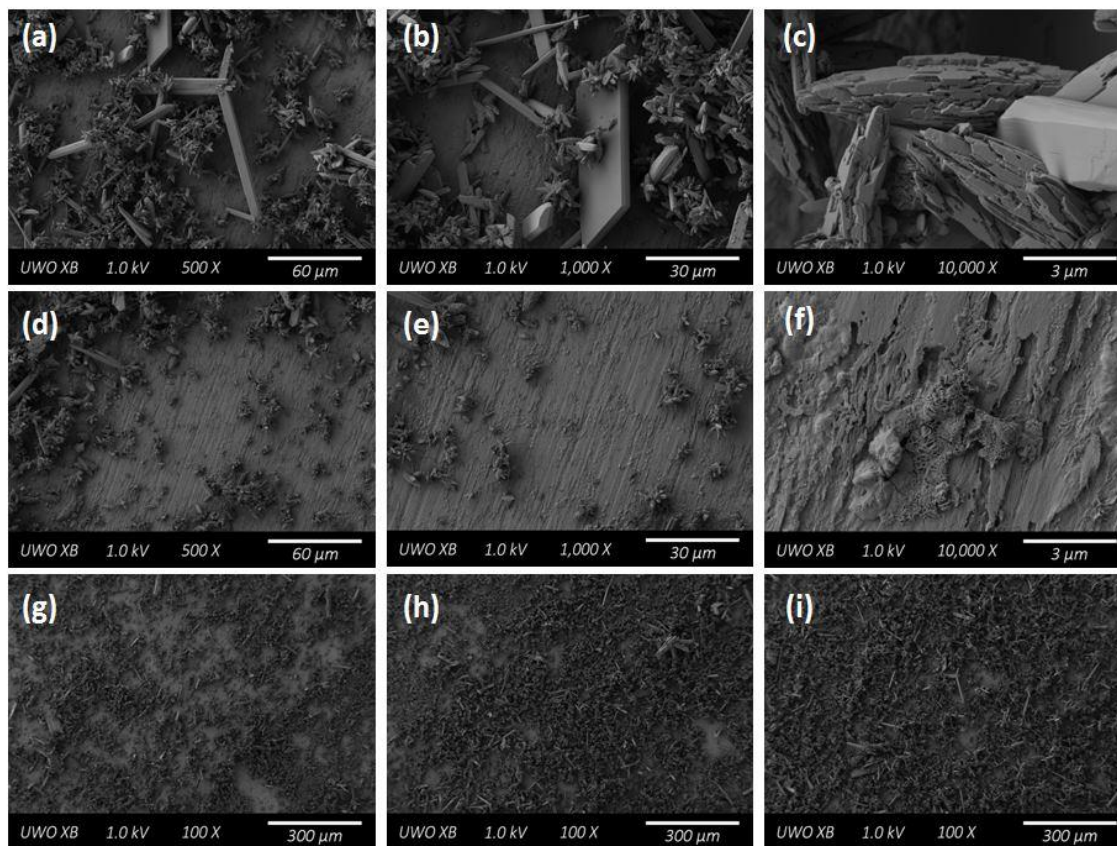


Figure A-79: SEM micrographs recorded on a specimen surface after 2 days of exposure to solution (iv) showing: (a-c) the morphology of crystal deposits; (d-f) the general surface morphology beneath the crystals; (g-i) three locations showing the distribution of crystal coverage.

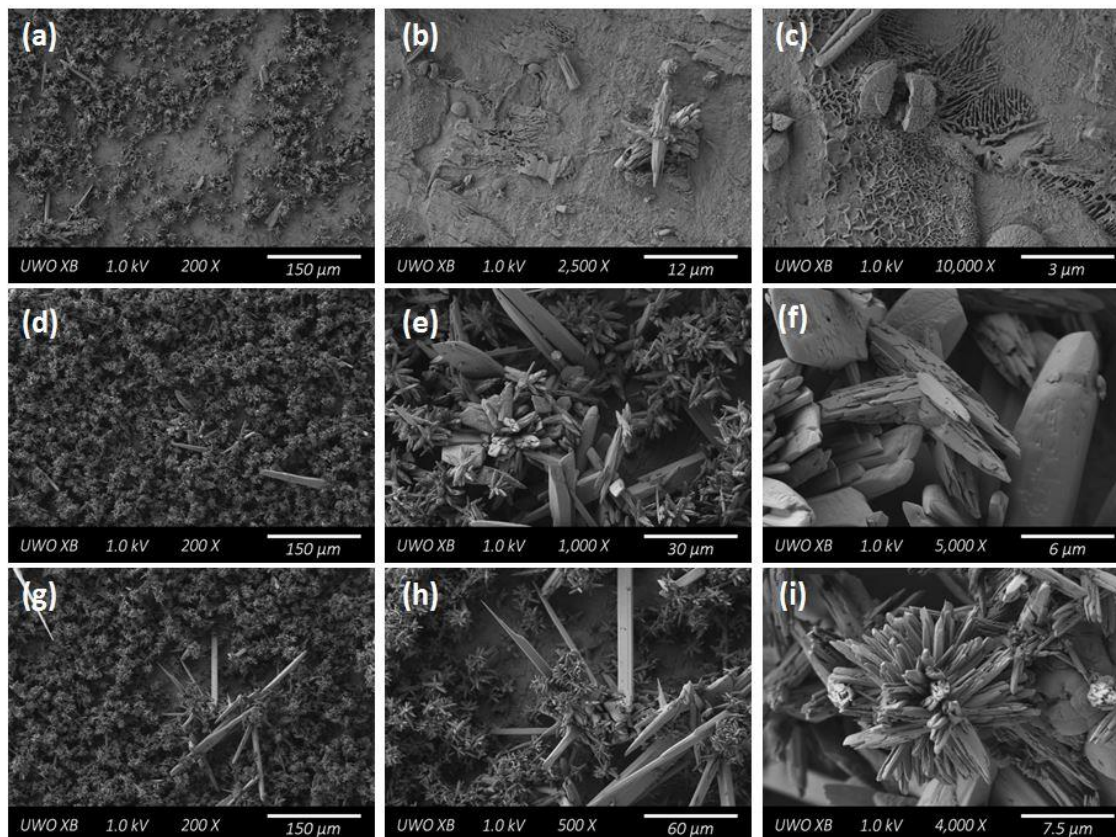


Figure A-80: SEM micrographs recorded on a specimen surface after 7 days of exposure to solution (iv) showing: (a-b) a region where the underlying surface remains visible; (c) the preferential dissolution of α -Fe from the pearlite grains; (d-f) a region of significant crystal coverage; (g-i) a secondary location of crystal coverage and the morphology of the formed crystals.

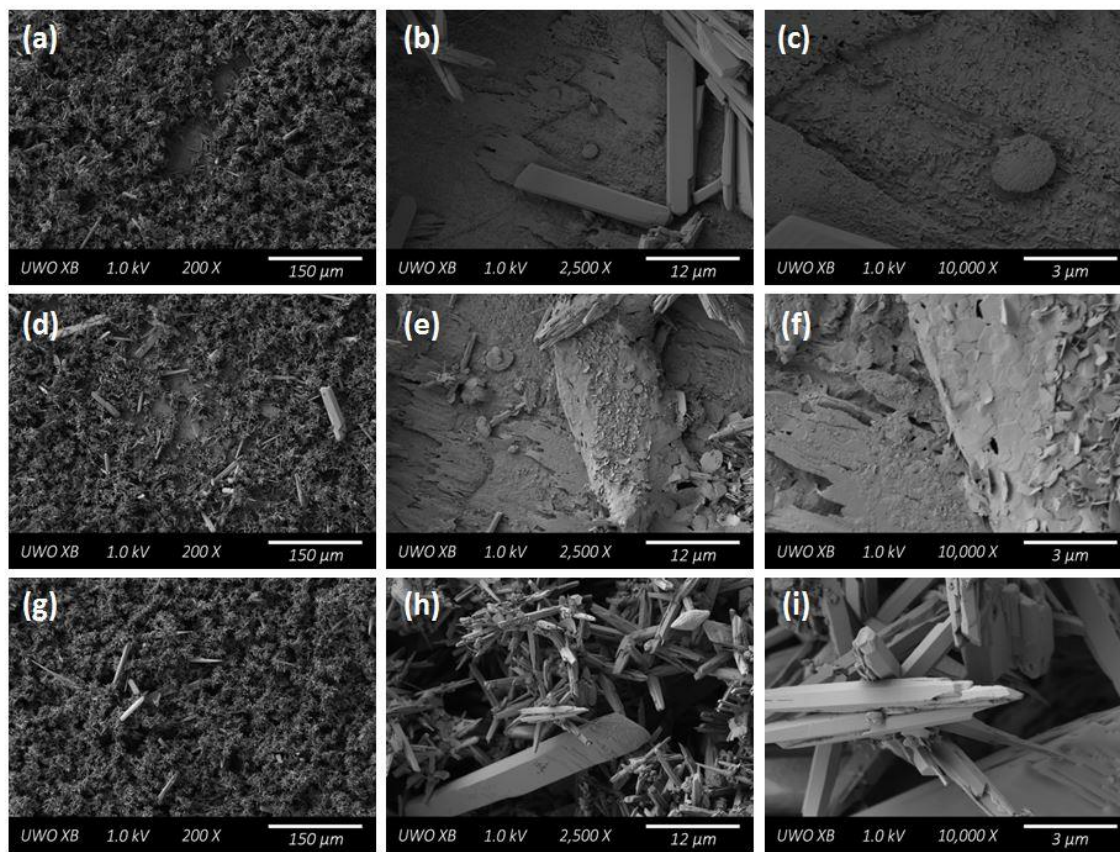


Figure A-81: SEM micrographs recorded on a specimen surface after 14 days of exposure to solution (iv) showing: (a-f) regions in which the underlying surface morphology remains visible; (g-i) a region of significant crystal coverage.

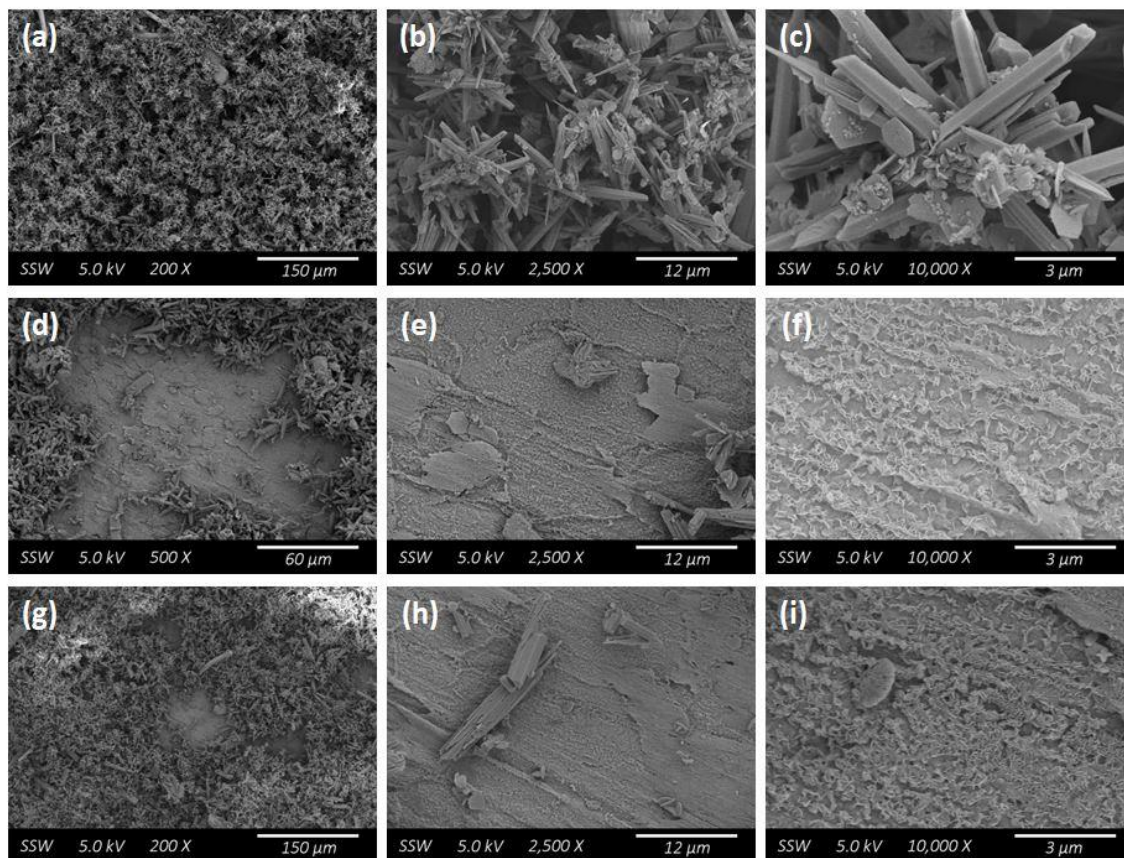


Figure A-82: SEM micrographs recorded on a specimen surface after 28 days of exposure to solution (iv) showing: (a-c) a region of significant crystal coverage; (d-i) two regions where the underlying surface morphology is visible.

Curriculum Vitae

Shannon Lee Wright Hill
Department of Chemistry, University of Western Ontario

EDUCATION

PhD Sept. 2011 – June 2016

Physical and Analytical Chemistry

University of Western Ontario (Western), London, ON

Thesis Title: The Corrosion of Carbon Steel under Deep Geologic Nuclear Waste Disposal Conditions

Supervisor: David W. Shoesmith

Honours BSc Sept. 2006 – April 2011

Comprehensive Chemistry

University of Ontario Institute of Technology (UOIT), Oshawa, ON

CONFERENCE PROCEEDINGS

S.L.W. Hill, N. Liu, Z. Qin, D. Zagidulin, D.W. Shoesmith "Interactions between carbon steel and UO₂ corrosion fronts inside a failed nuclear waste container" *17th International Conference on Environmental Degradation of Materials in Nuclear Power Systems – Water Reactors*, Ottawa, ON, Aug 9-12, 2015.

CONFERENCE PRESENTATIONS

1. **S.L.W. Hill**, M.J. Walzak, D. Zagidulin, D.W. Shoesmith "The Corrosion Evolution on Carbon Steel under Deep Geological Disposal Conditions for Spent Nuclear Fuel Waste: A 12 Month Surface Analysis Study" *The University Network of Excellence in Nuclear Engineering (UNENE) R&D Workshop*, Toronto, ON, December 15-16, 2015. **[Winner: 1st Place Poster]**
2. **S.L.W. Hill**, M.J. Walzak, D. Zagidulin, D.W. Shoesmith "The Corrosion Evolution on Carbon Steel under Deep Geological Disposal Conditions for Spent Nuclear Fuel Waste: A 12 Month Surface Analysis Study" *NACE Northern Area Eastern Conference*, Ottawa, ON, October 18-21, 2015. (Poster)
3. **S.L.W. Hill**, N. Liu, Z. Qin, D. Zagidulin, D.W. Shoesmith "Interactions between carbon steel and UO₂ corrosion fronts inside a failed nuclear waste container" *17th International Conference on Environmental Degradation of Materials in Nuclear Power Systems – Water Reactors*, Ottawa, ON, Aug 9-12, 2015. (Oral Presentation)
4. **S.L.W. Hill**, D. Zagidulin, D.W. Shoesmith "The evolution of corrosion on carbon steel under deep geologic nuclear waste disposal conditions" *CAMBR Distinguished Lecture and Research Day*, London, ON, April 17, 2015. (Poster)
5. **S.L.W. Hill**, D. Zagidulin, D.W. Shoesmith "The evolution of corrosion on carbon steel under deep geologic nuclear waste disposal conditions" *CORROSION 2015 Conference and Expo*, Dallas, TX, Mar 15-19, 2015. (Poster)

6. **S.L.W. Hill**, D.W. Shoesmith “The evolution of corrosion morphology and composition on carbon steel in a deep geological repository for spent nuclear fuel waste” *NACE Student Symposium 2014*, Hamilton, ON, Dec 12, 2014. (Oral Presentation)
7. **S.L.W. Hill**, J. Chen, D. Zagidulin, D.W. Shoesmith “Electrochemistry and corrosion of carbon steel in concentrated chloride solutions and simulated groundwaters” *Gordon Research Conferences – Aqueous Corrosion*, New London, NH, Jul 12-18, 2014. (Poster)
8. **S.L.W. Hill**, J. Chen, D. Zagidulin, D.W. Shoesmith “The corrosion of carbon steel in simulated groundwaters and concentrated chloride solutions” *CORROSION 2014 Conference and Expo*, San Antonio, TX, Mar 9-13, 2014. (Poster)
9. **S.L.W. Hill**, D.W. Shoesmith “Corrosion of Gr70 A516 carbon steel in high chloride environments under nuclear waste disposal conditions” *Surface Canada 2013*, London, ON, May 7-10, 2013. (Poster)
10. **S.L.W. Hill**, D.W. Shoesmith “Corrosion of carbon steel vessels inside a failed nuclear waste container” *CAMBR Distinguished Lecture and Research Day*, London, ON, Nov 13, 2012. (Poster)
11. **S.L.W. Hill**, D.W. Shoesmith “Corrosion of carbon steel vessels in failed nuclear waste containers for suppression of radionuclide release” *NACE Northern Area Eastern Conference*, Toronto, ON, Oct 28-31, 2012. [**Winner: 1st Place Poster**]

EDUCATIONAL PUBLICATIONS

Shannon Hill, Taylor Martino, Thomas Sutherland, Keith Griffiths. *Chemistry 3372 – Instrumental Analytical Chemistry Laboratory Manual*; Department of Chemistry, University of Western Ontario, London, ON, 2015.

Shannon Hill, Taylor Martino, Thomas Sutherland, Rob Harbottle, Keith Griffiths. *Chemistry 3372 – Instrumental Analytical Chemistry Laboratory Manual 2016*; Department of Chemistry, University of Western Ontario, London, ON, 2016.

AWARDS

1. UNENE first place student poster award (2015)
2. Graduate student teaching award (2015)
3. NACE Northern Area Eastern conference first place student poster award (2012)

SCIENTIFIC EXPERIENCE

Assistant Chemistry Technician 2007-2011
Faculty of Science, University of Ontario Institute of Technology, Oshawa, ON